transactions of the ASME

journal of heat transfer

Published Quarterly by
The American Society of
Mechanical Engineers
Volume 100 • Number 2
MAY 1978

EDITORIAL STAFF
Editor, **J. J. JAKLITSCH, JR.**
Production Editor,
ALLEN MORRISON
Editorial Prod. Asst.,
KIRSTEN DAHL

HEAT TRANSFER DIVISION
Chairman, **E. FRIED**
Secretary, **A. S. RATHBUN**
Senior Technical Editor, **E. M. SPARROW**
Technical Editor, **W. AUNG**
Technical Editor, **B. T. CHAO**
Technical Editor, **D. K. EDWARDS**
Technical Editor, **R. EICHHORN**
Technical Editor, **P. GRIFFITH**
Technical Editor, **J. S. LEE**
Technical Editor, **R. SIEGEL**

POLICY BOARD, COMMUNICATIONS
Chairman and Vice-President
I. BERMAN

Members-at-Large
R. C. DEAN, JR.
G. P. ESCHENBRENNER
M. J. RABINS
W. J. WARREN

Policy Board Representatives
Basic Engineering, **J. E. FOWLER**
General Engineering, **S. P. ROGACKI**
Industry, **J. E. ORTLOFF**
Power, **A. F. DUZY**
Research, **G. P. COOPER**
Codes and Stds., **P. M. BRISTER**
Computer Technology Com.,
A. A. SEIREG
Nom. Com. Rep.,
A. R. CATHERON

Business Staff
345 E. 47th St.
New York, N. Y. 10017
(212) 644-7789
Mng. Dir., Publ., **C. O. SANDERSON**

OFFICERS OF THE ASME
President, **S. P. KEZIOS**
Exec. Dir. & Sec'y, **ROGERS B. FINCH**
Treasurer, **ROBERT A. BENNETT**

EDITED and PUBLISHED quarterly at the offices of The American Society of Mechanical Engineers, United Engineering Center, 345 E. 47th St., New York, N. Y. 10017. Cable address, "Mechaneer," New York. Second-class postage paid at New York, N. Y., and at additional mailing offices.

CHANGES OF ADDRESS must be received at Society headquarters seven weeks before they are to be effective. Please send old label and new address.

PRICES: To members, $25.00, annually; to nonmembers, $50.00. Single copies, $15.00 each. Add $1.50 for postage to countries outside the United States and Canada.

STATEMENT from By-Laws. The Society shall not be responsible for statements or opinions advanced in papers or . . . printed in its publications (B 13, Par. 4).

COPYRIGHT © 1978 by the American Society of Mechanical Engineers. Reprints from this publication may be made on conditions that full credit be given the *TRANSACTIONS OF THE ASME, SERIES C—JOURNAL OF HEAT TRANSFER*, and the author and date of publication stated.

Downloaded 04 Feb 2011 to 194.85.80.107. Redistribution subject to ASME license or copyright; see http://www.asme.org/terms/Terms_Use.cfm

TECHNICAL NOTES

Announcements

J. A. Liburdy[1]
G. M. Faeth
Mechanical Engineering Department,
The Pensylvania State University,
University Park, Pa.

Heat Transfer and Mean Structure of a Turbulent Thermal Plume Along a Vertical Isothermal Wall

This investigation considers a two-dimensional turbulent thermal plume rising along a smooth vertical wall which is cooled to the ambient temperature. Mean velocity and temperature profiles within the plume, and the heat flux to the wall, were measured for various plume strengths and distances above the source. Integral analysis suggested an approach to local similarity, based on the local values of the thermal energy flux in the plume and the height above the source, at the limit of large Reynolds number where the local skin friction coefficient and Stanton number can be assumed to be nearly constant. The use of the local similarity hypothesis provided correlations for profiles of mean quantities, comparable to similarity correlations observed for other two-dimensional plumes. The wall plume was found to have greater velocities and temperatures than a free-line plume, in spite of direct losses to the wall. The local similarity hypothesis also provided a satisfactory correlation of wall heat transfer rates. The Nusselt number correlation is

$$Nu_x = 1.344\, Ra_x^{*0.18};\ 2 \times 10^{10} < Ra_x^* < 6 \times 10^{12}$$

for $Pr = 0.71$. *This expression is similar to correlations for turbulent natural convection with uniform heat flux, in fact, the present values are within 20 percent of the values found for natural convection with uniform heat flux for this range of* Ra_x^*.

Introduction

The turbulent thermal plume resulting from a line source of heat along a base of a vertical isothermal wall was investigated. This flow is encountered during unwanted fires, where the flame on a vertical burning surface serves as the heat source. Heat transfer to the surface from the plume over the fire, preheats the combustible material and is an important factor in understanding the mechanism of fire spread. Wall plumes are also found in other confined natural convection processes, such as the flow above baseboard heating elements.

Wall plumes are similar in many respects to free-line plumes, which have been studied by Rouse, et al. [1][2] and Lee and Emmons [2], among others, and the two flows will be compared. Grella and Faeth [3] studied the turbulent thermal wall plume along a vertical adiabatic surface, measuring mean temperature and velocity profiles. The present investigation extends the measurements to the case where the wall temperature is equal to the ambient temperature, which is representative of the early stages of wall heating by the plume.

The study was limited to the weakly buoyant region of the plume, where large property variations and radiation can be ignored. Profiles of mean velocity and temperature, as well as the heat flux to the wall, were measured for various source strengths and distances along the wall. The source was provided by an array of carbon monoxide diffusion flames, however, at the measuring positions the properties of the plume were essentially equivalent to air. Similar to the earlier plume investigations [1–3], integral analysis was undertaken in order to suggest convenient forms for data correlation. The model also provides a basis for determining plume entrainment, and estimating the effect of wall friction and heat loss on the characteristics of the flow.

Experimental Apparatus and Procedure

The apparatus was located within an interior room having plan dimensions of 4 × 6 m and a ceiling height of 4.5 m. The dimensions and arrangment of the assembly are illustrated in Fig. 1.

Test Apparatus. The test wall had a smooth front surface and was water-cooled through integral coils on its back surface (Dean Products Panal Coil, embossing pattern 301, Type S-13, ground flat). The flat, uncooled, side and floor panels helped to maintain a two-dimensional flow pattern near the centerline of the test wall. The cooling water was recirculated from a large storage tank located near the test area. Controlling the flow of cold makeup water to the storage tank, and the circulating flow itself, provided a means of maintaining the wall temperature uniform and nearly equal to the ambient temperature (within ±0.3 K). Wall temperatures were monitored with thermocouples, mounted in recesses drilled from the back side of the

---

[1] Present address: Department of Mechanical Engineering, Memphis State University, Memphis, Tenn.

[2] Numbers in brackets designate References at end of paper.

Contributed by the Heat Transfer Division for publication in the JOURNAL OF HEAT TRANSFER. Manuscript received by the Heat Transfer Division July 22, 1977.

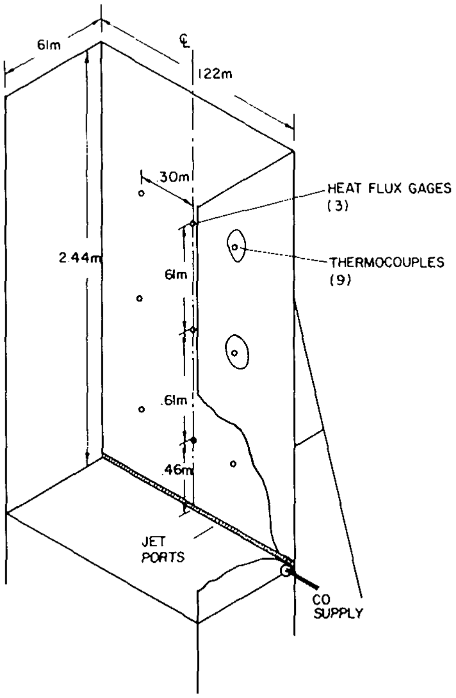

Fig. 1 Sketch of the test wall

wall, at the locations shown in Fig. 1.

The source of buoyancy was provided by an array of small carbon monoxide diffusion flames, having the same arrangement as in the earlier adiabatic wall plume study [3]. The heat source strength was varied by adjusting the flow rate of carbon monoxide. Long-term fuel flow rate stability was maintained by the use of critical flow orifices.

Instrumentation. Gas velocities were measured with a 5.08×10^{-6} m diameter tungsten hot wire sensor, having a length to diameter ratio of 200, coupled to a constant temperature anemometer [3]. The hot-wire signal was not linearized in order to obtain maximum sensitivity at low velocities. The sensors were calibrated over the complete temperature, velocity, and overheat ratio range of the experiments. The effect of temperature fluctuations on the mean velocity measurements was negligible for the overheat ratios used during the tests, since the maximum mean temperature difference was limited to 13.2 K, c.f. Table 1. This was verified by conducting tests using several different overheat ratios. Errors due to velocity fluctuations are considered in the Appendix. It is estimated that velocity fluctuations caused less than a five percent error in the mean velocity measurements for values of y/x less than 0.1. As usual, measurements near the outer edge of the flow are less accurate due to flow-reversal and high turbulence intensities. In spite of reduced accuracy, the data obtained in the outer region is presented here, in order to indicate qualitative features of the flow.

Gas temperatures were measured using a chromel-alumel thermocouple probe, constructed from 25.4×10^{-6} m diameter wires [3]. The ambient temperature was measured with a thermocouple suspended 1 m from the wall, at the height of the measuring location.

Heat flux to the wall was measured at three heights above the source (0.47, 0.94, and 1.82 m), using heat flux gages mounted flush with the front surface of the wall and centered on a coolant passage (Hy-Cal Sensible Heat Flow Transducers, BI-2 Series, 12.7 × 5.1 mm).

Experimental Accuracy. All measurements were made by integrating the signals for one minute intervals using an integrating digital voltmeter [3] in order to obtain proper averages. Measurements are reported along the centerline of the wall, there was less than a one percent temperature variation and a ten percent velocity variation, for distances up to 0.14 m on either side of the centerline. The repeatability of the profile measurements was within 15 percent, the wall heat flux measurement were reproducible within three percent. The effect of reduced measurement accuracy at the outer edge of the flow, introduced an error less than the repeatability level in the integrated quantities used to reduce the data, Q_x, etc., since mean values are relatively low in this region.

Analysis

The objective of the analysis was to provide a simple basis for correlating the data and interpreting the results. Therefore, detailed numerical calculations with a turbulence model were not attempted; the approach taken was an integral analysis, similar to earlier plume studies [1-3]. The weakly buoyant region was considered where property variations, under the Boussinesq approximation, and radiation, can be ignored. The experimental results were obtained no less than 0.47 m above a small, nonsooting fire source, where the maximum temperature was no more than 13.2 K higher than the ambient temperature. These conditions are properly representative of the weakly buoyant region of a plume. The flow was assumed to be two-dimensional and steady, with the wall and ambient temperatures taken to be equal and constant.

Integral Analysis. Employing the previous assumptions, the integral equations of conservation of mass, momentum, and energy become:

Nomenclature

C_f = skin friction coefficient, equation (7)
C_p = specific heat at constant pressure
C_x = buoyancy flux, equation (5)
E = entrainment, equation (1)
E_0 = entrainment coefficient, equation (7)
F = dimensionless velocity, equation (6)
Fr = Froude number, equation (15)
G = dimensionless temperature defect, equation (6)
$\mathrm{Gr}_x{}^*$ = modified Grashoff number, $g\beta x^3 Q_x / k\nu^2$
g = acceleration of gravity
H = dimensionless shear stress, equation (6)
h = heat transfer coefficient, $q_w/\Delta T_m$
I_i = profile integrals, equation (12)
k = thermal conductivity
k^* = parameter, equations (19) and (21)
$\dot{m}$ = fuel flow rate to source
Nu_x = Nusselt number, hx/k
Pr = Prandtl number, $C_p\mu/k$
Q_x = thermal energy flux in plume, equation (5)
q_w = heat flux to wall
$\mathrm{Ra}_x{}^*$ = modified Rayleigh number, $\mathrm{Gr}_x{}^* \cdot \mathrm{Pr}$
Re_x = Reynolds number, $\rho u_m x/\mu$
St = Stanton number, $h/\rho C_p u_m = q_w/\rho C_p u_m \Delta T_m$
T = temperature
u = mean velocity parallel to wall
v = mean velocity normal to wall
x = distance along wall from source
y = distance normal to wall
α_1, α_2 = entrainment parameters, equation (14)
β = coefficient of volumetric expansion
ΔT = temperature defect, $T - T_\infty$
η = dimensionless distance, y/x
μ = viscosity
ν = kinematic viscosity
ρ = density
σ = characteristic plume width
τ = shear stress

Subscripts

m = maximum value
w = at the wall
0 = initial condition
∞ = ambient condition

Table 1 Summary of test conditions and flow parameters

Test	x (m)	$\dot{m} \times 10^3$ (kg/ms)	Q_x (W/m)	u_m (m/s)	ΔT_m (K)	q_w (W/m^2)	$\left(\frac{\rho C_p u_m{}^3}{g\beta Q_x}\right)^{1/3}$	$\frac{g\beta x \Delta T_m}{(g\beta Q_x/\rho C_p)^{2/3}}$	Fr	k*	Re$_x$
1	0.47	6.20	59.8	.349	5.29	29.3	2.91	5.55	4.97	16.2	9700
2	0.47	9.43	156.4	.463	9.74	62.6	2.80	5.38	4.69	15.1	12900
3	0.47	12.40	283.8	.575	13.20	99.7	2.86	4.91	4.82	14.0	16000
4	0.94	9.43	116.2	.429	3.91	19.7	2.87	5.27	4.86	15.1	23900
5	0.94	12.40	239.2	.520	6.38	34.2	2.73	5.31	4.52	14.5	28900
6	0.94	15.50	325.1	.516	8.54	41.1	2.45	5.80	3.83	14.2	28700
7	1.82	12.40	160.4	.490	2.58	9.9	2.94	5.43	5.05	16.0	52800
8	1.82	15.50	305.7	.594	3.90	15.0	2.88	5.34	4.88	15.4	64000
				Averages							
				Isothermal wall plume			2.81	5.37	4.70	15.1	
				standard deviations			0.16	0.25	0.39	0.8	
				Adiabatic wall plume [3]			3.09	7.91	5.42	24.4	
				standard deviations			0.07	0.25	0.20	1.4	
				Free-line plume [1]			2.27	4.12	3.42	9.36	

Ambient conditions: 306K, 97.3 kN/m^2
Properties: $\rho = 1.11$ kg/m^3, g = 9.801 m/s^2, $C_p = 1.004\ kJ/kgK$, $\nu = 16.9 \times 10^{-6}$ m^2/s, Pr = 0.71

$$\frac{d}{dx}\int_0^\infty u dy = -v_\infty = E \tag{1}$$

$$\frac{d}{dx}\int_0^\infty \rho u^2 dy = \int_0^\infty g\rho\beta\Delta T dy - \tau_w \tag{2}$$

$$\frac{d}{dx}\int_0^\infty \rho u C_p \Delta T dy = -q_w \tag{3}$$

where E is the rate at which the plume entrains the ambient fluid. Morton, et al. [4] have proposed a relationship between plume velocities and entrainment. In the present study, however, an approach discussed by Fox [5] and Narain and Uberoi [6] was utilized in order to provide further information on the entrainment process of a wall plume. This involves consideration of the integral equation for the moment of momentum, which can be written as follows:

$$\frac{d}{dx}\int_0^\infty \rho u^3 dy = \int_0^\infty 2g\rho u\beta\Delta T dy - \int_0^\infty 2\tau\frac{\partial u}{\partial y}dy \tag{4}$$

The basic equations are completed by defining the plume thermal energy flux, Q_x, and buoyancy flux, C_x, as follows:

$$Q_x = C_p C_x/g\beta = \int_0^\infty \rho u C_p \Delta T dy \tag{5}$$

The assumption of dynamical similarity of mean quantities at large distances from the source is widely accepted for free turbulent jets and plumes. Dynamical similarity is less justified for wall jets and plumes, since the wall layer and outer boundary of the flow have slightly different growth rates [7–9]. The effect is not large, however, and since the assumption of dynamical similarity was useful during the adiabatic wall plume investigation [3], it was retained for the present study.

Taking $\sigma(x)$ to represent a characteristic width of the flow, the similarity variable $\eta = y/\sigma(x)$, and the following profile functions are defined

$$u/u_m = F(\eta),\ \Delta T/\Delta T_m = G(\eta),\ 2\tau/\rho u_m{}^2 = H(\eta) \tag{6}$$

assuming dynamical similarity of all mean quantities and the fluid stress. Also define an entrainment coefficient [4], a local skin friction coefficient, and a local Stanton number

$$E_0 = E/u_m,\ C_f = 2\tau_w/\rho u_m{}^2,\ \mathrm{St} = q_w/\rho C_p u_m \Delta T_m \tag{7}$$

all based on the maximum velocity and temperature defect within the plume.

Introducing equations (6) and (7) into equations (1)–(4) yields

$$\frac{d}{dx}(\sigma u_m I_1) = E_0 u_m \tag{8}$$

$$\frac{d}{dx}(\sigma u_m{}^2 I_2) = g\beta\sigma\Delta T_m I_4 - C_f u_m{}^2/2 \tag{9}$$

$$\frac{d}{dx}(\sigma u_m \Delta T_m I_5) = -\mathrm{St} u_m \Delta T_m \tag{10}$$

$$\frac{d}{dx}(\sigma u_m{}^3 I_3) = 2g\beta\sigma u_m \Delta T_m I_5 - u_m{}^3 I_6 \tag{11}$$

where the I_i are integrals of the profile functions

$$I_1 = \int_0^\infty F d\eta \quad I_4 = \int_0^\infty G d\eta$$
$$I_2 = \int_0^\infty F^2 d\eta \quad I_5 = \int_0^\infty FG d\eta \tag{12}$$
$$I_3 = \int_0^\infty F^3 d\eta \quad I_6 = \int_0^\infty F'H d\eta$$

For dynamical similarity, each of these integrals is a constant. Equations (8)–(12) reduce to the adiabatic wall plume case when St = 0, implying no heat loss to the wall and to the free-line plume case when both C_f = St = 0, implying no heat loss or wall friction.

Following [5] and [6] equations (8)–(11) can be manipulated to provide an expression for the entrainment coefficient

$$E_0 = \alpha_1 + \alpha_2/\mathrm{Fr}^2 \tag{13}$$

where

$$\alpha_1 = I_1\left(\frac{I_6}{I_3} - \frac{C_f}{2}\right),\ \alpha_2 = 2\left(\frac{I_1}{I_5}\right)\left(\frac{I_4 - I_5}{I_2 - I_3}\right) \tag{14}$$

and Fr is the Froude number, defined as follows

$$\mathrm{Fr}^2 = \rho C_p u_m{}^3/g\beta Q_x \tag{15}$$

Equations (13)–(15) indicate that the entrainment coefficient is not strictly constant, to the extent that Fr and C_f vary. For arbitrary initial conditions, the Froude number varies near the source, which modifies the value of the entrainment coefficient, however, far from the source, the Froude number approaches an asymptotic value for free-line plumes [2] and E_0 is nearly constant. Similarly, at large Reynolds numbers C_f is constant for rough walls, and a slowly varying function of Reynolds number for smooth walls, leading to a nearly constant E_0 for the adiabatic wall plume [3]. Through the Colburn analogy, St would also be nearly constant, under these conditions, for the isothermal wall plume.

Results at Large Reynolds Numbers. At the large Reynolds number limit, where C_f, St and E_0 can be taken to be constant, equations (8)–(10) yield a simple closed form solution. Only one initial condition is required, which is obtained by specifying the plume thermal energy flux as

$$Q_x = Q_{x0},\ x = x_0 \tag{16}$$

where x_0 is sufficiently removed from the source so that the flow corresponds to the weakly buoyant, high Reynolds number region, defined earlier. This requirement on x_0 must be met in order to obtain the subsequent variation of Q_x with x in a manner consistant with the other assumptions of the analysis (in fact, the large Reynolds number analysis leads to a singularity at $x_0 = 0$ for the isothermal wall plume, c.f., equation (22)). Therefore, unlike the free-line plume or the adiabatic wall plume, where Q_x is conserved and can be related directly to the source strength [1-3], for the isothermal wall plume, Q_{x0} depends upon poorly understood processes in the strongly-buoyant region near the source (which may also involve regions of laminar flow, or in the case of a fire-induced plume, regions of combustion) and is only indirectly related to the initial source strength. Therefore, pending the results of research on near source processes, Q_{x0} must be estimated, even when the source strength is known precisely.

The solution of equations (8)–(10) and (16) is

$$\frac{\sigma}{x} = \frac{E_0}{I_1}\left(1 + \frac{I_1\mathrm{St}}{3E_0I_5}\right) \tag{17}$$

$$u_m(\rho C_p/g\beta Q_x)^{1/3} = \mathrm{Fr}^{2/3} \tag{18}$$

$$g\beta x\,\Delta T_m(\rho C_p/g\beta Q_x)^{2/3} = k^*\mathrm{Fr}^{-2/3} \tag{19}$$

where

$$\mathrm{Fr}^2 = 6I_1I_4/(6E_0I_2I_5 - 2\mathrm{St}I_1I_2 + 3C_fI_1I_5) \tag{20}$$

$$k^* = 3I_1/(3E_0I_5 + I_1\mathrm{St}) \tag{21}$$

and

$$Q_x/Q_{x0} = (x_0/x)^{k^*\mathrm{St}} \tag{22}$$

In equations (17)–(22), any effect of a virtual origin, which should be small where these equations are appropriate, has been absorbed directly into the definition of x.

Equations (17)–(22) reduce to the forms appropriate for the adiabatic wall plume and the free-line plume by setting St = 0, or St = C_f = 0, respectively. For the free-line plume and adiabatic wall plume, Q_x is constant, implying a linear growth of the width of the plume, a constant maximum velocity, and maximum temperature defect inversely proportional to distance above the source.

For the isothermal wall plume, Q_x varies, and equations (17)–(19) imply local similarity based on the current values of Q_x and x. In this case, the plume width still grows in a linear fashion; however, the maximum velocity decreases and the maximum temperature defect decreases somewhat more rapidly than x^{-1}, due to the reduction of Q_x with height above the source. For constant values of St and C_f, equations (13), (14), (20), and (21) imply constant Froude number, k^* and E_0, the latter finding being also consistent with the assumptions of the analysis.

Heat Transfer Correlation. Since the previous results involve both skin friction coefficient and the Stanton number, the heat transfer characteristics of the flow were treated through the use of the Colburn analogy.

$$\mathrm{St}\mathrm{Pr}^{2/3} = C_f/2 \tag{23}$$

where C_f is taken to be a function of Reynolds number. In the present investigation the Reynolds number was based on the maximum velocity, and the height above the source

$$\mathrm{Re}_x = \rho u_m x/\mu \tag{24}$$

Employing equation (18), a more convenient form based on the thermal energy flux of the plume is obtained

$$\mathrm{Re}_x = \frac{\rho x}{\mu}\left(\frac{g\beta Q_x}{\rho C_p}\right)^{1/3}\mathrm{Fr}^{2/3} \tag{25}$$

Substituting equations (7) and (19) into equation (23) yields the following expression for the heat flux to the wall

$$xq_w\mathrm{Pr}^{2/3}/k^*Q_x = C_f/2 \tag{26}$$

The heat flux data was correlated in terms of equation (26), and plotted as a function of Reynolds number defined by equation (25). Alternative forms for correlating the data will be considered later.

Experimental Results and Discussion

Test Conditions. Eight test conditions were studied involving three heights above the source and four fuel flow rates to the burners, as summarized in Table 1. A virtual origin was not identified, and distances in the preceding correlations are taken as the height above the base of the wall, similar to the earlier wall plume study [3]. The thermal energy flux in the plume was determined by numerical integration of equation (5) using the property values given in Table 1. The Froude number, k^* and the Reynolds number were calculated from equations (18), (19), and (25), respectively. There is no systematic variation of Fr and k^* with Reynolds number, these parameters are nearly constant as suggested by the theory at the high Reynolds number limit.

Several of the parameters describing the flow are compared with measurements in free-line plumes [1], and adiabatic wall plumes [3] in Table 1. In the case of the free-line plume, the results were corrected so that Q_x refers to the energy flux in half the width of the plume, in order to provide a common basis for comparison. The maximum velocity and temperature parameters, Fr and k^* are seen to be relatively independent of Re_x for the present flow, similar to the results found for other two-dimensional plumes. In general, the wall plumes have higher values of u_m and ΔT_m for a given value of Q_x and x, than the free-line plume, with the highest values occurring in a adiabatic wall plume.

Mean Velocities and Temperatures. Taking $\sigma = x$, equations (6), (18), and (19) suggest the velocity and temperature defect plots shown in Fig. 2 and 3. Generally, these measurements exhibit local similarity to about the same degree that similarity was observed for the free-line plume [1] and the adiabatic wall plume [3]. Tests 2, 3, 4, and 5 were employed as test conditions for turbulence measurements in this flow, and represent the most reliable data from this investigation; these tests provide a good representation of local similarity, except near the wall. Poorer behavior is expected near the wall where the present high Reynolds number approximations, C_f, St, etc., constant, are least satisfactory. In addition, the wall layer in buoyant flows does not generally scale in quite the same manner as the outer portions of the flow [8, 9] and similarity of the complete profiles can only be obtained over a narrow region.

Comparable results for the free-line plume and the adiabatic wall plume are also shown in Figs. 2 and 3. Both wall plumes are narrower, and have greater velocities and temperatures than the free-line plume. There is considerable evidence for the presence of large scale meandering of free-line plumes [10–12]. It appears that the presence of the wall stabilizes the lateral motion and reduces the apparent spread of

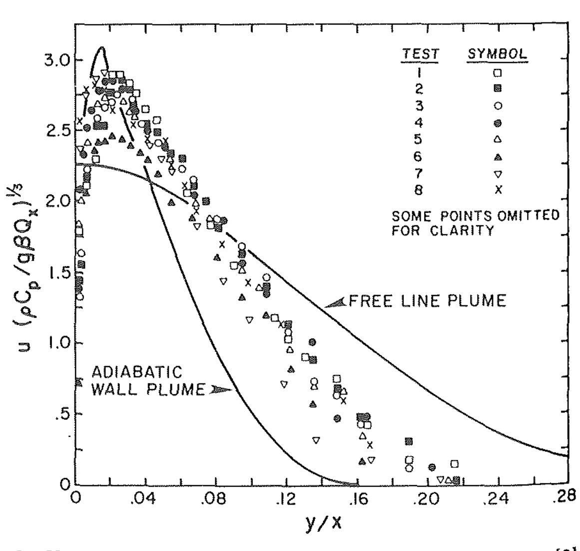

Fig. 2 Mean velocity profiles, compared with adiabatic wall plumes [3] and free-line plumes [1]

the flow. The isothermal wall plume is wider than the adiabatic wall plume due to the fact that its point of maximum buoyancy is shifted away from the wall.

Wall Heat Flux. The measurements of the heat flux to the wall are plotted according to equations (25) and (26) in Fig. 4, values for the skin friction coefficient are inferred from the Colburn analogy, equation (23). A least squares fit of this data yields

$$q_w x \mathrm{Pr}^{2/3}/k^* Q_x = 0.750 \mathrm{Re}_x^{-0.45} \tag{27}$$

for the Reynolds number range given in Table 1. From equations (23) and (26), the left-hand side of equation (27) is also equal to $\mathrm{St}\mathrm{Pr}^{2/3}$ and $C_f/2$. The standard error of the power of the Reynolds number in equation (27) is .05, with a correlation coefficient of 0.986 for the fitted line. While the experimental values of k^* and Fr were used in obtaining equation (27), the average values presented in Table 1 can also be used with little error, since these factors are nearly constant over the present test range.

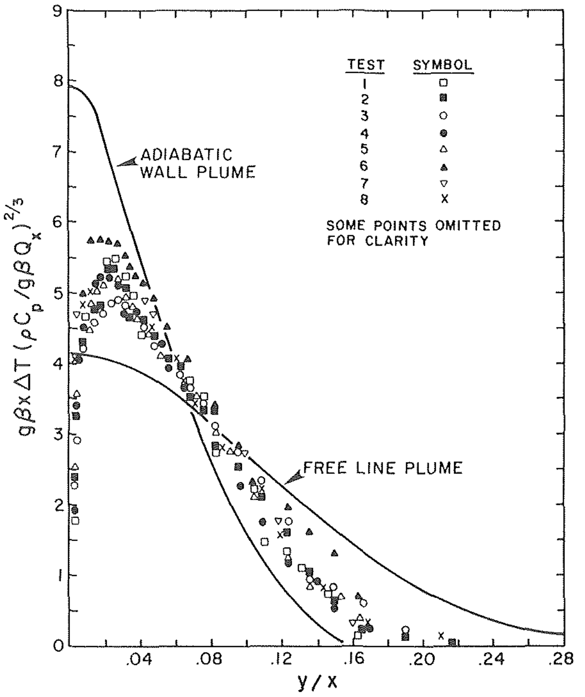

Fig. 3 Mean temperature profiles, compared with adiabatic wall plumes [3] and free-line plumes [1]

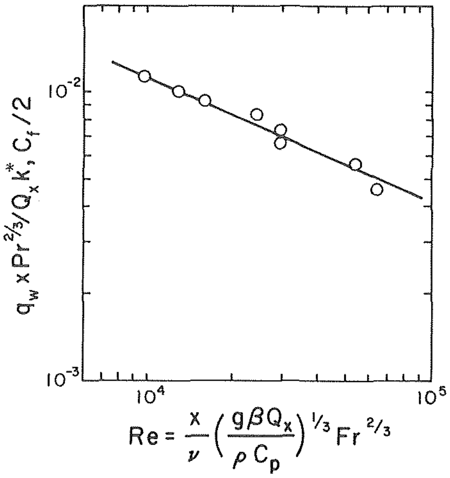

Fig. 4 Wall heat flux correlation

Equation (27) can be expressed in terms of the Nusselt number, as follows

$$\mathrm{Nu}_x = 0.750 \mathrm{Fr}^{0.37} \mathrm{Pr}^{-0.03} \mathrm{Ra}_x{}^{*0.18} \tag{28}$$

where $\mathrm{Ra}_x{}^*$ is a modified Rayleigh number based on the local thermal energy flux in the plume and the height above the source. Employing the average Froude number found from the present tests and evaluating the separate Prandtl number term (Pr given in Table 1), yields

$$\mathrm{Nu}_x = 1.344 \mathrm{Ra}_x{}^{*0.18},\ 2 \times 10^{10} < \mathrm{Ra}_x{}^* < 6 \times 10^{12} \tag{29}$$

The present measurements can be directly compared with natural convection studies, if it is noted that for natural convection with constant heat flux the local thermal energy flux in the flow is given by $Q_x = xq_w$. Therefore, the modified Rayleigh number adopted by Vliet and co-workers [9, 13 and 14], for natural convection with uniform heat flux, has the same meaning as $\mathrm{Ra}_x{}^*$ for the isothermal wall plume. Vliet [13] presents a correlation for turbulent natural convection in water, on vertical or inclined (unstable) constant heat flux surfaces as

$$\mathrm{Nu}_x = 0.302 \mathrm{Ra}_x{}^{*0.24} \tag{30}$$

which extends into the present $\mathrm{Ra}_x{}^*$ range for inclined surfaces. Later measurements by Vliet and Ross [14], in air, give results which are 15–30 percent lower than equation (30) for unstable and vertical wall configurations. At $\mathrm{Ra}_x{}^* = 10^{10}$, equation (29) gives a Nusselt number approximately ten percent higher than equation (30); at $\mathrm{Ra}_x{}^* = 10^{12}$, equation (29) is approximately 20 percent lower than equation (30). While it might be expected that the Nusselt numbers for these two processes should be similar, agreement to this degree is probably the result of a fortuitous range of $\mathrm{Ra}_x{}^*$, certainly the distribution of Q_x within the boundary layer for the two flows is quite different.

For natural convection with uniform heat flux on vertical surfaces, Vliet [9] observed transition for $3 \times 10^{12} < \mathrm{Ra}_x{}^* < 4 \times 10^{13}$, by observation of variation in the heat transfer coefficient as the wall; transition occurred at lower values of $\mathrm{Ra}_x{}^*$ for inclined surfaces (unstable). The point of transition was not determined during the present study, however, the hot-wire measurements indicated that the flow was turbulent at the lowest value of $\mathrm{Ra}_x{}^*$ tested ($\mathrm{Ra}_x{}^* = 2 \times 10^{10}$).

Variation of Plume Thermal Energy Flux. The local plume thermal energy flux plays an important role in the processes of the isothermal wall plume, since it controls the magnitude of temperatures and velocities within the plume, as well as the heat flux to the wall. Equation (22) provides one expression for the variation of Q_x with distance, if appropriate constant values can be chosen for k^* and St.

Fig. 4 indicates that the Stanton number varies significantly over the present test range. If the assumption of local similarity is maintained, as expressed by equations (17)–(19), an improved expression over the present test range can be obtained by integrating equation (3) directly, using data correlation of equation (27) for q_w and taking k^* and Fr to be constants. This yields the following expression for Q_x.

$$Q_x/Q_{x_0} = [1 - 0.250 k^* \mathrm{Fr}^{-0.30} \mathrm{Pr}^{-0.37} \mathrm{Ra}_{x_0}{}^{-0.15} [1 - (x_0/x)^{0.45}]]^{6.67} \tag{31}$$

Using the average values of k^* and Fr from Table 1, equation (31) becomes

$$Q_x/Q_{x_0} = [1 - 2.36 \mathrm{Pr}^{-0.37} \mathrm{Ra}_{x_0}{}^{-0.15} [1 - (x_0/x)^{0.45}]]^{6.67} \tag{32}$$

Equations (22) and (32) were compared with the present data, using measurements at several wall heights for a given source strength. Initial conditions were determined by the lowest position and the upper position were used to examine the accuracy of the equations. The results are summarized in Table 2. Both predictions are within experimental uncertainties; the more complete form given by equation (32) provides only a slight improvement over equation (22).

While equation (32) gives slightly better results than equation (22) over the present test range, it has less desirable asymptotic properties at large distances from the source, since

$$Q_{x\to\infty}/Q_{x_0} = [1 - 2.36\mathrm{Pr}^{-0.37}\mathrm{Ra}_{x_0}{}^{-0.15}]^{6.67} \qquad (33)$$

which provides a positive thermal energy flux in the plume at $x \to \infty$, rather than the expected value $Q_{x\to\infty} = 0$, which is given by equation (22). This behavior is due to the rapid decline of St with increasing Re_x, which was observed for the relatively low values of Re_x considered during the present experiments. By analogy with forced convection flows, this rate of decline should decrease at higher Reynolds numbers, eventually approaching a constant Stanton number limit for finite wall roughness. This behavior is represented more properly by equation (22) and equation (32) should be used with caution outside the present test range.

Integral Constants and the Entrainment Coefficient. The integrals defined in equation (12), and several other parameters characteristic of the flow are summarized in Table 3, along with their standard deviations for the eight tests. The table also includes results for the adiabatic wall plume and the free-line plume, although standard deviations are not available for the latter flow.

The value of I_1 depends upon the arbitrary selection of the characteristic width of the flow, the choice $\sigma = x$ has been made in Table 3, which implies that σ is approximately 6–15 displacement thicknesses, depending upon the flow.

The quantities $I_1 - I_5$ were determined by numerical integration of the data for the wall plumes, and calculated by integrating the Gaussian correlations of the temperature and velocity profiles provided for the free-line plume [1]. The ratios I_2/I_1, etc., for the wall plumes are similar to the free-line plume values, in spite of the fact that the wall plume profiles are not Gaussian near the wall, with the values for the isothermal wall plume falling between those of the other two flows. In all cases, I_4/I_1 is less than unity, indicating slower growth for the temperature scale than the velocity scale (put another way, Table 3 indicates $\eta(\Delta T_m/2) < \eta\,(u_m/2)$ in all cases).

Table 2 Measured and predicted variation of plume thermal energy flux

$\dot{m} \times 10^3$ (kg/ms)	x_0 (m)	Q_{x_0} (W/m)	x (m)	Q_x (W/m) measured	Eq. (32)[a]	Eq. (22)[b]
9.43	0.47	156.4	0.94	116.2	138.6	140.8
12.40	0.47	283.8	0.94	239.2	254.4	255.4
12.40	0.47	283.8	1.82	160.4	235.4	231.6
15.50	0.94	325.1	1.82	305.7	300.0	294.2
	average error (%)				14	15

[a] $Fr = 4.70$, $k^* = 15.1$
[b] $\mathrm{St} = 0.01$, $k^* = 15.1$

Table 3 Comparison of flow parameters for wall plumes and free plumes

Parameter	Isothermal wall plume	Adiabatic wall plume [3]	Free-line plume [1]
I_1[a]	0.101 ± 0.005	0.067 ± 0.004	0.157
I_2/I_1	0.700 ± 0.007	0.701 ± 0.007	0.707
I_3/I_1	0.556 ± 0.010	0.518 ± 0.011	0.577
I_4/I_1	0.901 ± 0.076	0.937 ± 0.040	0.883
I_5/I_1	0.660 ± 0.040	0.617 ± 0.040	0.662
I_6/I_1	0.48 ± 0.31[b]	0.43 ± 0.28[b]	0.46
E_0	0.096 ± 0.005[b]	0.067 ± 0.004	0.157
α_1	0.08 ± 0.05[b]	0.05 ± 0.03[b]	0.13
α_2	0.30 ± 0.67	0.47 ± 0.78	0.31
$\eta(u_m)$	0.022 ± 0.002	0.020 ± 0.002	0
$\eta(u_m/2)$	0.107 ± 0.010	0.066 ± 0.006	0.147
$\eta(\Delta T_m/2)$	0.095 ± 0.009	0.055 ± 0.002	0.130

[a] Value for $\sigma = x$
[b] Value taking $C_f = 0.015$, $\mathrm{St} = 0.009$

Several other parameters in Table 3 were calculated from the results of the analysis, assuming that C_f and St were constant for the wall plumes. The values chosen for C_f and St represent average values for the present test range, obtained from Fig. 4, although it will become evident that the assumed magnitudes of these parameters do not have a large effect on the results.

For the adiabatic wall plume and the free-line plume, the entrainment coefficient is equal to I_1, for $\sigma = x$, from equation (17). For the isothermal wall plume E_0 is slightly less than I_1 for the present test range, indicating a small effect of heat loss to the wall on the gross entrainment characteristics of the flow.

The parameter α_2 was determined from equation (14), using the measured profile integrals. Due to the uncertainties in the integrals, this parameter cannot be determined very accurately. The parameter α_1 was calculated from equation (13), using the computed values of E_0 and α_2, and the average value of Fr given in Table 1. Comparison of α_1 and E_0 indicates that the term involving the Froude number in equation (13) does not contribute greatly to the value of E_0. Therefore, far from the source, where the asymptotic value of Fr is approached, the entrainment process is dominated by shearing effects, similar to nonbuoyant flows.

The integral of the local shear stress and velocity gradient correlation across the flow, I_6, can be determined from equation (14) using the calculated value of α_1. The ratio I_6/I_1 is nearly identical for the three flows. Measurements of turbulence quantities in the isothermal wall plume have been recently undertaken in this laboratory, as an extension of the present investigation, which yield I_6 directly from the Reynolds stress distribution. The direct evaluation yields $(I_6/I_1) = 0.53 \pm 0.07$, which is in reasonably good agreement with the evaluation from the integral functions given in Table 3.

Influence of Wall Friction. Equations (17)–(21) provide a means of estimating the effects of wall friction and heat loss on the parameters describing the flow, if it is assumed that $I_1 - I_5$ are independent of Reynolds number. Two cases were considered, the large Reynolds number limit with $C_f = \mathrm{St} = 0$ and a Reynolds number typical of the present test range with $C_f = 0.015$ and $\mathrm{St} = 0.009$, from Fig. 4. The results are presented in Table 4, along with the standard deviation for the eight tests. The effect of Reynolds number, through the friction factor, is only about five percent for the range given in the table and is comparable to experimental accuracy represented by the standard deviations. This suggests that the present tests, over a limited range of Reynolds numbers, are reasonably representative of turbulent flows, at least on smooth surfaces.

The values of the flow parameters computed from the integral expressions of equations (20) and (21) in Table 4 are also in good agreement with the direct observations listed in Table 1. This indicates a reasonable degree of internal consistency for the results.

Concluding Remarks

The main results of the investigation are presented in Figs. 2–4. Profiles of mean velocity and temperature exhibit *local* similarity to about the same degree as similarity has been observed in previous two-dimensional plume studies. Local similarity is based on the current values of thermal energy flux in the plume and distance above the source, as suggested by this simplified integral model. Therefore, if Q_x and x are known, estimates of velocities and temperatures within the plume, and the heat flux to the wall, can readily be determined from the figures. The results are only valid in the weakly buoyant region of the plume, where radiation and variable property effects are small.

Table 4 Computed variation of flow parameters with skin friction coefficient[a]

C_f	St	E_0	$u_m(\rho C_p/g\beta Q_x)^{1/2}$	$g\beta x\Delta T_m(\rho C_p/g\beta Q_x)^{2/3}$	k^*	F_r
0	0	0.101	2.73	5.78	15.8	4.51
		(0.005)	(0.19)	(1.06)	(1.8)	(0.47)
0.015	0.009	0.096	2.67	5.64	15.1	4.37
		(0.005)	(0.19)	(1.00)	(1.6)	(0.45)

[a] Standard deviation in parenthesis

The greatest uncertainty in determining plume properties involves the estimation of Q_x at some point above the source. This value depends upon processes in the strongly buoyant region near the source, which are only poorly understood at present, particularly in a fire environment. Given an estimation of Q_x at some point, however, equations (22) and (32) provide subsequent values as a function of distance above the source. The use of equation (32) should be limited to the present test range, since its asymptotic behavior at large Reynolds numbers is not very satisfactory.

The wall plumes are narrower and have higher velocities and temperatures than a free-line plume at comparable conditions. This behavior appears to be due to the wall stabilizing the large lateral meandering observed with two-dimensional free plumes.

The heat transfer characteristics of the isothermal wall plume are similar to natural convection with a uniform heat flux, at comparable values of $\mathrm{Ra}_x{}^*$. In the present case, the effect of the Prandtl number has been inferred from the Colburn analogy and was not determined experimentally. Therefore, use of the results for substances having a Prandtl number substantially different than air should be approached with caution. Conditions for transition to turbulence were not determined in this investigation, however, turbulent flow was observed at lower $\mathrm{Ra}_x{}^*$ values for the wall plume than is the case for natural convection with uniform heat flux on a vertical surface.

The entrainment coefficient of the isothermal wall plume lies between the values found for the adiabatic wall plume and the free-line plume, suggesting that turbulent mixing is enhanced as the point of maximum buoyancy moves away from the stabilizing effect of a wall. The measurements indicate that major characteristics such as the Froude number, E_0 and k^* are only weakly influenced by wall friction and heat loss, through changes in C_f and St. Therefore, although the Reynolds number range of the present investigation was limited, the results may still be representative of turbulent wall plumes on smooth walls, at other conditions.

The conclusions of this study are not strongly dependent upon the simplified integral model which was used to suggest appropriate methods of data correlation. Similar to other integral models, an analysis of this type might be useful for treating flow development, the effect of variable wall temperature, the effect of stratified ambient conditions, etc., and the parameters given in Table 3 should be helpful for such attempts. However, this aspect of the model was not tested in the present investigation.

Acknowledgment

This research was supported by the United States Department of Commerce, National Bureau of Standards, Grant No. 5-9020, under the technical management of Dr. John Rockett of the Center for Fire Research.

References

1 Rouse, H., Yih, C. S., and Humphreys, H. W., "Gravitational Convection from a Boundary Source," *Tellus*, Vol. 4, 1952, pp. 201–210.

2 Lee, S. L., and Emmons, H. W., "A Study of Natural Convection Above a Line Fire," *Journal of Fluid Mechanics*, Vol. 11, 1961, pp. 353–368.

3 Grella, J. J., and Faeth, G. M., "Measurements in a Two-Dimensional Thermal Plume Along a Vertical Adiabatic Wall," *Journal of Fluid Mechanics*, Vol. 71, 1975, pp. 701–710.

4 Morton, B. R., Taylor, G. I., and Turner, J. S., "Turbulent Gravitational Convection from Maintained Sources," *Proceedings of the Royal Society*, London, Series A, Vol. 234, 1956, pp. 1–23.

5 Fox, D. G., "Forced Plume in a Stratified Fluid," *Journal of Geophysical Research*, Vol. 75, 1970, pp. 6818–6835.

6 Narain, J. P., and Uberoi, M. S., "The Swirling Turbulent Plume," ASME *Journal of Applied Mechanics*, Vol. 96, No. 2, pp. 337–342.

7 Poreh, M., Tseui, Y., and Cermak, J., "Investigations of a Turbulent Radial Wall Jet," ASME *Journal of Applied Mechanics*, Vol. 34, No. 2, 1967, pp. 457–463.

8 Cheesewright, H., "Turbulent Natural Convection from a Vertical Plane Surface," ASME JOURNAL OF HEAT TRANSFER, Vol. 90, No. 1, Feb. 1968, pp. 1–8.

9 Vilet, G. C., and Liu, C. K., "An Experimental Study of Turbulent Natural Convection Boundary Layers," ASME JOURNAL OF HEAT TRANSFER, Vol. 91, No. 4, Nov. 1969, pp. 517–531.

10 Fujii, T., Morioka, I., and Uehara, H., "Buoyant Plume of a Horizontal Line Heat Source," *International Journal of Heat and Mass Transfer*, Vol. 16, 1973, pp. 755–768.

11 Forstrom, R. J., and Sparrow, E. M., "Experiments on the Buoyant Plume Above a Heated Horizontal Wire," *International Journal of Heat and Mass Transfer*, Vol. 10, 1967, pp. 321–331.

12 Schorr, A. W., and Gebhart, B., "An Experimental Investigation of Natural Convection Wakes Above a Line Heat Source," *International Journal of Heat and Mass Transfer*, Vol. 13, 1970, pp. 557–571.

13 Vliet, G. C., "Natural Convection Local Heat Transfer on Constant-Heat-Flux Inclined Surfaces," ASME JOURNAL OF HEAT TRANSFER, Vol. 91, No. 4, Nov. 1969, pp. 511–517.

14 Vliet, G. C. and Ross, D. C., "Turbulent Natural Convection on Upward and Downward Facing Inclined Constant Heat Flux Surfaces," ASME JOURNAL OF HEAT TRANSFER, Vol. 97, No. 4, Nov. 1975, pp. 549–555.

15 Hinze, J. O., *Turbulence*, second edition, McGraw-Hill, New York, pp. 96–112, 1975.

APPENDIX

The effect of temperature fluctuations was reduced to a low level by operating the hot wire so that the temperature difference between the wire and the gas is large in comparison to the level of temperature fluctuations. This presented few difficulties during the present tests due to the relatively small temperature variation over the flow.

The major effect of turbulence on the present mean velocity measurements involved the influence of velocity fluctuations. Continued measurement of this flow has provided information on turbulence characteristics (the methods and complete results will be reported in the near future), which can be used to estimate the errors in the mean velocity measurements.

The stream wise turbulent intensity is approximately $0.2\,u_m$, and the turbulent intensity normal to the wall is approximately half this value, relatively independent of position in the flow (except very near the wall). From Hinze [15], for the present range of operating conditions and wire characteristics, the ratio of the measured mean velocity to the actual velocity is $1 + 3/16\,(u'/u)^2$, where u' is the longitudinal turbulent intensity parallel to the wall (this estimate is representative of the most adverse condition during these tests, but neglects terms of higher order than $(u'/u)^2$ in the error expression). Noting the relationship between u' and u_m stated above, the error in the mean velocity is less than five percent for $u/u_m \leqslant 0.5$. The variation in u/u_m is given in Fig. 1; except for a small zone very near the wall, this region lies in the range $y/x \leqslant 0.1$.

E. M. Sparrow,
S. V. Patankar,
R. M. Abdel-Wahed

Department of Mechanical Engineering,
University of Minnesota,
Minneapolis, Minn.

Development of Wall and Free Plumes Above a Heated Vertical Plate

An analysis has been made to determine the successive stages of development as the natural convection boundary layer on a steadily heated vertical plate evolves into a plume. Both the wall plume and the free plume are investigated. The wall plume develops along an adiabatic wall which is the vertical extension of the heated plate. The free plume is created as the boundary layer streams away from the upper edge of the plate. Since the plate is heated on only one of its faces, the free plume is initially unsymmetric. The development of these plumes does not admit similarity-type boundary layer solutions, and numerical techniques were, therefore, employed, with results being obtained for Prandtl numbers of 0.7, 2, 5, and 10. It was found that at sufficient downstream distances both plumes attain their respective fully developed behaviors (i.e., similar profiles at successive streamwise stations). For the wall plume, the development for all Prandtl numbers is completed at a position that is about five plate lengths above the leading edge of the heated plate. The development length for the free plume for Pr = 0.7 is about the same as that for the wall plume, but about 30 plate lengths are required for the development of the free plume when Pr = 10. The fully developed free plume is symmetric.

Introduction

The steady buoyancy-induced upflow above a steadily heated body is commonly referred to as a natural convection plume. Among such plumes, two general types may be identified—the free plume and the wall plume. The free plume is typified by the buoyant flow above a heated horizontal wire or cylinder. A typical wall plume is the flow along an adiabatic vertical plate, with the flow being induced by a heat source positioned adjacent to the lower edge of the plate. There is an extensive literature on free plumes that has recently been surveyed in [1].[1] Wall plumes have received substantially less attention [2, 3].

The published analyses for laminar plumes share a common set of characteristics. In all cases, they are based on similarity-type solutions of the laminar boundary layer equations and, therefore, pertain to plumes that are fully developed in the sense that the velocity profiles at successive streamwise stations are similar in shape. Solutions of this type do not take account of the fluid flow and heat transfer process adjacent to the heating surface which induces the plume. In addition, they do not describe the development of the similarity regime as the flow moves farther and farther away from the heating surface. In view of this lack of detail about the heating-surface flow and the subsequent developmental stages through which it passes, the similarity solutions are characterized as pertaining to a line (or point) source of heat.

The present analysis is concerned with both wall and free plumes which are induced by heating surfaces of finite extent. The primary focus of the research is to determine the successive stages in the evolution of the velocity and temperature distributions, starting at the heating surface and proceeding to the fully developed (i.e., similarity) regime.

The physical situations for which the wall and free plumes were studied are respectively illustrated in the left and right-hand diagrams of Fig. 1. The left-hand diagram shows a vertical plate whose lower portion ($0 \leq x < L_0$) is maintained at a uniform temperature T_w and whose upper portion ($x > L_0$) is adiabatic. If T_w is greater than the ambient temperature T_∞, a conventional natural convection boundary layer develops on the lower portion of the plate, with fluid moving upward. As the boundary layer flow encounters the adiabatic part of the plate, it becomes a wall plume. If the adiabatic section is sufficiently long, the plume will attain the similarity regime corresponding to a line heat source situated at the leading edge of an adiabatic plate. The similarity regime was analyzed in [2, 3].

The right-hand diagram depicts a wall having a vertical face of height L_0 maintained at a uniform temperature $T_w > T_\infty$. When the upward-moving boundary layer flow passes beyond the plate height, it becomes a free plume and can entrain fluid from the surroundings along both its flanks. At first, the free plume is unsymmetric because

---

[1] Numbers in brackets designate References at end of paper.

Contributed by the Heat Transfer Division for publication in the JOURNAL OF HEAT TRANSFER. Manuscript received by the Heat Transfer Division August 4, 1977.

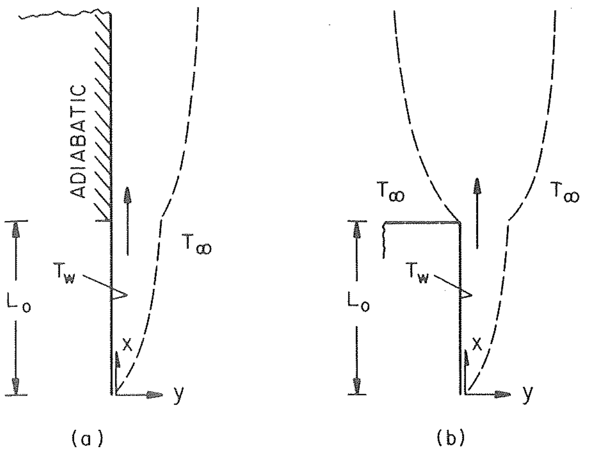

Fig. 1 The wall plume and free plume problems, diagrams (a) and (b), respectively

of its boundary layer origins. However, at sufficient heights above the plate, it becomes symmetric. The symmetric plume exhibits profile similarity and is identical to the much-studied plume above a horizontal line source of heat (surveyed in [1]).

The wall and free plume problems that were described in the foregoing do not permit similarity solutions of the laminar boundary layer equations. The solutions were, therefore, carried out using a numerical finite-difference technique. Nondimensionalization of the governing equations revealed that no new parameters are needed to accommodate the heated length L_0, so that the Prandtl number is the only prescribable parameter. It was assigned values of 0.7, 2, 5, and 10.

An interesting aspect of the solution for the free plume, to be elaborated later, is that its transverse position at any height x cannot be definitely related to the y coordinate of Fig. 1(b). This occurs because the boundary layer assumptions, in effect, banish the y-momentum equation, and without that equation the transverse position of the plume cannot be established. Although it is not generally recognized, this same state of affairs also exists in the analysis of the mixing of two parallel streams [4].

Analysis

The analysis to be performed here is based on the laminar boundary layer equations appropriate to natural convection flows. The use of the boundary layer equations for flow adjacent to a vertical plate is widely accepted. They should continue to be applicable to the wall plume problem of Fig. 1(a), especially since the temperature and velocity fields are continuous at $x = L_0$.

For the free plume problem of Fig. 1(b), there is a sharp discontinuity at $x = L_0$. Therefore, for the region adjacent to the discontinuity, it appears that the complete conservation equations should be employed as a basis for the solution. There is, however, clear evidence that the zone in which the complete equations are needed is relatively small and that downstream of this zone the boundary layer solution is valid. The most direct evidence comes from [5], where the symmetric buoyant wake just above an isothermal two-faced vertical plate was investigated. Finite-difference calculations based on the complete conservation equations were performed for values of x/L_0 up to 1.35, but it is implied that the boundary layer model is already valid before that point. Since the development lengths of the free plumes studied here are on the order of $10L_0$, it is evident that the boundary layer regime prevails throughout most of the development length. Furthermore, had it been desired to use the complete equations throughout the entire development length, the computer storage requirements and the computation times would have been prohibitive. In view of the foregoing considerations, it appeared reasonable to use the boundary layer equations for the solution of the free plume problem (as well as for the wall plume problem).

In the statement of the governing equations, it is convenient to introduce the following dimensionless variables

$$X = x/L_0,\ Y = (g\beta\Delta T/\nu^2 L_0)^{1/4} y \tag{1}$$

$$U = u/(g\beta\Delta T L_0)^{1/2},\ V = v/(g\beta\Delta T\nu^2/L_0)^{1/4} \tag{2}$$

$$\theta = (T - T_\infty)/\Delta T,\ \Delta T = T_w - T_\infty \tag{3}$$

where T_w refers to the uniform wall temperature that prevails over the length of plate between $x = 0$ and $x = L_0$. In terms of these new variables, the boundary layer form of the conservation equations can be written as

$$\frac{\partial U}{\partial X} + \frac{\partial V}{\partial Y} = 0 \tag{4}$$

$$U\frac{\partial U}{\partial X} + V\frac{\partial U}{\partial Y} = \theta + \frac{\partial^2 U}{\partial Y^2} \tag{5}$$

$$U\frac{\partial \theta}{\partial X} + V\frac{\partial \theta}{\partial Y} = \frac{1}{\mathrm{Pr}}\frac{\partial^2 \theta}{\partial Y^2} \tag{6}$$

It may be noted that these equations contain only one prescribable parameter—the Prandtl number.

With regard to the boundary conditions, separate cognizance has to be taken of the regions $0 < x < L_0$ and $x > L_0$, respectively corresponding to the heated surface and to the plume. For both the wall plume and free plume problems, the same boundary conditions are applicable in the range $0 < x < L_0$ $(0 < X < 1)$. At the wall, the velocities vanish and the temperature is T_w, whereas in the surroundings the streamwise velocity is zero and the temperature is T_∞. In terms of the transformed variables, these conditions become

$$U = V = 0 \text{ and } \theta = 1 \text{ at } Y = 0 \tag{7}$$

$$U = 0 \text{ and } \theta = 0 \text{ as } Y \to \infty \tag{8}$$

which are precisely those for the classical problem of the isothermal

Nomenclature

g = acceleration of gravity
L_0 = length of heated plate
Pr = Prandtl number
T = temperature
T_{aw} = local temperature on adiabatic wall
$T_{\max}$ = maximum temperature at any streamwise station
T_w = wall temperature of heated plate
T_∞ = ambient temperature
U = dimensionless streamwise velocity, equation (2)
u = streamwise velocity
$u_{\max}$ = maximum value of u at any streamwise station
V = dimensionless transverse velocity, equation (2)
v = transverse velocity
X = dimensionless streamwise coordinate, x/L_0
x = streamwise coordinate, Fig. 1
Y = dimensionless transverse coordinate, $(g\beta\Delta T/\nu^2 L_0)^{1/4} y$
Y' = dimensionless y' coordinate, $(g\beta\Delta T/\nu^2 L_0)^{1/4} y'$
y = transverse coordinate, Fig. 1
y' = transverse coordinate with $y' = 0$ when $u = u_{\max}$
β = thermal expansion coefficient
θ = dimensionless temperature, $(T - T_\infty)/(T_w - T_\infty)$
ν = kinematic viscosity

plate.

In the range $x > L_0$ $(X > 1)$, the adiabatic condition for the wall plume problem takes the form

$$\partial\theta/\partial Y = 0 \text{ at } Y = 0 \tag{9}$$

If equation (9) is substituted in lieu of $\theta = 1$ in equation (7), then both (7) and (8) continue to apply for the wall plume for $X > 1$.

For the free plume, the boundary conditions for $X > 1$ reflect the absence of solid boundaries. The streamwise velocity vanishes and the temperature is T_∞ in the surroundings adjacent to the respective flanks of the plume, so that

$$U = 0 \text{ and } \theta = 0 \text{ as } Y \to -\infty \tag{10}$$

$$U = 0 \text{ and } \theta = 0 \text{ as } Y \to \infty \tag{11}$$

For a symmetric plume, an additional boundary condition reflecting the symmetry can be specified. However, for an unsymmetric plume, such as that being treated here, equations (10) and (11) are the only physically based conditions that are available for the boundary-layer-type model.

It is interesting to note that equations (10) and (11) contain a total of four boundary conditions. On the other hand, equations (7) and (8) encompass five conditions, as do those for the wall plume. Therefore, it appears that there is a deficit of one boundary condition in the specification of the free plume problem in the region $X > 1$. Such a deficit is, in fact, encountered in the boundary layer analysis of all unsymmetric free shear layers, regardless of whether or not they admit similarity solutions.

In general, to enable solutions to be obtained for this class of problems, an additional boundary condition has to be imposed, and there is a degree of arbitrariness in what may be specified.[2] Fortunately, the boundary condition may be chosen without affecting the shape and magnitude of the velocity and temperature profiles at any cross section x = constant, the only influence being in the value of the transverse coordinate. Furthermore, the development of the successive profiles with x is unaffected. Therefore, such solutions, although not strictly complete, convey valuable information. The specification of the additional boundary condition used in the present problem will be described shortly.

Examination of the dimensionless form of the governing differential equations and boundary conditions indicates that there are no new parameters, even though both of the problems being studied experience a change of boundary conditions at $x = L_0$. Thus, the dimensionless results are universal in the sense that they do not depend parametrically on the length L_0 of the heated plate.

The solutions were carried out numerically by the use of the Patankar-Spalding method [8]. This solution procedure involves step-by-step marching in the streamwise direction. In the present investigation, the marching was initiated adjacent to the leading edge of the heated plate and was continued along the length of that plate and into the plume region. The solutions were started at $X = 0.001$ by making use of the velocity and temperature profiles from the well known integral solution for the isothermal vertical plate ([9], pp. 312–315). The location of the starting point of the computations was examined to make certain that $X = 0.001$ was sufficiently small so as not to affect the velocity and temperature profiles at $X = 1$.

The Patankar-Spalding method operates in X,ω coordinates rather than in X,Y coordinates, and the transformed conservation equations are available in [8]. The transverse coordinate ω is a dimensionless stream function defined as $\omega = (\psi - \psi_i)/(\psi_0 - \psi_i)$, in which ψ_i and ψ_0 are the values of the stream function at the inner and outer edges of the boundary layer. The stream function values ψ_i and ψ_0 vary with x as the boundary layer entrains more fluid, and the calculation of the entrainment rates is also described in [8]. For the computations, 200 grid points were deployed over the range of ω between zero and one, with a greater concentration of points in the region of highest gradients. In the X direction, the computations were begun with a step size ΔX of 0.001 near the leading edge of the plate. The step size was progressively increased along the length of the heated plate to a maximum value $\Delta X = 0.005$ at a rate that was coupled to the increasing thickness of the boundary layer. In the range of X between 1 and 10, the step size ΔX varied from 0.005 to 0.05, again coupled to the thickness of the layer (i.e., breadth of the plume). For $X > 10$, ΔX increased from 0.05 to a terminal value of 0.15. The adequacy of these step sizes was verified by auxiliary runs involving other step size patterns.

It is interesting to note that the aforementioned boundary condition deficit for the free plume problem for $X > 1$ is not directly felt by the Patankar-Spalding method since it operates with the stream function as the transverse coordinate rather than with Y. This is because the deficit is suffered by the velocity V, and it can be verified (e.g., [4], pp. 143–144 or [7], pp. 140–141) that the transformation from X,Y to X,ψ eliminates V from the x-momentum and energy equations.[3] The deficit is felt, however, when it is desired to restate the results from the solution coordinates into physical coordinates. To overcome the resulting indeterminacy, we have elected to define a transverse coordinate y' such that at each streamwise station, $y' = 0$ corresponds to the position of the maximum velocity.

Solutions for both the wall plume and the free plume were carried out for parametric values of the Prandtl number equal to 0.7, 2, 5, and 10. The final value of X was chosen sufficiently large so that the respective similarity regimes for the wall and free plumes were attained.

As a check on the finite-difference computations, the Nusselt numbers at $X = 1$ were compared with literature values based on similarity boundary layer solutions. The agreement was within 0.1 to 0.2 percent over the aforementioned range of Prandtl numbers.

Results and discussion

In the presentation that follows, results will first be given for the wall plume and then for the free plume.

Wall Plume. For the wall plume problem pictured in Fig. 1(*a*), the plume is bounded by an adiabatic plate whose temperature T_{aw} ($aw \sim$ adiabatic wall) will decrease in the flow direction as the plume broadens and entrains more fluid. The variation of T_{aw} with x is presented in Fig. 2 for the four Prandtl numbers investigated. To provide a dimensionless representation, the quantity $(T_{aw} - T_\infty)$ is ratioed with the temperature difference $(T_w - T_\infty)$ of the heated plate $(0 < X < 1)$. These results are referred to the left-hand ordinate.

In addition, there is a set of curves in Fig. 2 which slope upward to the right and are referred to the right-hand ordinate. Each curve shows, for a fixed Prandtl number, the x-dependence of the maximum velocity in the plume at each streamwise station.

The abscissa range starts at $x = L_0$ and extends to $x = 100L_0$. Results for $x < L_0$ are not shown because they correspond to the conventional isothermal plate problem.

It is seen from Fig. 2 that the adiabatic wall temperature drops off rapidly just beyond $x = L_0$ and then settles down to a slower, regular decrease which obeys a power law

$$(T_{aw} - T_\infty)/(T_w - T_\infty) \sim (x/L_0)^{-3/5} \tag{12}$$

The power-law regime is fully in effect for $x/L_0 > 8$ to 10 (depending on the Prandtl number) but, to within two percent, is already in effect at $X = 5$. The $-3/5$ power dependence is identical to that of the similarity solution for the laminar wall plume [2, 3]. Therefore, the x/L_0 value at which the power-law dependence takes hold can be regarded as being a measure of where the wall plume becomes fully developed.

It may also be noted from Fig. 2 that the adiabatic wall temperature

---

[2] For example, in the analysis of the mixing of the two parallel streams, it is common to assume that $v = 0$ along the downstream extension of the upstream splitter plate which separates the streams [4, 6, 7].

[3] This transformation is often referred to as the von Mises transformation.

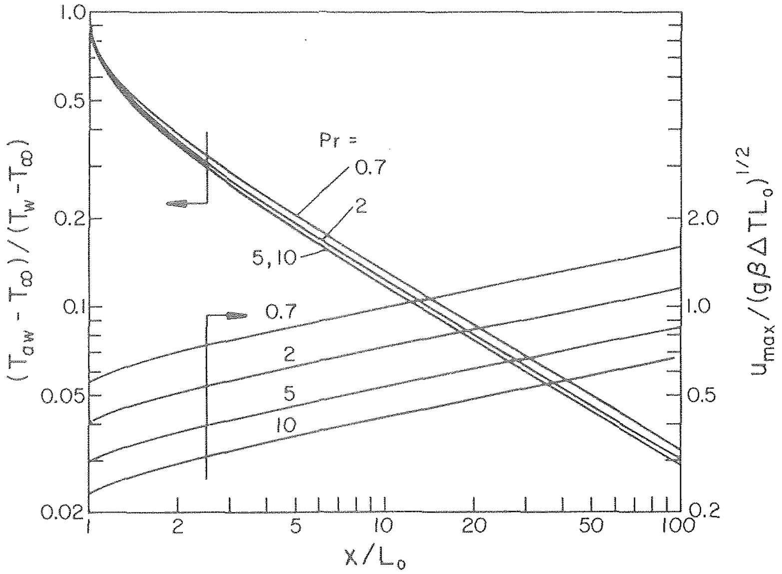

Fig. 2 Streamwise variations of the adiabatic wall temperature and of the maximum velocity for the wall plume

results are not very sensitive to Prandtl number. In particular, the curves for Pr = 5 and 10 are coincident for most of the range of x. This insensitivity may be made plausible by first noting that for a given temperature difference $(T_w - T_\infty)$ on the heated plate, the energy carried into the plume region across the line $x = L_0$ is different for different Prandtl numbers. With increasing Prandtl number, there is a smaller influx. Also, at higher Prandtl numbers, the fluid is less effective in transporting energy from the wall toward the edge of the plume. Thus, there is a match-up between energy-transporting capability and the amount of energy to be transported, and this causes the aforementioned insensitivity.

Attention may now be turned to the results of Fig. 2 for the maximum velocity at each streamwise station. It is seen from the figure that the maximum velocity increases as the plume rises, the increase being a consequence of the continuing action of buoyancy. The rate of increase of the velocity is somewhat more rapid near $x = L_0$ than at larger x where, ultimately, a power-law variation sets in

$$u_{\max}/(g\beta\Delta TL_0)^{1/2} \sim (x/L_0)^{1/5} \tag{13}$$

The straight line variation represented by equation (13) holds for $x/L_0 > 3$ to 5, with the larger x/L_0 for the higher Prandtl numbers. The $\frac{1}{5}$ power variation corresponds to the similarity wall plume [2, 3]. By taking note of the remarks following equation (12), it appears that the maximum velocity approaches its power-law asymptote somewhat more rapidly than the adiabatic wall temperature approaches its asymptote.

The appreciable Prandtl number influence which the $u_{\max}$ values for the wall plume inherited from the upstream flat-plate boundary layer is preserved with remarkable precision. The spacing between the respective $u_{\max}$ curves for the various Prandtl numbers is maintained over the entire range of x.

Another viewpoint on the development of the wall plume is given by the velocity and temperature profiles. In Figs. 3(a) and 3(b), $u/u_{\max}$ is plotted as a function of $Y/X^{2/5}$, respectively, for Pr = 0.7 and 10. In terms of these variables, the velocity profiles at all stations in the fully developed (i.e., similarity) regime fall together on a single line. Similarly, in left-hand and right-hand portions of Fig. 4, temperature profiles for Pr = 0.7 and 10 are plotted as $(T - T_\infty)/(T_{aw} - T_\infty)$ versus $Y/X^{2/5}$. As with the velocity, the form of these variables is borrowed from the similarity solution.

Velocity profiles are presented in Figs. 3(a) and 3(b) for streamwise stations at $X = 1, 2, 5$, and 10. The $X = 1$ profile represents that for

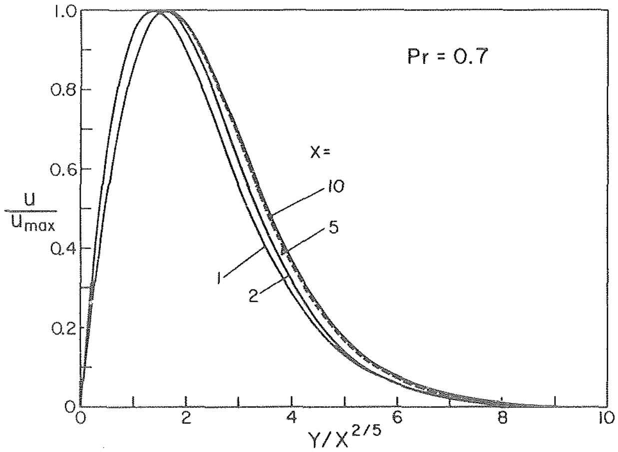

Fig. 3(a) Velocity profiles for the wall plume, Pr = 0.7

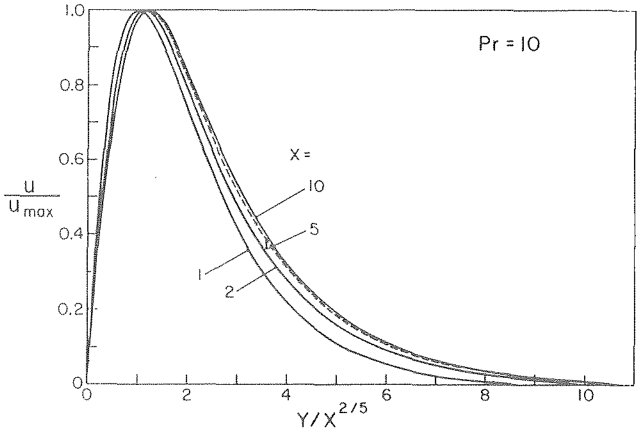

Fig. 3(b) Velocity profiles for the wall plume, Pr = 10

Fig. 3

the isothermal-plate boundary layer. All profiles for $X > 10$ coincide with that for $X = 10$, so that it may be regarded as the fully developed wall plume profile. A dashed line is employed to enable the profile for $X = 5$ to be distinguished from that for $X = 10$.

It is seen from these figures that there is not a great deal of difference between the velocity profiles for the isothermal-plate boundary layer and the fully developed wall plume. The development of the former into the latter follows an orderly progression. The profile at $X = 2$ is still in an intermediate stage of development, but that at $X = 5$ is very nearly fully developed. Although there is some residual development between 5 and 10, it appears reasonable to regard the velocity profile shape at $X = 5$ as being effectively fully developed. As further affirmation of this result, it may be recalled that when $X \geq 5$, $u_{\max}$ obeys the power law dependence for fully developed flow, equation (13).

From a comparison of Figs. 3(*a*) and 3(*b*), no significant differences are in evidence with regard to the effect of Prandtl number on the approach to the fully developed velocity field.

As a final remark with regard to Fig. 3, mention may be made of a comparison between the fully developed velocity profile calculated here and that from the similarity solution of [2]. Profiles for Pr = 0.7 are available from both investigations. Values taken from a photographically enlarged version of Fig. 1 of [2] and plotted on Fig. 3(*a*) were coincident with the profile for $X = 10$.

Turning next to Fig. 4, it should be noted that the profiles for $X = 1$ and $X = 10$ represent, respectively, the initial and final stages of the temperature field development for the wall plume. In contrast to the velocity profiles of Fig. 3, the temperature profiles undergo a significant change of shape as they progress from that for the isothermal flat plate to that for the fully developed wall plume. A major part of the adjustment in profile shape is accomplished between $X = 1$ and $X = 2$. By $X = 5$, the profile is already grazing the fully developed profile.

Thus, for practical purposes, the temperature field can be regarded as being fully developed for $X \geq 5$, as can the velocity field.

Free Plume. The presentation of results for the free plume will follow a pattern similar to that used for the wall plume results. There will, however, be a change in the temperature parameter to be employed. Instead of the adiabatic wall temperature T_{aw} which was relevant for the wall plume, attention is now focused on the maximum temperature $T_{\max}$ at each streamwise station. Owing to plume broadening and transverse conduction, $T_{\max}$ will decrease with x.

The streamwise variation of the maximum velocity and the maximum temperature are presented in dimensionless terms in Fig. 5. As is seen from the figure, the maximum velocity increases in the streamwise direction, while the maximum temperature decreases. These trends are the same as those for the wall plume.

Examination of the results in the neighborhood of $x = L_0$ indicates the dramatic changes that ensue as the boundary layer leaves the wall and becomes a free flow. On the wall, just upstream of $x = L_0$, $(T_{\max} - T_\infty)/(T_w - T_\infty) = 1$, since $T_{\max} = T_w$. However, in the plume, just downstream of $x = L_0$, values of $(T_{\max} - T_\infty)/(T_w - T_\infty)$ are encountered that are much less than one. Similarly, there is a sharp change in the maximum velocity. To help identify the change, the values of $u_{\max}/(g\beta\Delta TL_0)^{1/2}$ for the boundary layer flow just upstream of $x = L_0$ are plotted as open circles on the ordinate axis, with the Prandtl number ordering being the same as for the curves. The occurrence of abrupt changes in the velocity and temperature fields has already been observed in [5], where the complete conservation equations were used to study the near-wake region above a symmetrically heated vertical plate.

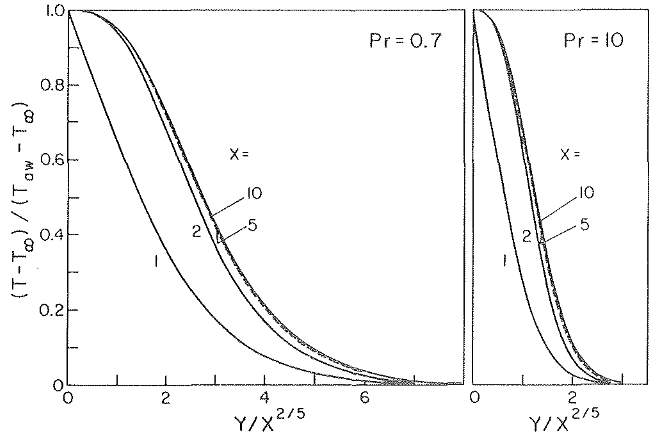

Fig. 4 Temperature profiles for the wall plume, Pr = 0.7 and 10

Downstream of the discontinuity, the further drop-off of the maximum temperature tends to be rather slow at first, but then becomes more rapid and finally takes on a power-law dependence

$$(T_{\max} - T_\infty)/(T_w - T_\infty) \sim (x/L_0)^{-3/5} \tag{14}$$

which is similar to equation (12). The value of x/L_0 at which the power law takes hold appears to increase with Prandtl number, varying from about 6 for Pr = 0.7 to about 30 for Pr = 10. It may be noted that the centerline temperature of a symmetric, fully developed free plume also varies as $x^{-3/5}$ [1].

The maximum velocity increases rapidly downstream of the discontinuity at $x = L_0$ and then tends toward the more gradual but steady power-law increase given by equation (13). The power-law dependence is in force for values of x/L_0 greater than 5 to 6. The $x^{1/5}$ variation of $u_{\max}$ is also characteristic of the centerline velocity of a symmetric, fully developed free plume.

Velocity profiles for Pr = 0.7 and 10 are presented in Figs. 6(*a*) and 6(*b*). The ordinate for these figures is $u/u_{\max}$ so that, as in Figs. 3(*a*) and 3(*b*), all the profiles have a maximum value of one. The abscissa variable is $Y'/X^{2/5}$, where

$$Y' = (g\beta\Delta T/\nu^2 L_0)^{1/4} y' \tag{15}$$

and y' is a transverse coordinate whose origin at any streamwise station coincides with the location of the maximum velocity. The background for the choice of the y' coordinate was discussed in detail in the Analysis section.

For purposes of orientation, it may be noted that the flank of the plume at positive Y' is a continuation of the edge of the upstream boundary layer. Owing to the discontinuity at $X = 1$, the velocity profile upstream of this point is, in effect, washed out, and therefore is not shown in the figures.

It is seen from the figures that in the early stages of its development, the plume is unsymmetric. Furthermore, its breadth is greater than

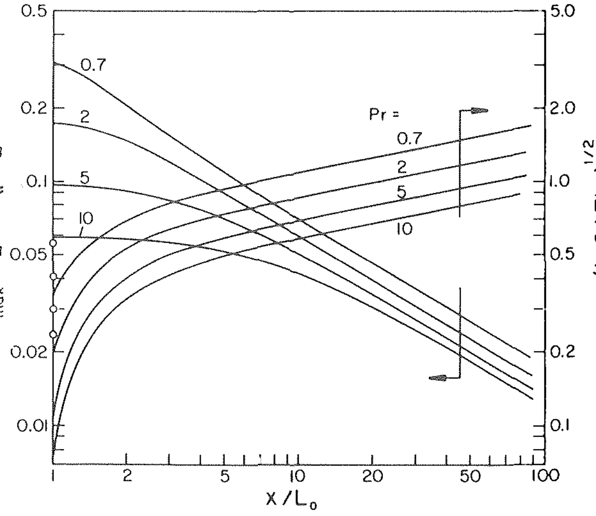

Fig. 5 Streamwise variations of the maximum temperature and maximum velocity for the free plume

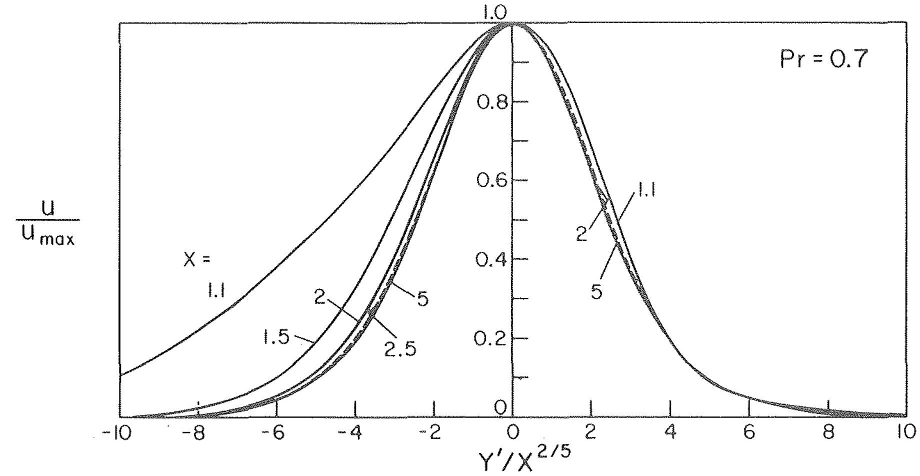

Fig. 6(*a*) Velocity profiles for the free plume, Pr = 0.7

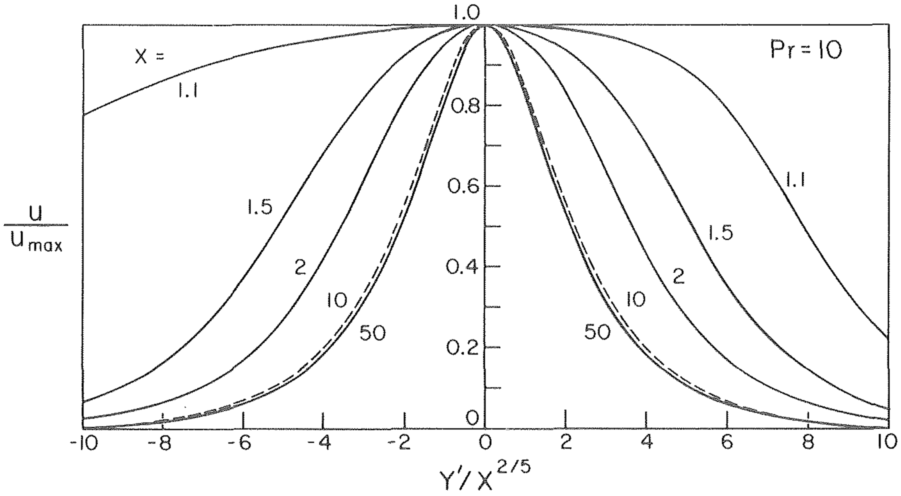

Fig. 6(*b*) Velocity profiles for the free plume, Pr = 10

Fig. 6

would be that of a fully developed plume at the same streamwise station. With increasing downstream distance, the successive profiles become more and more symmetric and tend to overlay one another. For Pr = 0.7, all profiles for $X > 5$ coincide with that for $X = 5$, whereas for Pr = 10 there is no further change in the profiles beyond $X = 50$.

Further inspection of Fig. 6(a) shows that for Pr = 0.7, the final developmental stage of the plume occurs between $X = 2.5$ and 5. Although it would appear that the plume can be pronounced fully developed at $X = 2.5$, Fig. 5 indicates that $U_{\max}$ has not quite attained its fully developed (i.e., straight line) behavior at that X. Therefore, $X = 4$ or 5 appears to be a better designation for the beginning of the fully developed regime for Pr = 0.7.

The velocity profile for $X = 5$ has been compared with that from the free-plume similarity solution of [10]. The two profiles were found to be coincident.

It is evident from Fig. 6(b) that the development of the plume is slower at higher Prandtl numbers. The final stage occurs between $X = 10$ and $X = 50$. A definite recommendation for the beginning of the fully developed regime will be made shortly, when the temperature profiles are examined.

The development of the temperature profiles is shown in Figs. 7(a) and 7(b), which pertain to Pr = 0.7 and 10, respectively. The ordinate of these figures is a dimensionless temperature variable which takes on a maximum value of one when $T = T_{\max}$. The abscissa variable is the same as that of Fig. 6, with y' defined to be zero at the transverse location where $u = u_{\max}$.

The temperature profiles for Pr = 0.7 develop quickly, so that the symmetric fully developed shape is attained for $X \simeq 2$. However, since $T_{\max}$ has not yet achieved its fully developed behavior at $X = 2$ (see Fig. 5), a development length of $X = 4$ or 5 appears appropriate, as was the case for the velocity field.

For Pr = 10, the temperature field development is relatively slow, and the final stages occur between 20 and 50. If account is taken of Fig. 5, then $X = 30$ appears to be an appropriate measure of the development length.

Concluding Remarks

This investigation has examined the development of both wall and free plumes above an isothermal, steadily heated vertical plate. The wall plume develops along an adiabatic wall which is the vertical extension of the one-sided heated plate. The free plume is created as the boundary layer from the heated plate streams away from the upper edge of the plate. The development of these plumes does not

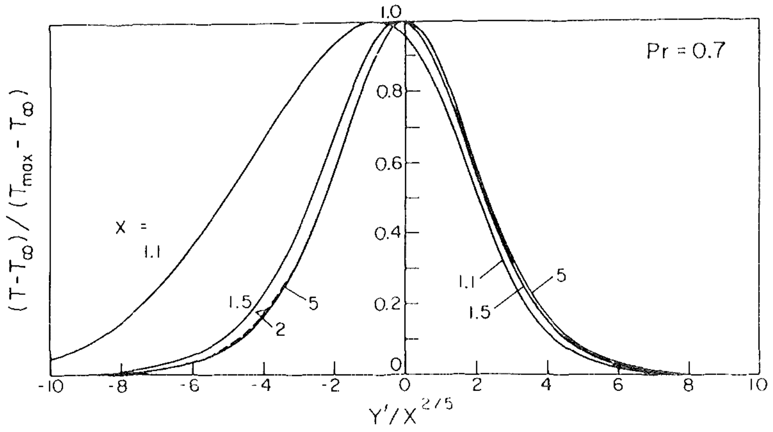

Fig. 7(*a*) Temperature profiles for the free plume, Pr = 0.7

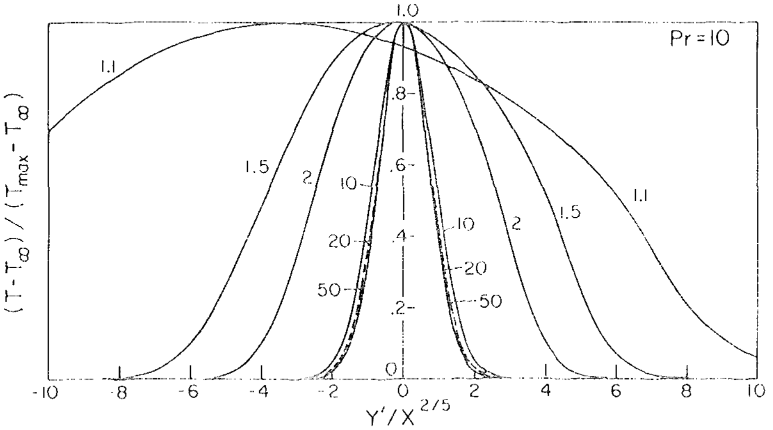

Fig. 7(*b*) Temperature profiles for the free plume, Pr = 10

Fig. 7

yield similarity-type boundary layer solutions.

It was found that at sufficient downstream distances, both plumes attain their respective fully developed behaviors. That behavior is characterized by velocity and temperature profiles that have similar shapes at successive streamwise locations. Furthermore, in the similarity regime, the maximum velocity at each streamwise station increases monotonically as $x^{1/5}$, while the maximum temperature decreases as $x^{-3/5}$.

Numerical solutions were carried out for Pr = 0.7, 2, 5, and 10 for both plume problems. The wall plume attains its fully developed behavior at a position that is about five plate lengths above the leading edge of the heated plate. Its development is not very sensitive to the Prandtl number. For the free plume, the development length for Pr = 0.7 is about the same as that for the wall plume. However, for Pr = 10, about 30 plate lengths are required for the attainment of fully developed behavior.

Acknowledgment

This research was performed under the auspices of NSF grant ENG-7518141.

References

1 Gebhart, B., "Natural Convection Flows and Stability," in *Advances in Heat Transfer*, Vol. 9, 1973, pp. 297–301.

2 Gebhart, B., and Jaluria, Y., "Buoyancy-Induced Flow Arising from a Line Thermal Source on an Adiabatic Vertical Surface," *International Journal of Heat and Mass Transfer*, Vol. 20, 1977, pp. 153–157.

3 Liburdy, J. A., and Faeth, G. M., "Theory of a Steady Laminar Thermal Plume Along a Vertical Adiabatic Wall," *Letters in Heat and Mass Transfer*, Vol. 2, 1975, pp. 407–418.

4 Schlichting, H., *Boundary Layer Theory*, sixth ed., McGraw-Hill, New York, 1968.

5 Hardwick, N. E., and Levy, E. K., "Study of the Laminar Free-Convection Wake Above an Isothermal Vertical Plate," ASME JOURNAL OF HEAT TRANSFER, Vol. 95, 1973, pp. 289–294.

6 Rosenhead, L., ed., *Laminar Boundary Layers*, Oxford, 1963.

7 Cebeci, T., and Bradshaw, P., *Momentum Transfer in Boundary Layers*, Hemisphere/McGraw-Hill, Washington/New York, 1977.

8 Patankar, S. V., and Spalding, D. B., *Heat and Mass Transfer in Boundary Layers*, Second ed., Intertext Books, London, 1970.

9 Eckert, E. R. G., and Drake, R. M., *Heat and Mass Transfer*, McGraw-Hill, New York, 1959.

10 Fujii, T., "Theory of the Steady Laminar Natural Convection Above a Horizontal Line Heat Source and a Point Heat Source," *International Journal of Heat and Mass Transfer*, Vol. 6, 1963, pp. 597–606.

A. Bejan
C. L. Tien

Department of Mechanical Engineering,
University of California,
Berkeley, Cal.

Natural Convection in a Horizontal Porous Medium Subjected to an End-to-End Temperature Difference

Natural convection in a porous medium filling a slender horizontal space with an end-to-end temperature difference is studied analytically. The end-to-end temperature difference gives rise to a horizontal counterflow pattern augmenting the heat transfer rate through the porous medium. Two basic geometries are considered: horizontal layer confined between two adiabatic and impermeable parallel plates, and horizontal cylinder surrounded by an adiabatic and impermeable cylindrical surface. Nusselt number relations are derived in terms of the Rayleigh number and the cavity aspect ratio. The end-wall permeability is shown to affect the heat transfer rate through the medium.

Introduction

The phenomenon of natural convection through porous media has been receiving increased attention due to its numerous applications, primarily in geophysical problems and thermal insulation. Natural-convection boundary layers in a porous medium have been extensively investigated recently (see, for instance, Cheng [1][1]). For natural convection in confined porous layers, most published works deal with the class of problems in which the heating and cooling are present on the long boundaries delineating the porous medium. Citing a few examples, the natural convection phenomenon in horizontal and sloping porous layers was studied by Bories and Combarnous [2] and Weber [3]. Natural convection in vertical porous layers was studied by Chan, Ivey, and Barry [4] and, more recently, Burns, Chow, and Tien [5]. Numerical estimates of the Nusselt number across moderately shallow rectangular spaces filled with a porous medium have been reported by Burns, Chow, and Tien [5] and Bankvall [6].

The objective of the present work is to study analytically the natural convection effect on heat transport through a porous layer confined in a horizontal space with the two ends maintained at different temperatures and the long horizontal walls adiabatic. Convection in this basic geometry has received little attention. Moreover, efforts on the corresponding natural convection problem in a horizontal enclosure filled with an incompressible fluid are few and quite recent. In a three-paper sequence, Cormack, et al. [7, 8] and Imberger [9] treated the flow in a parallel-plate horizontal channel with an imposed end-to-end temperature difference. The convection in horizontal tubes with one end warm and the other cold was studied numerically by Hong [10] and analytically by Bejan and Tien [11].

The following work is presented in two parts. The first part considers free convection in a horizontal parallel-plate space filled with a porous medium shown in Fig. 1. The method of solution consists of identifying the three major regions which, when combined, make up the natural convective pattern: a core region situated in the middle of the channel, plus two end regions. The temperature and velocity field is then derived analytically for each region subject to simplifying approximations characteristic to each region. As a conclusion to this part, we combine the three local solutions to estimate the axial rate of heat transfer (the Nusselt number) in horizontal layers with both

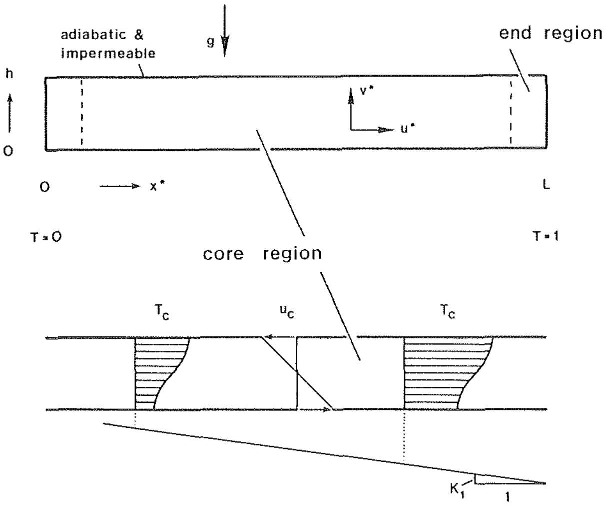

Fig. 1 Two-dimensional porous layer subjected to an end-to-end temperature difference, velocity and temperature distributions in the core region

---

[1] Numbers in brackets designate References at end of paper.

Contributed by the Heat Transfer Division for publication in the JOURNAL OF HEAT TRANSFER. Manuscript received by the Heat Transfer Division November 3, 1977.

ends impermeable, both ends permeable, and finally, in asymmetric layers with one end permeable and the other end permeable. Finally, we compare the present theoretical result for the Nusselt number in a space with two impermeable end walls with the numerical results of Burns, Chow, and Tien [5] and Bankvall [6] for free convection heat transfer in moderately shallow cavities filled with a porous medium.

In the second part, the analysis is repeated for natural convection in horizontal cylinders with different end temperatures (see Fig. 5). The cylindrical geometry can account for cases in which the width of the parallel-plate space of Fig. 1 is of the same order of magnitude as its vertical dimension h.

Two-Dimensional Horizontal Layer

The basic two-dimensional configuration is shown schematically in Fig. 1. The two short vertical walls are kept at different temperatures T_1 and T_2, while the long horizontal walls are adiabatic and impermeable. The rectangular space is filled with a porous medium. Assuming that Darcy's law applies, i.e., the Reynolds number based on pore diameter is less than one [12], the continuity, momentum, and energy equations are

$$\frac{\partial u}{\partial x} + \frac{\partial v}{\partial y} = 0, \quad u = -\frac{\partial P}{\partial x} \tag{1,2}$$

$$v = -\frac{\partial P}{\partial y} + \mathrm{Ra}\, T, \quad u\frac{\partial T}{\partial x} + v\frac{\partial T}{\partial y} = \frac{\partial^2 T}{\partial x^2} + \frac{\partial^2 T}{\partial y^2} \tag{3,4}$$

Equations (1–4) have already been nondimensionalized by defining

$$u, v = \frac{h}{\alpha}(u^*, v^*), \quad x, y = (x^*, y^*)/h \tag{5,6}$$

$$T = \frac{T^* - T_1}{T_2 - T_1}, \quad P = \frac{P^* K}{\alpha\mu} \tag{7,8}$$

where the asterisks denote the dimensional variables shown on Fig. 1 and listed in the nomenclature. Without loss of generality, it is assumed that the right end is warmer than the left, $T_2 > T_1$. The natural convection pattern is governed by the modified Rayleigh number

$$\mathrm{Ra} = \frac{g\beta h K(T_2 - T_1)}{\alpha\nu} \tag{9}$$

in which K, the medium permeability, is assumed uniform in both directions. Equations (1–4) contain the Boussinesq approximation whereby density differences are due solely to temperature differences.

We now poceed with deriving the velocity and temperature fields by solving equations (1–4) in each of the three major regions shown in Fig. 1.

The Flow in the Core Region. If the two-dimensional channel is very slender, $h/L \ll 1$, the central portion is sufficiently far removed from the two ends so that in the core region the streamlines are essentially parallel to the two horizontal walls. This observation is sufficient for deriving expressions for u and T, by setting $v = 0$ in equations (1–4). The resulting axial velocity and temperature in the core region is

$$u_c(y) = -\mathrm{Ra}\, K_1 \left(y - \frac{1}{2}\right) \tag{10}$$

$$T_c(x, y) = K_1 x + K_2 + \mathrm{Ra}\, K_1^2 \left(\frac{1}{4}y^2 - \frac{1}{6}y^3\right) \tag{11}$$

in which the two constants of integration K_1, K_2 have to be determined from temperature conditions in the two sections where the core region communicates with the end regions. Formulas (10) and (11) satisfy the adiabatic and impermeable boundary conditions at $y = 0, 1$. The velocity and temperature profiles for the core region have been sketched in Fig. 1. In contrast with fluid flow in a channel, the axial velocity u is finite (maximum) at the impermeable boundaries $y = 0, 1$.

The net rate of heat transfer $\dot{Q}$ through any cross section in the core region is characterized by a Nusselt number for axial heat transfer defined as

$$\mathrm{Nu} = \frac{\dot{Q}}{Wk(T_2 - T_1)} = \int_0^1 \left(\frac{\partial T_c}{\partial x} - u_c T_c\right) dy \tag{12}$$

Substituting expressions (10) and (11) into the Nu definition (12) and integrating yields

$$\mathrm{Nu} = K_1 \left(1 + \frac{1}{120}\mathrm{Ra}^2 K_1^2\right) \tag{13}$$

which shows that Nu depends on Ra and the yet unknown axial temperature gradient constant K_1. As mentioned before, K_1 will have to be determined by taking into account the flow pattern in the two end regions. The flow around an impermeable end and the flow through a permeable end are considered separately in the next two sections.

It is instructive to point out that K_1 is of the order of h/L or less, by considering the limit in which the horizontal layer is very slender, $h/L \rightarrow 0$. Under these circumstances the core region fills almost the entire layer of Fig. 1, and the temperature drop across the core region is approximately equal to or slightly less than the total ΔT maintained across the ends of the rectangular layer. Using expression (11), this statement can be written as

$$T_c\left(\frac{L}{h}, 1\right) - T_c(0, 0) \leqslant 1 \tag{14}$$

which, as $h/L \rightarrow 0$ and Ra remains finite, reduces to

$$K_1 \leqslant h/L \tag{15}$$

The equal sign corresponds to pure conduction through the porous

Nomenclature

B = function, equations (26), (70)
D = function, equation (76)
E = function, equation (77)
g = gravitational acceleration (m/s^2)
h = thickness (m)
K = permeability (m^2)
K_1 = axial temperature gradient constant
K_2 = constant
L = length (m)
Nu = Nusselt number, equations (12), (60)
P = pressure, equation (8)
$\dot{Q}$ = axial heat transfer rate (W)
r = radial distance, equation (43)
r_0 = cylinder radius (m)
Ra = Rayleigh number, equations (9), (44)
T = temperature, equation (7)
T_1 = cold end temperature (K)
T_2 = warm end temperature (K)
u = axial velocity, equation (5), and radial velocity, equation (42)
v = vertical velocity, equation (5), and tangential velocity, equation (42)
w = axial velocity, equation (42)
W = width of horizontal porous layer (m)
x = axial distance, Fig. 1
y = vertical distance, Fig. 1
z = axial distance, Fig. 5
$(\ )^*$ = dimensional variable
$(\ )_c$ = core solution
$(\ )_0$ = pertaining to the horizontal cylinder, Fig. 5
$(\ )_{0,\mathrm{I},\mathrm{II},\mathrm{III}\ldots}$ = zeroth, first, second, third order solution, equations (45), (46)
α = thermal diffusivity (m^2/s)
η = isothermal layer thickness
β = coefficient of volumetric thermal expansion (K^{-1})
δ = length of impermeable end-wall region
Δ = length of permeable end-wall region
θ = angular position, Fig. 5
ν = kinematic viscosity (m^2/s)
Ψ_{II} = stream function, Fig. 7

medium filling the rectangular space.

The Flow Around an Impermeable End-Wall. In this section we develop an integral solution or the velocity and temperature distribution in an impermeable end region. Matching the end solution with the core solution presented in the preceding section provides the necessary temperature end condition for estimating constants K_1 and K_2 appearing in equations (10), (11), and (13).

As shown in Fig. 2(a), the impermeable end region is assumed rectangular, with a length δ unknown at this point. The momentum and energy equations are to be satisfied in an integral manner in the volume occupied by the end region. Two integral conditions are obtained by integrating the momentum and energy equations vertically from 0 to 1 and horizontally from 0 to δ. However, before deriving the momentum integral we eliminate the pressure terms by cross-differentiating the momentum equations (2) and (3). The momentum and energy end conditions resulting from integrating in x and y are,

$$\int_0^\delta [u(x,1) - u(x,0)]\,dx + \int_0^1 v(0,y)\,dy = -\mathrm{Ra}\int_0^1 T(\delta,y)\,dy \quad (16)$$

$$\int_0^1 u_c T_c dy = K_1 - \int_0^1 \left(\frac{\partial T}{\partial x}\right)_{x=0} dy \quad (17)$$

Equations (16) and (17) already include the boundary conditions prevailing in the end region (see Fig. 3).

The next step consists of substituting reasonable velocity and temperature profiles into equations (16) and (17). The expressions selected for u, v and T in the end region are

$$u = -\mathrm{Ra}\,K_1\left(y - \frac{1}{2}\right)\left[1 + \left(\frac{x}{\delta} - 1\right)^3\right] \quad (18)$$

$$v = \frac{3}{2}\frac{\mathrm{Ra}\,K_1}{\delta}(y^2 - y)\left(\frac{x}{\delta} - 1\right)^2 \quad (19)$$

$$T = (T_c - \delta K_1)\left[2\frac{x}{\delta} - \left(\frac{x}{\delta}\right)^2\right] + K_1 x \quad (20)$$

which match the core solution at $x = \delta$ and satisfy the continuity equation (1) identically throughout the end region. The selection of such profiles is arbitrary accounting, in fact, for the approximate nature of the integral method. The chosen velocity and temperature distributions are qualitatively similar to the distributions determined numerically by Cormack, Leal and Seinfeld [8]. It is easy to verify that the choice of a different set of profiles in place of expressions (18–20) does not alter appreciably the integral solution, equations (21) and (22). Combining equations (18–20) with the integral conditions (16, 17) yields respectively,

$$\frac{1}{4}K_1\delta[\delta^{-2} - 1] = K_2 + \frac{1}{24}\mathrm{Ra}\,K_1^2 \quad (21)$$

$$\frac{1}{120}\delta\,\mathrm{Ra}^2 K_1^3 = K_2 + \frac{1}{24}\mathrm{Ra}\,K_1^2 \quad (22)$$

which, after eliminating δ, provides an implicit equation for K_2 as a function of K_1 and vice-versa. This relation is all we had hoped to achieve by analyzing the flow conditions in the vicinity of one of the two ends of the core region. The second relationship required for uniquely determining K_1 and K_2 follows from analyzing the flow pattern in the remaining extremity of the porous layer.

Dividing equations (21) and (22) side by side leads to an expression for the impermeable end length δ as a function of Ra K_1. This function is shown plotted in Fig. 3: as Ra K_1 tends to zero, δ approaches unity, whereas towards large values of Ra K_1 the end region reduces to a narrow vertical layer spread over the impermeable end wall.

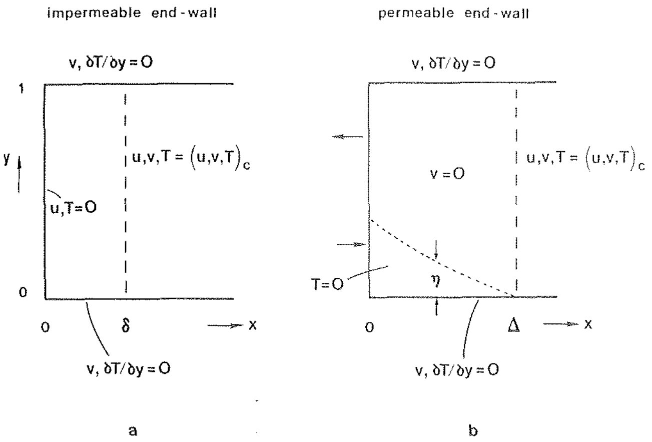

Fig. 2 Boundary conditions for end region integral analyses: (a) impermeable wall, (b) permeable wall

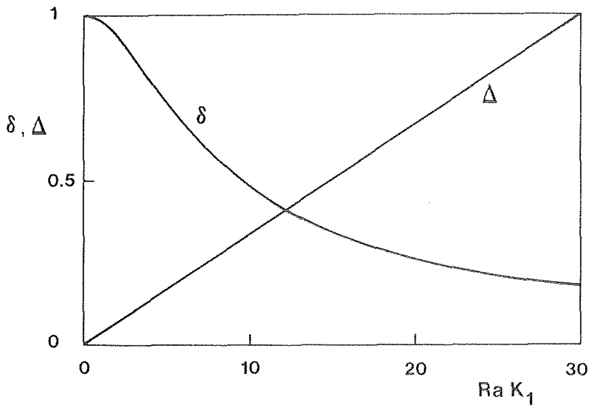

Fig. 3 End region lengths δ, Δ versus Ra K_1

The Flow through a Permeable End-Wall. Consider the permeable end region outlined in Fig. 2(b). Unlike the impermeable end-wall case treated in the preceding section, the permeable wall allows the fluid to migrate across the end boundary confining the horizontal porous layer. If, as in Fig. 2(b), the permeable end region is situated at the cold end of the horizontal layer, a stream of isothermal ($T = 0$) fluid will steadily creep into the rectangular channel through the lower portion of the permeable wall. The isothermal layer thickness η decreases to zero as the cold layer feels the effect of the warmer stream flowing along the top half of the channel. It is important to know the extent of the developing region Δ, beyond which the lowest sheet of fluid warms up above the entrance temperature T_1. In what follows, we present an integral technique for estimating Δ in terms of Ra and the core region axial gradient constant K_1.

The momentum and energy equations (2, 3) and (4) integrated across the channel height h yield

$$u(x,1) - u(x,0) - \frac{d}{dx}\int_0^1 v\,dy = -\mathrm{Ra}\frac{d}{dx}\int_0^1 T\,dy \quad (23)$$

$$\frac{d}{dx}\int_0^1 uT\,dy = \frac{d^2}{dx^2}\int_0^1 T\,dy \quad (24)$$

As in the preceding section, we must select reasonable profiles for u, v, T which satisfy mass continuity and the $y = 0, 1$ boundary conditions. The analysis is greatly simplified if for the end region of Fig. 2(b) we choose

$$u = u_c, \quad v = 0 \quad (25)$$

$$T = \begin{cases} B(x)\,F\left(\dfrac{y-\eta}{1-\eta}\right), & \eta < y < 1 \\ 0, & 0 < y < \eta \end{cases} \quad (26)$$

where the function $F(\xi) = {}^1\!/\!_4\xi^2 - {}^1\!/\!_6\xi^3$ represents the y dependence in the core temperature distribution, equation (11), and B and η are both functions of x. At the point where the end region communicates with the core region,

$$B(\Delta) = \mathrm{Ra}\, K_1{}^2, \quad \eta(\Delta) = 0 \tag{27,28}$$

while, from equation (11), $T_c(\Delta, 0) = 0$ yields

$$K_1\Delta + K_2 = 0 \tag{29}$$

Thus, the selected velocity and temperature distributions match the core solutions where the two regions come in contact. Substituting expressions (25) and (26) into equations (23) and (24) leads to two differential equations for $B(x)$ and $\eta(x)$

$$\frac{d}{dx}\,[B(1-\eta)] = 24\, K_1 \tag{30}$$

$$\frac{d}{dx}\left[B(1-\eta)\left(1+\frac{3}{2}\eta\right)\right] = 0 \tag{31}$$

Skipping some of the algebra, integrating equations (30) and (31) introduces two unknown constants which are determined as follows. The constant resulting from integrating (31) is determined from condition (27, 28). The resulting expression for $B(x)$ in terms of $\eta(x)$ is

$$\frac{B}{\mathrm{Ra}\, K_1{}^2} = \frac{1}{(1-\eta)\left(1+\frac{3}{2}\eta\right)} \tag{32}$$

which has a minimum at $\eta = 1/6$. Since $B(x)$ represents the temperature along the very top of the channel, it is reasonable to assume that B decreases gradually reaching its minimum just as the warm stream exits the end region to the left through the permeable wall (see Fig. 2(b)). This assumption constitutes the condition necessary for estimating the constant remaining from integrating equation (30), i.e., $\eta = 1/6$ at $x = 0$. The choice of η at $x = 0$ is of course arbitrary and adds to the approximate nature of the integral analysis. However, it can be verified that different values of η at $x = 0$ lead to expressions for Δ which come close to that (i.e., equation (33) obtained below) based on $\eta = 1/6$.

Finally, the integral of equation (30) is combined with condition (28) yielding the result we have been seeking,

$$\Delta = \frac{1}{30}\,\mathrm{Ra}\, K_1. \tag{33}$$

Combining now equations (33) and (29) we obtain the condition to be satisfied by the core constants K_1 and K_2 if, as in Fig. 2(b), the cold end has a permeable wall. The corresponding condition for a warm permeable wall is obtained by combining equation (33) with

$$T_c\left(\frac{L}{h} - \Delta, 1\right) = 1 \tag{34}$$

The length of the permeable end region, Δ, depends only on Ra K_1 and is shown superimposed on Fig. 3.

Axial Heat Transfer Rate. The heat transfer through the porous layer of Fig. 1 can now be calculated with the Nusselt number formula (13). Constant K_1 is determined by accounting for the fact that, for example, both end-walls of the cavity confining the porous medium are impermeable. The mathematical tools for estimating K_1 are equations (21) and (22) plus the centrosymmetry condition indicating that when the end-walls are identical the temperature field in the porous medium is symmetric about the center of the rectangular cavity.

$$T\left(\frac{1}{2}\frac{L}{h}, \frac{1}{2}\right) = \frac{1}{2} \tag{35}$$

Eliminating δ and K_2 between equations (21), (22) and (35) leads to the desired relationship between K_1 and the dimensionless groups characterizing the problem, Ra and L/h. This relationship is shown plotted in Fig. 4 where, for a given Ra and L/h, K_1 can be located through trial and error. The procedure for finding K_1 graphically is aided by the fact that $K_1 \ll h/L$, hence $K_1 = h/L$ may be used as a first guess. For more accurate results, K_1 can be found by numerically solving the sstem provided by equations (21), (22) and (35).

If both ends of the horizontal layer are permeable, K_1 and K_2 are calculated by combining equations (29), (33) and (34). The K_1 result is a quadratic

$$\frac{1}{60}\,\mathrm{Ra}\, K_1{}^2 + \frac{L}{h} K_1 - 1 = 0 \tag{36}$$

which, next to equation (13), represents the necessary device for calculating the Nusselt number. For comparison, equation (36) is also shown plotted in Fig. 4. For the same Ra and L/h, the axial temperature gradient in the core of a porous layer bounded by permeable end-walls is steeper than if the same layer was bounded by impermeable end-walls.

Finally, the intermediate configuration is handled by combining the integral conditions obtained for flow around an impermeable wall, equations (21) and (22), with the conditions valid for a permeable wall, equations (33) and (34). Eliminating K_2, δ and Δ from the four equations leads to a relationship between K_1 and the known parameters Ra and L/h. On Fig. 4, this relationship falls above the case with both ends permeable and below the case with both ends impermeable. We conclude that, for the same Rayleigh number and aspect ratio, the end-wall permeability yields a higher K_1 and consequently a higher Nusselt number for axial heat transport.

We can now compare the Nusselt number predicted by the present theory with published numerical heat transfer data for moderately shallow cavities filled with a porous medium [5, 6]. No experimental data are available for the system of Fig. 1. For $h/L = 0.5$ and Ra = 50 the Nusselt number calculated based on formula (13) and Fig. 4 when both ends are impermeable is 1.77. For the same h/L and Ra, Burns, Chow and Tien [5] and Bankvall [6] have found 1.54 and 1.43, respectively. For $h/L = 0.5$ and Ra = 100, this theory yields Nu = 2.80 compared with 2.81 reported by Burns, Chow and Tien and 2.30 by Bankvall. It should be pointed out that the accuracy in the numerical values indicated above is probably questionable due to the coarse grid employed for low aspect ratios. Since these studies were concerned primarily with the case of large aspect ratios, more accurate runs were made only for large aspect ratios. Still, the agreement is surprisingly good considering that $h/L = 0.5$ is actually very high for the present theory which was developed based on the assumption that a core re-

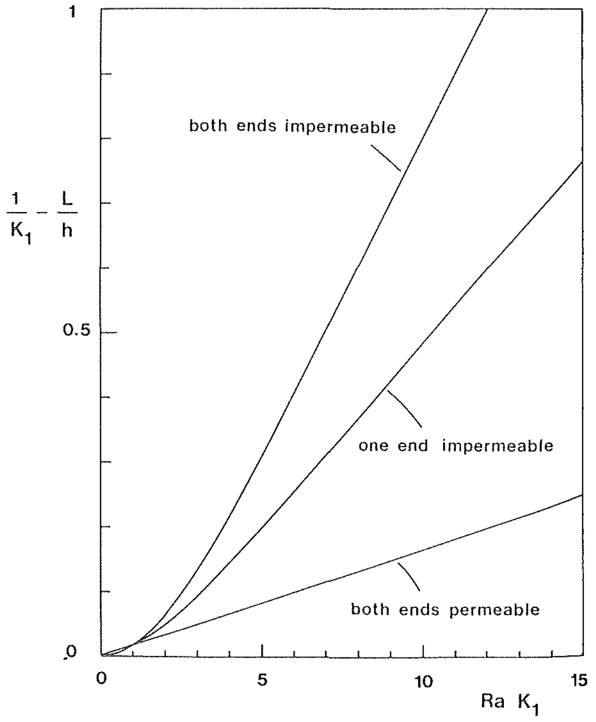

Fig. 4 Chart for constant K_1 as a function of Ra and L/h

gion exists ($h/L \ll 1$). The agreement improves as the Rayleigh number increases. This behavior is explained by the fact that at higher Rayleigh numbers the core region is less important, the heat transfer resistance associated with the two vertical end-walls dominating the resistance due to the counterflow heat exchanger pattern present in the core region (Fig. 1).

Horizontal Cylinder

The second part of this paper deals with natural convection in a long horizontal cylinder filled with a porous medium. The system schematic is shown in Fig. 5 along with the relevant quantities used in the analysis. The two end plates of the cylinder are maintained at different temperatures while the round horizontal wall is adiabatic and impermeable. The objective of the analysis is to predict the Nusselt number for axial heat transport through the porous medium. Three distinct situations will be considered: the case when the two end-walls are impermeable, the case with both end-walls permeable and, finally, the case when one end-wall is permeable and the other is not.

Since the method of solution for the horizontal cylinder proceeds on a path identical to the one presented previously for the two-dimensional porous layers, only the highlights of this analysis will be stressed. The nondimensional equations governing conservation of mass, momentum and energy in the cylindrical frame of Fig. 5 are

$$\frac{u}{r} + \frac{\partial u}{\partial r} + \frac{1}{r}\frac{\partial v}{\partial \theta} + \frac{\partial w}{\partial z} = 0, \quad u = -\frac{\partial P}{\partial r} + \mathrm{Ra}_0\, T \sin\theta \qquad (37,38)$$

$$v = -\frac{1}{r}\frac{\partial P}{\partial \theta} + \mathrm{Ra}_0\, T \cos\theta, \quad w = -\frac{\partial P}{\partial z} \qquad (39,40)$$

$$u\frac{\partial T}{\partial r} + \frac{v}{r}\frac{\partial T}{\partial \theta} + w\frac{\partial T}{\partial z} = \nabla^2 T \qquad (41)$$

in which P and T are defined in equations (7) and (8), and

$$u, v, w = \frac{r_0}{\alpha}(u^*, v^*, w^*), \quad r, z = (r^*, z^*)/r_0 \qquad (42,43)$$

$$\mathrm{Ra}_0 = \frac{g\beta r_0 K (T_2 - T_1)}{\alpha\nu} \qquad (44)$$

Below, we develop solutions to equations (37–41) subject to the boundary conditions of Fig. 5 in three main regions: the flow in the core region, the flow around in impermeable end-wall and the flow through a permeable end-wall.

The Flow in the Core Region. A perturbation analysis in Ra_0 as a small parameter was employed for deriving the main velocity and temperature field components in the core region. As usual, we assume series expressions for velocity and temperature,

$$(u, v, w)_c = (u, v, w)_0 + (u, v, w)_{\mathrm{I}}\, \mathrm{Ra}_0 + (u, v, w)_{\mathrm{II}}\, \mathrm{Ra}_0^2 + (u, v, w)_{\mathrm{III}}\, \mathrm{Ra}_0^3 + \ldots \qquad (45)$$

$$T_c = T_0 + T_{\mathrm{I}}\, \mathrm{Ra}_0 + T_{\mathrm{II}}\, \mathrm{Ra}_0^2 + T_{\mathrm{III}}\, \mathrm{Ra}_0^3 + \ldots \qquad (46)$$

Substituting expressions (45) and (46) into the governing equations and equating the terms containing the same power of Ra_0 leads to systems of equations for each set of coefficients (u, v, w, T). Before carrying out the perturbation analysis it is convenient to eliminate P between the three momentum equations (38–40) and obtain:

$$\frac{\partial u}{\partial \theta} - \frac{\partial}{\partial r}(rv) = \mathrm{Ra}_0 \left[\sin\theta \frac{\partial T}{\partial \theta} - r\cos\theta \frac{\partial T}{\partial r}\right] \qquad (47)$$

$$-\frac{\partial w}{\partial r} = \mathrm{Ra}_0 \sin\theta \frac{\partial T}{\partial z} \qquad (48)$$

Equations (47), (48) plus (37), (41) are the four relations needed for determining u, v, w, T. The zeroth order components are

$$(u, v, w)_0 = 0, \quad T_0 = K_1 z + K_2 \qquad (49,50)$$

corresponding to pure heat conduction in the cylindrical rod of Fig. 5. We see that in the $\mathrm{Ra}_0 \to 0$ limit, $K_2 \to 0$ while the axial gradient constant K_1 approaches r_0/L.

The first order solution reveals a free convection effect similar to the one discussed for two-dimensional layers,

$$(u, v)_{\mathrm{I}} = 0, \quad w_{\mathrm{I}} = -K_1 r \sin\theta \qquad (51,52)$$

$$T_{\mathrm{I}} = \frac{1}{8} K_1^2 \sin\theta (3r - r^3) \qquad (53)$$

Solution (51–53) satisfies the adiabatic and impermeable condition at $r = 1$. We see that the end-to-end ΔT induces a counterflow in the horizontal direction with the warmed branch occupying the top half of the cross section. The first order velocity and temperature distributions are sketched in Fig. 6.

The second order solution shows the first signs of radial and tangential motion,

$$u_{\mathrm{II}} = \frac{1}{48} K_1^2 \cos 2\theta (r^3 - r), \quad v_{\mathrm{II}} = \frac{1}{48} K_1^2 \sin 2\theta (r - 2r^3) \qquad (54,55)$$

$$(w, T)_{\mathrm{II}} = 0 \qquad (56)$$

The fact that the first order isotherms of Fig. 6 are not straight and horizontal as in the two-dimensional geometry of Fig. 1 causes eddies in each of the four quadrants of a vertical cross section. Fig. 7 shows the streamlines of this secondary flow, the streamfunction being defined as $\partial\Psi_{\mathrm{II}}/\partial\theta = -r u_{\mathrm{II}}$, $\partial\Psi_{\mathrm{II}}/\partial r = v_{\mathrm{II}}$. The net effect of this flow is an improved thermal contact between the upper layer and the lower layer by natural heat convection vertically downward. This effect becomes evident as we derive the third order solution for w and T which will later be used for calculating the Nusselt number for axial

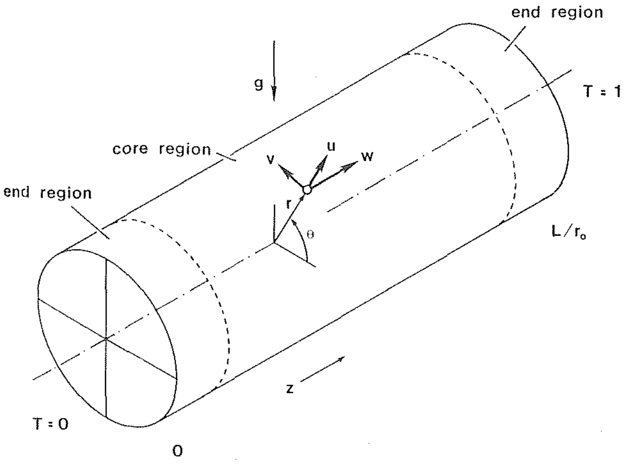

Fig. 5 Horizontal cylinder filled with a porous medium subjected to an end-to-end temperature difference.

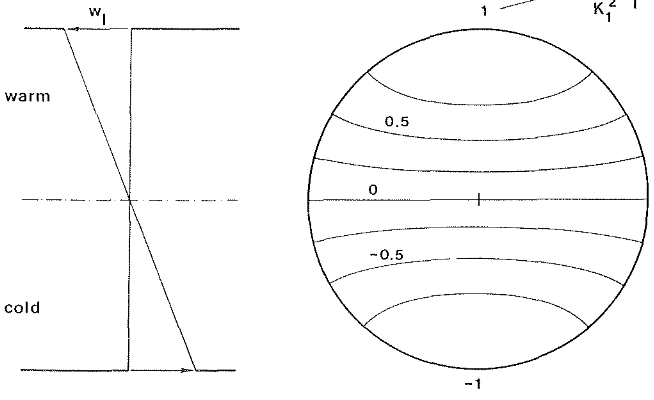

Fig. 6 First order solution for the core velocity and temperature distribution in the cylinder cross section.

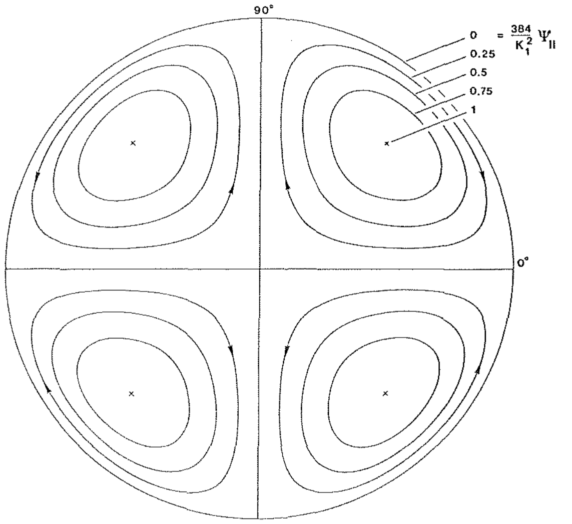

Fig. 7 Streamlines of second order velocity distribution in the core region

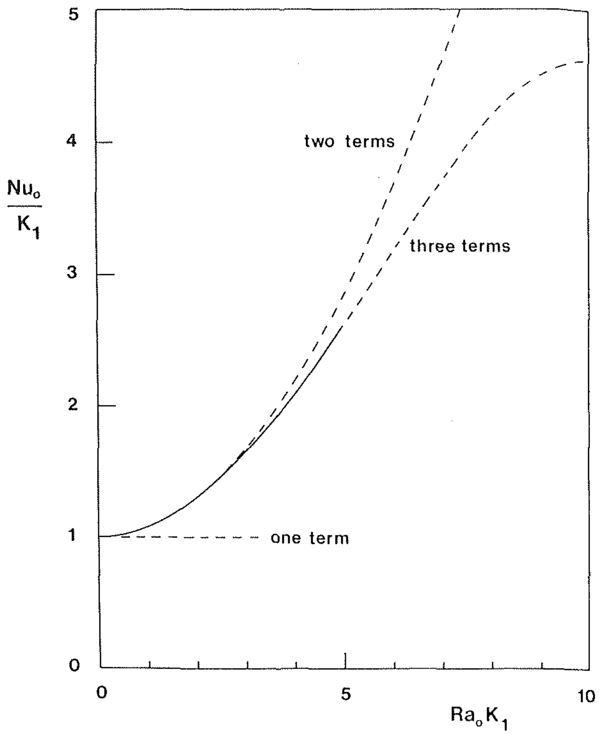

Fig. 8 The Nusselt number versus the Rayleigh number and K_1, equation (60)

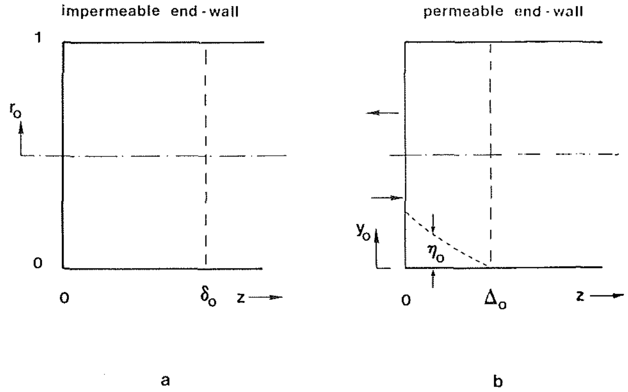

Fig. 9 Boundary conditions for end region integral analyses: (a) impermeable wall, (b) permeable wall

heat transfer [see equation (60)]. We obtain

$$w_{III} = 0 \tag{57}$$

$$T_{III} = \frac{K_1^4}{12288}\left[\frac{1}{5}(63r^3 - 35r^5 - 2r^7)\sin 3\theta + \frac{1}{3}(-73r + 36r^3 - 14r^5 + 5r^7)\sin\theta\right] \tag{58}$$

The Nusselt number Nu_0 for axial heat transfer is defined as

$$Nu_0 = \frac{\dot{Q}_0}{\pi r_0 k(T_2 - T_1)} = \frac{1}{\pi}\int_0^{2\pi}\int_0^1 \left(\frac{\partial T}{\partial z} - wT\right) r dr\, d\theta \tag{59}$$

Using the w, T expressions resulting from the perturbation analysis with coefficients up to the third order we obtain

$$Nu_0 = K_1\left(1 + \frac{7}{96}Ra_0^2 K_1^2 - \frac{3}{8192}Ra_0^4 K_1^4 + \ldots\right) \tag{60}$$

Taking only the first two terms, expression (60) is similar to the Nu result obtained for two-dimensional porous layers. The third terms represents the decrease in axial heat transfer due to improved vertical heat transfer caused by the eddies of Fig. 7. Expression (60) has been plotted on Fig. 8 suggesting that the three-term approximation for Nu_0 is probably satisfactory as long as $Ra_0 K_1$ is less than 5. For higher values of Ra_0 K_1 (large ΔT's, short cylinders), the perturbation analysis has to be carried beyond the third order solution presented here.

In order to estimate the Nusselt number we first have to determine the temperature gradient constant K_1 by taking into account the flow and temperature pattern in the two end regions. This work is presented in the next two sections.

The Flow Around an Impermeable End. The approximate velocity and temperature profiles assumed for the integral analysis of an impermeable end are

$$u = -\frac{3}{2}\frac{Ra_0 K_1}{\delta_0}(1 - r^2)\left(1 - \frac{z}{\delta_0}\right)^2 \sin\theta \tag{61}$$

$$v = -\frac{3}{2}\frac{Ra_0 K_1}{\delta_0}(1 - r^2)\left(1 - \frac{z}{\delta_0}\right)^2 \cos\theta \tag{62}$$

$$w = -Ra_0 K_1 r\left[3\frac{z}{\delta_0} - 3\left(\frac{z}{\delta_0}\right)^2 + \left(\frac{z}{\delta_0}\right)^3\right]\sin\theta \tag{63}$$

$$T = (T_c - K_1\delta_0)\left[2\frac{z}{\delta_0} - \left(\frac{z}{\delta_0}\right)^2\right] + K_1 z \tag{64}$$

Expressions (61–64) satisfy the boundary conditions listed in Fig. 9(a), as well as the continuity equation (37). The impermeable end region is located at the cold end and is assumed to have an axial length δ_0.

The momentum integral condition is deduced by first eliminating the pressure terms between equations (38) and (40) and again between equations (39) and (40). Multiplying the u result by $\sin\theta$ and the v result by $\cos\theta$, the two equations are summed up to yield an unique momentum condition

$$\left(\frac{\partial u}{\partial z} - \frac{\partial w}{\partial r}\right)\sin\theta + \left(\frac{\partial v}{\partial z} - \frac{\partial w}{r\partial\theta}\right)\cos\theta = Ra_0\frac{\partial T}{\partial z} \tag{65}$$

Using the assumed u, v, w, T profiles, equations (65) and (41) are then integrated over the entire volume occupied by the impermeable end region to yield the momentum and energy integral conditions for an impermeable end:

$$\frac{1}{4}K_1\left(\frac{3}{\delta_0^2} - 1\right) = \frac{K_2}{\delta_0} \tag{66}$$

$$\frac{1}{96}\mathrm{Ra}_0^2 K_1^3 - \frac{3}{8192}\mathrm{Ra}_0^4 K_1^5 = 2\frac{K_2}{\delta_0} \tag{67}$$

Conditions (66), (67) are equivalent to equations (21) and (22) obtained in Part I. Eliminating δ_0 they provide a relation between K_1 and K_2, as well as a way of estimating the extent of the impermeable end region in terms of $\mathrm{Ra}_0 K_1$ showing that δ_0 approaches $\sqrt{3}$ as $\mathrm{Ra}_0 K_1 \rightarrow 0$ (see Fig. 10).

The Flow Through a Permeable End. The objective of this integral analysis is to estimate the distance Δ_0 beyond which the cold isothermal fluid creeping along the bottom of the cylinder starts warming up, thus entering the core region. The situation is described schematically in Fig. 9(b). The assumed velocity and temperature distribution in the $0 < z < \Delta_0$ region is

$$u = 0, \quad v = 0 \tag{68}$$

$$w = -\mathrm{Ra}_0 K_1 r \sin\theta \tag{69}$$

$$T = \begin{cases} B_0(z)\dfrac{y_0 - \eta_0}{2(2-\eta_0)}, & \eta_0 < y_0 < 2 \\ 0, & 0 < y_0 < \eta_0 \end{cases} \tag{70}$$

where $y_0 = 1 + r\sin\theta$ is the vertical coordinate measured from the bottom of the cylinder and η_0 is isothermal layer thickness. Due to its simplicity, the temperature distribution (70) does not obey the $\partial T/\partial r = 0$ condition at $r = 1$. At $z = \Delta_0$ the temperature distribution is forced to match the core temperature for the top and bottom of the cross-section by setting

$$B_0(\Delta_0) = \frac{\mathrm{Ra}_0 K_1^2}{2}\left(1 - \frac{77}{11520}\mathrm{Ra}_0^2 K_1^2\right) \tag{71}$$

$$\eta_0(\Delta_0) = 0 \tag{72}$$

Writing $T_c = 0$ for $z = \Delta_0$, $\theta = -\pi/2$ and $r = 1$ in equation (46), and using equations (50, 53) and (58) we also must have

$$K_1\Delta_0 + K_2 = \frac{\mathrm{Ra}_0 K_1^2}{4}\left(1 - \frac{77}{11520}\mathrm{Ra}_0^2 K_1^2\right) \tag{73}$$

Substituting expressions (68–70) into the momentum equation (65) and the energy equation (41), and integrating over the circular cross section yields two differential equations for $B_0(z)$ and $\eta_0(z)$:

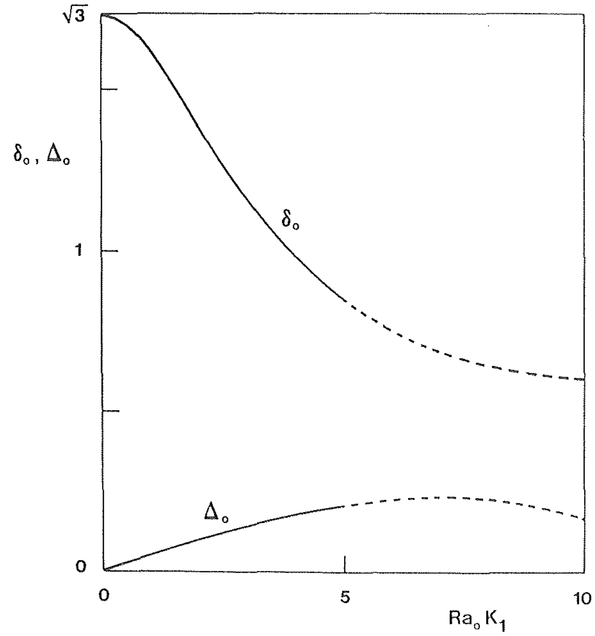

Fig. 10 End region lengths δ_0, Δ_0 versus $\mathrm{Ra}_0 K_1$

$$\frac{d}{dz}\left[\frac{B_0(z)D(\beta_0)}{2-\beta_0}\right] = \pi K_1, \quad \frac{d}{dz}\left[\frac{B_0(z)E(\beta_0)}{2-\beta_0}\right] = 0 \tag{74,75}$$

where

$$D(\beta_0) = \frac{1}{3}[1-(1-\beta_0)^2]^{3/2} + \frac{1}{2}(1-\beta_0)\{\cos^{-1}(\beta_0 - 1) + (1-\beta_0)[1-(1-\beta_0)^2]^{1/2}\} \tag{76}$$

$$E(\beta_0) = \frac{1}{3}(1-\beta_0)[1-(1-\beta_0)^2]^{3/2} + \frac{1}{8}\{\cos^{-1}(\beta_0-1) - (1-\beta_0)[1-(1-\beta_0)^2]^{1/2}[1-2(1-\beta_0)^2]\} \tag{77}$$

As in Part I, after equations (74) and (75) are integrated, $B_0(z)$ is chosen to reach its minimum right at the permeable wall, $z = 0$. We find this way $\eta_0(0) = 0.525$ and, using condition (72),

$$\Delta_0 = \frac{1.5787}{32}\mathrm{Ra}_0 K_1\left(1 - \frac{77}{11520}\mathrm{Ra}_0^2 K_1^2\right) \tag{78}$$

Equation (78) is shown plotted in Fig. 10, indicating again that the three-term perturbation solution approximation breaks down for values of $\mathrm{Ra}_0 K_1$ greater than about 5. Equations (73) and (78) are the needed temperature end conditions relating K_1 and K_2 if the cold end is permeable.

Axial Heat Transfer Rate. The Nusselt number for axial heat transport is provided by equation (60), with the temperature gradient constant K_1 determined from the two end conditions. For example, if both ends of the cylindrical enclosure are impermeable we use equations (66) and (67) plus the centrosymmetry condition

$$T_c = \frac{1}{2} \text{ at } r = 0, \quad z = \frac{1}{2}\frac{L}{r_0} \tag{79}$$

The implicit result for K_1 is shown on Fig. 11. For a given Ra_0 and aspect ratio L/r_0, K_1 can be found through trial and error, remembering that $K_1 \leqslant r_0/L$.

The procedure outlined at the end of Part I is repeated to calculate K_1 for a cylinder with both ends permeable and for a cylinder with only one end permeable. The resulting implicit expressions for K_1 are also plotted on Fig. 11, showing once again that the perturbation solution worked out in this study is adequate if $\mathrm{Ra}_0 K_1 < 5$.

Concluding Remarks

In order to understand the basic mechanism of heat transfer by natural convection through a porous medium, natural convection in a horizontal porous layer has been studied analytically. Two configurations have been considered. In the first part of this paper we studied the natural counterflow induced in a two-dimensional porous layer by an end-to-end temperature difference. In the second part we

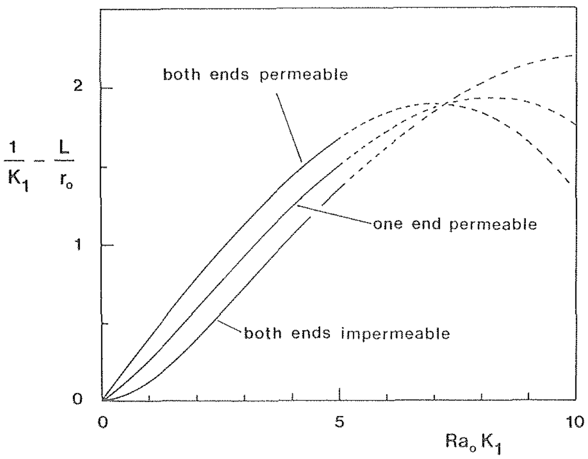

Fig. 11 Chart for constant K_1 as a function of Ra_0 and L/r_0

considered the same free convection phenomenon in a horizontal cylinder subjected to an end-to-end temperature difference.

The results demonstrate the dependence of the Nusselt number for axial heat transfer on the Rayleigh number and the aspect ratio of the horizontal porous medium. The influence of end-wall permeability on axial heat transfer has been examined. For a parallel-plate layer, the end-wall permeability significantly increases the rate of heat transfer through the porous medium. For a cylindrical porous medium, the effect of end-wall permeability on the Nusselt number is not as clear due to the asymptotic character of the perturbation analysis (valid when $Ra_0 K_1 < 5$).

Acknowledgment

A. Bejan acknowledges the support received from The Miller Institute for Basic Research in Science, University of California, Berkeley, in the form of a postdoctoral research fellowship.

References

1 Cheng, P., "Similarity Solutions for Mixed Convection from Horizontal Impermeable Surfaces in Saturated Porous Media," *International Journal of Heat and Mass Transfer*, Vol. 20, p. 893, 1977.

2 Bories, S. A. and Combarnous, M. A., "Natural Convection in a Sloping Porous Layer," *Journal of Fluid Mechanics*, Vol. 57, p. 63, 1973.

3 Weber, J. E., "Convection in a Porous Medium with Horizontal and Vertical Temperature Gradients," *International Journal of Heat and Mass Transfer*, Vol. 17, p. 241, 1974.

4 Chan, B. K. C., Ivey, C. M. and Barry, J. M., "Natural Convection in Enclosed Porous Media with Rectangular Boundaries," ASME JOURNAL OF HEAT TRANSFER, Vol. 92, p. 21, 1970.

5 Burns, P. J., Chow, L. C. and Tien, C. L., "Convection in a Vertical Slot Filled with Porous Insulation," *International Journal of Heat and Mass Transfer*, Vol. 20, p. 919, 1977.

6 Bankvall, C. G., "Natural Convection in Vertical Permeable Space," *Wärme-und Stoffübertragung*, Vol. 7, 1974, p. 22–30.

7 Cormack, D. E., Leal, L. G. and Imberger, J., "Natural Convection in a Shallow Cavity with Differentially Heated End-Walls. Part 1. Asymptotic Theory," *Journal of Fluid Mechanics*, Vol. 65, p. 209, 1974.

8 Cormack, D. E., Leal, L. G. and Seinfeld, J. H., "Natural Convection in a Shallow Cavity with Differentially Heated End-Walls. Part 2. Numerical Solutions," *Journal of Fluid Mechanics*, Vol. 65, p. 231, 1974.

9 Imberger, J., "Natural Convection in a Shallow Cavity with Differentially Heated End-walls. Part 3. Experimental Results," *Journal of Fluid Mechanics*, Vol. 65, p. 247, 1974.

10 Hong, S. W., "Natural Circulation in Horizontal Pipes," *International Journal of Heat and Mass Transfer*, Vol. 20, p. 685, 1977.

11 Bejan, A. and Tien, C. L., "Fully-Developed Natural Counterflow in a Long Horizontal Pipe with Different End Temperatures," accepted for publication in the *International Journal of Heat and Mass Transfer*.

12 Muskat, M., *The Flow of Homogeneous Fluids through Porous Media*, J. W. Edwards, Michigan, 1946.

Corrections to "Natural Convection in a Horizontal Porous Medium Subjected to an End-to-End Temperature Difference," by A. Bejan and C. L. Tein, published in the May 1978 issue of the ASME JOURNAL OF HEAT TRANSFER, pp. 191-198.

We wish to report two algebraic errors that appear in equations (22) and (33) of our paper on natural convection in a horizontal porous layer with different end temperatures. The corrected equations are

$$\frac{1}{240}\delta \mathrm{Ra}^2 K_1{}^3 = K_2 + \frac{1}{24}\mathrm{Ra}\,K_1{}^2 \tag{22}$$

$$\Delta = \frac{1}{120}\mathrm{Ra}\,K_1 \tag{33}$$

In the published version, two of the numerical coefficients (1/240 and 1/120 in the above equations) are erroneously reported as 1/120 and 1/30, respectively.

These errors explain the limited range of agreement between the heat transfer rate predicted by our published solution and the heat transfer rates calculated numerically by Hickox and Gartling [2]. As shown in Fig. 1 and Table 1, the corrected integral theory of our paper agrees very well with all the data reported numerically by Hickox and Gartling [1].

We wish to thank Mr. Ulrich Riebel of the University of Karlsruhe, West Germany, for pointing out these errors.

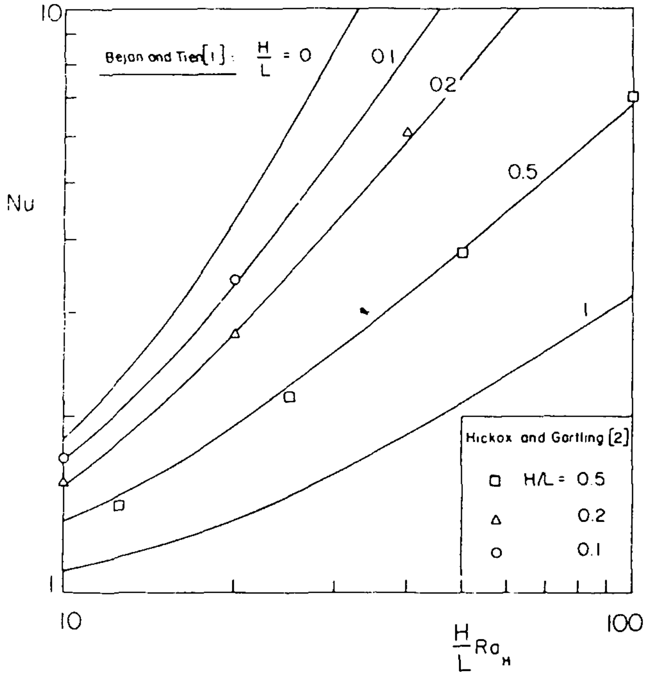

Fig. 1 The heat transfer rate in a shallow porous layer with different end temperatures

Table 1 Heat transfer results for natural convection in a porous layer heated from the side (height/length = 0.5)

Rayleigh number based on height	Conduction-referenced Nusselt number, Nu	
Ra	numerical, [1]	theoretical[a]
25	1.410	1.4577
50	2.155	2.2413

[a] corrected from Bejan and Tien paper

References

1 Hickox, C. E., and Gartling, D. K., "A Numerical Study of Natural Convection in a Horizontal Porous Layer Subjected to an End-to-End Temperature Difference," ASME JOURNAL OF HEAT TRANSFER, Vol. 103, 1981, pp. 797-802.

S. I. Abdel-Khalik
H-W. Li
Nuclear Engineering Department

K. R. Randall
Mechanical Engineering Department
University of Wisconsin,
Madison, Wis.

Natural Convection In Compound Parabolic Concentrators—A Finite-Element Solution

Natural convection heat transfer coefficients between absorber surfaces and cover plates for vertically oriented two-dimensional compound parabolic concentrators (CPC) are evaluated using finite-element techniques. Values of the critical Rayleigh number for different concentrations (2 < C < 10) with 1/3, 2/3, and full CPC heights are determined. Generalized charts for estimating the average absorber plate Nusselt number as a function of Rayleigh number and concentration for both full and truncated CPC cavities are given. The results are useful for evaluating the covective loss coefficients from such collectors.

Introduction

Compound parabolic concentrators have been recently proposed for solar energy collection [1].[1] For a given acceptance angle, these non-imaging concentrators can theoretically achieve the highest possible concentration [1–3]. Fig. 1 depicts a cross section of a two-dimensional CPC cavity (trough). For a full CPC with air as the cavity medium, the concentration C is given by: $C \equiv \ell/s$; $C_{\max} = 1/\sin \phi$, where ℓ and s are the aperture and absorber width, and ϕ is half the acceptance angle. All the incident light on the CPC with angles less than ϕ will reach the absorber surface. Radiation outside the acceptance angle will be rejected through the aperture surface (cover plate) after bouncing back and forth between the parabolic specular reflectors. The height/absorber ratio for a full CPC is given by: $h_{\text{full}}/s = (1 + \sin \phi)/2 \sin \phi \tan \phi$; this ratio becomes very large as C increases (Table 1). In practice, CPCs are usually truncated by cutting off a large portion of the top without much loss in performance. A summary of the main geometrical parameters for full and truncated CPCs with different concentrations is given in Table 1.

Knowledge of the loss coefficients for these collectors and their dependence on the different geometrical and operational parameters is necessary for evaluating their thermal performance. Numerous experimental and analytical studies on natural convection in simple rectangular enclosures have been reported in the literature [4–9]. The errors involved in using the results of these investigations for the more complicated CPC geometries can not be estimated without prior knowledge of the performance of the actual system. Earlier analytical studies of natural convection in enclosures have used either finite-difference or collocation techniques. These techniques become rather cumbersome when used over regions with irregular boundaries. Finite-element methods are well-suited for such problems.

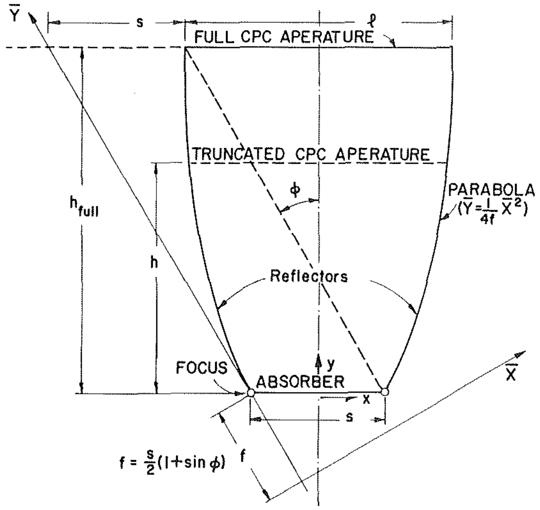

Fig. 1 Schematic diagram of a CPC cavity

Table 1 Geometrical parameters for CPC cavities considered in this investigation

Concen-tration†		Full CPC		Truncated CPC			
		$(h = h_{\text{full}})$		$(h = 2/3\, h_{\text{full}})$		$(h = 1/3\, h_{\text{full}})$	
C	ϕ	h/ℓ	h/s	h/ℓ	h/s	h/ℓ	h/s
2.0	30.0°	1.299	2.598	0.898	1.732	0.523	0.866
4.0	14.5°	2.420	9.681	1.678	6.454	1.009	3.227
6.0	9.6°	3.445	20.67	2.388	13.78	1.435	6.890
8.0	7.2°	4.465	35.72	3.091	23.81	1.850	11.91
10.0	5.7°	5.472	54.72	3.786	36.48	2.260	18.24

† For truncated CPC cavities, the concentrations given are those which would be obtained if the CPC's were to be extended to their full heights.

---

[1] Numbers in brackets designate References at end of paper.

Contributed by The Heat Transfer Division for publication in the JOURNAL OF HEAT TRANSFER. Manuscript received by the Heat Transfer Division November 21, 1977.

The use of finite-element methods to solve complex flow problems has expanded dramatically in recent years [10, 11]. Here, we shall use these methods to study natural convection in two-dimensional CPC cavities. Our main objective is to determine the convective loss coefficient from such collectors and its dependence on the different geometrical and operational parameters. Values of the critical Rayleigh number for different concentrations with full and truncated CPC geometries are also obtained. This study is limited to vertically oriented CPCs. In practice, the collectors are mounted so that they would face the sun; the tilt angle is nearly equal to the latitude.

Theoretical Analysis

The governing equations for steady buoyancy-driven flows in two-dimensional regions with no volumetric heating are [12]:

Continuity Equation

$$\frac{\partial u}{\partial x}+\frac{\partial v}{\partial y}=0 \qquad (1)$$

Momentum Equations:

$$u\frac{\partial u}{\partial x}+v\frac{\partial u}{\partial y}=\frac{-1}{\rho_0}\frac{\partial p}{\partial x}+\nu\left(\frac{\partial^2 u}{\partial x^2}+\frac{\partial^2 u}{\partial y^2}\right) \qquad (2)$$

$$u\frac{\partial v}{\partial x}+v\frac{\partial v}{\partial y}=-\frac{1}{\rho_0}\frac{\partial p}{\partial y}+g\beta(T-T_0)+\nu\left(\frac{\partial^2 v}{\partial x^2}+\frac{\partial^2 v}{\partial y^2}\right) \qquad (3)$$

Energy Equation:

$$u\frac{\partial T}{\partial x}+v\frac{\partial T}{\partial y}=\alpha\left[\frac{\partial^2 T}{\partial x^2}+\frac{\partial^2 T}{\partial y^2}\right] \qquad (4)$$

In the above equations, the Boussinesq approximation is utilized; y is the direction of gravity (Fig. 1) and the subscript 0 denotes conditions at the reference temperature T_0. Equations (1–4) can be written in terms of the following nondimensional variables:

$$\xi\equiv x/h,\quad \eta\equiv y/h,\quad u^*\equiv uh/\alpha$$

$$v^*\equiv vh/\alpha,\ p^*\equiv ph^2/\rho_0\alpha^2,\ \text{and}\ \theta\equiv\frac{T-T_\ell}{\Delta T_{\text{ref}}} \qquad (5)$$

The resulting equations can be rewritten in terms of the stream function ψ and vorticity ω to yield:

$$\frac{\partial^2\psi}{\partial\xi^2}+\frac{\partial^2\psi}{\partial\eta^2}=-\omega, \qquad (6)$$

$$\frac{\partial^2\theta}{\partial\xi^2}+\frac{\partial^2\theta}{\partial\eta^2}=\frac{\partial\psi}{\partial\eta}\frac{\partial\theta}{\partial\xi}-\frac{\partial\psi}{\partial\xi}\frac{\partial\theta}{\partial\eta}, \qquad (7)$$

and

$$\frac{\partial^2\omega}{\partial\xi^2}+\frac{\partial^2\omega}{\partial\eta^2}=\frac{1}{\text{Pr}}\left(\frac{\partial\psi}{\partial\eta}\frac{\partial\omega}{\partial\xi}-\frac{\partial\psi}{\partial\xi}\frac{\partial\omega}{\partial\eta}\right)-\text{Ra}\frac{\partial\theta}{\partial\xi} \qquad (8)$$

where,

$$u^*\equiv\frac{\partial\psi}{\partial\eta},\ v^*\equiv-\frac{\partial\psi}{\partial\xi},\ \text{and}\ \omega\equiv\frac{\partial v^*}{\partial\xi}-\frac{\partial u^*}{\partial\eta} \qquad (9)$$

Here, h is the height of the CPC cavity, and Pr and Ra are the Prandtl and Rayleigh numbers respectively as defined in the nomenclature.

Boundary Conditions. For a region surrounded by arbitrarily shaped solid boundaries, the no-slip condition at the wall yields:

$$\psi|_w=\text{constant}=0 \qquad (10a)$$

and

$$\left.\frac{\partial\psi}{\partial n}\right|_w=\text{zero} \qquad (10b)$$

where n is the normal direction at any point along the boundary. In addition, the temperature or heat flux may be prescribed at different segments along the boundary. For the CPC geometry shown in Fig. 1, the parabolic reflector walls are assumed to be adiabatic while the absorber is assumed to be isothermal at a temperature T_s higher than the uniform temperature T_ℓ of the cover plate. The sidewalls in a real concentrator will not be perfectly insulated; deviation from this ideal condition is design dependent. In addition, we assume the sidewalls to be perfect reflectors and the cover plate to be perfectly transparent to radiation so that radiation and convection effects would be uncoupled. In practice, the reflectivity of the parabolic surfaces will range from 0.75 to 0.95 [3] so that the sidewalls' temperature distributions will be slightly influenced by radiation.

The reference temperature difference ΔT_{ref} in equation (5) is set equal to $(T_s - T_\ell)$ while T_0 is equal to $(T_s + T_\ell)/2$. The boundary conditions for ω are obtained by combining equation (6) and the no-slip condition (10b) as outlined in Appendix A. A two-dimensional finite-element program has been developed to solve the above equations. The method of solution is described in Appendix A.

Results

The finite-element program described in Appendix A has been used to study natural convection in vertically oriented, two-dimensional CPC cavities (Fig. 1). Both full and truncated CPC's with different concentrations ($2.0 \le C \le 10.0$) have been investigated. A summary

Nomenclature

A_s = absorber area
C = concentration
$\mathbf{D}^{(e)}$ = element displacement matrix
E = total number of elements
F = function defined in equation (A-1)
$\mathbf{F}$ = $(M\times 1)$ vector containing the F values at the different nodes
g = gravitational acceleration
h = CPC cavity height
h_{full} = height of an untruncated CPC cavity
k = thermal conductivity
$\mathbf{K}$ = global conduction matrix
$\mathbf{K}^{(e)}$ = elemental conduction matrix
ℓ = aperture width
M = total number of nodes
n = direction of the normal at the boundary
Nu_s = average absorber plate Nusselt number
$\text{Nu}_{s,\text{cond}}$ = value of Nu_s under no-flow (conduction) conditions
$(\text{Nu}_s)_{E=\infty}$ = average absorber plate Nusselt number corresponding to infinite number of elements
p = static pressure
p^* = nondimensional pressure
Pr = Prandtl number $\equiv(\nu/\alpha)$
$\mathbf{Q}$ = global generation vector
Ra = Rayleigh number $\equiv(g\beta h^3\Delta T_{\text{ref}}/\alpha\nu)$
Ra_{crit} = critical Rayleigh number
s = absorber width
T = temperature
T_0 = reference temperature = $(T_s + T_\ell)/2$
T_s = absorber plate temperature
T_ℓ = cover plate temperature
ΔT_{ref} = reference temperature difference $\equiv (T_s - T_\ell)$
u = velocity component in the x direction
u^* = nondimensional velocity
v = velocity component in the y direction
v^* = nondimensional velocity
x,y = Cartesian coordinates
α = thermal diffusivity
β = coefficient of volume expansion
Δ = area of triangular element
η = nondimensional y coordinate
θ = nondimensional temperature
ν = kinematic viscosity
ξ = nondimensional x coordinate
ρ_0 = density at T_0
ϕ = half acceptance angle
ψ = stream function
$\psi|_w$ = stream function at the boundary (= zero)
ω = vorticity

of the main geometrical parameters for the different cases examined is given in Table 1. In all the following results a mesh of 200 triangular elements with 121 nodes (Fig. B-1) has been used. The effect of mesh size on the predicted Nusselt numbers is discussed in Appendix B; the differences between the predicted values using the 200-element mesh and those corresponding to the limit of infinite number of elements do not exceed 10 percent. The mesh size used is a compromise between accuracy and computing costs.

Variation of the average absorber plate Nusselt number $\mathrm{Nu}_{s,\mathrm{cond}}$ with concentration under no-flow (i.e., conduction) conditions is shown in Fig. 2. These results were directly obtained by solving the heat conduction equation subject to the temperature boundary conditions described in the previous section. For truncated CPC's, the concentration ratios used in Fig. 2 are those which would be obtained if the CPC's were to be extended to their full heights. The average absorber plate Nusselt number Nu_s is defined such that the total convective heat transfer rate from the absorber to the cover plate, q (watts), is given by: $q = \mathrm{Nu}_s k A_s (T_s - T_\ell)/h$, where k is the thermal conductivity of the cavity medium and A_s is the absorber area.

For a given cavity geometry, if the Rayleigh number exceeds the critical value, $\mathrm{Ra}_{\mathrm{crit}}$, the Nusselt number will, of course, be higher than that given by Fig. 2. Typical results showing the variation of Nu_s with Ra for a truncated CPC with $h/h_{\mathrm{full}} = 1/3$ and $C = 4.0$ are given in Fig. 3. These results were obtained using the finite-element program described in Appendix A. The critical Rayleigh number is obtained by extrapolating the convective Nusselt numbers to the conduction limit as shown in Fig. 3. Results similar to those shown in Fig. 3 have been used to determine the critical Rayleigh number for the different cases examined. These results (Fig. 4) show that the critical Rayleigh number increases markedly with concentration ratio reaching a value of approximately 7.5×10^5 for a full CPC with a concentration ratio of 10.0.

Variations of the average absorber plate Nusselt number with Rayleigh number and concentration ratio for full and truncated CPC cavities are shown in Figs. 5–7. The Nusselt numbers, Nu_s, are normalized relative to their corresponding conduction values $\mathrm{Nu}_{s,\mathrm{cond}}$ while the Rayleigh numbers, Ra, are normalized relative to their critical counterparts $\mathrm{Ra}_{\mathrm{crit}}$. For a given value of C and h/h_{full}, both $\mathrm{Nu}_{s,\mathrm{cond}}$ and $\mathrm{Ra}_{\mathrm{crit}}$ can be obtained from Figs. 2 and 4 respectively. The results given in Figs. 5–7 clearly show that convection is suppressed in high-concentration cavities where the height/aperture ratio is quite large (Table 1). Similar results for deep rectangular cavities with insulating side walls have been reported by Catton [13]. The restraining side walls affect the stability of the fluid layer and increase $\mathrm{Ra}_{\mathrm{crit}}$. (Fig. 4).

For truncated CPC cavities with $h/h_{\mathrm{full}} = 1/3$ and $C = 2.0$, the cavity is sufficiently "wide" so that a double-cell convection pattern is established. For all other cases examined here, a stable unicellular

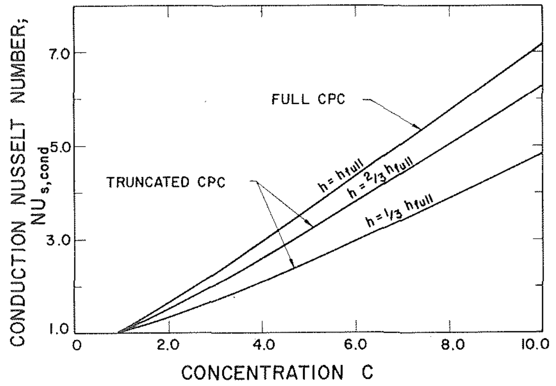

Fig. 2 Variation of the average absorber plate Nusselt number, $\mathrm{Nu}_{s,\mathrm{cond.}}$, with concentration ratio, C, under no-flow (conduction) conditions (See footnote after Table 1.)

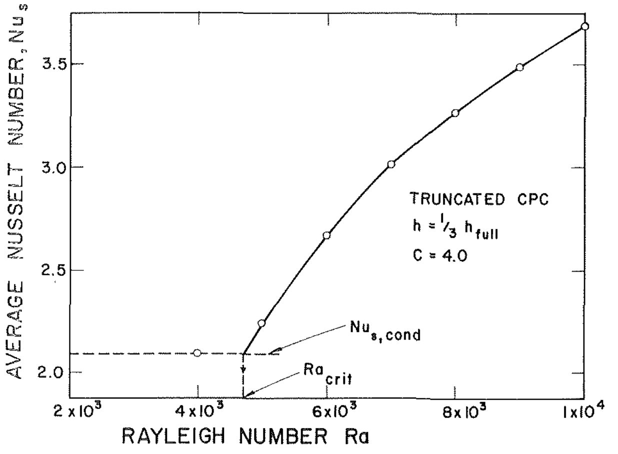

Fig. 3 Typical results showing variation of Nu_s with Ra for a truncated CPC with $h/h_{\mathrm{full}} = 1/3$ and $C = 4.0$

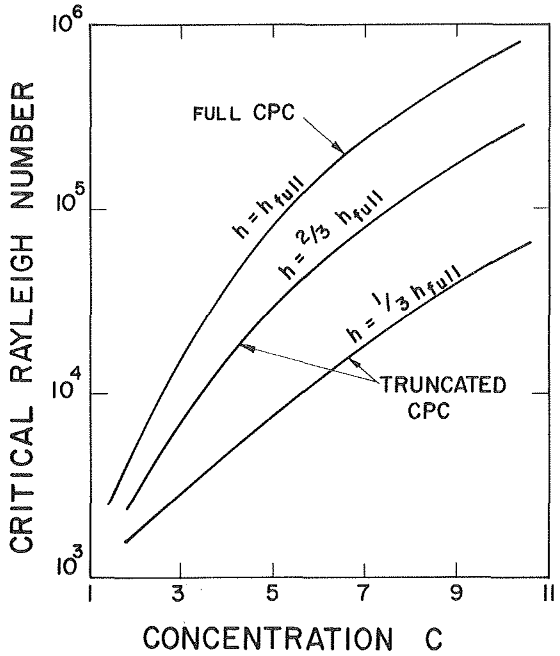

Fig. 4 Variation of the critical Rayleigh number, $\mathrm{Ra}_{\mathrm{crit}}$, with concentration for full and truncated CPC cavities (See footnote after Table 1.)

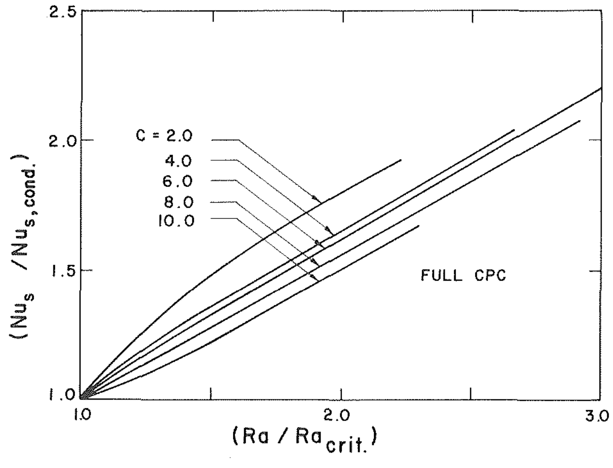

Fig. 5 Variation of $(\mathrm{Nu}_s/\mathrm{Nu}_{s,\mathrm{cond}})$ with $(\mathrm{Ra}/\mathrm{Ra}_{\mathrm{crit}})$ for full CPC cavities

pattern was obtained regardless of how the solution was initialized (i.e., even when the solution was initialized with a double-cell convection pattern). Typical plot showing the flow pattern in a cavity with a concentration of 4.0 at a Rayleigh number of 8.0×10^4 is given in Fig. 8. The temperature distributions along the side walls for different Rayleigh numbers are shown in Fig. 9.

Discussion and Conclusions

Finite-element methods have been used to study natural convection in vertically oriented, two-dimensional compound parabolic concentrators. Values of the critical Rayleigh number for full and truncated CPC cavities with different concentrations have been obtained. Generalized charts for estimating the average absorber plate Nusselt number as a function of Rayleigh number and concentration for CPC's with 1/3, 2/3, and full heights are given. These results clearly show that convection is suppressed at high concentrations as evidenced by the high critical Rayleigh numbers (Fig. 4) and the limited fractional increase in Nusselt numbers above their conduction values for a given fractional increase in Rayleigh number above Ra_{crit} (Figs. 5–7).

The generalized charts given in Figs. 5–7 can be readily used to determine the convective loss coefficients from two-dimensional CPC cavities. These figures cover wide ranges of concentration ($2 \leq C \leq 10$) and Rayleigh number ($2.0 \times 10^3 \leq Ra \leq 1.3 \times 10^6$) to be of use in practical systems (for a 5 cm deep CPC with T_s = 200°C and T_ℓ = 25°C, $Ra = 0.7 \times 10^5$). Caution should be exercised in extrapolating these results since at higher Rayleigh numbers than those shown in Figs. 5–7 a stable unicellular convection pattern can not be maintained and the numerical solution diverges. Similar behavior has been observed for simple rectangular cavities.

The grid size used in this investigation (200 elements) is a reasonable compromise between accuracy and computing cost. The Nusselt numbers given in Figs. 5–7 are less than 10 percent higher than those corresponding to the limit of inifinte number of elements (Appendix B). For a given concentration, the errors decrease with decreasing Rayleigh number reaching less than 1 percent for $Ra = Ra_{crit}$ (Fig. B3). Experimental verification of the results presented in this paper is necessary; however, such data do not exist at this time.

Acknowledgments

We are indebted to members of the Solar Energy Laboratory of the University of Wisconsin-Madison for stimulating our interest in this problem. Several discussions with Professors G. E. Myers and J. W. Mitchell of the Mechanical Engineering Department at the University of Wisconsin are appreciated.

Financial support for computing expenses has been provided by the U.S. Department of Energy under contract No. E(11-1)-2588.

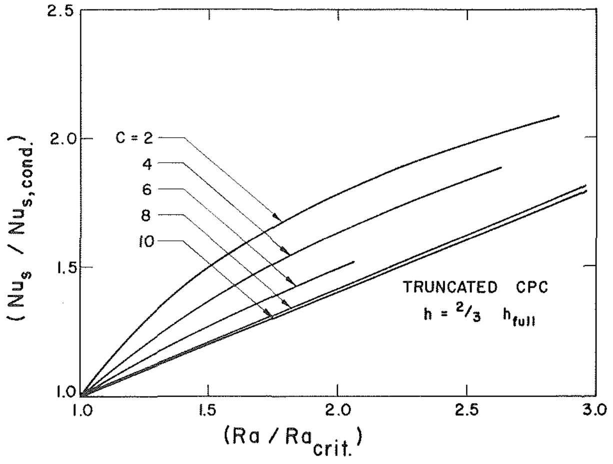

Fig. 6 Results similar to those in Fig. 5 for truncated CPC cavities with h/h_{full} = 2/3 (See footnote after Table 1.)

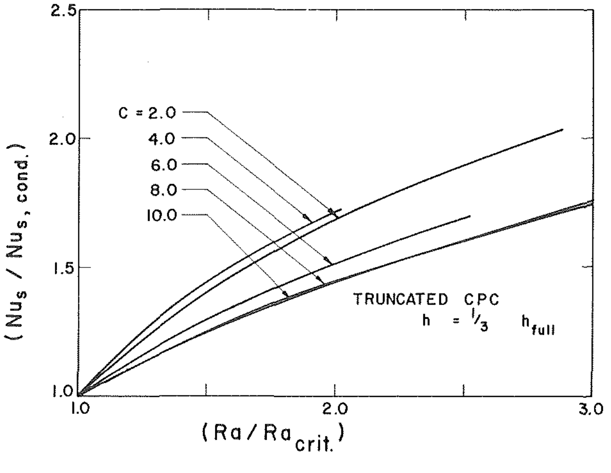

Fig. 7 Results imilar to those in Fig. 5 for truncated CPC cavities with h/h_{full} = 1/3 (See footnote after Table 1.)

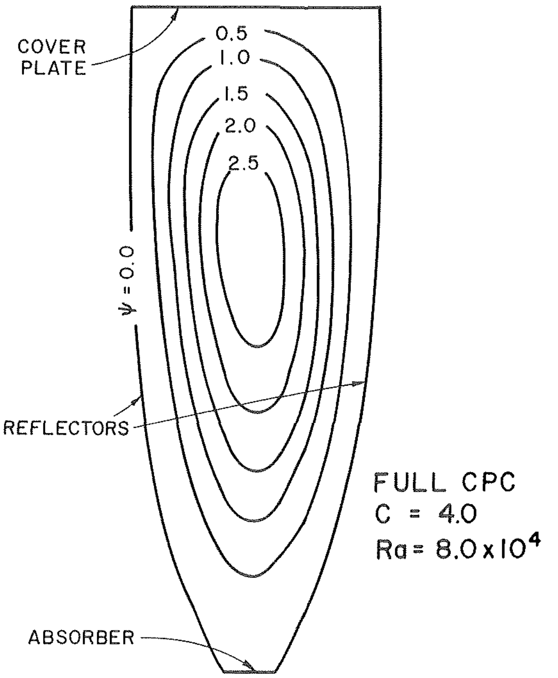

Fig. 8 Schematic diagram of the flow pattern in a full CPC cavity with $C = 4$ at $Ra = 8 \times 10^4$

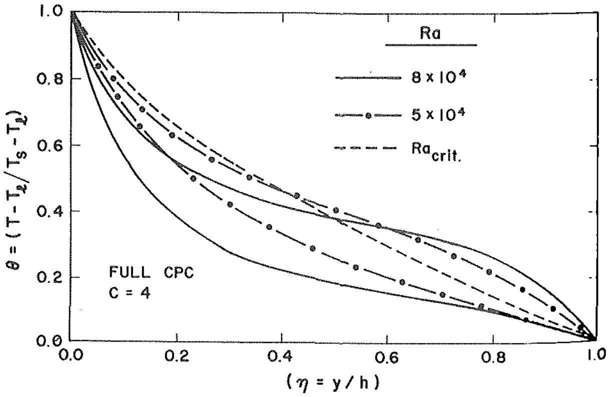

Fig. 9 Temperature distributions along the two insulated parabolic reflectors of a full CPC cavity with $C = 4$ at different values of Rayleigh number

References

1 Winston, R., "Principles of Solar Concentrators of a Novel Design," *Solar Energy*, Vol. 16, p. 89, 1974.

2 Rabl, A., "Comparison of Solar Concentrators," *Solar Energy*, Vol. 18, p. 93, 1976.

3 Rabl, A., "Optical and Thermal Properties of Compound Parabolic Concentrators," *Solar Energy*, Vol. 18, p. 497, 1976.

4 Randall, K. R., El-Wakil, M. M., and Mitchel, J. W., "Natural Convection Characteristics of Flat Plate Collectors," *Proc. Ann. Mtg. Am. Section of ISES*, Orlando, Florida, June 1977.

5 Arnold, J. N., Catton, I., and Edwards, D. K., "Experimental Investigation of Natural Convection in Inclined Rectangular Regions of Differing Aspect Ratios," ASME JOURNAL OF HEAT TRANSFER, Vol 19, p. 67, 1976.

6 Ozoe, H., Sayama, H., and Churchill, S. W., "Natural Convection in an Inclined Rectangular Channel at Various Aspect Ratios and Angles—Experimental Measurements," *Int. Journal of Heat and Mass Transfer*, Vol. 18, p. 1425, 1975.

7 Hollands, K. G. T., et al., "Free Convection Heat Transfer Across Inclined Air Layers," ASME JOURNAL OF HEAT TRANSFER, Vol. 98, p. 189, 1976.

8 Catton, I., Ayyaswamy, P., and Clever, R. M., "Natural Convection Flow in a Finite Rectangular Slot Arbitrarily Oriented with Respect to the Gravity Vector," *Int. Journal of Heat and Mass Transfer*, Vol. 17, p. 173, 1974.

9 Ozoe, H., Sayama, H., and Churchill, S. W., "Natural Convection in an Inclined Square Channel," *Int. Journal of Heat and Mass Transfer*, Vol. 17, p. 401, 1974.

10 Oden, J. T., et al., (Editors), *Proc. Int. Symp. On Finite Element Methods in Flow Problems*, Swansea, U.K., 1974.

11 Brebbia, C., and Connor, J. J., (Editors), *Proc. Symp. Numerical Methods in Fluid Dynamics*, Pentech Press, 1974.

12 Bird, R. B., Stewart, W. E., and Lightfoot, E. N., *Transport Phenomena*, Wiley, 1960.

13 Catton, I., "The Effect of Insulating Vertical Walls on the Onset of Motion in a fluid Heated from Below," *Int. Journal of Heat Mass Transfer*, Vol. 15, p. 665, 1972.

14 Myers, G. E., *Analytical Methods in Conduction Heat Transfer*, McGraw-Hill, 1971, Ch. 9.

APPENDIX A

Method of Solution

The steady-state partial differential equations (6–8) are solved using finite-element methods. These three equations can be written in the form:

$$\frac{\partial^2 F}{\partial \xi^2} + \frac{\partial^2 F}{\partial \eta^2} + Q(\xi,\eta) = 0 \qquad \text{(A-1)}$$

where F represents either ψ,θ,ω with the source term $Q(\xi,\eta)$ given by its respective function from equations (6–8). It can be easily shown that equation (A-1) is equivalent to the extremisation of the integral I given by [10, 11]:

$$I = \int\int_A \left\{\frac{1}{2}\left[\left(\frac{\partial F}{\partial \xi}\right)^2 + \left(\frac{\partial F}{\partial \eta}\right)^2\right] - Q^*(\xi,\eta)F\right\} dA \qquad \text{(A-2)}$$

The integral is performed over the two-dimensional region, A, of interest. The asterisk superscript in Q^* indicates that this function is prescribed and does not participate in the variation process.

The region is divided into E triangular elements with M vertices. Within each element, the function F is evaluated by linear interpolation between its values at the vertices. Extremisation of equation (A-2) leads to a set of simultaneous equations of the form [10, 11, 14]:

$$[\mathbf{K}][\mathbf{F}] = [\mathbf{Q}] \qquad \text{(A-3)}$$

where $\mathbf{K}$ is an $[M \times M]$ global "conduction" matrix given by:

$$[\mathbf{K}] = \sum_{e=1}^{E} [\mathbf{D}^{(e)}][\mathbf{K}^{(e)}][\mathbf{D}^{(e)}]^T \qquad \text{(A-4)}$$

Here $\mathbf{D}^{(e)}$ is the $[M \times 3]$ displacement matrix for element e with vertices i, j, and k so that $D_{i1}^{(e)} = D_{j2}^{(e)} = D_{k3}^{(e)} = 1$ with the remaining terms in $\mathbf{D}^{(e)}$ being zero. The elemental conduction matrix $\mathbf{K}^{(e)}$ is a $[3 \times 3]$ matrix whose elements are functions of the vertices' coordinates (see [14]). The $[M \times 1]$ vector $\mathbf{F}$ contains the F values at the vertices while the elements of the $[M \times 1]$ generation vector $\mathbf{Q}$ are functions of the Q values and coordinates of the vertices which depend on the interpolation scheme used. Detailed description of these different matrices may be found in [14].

For the problem at hand three coupled sets of equations corresponding to the variables ψ, θ, and ω are obtained:

$$[\mathbf{K}][\psi] = [\mathbf{Q}_\psi] \qquad \text{(A-5a)}$$

$$[\mathbf{K}][\theta] = [\mathbf{Q}_\theta] \qquad \text{(A-5b)}$$

and

$$[\mathbf{K}][\omega] = [\mathbf{Q}_\omega] \qquad \text{(A-5c)}$$

These equations are coupled through the generation vectors $\mathbf{Q}_\psi$, $\mathbf{Q}_\theta$, and $\mathbf{Q}_\omega$. The entires of these vectors are functions of ψ, θ, and ω values as well as the coordinates of the M vertices. The global conduction matrix is the same for all three equations since it depends only on the nodal arrangement.

The boundary conditions for ψ and θ are easily imposed by modifying the matrices $\mathbf{K}$ and $\mathbf{Q}$ [14]. For boundary conditions of the form $\partial F/\partial n = 0$, the $\mathbf{K}$ and $\mathbf{Q}$ matrices need not be modified [14]. The stream function has two boundary conditions (equations 10a,b), namely:

$$\psi|_w = 0 \qquad \text{(10a)}$$

and

$$\left.\frac{\partial \psi}{\partial n}\right|_w = 0 \qquad \text{(10b)}$$

The first boundary condition is used in solving equation (A-5a) while the latter is used to obtain the boundary values for ω as outlined below.

Equation (A-5a) can be rewritten as:

$$[\mathbf{K}][\psi] = [\mathbf{A}][\omega] \qquad \text{(A-6)}$$

where $\mathbf{A}$ is a diagonal matrix with A_{ii} equal to one third the sum of areas of all elements surrounding node i. This global area matrix is deduced from the element generation matrix:

$$[\mathbf{Q}_\psi^{(e)}] = \frac{\Delta}{3}\begin{bmatrix} 1 & 0 & 0 \\ 0 & 1 & 0 \\ 0 & 0 & 1 \end{bmatrix}\begin{bmatrix} \omega_i \\ \omega_j \\ \omega_k \end{bmatrix}$$

When equation (A-6) is solved without any modifications on $[\mathbf{K}]$ or $[\mathbf{A}][\omega]$, the boundary condition (10b) would be automatically imposed. In order to impose the other boundary condition (equation 10a), equation (A-6) is solved in reverse order to obtain values of ω on the boundary:

$$[\mathbf{A}^*][\omega] = ([\mathbf{K}][\psi])^* \qquad \text{(A-7)}$$

where $[\mathbf{A}^*]$ and $([\mathbf{K}][\psi])^*$ are modified matrices using ω values for the internal nodal points. This technique for evaluating the boundary values for ω has been checked using simple rectangular cavities and found to agree with the second order approximation:

$$\omega|_w = -\frac{2\psi_\delta}{(\Delta n)^2} \qquad \text{(A-8)}$$

Equation (A-8) can be readily obtained by expanding ψ in a Taylor series around a boundary point and substituting the boundary conditions (10a,b) to obtain ψ_δ which is the stream function at a point Δn away from the surface, which is then related to ω at the boundary using equation (6).

The procedure for solving equation (A-5a,b,c) is outlined below:

1 Values of θ are initialized with the conduction temperature distribution while ψ and ω values are initialized as zero.

2 Equation (A-5a) is modified for the boundary condition (10a). The generation matrix $\mathbf{Q}_\psi$ is evaluated using current values of ω and equation (A-5a) is solved for ψ.

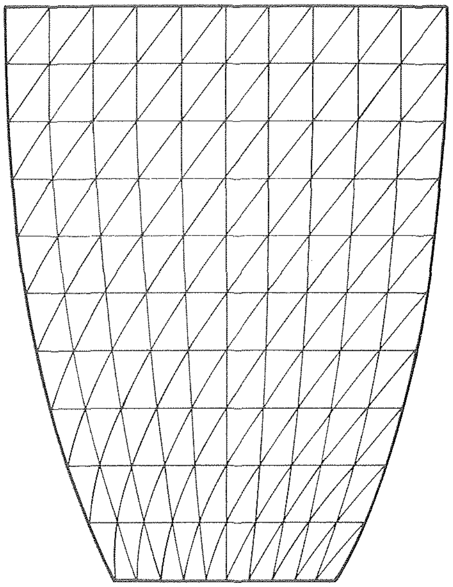

Fig. B1 Schematic diagram of the finite-element grid used in this investigation

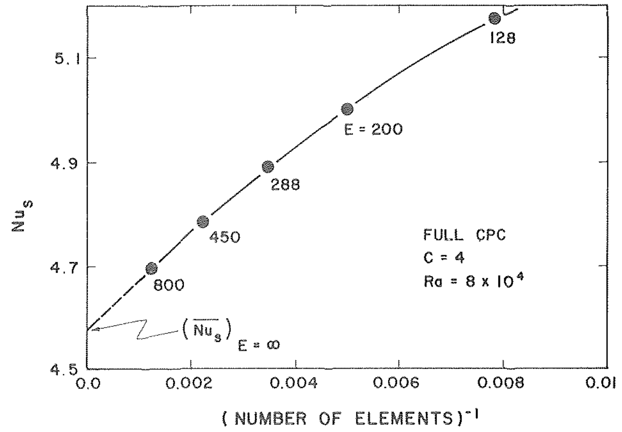

Fig. B2 Variation of average absorber plate Nusselt number with the inverse of number of elements of the grid for a full CPC cavity with $C = 4$ at $Ra = 8 \times 10^4$

3 Equation (A-5b) is modified using boundary conditions for θ. The current values of ψ and θ are used to find Q_θ and equation (A-5b) is solved for θ.

4 Equation (A-7) is solved with [A] and [K][ψ] modified using current values at the internal nodes to obtain values for ω along the boundary.

5 Equation (A-5c) is modified for the boundary values of ω. The generation matrix $[Q_\omega]$ is evaluated using current values of ψ, θ, and ω and equation (A-5c) is solved for ω.

6 Steps 2 through 6 are repeated until all the nodal values of ψ, θ, and ω converge to within 1 percent.

Table B1 Effect of grid size on computed values of average absorber plate Nusselt number

	$C = 2.0$		$C = 4.0$		$C = 10.0$	
$E\backslash Ra$	Ra_{crit}	9×10^3	Ra_{crit}	8×10^4	Ra_{crit}	1.3×10^6
128	—	2.830	—	5.174	—	9.689
200	1.639*	2.734	2.978	5.005	7.120	9.658
450	—	2.637	—	4.784	—	9.486
800	1.637	2.598	2.964	4.694	7.120	9.444
∞**	1.637	2.54	2.96	4.58	7.120	9.425

* Table values are Nu_s

** Values of $(Nu_s)_{E=\infty}$ are evaluated by extrapolation using graphs similar to Fig. B2.

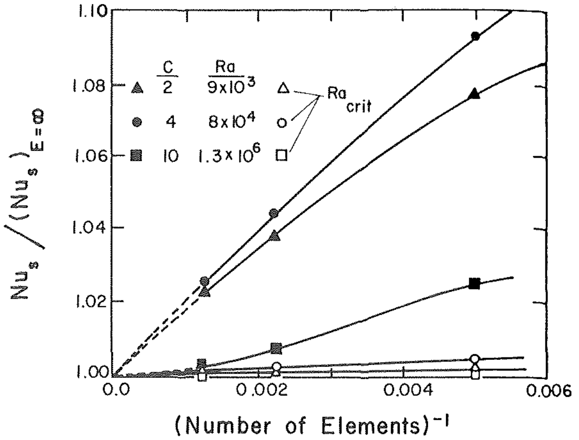

Fig. B3 Effect of grid size on the average absorber plate Nusselt number. Values of $(Nu_s)_{E=\infty}$ are obtained from Figures similar to B2 for the different cases examined

APPENDIX B

Grid Size Selection

In all the results presented in this study, a grid of 200 triangular elements with 121 nodes (Fig. B1) has been used. This mesh is selected as a compromise between accuracy and computation cost. Here, we investigate the effect of grid size on the predicted values of average absorber plate Nusselt number. Fig. B2 is a plot of Nu_s versus the inverse of number of elements in the mesh for a full CPC with a concentration of 4 at a Rayleigh number of 8.0×10^4. Different mesh sizes with up to 800 elements are compared; these are all arranged in a manner similar to Fig. B1. The results are extrapolated to the limit of infinite number of elements ($Nu_s = (Nu_s)_{E=\infty}$). Similar plots have been prepared for $C = 2, 4$, and 10 at the corresponding highest and lowest Rayleigh numbers examined in this investigation. A summary of these results in given in Table B1. Fig. B3 is a plot of $Nu_s/(Nu_s)_{E=\infty}$ for those different cases. The lowest Rayleigh numbers correspond to the conduction limit ($Ra = Ra_{crit}$). For a given concentration, the errors decrease as Ra is decreased reaching a value of less than 1 percent for $Ra = Ra_{crit}$. Fig. B3 clearly shows that the results obtained in this investigation are within 10 percent of those for infinite number of elements. The results presented in this paper should be verified experimentally; such data do not exist at this time.

Convection in an Enclosure-Source and Sink Located Along a Single Horizontal Boundary

L. A. Clomburg, Jr.
Chemical Engineering Dept.,
Massachusetts Institute of Technology,
Cambridge, Mass.

Laminar natural convection in a two-dimensional enclosure with both source (uniform heat flux density) and sink (temperature specified) located on the top horizontal boundary is investigated numerically. Temperature and velocity profiles are presented for a high Prandtl number fluid for length Rayleigh numbers in the range 10^7 to 10^9 for length to depth ratios of 1:1 to 4:1. To generalize the results, an order of magnitude analysis is used to determine the dependence of temperature, velocity, and boundary-layer thickness scales on aspect ratio and Rayleigh number. The numerical data are well correlated using these suggested scales. The analysis shows the Nusselt number and the maximum horizontal velocity to depend on the 1/6 and 1/3 powers of the Rayleigh number, independent of aspect ratio.

Introduction

In large Rayleigh number, steady natural convection flow within an enclosure, boundary layers will exist in the regions near the sources and sinks of energy. The core, or remainder of the volume of interest, will be partially or wholly enclosed by the boundary layers and will interact with them through energy, momentum, and material exchange. Many problems have been studied where the source and sink are isolated from one another. Two popular examples are the Rayleigh-Bernard problem—heating from below and cooling from above, and the Batchelor problem—heat exchange between isothermal sources and sinks located on opposite vertical boundaries of a rectangle. In both problems the boundary layers interact only indirectly through the core. Their solutions, functions of three dimensionless parameters: Rayleigh number, Prandtl number, and aspect ratio, have been studied by analytical, experimental, and numerical methods [4, 8].[1] Both the numerical and experimental techniques are time consuming, in that many cases are required to obtain a general solution. For this class of problems, matched asymptotic methods have proved useful for treating limiting cases of high and low parameter values. The techniques depend upon ascertaining the functional form of the core solution and then matching it with boundary layer solutions developed for the source and sink regions.

A class of problems which has been less studied has the source and sink located directly adjacent to one another. Examples of important physical situations which are influenced by these boundary conditions include atmospheric and oceanic circulation [9], convection within the earth's mantle [6], and the circulation of fluid within glass melts [3, 5, 7]. These problems depend on a multiple set of dimensionless parameters; thus their solution by experimental and pure numerical means is resource consuming. In addition, matched asymptotic methods are less useful because the source and sink boundary layers are directly coupled.

This paper treats the natural convection of a high Prandtl number fluid ($\Pr \gg 1$) within a rectangular enclosure which is both heated (uniform heat flux density) and cooled (isothermal sink) from above. The problem is among a class of problems that has been described previously [7]. That paper stressed modeling criteria for industrial glass melting furnaces, and presented a comparison of computed and experimental results for a single set of parameters. This paper examines the details of the boundary layer flow caused by the special boundary conditions with the objective of establishing the solution dependence on the aspect ratio and Rayleigh number parameters. Although the solution method is numerical, the emphasis of the paper is not on numerical techniques, but on how an understanding of the boundary layer physics (obtained here by examining a single representative solution) can be used with an order of magnitude analysis to develop a solution which is valid over a wide range of parameter values.

Problem Statement

The problem of interest is described mathematically by the continuity equation, the Navier-Stokes equations as modified by the Boussinesq approximation, and the energy equation, each assumed to be at steady state and two-dimensional, together with the relevant boundary conditions:

$$\frac{\partial U}{\partial X} + \frac{\partial V}{\partial Y} = 0 \qquad (1)$$

$$\frac{1}{\Pr}\left(\frac{\partial UU}{\partial X} + \frac{\partial VU}{\partial Y}\right) = -\frac{\partial P}{\partial X} - \mathrm{Ra}\theta + \nabla^2 U \qquad (2)$$

$$\frac{1}{\Pr}\left(\frac{\partial UV}{\partial X} + \frac{\partial VV}{\partial Y}\right) = -\frac{\partial P}{\partial Y} + \nabla^2 V \qquad (3)$$

---

[1] Numbers in brackets designate References at end of paper.

Contributed by the Heat Transfer Division and presented at the ASME-AIChE Heat Transfer Conference, St. Louis, Mo., Aug. 9-11, 1976. Manuscript received by the Heat Transfer Division February 3, 1977.

$$\frac{\partial U\theta}{\partial X} + \frac{\partial V\theta}{\partial Y} = \nabla^2\theta \tag{4}$$

$$Y = 0, 2A, 0 \le X \le 1 \quad U = V = \frac{\partial\theta}{\partial X} = 0$$

$$0 \le Y \le 2A, X = 1 \quad U = V = \frac{\partial\theta}{\partial X} = 0$$

$$0 \le Y \le A, X = 0 \quad U = V = \theta = 0$$

$$A \le Y \le 2A, X = 0 \quad U = V = 0, \quad \frac{\partial\theta}{\partial X} = -1 \tag{5}$$

In the above equations, constant fluid properties are assumed with the dimensionless variables being defined in the nomenclature. As shown in Fig. 1, the boundary conditions include insulated, no-slip walls for the left, right, and bottom boundaries of the enclosure. The source-sink energy pair which drives the flow is located on the top boundary. The sink, described by a constant temperature, is located on the left half, while the source, a constant heat flux density, occupies the right half. Along the entire top boundary, both horizontal and vertical velocity components are taken to be zero.

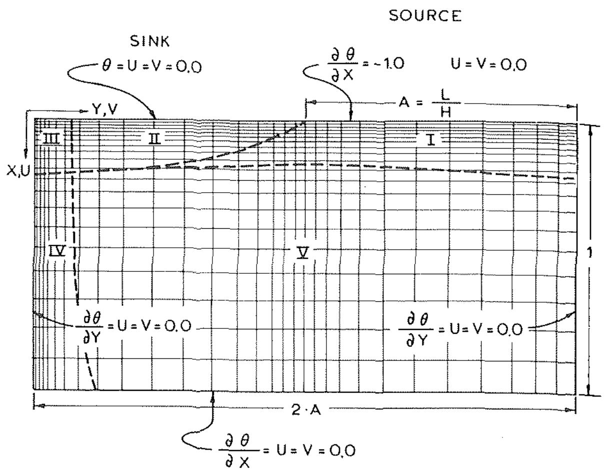

Fig. 1 Problem geometry and boundary conditions

Method of Solution

The above problem was solved for different Rayleigh numbers (Ra = $10^7, 10^8, 10^9$) and aspect ratios ($2A = 1, 2, 4$) at a large, fixed Prandtl number (Pr = 10^{10}) by iterative finite difference techniques. Rather than working directly with equations (1) to (3), the stream function concept was introduced to satisfy (1) directly, and equations (2) and (3) were combined to eliminate pressure as a variable:

$$U = \frac{\partial\psi}{\partial Y} \qquad V = -\frac{\partial\psi}{\partial X} \tag{6}$$

$$\frac{1}{\mathrm{Pr}}\left[\frac{\partial}{\partial X}(-U\nabla^2\psi) + \frac{\partial}{\partial Y}(-V\nabla^2\psi)\right] = \mathrm{Ra}\frac{\partial\theta}{\partial Y} + \nabla^2(-\nabla^2\psi) \tag{7}$$

$$Y = 0, 2A, \quad 0 \le X \le 1 \quad \psi = \frac{\partial\psi}{\partial Y} = 0$$

$$0 \le Y \le 2A, \quad X = 0, 1 \quad \psi = \frac{\partial\psi}{\partial X} = 0 \tag{8}$$

The spatial discretizations for equations (4) to (8) were obtained by sectioning the region of interest into 600 (20 × 30) unequally sized rectangular zones, and then using conservative difference formulations for the energy and vorticity ($\omega = -\nabla^2\psi$) transport equations. Hence, the flux density (in the X direction) of a scalar (θ or $-\nabla^2\psi$) across a vertical zone boundary was approximated as:

$$\mathbf{i}_X\left\{\theta_{i-1,j}\frac{|U| + U}{2} - \theta_{i,j}\frac{|U| - U}{2} - \frac{\theta_{i,j} - \theta_{i-1,j}}{\Delta X_{i-1/2}}\right\}$$

where $U \equiv U_{i-1/2,j}$ is the vertical velocity component evaluated on the zone boundary, and $\Delta X_{i-1/2}$ is the spacing between the centers of zones (i, j) and $(i - 1, j)$. The zone boundary velocities were obtained by first bilinearly averaging the zone center stream function values to obtain values on the zone corners, and then applying the difference analogs of equation (6) to those corner values. The vertical component of the vorticity in equation (7) was approximated as:

$$-\frac{1}{\Delta X_i}\left\{\frac{\psi_{i-1,j} - \psi_{i,j}}{\Delta X_{i-1/2}} + \frac{\psi_{i+1,j} - \psi_{i,j}}{\Delta X_{i+1/2}}\right\}$$

where ΔX_i is the spacing between zone boundaries. Equations (8) were satisfied using reflection boundary difference formulations. Hence, on the top boundary, the vorticity was:

$$-\frac{8}{(\Delta X_1)^2}\psi_{1,j}$$

Nomenclature

$A = \frac{L}{H}$ = geometry factor related to aspect ratio (= $2A$)
g = gravitational constant
H = enclosure depth
k = fluid thermal conductivity
L = enclosure half length
M = number of grid zones used in vertical direction (= 20 for this work)
$P = \frac{(p - p_0)H^2}{\rho\alpha\nu}$ = dimensionless pressure
Pr = ν/α = Prandtl number (= 10^{10} for this work)
q = heat flux density at source
$\mathrm{Ra} = \frac{g\beta qH^4}{k\nu\alpha}$ = depth Rayleigh number
Ra_L = length Rayleigh number
T = temperature

$u, U = \frac{uH}{\alpha}$ = dimensional and dimensionless vertical velocity
$v, V = \frac{vH}{\alpha}$ = dimensional and dimensionless horizontal velocity
$x, X = \frac{x}{H}$ = dimensional and dimensionless vertical position
$y, Y = \frac{y}{H}$ = dimensional and dimensionless horizontal position
α = thermal diffusivity
β = coefficient of thermal expansion
δ = dimensionless length scale for boundary layer

$\theta = \frac{k(T - T_0)}{qH}$ = dimensionless temperature
ν = kinematic viscosity
ρ = density
$\psi = \frac{\psi}{\alpha}$ = dimensionless steam function value
$\omega = -\nabla^2\psi$ = dimensionless vorticity

Subscripts and Superscripts

s = scaling quantity (see equations (16–20))
0 = sink temperature
* = modified dimensionless variables (equation (26))
+ = modified pressure superscript (equation (10))

Approximations to the various horizontal derivatives were similarly obtained. The buoyancy source term in equation (7) was estimated using the second order correct difference formulation:

$$\mathrm{Ra}\left\{\frac{\Delta Y_{j+1/2}}{\Delta Y_{j-1/2}+\Delta Y_{j+1/2}}\,\frac{\theta_{i,j}-\theta_{i,j-1}}{\Delta Y_{j-1/2}}\right.$$
$$\left.+\frac{\Delta Y_{j-1/2}}{\Delta Y_{j-1/2}+\Delta Y_{j+1/2}}\,\frac{\theta_{i,j+1}-\theta_{i,j}}{\Delta Y_{j+1/2}}\right\}$$

The relative zone dimensions, shown to scale in Fig. 1, were the same for each of the numerical solutions. The zone depths, which varied in a continuous manner, were chosen so that at least 7–8 zones would be within the region occupied by the top thermal boundary layer.[2] (The equation describing the variation of zone depth with vertical distance is $\ln \Delta X_i = 2.300 \sin^2 (\pi/2(i-1)/(M-1)) - 4.465$ $i = 1, M$.) Zone lengths also varied continuously with horizontal distance so that smaller zones were located near the left and right boundaries and near the point $(0, A)$ where the top boundary condition changed abruptly.

Steady-state solutions to the difference equations were obtained using alternating direction implicit line over-relaxation techniques for equations (4) and (7). Starting with an existing solution valid for different Ra and A, or with an isothermal motionless fluid, convergence for a particular numerical run was achieved within 200–300 iterations. Convergence was ascertained both by examining the residual error of the difference analogs to equations (4) and (7), and by computing a heat balance for the enclosure. The final residuals were 10^{-3} to 10^{-4} times the order of magnitude of the important terms of equations (4) and (7), while the heat balance closed within 0.1 percent (Details on the numerical procedure are available [1]). The numerical program has also been checked using data obtained from laboratory glycerin models, operated at high Rayleigh number, but with different endwall boundary conditions [7].

Base Case Solution

Shown in Figs. 2(a), (b), and (c) are contour plots for θ, ψ, and P for the base case solution (Ra = 10^8 and $2A = 2$). The boundary layer nature of the solution is immediately evident from the isotherm and streamline plots. Several regions are discernable. The core is largely isothermal—within the bottom 80 percent of the enclosure; the temperature differential is less than 8 percent of the maximum temperature (0.117 in the upper right corner). The core temperature is not that of the sink. For example, the lower right corner temperature of 0.019, representative of the core, is 16 percent of the maximum temperature. Under the source, isotherms are closely spaced and nearly horizontal where energy is being conducted inward from the boundary. Fluid is being entrained upward into the boundary layer at a nearly uniform rate to accept this energy ($|U_{\max}| \cong 20$ to 30). Flow under the top boundary is right to left with the maximum horizontal velocity component (V) increasing more rapidly than linearly as the boundary layer thickness thins slightly near $Y = 1$. An inner thermal boundary layer develops from the leading edge of the sink as the hot fluid is cooled from above. Material continues to be entrained into the outer boundary layer under the sink up to a point (0.202, 0.143) near the upper left corner. Between $Y = 1$ and $Y = 0.143$, V increases less rapidly than linearly as the outer boundary layer thickens. At the latter horizontal position the maximum horizontal velocity is 401, and the total circulation ($\psi_{\max}$) is 47.9. The flowing material turns downward in the upper left corner, and returns to the upper left region of the core with residual energy (with reference to the sink temperature) rather than descending the entire left wall.

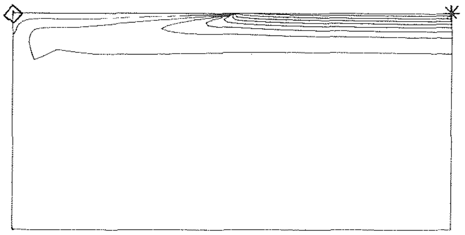

TEMPERATURE FIELD FOR RUN NUMBER 52

(0.117, 0.0, 0.0117)

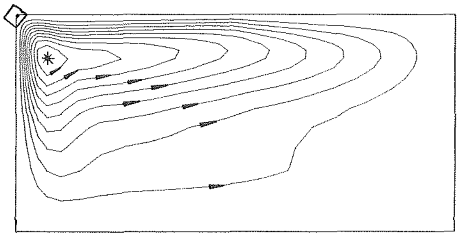

STREAM FUNCTION FIELD FOR RUN NUMBER 52

(46.9, 0.0, 4.69)

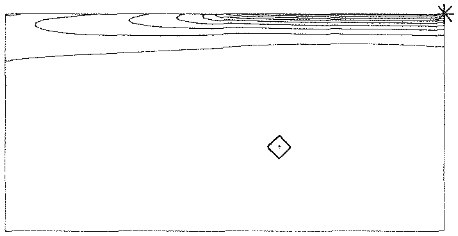

PRESSURE FIELD FOR RUN NUMBER 52

(6.18×10^5, -5.96×10^4, 6.78×10^4)

Fig. 2 Contour plots for the base case—A = 1, Ra_L = 10^8 (each plot contains 11 equally spaced contours. The maximum (*) and minimum (◇) values and the increment between contours is noted below each plot)

The pressure contour plot (Fig. 2(c)) also shows the boundary layer nature of the solution. Pressure is highest under the energy source, and decreases right to left due to the drag of the fluid on the top boundary. Moreover, within the core, the horizontal pressure gradient is small. The pressure field is not normally calculated using the algorithm described earlier. However, for purposes of providing physical insight, the pressure field was calculated by solving:

$$\nabla^2 P = -\mathrm{Ra}\frac{\partial \theta}{\partial X} - \frac{1}{\mathrm{Pr}}\left[\frac{\partial}{\partial X}\left(\frac{\partial UU}{\partial X} + \frac{\partial VU}{\partial Y}\right) + \frac{\partial}{\partial Y}\left(\frac{\partial UV}{\partial X} + \frac{\partial VV}{\partial Y}\right)\right] \quad (9)$$

with boundary pressures being obtained by line integration of equations (2) and (3) around the boundary with one modification. P in equations (2) and (3) is the pressure differential from that of an enclosure filled with motionless isothermal fluid at the sink temperature.

---

[2] It is the author's experience that relatively crude core zoning (roughly 10 × 10 zones) yields reasonably accurate results, provided the boundary layers are adequately resolved. This conclusion is based primarily on experimental evidence from a related problem [2, 7]. An indicator of the truncation error introduced by the finite mesh size is provided in Fig. 5; where the vertical velocity down the left wall is plotted for the largest velocity case (Ra = 10^9 and A = 1) for three different nonuniform zoning arrangements (1200, 600, and 345 total zones, respectively). As can be seen from the figure, there is good agreement between the maximum velocities predicted using the intermediate and finer zoning arrangements; but that the boundary layer thickness (and maximum stream function value) decreases slightly as the zoning is refined. The agreement between the temperatures was much better—the maximum temperature varied about one percent between the three grid arrangements. Additional support for the accuracy of the numerical solutions comes from the correlated results of Table 2 and Fig. 4. For the different cases (all computed with the same grid system), the boundary layer thickness varies by a factor of four; and yet the correlations remain valid. If the zoning were inadequate, one would expect that the high and low Rayleigh number results could not be so well correlated.

Since much of the core is largely motionless and isothermal at a temperature above that of the sink, a linear vertical pressure gradient will exist in the bottom of the enclosure, which will not drive any flow. Hence, the quantity P^+ is plotted in Fig. 2(c):

$$P^+ = P - \mathrm{Ra} \cdot X \cdot \theta(1, 2) \tag{10}$$

The line integration of equations (2) and (3) around the enclosure provides a check of the flow solution which is analogous to that of the overall energy balance. The results presented in Fig. 2(c) closed within 0.3 percent.

Order of Magnitude Analysis

Equations (1) and (5) are improperly scaled in the sense that since H, α/H, qH/k, and $\rho\alpha\nu/H^2$ do not reflect the magnitudes of the boundary layer thickness, the absolute velocity, and the temperature and pressure differentials within the enclosure, one cannot judge the relative magnitudes of the various terms in the equations. However, the base case solution can be examined to ascertain this information for different sets of simplified equations and boundary conditions. In regions I and II, as shown in Fig. 1, pressure and buoyancy forces balance in the vertical direction, whereas pressure balances viscous forces in the horizontal direction. For the energy equation, vertical conduction and both horizontal and vertical convection are important. Thus the regions are described approximately by:

$$\frac{\partial U}{\partial X} + \frac{\partial V}{\partial Y} = 0 \tag{1}$$

$$0 \cong -\frac{\partial P}{\partial X} - \mathrm{Ra}\theta \tag{11}$$

$$0 \cong -\frac{\partial P}{\partial Y} + \frac{\partial^2 V}{\partial X^2} \tag{12}$$

$$\frac{\partial(U\theta)}{\partial X} + \frac{\partial(V\theta)}{\partial Y} \cong \frac{\partial^2 \theta}{\partial X^2} \tag{13}$$

Boundary conditions include:

$$\begin{gathered} X = 0, \quad A \leq Y \leq 2A \quad U = V = 0 \\ \frac{\partial \theta}{\partial X} = -1 \\ X = 0, \quad 0 \leq Y \leq A \quad U = V = \theta = 0 \\ X \text{ large}, \theta \rightarrow \text{const.} \quad V \rightarrow V_{\text{core}} \\ Y = 2A \quad V\theta = 0 \end{gathered} \tag{14}$$

In addition θ, V, U, and P must match at the interface of regions I and II. Additional terms are required for regions III and IV because the boundary conditions $U = V = 0$ at $Y = 0$ are inconsistant with the above equations. Diffusion (of both energy and momentum) in the flow direction may still be neglected; but because of the impermeable no slip wall, all second derivatives in equations (2) to (4) are required in region III and all but $\partial^2 U/\partial X^2$ and $\partial^2 V/\partial X^2$ are required in region IV. In the core (region V), all second derivatives are small. Because of fluid drag down the left wall, material returns to the core in a region elevated above the enclosure bottom.

The question arises as to whether the dynamics of regions I and II are affected by those of regions III and IV. Since the inertial momentum terms are always small ($\mathrm{Pr} = 10^{10}$), regions III and IV can influence region I only by affecting the core temperature and pressure distributions. If θ_{core} (seen to be constant in Fig. 2(a)) does not approach $\theta_{\max}$ for increasing Ra and A, or more precisely if:

$$\frac{\theta_{\text{core}}}{\theta_{\max} - \theta_{\text{core}}} = \mathcal{O}\text{ (1 or less)} \tag{15}$$

then the dynamics of regions III and IV will be forced by those of regions I and II. Hence, the overall boundary layer distance, velocity, temperature, and pressure scales can be deduced simply from equations (1) and (11) to (14). Let δ, V_s, U_s, θ_s, and P_s be these unknown scales. In addition let $L/H = A$ be the proper length scale for the Y direction within regions I and II. Then, an order of magnitude analysis suggests that

$$\frac{U_s}{\delta} \approx \frac{V_s}{A} \tag{16}$$

$$\frac{P_s}{\delta} \approx \mathrm{Ra}\theta_s \tag{17}$$

$$\frac{P_s}{A} \approx \frac{V_s}{\delta^2} \tag{18}$$

$$\frac{U_s\theta_s}{\delta} \approx \frac{V_s\theta_s}{A} \approx \frac{\theta_s}{\delta^2} \tag{19}$$

In addition, the source thermal boundary condition requires that

$$\frac{\theta_s}{\delta} \approx 1 \tag{20}$$

These represent five independent algebraic expressions that may be solved to obtain the unknown scale factors. The solution is

$$\begin{gathered} \delta = \theta_s = A^{1/3}\mathrm{Ra}^{-1/6} \\ U_s = A^{-1/3}\mathrm{Ra}^{1/6} \\ V_s = A^{1/3}\mathrm{Ra}^{1/3} \\ P_s = A^{2/3}\mathrm{Ra}^{2/3} \end{gathered} \tag{21}$$

Rescaled, equations (1) to (4) become

$$\frac{\partial U^*}{\partial X^*} + \frac{\partial V^*}{\partial Y^*} = 0 \tag{22}$$

$$\frac{\partial P^*}{\partial X^*} + \theta^* = \epsilon \left[-\frac{1}{\mathrm{Pr}} \left(\frac{\partial U^* U^*}{\partial X^*} + \frac{\partial V^* U^*}{\partial Y^*} \right) + \frac{\partial^2 U^*}{\partial X^{*2}} + \epsilon^2 \frac{\partial^2 U^*}{\partial Y^{*2}} \right] \approx 0 \tag{23}$$

$$\frac{\partial P^*}{\partial Y^*} - \frac{\partial^2 V^*}{\partial X^{*2}} = -\frac{1}{\mathrm{Pr}} \left(\frac{\partial U^* V^*}{\partial X^*} + \frac{\partial V^* V^*}{\partial Y^*} \right) + \epsilon^2 \frac{\partial^2 V^*}{\partial Y^{*2}} \approx 0 \tag{24}$$

$$\frac{\partial U^* \theta^*}{\partial X^*} + \frac{\partial V^* \theta^*}{\partial Y^*} - \frac{\partial^2 \theta^*}{\partial X^{*2}} = \epsilon^2 \frac{\partial^2 \theta^*}{\partial Y^{*2}} \approx 0 \tag{25}$$

where $\epsilon = \mathrm{Ra}_L{}^{-1/6}$. From these equations, the new dimensionless variables

$$\begin{gathered} U^* \equiv \frac{uL}{\alpha} \mathrm{Ra}_L{}^{-1/6} \quad V^* \equiv \frac{vL}{\alpha} \mathrm{Ra}_L{}^{-1/3} \\ P^* \equiv \frac{(p - p_0)L^2}{\rho\alpha\nu} \mathrm{Ra}_L{}^{-2/3} \\ \theta^* \equiv \frac{k(T - T_0)}{qL} \mathrm{Ra}_L{}^{1/6} \end{gathered} \tag{26}$$

should be of order $1[\mathcal{O}(1)]$ in regions I and II, and should be functions of the variables

$$X^* \equiv \frac{x}{L} \mathrm{Ra}_L{}^{1/6} \quad Y^* \equiv y/L$$

independent of Ra_L, Pr, and A, provided that

$$\mathrm{Pr},\ \mathrm{Ra}_L{}^{1/6},\ \mathrm{Ra}_L{}^{1/6}/A \gg 1 \tag{27}$$

The last condition is that the ratio of the enclosure depth to boundary layer thickness is large.

Parameter Study

Additional numerical runs were obtained for Rayleigh numbers of 10^7 and 10^9 at fixed aspect ratio ($2A = 2$) and for aspect ratios of 1.0 and 4.0 for a fixed length Rayleigh number ($\mathrm{Ra}_L = \mathrm{Ra} \cdot A^4$). Contour plots of the temperature and stream function fields for these runs are shown in Fig. 3 while selected tabular results are given in Table 1. By examining first Fig. 3 and comparing it to Fig. 2, one can see the existence of each of the regions discussed for the base case (Run 52). Runs 45 and 49 emphasize the boundary layer nature of the problem even more clearly than run 52. $\theta_{\max}$ in Table 1 is the inverse of the Nusselt number:

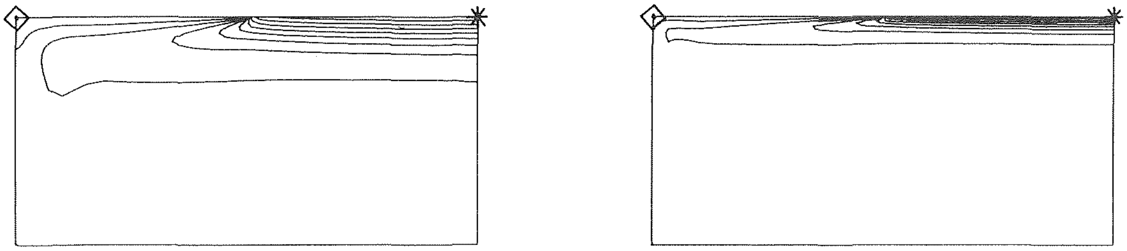

TEMPERATURE FIELD FOR RUN NUMBER 48

(0.174, 0.0, 0.0174)

TEMPERATURE FIELD FOR RUN NUMBER 45

(0.0782, 0.0 , 0.00782)

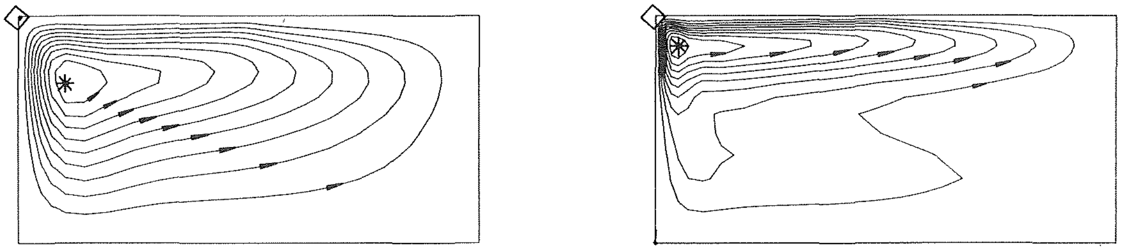

STREAM FUNCTION FIELD FOR RUN NUMBER 48

(29.8, 0.0, 2.98)

RUN 48 - $Ra_L = 10^7$, A=1

STREAM FUNCTION FIELD FOR RUN NUMBER 45

(72.0, 0.0 7.20)

RUN 45 - $Ra_L = 10^9$, A = 1

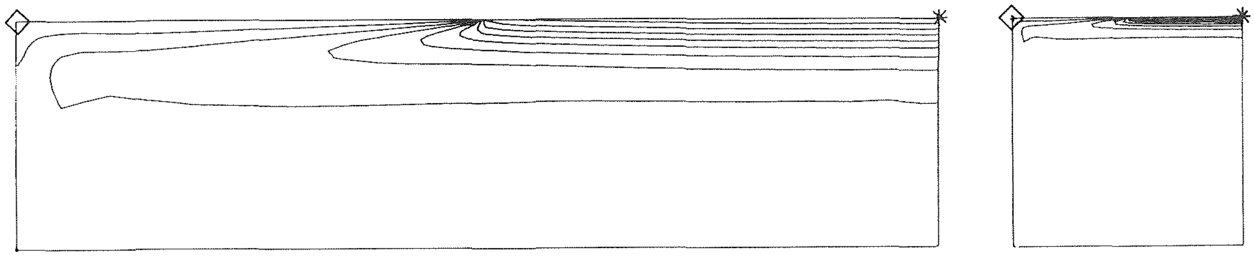

TEMPERATURE FIELD FOR RUN NUMBER 50

(0.239, 0.0, 0.0239)

TEMPERATURE FIELD FOR RUN NUMBER 49

(0.0566, 0.0, 0.00566)

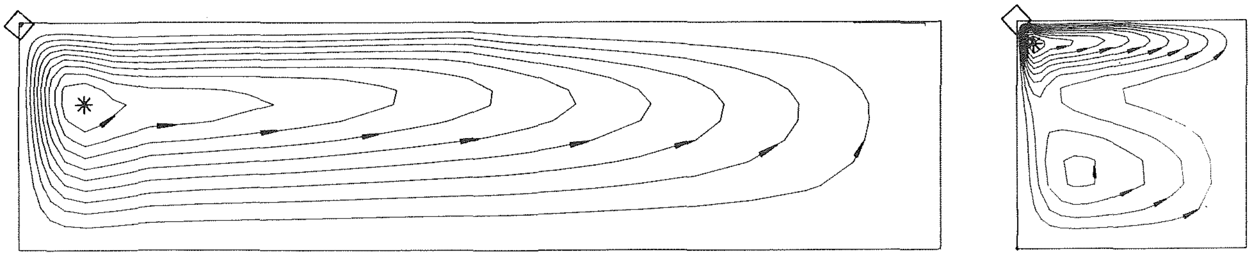

STREAM FUNCTION FIELD FOR RUN NUMBER 50

(42.7, 0.0 , 4.27)

RUN 50 – $Ra_L = 10^8$, A = 2

STREAM FUNCTION FIELD FOR RUN NUMBER 49

(48.2 , 0.0 , 4.82)

RUN 49 - $Ra_L = 10^8$, A = 1/2

Fig. 3 Effect of Rayleigh number and aspect ratio on isotherms and streamlines

$$\theta_{\max} = \frac{k(T_{\max} - T_0)}{qH}$$

Thus, for the cases run, the Nusselt number varies between 4.2 and 17.7. By the nature of the problem, the maximum temperature always occurs in the upper right corner of the enclosure. The reported value of θ_{core} is for the lower right corner. The maximum stream function values and the locations are given in the last two columns.

In Table 2, $\theta_{\max}$, θ_{core}, and $\psi_{\max}$ are rescaled according to equation (26). In column 3, $\theta^*_{\max}$ is of $\mathcal{O}(1)$ and varies about 5 percent for the five cases studied. Similarly $\psi^*_{\max}$ ($= \psi_{\max}\cdot \mathrm{Ra}_L{}^{-1/6}$) has the correct order of magnitude; however, its maximum to minimum variation is about 15 percent. The X^* and Y^* coordinates of the location of the eye agree for the runs at fixed Ra_L with varying A. (The variation of X^* is due to the fact that a fixed zoning arrangement was used for all five runs—this probably also explains the $\psi^*_{\max}$ variation.) However, the Y^* coordinate is a function of the length Rayleigh number. This is not unexpected since the Y length scale for regions III and IV should be more closely related to δ than to A.

An additional test of the validity of the order of magnitude analysis is shown in Fig. 4. Here, θ^* and V^* are plotted as a function of X^* for 6 values of Y^*. The range of the abscissa ($0 \leq X^* \leq 5$) of Fig. 4 covers depths between 0 and about $\frac{1}{9}$ to $\frac{1}{2}$ of the enclosure—see column 2 of Table 2. On the whole, the agreement is excellent, both in the magnitude of θ^* and V^* and the variation with X^*.

The poorest agreement in Fig. 4 exists in the velocity traverse at $Y^* = 0.25$, where V^* is high for run 46. This is due to the fact that the Y^* coordinate of the eye is 0.204 for this run, while it is 0.143 or less for each of the other four runs. Since extra fluid circulates around the eye due to the dynamics of regions III and IV, this is expected. One other point about Fig. 4 should be noted. The temperature traverses for the six values of Y^* plotted are all approaching the same limiting value (≈ 0.38) for large X^*. However, that limit is approached from different directions for $Y^* = 0.0$, ($\theta^*(X^*, 0) < 0.38$) and the other 5 values of Y^* (for example $\theta^*(X^* > 2, 0.25) > 0.38$). The result is that a horizontal temperature gradient exists in depth near the left wall of the enclosure. It is because of this temperature gradient that the deep secondary cell of run 49 exists.

From the above results, it is clear that the Nusselt number $qH/k(T_{\max} - T_0)$ and the dimensionless horizontal velocity (vH/α) will scale as $H/L\cdot \mathrm{Ra}_L{}^{1/6}$ and $H/L\cdot \mathrm{Ra}_L{}^{1/3}$ respectively so long as equations (1), (11) to (14) and (27) continue to hold. This will be true provided that the solution remains two-dimensional and steady and that the neglected terms in equations (11) to (14) are small. Experimental evidence with a glycerin (Pr ≈ 5000) model suggests that three dimensional motion will exist under the sink due to the cooling from above for Rayleigh numbers of order, 10^7. Roll cells, of nearly circular cross section, with their axes aligned with the major flow (Y) direction, develop in region II. However, these do not appear to drastically affect the temperature and velocity scales suggested by equations (16) to (20). Experimental evidence [2] suggests that vH/α and $\theta - \theta_{\text{core}}$ can be accurately predicted using the two dimensional model, but that θ_{core} is lowered somewhat. Physically, the effect is one of increasing the effective length of the sink surface.

Table 1 Effect of parameter variation on selected results

Run Number	Ra_L	A	$\theta_{\max}$ $\times 10^2$	θ_{core} $\times 10^2$	$\psi_{\max}$ value	$\psi_{\max}$ (X, Y)
50	10^8	2	23.87	3.99	42.7	(0.362, 0.286)
48	10^7	1	17.40	2.92	29.8	(0.299, 0.204)
52 (Base Case)	10^8	1	11.70	1.87	46.9	(0.202, 0.143)
45	10^9	1	7.82	1.19	72.0	(0.135, 0.099)
49	10^8	½	5.66	0.89	48.2	(0.089, 0.072)

Table 2 Rescaled selected results

Run Number	$\mathrm{Ra}_L{}^{1/6}/A$	$\theta^*_{\max}$	θ^*_{core}	$\psi^*_{\max}$ value	$\psi^*_{\max}$ (X^*, Y^*)
50	10.8	2.57	0.43	1.98	(3.91, 0.143)
48	14.7	2.56	0.43	2.03	(4.40, 0.204)
52 (Base Case)	21.5	2.52	0.40	2.18	(4.34, 0.143)
45	31.6	2.47	0.38	2.28	(4.27, 0.099)
49	43.1	2.44	0.38	2.24	(3.84, 0.143)

Conclusions

Natural convection, in a two-dimensional enclosure with both source and sink located along the same horizontal boundary, has been

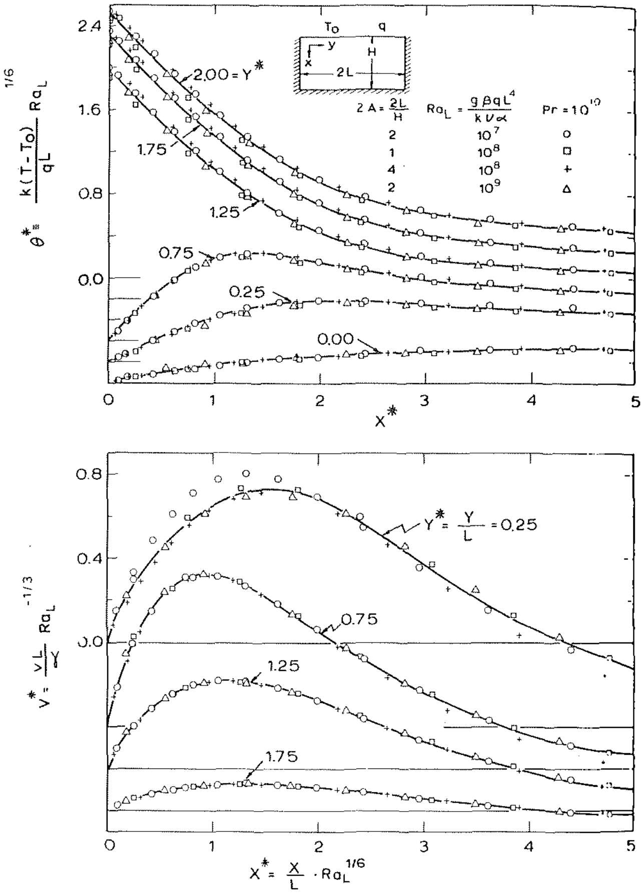

Fig. 4 Rescaled temperature and velocity traverses (note that the zero point along the ordinate for each traverse is displaced for clarity)

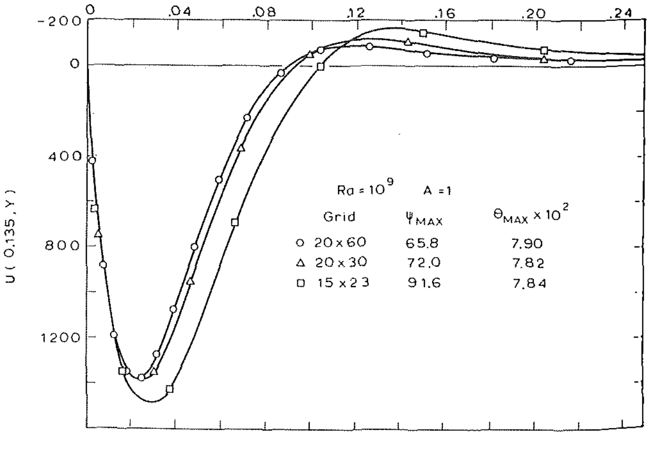

Fig. 5 Dependence of vertical velocity on zoning arrangement (the chosen X value, 0.135, is the X coordinate of the location where the stream function is a maximum)

investigated numerically as a function of Rayleigh number and aspect ratio for a high Prandtl number fluid. The solutions to the problem all exhibited the same boundary layer behavior in a narrow region under the top boundary. This information was used in an order of magnitude analysis to deduce not only the Rayleigh number and aspect ratio dependence of the Nusselt number, but also to develop a general two dimensional solution.

Acknowledgment

This work was sponsored by the National Science Foundation (Grant ENG 73-0832). The authors gratefully acknowledge the participation of N. W. E. Curlet, H. C. Hottel, J. L. Kim, A. F. Sarofim and K. J. Won in discussions pertaining to the material covered in this paper.

References

1 Clomburg, L. A. Jr., "Mathematical and Experimental Modeling of the Circulation Patterns in Glass Melts," Sc.D. Thesis in Chemical Engineering, M.I.T., Cambridge, Mass., 1971.

2 Curlet, N. W. E., "Experimental and Numerical Modeling of Three Dimensional Natural Convection in an Enclosure," Sc.D. Thesis in Chemical Engineering, M.I.T., Cambridge, Mass., 1976.

3 Goodson, R. E., "Modeling for Automatic Control and Process Design," *Automatic Control in Glass,* R. J. Mouly, ed., International Federation of Automatic Control, Pittsburgh, Penn. 1973, pp. 74–92.

4 Koschmieder, E. L., "Bernard Convection," *Advances in Chemical Physics,* Vol. XXVI, Interscience, New York, 1974, pp. 171–213.

5 Leyens, G., "Contribution to the Calculation of Two-Dimensional Convection Currents in Continuous Glass Tank Furnaces, Part I," *Glastech. Ber.*, Vol. 47, 1974, pp. 251–259.

6 McKenzie, D. P., Roberts, J. M., and Weiss, N. O., "Convection in the Earth's Mantle: Towards a Numerical Simulation," *Journal of Fluid Mech.*, Vol. 62, 1974, pp. 465–538.

7 Noble, J. J., Clomburg, Jr., Sarofim, A. F. and Hottel, H. C., "Mathematical and Experimental Modeling of the Circulation Patterns in Glass Melts," ASME JOURNAL OF HEAT TRANSFER, Vol. 94, 1972, pp. 149–154.

8 Ostrach, S., "Natural Convection in Enclosures," *Advances in Heat Transfer,* Academic Press, New York, 1972, pp. 161–227.

9 Schneider, S. H. and Kellogg, W. W., "The Chemical Basis for Climatic Change," *Chemistry of the Lower Atmosphere,* Plenum, 1973, pp 203–249.

Lun-Shin Yao

The Rand Corporation,
Santa Monica, Calif.

Free-Forced Convection in the Entry Region of a Heated Straight Pipe

The developing flow in the entry region of a horizontal pipe whose temperature is held constant and higher than the entry fluid temperature is analyzed. The asymptotic solution of the developing flow near the entrance of the heated straight pipe, distance $0(a)$, is obtained by perturbing the solution of the developing flow in an unheated straight pipe. The displacement of the boundary layer induces radial-directional and downward motion of the fluid particles in the inviscid core flow. The combination of these two motions results in two vortices developing along the pipe. The temperature in the core flow equals the entry fluid temperature. The forced convection boundary layer is affected by the buoyancy force and the axial pressure gradient induced by the boundary-layer displacement, and so is the heat transfer rate. The axial velocity has a concave profile with its maximum off the center line near the entrance, and it grows toward a uniformly distributed profile downstream. The downward stream caused by the displacement of the secondary boundary layer forces the axial velocity profile to turn counterclockwise continuously along the pipe if the flow is from left to right. The competition of two displacement effects supplies the physical explanation of why the flow pattern and the temperature distribution in heated pipes differ due to different degrees of heating.

Introduction

The laminar flow convective heat transfer in a pipe has been a research topic for about half a century. Continuous efforts have been devoted to the topic due to its practical applications in various engineering systems. It has been found that natural convection and variable material properties play important roles in the heat transfer and the fluid flow in a heated pipe. Frequently the prediction of the heat transfer by forced convection alone, without considering the secondary flow, can cause large errors.

In this paper, the hydrodynamically and thermally developing flow (entry flow) in a heated straight pipe is studied. The previous works of the hydrodynamically and thermally fully developed pipe flow, and the hydrodynamically fully developed but thermally developing pipe flow will be reviewed in order to elucidate the physics of the hydrodynamically developing flow in a heated straight pipe. Since the flow in heated pipes is similar to that in curved pipes, the corresponding works of the fully developed flow in curved pipes are also briefly reviewed in order to point out their similitudes.

Morton [1][1] found that the flow in a heated straight pipe is similar to that in a curved pipe. He followed the similar expansion techniques developed by Dean [2, 3] in solving the problem of a fully developed flow in curved pipes and was able to give the solution of laminar convection in uniformly heated horizontal pipes. He showed that the expansion parameter is the Rayleigh number, Ra (or the Grashof number, Gr). However, for a constant wall heat flux condition the heat transfer is enhanced by the speed of the flow and the length of the heated pipe. Therefore, the flow velocities and the heat transfer also depend on the Reynolds number, Re. Consequently, the solutions of constant wall heat flux depend on the product of the Rayleigh and the Reynolds numbers, RaRe. The Morton solution is only valid when RaRe, the ratio of the buoyancy force and the viscous force, is small in a heated pipe. When ReRa is large, viscous forces are important only in a thin boundary layer near the wall, and the motion outside the boundary layer is mostly confined to planes parallel to the plane of symmetry of the pipe. With these observations and assumptions, Mori and Futagami [4] presented a theoretical model similar to Baura's ideal [5] for the curved pipe flow of large Dean number, the ratio of the centrifugal force and the viscous force; the Nusselt number obtained from their model agrees well with their experimental data. Hong and Bergles [6] applied the model to study the effect of the temperature-dependent viscosity. Another interesting character of the flow in heated pipes, revealed by Mori, et al. [7] is that the secondary flow generated by heating can suppress the turbulence level when the inlet turbulence level is high and can enhance it when its level is low at the inlet. They also found that the critical Reynolds

---

[1] Numbers in brackets designate References at end of paper.

Contributed by the Heat Transfer Division for Publication in the JOURNAL OF HEAT TRANSFER. Manuscript received by the Heat Transfer Division August 25, 1977.

number of the flow in heated pipes converges to a value approximately equal to 3.8×10^3 at ReRa = 5×10^5 independently on the inlet disturbance level. A similar phenomenon was observed by Taylor [8] for the flow in curved pipes.

Ou and Cheng [9] studied the thermally developing flow and assumed that the axial velocity, parabolic profile is not affected by the buoyancy force. This limits their study for small Ra, or very close to the thermal entrance. For large Ra and away from the thermal entrance, the secondary flow streamline predicted by their analysis skews in a direction opposite to that observed by experiments. Hong, et al. [10] took the same assumption but argued that the effect of the secondary flow on the axial velocity profile can be neglected when Pr is large. Siegwarth, et al. [11] studied the effect of Pr and found that the interaction between the core flow and the boundary-layer flow seems negligible when $\mathrm{Pr} \rightarrow \infty$. But they concluded from their experiment that their solution for $\mathrm{Pr} \rightarrow \infty$ with large core velocity does not exist. In general, the interaction of the core flow and the boundary-layer flow is important for the pipe flow due to the finite cross-sectional area of the pipe even when Pr is large. This phenomenon can be explained and better understood from the mechanism of the flow development in the entry region of a heated straight pipe presented in this paper.

In general, the perturbation solution is valid when the governing parameter is small, and the boundary-layer asymptotic solution is good when the parameter is large. In the middle range, the finite difference solution [12, 13] can provide satisfactory results. However, it should be noted that the numerical damping introduced by the finite-difference discretization maintains the validity of the finite-difference solution only when the governing parameter is not too large. In fact, Collins and Dennis [14] have proved that the finite-difference solution of a fully developed curved pipe flow presented by Greenspan [15] has a large error introduced by the numerical damping when Dean number is not small.

In this paper the entry-developing flow in a heated straight pipe under the conditions of constant wall temperature is studied. Hieber and Sreenivasan [16] studied the problem for $\mathrm{Pr} \rightarrow \infty$. They neglected the interaction of the core flow and the boundary-layer flow. As pointed out by Siegwarth, et al. [11] the existence of the solution for $\mathrm{Pr} \rightarrow \infty$ is questionable. The reason becomes clear in the following analysis. The wall of the pipe is maintained at a higher temperature, T_w, the inlet fluid temperature, T_{in}. The governing parameters of the problem are (see equations (2)):

$$\mathrm{Re}, \quad \mathrm{Gr}, \quad \mathrm{Pr}, \quad \epsilon \tag{1}$$

The solution we will present is obtained by perturbing the entry flow in unheated straight pipes. Atkinson and Goldstein [17] gave the first solution of the developing flow in the entry region of an unheated straight pipe. Later, Van Dyke [18] pointed out in his study of the entry flow in a channel that Atkinson and Goldstein's solution is not valid near the entrance of the pipe. Also, in his paper, Van Dyke indicated the correct asymptotic expansion procedure for the entry developing flow. Independently, a similar, more detailed mathematical analysis was given by Wilson [19]. The zeroth order solution presented in this paper is obtained by following this procedure. A comprehensive summary of the similitude between the developing flow in a heated straight pipe and in an unheated curved pipe was given by Yao [20].

Heated Straight Pipe

It should be noted that the fully developed flow in heated straight pipes under the condition of constant wall temperature is simply the Poiseuille flow. This is because the fluid temperature is identical to the wall temperature at the fully developed stage. The developing flow in heated straight pipes can be categorized into the following three cases:

1 When ϵ and Gr are small, the entry flow deviates slightly from the developing Poiseuille flow. There are two regions, $0(a)$ and $0(a\mathrm{Re})$, which are similar to the entry flow in an unheated straight pipe [20].

2 When ϵ is small and Gr is large, the axial characteristic lengths are $0(a)$, and $0(a/\sqrt{\epsilon})$, and $0(a\mathrm{Re})$. The secondary flow becomes one of the dominant flow components as the fluid moves into the region of $0(a/\sqrt{\epsilon})$. Further downstream, the difference between the wall temperature and the core flow temperature decreases, and the flow gradually approaches the Poiseuille flow in the region of $0(a\mathrm{Re})$.

3 When ϵ is large, the region of $0(a)$ does not exist. There are two regions, $0(a/\sqrt{\epsilon})$ and $0(a\mathrm{Re})$, which are similar to case 2.

The solution presented in this paper is limited to the region distance $0(a)$ from the inlet for constant wall temperature. The solution exists, apparently, when ϵ is small. It should be noted that the entry flow is not restricted by the critical Reynolds number, $\mathrm{Re}_{cri} = 1000$, of the fully developed flow in an unheated straight pipe. In other words, the entry flow can be laminar even when $\mathrm{Re} > 1000$, but the flow transition may occur before it becomes fully developed. Therefore, the value of ϵ can be small under a large overheating condition as long as Re is large.

As the fluid enters the pipe, a boundary layer develops on the wall with a secondary flow developed inside the boundary layer by the buoyancy forces due to the temperature difference between the wall and the inlet fluid. The central inviscid flow will be accelerated by the displacement of the axial boundary layer like that in an unheated straight pipe. This motion generates node-like sinks along the center line of the pipe and causes fluid particles to move toward the center of the pipe. Simultaneously, the displacement of the secondary boundary layer induces a uniform, downward stream on the cross section of the pipe. The combination of the downward stream with the radiial stream responds to the development of two vortices in the central core of the pipe. A saddle-point-like stagnation point, initially coincident with the center line, moves downward along the vertical symmetry line of the pipe, and the saddle-point-like stagnation point will stay in the core of the pipe within the region of $0(a)$. The axial velocity profile turns to accommodate the downward stream generated

Nomenclature

a = radius of the pipe
A = variable viscosity function, equation (13)
D = Dean number = $\alpha^{-1/2}$. Re
f_0, F_1, F_2 = dimensionless stream functions
g = gravitational acceleration = 32.2 ft/s^2
G = dimensionless temperature function
Gr = Grashof number = $\gamma g a^3 \Delta T/\nu^2$
I_0, I_1, I_2 = Bessel functions
k = thermal conductivity
N_0, N = viscosity ratio, equation (13)
P = pressure
Pr = Prandtl number
r, ϕ, z = coordinates, Fig. 1 (ft)
$\bar{r}$ = coordinate normal to the wall
Re = Reynolds number, $W_{in}a/\nu$
T = temperature (°F)
$\Delta T = T_w - T_{in}$ (°F)
T_w = wall temperature (°F)
T_{in} = inlet temperature (°F)
u, v, w = velocities in the boundary layer (ft/s)
U, V, W = velocities of the inviscid core flow (ft/s)
X, Y, z = coordinates, Fig. 1
$\bar{\alpha}$ = curvature ratio
α = constant for viscosity, equation (13)
β_1, β_2 = constants, Table 1
γ = expansion coefficient
$\delta_1 = 1/\sqrt{\mathrm{Re}}$
$\epsilon = \mathrm{Gr}/\mathrm{Re}^2$, equation (7)
θ_0, Θ = dimensionless temperature = $T - T_{in}/T_w - T_{in}$
Θ_c = dimensionless temperature at $r = 0$
κ = thermal diffusivity
η = Blasius variable

Subscripts

0, 01, 10, 11, 20 = indicate the order of the perturbing functions by the displacement of the secondary boundary layer: a favorable pressure gradient develops along the bottom wall of the pipe; on the contrary, an unfavorable pressure gradient develops along the top wall of the pipe. It is found that the temperature in the central core of the pipe does not change within the region of $0(a)$ and is identical to the inlet temperature. It is expected that the strength of the sinks along the pipe center line will gradually decrease and the downward-stream pattern will become dominant as the fluid moves downstream of the region, a distance $0(a)$ from the inlet when Gr is large.

Governing Equations

Near the inlet it is natural to refer lengths to the radius, a, of the pipe, the velocities to the uniform inlet velocity, W_{in} (Fig. 1). The pressure is nondimensionalized by $\rho_{in}W_{in}{}^2$, where ρ_{in} is the density. The dimensionless temperature is defined in terms of the inlet temperature, T_{in}, and the constant wall temperature, T_w, as $\Theta = (T - T_{in})/(T_w - T_{in})$. The dimensionless equations of motion and energy with the Boussinesq approximation in cylindrical coordinates become

$$\frac{1}{r}\frac{\partial(rU)}{\partial r}+\frac{1}{r}\frac{\partial V}{\partial\phi}+\frac{\partial W}{\partial z}=0 \qquad (2a)$$

$$U\frac{\partial U}{\partial r}+\frac{V}{r}\frac{\partial U}{\partial\phi}+W\frac{\partial U}{\partial z}-\frac{V^2}{r}=-\frac{\partial P}{\partial r}+\epsilon(\Theta-\Theta_c)\cos\phi+\frac{1}{\mathrm{Re}}\left(\nabla^2U-\frac{U}{r^2}-\frac{2}{r^2}\frac{\partial V}{\partial\phi}\right) \qquad (2b)$$

$$U\frac{\partial V}{\partial r}+\frac{V}{r}\frac{\partial V}{\partial\phi}+W\frac{\partial V}{\partial z}+\frac{UV}{r}=-\frac{\partial P}{r\partial\phi}+\epsilon(\Theta-\Theta_c)\sin\phi+\frac{1}{\mathrm{Re}}\left(\nabla^2V-\frac{V}{r^2}+\frac{2}{r^2}\frac{\partial U}{\partial\phi}\right) \qquad (2c)$$

$$U\frac{\partial W}{\partial r}+\frac{V}{r}\frac{\partial W}{\partial\phi}+W\frac{\partial W}{\partial z}=-\frac{\partial P}{\partial z}+\frac{1}{\mathrm{Re}}\nabla^2W \qquad (2d)$$

$$U\frac{\partial\Theta}{\partial r}+\frac{V}{r}\frac{\partial\Theta}{\partial\phi}+W\frac{\partial\Theta}{\partial z}=\frac{1}{\mathrm{PrRe}}\nabla^2\Theta \qquad (2e)$$

where

$$\nabla^2=\frac{\partial^2}{\partial r^2}+\frac{1}{r}\frac{\partial}{\partial r}+\frac{1}{r^2}\frac{\partial^2}{\partial\phi^2}+\frac{\partial^2}{\partial z^2} \qquad (3)$$

is the Laplace operator, Θ_c is the temperature along the center line of the pipe. The parameters ϵ, Re, and Pr are defined in equation (1).

The entry condition is uniform inlet axial velocity and temperature; the reference pressure at the inlet is set equal to zero. It may be noted that, in the absence of viscosity, the exact solution of equations (2) satisfying the above inlet condition and slip wall condition is

$$W = 1, U = V = P = \Theta = 0 \qquad (4)$$

Solutions

As the fluid flows into the pipe, the viscous forces are confined to the thin boundary layer near the wall of the pipe. For a heated pipe the secondary flow is created by the buoyancy forces inside the thermal boundary layer. The ratio of the thicknesses of the thermal boundary layer to the momentum boundary layer depends on the Prandtl number. Viscous forces and heat conduction can be ignored away from the boundary layer; the flow is isothermal and inviscid in the central core of the pipe. The core flow is accelerated due to the displacement effect of the boundary layer, and fluid particles will be pushed from the wall toward the center of the pipe. Simultaneously, a downward stream is developed due to the displacement effect of the secondary boundary layer. The combination of the radial-direction motion with the downward one gives the stream pattern of two developing vortices on the cross section normal to the axis of the pipe. The downward stream will also skew the axial velocity by accelerating it below the center and decelerating it above the center of the pipe. The analysis shows that the development of the secondary flow due to the heating effect near the entrance when ϵ is small can be obtained by perturbing the solution of the developing flow in an unheated pipe.

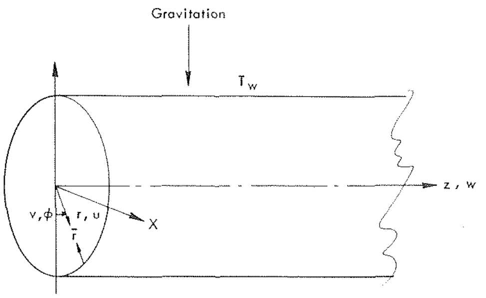

Fig. 1 Coordinate systems

Zeroth-Order Solution in the Inviscid Flow. The solution of the inviscid core flow can be obtained by expanding the dependent variables into series in δ, which are

$$U = U_0 + \delta U_1 + \ldots, \quad V = V_0 + \delta V_1 + \ldots, \quad W = W_0 + \delta W_1 + \ldots \quad P = P_0 + \delta P_1 + \ldots, \quad \Theta = \Theta_0 + \delta\Theta_1 + \ldots, \quad \Theta_c = \Theta_0^c + \delta\Theta_1^c + \ldots \qquad (5)$$

where δ is the expansion parameter and can be determined by matching with the zeroth-order boundary-layer flow. It can be shown that it is equal to $1/\sqrt{\mathrm{Re}}$. The governing equations of the first order can be obtained by taking the limit of $\mathrm{Re}\to\infty$ from equations (2). The zeroth solutions which satisfy the uniform inlet velocity and temperature conditions and the slip condition at the pipe wall are just the undisturbed flow, which is given in equation (4).

Zeroth-Order and First-Order Boundary-Layer Flow. Near the pipe wall, the viscous forces and heat conduction normal to the wall become important. The radial coordinate r is stretched to reflect this physical fact. Accordingly, we introduce the inner variables, as in the classical boundary layer,

$$r = 1 - \delta\bar{r}, \quad U = -\delta u, \quad V(r, \phi, z) = v(\bar{r}, \phi, z), \quad \text{etc.} \qquad (6)$$

A combination of equations (2) and (6), after neglecting the smaller order terms, yields

$$\left.\begin{aligned}
&\frac{\partial u}{\partial\bar{r}}+\frac{\partial v}{\partial\phi}+\frac{\partial w}{\partial z}=0\\
&u\frac{\partial v}{\partial\bar{r}}+v\frac{\partial v}{\partial\phi}+w\frac{\partial v}{\partial z}=-\frac{\partial P}{\partial\phi}+\epsilon(\theta-\theta_c)\sin\phi+\frac{\partial^2v}{\partial\bar{r}^2}\\
&u\frac{\partial w}{\partial\bar{r}}+v\frac{\partial w}{\partial\phi}+w\frac{\partial w}{\partial z}=-\frac{\partial P}{\partial z}+\frac{\partial^2w}{\partial\bar{r}^2}\\
&u\frac{\partial\theta}{\partial\bar{r}}+v\frac{\partial\theta}{\partial\phi}+w\frac{\partial\theta}{\partial z}=\frac{1}{\mathrm{Pr}}\frac{\partial^2\theta}{\partial\bar{r}^2}
\end{aligned}\right\} \qquad (7)$$

The analysis of the first-order boundary-layer flow can be easily extended to the case that fluid properties depend on the temperature. For most liquids, the principal departure from constant-property flow is due to the viscosity variation. Including the variable viscosity of the fluid, the terms of the viscous forces in equations (7) will be replaced by

$$\frac{\partial^2v}{\partial\bar{r}^2}\to\frac{\partial}{\partial\bar{r}}\left(N\frac{\partial v}{\partial\bar{r}}\right),\quad \frac{\partial^2w}{\partial\bar{r}^2}\to\frac{\partial}{\partial\bar{r}}\left(N\frac{\partial w}{\partial\bar{r}}\right) \qquad (8)$$

where

$$N = \mu/\mu_\infty$$

is the viscosity normalized by the viscosity in the central core. The associated boundary conditions of equations (7) are

$$\left.\begin{array}{ll}\text{At } z = 0, u = v = \theta = 0, w = 1 & \text{(entrance condition)}\\ \text{At } \bar{r} = 0, u = v = w = 0 & \text{(no-slip condition at wall)}\\ \qquad\theta = 1, \text{ or} & \text{(constant wall temperature)}\\ \text{As } \bar{r} \to \infty, v \to 0, w \to 1, \theta \to 0 & \text{(matching condition with}\\ & \text{zeroth-order inviscid}\\ & \text{core flow)}\end{array}\right\} \quad (9)$$

Under the constant wall temperature, the zeroth-order boundary-layer solutions of equations (7) satisfying the conditions (8) have been published by Yao and Catton [21, 22] for Pr = 0.01, 1, 10 of the constant property flow and Pr = 8 of the water flow (variable viscosity). Their results will be summarized briefly below in order to make this paper self-contained.

The dependent variables can be expressed as

$$w = f_0'(\eta) + \epsilon(2z)^2F_1'(\eta)\cdot \cos\phi + \delta\cdot(2z)^{1/2}(f_3'(\eta) - f_0) \quad (10a)$$

$$v = \epsilon(2z)\cdot F_2'(\eta)\cdot \sin\phi + \ldots \quad (10b)$$

$$u = \frac{1}{\sqrt{2z}}(\eta f_0' - f_0) + \epsilon(2z)^{3/2}(\eta F_1' - 5F_1 - F_2)\cdot\cos\phi + \delta(\eta f_3' - 2f_3) + \ldots \quad (10c)$$

$$\theta = \theta_0(\eta) + \epsilon(2z)^2\cdot G_1(\eta)\cdot\cos\phi + \delta(2z)^{1/2}g_2(\eta) + \ldots \quad (10d)$$

where $\eta = \bar{r}/\sqrt{2z}$ is the Blasius variable. The terms of $0(\delta)$ in equations (10) represent the effect of the core flow acceleration due to the axial boundary-layer displacement, which can be determined by matching the first-order core flow. The f_0 in the last term of equation (10a) represents the transverse curvature effect. Substitution of equations (10) into equations (7), and collecting terms of equal order yield

$$(N_0f_0'')' + f_0f_0'' = 0, \quad \theta_0'' + \mathrm{Pr}f_0\theta_0' = 0 \quad (11a,b)$$

and

$$\left.\begin{array}{l}(N_0F_1'')' + f_0F_1'' - 4f_0'F_1' - 5f_0''F_1 + f_0''F_2 = (A\cdot G\cdot f_0'')'\\ (N_0F_2'')' + f_0F_2'' - 2_0'F_2' = -\theta_0\\ \dfrac{1}{\mathrm{Pr}}G_1'' + f_0G_1' - 4f_0'G_1 = -\theta_0'(5F_1 + F_2)\end{array}\right\} \quad (12)$$

where

$$N_0 = \frac{1}{1 + \alpha(T_w - T_{in})\theta_0}, \quad A = \frac{-\alpha(T_w - T_{in})}{[1 + \alpha(T_w - T_{in})\theta_0]^2} \quad (13)$$

and α is the coefficient of the variable viscosity. For water in the temperature range between 40°F (4.4°C) and 100°F (37.8°C), $\alpha \simeq 0.0151\ (°\mathrm{F})^{-1}$; for the constant property flow, $\alpha = 0$. The boundary conditions (9) become

$$\left.\begin{array}{l}f_0 = f_0' = 0 \text{ and } \theta_0 = 1 \text{ at } \eta = 0\\ f_0' \to 0 \text{ and } \theta_0 \to 0 \text{ as } \eta \to \infty\end{array}\right\} \quad (14a)$$

and

$$\left.\begin{array}{l}F_1 = F_1' = F_2 = F_2' = G_1 = 0 \text{ at } \eta = 0\\ F_1', F_2', \text{ and } G_1 \to \infty \text{ as } \eta \to \infty\end{array}\right\} \quad (14b)$$

The numerical values of stream functions f_0, θ_0, F_1, F_2, and G_1 can be found in Yao and Catton [21, 22].

The velocity normal to the wall along the outer edge of the boundary layer is required to solve the first-order inviscid core flow (matching conditions). The matching conditions can be obtained by taking the limit of equation (10c) for $\eta \to \infty$, which gives

$$U_1(r = 1) = -\lim_{\eta\to\infty}\left\{\frac{1}{\sqrt{2z}}(\eta f_0' - f_0) + \epsilon(2z)^{3/2} \times (\eta F_1' - 5F_1' - F_2)\cos\phi + \ldots\right\}$$

$$= \frac{\beta_1}{\sqrt{2z}} - \epsilon\beta_2(2z)^{3/2}\cos\phi + \ldots \quad (15a)$$

where

$$\beta_1 = \lim_{\eta\to\infty}(\eta - f_0), \beta_2 = \lim_{\eta\to\infty}(5F_1 + F_2) \quad (15b,c)$$

The values of β_1 and β_2 for Pr = 0.01, 1., 10 of the constant property flow and for Pr = 8 of the water flow are taken from Yao and Catton [11, 12] and are listed in Table 1.

First-Order Inviscid Core Flow. The equations of the second-order inviscid core flow are found by substituting equations (4) and (5) into equations (2). They are

$$\frac{1}{r}\frac{\partial(rU_1)}{\partial r} + \frac{1}{r}\frac{\partial V_1}{\partial\phi} + \frac{\partial W_1}{\partial z} = 0 \quad (16a)$$

$$\frac{\partial U_1}{\partial z} = -\frac{\partial P_1}{\partial r} + \epsilon(\Theta_1 - \Theta_1^c)\cos\phi \quad (16b)$$

$$\frac{\partial V_1}{\partial z} = -\frac{\partial P_1}{r\partial\alpha} + \epsilon(\Theta_1 - \Theta_1^c)\sin\phi \quad (16c)$$

$$\frac{\partial W_1}{\partial z} = -\frac{\partial P_1}{\partial z} \quad (16d)$$

$$\frac{\partial\Theta_1}{\partial z} = 0 \quad (16e)$$

The temperature of the inviscid core flow, up to this order, is still not changed and is equal to the inlet temperature. This is confirmed by equation (16e), the solution of which is $\Theta_1 \equiv 0$. Therefore, there is no buoyancy force acting on the fluid in the central core of the pipe. Equations (16a) through (16d) can be separated into two parts: the accelerating axial flow due to the displacement effect of the axial boundary layer and the downward stream due to the displacement effect of the secondary boundary layer. The equations governing the two phenomena are found by substituting

$$U_1 = U_{10} + \epsilon U_{11}\cos\phi + \ldots, \quad V_1 = \epsilon V_{11}\sin\phi + \ldots$$

$$W_1 = W_{10} + \epsilon W_{11}\cos\phi + \ldots, \quad P_1 = P_{10} + \epsilon P_{11}\cos\phi + \ldots \quad (17)$$

into equations (16). After collecting the terms without ϵ and with ϵ, we have

$$\frac{1}{r}\frac{\partial(rU_{10})}{\partial r} + \frac{\partial W_{10}}{\partial z} = 0 \quad (18a)$$

$$\frac{\partial U_{10}}{\partial z} = -\frac{\partial P_{10}}{\partial r}, \quad \frac{\partial W_{10}}{\partial z} = -\frac{\partial P_{10}}{\partial z} \quad (18b,c)$$

and

$$\frac{1}{r}\frac{\partial(rU_{11})}{\partial r} + \frac{V_{11}}{r} + \frac{\partial W_{11}}{\partial z} = 0, \quad \frac{\partial U_{11}}{\partial z} = -\frac{\partial P_{11}}{\partial r} \quad (19a,b)$$

$$\frac{\partial V_{11}}{\partial z} = \frac{P_{11}}{r}, \quad \frac{\partial W_{11}}{\partial z} = -\frac{\partial P_{11}}{\partial z} \quad (19c,d)$$

Displacement Effect 0(δ). The appropriate matching condition for equations (18) is

$$U_{10} = -\beta_1/(2z)^{1/2} \text{ at } r = 1 \quad (20a)$$

and the entry conditions are

Table 1 Constants from the computation of the boundary-layer flow

(1) Constant Property (Yao and Catton [21])

Pr	0.01	1	10
β_1	1.2167	1.2167	1.2167
β_2	3.9454	0.8534	0.3158

(2) Variable Viscosity (Pr = 8) (Yao and Catton [22])

$\alpha\Delta T$	0	0.5	1
β_1	1.2167	1.0617	0.9497
β_2	0.3522	0.3106	0.2835

$$P_{10} = W_{10} = 0 \text{ at } z = 0 \tag{20b}$$

Integrating equation (18c) with respect to z and using (20a) gives

$$W_{10} = P_{10} \tag{21}$$

Eliminating U_{10} and W_{10} from equations (18a), (18b), and (21) results in

$$\frac{\partial^2 P_{10}}{\partial r^2} + \frac{1}{r}\frac{\partial P_{10}}{\partial r} + \frac{\partial^2 P_{10}}{\partial z^2} = 0 \tag{22}$$

The solution of equation (22) satisfying condition (20a) can be found by Fourier Transform in the sense of generalized functions [23]. It is

$$P_{10} = -\frac{\beta_1}{\sqrt{\pi}} \int_0^\infty \alpha^{-1/2} \frac{I_0(\alpha r)}{I_1(\alpha)} \sin \alpha z \, d\alpha \tag{23a}$$

where Is are modified Bessel functions. Substituting equation (23a) into equations (18b) and 18c), we obtain

$$W_{10} = \frac{\beta_1}{\sqrt{\pi}} \int_0^\infty \alpha^{-1/2} \frac{I_0(\alpha r)}{I_1(\alpha)} \sin \alpha z \, d\alpha \tag{23b}$$

and

$$U_{10} = -\frac{\beta_1}{\sqrt{\pi}} \int_0^\infty \alpha^{-1/2} \frac{I_1(\alpha r)}{I_1(\alpha)} (\cos \alpha z - 1) d\alpha \tag{23c}$$

The asymptotic values of equations (23) for large z can be easily found:

$$W_{10} = -P_{10} = \beta_1 \cdot 2(2z)^{1/2} \cdot \left[1 + \frac{1}{4}\frac{r^2}{(2z)^2} + \ldots\right] \tag{24a}$$

$$U_{10} = -\beta_1 \cdot r \cdot (2z)^{-1/2} \tag{24b}$$

Equations (23) or (24) represent the accelerating flow due to the displacement effect of the boundary layer in an unheated pipe.

Secondary Displacement Effect 0($\delta\epsilon$). For the constant wall temperature, the matching condition for equations (19) is found from equations (15) and is

$$U_{11} = \beta_2 (2z)^{3/2} \text{ at } r = 1 \tag{25a}$$

The entry conditions are

$$P_{11} = W_{11} = 0 \text{ at } z = 0 \tag{25b}$$

Solving equations (19) with condition (25) yields

$$-W_{11} = P_{11} = -\frac{6\beta_2}{\sqrt{\pi}} \int_0^\infty \alpha^{-5/2} \frac{I_1(\alpha r)}{I_0(\alpha) + I_2(\alpha)} \sin \alpha z \cdot d\alpha \tag{26a}$$

$$V_{11} = -\frac{6\beta_2}{r\sqrt{\pi}} \int_0^\infty \alpha^{-5/2} \frac{I_1(\alpha r)}{I_0(\alpha) + I_2(\alpha)} (\cos \alpha z - 1) d\alpha \tag{26b}$$

and

$$U_{11} = -\frac{3\beta_2}{\sqrt{\pi}} \int_0^\infty \alpha^{-5/2} \frac{I_0(\alpha r) + I_2(\alpha r)}{I_0(\alpha) + I_2(\alpha)} (\cos \alpha z - 1) d\alpha \tag{26c}$$

For a large z, they can be approximated by

$$W_{11} = -P_{11} \sim 3\beta_2 \cdot r \cdot \left[(2z)^{1/2} + \tfrac{1}{2} \Big(1 - \frac{r^2}{4} (2z)^{-3/2} + \ldots \right] \tag{27a}$$

$$-V_{11} = U_{11} \sim \beta_2 (2z)^{3/2} + \ldots \tag{27b}$$

First-Order Boundary-Layer Flow 0(δ). The differential equations for the first-order boundary-layer flow are

$$\begin{aligned}[N_0 f_3'']' + f_0 f_3'' - f_0' f_3' + 2 f_0'' f_3 = {} & -2\beta_1 + N_0' f_0' \\ & + (\eta f_0 + 2N_0) f_0'' + [A g_2 f_0'']' \end{aligned} \tag{28a}$$

$$g_2'' + \Pr(f_0 g_2' - f_0' g_2) = \theta_0' \cdot [1 + \Pr(\eta f_0 - 2f_3)] \tag{28b}$$

The associated boundary conditions are

$$\left.\begin{aligned} & f_3 = f_3' = g_2 = 0 \text{ at } \eta = 0 \\ & f_3' \to 2\beta_1 + f_0,\ g_2 \to 0 \text{ as } \eta \to \infty \end{aligned}\right\} \tag{29}$$

Results and Discussion

Boundary-Layer Flow. A detailed discussion of the zeroth-order boundary-layer flow and its stability can be found in Yao and Catton [21, 22] and will not be repeated here.

Functions f_3, f_3', and g_2, the acceleration effect on the boundary-layer flow due to the displacement of the axial boundary layer, are presented in Figs. 2–4. The value of f_3 is reduced by the variable viscosity, and so is the overshot of the velocity profile, f_3'. The magnitude of the perturbed temperature is smaller for the water flow due to its variable viscosity. This is simply due to the fact that the thickness of

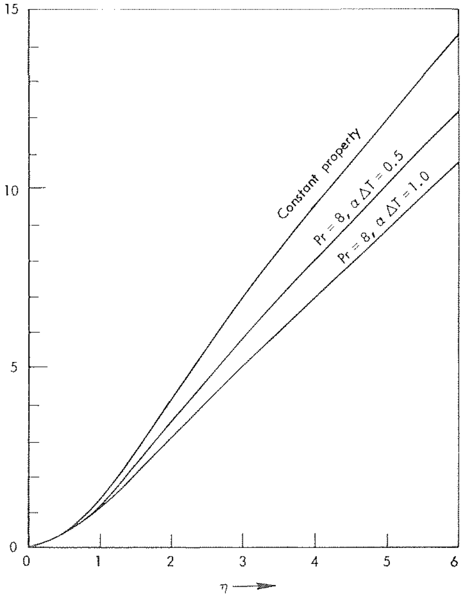

Fig. 2 Function f_3

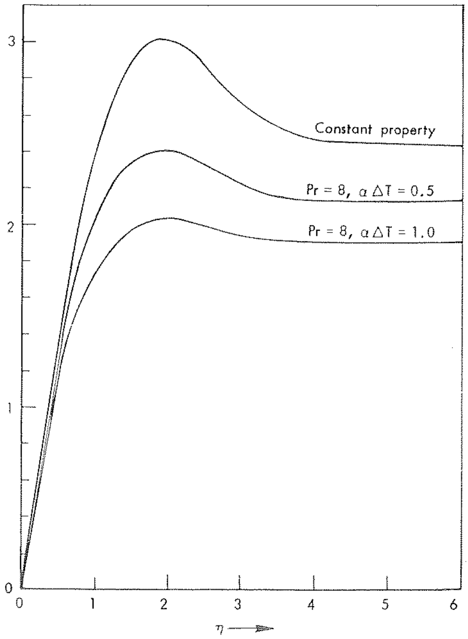

Fig. 3 Function f_3'

the boundary layer is thinned by heating.

The local Nusselt number can be written as

$$\frac{\mathrm{Nu}}{\mathrm{Nu}_0} = 1 + \epsilon(2z)^2 \cdot \frac{G_1'(0)}{\theta_0'(0)} \cdot \cos\phi + \delta(2z)^{1/2}\frac{g_2'(0)}{\theta_0'(0)} + \ldots \qquad (30)$$

where "0" denotes the forced convection without considering the buoyancy forces and the interaction of the boundary-layer flow and the core flow. The values of $\theta_0'(0)$, $G_1'(0)$, and $g_2'(0)$ are given in Table 2. The last term of equation (30) shows that the acceleration of the core flow due to the displacement of the axial boundary layer will increase the local heat transfer rate except for very small Prandtl numbers ($\mathrm{Pr} = 0.01$). The third term, $0(\epsilon)$, of equation (30) represents the effect of the secondary boundary layer on the Nusselt number, which enhances the heat transfer along the bottom wall, $-90° \le \phi \le 90°$, of the pipe and degrades the heat transfer along the top wall, $90° \le \phi \le 270°$, of the pipe.

Similar interpretation can be given to the axial shear stress,

$$\frac{\tau_{rz}}{(\tau_{rz})_0} = 1 + \epsilon(2z)^2 \frac{F_1''(0)}{f_0''(0)} \cdot \cos\phi + \delta(2z)^{1/2}\frac{f_3''(0)}{f_0''(0)} \qquad (31)$$

The circumferential stress is

$$\tau_{r\varphi} \sim \epsilon(2z)^{1/2}F_2''(0)\sin\phi \qquad (32)$$

Inviscid Core Flow. Equations (23*a*,*b*) and (26*a*) are numerically integrated by using the Fast Fourier Transform. The details of the numerical method are given by Yao [20]. W_{10}/β_1 (or $-P_{10}/\beta_1$) and W_{11}/β_2 (or $-P_{11}/\beta_2$) are evaluated at $r = 0.5$ as functions of z, and plotted in Fig. 6. The values of W_{10}/β_1 (or $-P_{10}/\beta_1$) at $r = 0$ differ only slightly from their values at $r = 0.5$ and are not presented in Fig. 5. Along the center line, functions W_{11} and P_{11} are identical to zero. W_{10} is the flow acceleration due to the displacement effect of the axial boundary layer. The flow is quickly accelerated near the entrance, and

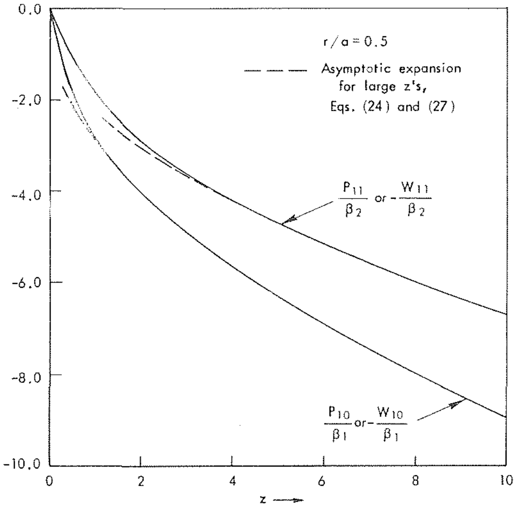

Fig. 5 Displacement effect: pressure P_{10}/β_1, velocity W_{10}/β_1; and secondary-flow effect: pressure P_{11}/β_2, velocity W_{11}/β_2, on the cross sections at $z = 0.1, 0.5, 1.0, 2.5$

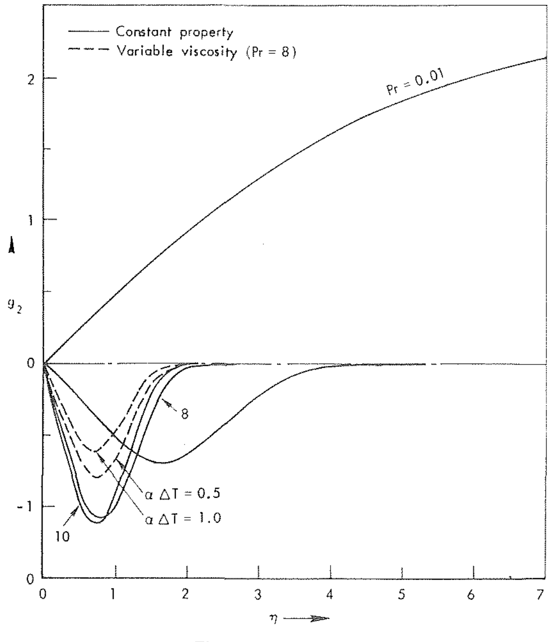

Fig. 4 Function g_2

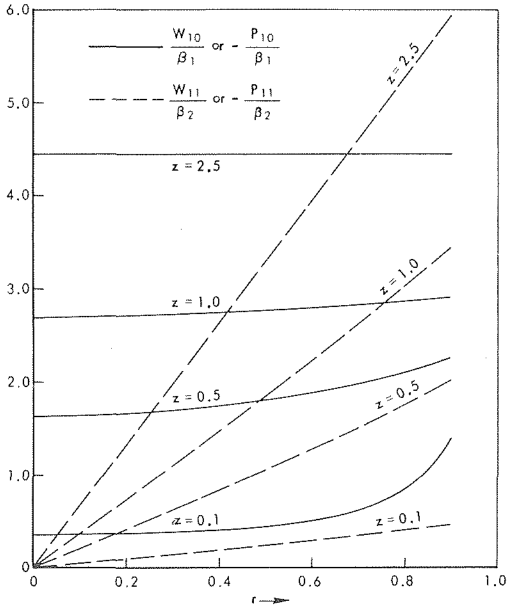

Fig. 6 Displacement effect W_{10}/β_1 (or $-P_{10}/\beta_1$), and secondary flow W_{11}/β_2 (or P_{11}/β_2)

Table 2 Coefficient for heat transfer and shear stress

	$\theta_0'(0)$	$G_1'(0)$	$g_2'(0)$	$f_0''(0)$	$F_1''(0)$	$F_2''(0)$	$F_3''(0)$
(1) Constant Property							
Pr = 0.01	−0.07628	−0.0064	0.5423	0.4695	0.0910	0.9274	3.1744
1.0	−0.4695	−0.0467	−0.3856	0.4695	0.0467	0.6174	3.1744
8.0	−0.9552	−0.06627	−1.6678	0.4695	0.0230	0.4150	3.1744
10.0	−1.0295	−0.0677	−1.8669	0.4695	0.0209	0.3942	3.1744
(2) Variable Viscosity (Pr = 8)							
αΔT = 0.5	−1.0397	−0.0542	−1.2989	0.6665	0.0265	0.5363	3.4338
= 1.0	−1.1036	−0.0465	−1.0180	0.8408	0.0284	0.6389	3.4649

the acceleration declines and is proportional to $z^{-1/2}$ downstream. The distributions of W_{10} (or P_{10}) on the cross section normal to the pipe axis are given in Fig. 6. Near the entrance, $z = 0.1$, the axial velocity is higher close to the boundary layer than along the center line of the pipe. The delay of the flow acceleration near the center line causes the axial velocity profile to become concave. The velocity profile has its maximum velocity off the center line. The peaks are eroded downstream and eventually disappear at $z = 2.5$ (see Fig. 5). The overshoot of the axial velocity profile (see Fig. 3) moves into the boundary layer and can be estimated from equation (10*a*). Further downstream, the overshoot of the axial velocity profile moves toward the wall and disappears. A similar interpretation can be given to P_{10}, which is the pressure drop.

The displacement effects of the secondary boundary layer are represented by functions W_{11} and P_{11}. Physically, the secondary boundary layer causes the axial flow to turn counterclockwise around the horizontal line passing through the center of the pipe and normal to the axis of the pipe, $Y = r \cos \phi = 0$, and does not cause any net mean acceleration of the flow. The turning rate is higher near the entrance and gradually matches the rate which is proportional to $z^{-1/2}$.

The asymptotic expansions, equations (24*a*) and (27*a*), of equations (23*a, b*) and (26*a*) for large z's are also plotted in Fig. 6. They show that the asymptotic values of W_{10} (or P_{10}) match their exact value approximately at $z = 2$. For W_{11} (or P_{11}), the asymptotic values start to be valid at $z = 4$. The comparison of the asymptotic expansions with the exact evaluation of the sine integrals suggests that simpler asymptotic expansions can be used for practical application when z is larger than four, which will cover most ranges of practical interest when ϵ is small. The velocity components and the pressure, in terms of their asymptotic forms, are

$$P = -\delta \cdot (2z)^{1/2} \cdot \left\{ 2\beta_1 \left[1 + \frac{r^2(2z)^{-2}}{4} + \dots \right] \right.$$

$$\left. + \epsilon \cdot 3\beta_2 \cdot r \cos \phi \cdot \left[1 + ½ \left(1 - \frac{r^2}{4} \right) (2z)^{-2} + \dots \right] \right\} \qquad (33a)$$

$$W = 1 - P \qquad (33b)$$

$$U = -\delta \cdot \{\beta_1[r(2z)^{-1/2} + \dots] - \epsilon\beta_2[(2z)^{3/2} \cdot \cos \phi + \dots]\} \qquad (33c)$$

$$V = -\delta\epsilon\beta_2[(2z)^{3/2} \cdot \sin \delta + \dots] \qquad (33d)$$

Pressure Drop. The pressure head will drop along the pipe when the flow is accelerated. The first term of equation (33*a*) represents the pressure drop in an unheated pipe due to the displacement of the axial boundary layer. The pressure drops faster close to the edge of the boundary layer than along the center line of the pipe where $r = 0$. The difference in the pressure distribution on the cross section of the pipe disappears for large z, and the pressure distribution approaches

$$P \sim -\delta \cdot 2\beta_1(2z)^{1/2} \qquad (34)$$

The pressure distribution is disturbed when the pipe wall is heated, which is represented by the second term of equation (33*a*). This term can be rewritten in $(\overline{X}, \overline{Y}, z)$ coordinates as $\delta\epsilon 3\beta_2 Y(2z)^{1/2}$, which shows that the displacement effect of the secondary boundary layer introduces an unfavorable pressure gradient over the upper half of the pipe flow, $Y > 0$, and a favorable one over the lower half of the pipe, $Y < 0$.

Axial-Velocity Profiles of the Core Flow. The axial velocity of the core flow can be viewed as a superposition of three components. The first one is the undisturbed flow at the inlet, i.e., $W = 1$. The second one is the accelerated flow due to the displacement effect of the axial boundary layer in an unheated pipe. The last component is due to the displacement of the secondary boundary layer. Similar to the pressure distribution, the third term in (X, Y, z) coordinates is $-\delta\epsilon 3\beta_2 Y(2z)^{1/2}$, which means that the axial velocity profile turns counterclockwise around $Y = 0$. In the region of $z \sim 0(a)$, both the second and the third terms increase as $z^{1/2}$. However, the second term may be dropped when the third term is still growing downstream beyond the region of $0(a)$ when Gr is not small. For the cases of small Gr (or ReGr), the second and the third terms will continue growing and the flow will approach its fully developed state.

Velocities on the Cross Section. The radial velocity component U is given in equation (33*c*). The first term is due to the displacement effect of the axial boundary layer, which displaces the fluid away from the wall and toward the center of the pipe. The second term represents the motion when the fluid leaves the boundary layer over the upper half of the pipe ($\pi/2 < \phi < 3\pi/2$), and enters the boundary layer over the lower half of the pipe ($-\pi/2 < \delta < \pi/2$). The first kind of motion declines downstream, and the second one increases due to heating. They become the same order of magnitude when $z \sim 0(a/\sqrt{\epsilon})$. Beyond this point, the analysis is not valid anymore. For the case of large Gr, the second term becomes dominant and the axial length scale will be $a/\sqrt{\epsilon}$). For a small Gr, $a/\sqrt{\epsilon}$ is larger than $a \cdot$ Re. This suggests that the next length scale will be $a \cdot$ Re; physically, it suggests that the flow development will be similar to be unheated, straight pipe and the solution of the slightly heated pipe can be obtained by perturbing the solution of an unheated pipe. Along the line of $\phi = 0$, where $V = 0$, there is a stagnation point at (from equation (33*c*))

$$r = \frac{\beta_2}{\beta_1} [\epsilon(2z)^2] \qquad (35)$$

This is also a saddle point, point P in Fig. 7.

Streamlines on the Cross Section. The projection of the streamline on a cross section can be computed (from equations (33c) and (33*d*)) by

$$\frac{1}{r}\frac{dr}{d\varphi} = \frac{\beta_1 r(2z)^{-1/2} - \epsilon\beta_2 \cos \phi (2z)^{3/2}}{\epsilon\beta_2 \sin \phi (2z)^{3/2}} \qquad (36)$$

Equation (36) shows that all streamlines are tangent to the vertical line, $\phi = 0, \pi$, and are plotted in Fig. 7. If z is not too large, the second term in the numerator of equation (36) can be neglected and equation

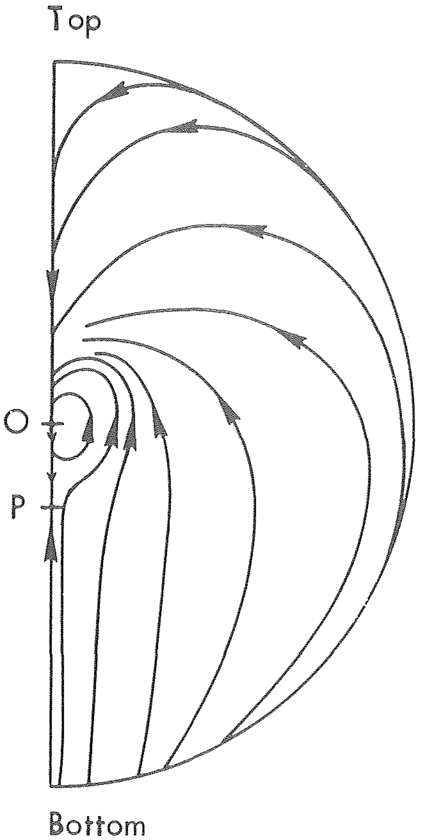

Fig. 7 Streamlines on the cross section

(36) can be integrated to give

$$\tan\frac{\phi}{2} = e^{-\epsilon\beta_2(2z)^2/\beta_1 r} + \text{constant} \tag{37}$$

For $\epsilon = 0$, an unheated straight pipe, equation (37) becomes $\phi =$ constant. The streamlines on the cross section are a radial straight line. Within the limit of the analysis, the second term on the numerator of equation (36) can never be larger than the first one. Nevertheless, stretching somewhat our interpretation of equation (36) and considering it for large z can predict what may occur for the flow development further downstream. Equation (36) becomes, after neglecting the first term of the numerator and integrating,

$$\bar{x} = \text{constant} \tag{38}$$

which shows that the streamlines on the cross section, due to the displacement effect of the secondary boundary layer, are vertical straight lines. The magnitude of this downward flow is

$$\sqrt{U_{11}^2 + V_{11}^2} = \beta_2(2z)^{3/2} \tag{39}$$

which increases downstream. This flow, when Gr is large, will eventually become the dominant flow pattern, which is observed by Mori and Futagami [7]. Also, the downward stream forms a stagnation-like flow locally along the bottom wall of the pipe. The convective effect of this locally stagnant flow prevents the boundary layer from growing. Thus, the boundary layer will remain thin as the flow moves downstream. Therefore, the flow acceleration due to the displacement effect of the axial boundary layer will fade out. This suggests that the flow development in the region of $0(a/\sqrt{\epsilon})$ is mainly in changing the slope of the axial velocity profile to balance the gradually enhanced flow in the secondary boundary layer. Also, the unfavorable pressure gradient near the top wall of the pipe gradually grows and eventually triggers the separation of the boundary layer further downstream. The phenomenon of the flow development will be similar to that of a curved pipe given by Yao and Berger [24].

References

1 Morton, B. R., "Laminar Convection in Uniformly Heated Horizontal Pipee at Low Rayleigh Numbers," *Quarterly Journal of Mechanics and Applied Mathematics,* Vol. 12, 1959, pp. 410–420.

2 Dean, W. R., "Note on the Motion of Fluid in a Curved Pipe," *Philosophical Magazine,* Vol. 4, 1927, pp. 208–223.

3 Dean, W. R., "The Stream-Line Motion of Fluid in a Curved Pipe," *Philosophical Magazine,* Vol. 5, 1928, pp. 673–695.

4 Mori, Y., and Futagami, K., "Forced Convective Heat Transfer in Uniformly Heated Horizontal Tubes," *International Journal of Heat and Mass Transfer,* Vol. 10, 1967, pp. 1801–1813.

5 Barua, S. N., "Secondary Flow in Stationary Curved Pipes," *Quarterly Journal of Mechanics and Applied Mathematics,* Vol. 16, 1963, pp. 61–77.

6 Hong, S. W., and Bergles, A. E., "Theoretical Solutions for Combined Force and Free Convection in Horizontal Tubes with Temperature-Dependent Viscosity," ASME, JOURNAL OF HEAT TRANSFER, Vol. 98, 1976, pp. 459–465.

7 Mori, Y., Futagami, K., Tokuda, S., and Nakamura, M., "Forced Convective Heat Transfer in Uniformly Heated Horizontal Tubes," *International Journal of Heat and Mass Transfer,* Vol. 9, 1965, pp. 453–463.

8 Taylor, G. I., "The Criterion for Turbulence in Curved Pipes," *Proceedings of the Royal Society,* Vol. A124, 1927, p. 243.

9 Ou, J. W., and Cheng, K. C., "Natural Convection Effects on Graetz Problem in Horizontal Isothermal Tubes," *International Journal of Heat and Mass Transfer,* Vol. 20, 1977, pp. 953–960.

10 Hong, S. W., Morcos, S. M., and Bergles, A. E., "Analytical and Experimental Results for Combined Forced and Free Laminar Convection in Horizontal Tubes," *Heat Transfer 1974,* Vol. III, Fifth International Heat Transfer Conference, Tokyo, 1974, pp. 159–163.

11 Siegwarth, D. P., Mikesell, R. D., Readal, T. C., and Hanrathy, T. J., "Effect of Secondary Flow on the Temperature Field and Primary Flow in a Heated Horizontal Pipe," *International Journal of Heat and Mass Transfer,* Vol. 12, 1969, pp. 1535–1551.

12 Huang, G. J., and Cheng, K. C., "Boundary Vorticity Method for Convective Heat Transfer with Secondary Flow-Application to the Combined Free and Forced Laminar Convection in Horizontal Tubes," *Heat Transfer 1970,* Vol. IV, Fourth International Heat Transfer Conference, Paris, 1970, NC 3.5.

13 Cheng, K. C., and Hong, S. W., "Combined Free and Forced Laminar Convection in Inclined Tubes," *Applied Science Research,* Vol. 27, 1972, pp. 19–38.

14 Collins, W. M., and Dennis, S. C. R., "The Steady Motion of a Viscous Fluid in a Curved Tube," *Quarterly Journal of Mechanics and Applied Mathematics,* Vol. 28, Part 2, 1975, pp. 133–156.

15 Greenspan, D., "Secondary Flow in a Curved Pipe," *Journal of Fluid Mechanics,* Vol. 57, Part 1, 1973, pp. 167–176.

16 Hieber, C. A., and Sreenivasan, S. K., "Mixed Convection in an Isothermally Heated Pipe," *International Journal of Heat and Mass Transfer,* Vol. 17, 1974, pp. 1337–1348.

17 Atkinson, G. S., and Goldstein, S., Unpublished work described in *Modern Developments in Fluid Dynamics,* Vol. 1 (S. Goldstein, ed.), Oxford, 1938, pp. 304.

18 Van Dyke, M., "Entry Flow in a Channel," *Journal of Fluid Mechanics,* Vol. 44, Part 4, 1970, pp. 813–823.

19 Wilson, S. D. R., "Entry Flow in a Channel, Part 2," *Journal of Fluid Mechanics,* Vol. 46, Part 4, 1971, pp. 787–799.

20 Yao, L. S., "Entry Flow in a Heated Tube," The Rand Corporation, R-2111-ARPA, 1977.

21 Yao, L. S., and Catton, I., "Buoyancy Cross-Flow Effects on the Boundary Layer of a Heated Horizontal Cylinder," ASME, JOURNAL OF HEAT TRANSFER, Vol. 99, No. 1, 1977, pp. 122–124.

22 Yao, L. S., and Catton, I., "The Buoyancy and Variable Viscosity Effects on a Water Laminar Boundary Layer along a Heated Longitudinal Horizontal Cylinder," The Rand Corporation, R-1966-ARPA, 1977.

23 Lighthill, M. J., *Introduction to Fourier Analysis and Generalized Functions,* Cambridge University Press, 1958.

24 Yao, L. S., and Berger, S. A., "Entry Flow in a Curved Pipe," *Journal of Fluid Mechanics,* Vol. 67, 1975, pp. 177–196.

Fabio Gori

Fisica Tecnica,
Facoltà di Ingegneria,
Università di Firenze,
Firenze, Italy

Variable Physical Properties in Laminar Heating of Pseudoplastic Fluids with Constant Wall Heat Flux

A theoretical investigation of the combined influence of natural convection and consistency variations in laminar heating of non-Newtonian fluids has been carried out. The heating of a power law fluid with an initially fully developed velocity profile flowing upward through a vertical tube with a constant wall heat flux was considered. The system of governing equations, complete with the convective terms, was solved numerically. Detailed comparisons with previous theoretical and experimental results were performed to check the integrity of the solutions obtained with the present approach. Local heat transfer coefficients, as a function of Graetz number, were presented. Local heat transfer results showed that for pseudoplastic fluids with smaller Prandtl number the parameter Pr was very important in the inlet and in the intermediate part of the tube.

Introduction

The problem of heating of pseudoplastic fluids in laminar flow in a vertical tube with constant wall heat flux has been of interest for a number of years. The interest has increased in the flow and heat transfer characteristics of these fluids because of their importance in industry.

Several authors [1–7][1] have presented heat transfer results for laminar forced convection of Newtonian and non-Newtonian fluids with constant physical properties and with fully developed or flat axial velocity profile at the inlet.

The prediction of the rate of heat transfer to a non-Newtonian fluid is complicated by the variation of the fluid physical properties with the temperature. This variation affects the temperature field and the rate of heat transfer.

Some papers [8–10] have considered a temperature-dependent consistency and they have assumed that natural convection effects are negligible.

Many pseudoplastic fluids are so highly viscous that such an assumption is valid, but for less viscous pseudoplastic fluids the natural convection effects on heat transfer can be important.

Other studies [11–12] have shown that the buoyancy effects, which increase with the Grashof over Reynolds number ratio Gr/Re, can increase the heat transfer significantly.

A complete analysis including both temperature varying consistency and density has been carried out in [13] for Newtonian fluids flowing in a vertical tube with a constant wall heat flux and in [14, 15] for Newtonian and non-Newtonian fluids flowing in a vertical annulus.

The purpose of the present paper is to present numerical solutions for velocity and temperature profiles and heat transfer coefficients for constant flux heating of a pseudoplastic fluid in a vertical tube when density and consistency are simultaneously temperature-varying properties.

In a precedent paper [16] the author has considered the heating in a vertical tube with a constant wall temperature and he proposed an expression for the correlation of the average heat transfer results.

Equations

Power law constitutive equation is assumed

$$\Gamma_{zr} = m \left|\frac{\partial V_z}{\partial r}\right|^{n-1} \frac{\partial V_z}{\partial r}, \tag{1}$$

where the consistency, m, is a function of temperature given by

$$m = m_r/\{1 + B(T - T_r)\}^n \tag{2}$$

and m_r is the value of consistency at the inlet temperature and B is a constant.

It is further assumed that specific heat $\tilde{c}_p$, thermal conductivity k, and pseudoplastic index n are constant and the density in the buoyancy force varies linearly with the temperature.

The steady flow is laminar and it is fully developed at the entrance

---

[1] Numbers in brackets designate References at end of paper.

Contributed by the Heat Transfer Division for publication in the JOURNAL OF HEAT TRANSFER. Manuscript received by the Heat Transfer Division February 17, 1977.

of the tube while fluid inlet temperature is uniform and constant.

Viscous dissipation was neglected and the symmetry about the tube center line was assumed. The dimensionless continuity, z-momentum and energy equations are

$$\frac{\partial V}{\partial \eta} + \frac{W}{\xi} + \frac{\partial W}{\partial \xi} = 0 \tag{3}$$

$$\frac{1}{\mathrm{Pr}}\left(W\frac{\partial V}{\partial \xi} + V\frac{\partial V}{\partial \eta}\right) = -\frac{dP}{d\eta} + \frac{\mathrm{Gr}}{\mathrm{Re}}\Theta + \left|\frac{\partial V}{\partial \xi}\right|^{n-1}\frac{m}{m_r}\left\{\frac{1}{\xi}\frac{\partial V}{\partial \xi} + n\frac{\partial^2 V}{\partial \xi^2} + \frac{1}{m/m_r}\frac{\partial m/m_r}{\partial \Theta}\frac{\partial \Theta}{\partial \xi}\frac{\partial V}{\partial \xi}\right\} \tag{4}$$

$$V\frac{\partial \Theta}{\partial \eta} + W\frac{\partial \Theta}{\partial \xi} = \frac{\partial^2 \Theta}{\partial \xi^2} + \frac{1}{\xi}\frac{\partial \Theta}{\partial \xi} \tag{5}$$

The mass flow conservation, as given by the integrated continuity equation, was considered.

$$\int_0^1 V\xi d\xi = 1/2 \tag{6}$$

The boundary conditions were:
at the wall

$$V = W = 0, \frac{\partial \Theta}{\partial \xi} = 1 \tag{7}$$

at the center line

$$\frac{\partial V}{\partial \xi} = \frac{\partial \Theta}{\partial \xi} = W = 0 \tag{8}$$

The parameter M is defined as $M = Bq_wR/k$. (9)

The parameters of the problem are the index of pseudo-plasticity n, the Prandtl number Pr, the Grashof over Reynolds number ratio Gr/Re and the parameter M characterizing the variation of the consistency with the temperature.

Local Nusselt number, $\mathrm{Nu}_{\mathrm{loc}}$, may be calculate, once the velocity and temperature profiles have been determined, using the equation

$$\mathrm{Nu}_{\mathrm{loc}} = \frac{2}{\Theta_w - \Theta_b} \tag{10}$$

Numerical Solution

The governing equations (3)–(6), with the boundary conditions (7)–(8), were solved numerically with the aid of a CDC 7600 computer.

The numerical technique employed a modification of the implicit-explicit finite difference method proposed by Bodoia, et al. [17, 18] for flow between parallel plates and applied by Hornbeck for flow in a pipe [19, 20].

Details of this procedure may be found in the papers by Marner, et al. [21, 22], where a similar modification for mixed convection and constant consistency was used. Radial and axial velocity in the convective terms and $|\partial V/\partial \xi|^{n-1}$ were evaluated at the previous axial step to linearize the momentum and energy equations.

Once the radial Θ profile had been calculated from the solution of equation (5), the V profile and the dimensionless pressure P were obtained from the simultaneous solutions of equations (4) and (6). The radial dimensionless velocity W was computed in an explicit way from equation (3) starting from the tube center line.

It could be observed that it was not necessary to introduce any other hypothesis, in comparison to the analysis of Marner, et al. [21, 22], for the introduction of the consistency variation term in equation (4).

A similar procedure was employed in the precedent paper [16] with the boundary condition of constant wall temperature.

The axial mesh sizes were $\Delta\eta = 2.5 \times 10^{-6}$ in the inlet and $\Delta\eta = 0.001$ at the end of the tube; while the radial mesh sizes were $\Delta\xi = 0.1$ in the inner part of the tube and $\Delta\xi = 0.00625$ near the wall ($\xi > 0.8$); the procedure of Hornbeck [23] was used at the point where the radial mesh size was changed.

To check the convergence of the solution the following identity was verified

$$\pi R^2 \rho \hat{c}_p V_m (T_b - T_r) = \int_0^z q_w 2\pi R dz \tag{11}$$

or in dimensionless form

$$\Theta_b = 2\eta. \tag{12}$$

Using a radial grid with 41 nodes equation (11) was verified with a precision of 2–3 percent in the inlet while in the other part of the tube it was less than 1 percent.

Discussion of Results

The solutions of the present paper for fully developed flow were in good agreement with the asymptotic $\mathrm{Nu}_{\mathrm{loc}}$ values, calculated using the analytical expression derived by Beek, et al. [2], with a maximum deviation of 0.3 percent.

For constant physical properties the present solutions were compared with the theoretical results obtained for $n = 0.5$ in (4), (8), (9) and (10) and for $n = 1/3$, $n = 0.2$ in (9). The discrepances were 3–4 percent.

An infinite Pr value would have been necessary for the comparison with the theoretical solutions which had dropped the convective terms in the momentum equation; the author assumed in this work a very large Pr value ($\mathrm{Pr} = 10^3 - 10^5$) because, for greater Pr number, the differences between the solutions were negligible.

When the natural convection effects were negligible and a moderate variation of consistency was considered, the $\mathrm{Nu}_{\mathrm{loc}}$ solutions of this work could be checked with the theoretical results of Forrest, et al. [10] and with the empirical equation proposed by Mizushina, et al.

Nomenclature

B = coefficient defined by equation (2)
$\hat{c}_p$ = fluid specific heat
g = acceleration of gravity
Gr = $\rho^2\beta_r g q_w R^{2n+2} V_m{}^{2-2n}/km^2$ = Grashof number
G = mass flow rate
Gz = $G\hat{c}_p/kL$ = Graetz number
h = local heat transfer coefficient
h_{av} = average heat transfer coefficient
k = thermal conductivity
L = tube length
m = fluid consistency
M = coefficient defined by equation (9)
n = index of pseudoplasticity
$\mathrm{Nu}_{\mathrm{loc}} = h2R/k$ = local Nusselt number
$\mathrm{Nu}_{\mathrm{av}} = h_{av}\, 2\, R/k$ = average Nusselt number
p = pressure
$P = (p + \rho_r gz)/\rho_r V^2\ \mathrm{Pr}$ = dimensionless pressure
$\mathrm{Pr} = m\hat{c}_p/k\ (V_m/R)^{n-1}$ = Prandtl number
q_w = wall heat flux
r = radial coordinate
R = tube radius
$\mathrm{Re} = \rho V_m{}^{2-n} R^n/m$ = Reynolds number
T = temperature
$V = V_z/V_m$ = dimensionless axial velocity
V_m = mean axial velocity
V_r = radial velocity
V_z = axial velocity
$W = V_r\ \mathrm{Re\ Pr}/V_m$ = dimensionless radial velocity
z = axial coordinate
β = coefficient of thermal cubic expansion
Γ_{zr} = shear stress
$\eta = z/R\ \mathrm{Re\ Pr}$ = dimensionless axial coordinate
$\Theta = (T - T_r)/(q_wR/k)$ = dimensionless temperature
$\xi = r/R$ = dimensionless radial coordinate
ρ = fluid density

Subscripts

b = evaluated at bulk temperature
r = evaluated at inlet temperature
w = evaluated at wall temperature

[8] which correlated the experimental results. Table 1 presents a very good agreement. The Nu_{loc} solutions were also compared with the experimental and theoretical results of Mitsuishi, et al. [9] for forced convection and higher variations of consistency with temperature. The comparison for $n = 1/3$, $M = 10$, and $Pr = 10^5$ showed a maximum deviation of 5 percent.

As observed by Lawrence, et al. [24], for flow in a vertical tube with a constant wall heat flux, the velocity and temperature profiles never become "fully developed" for the variations of the physical properties with the temperature. When the density and the consistency are simultaneously variable with the temperature, the results of this work are in accordance with the observation made in [24].

For constant consistency and mixed convection the dimensionless velocity and temperature profiles, obtained in this work in the last part of the vertical tube ($\eta = 0.6$), could be compared with the experimental data of Greene [25] and with the theoretical ones of Marner, et al. [12].

Fig. 1 presents dimensionless temperature and axial velocity profiles. For $n = 0.845$, $Gr/Re = 43.6$, and $Pr = 10^5$ the agreement with the theoretical temperature profile of [12] is very good and for $n = 0.5$, $Gr/Re = 58$, and $Pr = 10^5$ the deviation from the theoretical velocity profile of [12] is very small. It is important to emphasize that the profiles obtained in [12] were determined from a simultaneous solution of the continuity, energy and momentum equations.

From Fig. 1 the comparison with the experimental temperature profile of [25] shows that the agreement is good near the wall but less good in the central part of the tube section. Most of the difference is probably due to the variations of the consistency with the temperature. To show a qualitative trend of the temperature profile of this work, a small variation of the consistency ($M = 1$) was introduced in the present approach for $n = 0.845$, $Gr/Re = 43.6$, and $Pr = 10^5$. The temperature profile obtained in this work in the last part of the vertical tube ($\eta = 0.6$) was represented in Fig. 1 and it shows a better agreement with the experimental data of [25] in the central part of the tube section.

Table 1 Comparison with reference [8, 10] for $n = 0.5$, $M = 1$, $Pr = 10^5$

	Nu_{loc} results		
Gz	Ref.(8)	Ref.(10)	This work
274000	100.40	98.03	98.49
66000	62.67	60.57	60.83
13600	37.16	35.59	35.83
840	14.78	13.99	14.15
105	7.41	7.35	7.46
10	4.82	4.91	4.94

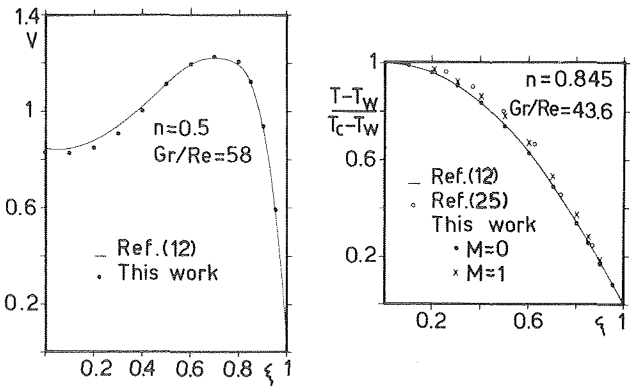

Fig. 1 Comparison with reference [12, 25] for mixed convection

A review of the literature concerning the combined influence of buoyancy force and consistency variations showed that the comparison of Nu_{loc} results was possible only for Newtonian fluids. Fig. 2 presents the comparison with the theoretical solutions of Mitsuishi, et al. [13] for $n = 1$, $Gr/Re = 80$, $M = 10$, and $Pr = 10^5$. The maximum deviation, with the results of this work, is 4–5 percent in the range of large Gz number.

Representative Nu_{loc} results of this work are given in Fig. 3 for $n = 0.3$ and in Fig. 4 for $n = 0.6$. In each figure four curves are shown: for fully developed axial velocity profile and constant physical properties for $Pr = 10$, $Pr = 10^3$, and $Pr = 10^5$ with the simultaneous influence of natural convection and consistency variations.

Figs. 3 and 4 show that the local heat transfer coefficients, for given n, M, Gr/Re and at given value of Gz number, are greater for the fluids with a higher Pr number, because the velocity profile distortion, due to the variations of the physical properties, is greater.

The trend is in accordance with the Nu_{loc} results of Rosen, et al. [26] (Newtonian fluids), with the Nu_{av} results of Rosenberg, et al. [27] (Newtonian fluids) and of Marner, et al. [21, 22] (Newtonian and pseudoplastic fluids). In these papers [21, 22], [26, 27] the boundary condition was for constant wall temperature, but the effects of the variable physical properties are qualitatively independent of the heat supply mechanism.

In the paper by McKillop, et al. [28] the inlet condition was for flat axial velocity profile and the local heat transfer solutions, at a given value of Gz number, are greater for the fluids with a smaller Pr number. Some observations could be made for the Nu_{loc} solutions obtained in [28] between fluids with different Pr number (having used the coefficients for Nusselt number correlation equation). The percentage difference of Nu_{loc} numbers was smaller for variable consistency than for constant physical properties showing that the consistency variations produces a greater increase of Nu_{loc} for fluids with a higher Pr number.

While McKillop, et al. [28] used a flat axial velocity profile in the inlet, this work and the aforementioned papers [21], [22, 26, 27] employed a fully developed axial velocity profile but similar effects of the Pr number on the heat transfer, for flow with variable physical properties, were recognizable. In conclusion, the variations of density and consistency with temperature produce a greater increase of the heat transfer for fluids with a higher Pr number.

From Figs. 3 and 4 it is evident that the theoretical results obtained for $Pr = 10^5$ are not significantly different from the solutions determined for $Pr = 10^3$. It is also evident that the parameter Pr is very important when its value is in the range 10–10^3, for great and intermediate Gz values.

For $n = 0.3$ (Fig. 3) the variable physical properties ($M = 10$, $Gr/Re = 20$) determine an increase of Nu_{loc}, for $Pr = 10^3$ in comparison with the fully developed curve, of 18 percent in the intermediate Gz values ($Gz = 500$).

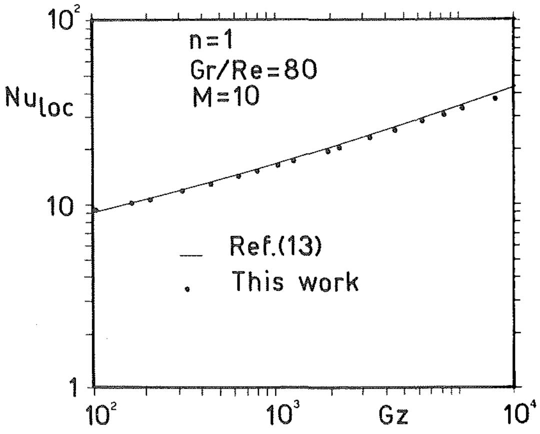

Fig. 2 Comparison with reference [13] for $n = 1$, $M = 10$, $Gr/Re = 80$, $Pr = 10^5$

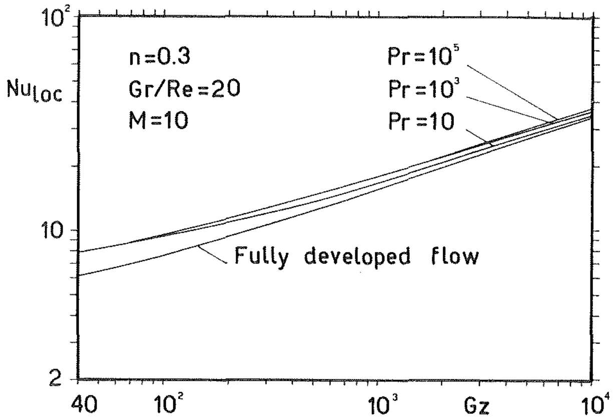

Fig. 3 Results of this work for $n = 0.3$, $M = 10$, Gr/Re = 20 and various Pr

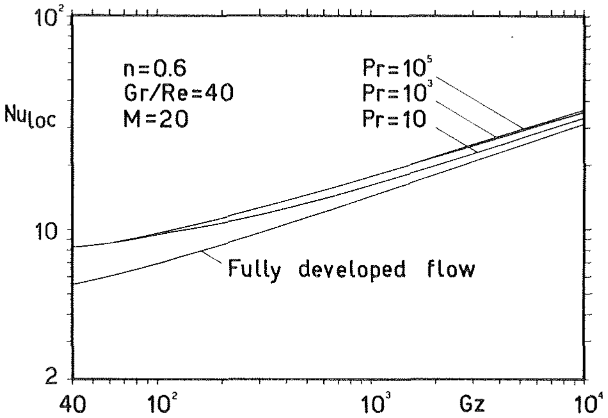

Fig. 4 Results of this work for $n = 0.6$, $M = 20$, Gr/Re = 40 and various Pr

For a pseudoplastic fluid with a small Pr number the increase of $\mathrm{Nu}_{\mathrm{loc}}$ is smaller; when Pr = 10 the increment is only 9 percent, for Gz = 500.

In Fig. 4 the curves of $\mathrm{Nu}_{\mathrm{loc}}$ versus Gz are presented for $n = 0.6$ and higher variations of physical properties ($M = 20$, Gr/Re = 40). For Pr = 10^3 the increase of $\mathrm{Nu}_{\mathrm{loc}}$ is 27 percent for Gz = 500 and 15 percent for Gz = 10^4. The curve obtained for Pr = 10 shows an increment of $\mathrm{Nu}_{\mathrm{loc}}$ of 16 percent for Gz = 500 and 7.5 percent for Gz = 10^4.

These considerations confirm the importance of the Pr number, in the range of Gz values mentioned previously, in the theoretical analysis of constant flux laminar heating of pseudoplastic fluids in a vertical tube.

Conclusions

A numerical study of constant wall flux heating of pseudoplastic fluids in a vertical tube has been carried out.

The analysis has considered the simultaneous influence of natural convection and consistency variation on local heat transfer.

The parameters of the problem are the pseudoplasticity index n, the Grashof over Reynolds number ratio Gr/Re, the parameter M characterizing the variations of consistency with temperature and the Prandtl number Pr.

The analysis has shown that when Pr number value is smaller than 10^3 it is an important parameter and its value affects significantly the local heat transfer coefficient. If Pr number is greater than 10^3 the differences with $\mathrm{Nu}_{\mathrm{loc}}$ results, obtained for Pr = 10^3, are negligible.

It would been necessary to compare the theoretical results of this work with the experimental ones but it has been impossible due to the lack of experimental studies in the literature.

It is clear that further work is necessary in the area of experimental constant flux heating of pseudoplastic fluids in a vertical tube.

References

1 Schenk, J., and Van Laar, J., "Heat Transfer in Non-Newtonian Laminar Flow in Tubes," *Appl. Sci. Res.*, Vol. A No. 7, 1958, pp. 449–462.

2 Beek, W. J., and Eggink, R., *de Ingenieur*, Vol. 74, 1962, p. 81.

3 Heaton, H. S., Reynolds, W. C., and Kays, W. M., "Heat Transfer in Annular Passages. Simultaneous Development of Velocity and Temperature Fields in Laminar Flow," *International Journal of Heat and Mass Transfer*, Vol. 7, 1964, pp. 763–781.

4 McKillop, A. A., "Heat Transfer for Laminar Flow of Non-Newtonian Fluids in Entrance Region of a Tube," *International Journal of Heat and Mass Transfer*, Vol. 7, 1964, pp. 853–862.

5 Ulrichson, D. L., Schmitz, R. A., "Laminar-Flow Heat Transfer in the Entrance Region of Circular Tubes," *International Journal of Heat and Mass Transfer*, Vol. 8, 1965, pp. 253–258.

6 Worsøe-Schmidt, P. M., "Heat Transfer in the Thermal Entrance Region of Circular Tubes and Annular Passages With Fully Developed Laminar Flow," *International Journal of Heat and Mass Transfer*, Vol. 10, 1967, pp. 541–551.

7 Manohar, R., "Analysis of Laminar-Flow Heat Transfer in the Entrance Region of Circular Tubes," *International Journal of Heat and Mass Transfer*, Vol. 12, 1969, pp. 15–22.

8 Mizushina, T., Kuriwaki, Y., "Heat Transfer to Laminar Flow of Pseudoplastic Fluids," Mem. Fac. Eng., Kyoto University, XXX, Vol. 4, 1968, pp. 511–524.

9 Mitsuishi, N., and Miyatake, O. "Heat Transfer With Non-Newtonian Laminar Flow in a Tube Having a Constant Wall Heat Flux," *Int. Chem. Eng.*, Vol. 9, No. 2, 1969, pp. 352–357.

10 Forrest, G., and Wilkinson, W. L., "Laminar Heat Transfer to Power Law Fluids in Tubes with Constant Wall Heat Flux," *Trans. Instn Chem. Engrs*, Vol. 52, 1974, pp. 10–16.

11 DeYoung, S. H., and Scheele, G. F., "Natural Convection Distorted Non-Newtonian Flow in a Vertical Pipe," *AIChE Journal*, Vol. 16, No. 5, 1970, pp. 712–717.

12 Marner, W. J., and Rehfuss, R. A., "Buoyancy Effects on Fully Developed Laminar NonNewtonian Flow in a Vertical Tube," *Chemical Engineers Journal*, Vol. 3, 1972, pp. 294–300.

13 Mitsuishi, N., Miyatake, O., and Yanagida, M., "Heat Transfer of Laminar Flow in Vertical Tubes With Constant Wall Heat Flux," *Journal of Chem. Eng.*, Japan, Vol. 1, No. 2, 1968, pp. 120–124.

14 Tanaka, M., and Mitsuishi, N., "Numerical Solutions for Laminar Heat Transfer in Concentric Annuli," *Heat Transfer—Jap. Res.*, Vol. 3, No. 1, 1974, pp. 69–79.

15 Tanaka, M., and Mitsuishi, N., "Non-Newtonian Laminar Heat Transfer in Concentric Annuli," *Heat Transfer—Jap. Res.*, Vol. 4, No. 2, 1975, pp. 26–36.

16 Gori, F., "Effects of Variable Physical Properties in Laminar Flow of Pseudoplastic Fluids," *International Journal of Heat and Mass Transfer*, to be published.

17 Bodoia, J. R., and Osterle, J. F., "Finite Difference Analysis of Plane Poiseuille and Couette Flow Developments. *Appl. Sci. Res.*, Vol. A, No. 10, 1961, pp. 265–276.

18 Bodoia, J. R., and Osterle, J. F., "The Development of Free Convection Between Heated Vertical Plates," ASME JOURNAL OF HEAT TRANSFER, Vol. 84, No. 1, 1962, pp. 40–44.

19 Hornbeck, R. W., "Laminar Flow in the Entrance Region of a Pipe," *Appl. Sci. Res.*, Vol. A, No. 13, 1964, pp. 224–232.

20 Hornbeck, R. W., "An All-Numerical Method for Heat Transfer in the Inlet of a Tube," ASME Paper No. 65-WA/HT-36, 1965.

21 Marner, W. J., and McMillan, H. K., "Combined Free and Forced Laminar Convection in a Vertical tube With Constant Wall Temperature," ASME JOURNAL OF HEAT TRANSFER, Vol. 92, 1970, pp. 559–561.

22 Marner, W. J., and McMillan, H. K., "Combined Free and Forced Laminar Non-Newtonian Convection in a Vertical Tube With Constant Wall Temperature," *Chem. Eng. Sci.*, Vol. 27, 1972, pp. 473–488.

23 Hornbeck, R. W., "NonNewtonian Laminar Flow in the Inlet of a Pipe," ASME Paper No. 65-WA/FE-4, 1965.

24 Lawrence, W. T., and Chato, J. C., "Heat-Transfer Effects on the Developing Laminar Flow Inside Vertical Tubes," ASME Paper No. 65-WA/HT-11, 1965.

25 Greene, H. L., PhD dissertation, Cornell University, 1966.

26 Rosen, E. M., and Hanratty, T. J., "Use of Boundary-Layer Theory to Predict the Effect of Heat Transfer on the Laminar-Flow Field in a Vertical Tube With a Constant-Temperature Wall," *AIChE Journal*, Vol. 7, No. 1, 1961, pp. 112–123.

27 Rosenberg, D. E., and Hellums, J. D., "Flow Development and Heat Transfer in Variable-Viscosity Fluids," *I. & E. C. Fund.*, Vol. 4, No. 4, 1965, pp. 417–422.

28 McKillop, A. A., Harper, J. C., Bader, H. J., and Korayem, A. Y., "Variable Viscosity Entrance-Region Flow of NonNewtonian Liquids," *International Journal of Heat and Mass Transfer*, Vol. 13, 1970, pp. 901–909.

O. T. Hanna
O. C. Sandall

Department of Chemical and Nuclear Engineering,
University of California,
Santa Barbara, Calif.

Heat Transfer in Turbulent Pipe Flow for Liquids Having a Temperature-Dependent Viscosity

Analytical approximations are developed to predict the effect of a temperature-dependent viscosity on convective heat transfer through liquids in fully developed turbulent pipe flow. The analysis expresses the heat transfer coefficient ratio for variable to constant viscosity in terms of the friction factor ratio for variable to constant viscosity, T_w, T_b, and a fluid viscosity-temperature parameter β. The results are independent of any particular eddy diffusivity distribution. The formulas developed here represent an analytical approximation to the model developed by Goldmann. These approximations are in good agreement with numerical solutions of the model nonlinear differential equation. To compare the results of these calculations with experimental data, a knowledge of the effect of variable viscosity on the friction factor is required. When available correlations for the friction factor are used, the results given here are seen to agree well with experimental heat transfer coefficients over a considerable range of μ_w/μ_b.

Introduction

The problem of forced convection heat transfer to liquids having a strong temperature dependence of viscosity has been of interest, both theoretically and in a practical sense, for a long time. In the case of turbulent flow, the nonlinearity of the problem has rendered it largely intractable analytically, so that up to now, results reported for this problem have been either empirical correlations [1–4][1] or numerical integrations of various models [5, 6]. This problem is becoming of even greater importance as process requirements, as well as improved heat-exchanger materials, result in practical heat transfer situations which involve very large temperature differences. The analysis developed here is intended to provide a rational basis for extrapolation to conditions which are beyond those for which reliable data or correlations are available.

The viscosity of most liquids is usually quite sensitive to temperature variations. Although some calculations have been done in the past for $\mu \propto T^{-n}$, viscosity variations with temperature are usually best expressed as $\mu \propto e^{\beta/T}$, as shown in Fig. 1. Although analytical results can be obtained for both of these viscosity variations, comparisons with numerical integration of the model and with experimental data are restricted here to exponential variations, as found in practice.

In this work, the problem of fully-developed turbulent forced convection is considered for the case of liquids having a strong temperature-dependence of viscosity. Most liquids (with the exception of liquid metals) have Prandtl numbers which are relatively large, i.e., in the range from about two to 10,000 or so. Thus it is natural to invoke some "large Prandtl number" assumptions for the analysis. However, it will be shown that there is reason to believe that the correction derived here for variable viscosity is not restricted to large Prandtl numbers but may be rather generally applicable to various turbulent heat transfer problems involving liquids, if the results are interpreted properly.

Model

The model used in this study for the effect of variable viscosity on the eddy diffusivity is due to Goldmann [6]. This model has also been used by Petukhov [2] in his study of variable property heat transfer. In the Goldmann model, it is assumed that ϵ/ν for variable properties has the same functional relationship in terms of y^{++} as does ϵ/ν in terms of y^+ for constant properties. Here y^{++} is defined as

$$y^{++} \equiv \int_0^y \frac{\sqrt{\tau_0/\rho}}{\nu}\, dy$$

It may be seen that $y^{++} = y^+$ for the case of constant properties.

The energy equation corresponding to steady, incompressible, turbulent, "fully developed" forced convection in Cartesian geometry may be written as

$$u \frac{\partial T}{\partial x} = \frac{\partial}{\partial y}\left[(\alpha + \epsilon)\frac{\partial T}{\partial y}\right] \tag{1}$$

Viscous dissipation is assumed to be negligible. We assume thermally developed conditions corresponding to a uniform surface heat flux. Of course, rigorously there cannot be a fully developed velocity or

---

[1] Numbers in brackets designate References at end of paper.

Contributed by the Heat Transfer Division for publication in the JOURNAL OF HEAT TRANSFER. Manuscript received by the Heat Transfer Division July 22, 1977

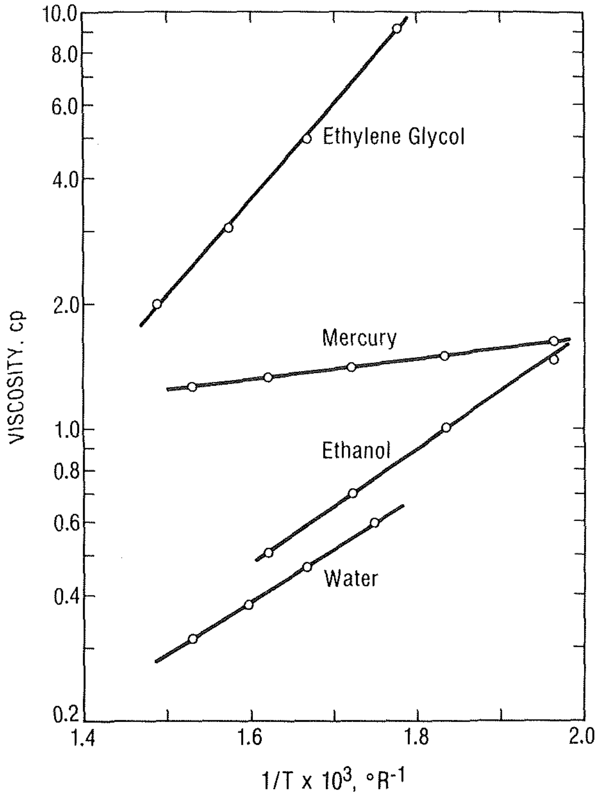

Fig. 1 Viscosity variation with temperature for some common liquids. Data taken from *The Handbook of Chemistry and Physics*

temperature profile when viscosity varies with temperature. However, we assume that, for large distances downstream from the start of heating, viscosity variations will not produce any signficant variations in the convective terms. Thus we regard the transport far downstream as having a very weak developing character, so that to a good approximation the convective terms in the energy equation are negligible.

Under the above assumptions, many previous studies [2, 5, 7] have shown that for Pr greater than 0 (1), we may integrate equation (1) with respect to y to get

$$-\frac{q_w}{C_p\rho} = (\alpha + \epsilon)\frac{dT}{dy} \tag{2}$$

Although equation (2) is based on Cartesian geometry, this result is known to hold closely for circular ducts as well. Based on previous studies [5, 7], we also expect the analysis for constant surface heat flux to hold for constant surface temperature, particularly at larger Prandtl numbers.

If we now change coordinates from y to

$$y^{++} \equiv \int_0^y \frac{\sqrt{\tau_0/\rho}}{\nu}\,dy$$

we get

$$-B\frac{dT}{dy^{++}} = \frac{1}{\dfrac{\alpha}{\nu} + \dfrac{\epsilon}{\nu}} \tag{3}$$

where

$$B = \rho C_p u^*/q_w$$

Here, by the Goldmann model for the variable viscosity eddy diffusivity, the quantity ϵ/ν is the same function of y^{++} as is ϵ/ν for constant properties a function of y^+.

Derivation of Analytical Results

We wish to develop an analytical approximation for the solution of the nonlinear differential equation, equation (3), where $\nu(T)$ is a function of temperature. We note the algebraic identity

$$\frac{1}{\dfrac{\alpha}{\nu} + \dfrac{\epsilon}{\nu}} - \frac{1}{\dfrac{\alpha}{\nu_0} + \dfrac{\epsilon}{\nu}} = -\frac{\alpha}{\nu_0}\,\frac{\left(\dfrac{\nu}{\nu_0} - 1\right)}{\left(\dfrac{\alpha}{\nu_0} + \dfrac{\epsilon}{\nu}\right)\left(\dfrac{\alpha}{\nu} + \dfrac{\epsilon}{\nu}\right)} \tag{4}$$

where ν_0 is the kinematic viscosity at some reference temperature.

Substituting from equation (3) for $1/(\alpha/\nu + \epsilon/\nu)$ in the right hand side of equation (4) yields

$$\frac{1}{\dfrac{\alpha}{\nu} + \dfrac{\epsilon}{\nu}} - \frac{1}{\dfrac{1}{\mathrm{Pr}_0} + \dfrac{\epsilon}{\nu}} = \frac{\dfrac{B}{\mathrm{Pr}_0}\left(\dfrac{\nu_0}{\nu} - 1\right)}{\dfrac{1}{\mathrm{Pr}_0} + \dfrac{\epsilon}{\nu}}\,\frac{dT}{dy^{++}} \tag{5}$$

Here $\mathrm{Pr}_0 \equiv \nu_0/\alpha$ is the Prandtl number based on the reference kinematic viscosity, which is as yet unspecified. Using this expression in

Nomenclature

A = constant in equation (13), differs for heating and cooling
B = constant = $\rho C_p u^*/q_w$, K^{-1}
C_p = heat capacity at constant pressure, cal/g K
f = friction factor = $2\tau/\rho u_b{}^2$
h = heat transfer coefficient, $h = q_w/(T_w - T_b)$, cal/cm^2 K
I = integral = $\displaystyle\int_0^{\bar{y}} \frac{dy^{++}}{\dfrac{1}{\mathrm{Pr}_0} + \epsilon^+}$
k = thermal conductivity, cal/cm K s
Pr = Prandtl number = ν/α
q_w = wall heat flux, cal/cm^2 s
St = Stanton number = $h/\rho C_p u_b$
St$_0$ = constant property Stanton number at reference (bulk) temperature
T = temperature, K
T_b = bulk temperature, K
T_c = centerline temperature, taken to be the same as bulk temperature, K
T_w = wall temperature, K
u_b = bulk velocity, cm/s
u^* = friction velocity = $\sqrt{f/2}\,u_b$, cm/s
y = distance measured from wall, cm
y^+ = dimensionless distance from wall = yu^*/ν
y^{++} = dimensionless distance from wall = $\displaystyle\int_0^y \frac{\sqrt{\tau/\rho}}{\nu}\,dy$
$\bar{y}$ = the value of y^{++} at the centerline
α = thermal diffusivity = $k/\rho C_p$, cm^2/s
β = constant, K
ϵ = eddy diffusivity, cm^2/s
ν = kinematic viscosity, cm^2/s
ρ = fluid density, g/cm^3
μ = dynamic viscosity, g/cm-s
Pr$_0$ = reference Prandtl number = ν_0/α
τ = shear stress at the wall, g/cm s^2

Subscripts

b = bulk condition
c = centerline condition, taken to be the same as bulk condition
0 = reference condition (bulk)
w = wall condition

the original differential equation, equation (3), and integrating with respect to y^{++} from $y^{++} = 0$ to $\bar{y}$, the point where $T = T_c$ (centerline temperature), we find

$$-B(T_c - T_w) = \int_0^{\bar{y}} \frac{dy^{++}}{\dfrac{1}{\mathrm{Pr}_0} + \dfrac{\epsilon}{\nu}} + \frac{B}{\mathrm{Pr}_0} \int_{T_w}^{T_c} \frac{\left(\dfrac{\nu_0}{\nu} - 1\right) dT}{\dfrac{1}{\mathrm{Pr}_0} + \dfrac{\epsilon}{\nu}} \tag{6}$$

Equation (6) represents an exact integral equation which is equivalent to equation (3). The second term on the right of equation (6) clearly represents what can be considered a "correction" to account for effects of viscosity variation on the temperature profile, since this term vanishes when ν = constant = ν_0.

We now consider the question of approximating this variable viscosity correction term. If we take the reference kinematic viscosity, ν_0, to be the centerline value, then the integrand in the correction term is largest in magnitude near the wall, and it goes to zero outside the major "thermal layer". Certainly for large Prandtl number fluids the main thermal layer or region is rather close to the wall and in fact this is reasonably true even for Prandtl numbers as low as order unity. Thus, at large Prandtl numbers, we could replace ϵ/ν by $K \cdot y^{++3}$ in the correction term and rescale y^{++} in the usual way [7]. Then the correction term would appear as

$$\frac{B}{\mathrm{Pr}_0} \int_{T_w}^{T_c} \frac{\left(\dfrac{\nu_c}{\nu} - 1\right) dT}{\dfrac{1}{\mathrm{Pr}_0} + \epsilon^+} \doteq B \int_{T_w}^{T_c} \frac{\left(\dfrac{\nu_c}{\nu} - 1\right) dT}{1 + Kz^3} \tag{7}$$

where $z \equiv \mathrm{Pr}_0^{1/3}\, y^{++}$. In this form, the correction term represented by equation (7) would appear to be *close* to (but smaller than) the value

$$B \int_{T_w}^{T_c} \left(\frac{\nu_c}{\nu} - 1\right) dT$$

By the second mean value theorem for integrals, the right hand side of equation (7) can be written as

$$Bf(\xi) \int_{T_w}^{T_c} \left(\frac{\nu_c}{\nu} - 1\right) dT$$

where $f(\xi)$ is an unknown value of $1/(1 + Kz^3)$ evaluated somewhere between the limits of integration. A useful approximation should correspond to replacing the quantity $f(\xi)$ by an unknown constant $1/A$, which should be less than unity. Thus we will write the R.H.S. of equation (7) as

$$(B/A) \cdot \int_{T_w}^{T_c} \left(\frac{\nu_c}{\nu} - 1\right) dT$$

where A should be somewhat greater than unity. A numerical value for A will be chosen in order to cause the analytical results to agree well with available experimental data, if this is possible. Since the evaluation of the analytical result is different for heating and cooling, separate values of A will be determined for each of these two conditions.

Thus we approximate the correction term of equation (6) as

$$\frac{B}{\mathrm{Pr}_0} \int_{T_w}^{T_c} \frac{\left(\dfrac{\nu_c}{\nu} - 1\right) dT}{\dfrac{1}{\mathrm{Pr}_0} + \dfrac{\epsilon}{\nu}} \doteq \frac{B}{A} \int_{T_w}^{T_c} \left(\frac{\nu_c}{\nu} - 1\right) dT \tag{8}$$

Although the approximation represented by equation (8) has been presented in the context of relatively "large" Prandtl numbers, this point requires further discussion. In the first place, this approximation, while appearing quite plausible, is not strictly an *asymptotic* approximation. That is, for example, the term Kz^3 in equation (7) does not necessarily become relatively smaller as $\mathrm{Pr}_0 \to \infty$. This is because as $\mathrm{Pr}_0 \to \infty$, both laminar and turbulent transport are of the same order of magnitude within the thin thermal layer. On the other hand, it would be expected that equation (8) would be reasonable for perhaps any Prandtl number larger than order unity, since the result is independent of the particular form of ϵ, and since the preceding discussion appears to be plausible even for moderate Prandtl numbers. Of course, the value of the first integral on the right hand side of equation (6) is strictly a function of temperature through its upper limit. However, for large Pr_0, the integral is independent of the upper limit, and this is known to hold rather well even for moderate Pr_0 [7]. If we also use this approximation, namely that

$$I = \int_0^{\bar{y}} \frac{dy^{++}}{\dfrac{1}{\mathrm{Pr}_0} + \dfrac{\epsilon}{\nu}}$$

has the same value for both constant and variable viscosity, then equation (6) becomes

$$-B(T_c - T_w) = I + \frac{B}{A}\left[\int_{T_w}^{T_c} \frac{\nu_c}{\nu} dT - (T_c - T_w)\right] \tag{9}$$

It is convenient to introduce the quantity

$$H \equiv \int_{T_w}^{T_c} \frac{\nu_c}{\nu} dT \tag{10}$$

Then equation (9) becomes

$$-B(T_c - T_w) = I + \frac{B}{A}\left[H - (T_c - T_w)\right] \tag{11}$$

For the same temperature difference but with viscosity constant at the bulk temperature value, equation (11) reduces to

$$-B_0(T_c - T_w) = I \tag{12}$$

By eliminating I between equations (11) and (12), and noting that $B_0/B = (\mathrm{St}/\sqrt{f/2})/(\mathrm{St}/\sqrt{f/2})_0$, we finally get

$$\frac{\mathrm{St}/\sqrt{f/2}}{(\mathrm{St}/\sqrt{f/2})_0} = \left(1 - \frac{1}{A}\right) + \frac{H}{A(T_c - T_w)} \tag{13}$$

Here the subscript 0 refers to the constant property solution evaluated at the centerline temperature. The centerline temperature T_c can normally be replaced by the bulk temperature T_b with less than five percent error for Pr greater than about ten [8]. Use of T_b in place of T_c greatly simplifies the results.

Since the nature of the approximations made in deriving equation (10) involves several quite plausible but untested assumptions, its usefulness will be determined by a comparison with numerical solutions of the original nonlinear differential equation (3), as well as by comparison with experimental data. Since the final result is in the form of a ratio of variable property to constant property transport coefficients, and since the arguments leading up to this formula do not seem to be tied severely to a large Prandtl number assumption, it is hoped that this result will prove to be fairly general. Thus we would expect that this correction might be appropriate for virtually all liquids, with the exception of liquid metals, since liquid Prandtl numbers are normally greater than unity.

To evaluate the integral H, we have assumed that the viscosity variation with temperature follows the equation $\nu \propto e^{\beta/T}$. This form has been found to correlate the viscosity-temperature relation for most liquids over a wide range of temperatures. Typical examples of liquids which have such a viscosity variation are shown in Fig. 1. In this case, H is given by

$$H = e^{\beta/T_c} \int_{T_w}^{T_c} e^{-\beta/T} dT \tag{14}$$

This integral can be expressed in terms of tabulated exponential integrals. Instead, we will develop simple and accurate asymptotic approximations which cover the range of virtually all practical applications. The cases of heating and cooling are treated separately. A derivation of these simple approximations, together with an assessment of their accuracy, is given in the Appendix. The results are as follows:

Heating

$$H \doteq -T_w e^{\beta(1/T_c - 1/T_w)} \cdot \left[\frac{1 - e^{-(T_w/T_c - 1)(\beta/T_w + 2)}}{\dfrac{\beta}{T_w} + 2} \right] \qquad (15)$$

Cooling

$$H \doteq T_c \left[\frac{1 - e^{-(T_c/T_w - 1)(\beta/T_c + 2)}}{\dfrac{\beta}{T_c} + 2} \right] \qquad (16)$$

As shown in the Appendix, these two approximations are both very good for a wide range of possible conditions.

Discussion of Results

To assess the accuracy of the approximation formula, equation (13), in relation to the original model, equation (3), numerical integrations of equation (3) were performed for β in the range $1{,}000 \le \beta \le 10{,}000$. This range is expected to cover most applications. To expedite numerical integration of equation (3), the wall temperature was fixed at 600°R and for β values of 1,000, 5,000, and 10,000, three different values of B (equivalent to heat flux) were chosen. This defined nine specific cases for both heating and cooling which correspond to the ν_w/ν_b values as shown in Table 1. The specification of the eddy diffusivity for these numerical integrations was $\epsilon/\nu = 0.00091\, y^{++3}$, which is the limiting form of the Notter and Sleicher [9] expression for the wall region. Thus the numerical integrations correspond to the case of large Prandtl numbers. By choosing appropriate values of the parameter A in equation (13), ($A_{\text{cooling}} = 1.08, A_{\text{heating}} = 1.26$) very good agreement was found between the numerical and analytical results for the 18 cases mentioned above. The maximum deviation in these cases is 8.2 percent; the mean absolute deviation is 1.6 percent for the viscosity range $0.39 < \nu_w/\nu_c < 38$. This agreement shows that the analytical approximation to the model is quite good, but this in itself does not answer the question of agreement between the model used and results of experiments.

Since the original model and its approximate solution involve several possible sources of error, we now focus attention on a direct comparison between the analytical approximation, equation (13), and available experimental data. Our procedure is to select heat transfer conditions corresponding to the 18 cases used in the previous paragraph for comparision with the numerical integrations.

Perhaps the broadest source of experimental data available for this comparison has been compiled by Petukhov [2]. In this reference, considerable experimental results are shown for both heating and cooling. Petukhov shows that if the data are plotted as St/St_0 versus μ_w/μ_b, then the following empirical correlations provide a reasonably good representation of the data.

$$\frac{St}{St_0} = \left(\frac{\mu_w}{\mu_b}\right)^n \quad \begin{array}{l} \text{Heating: } n = 0.11 \\ \text{Cooling: } n = 0.25 \end{array} \qquad (17)$$

Another less extensive but important set of experimental data which are useful for comparison purposes are due to Allen and Eckert [10] and Malina and Sparrow [11]. These data will also be used in the comparison to follow.

To carry out a comparison, the analytical formula, equation (13), was evaluated using several values of A for the 18 heat transfer conditions studied previously. By comparing these results with the empirical correlations of Petukhov [2] we obtain the results shown in Table 1. In order to determine the analytical values it is necessary to specify the effect of variable viscosity on the friction factor. For the calculations shown in Table 1, the following empirical correlations of Petukhov [2] for the friction factor were used.

Heating

$$\frac{f}{f_0} = \frac{1}{6}\left(7 - \frac{\mu_b}{\mu_w}\right) \qquad (18)$$

Cooling

$$\frac{f}{f_0} = \left(\frac{\mu_w}{\mu_b}\right)^{0.24} \qquad (19)$$

Equation (18) is based on the heating data of Allen and Eckert [10] for water at Pr = 8. Equation (19) for cooling is based on the data of Rohonczy [12] for water with $1.3 \le \text{Pr} \le 5.8$.

In Table 1 results are shown for the empirical correlations of Petukhov, equation (17), and the analytical prediction, equation (13). The predictions of the model are compared to both the Petukhov and Seider-Tate (3) correlations in Fig. 2. The choices of A(cooling) = 1.05 and A(heating) = 2.4 are seen to lead to very good agreement for a rather wide range of μ_w/μ_b values. Because of the form of the heating correlation for the friction factor, it was felt that it would be unwise to use equation (18) to extrapolate f/f_0 values beyond the range of the experimental data. This limited the heating calculations to $\mu_w/\mu_b > 0.38$. As Petukhov's diagram shows, there is substantial scatter in the data when it is plotted in this way. It is possible that some of this scatter represents the fact that the quantity μ_w/μ_b cannot, by itself, account completely for the effects of variable viscosity. The model results depend explicitly on three parameters, β, T_w and T_c rather than merely on the quantity μ_w/μ_b. However, the numerical evaluation of the analytical solution shows that the variable μ_w/μ_b correlates most of the nonisothermal effects.

The recent large Prandtl number empirical correlation of Sleicher and Rouse [4] predicts values of St/St_0 in good agreement with Petukhov for heating under the conditions of our calculations. However for the conditions of our cooling calculations, equation (13) of Sleicher and Rouse, which is based on heating data, predicts values of St/St_0 significantly higher than the Petukhov correlation.

In Table 2 results are shown for the analytical predictions compared

Table 1 Comparison of the Stanton number predictions of the analytical formulae with the correlations of Petukhov

$T_w = 600°\text{R}$

HEATING CASES (A = 2.4)				COOLING CASES (A = 1.05)			
β		St/St_0		β		St/St_0	
(°R)	μ_w/μ_c	Model	Petukhov	(°R)	μ_w/μ_c	Model	Petukhov
10,000	0.833	1.023	1.020	10,000	3.21	0.710	0.747
10,000	0.678	1.049	1.044	10,000	6.06	0.624	0.637
10,000	0.413	1.099	1.102	10,000	37.77	0.516	0.403
5,000	0.831	1.023	1.021	5,000	1.95	0.810	0.846
5,000	0.672	1.051	1.045	5,000	3.00	0.727	0.760
5,000	0.391	1.105	1.109	5,000	12.35	0.592	0.533
1,000	0.929	1.009	1.008	1,000	1.16	0.948	0.964
1,000	0.694	1.046	1.041	1,000	1.31	0.910	0.935
1,000	0.425	1.101	1.099	1,000	2.11	0.774	0.830

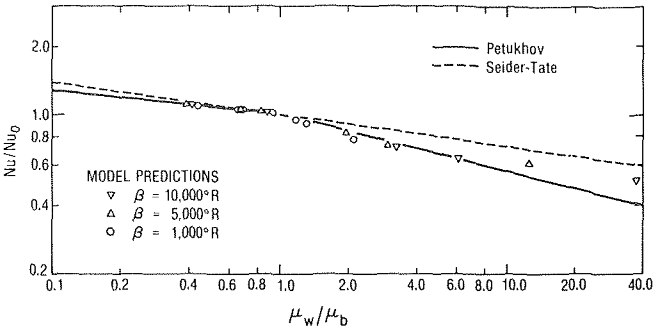

Fig. 2 Heat transfer predictions of the model compared to empirical correlations. $T_w = 600°R$

to the very precise heating measurements of Allen and Eckert [10] and Malina and Sparrow [11] and the corresponding values from the Petukhov correlation. Each value given for $(St/St_0)_{exp}$ represents an arithmetic average of values for either four or five Reynolds numbers as given by Malina and Sparrow. It is seen that the effect of variable viscosity on (St/St_0) is somewhat smaller in these experiments than that predicted by the Petukhov correlation or our analytical formula.

Summary

An approximate relationship, equation (13), is derived for the effect of variable viscosity on the fully-developed heat transfer rate to turbulent liquids. The correction, H, in equation (10), has been evaluated for viscosity variations of $\mu \propto e^{\beta/T}$ in case of heating (equation (15)) and cooling (equation (16)). The analytical formulae are found to be in excellent agreement with the numerical integrations of the model equation, (3). If the values $A(\text{cooling}) = 1.05$ and $A(\text{heating}) = 2.4$ are adopted, the analytical formulae also compare very favorably to the variable property heat transfer correlations of Petukhov for liquids.

References

1 Hufschmidt, W. E., Burch, and Riebold, W., "Die Bestimung Ortlicher und Mittlerer Warmeubergangzahlen in Rohrer bei Hohen Warmestromdichten," *Int. J. Heat Mass Transfer*, Vol. 9, 1966, p. 539.

2 Petukhov, B. S., "Heat Transfer and Friction in Turbulent Pipe Flow with Variable Physical Properties," *Adv. Heat Transf.*, Vol. 6, 1970, p. 503.

3 Sieder, C. A., and Tate, G. E., "Heat Transfer and Pressure Drop of Liquids in Tubes," *Ind. Eng. Chem.*, Vol. 28, 1936, p. 1429.

4 Sleicher, C. A., and Rouse, M. W., "A Convenient Correlation for Heat Transfer to Constant and Variable Property Fluids in Turbulent Pipe Flow," *Int. Journal of Heat and Mass Transfer*, Vol. 18, 1975, p. 677.

5 Deissler, R. G., NACA Tech. Rept. 1210, 1955.

6 Goldmann, Kurt, "Heat Transfer to Supercritical Water and Other Fluids with Temperature-Dependent Propterties," *C.E.P. Symposium Series*, Vol. 50, No. 11, 1954, p. 105.

7 Hanna, O. T., and Sandall, O. C., "Developed Turbulent Transport in Ducts for Large Prandtl or Schmidt Numbers," *AIChE Journal*, Vol. 18, 1972, p. 527.

8 Knudsen, J. G., and Katz, D. L., *Fluid Dynamics and Heat Transfer*, McGraw-Hill, New York, NY, 1958.

9 Notter, R. H., and Sleicher, C. A., "The Eddy Diffusivity in the Turbulent Boundary Layer Near a Wall," *Chem. Eng. Sci.*, Vol. 26, 1971, p. 161.

10 Allen, R. W., and Eckert, E. R. G., "Friction and Heat-Transfer Measurements to Turbulent Pipe Flow of Water (Pr = 7 and 8) at Uniform Wall Heat Flux," ASME JOURNAL OF HEAT TRANSFER.

11 Malina, J. A., and Sparrow, E. M., "Variable-Property, Constant-Property and Entrance Region Heat Transfer Results for Turbulent Flow of Water and Oil in a Circular Tube," *Chem. Eng. Sci.*, Vol. 19, 1964, p. 953.

12 Rohonczy, G., Schweizer Arch. No. 5, 1939, as referred to in Petukhov [2].

APPENDIX

Approximation Formula for

$$H \equiv \int_{T_w}^{T_c} \frac{\nu_c}{\nu}\, dT \text{ for } \nu \propto e^{\beta/T}$$

The integral H can be written as

$$H = e^{\beta/T_c} \int_{T_w}^{T_c} e^{-\beta/T} dT$$

If we introduce $1/T \equiv u$, this can be written as

$$H = e^{\beta/T_c} \int_{u=1/T_c}^{1/T_w} \frac{e^{-\beta u} du}{u^2} \tag{A1}$$

The integral expression in H can be written as the difference between two generalized exponential integrals, but instead we develop a simple and accurate approximation for large β which should apply to the entire range of conditions which are met in practice. The cases of heating and cooling must be treated separately, since the maximum contribution to the integral in H comes from opposite locations in these two cases. In either case, H is reduced to an algebraic factor times the integral

$$\int_0^c e^{-\sigma z} dz/(1+z)^2$$

where the values of c and σ are different for heating and cooling. An excellent approximation to this integral is given by

$$\int_0^c \frac{e^{-\sigma z} dz}{(1+z)^2} \doteq \frac{1 - e^{-c(\sigma+2)}}{\sigma + 2} \tag{A2}$$

This approximation can be derived by merely replacing $(1 + z)$ by e^z in equation (A1) and integrating the exponential. This approximation is asymptotic both for $c \to 0$ and $\sigma \to \infty$, with errors of $0(c^3)$ and $0(1/\sigma^3)$, respectively. The values of c to be found in practice are roughly in the range (0.02–0.5) while the values of σ will normally be in the range $(2 < \sigma < 20)$.

To illustrate the accuracy of this approximation, values of the integral in equation (A2) are shown in Table 3 compared to the approximation for typical pairs of c and σ. The agreement is normally better than one percent. In the very extreme case (i.e., large c, small σ) $c = 0.5$, $\sigma = 2$, we find an error of about four percent.

For the case of heating, we introduce into equation (A1) the substitution $u = (1 + z)/T_w$. Then using equation (A2), the value of H becomes

$$H = -T_w e^{\beta(1/T_c - 1/T_w)} \int_{z=0}^{T_w/T_c - 1} \frac{e^{-\beta/T_w z} dz}{(1+z)^2}$$

Table 2 Comparision of the analytical formula with heating data of Malina and Sparrow [11] for Pr = 3, 48, 75 and with heating data of Allen and Eckert [10] for Pr = 8

$T_w - T_b = 50°R$

				$(St/St_0)_{pred.}$	
Pr	β	μ_w/μ_b	$(St/St_0)_{exp}$	This Work	Petukhov [2]
3	3090	0.673	1.02	1.05	1.04
8	3090	0.594	1.04	1.07	1.06
48	8745	0.404	1.05	1.10	1.11
75	8745	0.376	1.07	1.10	1.11

Table 3 Comparison of Numerical and Analytical Approximation of

$$I \equiv \int_0^c e^{-\sigma z} dz/(1+z)^2$$

c	σ	$I_{\text{Numerical}}$	$I_{\text{approx.}} = \dfrac{1 - e^{-c(\sigma+2)}}{\sigma + 2}$
0.2	2	0.139	0.138
0.5	2	0.225	0.216
0.02	2	0.0192	0.0192
0.2	20	0.0450	0.0449
0.02	10	0.0178	0.0178
0.1	6	0.0690	0.0688

$$H \doteq -T_w e^{\beta(1/T_c - 1/T_w)} \left[\frac{1 - e^{-(T_w/T_c - 1)(\beta/T_w + 2)}}{\dfrac{\beta}{T_w} + 2} \right] \quad \text{Heating}$$

For cooling, we introduce into equation (A1) the substitution $u = (1 + z)/T_c$. Then using equation (A2), the value of H becomes

$$\frac{H}{T_c} = \int_{z=0}^{(T_c/T_w - 1)} \frac{e^{-\beta/T_c z} dz}{(1 + z)^2} = \frac{1 - e^{-(T_c/T_w - 1)(\beta/T_c + 2)}}{\dfrac{\beta}{T_c} + 2} \quad \text{Cooling}$$

K. H. Chu
R. Greif
Department of Mechanical Engineering,
University of California, Berkeley,
Berkeley, Calif.

Theoretical Determination of Band Absorption for Nonrigid Rotation with Applications to CO, NO, N_2O, and CO_2

Results are determined for infrared absorption in a fundamental manner directly from the basic spectroscopic variables. Comparison with experimental data shows good agreement for small and moderate optical depths, but substantial differences result for very large optical depths. The basis for the discrepancy is discussed and further work is recommended.

Introduction

In a previous study, the spectral absorption coefficient and the total band absorptance were derived in a fundamental manner directly from the basic spectroscopic variables for a vibration-rotation band for rigid rotation [1].[1] A comparison of the theoretical results with the experimental data for diatomic gases, in particular for carbon monoxide and nitric oxide, showed very good agreement. In the present study new relations are derived for nonrigid rotation. Comparisons are then made with the experimental data for carbon monoxide and nitric oxide and for the linear triatomic gases, nitrous oxide and carbon dioxide.

Analysis

The distinguishing feature of nonrigid rotation is the nonuniform spacing of the spectral lines, which requires a separate specification for the P and the R branches [2, 3] according to (for nonsymmetric molecules):

$$d_P = (B' + B'') + 2(B'' - B')J = d_1 + 2d_2J \tag{1a}$$

$$d_R = |(B' + B'') - 2(B'' - B')(J + 1)| = |d_1 - 2d_2(J + 1)| \tag{1b}$$

(The symmetric molecule case is briefly noted in Appendix A.) The result for the absorption coefficient for linear nonsymmetric, nonrigid molecules which have the dispersion form is obtained by summing the contribution for each line [4] and is given by

$$\frac{k}{bS_0/\pi} = \sum_{J=1,2,\ldots} \frac{\mathrm{J} \exp\left[-hcB''J(J+1)/kT\right]}{[(\nu - \nu_0) + d_1J + d_2J^2]^2 + b^2} + \sum_{J=1,2,\ldots} \frac{\mathrm{J} \exp\left[-hcB''J(J+1)/kT\right]}{[(\nu - \nu_0) - d_1J + d_2J^2]^2 + b^2} \tag{2}$$

where $S_0 = \alpha hcB''/kT$. Following [1, 5], the sums of these series are obtained by using the residue theorem, and the approximate result is given by

$$k = \pm \frac{\alpha hcB''}{2\pi d_1 kT} \frac{\exp\left\{\frac{-hcB''}{kT}\left[\frac{\tau}{2\pi}\left(\frac{\tau}{2\pi} - 1\right) - \left(\frac{\beta}{2\pi}\right)^2\right]\right\}}{\cosh\beta - \cos\tau} \cdot \left\{(\tau \sinh\beta - \beta\sin\tau) + \frac{d_2}{\pi d_1}\left[(\tau^2 - \beta^2)\sinh\beta - 2\tau\beta\sin\tau\right]\right\} \tag{3}$$

where the + sign refers to $\tau > 0$ and the − sign to $\tau < 0$, with $\tau = 2\pi(\nu - \nu_0)/d_1$ and $\beta = 2\pi b/d_1$. Using equation (3) it is possible to obtain explicit results for the total band absorptance in terms of the basic spectroscopic variables. Equation (3) is approxmiate because the line integrals have been neglected [1, 6].

For small values of the broadening parameter, β, the following expression is obtained:

$$k = \left(1 + \frac{d_2\tau}{\pi d_1}\right) k_r \tag{4}$$

where the absorption coefficient for rigid rotation, k_r, is

$$k_r = \pm \frac{\alpha hcB''}{2\pi d_1 kT} \frac{\exp\left\{\frac{-hcB''}{kT}\left[\frac{\tau}{2\pi}\left(\frac{\tau}{2\pi} - 1\right)\right]\right\}}{1 + (\beta^2/2) - \cos\tau} \beta(\tau - \sin\tau) \tag{5}$$

with $k > k_r$ for $\tau > 0$ (R branch) and $k < k_r$ for $\tau < 0$ (P branch). Note that the contribution to the total band absorption in the region of small values of τ is small. Hence, errors in this region are not of im-

---

[1] Numbers in brackets designate References at end of paper.

Contributed by the Heat Transfer Division for publication in the JOURNAL OF HEAT TRANSFER. Manuscript received by the Heat Transfer Division July 25, 1977.

portance.[2]

The total band absorptance [7–14] is defined by $A = \int_{-\infty}^{\infty}[1 - \exp(-kX)]d(\nu - \nu_0)$. For small β it is convenient to cast this in the form

$$A = \sum_{-\infty}^{-1} A_n + \sum_{1}^{\infty} A_n \tag{6}$$

with A_n approximated by

$$\begin{aligned} A_n &= \frac{d_1}{\pi} \int_0^{\pi} \left\{1 - \exp\left[\frac{-y_n\beta}{1 + (\beta^2/2) - \cos\tau'}\right]\right\} d\tau' \\ &= \beta d_1 \int_0^{y_n/\beta} \exp\left[-\left(1 + \frac{\beta^2}{2}\right)\zeta\right] I_0(\zeta)d\zeta \end{aligned} \tag{7}$$

with $\tau' = \tau - 2\pi n + 2\pi n^2(d_2/d_1)$ and, $y_n = (\alpha hcB''X|n|/d_1kT)(1 + 2nd_2/d_1)\exp(-hcB''n^2/kT)$. For $y_n\beta/2 \ll 1$ and $u/\beta \ll 1$, with $u = (\alpha x/d_1)(hcB''/kT)^{1/2}$, we obtain

$$\frac{A}{2F} = u\left\{1 - [.157 + 0.470E^2]\frac{u}{\beta}\right\} \tag{8}$$

with $F = (d_1/2)(kT/hcB'')^{1/2}$ and $E = (d_2/d_1)(kT/hcB'')^{1/2}$.

Continuing with the small β condition and requiring $y_n/\beta \gg 1$ (and $y_n\beta/2 \ll 1$, cf. equation (7)) we obtain

$$A_n = d_1 \operatorname{erf}[(y_n\beta/2)^{1/2}] \tag{9}$$

The total band absorptance, A, may now be obtained by numerically summing the values of A_n or alternatively by using the Euler-MacLaurin formula to obtain

$$\begin{aligned} \frac{A}{2F} &= \int_1^{\infty} \operatorname{erf}\left[\left\{\frac{u\beta z e^{-z^2}}{2}(1 + 2Ez)\right\}^{1/2}\right] dz \\ &\quad + \int_1^{\infty} \operatorname{erf}\left[\left\{\frac{u\beta z e^{-z^2}}{2}(1 - 2Ez)\right\}^{1/2}\right] dz \end{aligned} \tag{10}$$

For small values of $u\beta$ the series representation for the error function may be used which yields

$$\frac{A}{2F} = 2.06\left(\frac{2\beta u}{\pi}\right)^{1/2}\{1 + 0.750E^2\} \tag{11}$$

This result may also be obtained by using equation (9) directly.

For very large values of $u\beta$ an asymptotic relation may be obtained for the absorption using equation (10). The result is

$$\frac{A}{2F} \sim 2[\sqrt{2\,\ell n\,(u\beta)} + 2E\,\ell n\,(u\beta)]. \tag{12}$$

Recall that β is small, so that equation (12) is therefore limited to extremely large values of u.

The limiting relations for the total band absorptance, A, that were given above were based on the approximate relation, equation (5), for the absorption coefficient, which is limited to small values of the broadening parameter β. Another important condition corresponds to moderately large values of β[3] and the absorption coefficient for rigid rotation is now given by

$$k_r = \frac{\alpha hcB''|\tau|}{2d_1kT}\exp\left\{\frac{-hcB''}{kT}\left(\frac{\tau}{2\pi}\right)^2\right] \tag{13}$$

It was previously noted that in the region of very large positive and negative values of τ the contribution to the absorption is negligible. Substituting this result into the definition for the total band absorptance yields

$$\begin{aligned} \frac{A}{2F} &= \int_0^{\infty} \{1 + \exp[-u(1 + 2E\eta)\eta e^{-\eta^2}]\}d\eta \\ &\quad + \int_0^{\infty} \{1 + \exp[-u(1 - 2E\eta)\eta e^{-\eta^2}]\}d\eta \end{aligned} \tag{14}$$

where $\eta = (\tau/2\pi)(hcB''/kT)^{1/2}$.

For small values of u, equation (14) gives

$$\frac{A}{2F} = u[1 - (0.157 + 0.470E^2)u] \tag{15}$$

For large values of u the band absorptance varies according to

$$\frac{A}{2F} \sim 2\sqrt{\ell nu} + 2E\,\ell nu \tag{16}$$

In closing this section it is repeated that it is restricted to linear nonsymmetric molecules. The procedure for linear symmetric molecules is briefly noted in Appendix A.

Discussion of Results and Conclusions

Results for the absorption coefficient of gases have been derived based on the quantum mechanical representation of the intensity. Using these results, relations for the total band absorptance and its derivatives have then been obtained directly from the basic spectroscopic variables over ranges of the parameters that are rigorously defined. Results for intermediate ranges of the parameters have also been obtained, but these require, in general, numerical computation. The quantities, u, β and F are defined in Table 1 and numerical values are then obtained from the constants given in Table 2.

In a previous study assuming rigid rotation [1], the theoretical results obtained were in good agreement with the experimental data for both the 4.7 micron band of carbon monoxide (Burch, et al. [23], Abu-Romia and Tien [24]) and the 5.35 micron band of nitric oxide (Green and Tien [22]). The optical depths, u, varied from 0.017 to 354. Now, carrying out the calculations for nonrigid rotation, as presented in this study, yields only slight changes with respect to the rigid rotation results for carbon monoxide (generally less than one percent) but larger changes are obtained for nitric oxide.[4] The results for nitric oxide show an improvement in the agreement with the data for the nonrigid rotation calculations (cf. Table 3).

The results for the 4.5 micron band of nitrous oxide are presented in Table 4 and show fair agreement with the experimental data of Burch, et al. [23]. The results for rigid rotation prove to be very close to those for nonrigid rotation and are therefore not presented separately. The range of optical depths is from 0.1 to 7500, and it is seen that at the larger optical depths the theoretical values are consistently lower than the experimental data. This trend is clearly confirmed in the results for carbon dioxide as shown in Table 5, which refers to the data of Edwards [20]. The optical depths now extend up to 220,000, and the theoretical values for the band absorptance, at the large optical depths, are substantially less than the experimental data. Comparisons with the data of Hottel [16] show the same trend.

For small values of the optical depth, u, and small broadening, β, the effects of overlapping between neighboring spectral lines may be neglected. For this condition the total absorption may be obtained by simply adding the contribution from each line, and an accurate specification of the spacing between the lines is not important. It is only when the contributions from the wings of neighboring lines begin to overlap that the spacing becomes important and the nonrigid effects become significant.

For moderately large optical depths the contribution from the wings of the lines becomes important, and the absorption is then influenced by overlapping. For this condition an accurate value for the line spacing should be considered. Since most of the contribution comes from the lines in the central portion of the band (which have a small rotational quantum number J) the difference in line spacing between the rigid and nonrigid rotator, which is proportional to J, is very small in this region. Therefore, the theoretical results obtained for rigid and nonrigid rotation are close.

For large optical depths the central portion of the band becomes

---

[2] It is also emphasized that for very large negative and positive values of τ the contribution to the absorption is negligible.

[3] Equation (4) also proves to be valid for this condition.

[4] It is also noted that the values of u and β for nonrigid rotation (u_{NR}, β_{NR}) differ slightly from the corresponding values based on rigid rotation (u_R, β_R). When there is no subscript the nonrigid values are used.

Table 1 Limiting relations for the total band absorptance, A. ($3\sqrt{\pi/128} = 0.470$, $\sqrt{\pi/128} = 0.157$)

	Rigid Rotator	Nonrigid Rotator
	Small β	
Small u (Small u/β)	$u\left[1 - 0.157\left(\frac{u}{\beta}\right) + 0.028\left(\frac{u}{\beta}\right)^2\right]$	$u\left[1 - (0.157 + 0.470E^2)\frac{u}{\beta}\right]$
Moderate u (Small $u\beta$)	$2.06\left(\frac{2\beta u}{\pi}\right)^{1/2}$	$2.06\left(\frac{2\beta u}{\pi}\right)^{1/2}(1 + 0.750E^2)$
Large u (Large $\mu\beta$)	$2\sqrt{2\,\ell n\,(u\beta)}$	$2[\sqrt{2\,\ell n\,(u\beta)} + 2E\,\ell n\,(u\beta)]$
	Moderately Large β	
Small u	$u[1 - 0.157u + 0.028u^2]$	$u[1 - (0.157 + 0.470E^2)u]$
Large u	$2\sqrt{\ell n\,u}$	$2\sqrt{\ell n\,u} + 2E\,\ell n\,u$

Note: For $\left.\begin{cases}\text{Diatomic or}\\ \text{Linear Asymmetric Triatomic Molecules}\end{cases}\right\}$ $u = \alpha x/2F, \quad \beta = 2\pi b/d_1$

For Linear Symmetric Triatomic Molecules $u = 2\alpha x/2F, \quad \beta = 2\pi b/2d_1$

$$F = \frac{d_1}{2}\left(\frac{kT}{hcB''}\right)^{1/2}, \quad E = \frac{d_2}{d_1}\left(\frac{kT}{hcB''}\right)^{1/2}, \quad d_1 = B'' + B', \quad d_2 = B'' - B'$$

Note: $B'' = \left.\begin{cases} B_e - \alpha_e(v'' + 1/2) & \text{for diatomic}\\ B_e - \alpha_1(v_1'' + 1/2) - \alpha_2(v_2'' + 1/2) - \alpha_3(v_3'' + 1/2) & \text{for linear triatomic}\end{cases}\right\}$

Similar relation for B'

Table 2 Tabulation of variables. For CO, $\alpha_e = 0.01748$ [3, p. 522] and for NO, $\alpha_e = 0.0178$ [3, p. 558]; other variables in [1]. Note $P_e = P_T + (\beta - 1)P_a = b_o\,P_e$

	N_2O		CO_2	
B_e	0.419		0.395	
(cm^{-1}	[15, p. 272]		[3, p. 21]	
b_0	0.157		0.1	
(atm^{-1} cm^{-1})	[17, p. 1498]		[18, p. 378]	
B	1.12*		1.3	
	[15, p. 275]		[19, p. 541]	
α_1	0.0345		0.00121	
(cm^{-1}	[21, p. 596]		[21, p. 598]	
α_2	−0.00056		−0.00072	
(cm^{-1})	[21, p. 596]		[21, p. 598]	
α_3	0.00179		0.00309	
(cm^{-1})	[21, p. 596]		[21, p. 598]	
	4.5μ	2.7μ	4.3μ	15μ
α	2035*	70.8	2706	240
(atm^{-1} cm^{-2})	[15, p. 275]	[18, p. 310]	[18, p. 310]	[18, p. 310]

* Values correspond to 273 K. Other values correspond to 300 K.

Table 3 Comparison of experimental and theoretical results (rigid and nonrigid rotation) for the 5.35 micron fundamental band of nitric oxide (experimental data and correlation from Green and Tien ([22])).

Effective Pressure P_e (atm)	Pressure Path Length P_aL (atm-cm)	Optical Depth		Broadening Parameter		Experimental Data A_E (cm^{-1})	Theoretical Results		Correlation A_C (cm^{-1})
		u_R	u_{NR}	β_R	β_{NR}		$A_{TH,R}$ (cm^{-1})	$A_{TH,NR}$ (cm^{-1})	
1.0	0.845	2.69	2.71	0.101	0.102	35.76	31.0	33.3	36.2
1.0	1.22	3.89	3.92	0.101	0.102	45.25	37.0	39.7	44.3
1.0	2.45	7.81	7.87	0.101	0.102	67.37	53.0	55.2	64.6
1.0	3.09	9.84	9.92	0.101	0.102	70.83	59.0	61.4	73.0
2.025	1.71	5.45	5.49	0.205	0.207	64.99	62.0	64.6	65.6
2.025	2.47	7.87	7.93	0.205	0.207	84.7	73.0	76.0	80.2
2.025	4.96	15.80	15.93	0.205	0.207	113.92	97.0	100.5	111.6
2.025	6.24	19.88	20.04	0.205	0.207	119.18	105.6	109.1	121.9
3.05	2.575	8.20	8.26	0.309	0.312	91.44	88.1	91.5	92.0
3.05	3.725	11.87	11.96	0.309	0.312	113.87	101.6	105.1	108.6
3.05	7.47	23.80	23.99	0.309	0.312	142.7	127.5	130.9	139.9
2.98	9.195	29.29	29.52	0.302	0.305	142.7	134.0	137.2	148.7
4.075	3.44	10.96	11.05	0.413	0.417	108.15	109.5	113.0	111.7
4.075	4.975	15.85	15.98	0.413	0.417	131.42	123.3	126.7	128.3
4.075	9.97	31.76	32.01	0.413	0.417	157.54	146.7	149.5	159.6
4.075	12.56	40.01	40.33	0.413	0.417	157.40	153.2	155.9	169.9

Table 4 Comparison of experimental and theoretical results for the 4.5 micron fundamental band of nitrous oxide at 303 K (Experimental data of Burch, et al. [23])

P_e (mm Hg)	$P_{N_2O}L$ (atm-cm)	β_{NR}	u_{NR}	A_E (cm^{-1})	A_{TH} (cm^{-1})
11.5	0.0186	0.0180	1.824	5.93	5.50
21.6		0.0337		7.21	7.29
42.4		0.0662		9.31	9.97
91.2		0.142		12.2	13.97
186.0		0.290		15.8	18.51
360.0		0.562		18.7	23.05
749.0		1.169		22.0	27.58
1920.0		2.373		24.4	30.72
3035.0	0.0186	4.738	1.824	24.9	32.49
112	0.74	0.175	72.58	70.4	72.25
181		0.283		77.6	78.87
292		0.456		83.7	84.32
479		0.748		86.8	89.26
767		1.197		90.0	93.41
1530		2.388		92.2	98.97
3080	0.74	4.808	72.58	93.5	104.16
3.2	1.4	0.0050	137.31	31.7	25.21
6.2		0.0097		38.7	35.09
10.8		0.0169		46.4	46.31
30.0		0.0468		63.7	60.73
74.0		0.116		80.0	75.46
232.0		0.362		92.8	88.38
7360.0		1.149		98.8	98.26
3035.0	1.4	4.738	137.31	101.2	108.54
28	11.6	0.0347	1137.74	102	88.38
61		0.0952		108	95.27
203	11.6	0.317	1137.74	115	104.39
22.4	18.8	0.035	1843.93	103.2	90.79
42.4		0.066		108.7	96.21
106		0.166		115.2	103.22
406		0.634		120.2	112.39
742	18.8	1.158	1843.93	121.8	116.30
56	23.7	0.0874	2324.53	115.6	100.14
103		0.161		120.1	104.63
213	23.7	0.333	2324.53	125.3	109.66
44.8	76.4	0.070	7493.41	125	107.02
168		0.262		129	115.79
211	76.4	0.329	7493.41	129	117.16

opaque and the contribution from the lines far from the band center with large rotational quantum number J become important. In this region, there is a significant difference in the line spacing between the rigid and nonrigid models. As asymptotic relation is derived for the nonrigid rotator model at very large optical depths which gives a linear combination of logarithmic and square root logarithmic functions. Although this is encouraging since many data are correlated with a logarithmic dependence for large optical depths, the numerical results are not in good agreement with the data as exemplified by Table 5 for carbon dioxide. It would appear that this discrepancy is primarily due to the folding back of the R branch.[5] The wavenumbers of the lines in the R branch are given by the relation $\nu_R = \nu_0 + d_1J - d_2J^2$. The $-d_2J^2$ term, resulting from the nonrigid rotation, causes ν_R to first increase, then reach a maximum and then decrease. Hence the R branch folds back and first overlaps on itself and then overlaps with the P branch. With such folding, the broadening parameter β, for example, requires further study. In the present analysis, the method used to obtain the total band absorptance, A, breaks down when the R branch folds back, and this contribution has not been considered. Due to the small intensity of these lines, the error introduced can be neglected for small and moderate optical paths, u, but for large optical paths the error may be large. The folding back of the R branch near

Table 5 Comparison of experimental and theoretical results for carbon dioxide at 294 K. (Experimental data of Edwards [20] and ϵ_E are calculated from these data). β_{NR} was used for the theoretical results, β_R is listed as a parameter.

P_T (atm)	P_e (atm)	$P_{CO_2}L$ (atm-cm)	β_R	15μ				4.3μ				2.7μ					
				u_{NR}	A_E	A_{Th}	$\epsilon_{Th,15}$	u_{NR}	A_E	A_{Th}	$\epsilon_{Th,15}$	u_{NR}	A_E	A_{Th}	$\epsilon_{Th,2.7}$	ϵ_{Th}	ϵ_E
0.5	0.508	3.45	0.204	94.17	62	75.25	.079	1066.98	110	95.85	.00121	27.96	73	55.19	.000003	.080	.064
1.0	1.016	6.85	0.408	186.98	95	89.03	.093	2188.49	128	105.09	.00133	55.51	119	75.42	.000005	.094	.101
0.51	0.663	19.79	0.266	540.20	113	94.08	.098	6120.43	143	109.03	.00139	160.38	169	89.56	.000005	.099	.120
1.0	1.071	30.81	0.430	841.02	130	100.72	.105	9528.57	157	114.45	.00145	249.62	209	92.67	.000006	.106	.137
1.0	1.300	38.87	0.522	1061.03	136	103.56	.108	12021.27	165	116.90	.00148	315.01	208	92.67	.000006	.109	.144
1.0	1.168	72.37	0.469	1975.47	154	106.95	.112	22381.77	173	119.68	.00152	586.50	217	96.29	.000006	.114	.163
2.0	2.6	77.86	1.044	2125.33	160	112.37	.117	24079.65	196	124.32	.00158	631.00	246	101.98	.000006	.119	.169
1.0	1.300	129.39	0.522	3531.94	163	111.26	.116	40016.26	183	123.37	.00156	1048.61	261	100.83	.000006	.118	.169
9.9	10.604	304.30	4.260	8306.42	193	127.94	.133	94110.42	236	137.84	.00174	2466.12	296	117.80	.000007	.135	.204
9.9	12.87	385.99	5.170	10536.30	203	130.12	.136	119374.57	287	139.75	.00177	3128.16	338	120.05	.000007	.138	.216
5.0	6.5	646.97	2.611	17660.22	209	129.28	.135	200087.48	268	139.02	.00176	5243.20	317	119.13	.000007	.137	.221
9.9	11.56	712.77	4.645	19456.35	217	132.72	.138	220437.36	289	141.92	.00180	5776.46	317	122.52	.000008	.140	.230

---

[5] In certain regions, however, the effects of hot bands, isotopic bands, overtone bands, etc., may be important.

the band center may not be very important, because this region will become opaque before the contribution (from the lines folding back) becomes significant. Thus the contribution to the total band absorptance, A, from the lines folding back in the region near the center of the band, is small. However, far from the center of the band where the intensities of the R and P branches are small, the presence of the lines folding back will significantly increase the value of A for large optical depths. Thus, if methods were introduced to treat the folding back of the R branch, better agreement with the experimental data could be expected.

In summary, the nonrigid rotator model is used to predict the value of the total band absorptance, A. For small and moderately large optical depths, the theoretical results from the nonrigid rotator model give good agreement with the experimental values and a slight improvement over the values predicted by the rigid rotator model. For very large optical depths, the theoretical values are substantially less than the experimental data, although an asymptotic dependence $2E\ \ell n\, u + 2\sqrt{\ell n\, u}$ is predicted (cf. Table 1 for moderately large β). To remedy the discrepancy at large optical depths, the folding back of the R branch should be considered in detail and a calculational procedure devised to obtain the total band absorptance. If this effect does not yield accurate results, the contributions from hot bands, isotopic bands, overtone bands, etc., will have to be included.

Acknowledgment

The authors acknowledge with appreciation the support of this research by the National Science Foundation under grant ENG 76-14401.

References

1 Hashemi, A., Hsieh, T. C., and Greif, R., "Theoretical Determination of Band Absorption with Specific Application to Carbon Monoxide and Nitric Oxide," ASME JOURNAL OF HEAT TRANSFER, Vol. 98, 1976, pp. 432–437.

2 Edwards, D. K., "Molecular Gas Band Radiation," *Advances in Heat Transfer*, T. F. Irvine and J. P. Hartnett, eds., Vol. 12, Academic Press, New York, 1976, pp. 116–195.

3 Herzberg, G., *Infrared and Raman Spectra*, Von Nostrand Reinhold Company, New York, 1945.

4 Elsasser, W. M., *Heat Transfer by Infrared Radiation in the Atmosphere*, Blue Hill, Milton, Mass., 1972.

5 Copson, E. T., *"An Introduction to the Theory of Functions of a Complex Variable,"* Oxford University Press, 1955.

6 Hsieh, T. C., and Greif, R., "Theoretical Determination of the Absorption Coefficient and the Total Band Absorptance Including a Specific Application to Carbon Monoxide," *International Journal of Heat and Mass Transfer*, Vol. 15, 1972, pp. 1477–1487.

7 Edwards, D. K., and Menard, W. A., "Comparison of Modesl for Correlation of Total Band Absorptance," *Appl. Optics*, Vol. 3, 1964, pp. 1621–1625.

8 Tien, C. L., "Thermal Radiation Properties of Gases," *Advances in Heat Transfer*, J. P. Hartnett and T. F. Irvine, eds., Vol. 5, Academic Press, New York, 1968, pp. 253–324.

9 Cess, R. D., and Tiwari, S. N., "Infrared Radiative Energy Transfer in Gases," *Advances in Heat Transfer*, J. P. Hartnett and T. F. Irvine, eds., Vol. 8, Academic Press, New York, 1972, pp. 229–283.

10 Tien, C. L., and Lowder, J. E., "A Correlation for Total Band Absorptance of Radiating Gases," *International Journal of Heat and Mass Transfer*, Vol. 9, 1966, pp. 698–701.

11 Edwards, D. K., and Balakrishnan, A., "Thermal Radiation by Combustion Gases," *International Journal of Heat and Mass Transfer*, Vol. 16, 1973, pp. 24–40.

12 Cess, R. D., and Ramanathan, V., "Radiative Transfer in the Atmosphere of Mass and that of Venus above the Cloud Deck," *J. Quantitative Spectroscopy and Radiative Transfer*, Vol. 12, 1972, pp. 933–945.

13 Tiwari, S. N., "Band Models and Correlation for Infrared Radiation," AIAA 10th Thermophysics Conference, May, 1975, AIAA 75-699.

14 Lapp, M., Gray, L. D., and Penner, S. S., "Equilibrium Emissivity Calculations for CO_2," International Heat Transfer Conference, Part IV, ASME, 1961, p. 812.

15 Tien, C. L., Modest, M. F., and McCreight, C. R., "Infrared Radiation Properties of Nitrous Oxide," *J. Quantitative Sepctroscopy and Radiative Transfer*, Vol. 12, 1972, pp. 267–277.

16 Hottel, H. C., Chapter 4 in *Heat Transmission*, W. H. McAdams, McGraw-Hill Book Col, Inc., New York, N. Y., 1954. Also, see Hottel, H. C. and Sarofim, A. F., *Radiative Transfer*, McGraw-Hill Book Co., Inc., New York, N. Y., 1967.

17 Gray, L. D., "Spectral Absorption of the 4.6 micron Bands of N_2O," *Applied Optics*, Vol. 4, 1965, p. 1494.

18 Penner, S. S., *Quantitative Molecular Spectroscopy and Gas Emissivities*, Addison-Wesley, Reading, Mass., 1959.

19 Siegel, R., and Howell, J. R., *Thermal Radiation Heat Transfer*, McGraw-Hill, Inc., New York, N. Y. 1972.

20 Edwards, D. K., "Absorption by Infrared Bands of Carbon Dioxide Gas at Elevated Temperatures," *Journal of the Optical Society of America*, Vol. 50, 1960, pp. 617–626.

21 Herzberg, G., *Molecular Spectra and Molecular Structure*, III, Van Nostrand Reinhold Co., New York, 1966.

22 Green, R. M., and Tien, C. L., "Infrared Radiation Properties of Nitric Oxide at Elevated Temperatures," *J. Quantitative Spectroscopy and Radiative Transfer*, Vol. 10, 1970, pp. 805–817; also Green, R. M., "The Infrared Radiation Properties of Nitric Oxide at Elevated Temperature," Ph.D. Dissertation, U.C., Berkeley, 1969.

23 Burch, D. E., Gryvnak, D. A., Singleton, E. B. France, W. L., and Williams, D., "Infrared Absorption by Carbon Dioxide, Water Vapor, and Minor Atmospheric Constituents," Research Report AFCRL-62-698, July 1962.

24 Abu-Romia, M. M., and Tien, C. L., "Measurements and Correlations of Infrared Radiation of Carbon Monoxide at Elevated Temperatures," *Journal Quant. Spectrosc. and Radiat. Transfer*, Vol. 6, 1966, pp. 143–167.

Appendix A

Absorption of Linear Symmetric Molecules

For the symmetric molecule, alternative rotation lines are missing. This causes some changes in the basic equations which are outlined below. The line spacing is now given by

$$d_P = (B' + B'') + 2(B'' - B')J = d_1 + 2d_2J,\ J = 2, 4, 6 \quad \text{(A-1a)}$$

$$d_R = |(B' + B'') - 2(B'' - B')(J + 1)| = |d_1 - 2d_2(J + 1)|,\ J = 0, 2, 4 \quad \text{(A-1b)}$$

so that the absorption coefficient becomes

$$\frac{k}{bS_0/\pi} = \sum_{J=2,4,\ldots} \frac{J \exp\left[-hcB''J(J+1)/kT\right]}{[(\nu - \nu_0) + d_1J + d_2J^2]^2 + b^2} + \sum_{J=1,3,\ldots} \frac{J \exp\left[-hcB''J(J+1)/kT\right]}{[(\nu - \nu_0) - d_1J + d_2J^2]^2 + b^2} \quad \text{(A-2)}$$

where $S_0 = 2\alpha hcB''/kT$. Proceeding in the manner presented in the analysis for linear nonsymmetric molecules yields the same relations for the band absorptance provided that the optical depth is now given by $u = (2\alpha x/d_1)$. $(hcB''/kT)^{1/2}$, $\beta = 2\pi b/2d_1$ and $\tau = 2\pi(\nu - \nu_0)/2d_1$. Note that these relations for S_0, u, β and τ differ from the previous expressions by a factor of 2 due to the missing lines. The specifications for E and F remain the same (cf. Table 1).

G. L. Hubbard
C. L. Tien

Department of Mechanical Engineering,
University of California, Berkeley,
Berkeley, Calif.

Infrared Mean Absorption Coefficients of Luminous Flames and Smoke

A simple procedure has been developed for the calculation of the Planck mean emission and absorption coefficients and the Rosseland mean absorption coefficient for infrared radiation of the soot-gas mixtures commonly occurring in luminous flames and smoke. Specific results are presented for mixtures involving carbon dioxide, water vapor and carbon soot, the dominant species in most combustion systems. The close agreement between the various averages clearly demonstrates the usefulness of the mean absorption coefficient concept for applications.

Introduction

Infrared radiative heat transfer is an important component of many engineering problems involving smoke and flames. In such applications, consideration must be given to particulate matter as well as the usual absorbing-emitting gaseous species. The two dominant gaseous species from a thermal radiation standpoint are carbon dioxide and water vapor, the common combustion products. The small solid particles known as soot are the result of incomplete combustion of the fuel. The soot contribution is often dominant in many flame and smoke calculations.

A large number of experimental and analytical investigations of flame and smoke radiation have been reported recently [1–7],[1] having been well summarized in a recent paper [7]. The experimental results generally are presented for one specific geometry using arbitrary empirical correlations. Lack of a simple theoretical model makes interpretation and comparison of various data difficult and generalization to application in actual flames almost impossible. On the theoretical side most current models require overly detailed input information, and are often too complex to allow practical use of them in an actual problem. There does exist, however, a large body of analytical results, including some for smoke and flame situations, in which the intervening medium has been assumed to be gray. These results are generally relatively simple to generate and to apply to any particular problem. The difficulty lies in finding an appropriate mean absorption coefficient to use, with the need to resort to experiments when facing each new problem.

In this paper, a simple method for calculating the mean absorption coefficient is presented. It requires knowledge only of the temperature, volume fraction of soot, and partial pressures of the various absorbing species for its application. When the dominant absorbing gaseous species are CO_2 and H_2O, as in most systems, graphical results are given for the convenience of practical calculations.

Analysis

The equation of transfer along a line of sight, s, for a nonscattering medium in local thermodynamic equilibrium is given as

$$\frac{dI_\omega}{ds} = \kappa_\omega(I_{b\omega} - I_\omega) \qquad (1)$$

where I_ω is the spectral radiative intensity, κ_ω the monochromatic absorption coefficient, and $I_{b\omega}$ the blackbody intensity.

Equation (1) can be directly integrated over all wavenumbers and for an arbitrary path to find the total intensity at a point s

$$I(s) = \int_0^\infty I_\omega(0)e^{-\tau_\omega(s)}d\omega + \int_0^\infty \int_0^s I_{b\omega}(s')e^{\tau_\omega(s')-\tau_\omega(s)}\kappa_\omega(s')ds'd\omega \qquad (2)$$

where the optical depth τ is given by

$$\tau_\omega(s) = \int_0^s \kappa_\omega(s')ds' \qquad (3)$$

Evaluation of equation (2) directly, even using numerical means, is impractical due to the rapid and complex variation of κ_ω with wavenumber. There are, however, two limiting cases in which the path and wavenumber dependencies can be separated in such a way as to make evaluation practical.

If the optical depth is small for all wavenumbers and positions in question, the exponentials can be expanded in a Taylor series. If it is also assumed that $I_\omega(0) = \epsilon I_{b\omega}(T_0)$, where ϵ is independent of ω and T_0 is any temperature, equation (2) reduces to

$$I(s) \sim I_0\left[1 - \int_0^s \kappa_{P,a}(s, T_0)ds\right]$$

---

[1] Numbers in brackets designate References at end of paper.

Contributed by the Heat Transfer Division for publication in the JOURNAL OF HEAT TRANSFER. Manuscript received by the Heat Transfer Division October 7, 1977.

$$+ \int_0^s I_b(s')\kappa_{P,e}(s')ds', \; \tau_\omega \ll 1 \quad (4)$$

Here $\kappa_{P,a}$ and $\kappa_{P,e}$ are the Planck mean absorption and emission coefficients, respectively,

$$\kappa_{P,a}(T; T_0) \triangleq \frac{1}{\sigma T_0^4} \int_0^\infty \kappa_\omega(T) B_\omega(T_0) d\omega \quad (5)$$

$$\kappa_{P,e}(T) \triangleq \frac{1}{\sigma T^4} \int_0^\infty \kappa_\omega(T) B_\omega(T) d\omega \quad (6)$$

where $B_\omega(T)$ is the spectral blackbody emissive power, and σ is the Stefan-Boltzmann constant. Since $\kappa_{P,a}$ and $\kappa_{P,e}$ are functions only of T_0 and local conditions (not the distance traveled) they can be tabulated once and for all, eliminating the need for any further spectral integrations.

It is also possible to get an asymptotic solution in the limit $\tau_\omega \gg 1$. In this case Watson's lemma is used, yielding

$$I(s) \sim I_b(s) - \frac{1}{\kappa_R(s)} \frac{dI_b}{ds}, \; \tau \gg 1 \quad (7)$$

where the Rosseland mean absorption $\kappa_R(T)$ is defined by

$$\frac{1}{\kappa_R(T)} \triangleq \int_0^\infty \frac{1}{\kappa_\omega(T)} \frac{\partial B_\omega(T)}{\partial(\sigma T^4)} d\omega \quad (8)$$

Notice again that the spectral and path variations are again separated, provided that the diffusion approximation, equation (7), is used.

Between these two limits the concept of a mean absorption coefficient is not generally useful. If κ_M is defined so that the emissivity of a homogeneous gas-soot mixture of pathlength L is given by

$$\epsilon_M = 1 - e^{-\kappa_M L} \quad (9)$$

it is found that κ_M depends not only on the properties of the gas, but on L itself, unless κ_ω is independent of ω. However, for many soot-gas mixtures, κ_ω varies sufficiently slowly with ω that equation (9) can be applied using $\kappa_M = \kappa_{P,e}$ in optically thin cases and $\kappa_M = \kappa_R$ in optically thick ones. For pure soot, assuming $\kappa_\omega = \text{const}/\lambda$, it has been shown [6] that this scheme results in a maximum error in ϵ_M of seven percent.

In a mixture of soot and various gases, the monochromatic absorption coefficient, κ_ω, is just the sum of the κ_ω's for the components. That is, for N absorbing species

$$\kappa_\omega = \kappa_{\omega,s} + \sum_{i=1}^{N} \kappa_{\omega,i} \quad (10)$$

Soot particles in smoke and flames are generally much smaller in size than one characteristic wavelength of radiation. In addition, scattering is usually negligible relative to absorption. In this limit, referred to as the Rayleigh absorption limit, the spectal absorption efficiency is given by [8]

$$A_\omega = 24\pi D\omega \frac{nk}{[n^2 - k^2 + 2]^2 + 4n^2k^2} \quad (11)$$

where $(n - ik)$ is the complex index of refraction. If the number of particles per unit volume with diameters between D and $D + dD$ is denoted by $F(D)dD$, then the spectral absorption coefficient is

$$\kappa_{\omega,s} = \int_0^\infty A_\omega \frac{\pi D^2}{4} F(D)dD$$

$$= 36\pi\omega f_v \frac{nk}{[n^2 - k^2 + 2]^2 + 4n^2k^2} \quad (12)$$

or

$$\kappa_{\omega,s} = C_0(\omega) f_v \omega \quad (13)$$

where f_v is the volume fraction of soot. Generally, f_v is of the order 1×10^{-6} (1 ppm) and C_0 varies from 2 to 6. Often C_0 is taken as constant although that will not be done here.

For the absorbing gases, the Elsasser narrow-band model is used. Here an array of equally intense, equally wide, equally spaced absorption lines is assumed to exist in a given spectral region. For these conditions

$$\kappa_{\omega,i} = \left(\frac{S_\omega P_i}{d_\omega}\right) \left(\frac{\sinh \beta_\omega}{\cosh \beta_\omega - \cos z_\omega}\right) \quad (14)$$

where $z_\omega = 2\pi\omega/d_\omega$, $\beta_\omega = 2\pi\gamma_\omega{}^0 P_e/d_\omega$, S_ω is the line intensity, d_ω the line spacing, and $\gamma_\omega{}^0$ is the line half-width at unit pressure. All of these are functions of local temperature and are allowed to vary slowly with ω. The equivalent pressure, P_e, accounts for collision induced line broadening.

Equations (10), (13) and (14) are now substituted into the definitions of $\kappa_{P,e}$, $\kappa_{P,a}$ and κ_R. The integrals over wavenumber are accomplished in two steps. First everything but z_ω is assumed constant over one line spacing yielding

$$\bar{\kappa}_\omega = \frac{1}{d_\omega} \int_{\omega_1}^{\omega_2} \kappa_\omega d\omega = C_0 f_v \omega + \sum_{i=1}^{N} \frac{S_{\omega,i}}{d_{\omega,i}} P_i \quad (15)$$

$$\overline{\kappa_\omega{}^{-1}} = \frac{1}{d_\omega} \int_{\omega_1}^{\omega_2} \kappa_\omega{}^{-1} d\omega = \frac{1}{C_0 f_v \omega} - \sum_{i=1}^{N} \frac{\xi_i}{C_0 f_v \omega} \left[1 + \xi_i{}^2 + \frac{2\xi_i}{\tanh \beta_{\omega,i}}\right]^{-1/2} \quad (16)$$

where $\omega_1 = \omega - d_\omega/2$, $\omega_2 = \omega + d_\omega/2$ and $\xi_i = (S_{\omega,i}P_i)/(d_{\omega,i}C_0 f_v \omega)$.

The second step is to integrate over all wavenumbers using these average values. Considering that each absorption band, j, is narrow enough that B_ω can be assumed constant, then equation (6) yields

$$\kappa_{P,e}(T, P_i) = \int_0^\infty C_0 f_v \omega \frac{B_\omega}{\sigma T^4} d\omega$$

Nomenclature

a = integrated band intensity
A_ω = spectral absorption efficiency for soot
B = Planck blackbody emissive power
C_0 = function defined by equation (13)
C_2 = second radiation constant, 1.4388 cm-K
d = mean line spacing
D = soot particle diameter
f_v = volume fraction of soot
F = soot particle size distribution function
I = radiant intensity
n = real part of the index of refraction
k = imaginary part of the index of refraction
P_i = partial pressure for species i
P_e = equivalent line broadening pressure
s = path length
S = integrated line intensity
T = gas-soot mixture temperature
T_0 = characteristic temperature of incoming radiation
β_ω = line broadening parameter, $2\pi\gamma_\omega{}^0 P_e/d_\omega$
$\gamma_\omega{}^0$ = mean line half-width at unit pressure
Δ = band half-width
ϵ = emissivity
ζ = dimensionless wavenumber, $\omega C_2/T$
κ = absorption coefficient
$\kappa_{P,a}$ = Planck mean absorption coefficient
$\kappa_{P,e}$ = Planck mean emission coefficient
κ_R = Rosseland mean absorption coefficient
λ = wavelength
σ = Stefan-Boltzmann constant
τ = optical depth
χ_i = gas-soot ratio parameter, p_i/f_v
ω = wavenumber

Subscripts

b = blackbody
i = gas species i
j = absorption band j
M = mixture
P = Planck mean
R = Rosseland mean
s = soot
ω = spectral value

$$+\sum_{i=1}^{N} P_i \sum_j \frac{B_{\omega j}}{\sigma T^4} \int_{\Delta\omega j} \frac{S_{\omega,i}}{d_{\omega,i}} d\omega \quad (17)$$

or,

$$\frac{\kappa_{P,e}(T, \chi_i)}{f_v} = \kappa_{P,s}(T) + \sum_{i=1}^{N} \chi_i \kappa_{P,i}(T) \quad (18)$$

where $\chi_i = P_i/f_v$ is a measure of the relative amount of soot and gas. The term $\kappa_{P,s}$ represents the contribution due to the soot and is given by

$$\kappa_{P,s} = \int_0^\infty C_0(\omega)\omega \frac{B_\omega(T)}{\sigma T^4} d\omega = \frac{T}{C_2} \int_0^\infty C_0(\omega) \frac{15}{\pi^4} \frac{\zeta^4}{(e^\zeta - 1)} d\zeta \quad (19)$$

where $C_2 = hc/k = 1.4388$ cm-K is the second radiation constant and $\zeta = C_2\omega/T$. If C_0 is constant the value of the integral is 3.83 C_0, as obtained before [9]. The term $\kappa_{P,i}$ is sometimes called the Planck mean absorption coefficient itself [10] and is given by

$$\kappa_{P,i}(T) = \sum_j \frac{B_{\omega j}}{\sigma T^4} \int_{\Delta\omega j} \frac{S_{\omega,i}}{d_{\omega,i}} d\omega = \sum_j a_j(T) \frac{B_{\omega j}(T)}{\sigma T^4} \quad (20)$$

where a_j is the integrated band intensity. Generally, the product, $a_j(T)\cdot T$, is a constant, $a_j(T_0)\cdot T_0$, for most important bands so that

$$\frac{\kappa_{P,a}(T, \chi_i; T_0)}{f_v} \simeq \kappa_{P,s}(T_0) + \sum_{i=1}^{N} \left(\chi_i \frac{T_0}{T}\right) \kappa_{P,i}(T_0) \quad (21)$$

or

$$\frac{\kappa_{P,a}(T, \chi_i; T_0)}{f_v} \simeq \frac{\kappa_{P,e}(T_0, \chi_i T_0/T)}{f_v} \quad (22)$$

Calculation of κ_R requires knowledge of the spectral distribution of S/d as well as its integral since κ_ω^{-1} is not a linear function of ξ_i. The exact distribution is very complex and must be simplified greatly if a closed-form expression for κ_R is desired. The shape chosen here is taken from the exponential wide-band model [11], where β_ω does not vary with ω inside each band and

$$\frac{S_\omega}{d_\omega} = \frac{a_j(T)}{\Delta_j(T)} \exp\left(-2 \frac{|\omega - \omega_j|}{\Delta_j(T)}\right). \quad (23)$$

Here Δ_j is the band half-width and ω_j is the spectral location of the band center. This model was developed to enable prediction of the integrated band absorptance. The values of a_j and Δ_j are selected to get a maximum agreement with experiment over a large range of pathlengths. Since the model is somewhat arbitrary, these values of a_j do not agree exactly with those generally accepted [10]. In addition, this model used the Goody narrow-band model rather than the Elsasser model used here. However, the two models do not differ greatly so the difference should not be significant.

Use of equation (23) implicitly assumes that there is no overlapping of bands. This is not a good assumption at high temperatures where Δ_j is large. Fortunately under such conditions the soot generally dominates since $a_j \propto T^{-1}$ and so the error is not significant. If it is now assumed $C_0\omega$ and $\partial B_\omega/\partial(\sigma T^4)$ are constant over each of the bands, equation (8) yields

$$\frac{f_v}{\kappa_R(T, \chi_i, P_e)} = \frac{1}{\kappa_{R,s}(T)} - \sum_{i=1}^{N} \sum_j \frac{\Delta_j}{C_{0_j}\omega_j} \ell n \{G_j + (G_j{}^2 - e^{-2\beta_j})^{1/2}\} \frac{\partial B_{\omega j}}{\partial(\sigma T^4)} \quad (24)$$

or

$$\frac{f_v}{\kappa_R(T, \chi_i, P_e)} = \frac{1}{\kappa_{R,s}(T)} - \sum_{i=1}^{N} \frac{1}{\kappa_{R,i}(T, \chi_i, P_e)} \quad (25)$$

where

$$\frac{1}{\kappa_{R,s}(T)} = \int_0^\infty \frac{1}{C_0\omega} \frac{\partial B_\omega}{\partial(\sigma T^4)} d\omega = \frac{C_2}{T} \int_0^\infty \frac{1}{C_0} \frac{15}{4\pi^4} \frac{\zeta^3 e^\zeta}{(e^\zeta - 1)^2} d\zeta \quad (26)$$

and

$$G_j = \frac{\frac{a_j}{C_{0_j}\omega_j\Delta_j} \chi_i \tanh \beta_j + 1}{\tanh \beta_j + 1}. \quad (27)$$

For the case where C_0 is constant, $\kappa_{R,s} = 3.6 C_0 T/C_2$ [9]. For high pressures and temperatures, where $\beta_j \to \infty$, this result reduces to

$$\frac{1}{\kappa_{R,i}} = \sum_j \frac{\Delta_j}{C_{0_j}\omega_j} \ell n \left\{1 + \frac{a_j}{C_{0_j}\omega_j\Delta_j} \chi_i\right\}. \quad (28)$$

The values of $\kappa_{R,i}$ in contrast to $\kappa_{P,i}$ have not appeared previously and have no meaning as $f_v \to 0$. This can be easily seen by noting as $f_v \to 0$, $\chi_i \to \infty$ and $\kappa_R = f_v \cdot \kappa_{R,i} \to 0$. This is to be expected as the Rosseland mean absorption coefficient is not properly defined in pure gases due to the presence of transmission windows [10]. In fact, the present analysis is really correct only if the system is optically thick even in those windows. That implies that the soot alone must make the system optically thick.

Results and Discussion

The calculation of $\kappa_{P,s}$ and $\kappa_{R,s}$ requires specification of the complex index of refraction for soot at all wavelengths. A dispersion theory model is used in which the constants are adjusted to fit experimental data [12]. The integrals in equations (19) and (26) are then evaluated numerically using Simpson's rule, the results being shown in Fig. 1. Note that the maximum deviation between $\kappa_{P,s}$ and $\kappa_{R,s}$ is 17 percent versus only 6 percent if C_0 is taken as constant. This is because C_0 drops with increasing wavelength, increasing the variation of $\kappa_{\omega,s}$.

For evaluation of the contribution of CO_2 and H_2O to the Planck mean absorption coefficient, the value of the integrated band intensity of each band is needed. The values at standard conditions are those generally accepted [10] and the variation in temperature is determined from a simplified quantum theory [11]. For H_2O, the 20 μ pure rotation and the 6.3 μ, 2.7 μ, 1.9 μ and 1.4 μ vibration-rotation bands were included. For CO_2 the vibration-rotation bands considered are at 15 μ, 10.4 μ, 9.4 μ, 4.3 μ, 2.7 μ and 2.0 μ. The results are shown in Fig. 2. This quantity is identical with the Planck mean absorption coefficient for pure gases quoted elsewhere [10]. The rapid drop if $\kappa_{P,i}$ with temperature results from the T^{-1} variation of a_j and the shift of blackbody curve away from the infrared, where the absorption bands are located.

Data for the Rosseland mean absorption coefficient are taken from the exponential wide-band model correlation [11]. As noted previously, the values of a_j here do not always agree precisely with those

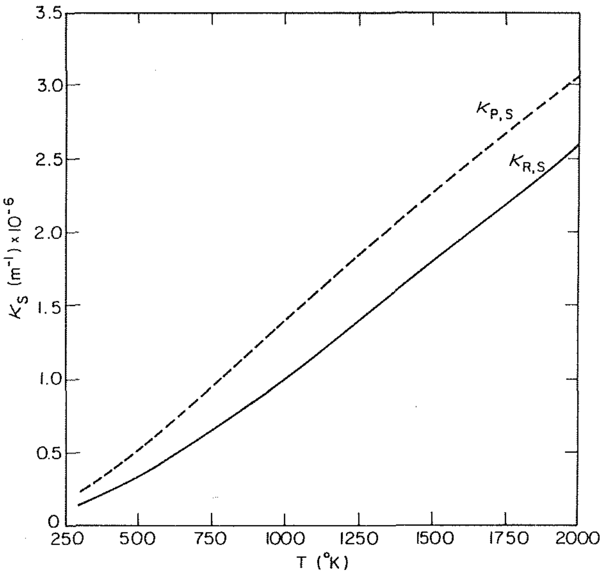

Fig. 1 Mean absorption coefficients for pure soot

used earlier but are used to insure consistency with the values for Δ_j and β_j. The quantity $1/\kappa_{R,i}$ is shown in Figs. 3 and 4 for H_2O and CO_2, respectively. The equivalent pressure is calculated from

$$P_e = P + P_i(8.6\sqrt{T^*/T} - 0.5) \text{ for } H_2O$$

$$\simeq (P + 0.3P_i)^{0.7} \text{ for } CO_2$$

where T^* , 100 K and all pressures are in atm. The exponent for the CO_2 case varies somewhat from band to band, 0.7 being an average value. Since most fires are at atmospheric conditions, and the partial pressure of carbon dioxide rarely exceeds 0.2 atm, P_e never deviates significantly from 1 atm and so only that case is shown. For water vapor, however, that is not true. If the temperature is low, the effective pressure can rise to nearly two atms without P_{H_2O} exceeding the saturation pressure. Since the effect of P_e is relatively small in this range, the simple correction shown on Fig. 3 is completely sufficient and easy to use.

Using equations (18) and (25) it is possible to readily calculate $\kappa_{P,e}$ and κ_R with the aid of Figs. 1 through 4. This is done in Figs. 5 and 6 for two sets of conditions. In the first $P_{CO_2} = P_{H_2O}$, and in the second $P_{CO_2} = 2P_{H_2O}$. The Planck mean emission coefficient does not depend on P_e but the Rosseland mean does, the cases here corresponding to $P_e = 1$ atm. However, changing P_e to two atm results in a maximum change of these results of only ten percent, a difference which is probably negligible for most purposes. Of course, other cases could be easily generated if needed.

Figs. 5 and 6 demonstrate how insensitive the Rosseland mean

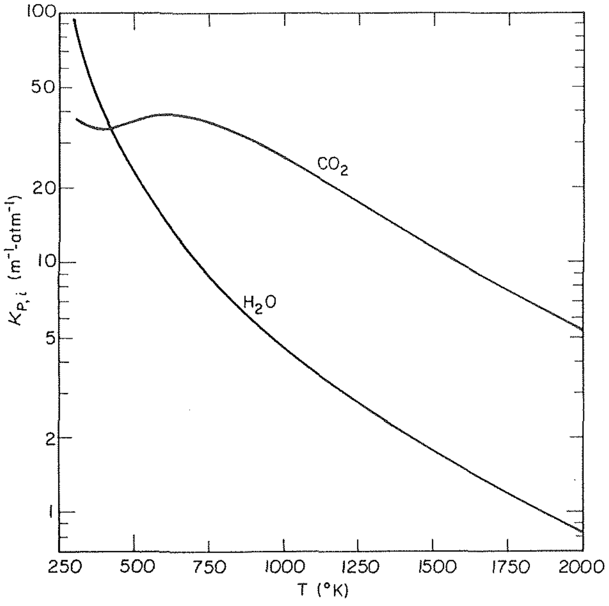

Fig. 2 **Contributions of CO_2 and H_2O to the Planck mean absorption coefficient**

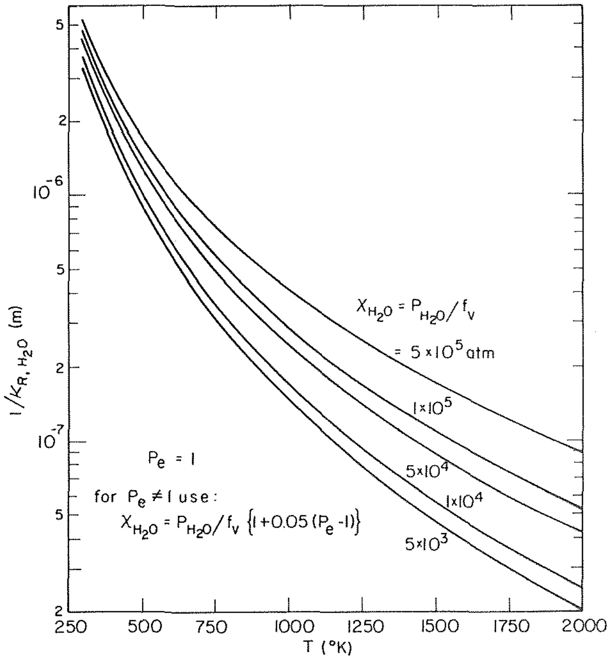

Fig. 3 **Contribution of H_2O to the Rosseland mean absorption coefficient**

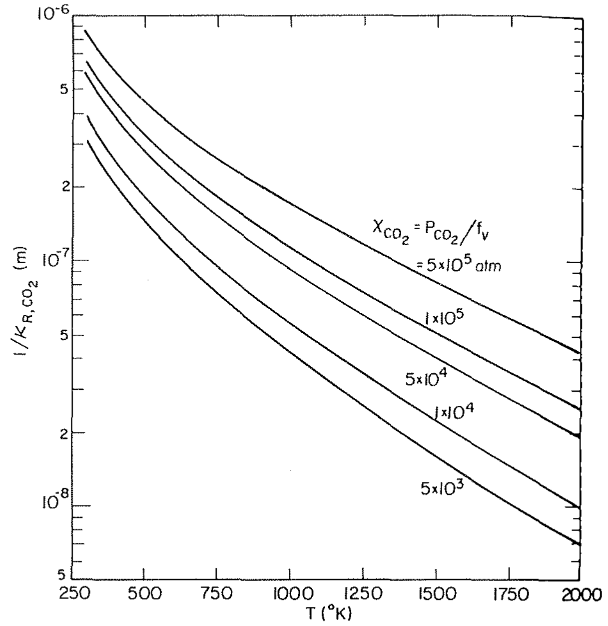

Fig. 4 **Contribution of CO_2 to the Rosseland mean absorption coefficient**

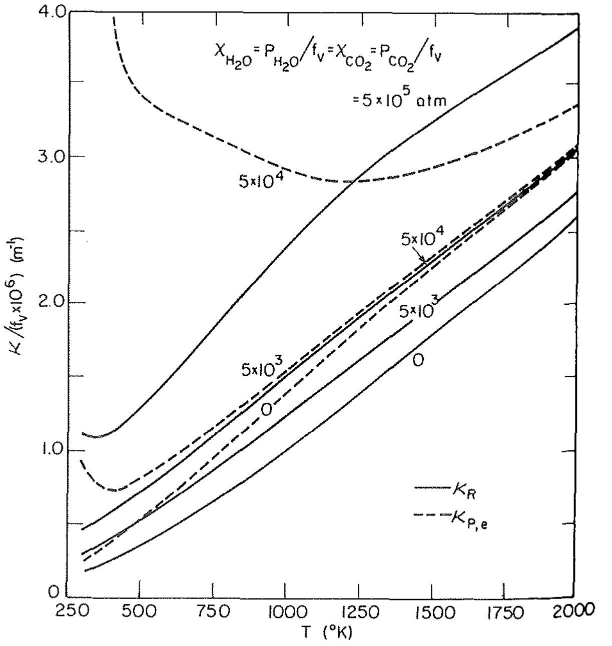

Fig. 5 **Mean absorption coefficients for luminous flames and smoke ($X_{H_2O} = X_{CO_2}$)**

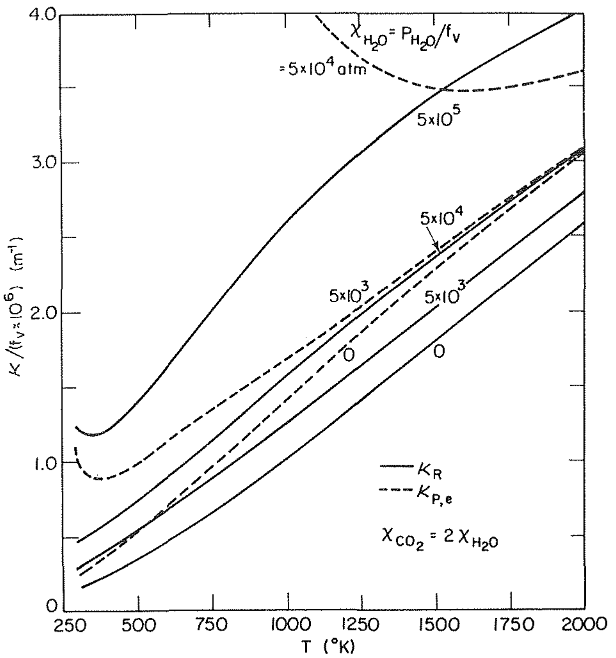

Fig. 6 Mean absorption coefficients for luminous flames and smoke ($\chi_{CO_2} = 2\chi_{H_2O}$)

Table 1 Values of the soot volume fraction f_v and the soot temperature (T_s) for various fuels [6]

		C/H	$f_v \times 10^6$	T_s (K)
Gas fuels	methane, CH_4	0.25	4.49	1289
	ethane, C_2H_6	0.33	3.30	1590
	n-butane, $(CH_3)(CH_2)_2(CH_3)$	0.40	6.41	1612
	propane, C_3H_8	0.38	7.09	1561
	isobutane, $(CH_3)_3CH$	0.40	9.17	1554
	ethylene, C_2H_4	0.50	5.55	1722
	propylene, C_3H_6	0.50	13.6	1490
	isobutylene, $(CH_3)_2CCH_2$	0.50	18.7	1409
	1,3-butadiene, $CH_2CHCHCH_2$	0.66	29.5	1348
Solid fuels	wood $\simeq (CH_2O)_n$	0.50	0.362	1732
	plexiglas, $(C_5H_8O_2)_n$	0.63	0.272	1538
	polystyrene, $(C_8H_8)_n$	1.00	0.674	1486

absorption coefficient is to the quantity of gas present, especially in the important region $\chi < 10^4$ atm. Thus, for optically thick systems, the radiative transfer is due primarily to the soot. For pure soot, $\kappa_{P,e}$ and κ_R differ by at most 17 percent. As the partial pressure of gas increases, $\kappa_{P,e}$ rises relatively rapidly because of its linear dependence on χ_i. Hence, in optically thin systems, especially at low temperatures when the 20 μ H_2O and 15 μ CO_2 bands are important, the gas plays an important role in the heat transfer process. At high temperatures the effect is much smaller since $\kappa_{P,i}$ drops rapidly with T as discussed earlier. The reason the differences are larger in Fig. 6 is basically because there is 50 percent more gas present than for the same value of χ in Fig. 5.

Many engineering systems are neither optically thin nor optically thick, of course, and for this method to be useful it must be possible to estimate κ_M for these cases. If the temperature is high this presents little problem because of the basic agreement between $\kappa_{P,e}$ and κ_{ℓ} in that region. At low temperatures or high partial pressures that is not true; however, a numerical comparison with Felske and Tien [1] shows a maximum error in ϵ of 15 percent exists if κ is taken as κ_R, even when the optical depth of the soot alone is 0.3. This is not unexpected, based on the pure soot results [6] which show a maximum error of 7 percent in ϵ over all optical depths. Under the condition $P_iL < 1 \times 10^{-4}$ m-atm, $\kappa_\omega L \ll 1$ even at the band heads, and $\kappa_{P,e}$ should be used. It should be noted, however, that these two limits, $\kappa_{P,e}$ and κ_R, do not necessarily bound the results, as can be seen from the pure soot case [6].

As an example, consider radiative transfer in a polystyrene, $(C_8H_8)_n$, pool fire 30 cm across. Experimental data [3,7] show that a reasonable mean flame temperature is 1486 K, and a mean value for f_v is 0.675×10^{-6} (see Table 1). For complete combustion, the product gas will contain twice as much CO_2 as H_2O, the actual values depending on conditions. The numbers used here are $P_{H_2O} = 0.075$ atm and $P_{CO_2} = 0.15$ atm. Thus $\chi_{H_2O} = 0.075 \text{ atm}/6.74 \times 10^{-7} = 1.1 \times 10^5$ atm, with $P_e = 1.2$ atm. The values $\kappa_{P,e}/f_v$ and κ_R/f_v can now be read directly from Fig. 6 or computed using Figs. 1 through 4 with equations (18) and (28). The former is useful for quick estimates but the latter method is somewhat more accurate because the interpolation is simpler. These values are then multiplied by f_v, giving $\kappa_{P,e} = 3.6$ m^{-1} and $\kappa_R = 1.74$ m^{-1}. Multiplying these by the pathlengths, $s = 0.3$ m, gives $\tau_P = \kappa_{P,e}\, s = 1.1$ and $\tau_R = \kappa_R\, s = 0.52$. Hence, this case is neither optically thin or thick. Based on the previous discussion, κ_R is probably the best value to use, thus $\kappa_M = 1.74$ m^{-1}. The emissivity would be $\epsilon_M = 1 - \exp(-\kappa_M L) \simeq 0.40$.

Conclusion

A method has been presented to allow the determination of the mean absorption coefficient of gas-soot mixtures. This permits the use of the gray-gas approximation when solving the equation of transfer, and hence greatly simplifies radiative transfer problems in luminous flames and smoke. Quantitative results have been presented for the case where water vapor and carbon dioxide are the dominant absorbing gaseous species, as in most important engineering systems. For these conditions, close agreement has been found between the various mean absorption and emission coefficients, helping to verify the usefulness of the mean absorption coefficient concept. For many such systems, the contribution of gas absorption has been shown to be small. Unless $P_iL < 10^{-4}$ atm-m, where the optically thin limit is valid, it is best to use κ_R for calculational purposes. Provided this gives an emissivity greater than 0.3, reasonable confidence can be had in the results. If neither of these limits is valid, this greatly simplified approach fails and a more complete theory must be used. Fortunately, a great many engineering systems fall in one of the two categories.

References

1 Felske, J. D., and Tien, C. L., "Calculation of the Emissivity of Luminous Flames," *Combustion Science and Technology,* Vol. 7, 1973, pp. 25–31.

2 Taylor, P. B., and Foster, P. J., "The Total Emissivity of Luminous and Non-Luminous Flames," *International Journal of Heat and Mass Transfer,* Vol. 17, 1974, pp. 1591–1605.

3 Markstein, G. H., "Radiative Energy Transfer from Gaseous Diffusion Flames," *Fifteenth Symposium (International) on Combustion,* The Combustion Institute, 1974, p. 1285.

4 Lee, C. K., "Estimate of Luminous Flame Radiation from Fire," *Combustion and Flames,* Vol. 24, 1975, pp. 239–244.

5 Sato, T., Kunitomo, T., and Hashimoto, T., "On the Monochromatic Distribution of the Radiation from the Luminous Flame," Bulletin of *JSME,* Vol. 12, 1969, pp. 1135–1143.

6 Yuen, W. W., and Tien, C. L., "A Simple Calculation Scheme for the Luminous Flame Emissivity," *Sixteenth Symposium (International) on Combustion,* The Combustion Institute, 1976, p. 1481–1487.

7 Buckius, R. O., and Tien, C. L., "Infrared Flame Radiation," *International Journal of Heat and Mass Transfer,* Vol. 20, 19/7, pp. 93–106.

8 Mie, G., "Optics of Turbid Media," *Annalen der Physik,* Vol. 25, 1908, pp. 377–445.

9 Felske, J. D., and Tien, C. L., "The Use of the Milne-Eddington Absorption Coefficient for Radiative Heat Transfer in Combustion Systems," ASME JOURNAL OF HEAT TRANSFER, Vol. 99, 1977, pp. 458–465.

10 Tien, C. L., "Thermal Radiation Properties of Gases," *Advances in Heat Transfer,* Vol. 5, 1967, pp. 253–324.

11 Edwards, D. K., Molecular Gas Band Radiation," *Advances in Heat Transfer,* Vol. 12, 1976, pp. 116–193.

12 Dalzell, W. H., and Sarofim, A. F., "Optical Constants of Soot and Their Applications to Heat Flux Calculations," ASME JOURNAL OF HEAT TRANSFER, Vol. 91, 1969, pp. 100–104.

S. N. Tiwari
Professor.
Mem. ASME

S. K. Gupta
Research Associate.

School of Engineering,
Old Dominion University,
Norfolk, Va.

Accurate Spectral Modeling for Infrared Radiation

Direct line-by-line integration and quasi-random band model techniques are employed to calculate the spectral transmittance and total band absorptance of the 4.7μ *CO,* 4.3μ CO_2*,* 15μ CO_2*, and* 5.35μ *NO bands. Results are obtained for different pressure and path lengths. These are compared with available theoretical and experimental investigations. Total band absorptance values are available in the literature for certain pressure and path length conditions for these gases. Total absorptances have been calculated for the same physical conditions, employing line-by-line and quasi-random band models and the continuous correlations of Tien and Lowder, Cess and Tiwari, and Felske and Tien. In almost all cases, the line-by-line results are found to be in excellent agreement with the experimental values. The range of validity of other models are discussed.*

1 Introduction

In radiative transfer analyses, involving infrared active molecules, it often becomes essential to employ meaningful, computationally fast and accurate spectral models for absorption by the absorbing-emitting molecules. The most accurate theoretical procedure to compute the absorptance of a vibration-rotation band is probably the direct integration (line-by-line) method. This employs an appropriate line profile (Lorentz, Doppler, Voigt, etc.) for the given pressure and temperature conditions, and calculates absorption at a large number of frequencies within the spectral range of interest. Although it requires the knowledge of individual line parameters and involves lengthy calculations, the line-by-line method is quite reliable.

Several "narrow" and "wide" band models and band model correlations for infrared spectral absorption have been proposed in the literature [1–10].[1] Narrow band models (viz., Elsasser, statistical, random-Elsasser, and quasi-random) can be used for spectral absorptance computations when high resolution is not required. Although the use of these models results in considerable reduction of computational time, the results, in general, have a lower degree of accuracy than those obtained by the line-by-line method [12–14]. The quasi-random band model, introduced by Wyatt, et al. [3], is the best among the narrow band models to represent the absorption of a vibration-rotation band accurately. In many engineering applications involving a single absorbing-emitting gas, it is possible to make use of the so-called wide band models [4–9]. The relations for total band absorptance of a wide band are obtained from the absorptance formulations of the narrow bands by employing an exponential variation of the line intensities. As such, these models are called the exponential wide band models. In addition, several correlations for the total band absorptance of a wide band are available in the literature [4, 10]. For some gases, these correlations satisfactorily represent the band absorptance over certain ranges of physical conditions. Results of various wide band models and correlations were compared in [2, 11]. It was noted that different band models and correlations predict the total absorptance of a band with varying degree of accuracy. Recently, attempts have also been made to express band absorptance relations directly in terms of the basic spectroscopic variables [15, 16]. All these results indicate that while a particular formulation (band model relation or correlation) may be applicable to linear molecules, it may give erroneous results when applied to asymmetric or spherical top molecules.

The purpose of this study is to calculate the spectral transmittance and total band absorptance of 4.7μ CO, 4.3μ CO_2, 15μ CO_2, and 5.35μ NO bands by employing the direct line-by-line integration and quasi-random band model techniques. Specific results are obtained for the temperature, pressure, and path length conditions for which experimental measurements are available. Various theoretical and experimental results are compared in order to establish the validity of a particular formulation to specific applications. General results for band absorptance are obtained for different temperatures, pressures, and path lengths, and these are compared with the results of various correlations.

2 Governing Equations

For a homogeneous path, the spectral absorptance, α_ω, at wavenumber ω is defined as

$$\alpha_\omega = 1 - \tau_\omega = 1 - \exp(-\kappa_\omega X) \tag{1}$$

where τ_ω represents the spectral transmittance, κ_ω is the volumetric absorption coefficient, and $X = py$ is the pressure path length. The total (integrated) band absorptance, over a spectral interval $\Delta\omega$, is given by

$$A = \int_{\Delta\omega} \alpha_\omega d\omega = \int_{\Delta\omega} [1 - \exp(-\kappa_\omega X)] d\omega \tag{2}$$

---

[1] Numbers in brackets designate References at end of paper.

Contributed by the Heat Transfer Division and presented at the AIChE-ASME Heat Transfer Conference, Salt Lake City, Utah, August 15–17, 1977. Revised manuscript received by the Heat Transfer Division December 21, 1977. Paper No. 77-HT-69.

The total band absorptance of a wide band, in turn, is given by

$$A = \int_{-\infty}^{\infty} [1 - \exp(-\kappa_\omega X)] d(\omega - \omega_0) \qquad (3)$$

where the limits of integration are over the entire band pass and ω_0 is the wavenumber at the center of the wide band.

For the present study, it is convenient to define the integrated band absorptance in a nondimensional form as

$$\bar{A} = A/A_0 \qquad (4)$$

where A_0 is the band width parameter [5–8]. Also, the optical path length is defined as

$$u = SX/A_0 = Spy/A_0 \qquad (5)$$

where S represents the integrated band intensity.

Various theoretical formulations of narrow and wide band models are reviewed in [2, 7–9]. The wide band correlations, whose results are compared in this study, are discussed here briefly. A three-piece correlation was introduced first by Edwards and Menard [4–5]. The first continuous correlation was proposed by Tien and Lowder [6–7], and this is of the form

$$\bar{A}(u, \beta) = \ln(uf(t)\{(u + 2)/[u + 2f(t)]\} + 1) \qquad (6)$$

where

$$f(t) = 2.94[1 - \exp(-2.60\, t)],\ t = \beta/2,\ \beta = 2\pi\gamma_L/d$$

A continuous correlation introduced by Cess and Tiwari is given by

$$\bar{A}(u, \beta) = 2\ \ln(1 + u/\{2 + [u(c + \pi/2\beta)]^{1/2}\}) \qquad (7)$$

Different values for constant c in equation (7) are suggested in [2]. If it is desired to use only one value of c for all β and path lengths, the value of $c = 0.1$ is recommended. Felske and Tien [10] have proposed a continuous correlation of the form

$$\bar{A}(u, \beta) = 2\, E_1(t\rho_u) + E_1(\rho_u/2) - E_1[(\rho_u/2)(1 + 2t)] + \ln[(t\rho_u)^2/(1 + 2t)] + 2\gamma \qquad (8)$$

where

$$\rho_u = \{(t/u)[1 + (t/u)]\}^{-1/2},\ \gamma = 0.5772156$$

Since this correlation involves exponential integral functions, it requires relatively longer computational time when used in radiative transfer analyses [11]. Based on the theoretical formulation of Edwards and Menard [4–5], Green and Tien have proposed a piecewise correlation for NO in [25]. Results of these correlations are compared with other theoretical and experimental results in Sections 4 and 5.

3 Computational Procedure

The procedure used for computing the spectral transmittance and total band absorptance by employing the line-by-line and quasi-random band models are described in detail in [3, 12, 18–20]. These are discussed here briefly.

The direct integration (line-by-line) method consists of calculating the absorption coefficient, and then the transmittance, at a large number of frequency locations within the spectral range of interest. Since the absorption coefficient is a fast varying function of the frequency (varying by orders of magnitude over the width of a line), it has to be evaluated at very closely spaced locations. The total absorption coefficient at any frequency location is made up of contributions from a large number of lines in the vicinity of that frequency. This method yields results with a high degree of accuracy. However, the evaluation of total absorptance of a band with a large number of lines requires a considerably long computational time. Drayson [18] and Kunde and Maguire [20] have proposed a scheme for the evaluation of transmittance using this method. The procedure and computer program developed for this work is a modification of the methods discussed in the above references. It makes use of the Lorentz line profile for absorption coefficient and is relatively simple and efficient. The entire procedure is discussed in detail in [12]. The line parameters needed in the calculation are obtained from McClatchey, et al. [21].

The quasi-random band model was introduced by Wyatt, Stull and Plass [3]. A revised version of this model was applied by Kunde [19] to several planetary atmospheric problems and satisfactory results were obtained. The method consists of dividing the entire spectrum into narrow frequency intervals. The lines in each interval are grouped into five intensity decades. Average transmittance for the interval is computed for lines in each decade separately and the final transmittance is obtained by multiplying them for the five decades. It is to be noted here that adopting smaller width for the intervals increases accuracy of the results but also steeply increases the cost of computation. A width of five cm^{-1} was found to be consistent with the required accuracy and was adopted for the present work. The numerical procedure used in the present work is different than that used by other workers [3, 19]. It is very accurate and computationally much faster than the other numerical schemes. The details of this method are discussed in [12].

4 Specific Comparisons

For the gases under consideration, experimental band absorptance results are available in the literature [17, 22, 23]. For the 4.7μ CO fundamental band experimental results were obtained from Burch, et al. [22] and Abu-Romia and Tien [23]. For the 15μ and 4.3μ CO_2 bands experimental results were obtained from Burch, et al. [22] and for the 5.35μ NO band the results were obtained from Green and Tien [17]. By employing the line-by-line (LBL) and quasi-random band (QRB) models, specific results were obtained for exactly the same temperature, pressure, and path length conditions for which experimental measurements were available. For the same conditions, results were also obtained by employing the continuous correlations of Tien and Lowder [6–7], Cess and Tiwari [8], and Felske and Tien [10]. The correlation quantities required in the calculation were obtained from [5–7]. Various theoretical and experimental band absorptance results are compared in this section.

For the 4.7μ CO fundamental band, the spectral band considered is between 1975–2265 cm^{-1}. In this range, there are 254 spectral lines. The line parameters for this band were obtained from McClatchey, et al. [21]. By employing the LBL and QRB models, spectral transmittance results were obtained for this band in the spectral range 2070–2220 cm^{-1} for conditions $T = 300$ K, $P_e = 51$ mm Hg and $X =$

Nomenclature

A = total band absorptance, cm^{-1}
A_0 = band width parameter (correlation quantity), cm^{-1}
$\bar{A}(u, \beta)$ = dimensionless band absorptance, $\bar{A} = A/A_0$
d = average line spacing, cm^{-1}
p or P = gas pressure, atm
$S, S(T)$ = total band intensity, $\text{atm}^{-1}\text{-cm}^{-2}$
t = line structure parameter, $t = \beta/2$
T = temperature, K
u = dimensionless coordinate, $u = Spy/A_0$
y = physical coordinate
α_ω = spectral absorptance
β = line structure parameter, $\beta = 2t$
γ_L = rotationally averaged line half-width, cm^{-1}
κ_ω = volumetric spectral absorption coefficient, $(\text{atm-cm})^{-1}$
τ_ω = spectral transmittance
ω = wave number, cm^{-1}
ω_0 = wave number at the band center, cm^{-1}

22.8 cm-atm [13]. A comparison of these with experimental results (see Fig. 1) indicates that the LBL results are in good agreement with the experimental values while QRB results exhibit appreciable differences (particularly in the P and R branches of the band). By employing the LBL and QRB models and the continuous correlations, total absorptance results were obtained for this band at T = 300 K. The results are presented in Table 1 along with other theoretical and experimental results. The comparison shows that the LBL and QRB results are in good agreement with the experimental results (LBL being slightly better than QRB). Among other theoretical results, the results of HHG (Hashemi, Hsieh and Greif [16]) provides the best agreement with the experimental and LBL results. Among the results of the correlations, it can be seen that, for the very low pressures, Tien and Lowder's correlation yields higher values of absorptance and Cess and Tiwari and Felske and Tien's correlations show better agreement. For medium and high pressures, however, Tien and Lowder's correlation yields better agreement while Cess and Tiwari and Felske and Tien's correlations yield much lower values. One may conclude, therefore, that use of the Tien and Lowder's correlation is justified in radiative transfer analyses involving CO at relatively high pressures.

The line parameters for the 15μ CO$_2$ fundamental band were obtained from [21]. There are more than 7,200 lines in the spectral range (550–800 cm^{-1}) of this band. Spectral transmittances were calculated for this band by using the LBL and QRB models for T = 300 K, P_e = 1100 mm Hg, and X = 1.55 cm-atm [13]. These are illustrated in Fig. 2 along with experimental results. The agreement between the three results is seen to be excellent. For this band, total band absorptance results were calculated by employing the LBL and QRB models and the continuous correlations at T = 300 K. The QRB results for this band are given also by Kunde [19] and Young [24]. The results are presented in Table 2 for six illustrative cases. Because of

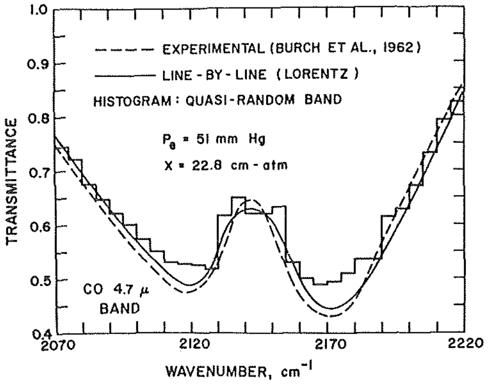

Fig. 1 Comparison of transmittances of the CO fundamental band at T = 300 K.

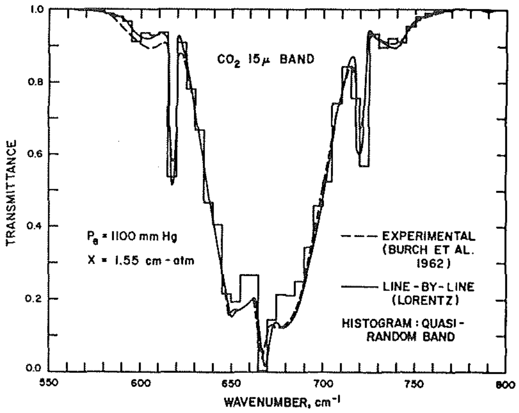

Fig. 2 Comparison of transmittances of the 15μ CO$_2$ band at T = 300 K

Table 1 Comparison of absorptance results for the 4.7μ fundamental band of carbon monoxide at T = 300 K (experimental data of Burch, et al. [22]); HHG = Hashemi, A., Hseih, T. C., and Greif, R. [16] LBL = line-by-line, QRB = quasi-random band

				Absorptance Results, A (cm^{-1})							
					Theoretical				Correlation		
Eff. Pr. [16] P_e (atm)	Eff. Pr. [22] P_e (atm)	Pr. Path Length [22] $P_a y$ (atm-cm)	Opt. Path u	Exp. [22]	HHG [16]	Edwards and Menard [4, 5]	Present LBL	Present QRB	Tien and Lowder [6]	Cess and Tiwari [2, 8]	Felske and Tien [10]
0.0329	0.0329	0.0110	0.0686	0.84	0.92	1.3	0.737	0.974	1.0132	0.8091	0.8318
0.0345	0.0345	1.3752	8.5771	14.2	12.6	17.0	12.86	13.00	7.9414	11.9875	11.3233
0.337	0.3368	0.0028	0.0175	0.64	0.64	0.68	0.650	0.678	0.6402	0.4906	0.5789
0.317	0.3171	0.4366	2.7231	20.5	21.4	22.9	20.55	19.88	22.6158	16.6929	17.1523
0.312	0.3118	15.175	94.647	110.0	108.0	119.7	110.24	104.45	113.3707	75.2403	83.3990
3.97	3.974	0.0028	0.0175	0.69	0.68	0.68	0.723	0.726	0.6635	0.5925	0.6543
3.91	3.908	0.0753	0.4696	16.3	16.5	17.4	16.50	16.11	15.6790	16.2476	12.7278
3.91	3.908	1.3752	8.5771	102.6	113.5	97.5	101.95	94.49	100.0165	58.6714	69.7050
3.91	3.908	15.175	94.647	183.4	187.6	188.6	185.31	184.43	193.0015	133.2973	155.5740
1.01	0.015	47.421	295.765	184.6	183.4	197.7	187.05	186.93	196.6126	138.9117	160.9919

Table 2 Comparison of absorptance results for the 15μ fundamental band of carbon dioxide at T = 300 K (experimental data of Burch, et al. [22] and Kunde [19]); LBL = line-by-line; QRB = quasi-random band

						Absorptance Results, A (cm^{-1})							
											Correlation		
							Theoretical						
Path Length y (cm)	Eff. Pr. [22] P_e (mm Hg)	Eff. Pr. [19] P_e (atm)	Pr. Path Length [19, 22] $P_a y$ (atm-cm)	Pr. Path Length [22] $P_a y$ (atm-cm)	Opt. Path u	Exp. [22]	Young [25] QRB	Kunde [19] QRB	Present LBL	Present QRB	Tien and Lowder [6]	Cess and Tiwari [2, 8]	Felske and Tien [10]
400	15.6	0.0205	5.73	5.7474	87.378	34.6	43.3	34.4	35.44	37.49	17.36	16.08	15.72
400	63.6	0.0837	5.73	5.7474	87.378	54.7	67.3	53.6	56.42	57.54	39.11	27.81	28.90
400	304.0	0.4000	5.73	5.7474	87.378	81.9	94.0	79.2	83.23	83.47	69.93	46.25	51.68
400	767.0	1.0092	5.73	5.7474	87.378	95.3	103.9	93.2	86.39	96.91	88.41	58.89	67.85
1,600	3.77	0.0050	5.56	5.5558	84.465	21.7	26.7	20.1	19.88	24.7	5.48	8.57	8.02
1,600	6.24	0.0083	9.20	9.1958	139.804	32.6	39.3	30.4	30.81	34.18	12.58	13.43	12.91

the large computer time required for the LBL computation, only six sample cases were considered. The time required by the QRB model was remarkably low (approximately a factor of 14 lower than the LBL computation) for this band. An inspection of the Table shows that the LBL results agree very well with the experimental results. The present QRB results are higher than the experimental values for very low pressures, but they agree well at moderate and high pressures. Young's results are consistently higher than the experimental values for very low pressures, but they agree well at moderate and high pressures. Young's results are consistently higher while Kunde's results agree very well. Looking at the results of continuous correlations, it is noted that Tien and Lowder's results are very low at lower pressures but compare better at the higher pressures. The results of Cess and Tiwari and Felske and Tien's correlation are consistently lower for all cases considered.

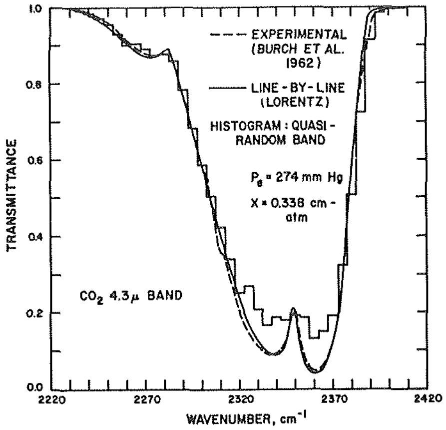

Fig. 3 Comparison of transmittances of the 4.3μ CO_2 band at T = 300 K

The line parameters for 4.3μ CO_2 band were also obtained from [21]. There are approximately 5,565 lines in the spectral range (2220–2420 cm^{-1}) of this band. Experimental and theoretical transmittance results for this band are compared in Fig. 3 for T = 300, P_e = 274 mm Hg, and X = 0.338 cm-atm [13]. The agreement between the experimental and LBL results is seen to be excellent. The QRB results, however, exhibit a slightly lower absorption. By employing the LBL and QRB models and the continuous correlations, total band absorptance results were obtained for T = 300 K. For this band also, only six sample cases were considered because of the large time requirement of the LBL computations. No other theoretical results for this band seem to be available in the literature. The results of present computations are presented in Table 3 along with the experimental values of Burch, et al. [22]. The table indicates excellent agreement between the experimental and present LBL results. The QRB results also are seen to compare very well. Among the results of correlations, Tien and Lowder's results are seen to be lower for low pressures but they compare better at high pressures. Cess and Tiwari and Felske and Tien's results are again found to be consistently low.

For the 5.35μ NO band, the line parameters were obtained from the compilation of Goldman and Schmidt [25]. The spectral range considered for this band is 1750–2000 cm^{-1} where there are approximately 1450 rotational lines. The integrated intensity for this band was found to be 112 cm^{-2} atm^{-1}. Goldman used a value of S = 122 cm^{-2} atm^{-1} in the generation of line parameters. This difference can be attributed to the presence of additional lines in the wings of the band beyond the above spectral range. The band correlation parameters were obtained from Green and Tien [17]. The u and β values for this band are listed also in [16]. By employing the LBL and QRB models and the correlations, total band absorptance results were calculated for T = 300 K. These are presented in Table 4 along with theoretical results of HHG [16] and theoretical and experimental

Table 3 Comparison of absorptance results for the 4.3μ fundamental band of carbon dioxide of T = 300 K (experimental data of Burch, et al. [22]); LBL = line-by-line; QRB = quasi-random band

						Absorptance Results, A (cm^{-1})					
							Theoretical		Correlation		
Cell Length y (cm)	Eff. Pr. P_e (mm Hg)	Eff. Pr. P_e (atm)	Pr. Path Length $P_a y$ (atm-cm)	Pr. Path Length [22] $P_a y$ (atm-cm)	Opt. Path u	Exp. [22]	Present LBL	Present QRB	Tien and Lowder [6]	Cess and Tiwari [2, 8]	Felske and Tien [10]
1.55	203	0.2671	0.0108	0.011	1.0663	11.7	12.03	11.75	11.19	6.79	7.43
1.55	812	1.0684	0.0234	0.0235	2.3103	29.1	30.03	27.92	26.40	15.00	17.78
1.55	137	0.1803	0.195	0.1948	19.253	48.3	47.80	45.00	40.14	28.83	27.92
12.8	810	1.0658	0.043	0.044	4.2455	41.2	41.90	38.71	36.84	20.94	24.62
12.8	24	0.0318	0.169	0.17	16.686	23.3	22.94	22.50	14.62	12.95	12.80
12.8	218	0.2868	2.55	2.5493	251.767	107.0	106.96	105.27	96.01	66.95	77.54

Table 4 Comparison of absorptance results for the 5.35μ fundamental band of nitric oxide at T = 300 K (experimental data of Green and Tien [17]); HHG = Hashemi, A., Hseih, T. C., and Greif, R. [16], LBL = line-by-line; QRB = quasi-random band

			Absorptance Results, A (cm^{-1})							
				Theoretical				Correlation		
Eff. Pr. P_e (atm)	Pr. Path Length $P_a y$ (atm-cm)	Opt. Path* u	Exp. [17]	Green and Tien [24]	HHG [16]	Present	Present	Tien and Lowder [6]	Cess and Tiwari [2, 8]	Felske and Tien [10]
1.0	0.845	2.69	35.76	36.2	31.0	37.93	45.09	28.91	18.43	19.60
1.0	2.45	7.81	67.37	64.6	53.0	64.33	75.83	48.43	30.78	33.06
2.025	1.71	5.45	64.99	65.6	62.0	69.51	78.24	54.38	32.23	35.87
2.025	4.96	15.80	113.92	111.6	97.0	108.90	119.13	81.66	50.56	57.22
3.05	2.575	8.20	91.44	92.0	88.1	97.09	104.93	72.45	42.99	49.18
3.05	7.47	23.80	142.7	139.9	127.5	136.87	144.21	102.45	64.77	75.03
2.98	9.195	29.29	142.7	148.7	134.0	143.84	151.08	107.96	69.13	80.17
4.075	3.44	10.96	108.15	111.7	109.5	113.64	119.83	85.95	51.75	60.21
4.075	9.97	31.76	157.54	159.6	146.7	153.59	159.47	117.16	75.75	88.42
4.075	12.56	40.01	157.40	169.9	153.2	160.53	166.55	124.01	81.50	95.24

* u-values were obtained from [16]

results of Green and Tien [17]. It is seen that the present LBL results are in excellent agreement with the experimental values. Also, except for a few cases, the present QRB results are within ten percent of the experimental results. Among the correlation results, Tien and Lowder's results, although lower, compare best with the experimental values. Cess and Tiwari and Felske and Tien's correlations yield much lower values.

In this section, results were presented only for $T = 300$ K. Similar results were obtained for $T = 500$ K by converting the line intensities and half-widths to correspond to this temperature [21]. It should be noted that the same procedure can be used to obtain results for combustion temperatures without involving any additional computation effort. Results presented in this section consistently show that the LBL results are in excellent agreement with the experimental values. In most cases QRB results are better than results of any other theoretical formulation. The results of various correlations agree with varying degree of accuracy depending upon the nature of the gas. Spectral and correlation parameters for the various bands investigated here are presented in Table 5.

In order to give an idea of comparative computational time and cost involved in calculating the total band absorptance, let us consider, for example, the case of 15μ CO_2 band results presented in Table 3. All these results were obtained from programs run on the CDC-Cyber 175 machine. The time and cost for computing these results by using the LBL and QRB models are as follows:

Model	Time (s)	C. R. Units	Cost
LBL	550	2244	58.00 dollars
QRB	40	180	7.00 dollars

This indicates that the time, computer resource (CR) units and cost in dollars associated with QRB calculations are approximately an order of magnitude lower than for the LBL computations. This will be true for any band which has a large number of (several thousand) lines. For bands which have smaller number of lines, this difference is less dramatic. A single program was used to compute the absorptance for all four bands (4.7μ CO, 15μ CO_2, 4.3μ CO_2, and 5.35μ NO) using all three correlations (Tien and Lowder, Cess and Tiwari, and Felske and Tien). The computer resource units used by this program are, in general, a factor of five lower than those used by the QRB program. It will be safe to assume, therefore, that the use of the various correlations results in at least another order of magnitude reduction in computer usage.

5 General Parametric Comparisons

General band absorptance results were obtained by employing the LBL and QRB models and the continuous correlations of Tien and Lowder, Cess and Tiwari, and Felske and Tien. The sources of various correlation quantities and line parameters used in the computation are already mentioned in the previous section. For different gases (4.7μ CO, 15μ CO_2, 4.3μ CO_2, and 5.35μ NO), results were obtained for $P = 0.01$, 0.1, 1.0, and 10 atm and for $T = 300$ K and 500 K. The results for $T = 300$ K are compared in Figs. 4–6 for a few illustrative cases. Extensive results for other conditions are available in [26]. In this section, line-by-line results are treated as exact results.

For CO fundamental band results presented in Figs. 4 and 5 show that the QRB values are in excellent agreement with the exact (LBL) results except for very low pressures and small optical paths. It is evident that all three correlations exhibit poor agreement with the exact results at the very low pressure of 0.01 atm. At 0.1 atm, however, Cess and Tiwari and Felske and Tien correlations yield better agreement than does the Tien and Lowder correlation. At 1.0 atm, all three correlations yield reasonable agreement, although Tien and Lowder correlation yields higher values than the LBL results while the others yield lower values. At 10 atm, Tien and Lowder correlation yields much better agreement than do the others.

Results presented in Fig. 6 show that for 15μ CO_2 band also the QRB results are in excellent agreement with the LBL results except for very low pressures and small optical paths. Of the three correlations, the Tien and Lowder correlation shows fair agreement with the exact results for the entire range of physical conditions. The Cess and

Table 5 Spectral and co-relation parameters of the bands at 300 K.

	$S(\text{cm}^{-2}\,\text{atm}^{-1})$	$A_0(\text{cm}^{-1})$	$B^2 = t/P_e$†
$CO(4.7\mu)$	237.7	38.11	0.0838
$CO_2(4.3\mu)$	1966.6	19.92	0.2425
$CO_2(15\mu)$	339.7	22.34	0.0841
$NO(5.35\mu)$	122.0	29.93	0.0505

† P_e = Effective or equivalent pressure

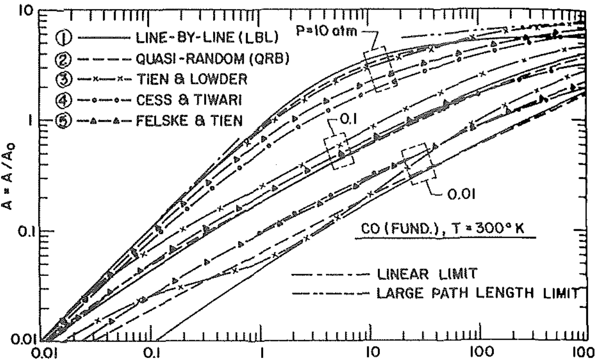

Fig. 4 Comparison of band absorptance for the CO fundamental band at $T = 300$ K

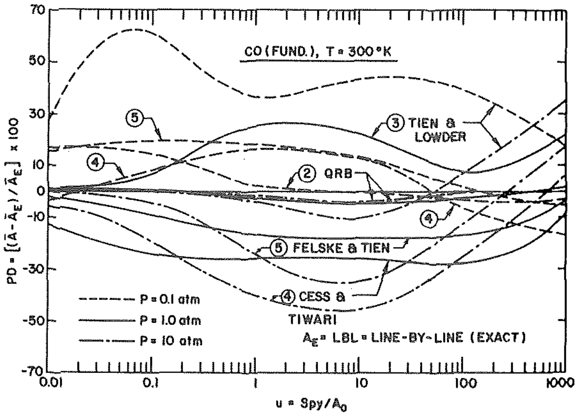

Fig. 5 Errors in the total band absorptance by using the various correlations and QRB formulation for the CO fundamental band at $T = 300$ K

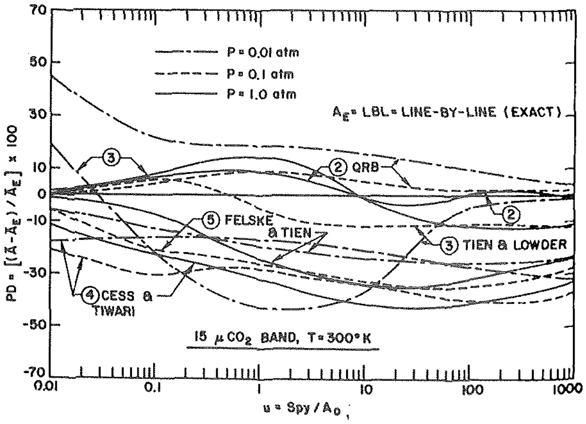

Fig. 6 Errors in the total band absorptance by using the various correlations and QRB formulation for the 15μ CO_2 band at $T = 300$ K

Tiwari and Felske and Tien correlations, on the other hand, yield consistently lower values than the LBL results.

For the 4.3μ CO_2 band also, the QRB results (see Table 6) show an excellent agreement with the LBL results. Among the correlations, Cess and Tiwari and Felske and Tien correlations exhibit much better agreement with LBL results at lower pressures, while Tien and Lowder correlation yields much higher values. At moderate and high pressures, however, Tien and Lowder correlation shows much better agreement while the other yield results which are consistently lower.

For the NO fundamental band, the QRB results (see Table 7) show poor agreement with the LBL results for 0.01 atm and only fair agreement at 0.1 atm. For 1.0 atm the agreement is good and it is excellent at 10 atm. Tien and Lowder correlation yields poor agreement at lower pressures and fair agreement at medium and high pressures. Cess and Tiwari and Felske and Tien correlations, on the other hand, yield consistently lower values for the entire range of physical conditions.

Results presented in this section indicate that, except for very low pressures, the QRB results are in general agreement with the LBL

Table 6 **Comparison of integrated absorptances for CO_2 4.3μ band (T = 300 K); $\overline{A}_E$ = LBL = line-by-line results (exact), $PD = [(\overline{A} - \overline{A}_E)/\overline{A}_E] \times 100$, QRB = quasi-random results**

	Opt.	Integrated Absorptance, $\overline{A} = A/A_0$ (Nondimensional)								
P	Path	LBL	QRB		Tien and Lowder		Cess and Tiwari		Felske and Tien	
(atm)	*u*	$\overline{A}_E$	$\overline{A}$	*PD*	$\overline{A}$	*PD*	$\overline{A}$	*PD*	$\overline{A}$	*PD*
0.01	0.01	0.00620	0.00914	47.0	0.0092	48.0	0.0066	6.5	0.0055	−11.3
	0.1	0.02981	0.03704	24.0	0.0544	82.0	0.0377	26.0	0.0401	34.5
	1.0	0.12012	0.13533	12.7	0.1425	18.6	0.1567	30.0	0.1542	28.4
	10	0.42952	0.45536	6.0	0.5157	20.0	0.5093	18.6	0.4977	15.9
	100	1.36398	1.37231	0.6	1.9162	40.0	1.3407	−1.7	1.4050	3.0
	1000	3.48728	3.35253	−3.9	4.0602	16.4	2.8021	−19.6	3.1926	−8.5
0.1	0.01	0.00950	0.00959	1.0	0.0099	4.2	0.0083	−12.6	0.0095	0.0
	0.1	0.06973	0.06966	−0.1	0.0876	25.6	0.0593	−15.0	0.0697	0.0
	1.0	0.31680	0.31561	−0.4	0.4751	50.0	0.2995	−5.5	0.3220	1.6
	10	1.16636	1.13011	−3.1	1.5749	35.0	1.0083	−13.6	1.0792	−7.5
	100	3.24933	3.06648	−5.6	3.5707	9.9	2.3740	−27.0	2.6963	−17.0
	1000	5.52244	5.47292	−0.9	5.8360	5.7	4.2643	−22.8	4.9229	−10.9
1.0	0.01	0.00994	0.00999	0.5	0.0100	0.6	0.0091	−8.4	0.0099	−0.4
	0.1	0.09499	0.09464	−0.4	0.0969	2.0	0.0754	−21.0	0.0905	−4.7
	1.0	0.67912	0.64769	−4.6	0.7613	12.1	0.4561	−32.8	0.5570	−18.0
	10	2.55122	2.35619	−7.6	2.7390	7.4	1.6189	−36.5	1.9140	−25.0
	100	4.89961	4.79504	−2.1	5.0633	3.3	3.4993	−28.6	4.0822	−16.7
	1000	6.92736	6.85839	−1.0	7.3705	6.4	5.6751	−18.0	6.3861	−7.8
10	0.01	0.00989	0.00996	0.7	0.0100	1.1	0.0094	−5.0	0.0099	0.1
	0.1	0.09752	0.09808	0.6	0.0982	0.7	0.0824	−15.5	0.0963	−1.3
	1.0	0.85205	0.84544	−0.8	0.8244	−3.2	0.5454	−36.0	0.7334	−14.0
	10	3.44692	3.39145	−1.6	3.1404	−8.9	2.0124	−42.0	2.5426	−25.6
	100	5.58567	5.60593	0.4	5.6428	1.0	4.2069	−24.7	4.8188	−13.7
	1000	8.21852	8.26854	0.4	7.9753	−3.0	6.5340	−20.5	7.1321	−13.2

Table 7 **Comparison of integrated absorptances for NO fundamental band (T = 300 K); $\overline{A}_E$ = LBL = line-by-line results (exact), $PD = [(\overline{A} - \overline{A}_E)/\overline{A}_E] \times 100$, QRB = quasi-random band results**

	Opt.	Integrated Absorptance, $\overline{A} = A/A_0$ (Nondimensional)								
P	Path	LBL	QRB		Tien and Lowder		Cess and Tiwari		Felske and Tien	
(atm)	*u*	$\overline{A}_E$	$\overline{A}$	*PD*	$\overline{A}$	*PD*	$\overline{A}$	*PD*	$\overline{A}$	*PD*
0.01	0.01	0.00607	0.01306	115.0	0.0068	12.0	0.0045	−26.0	0.0032	−47.0
	0.1	0.02375	0.03955	67.0	0.0180	−24.0	0.0208	−12.4	0.0204	−14.1
	1.0	0.08086	0.13251	64.0	0.0303	−63.0	0.0756	−6.5	0.0706	−12.7
	10	0.28949	0.43065	49.0	0.1181	−59.0	0.2420	−16.4	0.2248	−22.0
	100	0.92456	1.25337	35.0	0.7263	−21.5	0.6930	−25.0	0.6746	−27.0
	1000	2.55159	3.16153	24.0	2.4413	−4.3	1.6805	−34.0	1.7994	−29.0
0.1	0.01	0.00894	0.00977	9.3	0.0093	4.0	0.0068	−24.0	0.0067	−25.0
	0.1	0.06350	0.07755	22.0	0.0578	−9.0	0.0394	−38.0	0.0422	−34.0
	1.0	0.25462	0.34331	35.0	0.1600	−37.0	0.1657	−35.0	0.1639	−36.0
	10	0.86630	1.12599	30.0	0.5737	−34.0	0.5396	−38.0	0.5304	−39.0
	100	2.51921	3.06630	22.0	9.0365	−19.0	1.4088	−44.0	1.4866	−41.0
	1000	5.27990	5.75481	9.0	4.1978	−20.0	2.9078	−45.0	3.3235	−37.0
1.0	0.01	0.00991	0.01001	1.0	0.0099	−0.1	0.0083	−16.0	0.0095	−4.1
	0.1	0.09378	0.09655	3.0	0.0890	−5.1	0.0608	−35.0	0.0719	−23.0
	1.0	0.63506	0.72239	14.0	0.5047	−21.0	0.3121	−51.0	0.3383	−47.0
	10	2.23890	2.63281	18.0	1.6738	−25.0	1.0546	−53.0	1.1378	−49.0
	100	5.04365	5.40347	7.1	3.6985	−27.0	2.4628	−51.0	2.8097	−44.0
	1000	6.79166	7.14657	5.2	5.9678	−12.0	4.3799	−36.0	5.0510	−26.0
10	0.01	0.00991	0.00997	0.6	0.0100	0.9	0.0091	−8.1	0.0099	−0.1
	0.1	0.09792	0.09851	0.6	0.0972	−0.7	0.0763	−22.0	0.0914	−6.6
	1.0	0.87160	0.87741	0.7	0.7725	−11.0	0.4660	−47.0	0.5750	−34.0
	10	3.98050	4.04590	1.6	2.8026	−30.0	1.6608	−58.0	1.9767	−50.0
	100	6.22197	6.41691	3.1	5.1503	−17.0	3.5744	−43.0	4.1673	−33.0
	1000	7.41852	7.64331	3.0	7.4606	0.6	5.7666	−22.0	6.4721	−13.0

results for all bands under investigation. It is also noted that no one correlation can be expected to yield accurate results for all gases under all conditions.

6 Conclusions

It has been demonstrated that the line-by-line model is probably the best theoretical approach to calculate the spectral transmittance and total absorptance of a vibration-rotation band. Although it requires a considerably long computational time, the results obtained by this model are in excellent agreement with the available experimental results. The quasi-random band model requires relatively less computational time and yields accurate results in most cases. As such, use of these theoretical models is suggested for radiative transfer analyses requiring a high degree of accuracy.

Relative validity of various correlations (Tien and Lowder, Felske and Tien, and Cess and Tiwari), under different pressure and path length conditions, has been established. These correlations require significantly less computational time and yield results with varying degree of accuracy depending upon the nature of the gas. The computer time required by the Felske and Tien correlation is relatively longer than by the Tien and Lowder and Cess and Tiwari correlations. Results of specific and general parametric comparisons indicate that the use of the Tien and Lowder correlation is justified to all gases under investigation at relatively high pressures. Use of the Felske and Tien, and Cess and Tiwari correlations is recommended for lower and moderate pressures.

Acknowledgment

This work was supported by the NASA-Langley Research Center through the Grant No. NSG-1282.

References

1 Goody, R. M., *Atmospheric Radiation I: Theoretical Basis,* Oxford Univ. Press, London and New York, 1964.

2 Tiwari, S. N., "Models for Infrared Atmospheric Radiation," TR-76-T10, June 1976, School of Engineering, Old Dominion University, Norfolk, Va. Also, in *Advances in Geophysics,* Vol. 20, Academic Press, 1978.

3 Wyatt, P. J., Stull, V. R., and Plass, G. N., "Quasi-Random Model of Band Absorption," *Journal of the Optical Society of America,* Vol. 52, No. 11, Nov. 1962, pp. 1209–1217.

4 Edwards, D. K. and Menard, W. A., "Comparison of Methods for Correlation of Total Band Absorption," *Applied Optics,* Vol. 3, No. 5, May 1964, pp. 621–625.

5 Edwards, D. K., Glassen, L. K. Hauser, W. C., and Tuchscher, J. S., "Radiation Heat Transfer in Nonisothermal Nongray Gases," ASME JOURNAL OF HEAT TRANSFER, Vol. 89, No. 3, Aug. 1967, pp. 219–229.

6 Tien, C. L. and Lowder, J. E., "A Correlation for Total Band Absorptance of Radiating Gases," *International Journal of Heat and Mass Transfer,* Vol. 9, No. 7, July 1966, pp. 698–701.

7 Tien, C. L., "Thermal Radiation Properties of Gases," *Advances in Heat Transfer,* Vol. V, Academic Press, New York, 1968.

8 Cess, R. D. and Tiwari, S. N., "Infrared Radiative Energy Transfer in Gases," *Advances in Heat Transfer,* Vol. VIII, Academic Press, New York, 1972.

9 Edwards, D. K., "Molecular Gas Band Radiation," *Advances in Heat Transfer,* Vol. XII, Academic Press, New York, 1976.

10 Felske, J. D. and Tien, C. L., "A Theoretical Closed Form Expression for the Total Band Absorptance of Infrared-Radiating Gases," *International Journal of Heat and Mass Transfer,* Vol. 17, No. 1, Jan. 1974, pp. 155-158.

11 Tiwari, S. N., "Application of Infrared Band Model Correlations to Nongray Radiation." Accepted for publication in the *International Journal of Heat and Mass Transfer*.

12 Gupta, S. K. and Tiwari, S. N., "Evaluation of Upwelling Infrared Radiance from Earth's Atmosphere," TR-75-T14, Nov. 1975. School of Engineering, Old Dominion University, Norfolk, Va.

13 Gupta, S. K. and Tiwari, S. N., "Evaluation of Transmittance of Selected Infrared Bands," TR-76-T7, April 1976, School of Engineering, Old Dominion University, Norfolk, Va.

14 Tiwari, S. N., and Gupta, S. K., "Evaluation of Upwelling Infrared Radiance from the Earth's Troposphere," ASME-AIChE Heat Transfer Conference, Aug. 1976, ASME 76-HT-5.

15 Hsieh, T. C. and Greif, R., "Theoretical Determination of the Absorption Coefficient and the Total Band Absorptance Including a Specific Application to Carbon Monoxide," *International Journal of Heat and Mass Transfer,* Vol. 15, No. 8, Aug. 1972, pp. 1477–1487.

16 Hashemi, A., Hsieh, T. C., and Greif, R., Theoretical Determination of Band Absorptance with Specific Application to Carbon Monoxide and Nitric Oxide," Paper No. 76-HT-1. To appear in ASME JOURNAL OF HEAT TRANSFER.

17 Green, R. M., and Tien, C. L., "Infrared Radiation Properties of Nitric Oxide at Elevated Temperatures," *Journal of Quantitative Spectroscopy and Radiative Transfer,* Vol. 10, 1970, pp. 805–817.

18 Drayson, S. R., "Atmospheric Transmission in the CO_2 Bands Between 12μ and 18μ," *Applied Optics,* Vol. 5, No. 3, 1966, pp. 385–392.

19 Kunde, V. G., "Theoretical Computations of the Outgoing Infrared Radiance from a Planetary Atmosphere," TR D-4045, Aug. 1967, NASA.

20 Kunde, V. G. and Maguire, W. C., "Direct Integration Transmittance Model," *Journal of Quantitative Spectroscopy and Radiative Transfer,* Vol. 14, No. 8, Aug. 1974, pp. 803–817.

21 McClatchey, R. A., Benedict, W. S., Clough, S. A., Burch, D. E., Calfee, R. F., Fox, K., Rothman, L. S., and Garing, J. S., "AFCRL Atmospheric Line Parameters Combilation," AFCRL-TR-73-0096, Jan. 1973, Air Force Cambridge Research Laboratories, Bedford, Mass.

22 Burch, E. E., Gryvnak, D. A., Singleton, E. B., France, W. L., and Williams, D., "Infrared Absorption by Carbon Dioxide, Water Vapor, and Minor Atmospheric Constituents," AFCRL-62-698, July 1962, Air Force Cambridge Research Laboratories, Bedford, Mass.

23 Abu-Romia, M. M., and Tien, C. L., "Measurements and Correlations of Infrared Radiation of Carbon Monoxide at Elevated Temperatures," *Journal of Quantitative Spectroscopy and Radiative Transfer,* Vol. 6, 1966, pp. 143–167.

24 Young, C., "A Study of the Influence of Carbon Dioxide on Radiative Transfer in the Stratosphere and Mesosphere," Technical Report, March 1964, Dept. of Meteorology and Oceanography, College of Engineering, University of Michigan, Ann Arbor, Mich.

25 Goldman, A., and Schmidt, S. C., "Infrared Spectral Line Parameters and Absorptance Calculations of NO at Atmospheric and Elevated Temperatures for the $\Delta v = 1$ Bands Regions," *Journal of Quantitative Spectroscopy and Radiative Transfer,* Vol. 15, 1975, pp. 1277–138.

26 Tiwari, S. N., and Gupta, S. K., "Accurate Spectra Modeling for Infrared Radiation," TR-77-T, April 1977, School of Engineering, Old Dominion University, Norfolk, Va.

W. L. Grosshandler
Assistant Professor,
Washington State University,
Pullman, Wash.
Mem. ASME

R. F. Sawyer
Professor,
Department of Mechanical Engineering,
University of California,
Berkeley, Calif.
Mem. ASME

Radiation From a Methanol Furnace

Monochromatic intensity measurements are taken in a water-cooled furnace, 20 cm in diameter, burning methanol and a methanol/coal slurry. The primary interest is to determine the contribution of particulate radiation to the total intensity. Temperature, carbon dioxide, carbon monoxide, water, methanol, and particulate concentration levels are quantitatively measured throughout the furnace chamber. A computer code is discussed which integrates the equation of transfer over a nonhomogeneous path containing combustion gases and particulates. This allows comparison of the measured intensity with a theoretical prediction based upon known concentration and temperature profiles. The intensity and emittance measurements from the methanol furnace are compared with measurements in other experimental furnaces burning oil and gas.

Introduction

Methanol is an attractive alternate fuel for gas turbines, furnaces, and internal combustion engines because of its physical and chemical properties. Being a stable liquid at ordinary pressure and temperature, it can be stored and transported much more cheaply and safely than either methane or hydrogen. In pilot-plant and full-scale boiler demonstrations, pollutants such as carbon monoxide and nitric oxide are lower when burning methanol than when burning methane. Additionally, existing carbon deposits within the furnace are removed by burning methanol [1].[1]

Currently, the cost of producing methanol is its major drawback. In terms of dollars per million kilojoules, methanol is about 50 percent more expensive to produce than methane and 12 percent more than hydrogen when coal is the raw material. Relative to well-head natural gas, methanol costs triple the price [1]. There is some discussion of producing methanol as a byproduct from the steel and electric utility industries. Coal would be the primary fuel for steel, but the electric utility could combine nuclear fuel and coal in an advanced cycle [2]. The economic attractiveness of methanol is certain to improve relative to conventional fuels if the above methods are proved feasible and as the cost of natural gas and petroleum continues to rise.

With methanol usage likely to increase, it becomes important to predict its behavior in combustion systems. Based upon studies by Street and Thomas [3], there is reason to believe that methanol will produce much less soot than most other organic fuels in turbulent diffusion flames typically found in furnaces and gas turbines. Emission from soot and particulates is the dominant source of radiation in coal and oil flames. Even in natural gas flames, soot emission can contribute to the total radiation. If there is no soot in a methanol flame, the total radiation could be less than for these other fuels. This provides the incentive for measuring the monochromatic intensity of a methanol flame in a model furnace. With this type of measurement, the particulate radiation can be distinguished from gaseous radiation. Also, the effect on flame emittance of mixing small amounts of pulverized coal with the methanol can be assessed.

Experimental Apparatus

A complete description of the experimental facility is given in [4]. Briefly, the combustion chamber of the furnace is 19.6 cm in diameter by one meter long with a water-cooled stainless steel wall. Access ports are provided along the axis of the chamber to allow optical measurements and probing of the flame. Fig. 1 shows a cutaway view of the furnace burner. Methanol, flowing at 3 g/s, enters through a pressure jet nozzle at the center of the burner. The nozzle is surrounded by a swirling primary air stream. The bulk of the air is brought in past the secondary swirl vanes with a swirl number of 0.6. 20 micron dia coal is introduced directly into the methanol fuel tank as 5.3 percent of the total fuel mass. The tank is continuously rotated to prevent separation of the coal/methanol slurry. A larger internal diameter fuel

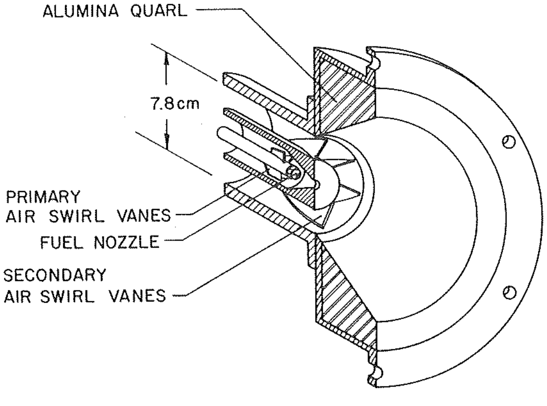

Fig. 1 *Cross section of burner assembly*

---

[1] Numbers in brackets designate References at end of paper.

Contributed by the Heat Transfer Division of THE AMERICAN SOCIETY OF MECHANICAL ENGINEERS and presented at the AIChE-ASME Heat Transfer Conference, Salt Lake City, Utah, August 15–17, 1977. Manuscript received by the Heat Transfer Division September 30, 1977. Paper No. 77-HT-14.

nozzle, used only when burning the slurry, prevents particle buildup. However, since the fuel mass flow rate is held constant, the character of the fuel spray changes, producing larger droplets with a smaller divergence angle. For all of the experimental runs, the overall fuel/air equivalence ratio is held constant at 0.9 and the thermal power is 60 kW.

The infrared radiation is measured with a Perkin-Elmer model 98 monochromator. In addition to the radiant intensity, the experimental apparatus is also instrumented to measure flame temperature, concentrations of carbon dioxide, carbon monoxide, water vapor, and methanol, and particulate levels.

Experimental Results

Flame Structure. The temperature data were taken through each of the twelve access ports located every 7.1 cm along the furnace axis. About 20 data points were taken at each port, the distance between points being dictated by the temperature gradients encountered. This information, uncorrected for thermocouple radiation losses, is shown on the temperature map in Fig. 2. The radial distance is expanded by a factor of two to improve readability. The fuel nozzle is located at the left of the figure on the centerline. The most striking feature is the asymmetry about the centerline. This could easily be attributed to buoyant forces if the temperature map were of a vertical slice through the furnace centerline; but since it is a horizontal slice, the effect of buoyancy is more subtle.

The importance of buoyancy in the tangential direction can be estimated by comparing the tangential Reynolds number, Re_θ, to the square root of the Grashof number, Gr:

$$\frac{\mathrm{Gr}^{1/2}}{\mathrm{Re}_\theta} = \frac{[(T_g - T_w)gD]^{1/2}}{(V_\theta T_g{}^{1/2})}$$

where D is the furnace diameter, g is the gravitational acceleration, T_g and T_w are the temperature of the hot gas and cold wall, respectively, and V_θ is the tangential velocity. For the present operating conditions, $\mathrm{Gr}^{1/2}/\mathrm{Re}_\theta$ is of the order of unity in the first half of the furnace. The fluid set in motion by the buoyant force is, thus, of the same order as that induced by the swirl generator. The velocities are parallel on the lower portion of Fig. 2 and counter on the upper portion. The incoming swirl number is such that the tangential momentum is 60 percent of the incoming axial momentum. Therefore the buoyant effect on the tangential velocity is enough to modify the expected symmetrical flame structure.

The maximum temperature obtained is 1725 K. If the thermocouple is corrected for radiation loss, the measured temperature is still over 250 K below the adiabatic equilibrium temperature, 2150 K. This is due to heat loss to the walls and the mixing structure of the flow.

An adiabatic equilibrium calculation indicates that at an equivalence ratio of 0.9, the mole fraction of major species is as follows:

Species:	N_2	H_2O	CO_2	O_2	CO	CH_3OH
Mole Fraction:	0.658	0.204	0.102	0.022	0.001	$<10^{-5}$

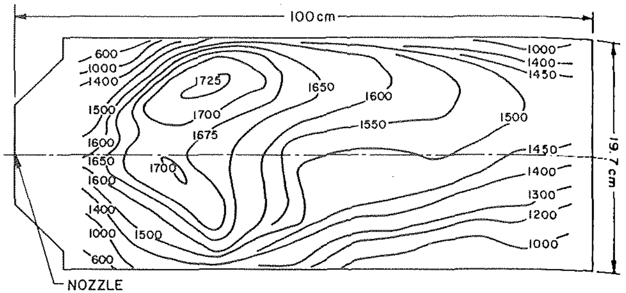

TEMPERATURE, K (UNCORRECTED)

Fig. 2 Horizontal temperature distribution in methanol-fired furnace (uncorrected for thermocouple heat transfer)

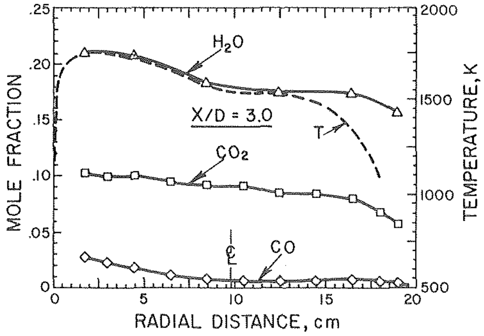

Fig. 3 Radial temperature and concentration profiles in a methanol-fired furnace

Actual measurements in the furnace show that the maximum water concentration occurs in the primary reaction zone near the burner and drops off to about 0.18 mole fraction near the furnace exit. The carbon dioxide concentration is below the equilibrium value and varies little in the axial direction along the last two-thirds of the furnace. The carbon monoxide concentration is well above the equilibrium value and reaches a peak of 0.08 mole fraction deep within the fuel jet near the furnace entrance. The carbon monoxide is consumed as the gas moves through the furnace, but even at the exit, the concentration remains above the equilibrium value.

The only other species which is both infrared-active and of sufficient concentration to contribute to the radiation heat transfer is methanol. At an axial position to diameter ratio (X/D) of 0.65, the maximum methanol mole fraction is 0.0029. Elsewhere in the furnace, methanol is detected but is generally less than 100 ppm.

Radial concentration and temperature profiles are shown in Fig. 3 for $X/D = 3.0$. The horizontal axis is the distance from the far wall of the furnace with the centerline at 9.8 cm. The vertical axis is mole fraction and temperature (corrected for radiation loss). The concentration profiles level off by $X/D = 3.0$ and do not alter greatly in

Nomenclature

A = furnace surface area
$A(r)$ = particle cross-sectional area
$\tilde{A}$ = total particle cross-sectional area per unit gas volume
D = diameter of furnace
g = gravitational acceleration
Gr = Grashof number
I_λ = monochromatic intensity
$I_{b\lambda}$ = monochromatic blackbody intensity
K_a = absorption coefficient
ℓ = path length
n = real component of index of refraction
$N(r)$ = size frequency distribution function per unit volume
$\dot{q}$ = energy rate
r = particle radius
r^* = radius separating large and small particle limits
Re_θ = tangential Reynolds number
T_g = gas temperature
T_w = wall temperature
$V(r)$ = particle volume
$\tilde{V}$ = total particle volume per unit volume of gas
V_θ = tangential velocity
X/D = axial distance to diameter ratio
ϵ_p = particle hemispherical emissivity
κ = complex component of index of refraction
λ = wavelength
τ_λ = monochromatic transmittance

the last half of the furnace. The temperature continues to drop as heat is transferred by convection and radiation to the water-cooled walls.

Temperature and concentration measurements were also taken with the coal/methanol slurry as the fuel. Because fuel delivery problems necessitated increasing the nozzle orifice, the fuel jet momentum is less. Therefore, the spray cone angle is smaller and the droplets are larger, forming a longer and thinner flame than when burning pure methanol. Enough measurements were not made to completely map the temperature and concentration distributions, but radial temperature profiles (corrected for radiation loss), carbon dioxide concentrations, and particulate levels for $X/D = 3.0$ are shown in Fig. 4. The particulate levels are given in units of grams of solid per cubic meter of gas at the local temperature. Levels near 0.001 g/m^3 are found in the pure methanol flame as compared to about 0.10 g/m^3 in the latter regions of the slurry flame. As a reference, the incoming pulverized coal level averaged across the inlet is 1.5 g/m^3 (corrected to 1500 K). Inspection of particle samples under a microscope shows that two categories exist. The large particles, one to ten micrometers in diameter, are coal, while the vast number of submicron particles are presumably flyash or soot. There are few particles of intermediate size.

Radiation Measurements. The gaseous species which are important to the radiation heat transfer are listed in Table 1. Both the 15 μm CO_2 band and the 9.67 μm CH_3OH band are strong absorbers. However, at typical flame temperatures, the Planck energy distribution biases the intensity toward shorter wavelengths. Therefore, most of the energy lies in the wavelength region between one and eight micrometers. Spectra taken at $X/D = 3.0$ are shown in Fig. 5. The abscissa is the infrared wavelength in micrometers while the ordinate is spectral intensity leaving the flame in a horizontal direction perpendicular to the furnace axis in units of Watts per square centimeter per micrometer per sterradian. The largest contribution to intensity is from the 4.26 μm carbon dioxide peak followed by the combined water and carbon dioxide peak centered near 2.7 μm. Smaller water peaks occur at 1.38 and 1.88 μm. The 6.27 μm water band extends from below 5 μm to greater than 8 μm. Since it is the area under the peak and not the absolute maximum which is important, this band also makes an appreciable contribution to the total heat transferred from the flame. Carbon monoxide contributes to the intensity at 4.67 μm, but the peak cannot be resolved from the neighboring carbon dioxide band. The C-H vibration of methanol between 3.3 and 3.6 μm is visible only in spectra taken close to the fuel nozzle.

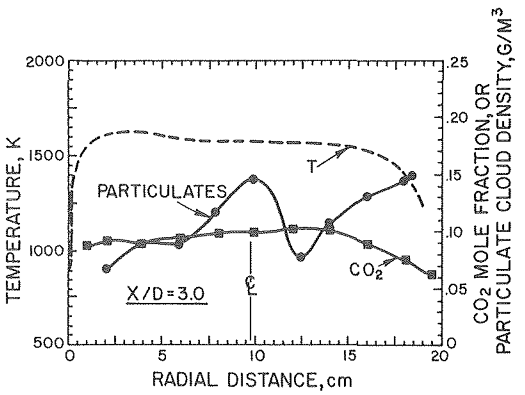

Fig. 4 Radial temperature, CO_2 concentration, and particulate level profiles in a slurry-fired furnace

Table 1 Infrared bands of gaseous species important in methanol combustion

CO	CO_2	H_2O	CH_3OH
4.67 μm	15.0 μm	6.27 μm	9.67 μm
2.35 μm	4.26 μm	2.70 μm	3.52 μm
	2.70 μm	1.88 μm	3.36 μm
		1.38 μm	2.72 μm

The combined effect on intensity of adding 5.3 percent coal to the methanol and changing fuel nozzles can be seen by comparing the solid line in Fig. 5 to spectra of the pure methanol flame (the dotted line). The continuous radiation due to particles in the flame is noticeable between the 1.38, 1.88, and 2.7 μm bands. The contribution to intensity in the 3 to 4 μm range cannot be attributed entirely to particles. At a temperature of 1500 K, the maximum intensity of a gray body occurs at 1.93 μm. At a wavelength of 4 μm, the intensity is reduced by a factor of three. The relatively large value of intensity at this wavelength is due to continuous radiation from the far wall of the furnace. Even though the walls are water-cooled to below 373 K, coal builds up on the surface when burning the slurry and acts as insulation. Hot particles impact on top of this layer and radiate into the line of sight. If it is assumed that the walls are black, the surface temperature can be estimated to be about 700 K.

Radiation measurements were taken at several locations along the furnace axis for both fuel systems. The spectra were numerically integrated to determine the total intensity in a direction normal to the furnace axis in a horizontal plane. The results are shown in Fig. 6. The abscissa is the distance along the furnace axis measured from the fuel nozzle, in centimeters, and the ordinate is the total intensity in units of Watts per square centimeter per sterradian. The methanol flame intensity increases to a maximum value of 1.7 W/cm^2 $-$ sr as the fuel oxidizes and then decreases as heat is transferred to the walls. The two sets of points for methanol at 67 and 86 cm were taken on different days to assess reproducibility. With the slurry as fuel, the effect of the coal and larger nozzle is to reduce the intensity early in the flame and to move the point of maximum intensity further down stream. The anomalously high data point at 34 cm is suspect and may be due to operational difficulties. Near the exit of the furnace, as the importance of the inlet jet momentum declines and the coal particles burn out, the intensities of the two fuel systems approach a common value.

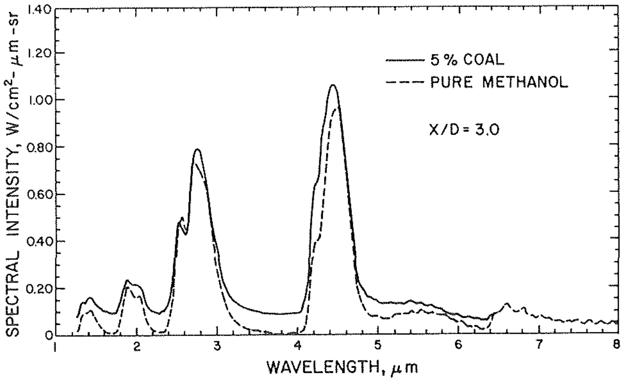

Fig. 5 Measured spectral intensity from methanol and slurry-fired furnace

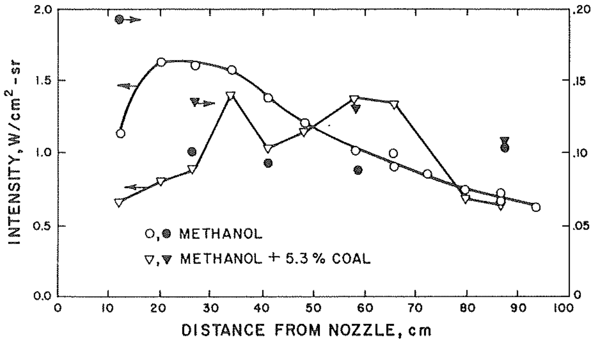

Fig. 6 Intensity and emittance of experimental furnace

The equivalent homogeneous emittance for the methanol furnace can be estimated based upon an average fourth power of temperature and the integrated measured intensity. This estimate has been made for both fuels and is also shown plotted in Fig. 6. Note that although the intensity from the slurry flame is lower than that of the pure methanol flame, the emittance from the slurry flame is generally higher. This is due to the increased particles and lower temperatures in the slurry flame.

Discussion of Results

Comparison with Numerical Calculations. With the major gaseous species, particle concentrations and temperature radial distributions known at any given axial position, it is theoretically possible to integrate the equation of transfer across the line of sight to determine the monochromatic intensity leaving the furnace. This procedure is much simplified if energy scattered into the line of sight is negligible compared to the energy emitted. For gaseous systems and particles of diameter much less than the wavelength of light (λ), scattering can be neglected. For particles much larger than λ, the ratio of the scattering coefficient to the absorption coefficient approaches the value of the reflectivity of the particle divided by its emissivity. For coal and soot particles, this ratio is less than 0.25. For systems in which gaseous radiation dominates the particle radiation (such as in the experimental furnace), it thus becomes reasonable to neglect scatter into the line of sight. The integrated equation of transfer becomes

$$I_\lambda(\ell) = I_\lambda(0)\tau_\lambda(0, \ell) - \int_0^\ell I_{b\lambda}(\ell')\frac{\partial}{\partial \ell'}\tau_\lambda(\ell', \ell)d\ell' \qquad (1)$$

with

$$\tau_\lambda(\ell_1, \ell_2) \equiv \exp\left(-\int_{\ell_1}^{\ell_2} K_a d\ell\right) \qquad (2)$$

I_λ is the monochromatic intensity, τ_λ is the monochromatic transmittance, $I_{b\lambda}$ is the Planck blackbody intensity, ℓ is the path length, and K_a is the monochromatic absorption coefficient.

The value of the absorption coefficient varies along the line of sight as a result of contributions from different combustion gases and particulates at varying temperatures. Different models can be used to calculate the absorption coefficient of each species. For carbon monoxide [5] and the 4.26 μm band of carbon dioxide [6], the individual vibration-rotation line strengths can be determined using a diatomic anharmonic oscillator, nonrigid rotor model. The total absorption coefficient can be found by rigorously summing over both the P and R branches of the spectrum for all significant vibrational transitions. The 2.7 μm band of CO_2 cannot be treated exactly as a simple diatomic oscillator, but Malkmus [7] discusses how this simple approximation can be extended with empirical correlations to allow evaluation of the absorption coefficient of this band. The absorption properties of water cannot be calculated conveniently from first principles, but tabulated experimental results [8] can be used. The contribution of methanol to the absorption coefficient can be neglected since large concentrations exist only in the cooler fuel jet at the furnace entrance.

The Curtis-Godson approximation is used to sum up the absorption effects along the inhomogeneous path. This approximation becomes exact in the limits of large and small optical depths (see, for example, [8], p. 138).

The contribution of particulates to the absorption coefficient can be determined easily in the small and large particle limits [9, pp. 408–410]:

$$K_a = \frac{36\pi}{\lambda}\frac{n\kappa}{(n^2 - \kappa^2 + 2)^2 + 4n^2\kappa^2}\tilde{V}, \quad \frac{2\pi r}{\lambda} \ll 1 \qquad (3)$$

or

$$K_a = \epsilon_p\tilde{A}, \quad \frac{2\pi r}{\lambda} \gg 1 \qquad (4)$$

where n and κ are the real and complex components, respectively, of the index of refraction, r is the particle radius, ϵ_p is the hemispherical emissivity of the particle, and $\tilde{V}$ and $\tilde{A}$ are the particle volume and area per unit volume of cloud. If the particle size distribution spans both limits, an approximate absorption coefficient can be found by evaluating $\tilde{V}$ and $\tilde{A}$ as

$$\tilde{V}(r^*) = \int_0^{r^*} N(r)V(r)dr, \qquad (5)$$

$$\tilde{A}(r^*) = \int_{r^*}^{\infty} N(r)A(r)dr \qquad (6)$$

where $N(r)$ is the size frequency distribution per unit volume and r^* is that value of radius such that if all particles were of this size, the small and large particle limits would predict the same value for K_a. The total particle absorption coefficient is the sum of the contributions from the small and large particles.

The monochromatic transmittance between any two positions along the line of sight can be determined by summing the contributions of the gaseous species and particulates to the absorption coefficient. The equation of transfer can then be numerically integrated along the line of sight to give the theoretical monochromatic intensity.

A program called RADCALC has been written to perform this type of calculation. The general procedure outlined by Ludwig, Malkmus, Reardon and Thompson [8] is followed. While written to determine the intensity from the experimental furnace, the program is completely general and can be used to calculate the monochromatic and total intensity from any nonhomogeneous mixture containing varying amounts of carbon dioxide, carbon monoxide, water vapor, nitrogen, oxygen, and particulates in the temperature range between 300 K and 2500 K and in the wavelength range between 1.25 μm and 8.33 μm. Details are given in [14].

The results of two RADCALC computations are shown as the solid lines in Figs. 7 and 8. The dotted lines are included to allow comparison with the measured results. For the pure methanol (Fig. 7), the spectral variation is well modeled throughout the wavelength range. However, the magnitude of the bands is consistently under-predicted. This discrepancy can be accounted for by estimating the intensity

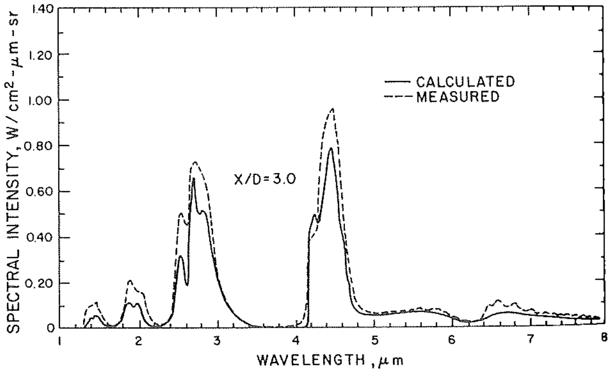

Fig. 7 Calculated spectral intensity in methanol-fired furnace

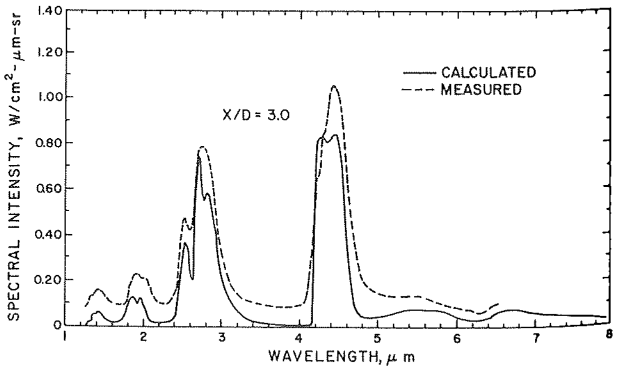

Fig. 8 Calculated spectral intensity in slurry-fired furnace

which is reflected from the far wall of the furnace into the line of sight. In the program, the wall is assumed cold and black, but the reflectivity of weathered stainless steel is about 0.2. Therefore the measured intensity can be expected to be larger than the calculated intensity by a factor of 20 percent or less, depending upon the monochromatic transmittance of the gas volume. When integrated over wavelength, the measured intensity is larger than the calculated intensity by 27 percent.

When burning the slurry, the assumption that the walls are black is valid, but since the walls are now hotter, the energy emitted into the line of sight can become important. This explains the underprediction of intensity in the 3 to 4 μm range of Fig. 8. The discrepancy in the shorter wavelengths is the result of two additional factors: particle sampling resulting in possible loss of mass on the probe walls, and the use of an empirical size frequency distribution. The size frequency distribution used is based upon measurements taken by Milne, Greene, and Beachey [10] on a similar pulverized coal sample. To allow for a reduction in particle diameter as combustion proceeds, the mean particle diameter is assumed to decrease as the one-half power of the measured particle loading. For a given particle load, it can be shown that decreasing the particle diameter of a monodispersed cloud from 1.0 μm to 0.03 μm can increase the intensity from two to three times across the spectrum. Averaged over wavelength, the calculated total intensity is 33 percent below the measured total intensity for the slurry flame.

To determine the sensitivity of monochromatic intensity to species concentration, RADCALC was used to predict the intensity from a gas volume assuming homogeneous, adiabatic, equilibrium levels across the furnace but a nonhomogeneous temperature distribution. The only noticeable difference occurred in the 4.3 μm band because the equilibrium value of CO_2 is generally above the actual furnace level while the CO equilibrium concentration is generally below.

A wide-band homogeneous model can be checked against RADCALC by averaging concentrations and temperature across the furnace. The Tien-Lowder correlation of the Edwards exponential wide-band model [11] was used with the homogeneous concentration levels of 0.09 for CO_2 and 0.185 for H_2O. The temperature used, 1549 K, was the average of the fourth power of temperature measured across the furnace. The integrated band intensities predicted by the model are in resonable agreement with the experiment. For this case, the homogeneous calculation is 0.78 $W/cm^2 - sr$ as compared to 0.74 $W/cm^2 - sr$ from RADCALC and 1.02 $W/cm^2 - sr$ from the experiment.

Comparison with Other Experimenters. With the intensity from the methanol furnace known, it is interesting to compare the results with those of other experimenters. The radiative properties of methanol can then be qualitatively ranked with other fuels. Comparison can be made by nondimensionalizing the intensity with the incoming energy rate of the fuel ($\dot{q}$) and the internal surface area of the furnace (A). The parameter $\pi I/(\dot{q}/A)$ can be viewed as the fraction of incoming energy which is transferred by radiation to the walls. Values greater than one are possible since the intensity used is the normal value, which can be greater than the average hemispherical value. Also, the entire unobstructed surface area of the walls is not available to each volume of gas. Fig. 9 is a plot of nondimensionalized intensity versus X/D for the present study (solid symbols) along with earlier work done by the International Flame Research Foundation [12, 13] (open symbols). For small X/D, the intensity from both the gas-oil and gas-carbon-black slurry flames is up to three times greater than that of the methanol flames, but the coke oven gas flame is less than or equal to the methanol flames. The intensity of both the most luminous and least luminous of the IFRF flames approaches a constant value of about 0.4 at the furnace exit, but the methanol flame intensities continue to drop. This effect is from the water-cooled walls in the methanol furnace as compared to the adiabatic walls in the IFRF furnace.

Sato, et al. [15] have measured the monochromatic emittance of city gas in a cylindrical furnace, 40 cm in diameter. Their results for an X/D of about 3.0 are shown in Fig. 10 compared to similar measurements from the methanol and slurry flames. Higher levels of carbon monoxide increase the emittance of the methanol furnace at a wavelength between 4.5 and 5.0 μm when compared to the city gas flame. The continuous emission from the pure methanol flame is also greater than that of the gas flame. This may be due to different measurement techniques and furnace wall conditions.

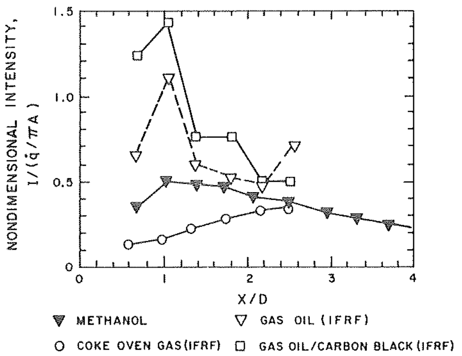

Fig. 9 Flame intensities of various fuel systems

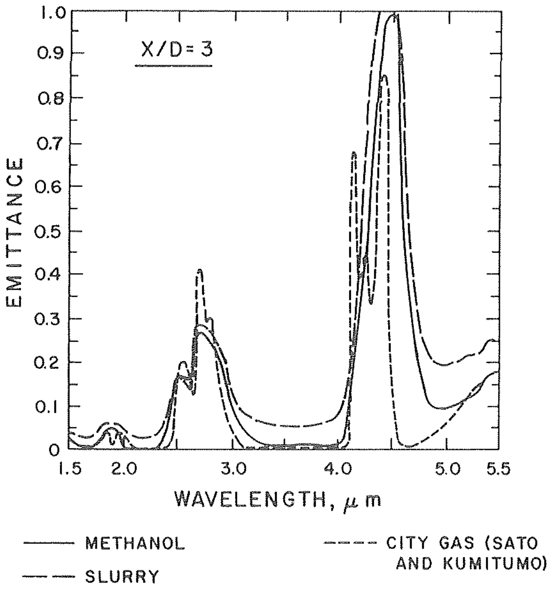

Fig. 10 Spectral emittance of methanol, slurry and city gas flames

Conclusions

In summary, the monochromatic intensity has been measured in a model water-cooled furnace burning methanol and a methanol/coal slurry. The chemical and temperature structure has also been experimentally determined. A numerical program has been written to calculate the monochromatic intensity from a nonhomogeneous mixture of combustion gases. This allows comparison of the measured intensity with the theoretical intensity. The following conclusions can be drawn:

1 The infrared spectra of a methanol diffusion flame contains little significant particulate radiation.

2 The emittance of a furnace burning methanol can be enhanced by the addition of pulverized coal to the fuel, although the total intensity may not be enhanced.

3 The radiative emission character of a furnace burning methanol is not significantly different from a furnace using other clean burning fuels, such as coke-oven gas and city gas.

References

1 Reed, T. B., and Lerner, R. M., "Methanol: A Versatile Fuel for Imme-

diate Use," *Science*, Vol. 182, 1973.

2 Steinberg, M, Salzano, F, Beller, M, and Manowitz, B., "Methanol as a Fuel in the Urban Energy Economy and Possible Source of Supply," Brookhaven National Laboratory 17800, April 1973.

3 Street, J. C., and Thomas, A., "Carbon Formation in Premixed Flames," *Fuel*, Vol. 34, 1955, p. 4.

4 Grosshandler, W. L., "The Furnace Combustion and Radiation Characteristics of Methanol and a Methanol/Coal Slurry," Lawrence Berkeley Laboratory Report LBL-5947, Jan. 1977.

5 Malkmus, W., and Thompson, A., "Infrared Emissivity of Diatomic Gases for the Anharmonic Vibrating-Rotator Model," *Journal of Quant. Spectrosc. and Radiat. Transfer*, Vol. 2, 1961, p. 17.

6 Malkmus, W., "Infrared Emissivity of Carbon Dioxide (4.3-μ Band)," *Journal of Optical Soc. Amer.*, Vol. 53, 1963, p. 951.

7 Malkmus, W., "Infrared Emissivity of Carbon Dioxide (2.7-μ Band)," General Dynamics/Astronautics AE63-0047, 1963.

8 Ludwig, C. B., Malkmus, W., Reardon, J. E., and Thompson, J. A., *Handbook of Infrared Radiation From Combustion Gases*, NASA SP-3080, 1973.

9 Hottel, H. C., and Sarofim, A. F., *Radiative Transfer*, McGraw-Hill Book Co., 1967.

10 Milne, T. A., Greene, F., and Beachey, J., "Pulverized Coal Combustion Studies on Flat Flame Burners," Western States Section/The Combustion Institute, Spring 1974.

11 Tien, C. L., and Lowder, J. E., "A Correlation for Total Band Absorptance of Radiating Gases," *Int. Journal of Heat and Mass Trans.*, Vol. 9, 1965, p. 698.

12 International Flame Research Foundation, "The Radiation from Turbulent Jet Diffusion Flames of Liquid Fuel/Coke-Oven Gas Mixtures," *Journal of Inst. Fuel*, Vol. 29, 1956, p. 23.

13 International Flame Research Foundation (Hubbard, E. H.), "Comparison of Different Methods of Fluid-Atomizing Oil Flames and the Effect on Flame Emissivity and Radiation of the Addition of Carbon Black to Liquid Fuels," *Journal of Inst. Fuel*, Vol. 32, 1959, p. 328.

14 Grosshandler, W. L., "A Study of a Model Furnace Burning Methanol and a Methanol/Coal Slurry," Ph.D. Thesis, University of California, Berkeley, 1976.

15 Sato, T., Kumitomo, T., Yoshii, S., and Hashimoto, T., "On the Monochromatic Distribution of the Radiation from the Luminous Flame," *Bulletin of Japan Soc. Mech. Engr.*, Vol. 12, 1969, p. 1135.

T. M. Shih[1]
P. J. Pagni

Department of Mechanical Engineering,
University of California, Berkeley,
Berkeley, Calif.

Laminar Mixed-Mode, Forced and Free, Diffusion Flames

To explore the intersection of previous studies of inert mixed-mode flows and single-mode diffusion flames, this analysis describes a laminar, forced and free, mixed-mode diffusion flame adjacent to a vertically burning fuel slab. Shvab-Zeldovich variables, boundary-layer and local similarity approximations are used. Five flaming and chemical parameters are found necessary to describe this combusting system. The solution obtained herein includes profiles of velocity, Shvab-Zeldovich variables and thereby enthalpy and species, as well as surface fluxes, flame sheet locations and excess pyrolyzate. For comparison, the finite-difference method is also employed. The local similarity solution for surface gradients lies within 20 percent of the finite-difference results. Good agreement with the aforementioned simpler limiting cases is also obtained. The results indicate that the flow characteristics of a mixed-mode flame are more complicated than a simple superposition of the two limiting flame cases.

1 Introduction

Compartment fires induce an internal fluid mechanics which couples with the local flame buoyancy to produce mixed, free and forced, convective boundary layers on burning surfaces within the enclosure. As a first step toward understanding the complex full scale turbulent phenomenon, a steady, two-dimensional, laminar diffusion flame on a pyrolyzing, vertical, fuel slab is analyzed here. Fig. 1 shows a system schematic. It is assumed that the initial transient burning has been completed. Radiation is neglected. The fuel flux escaping downstream at the top of the fuel slab, called excess pyrolyzate, is the primary unknown. Detailed profiles, surface fluxes, flame locations, and temperatures are also obtained.

The small-scale, mixed-mode combusting problem considered lies at a point of intersection of several previous fundamental studies. The limits of pure forced and pure free convective combusting boundary layers have been analyzed by Emmons [1],[2] Kosdon, Williams, and Buman [2], Kim, de Ris, and Krosser [3] and Pagni and Shih [4]. Inert mixed-mode convective flow has been studied by Merkin [5], Lloyd and Sparrow [6] and Gryzagogridis [7].

In this diffusion flame analysis, it is assumed that all detailed chemical reaction mechanisms can be represented by a single global stoichiometry. With the additional assumptions of unit Lewis number and transport properties independent of composition [8], Shvab-Zeldovich variables are then introduced to eliminate heat and mass generation terms in the species and enthalpy conservation equations. Density variations are incorporated via the Howarth-Dorodnitzyn transformation. Boundary-layer and infinite chemical kinetics approximations are introduced. The oxidant and fuel react only in a flame sheet much thinner, as shown in Fig. 1, then the boundary-layer thickness.

The local similarity approximation is applied to the governing equations derived from the above model. The resulting two-point boundary value problem is solved by the parametric expansion method [9]. Results are compared with those obtained by the finite-difference technique [10, 11]. Acceptable agreement in the wall gradients suggests that local similarity, though less accurate than local nonsimilarity [12, 13], can serve as a first approximation for the complicated combusting mixed-mode problem.

2 Combusting Free and Forced Flow

The continuity, momentum, enthalpy and species equations describing a steady, two-dimensional combusting boundary-layer flow over a vertical pyrolyzing fuel slab, neglecting dissipation and radiation, are, respectively:

$$\frac{\partial}{\partial x}(\rho u) + \frac{\partial}{\partial y}(\rho v) = 0 \tag{1a}$$

$$\rho u \frac{\partial u}{\partial x} + \rho v \frac{\partial u}{\partial y} = \frac{\partial}{\partial y}\left(u \frac{\partial u}{\partial y}\right) + g(\rho_\infty - \rho) \tag{1b}$$

$$\rho u \frac{\partial h}{\partial x} + \rho v \frac{\partial h}{\partial y} = \frac{\partial}{\partial y}\left(\frac{k}{c_p}\frac{\partial h}{\partial y}\right) + \dot{q}''' \tag{1c}$$

$$\rho u \frac{\partial Y_i}{\partial x} + \rho v \frac{\partial Y_i}{\partial y} = \frac{\partial}{\partial y}\left(\rho D \frac{\partial Y_i}{\partial y}\right) + \dot{m}_i''' \tag{1d}$$

where $h \equiv \int_{T_\infty}^{T} c_p dT$ and $\dot{q}'''$ and $\dot{m}_i'''$ are the volumetric heat and mass generation rates, respectively. Assuming constant enthalpy and fuel concentration at the wall, the boundary conditions are:

---

[1] Research Fellow, Division of Applied Science, Harvard University, Cambridge Mass.

[2] Numbers in brackets designate References at end of paper.

Contributed by the Heat Transfer Division for publication in the JOURNAL OF HEAT TRANSFER. Manuscript received by the Heat Transfer Division June 20, 1977.

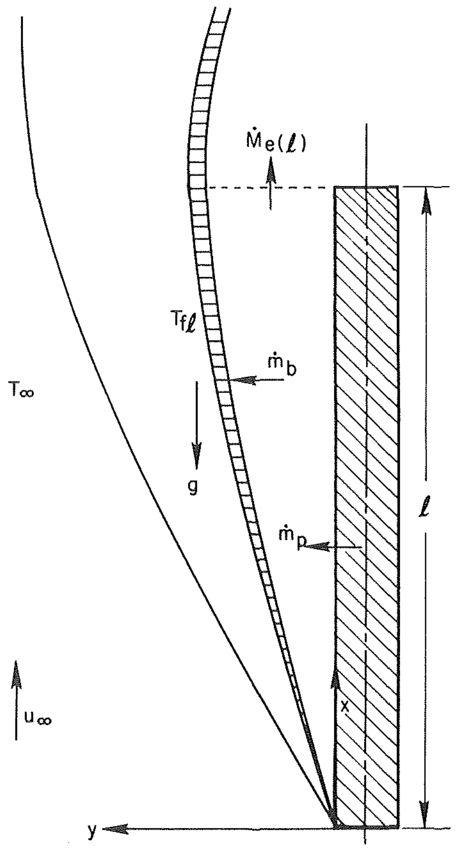

Fig. 1 System schematic of a steady, two-dimensional, laminar, mixed-mode convective flame on a vertical pyrolyzing fuel slab

$$\text{At } y = 0, u = 0, h = h_w, Y_f = Y_{fw}, \frac{k}{c_p}\frac{\partial h}{\partial y} = \dot{m}_p L, \dot{m}_p = \frac{-\rho D \dfrac{\partial Y_f}{\partial y}}{Y_{ft} - Y_{fw}} \tag{2a}$$

$$\text{At } y \to \infty, u = u_\infty, h = 0, Y_{0x} = Y_{0x,\infty} \tag{2b}$$

Since similarity solutions exist in both limits of forced and free convective flames [1–4], similarity variables should at least simplify equations (1, 2) in the mixed-mode case. Based on the transformations used in the limiting cases, the following general transformation is adopted

$$\eta = \int_{0^*}^{y} (\rho/\rho_\infty)dy/Ax^a\nu_\infty \quad \text{and} \quad f(x, \eta) = \psi(x, y)/Cx^c \tag{3}$$

where $\psi(x, y)$ is the stream function defined by

$$\partial\psi/\partial y = \rho u/\rho_\infty \quad \partial\psi/\partial x = -\rho v/\rho_\infty \tag{4}$$

and constants A, a, C and c are to be determined. Equations (3, 4) yield

$$u = f'(x, \eta)Cx^{c-a}/A\nu_\infty, v = \left(a\eta x^{c-1}f' - cx^{c-1}f - x^c \frac{\partial f}{\partial x}\right) C\rho_\infty/\rho \tag{5}$$

Here the prime denotes derivative with respect to η. The source terms in equations (1, 2) can be eliminated by introducing Shvab-Zeldovich variables defined as

$$\beta = Y_f/\nu_f M_f - Y_{0x}/\nu_{0x}M_{0x}, \gamma = -h/Q_p\nu_{0x}M_{0x} - Y_{0x}/\nu_{0x}M_{0x} \tag{6}$$

It is convenient to normalize the Shvab-Zeldovich concentration and enthalpy as

$$J = \frac{\beta - \beta_\infty}{\beta_w - \beta_\infty} = \frac{\gamma - \gamma_\infty}{\gamma_w - \gamma_\infty} \tag{7}$$

and

$$\phi = h/h_w = \gamma/\gamma_w = J + (1 - J)D_3, \eta \le \eta_{fl}$$

with

$$\phi = h/h_w = (\gamma - \beta)/\gamma_w = (D_3 + r)J/r, \eta \ge \eta_{fl} \tag{8}$$

where

$$r \equiv Y_{0x,\infty}\nu_f M_f/Y_{fw}\nu_{0x}M_{0x} \quad \text{and} \quad D_3 \equiv Q_p Y_{0x,\infty}/h_w \tag{9a,b}$$

Unit Chapman constant, i.e., $\rho\mu/\rho_\infty\mu_\infty = 1$, is also assumed. Substituting in equations (1, 2) yields

$$f''' - f'^2AC(c - a)x^{a+c-1} + ff''ACcx^{a+c-1} + \phi \frac{h_w}{c_pT_\infty}\frac{A^3}{C}g\nu_\infty{}^2x^{3a-c} = ACx^{a+c}\left(f'\frac{\partial f'}{\partial x} - f''\frac{\partial f}{\partial x}\right) \tag{10a}$$

---

* These assumptions are justified in [1–4].

Nomenclature

B = mass transfer number, $(Q_pY_{0x}, -h_w)/L$
c_p = specific heat
D = species diffusivity
D_3 = third Damköhler number, $Q_pY_{0x,\infty}/h_w$
f = similarity stream function in boundary layer
Gr_x = Grashof number, $g(T_w - T_\infty)x^3/\nu_\infty{}^2T_\infty$
g = acceleration of gravity
h = specific enthalpy
J = normalized Shvab-Zeldovich concentration, $(\beta - \beta_\infty)/(\beta_w/\beta_\infty)$ or $(\gamma - \gamma_\infty)/(\gamma_w - \gamma_\infty)$
k = conductivity
L = total enthalpy required to pyrolyse unit mass of solid initially at T_∞
M = molecular weight
$\dot{M}$ = total mass flux
$\dot{m}$ = local mass flux
Pr = Prandtl number ν/α
$\dot{q}''$ = local heat flux
Q_p = heat of reaction per unit mass of oxygen
Re_x = Reynolds number, $u_\infty x/\nu_\infty$
r = mass consumption number, $Y_{0x,\infty}\nu_fM_f/Y_{fw}\nu_{0x}M_{0x}$
T = temperature
u = x-direction velocity
v = y-direction velocity
Y_i = mass fraction of i species
$\alpha = k/\rho c_p$
β = Shvab-Zeldovich variable, $Y_f/\nu_fM_f - Y_{0x}/\nu_{0x}M_{0x}$
γ = Shvab-Zeldovich variable, $-h/Q_p\nu_{0x}M_{0x} - Y_{0x}/\nu_{0x}M_{0x}$
δ = boundary-layer thickness
ϵ_3, ϵ_5 = remainders in the parametric expansion method
η = local similarity variable
μ = viscosity
ν = kinematic viscosity, or stoichiometric coefficient
ξ = mixed convection number, $\mathrm{Gr}_x/\mathrm{Re}_x{}^2$
ρ = density
τ_w = shear stress at wall
$\phi = h/h_w$

Subscripts

e = excess
f = fuel
$f\ell$ = flame
ℓ = slab length
$0x$ = oxygen
p = pyrolyzed
t = total
w = wall
∞ = ambient

$$J'' + \Pr fJ'ACcx^{a+c-1} = \Pr ACx^{a+c}\left(f'\frac{\partial J}{\partial x} - J'\frac{\partial f}{\partial x}\right) \quad (10b)$$

with the boundary conditions

$$x^{a+c-1}\left[\frac{x}{c}\frac{\partial f(x, 0)}{\partial x} + f(x, 0)\right] = \frac{B}{\Pr}\frac{J(x, 0)}{ACc},$$

$$f'(x, 0) = 0, J(x, 0) = 1, \quad (11a)$$

$$f'(x, \infty) = \frac{A}{C}u_\infty \nu_\infty x^{a-c}, J(x, \infty) = 0 \quad (11b)$$

where

$$B \equiv (Q_p Y_{0x,\infty} - h_w)/L \quad (12)$$

The transformation constants can now be chosen to minimize the x dependence in equations (10). Two choices exist, corresponding respectively to forced or free similarity, i.e.,

$$a = \frac{1}{2}, c = \frac{1}{2}, A = 2/(u_\infty \nu_\infty)^{1/2} \text{ and } C = (u_\infty \nu_\infty)^{1/2} \quad (13)$$

and

$$a = \frac{1}{4}, c = \frac{3}{4}, A = (4c_p T_\infty/gh_w \nu_\infty{}^2)^{1/4}$$

$$\text{and } C = (64gh_w \nu_\infty{}^2/c_p T_\infty)^{1/4} \quad (14)$$

If equations (13) are chosen, the boundary conditions in equations (11) become independent of x, whereas equations (14) produce $f' \sim x^{-1/2}$ at the edge of the boundary layer. Introducing $\xi = \mathrm{Gr}_x/\mathrm{Re}_x{}^2 = xg(T_w - T_\infty)/T_\infty u_\infty{}^2$ and equations (13) in equations (10, 11) yields the general governing equations

$$f''' + ff'' + 8\xi\phi = 2\xi\left(f'\frac{\partial f'}{\partial \xi} - f''\frac{\partial f}{\partial \xi}\right), \quad (15a)$$

$$J'' + \Pr fJ' = 2\xi \Pr\left(f'\frac{\partial J}{\partial \xi} - J'\frac{\partial f}{\partial \xi}\right) \quad (15b)$$

subject to the boundary conditions

$$2\xi\frac{\partial f(\xi, 0)}{\partial \xi} + f(\xi, 0) = \frac{B}{\Pr}J'(\xi, 0), f'(\xi, 0) = 0, J(\xi, 0) = 1, \quad (16a)$$

$$f'(\xi, \infty) = 2, J(\xi, \infty) = 0 \quad (16b)$$

The problem defined by equations (15 and 16) could be accurately modelled by a two or three-equation local nonsimilarity approximation [12, 13]. However, since the simpler inert mixed-mode flow problem has not been solved by this more accurate method, it seems appropriate to use local similarity as a first approximation. Furthermore, the flame problem involves many assumptions not present in the inert case, which are assailable at the same level of accuracy as local similarity, e.g., radiation may easily be $\gtrsim$10 percent of the convective heating at the wall; the flame-sheet approximation simplifies the profiles near the flames, etc. Using local nonsimilarity to strive diligently for high numerical accuracy in the convective problem would thus violate consistency.

The combusting mixed-mode problem in the local similarity approximation is obtained by neglecting as small the right side of equations (15),

$$f''' + ff'' + 8\xi\phi = 0 \quad (17a)$$

$$J'' + \Pr fJ' = 0 \quad (17b)$$

subject to the boundary conditions

$$f(\xi, 0) = BJ'(\xi, 0)/\Pr, f'(\xi, 0) = 0, J(\xi, 0) = 1 \quad (18a)$$

$$f'(\xi, \infty) = 2, J(\xi, \infty) = 0 \quad (18b)$$

All streamwise dependence is contained in the similarity variable η and the local similarity parameter ξ.

These equations contain five parameters ξ, B, r, D_3 and Pr. The mixed convection number, $\xi \equiv \mathrm{Gr}_x/\mathrm{Re}_x{}^2$, denotes the relative magnitude of buoyancy to inertia. The convective mass transfer number, equation (12), gives the ratio of the chemical energy evolved in combustion to the effective enthalpy of pyrolysis. When no mass transfer occurs at the wall, B does not enter the problem. Named by analogy to B, the mass consumption number, equation (9a), is the ratio of the relative available oxygen, $Y_{0x,\infty}/Y_{fw}$, to the stoichiometrically required oxygen, $\nu_{0x}M_{0x}/\nu_f M_f$. It ranges from zero to unity for common polymeric fuels with large values denoting small flame heights and small values, i.e., insufficient oxygen, giving large flame heights. Although it contains Y_{fw}, this parameter is completely defined *a priori* for a given system as shown in Appendix A. A group related to the third Damköhler number, equation (9b), is the ratio of the chemical energy evolved per unit mass of the ambient gas to the specific enthalpy at the wall. Typically, $D_3 \approx 4.0$ for solid polymeric fuels.

3 Results and Discussion

The parametric expansion method [9], is used to numerically solve the two-point boundary value problem, equations (17 and 18), for $f(\eta)$ and $J(\eta)$. This procedure is summarized in Appendix B. The surface shear stress and heat flux can be obtained from equations (5 and 8) respectively as

$$\tau_w = \mu_w \left.\frac{\partial u}{\partial y}\right|_w = \rho_\infty u_\infty{}^2 \mathrm{Re}_x{}^{-1/2} f''(\xi, 0)/2, \quad (19)$$

$$q_w = \frac{k_w}{c_{p_w}}\left.\frac{\partial h}{\partial y}\right|_w = h_w \rho_\infty u_\infty \mathrm{Re}_x{}^{-1/2} J'(0)(1 - D_3)/2 \Pr \quad (20)$$

using equations (3 and 13). Figs. 2(*a*) and 2(*b*) show the nondi-

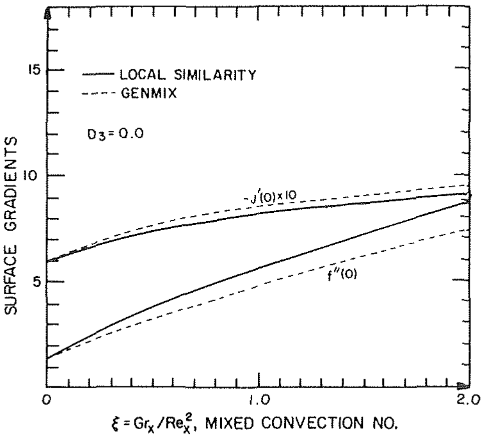

Fig. 2(*a*) Nondimensionalized surface shear stress and heat flux versus ξ for inert mixed-mode flow

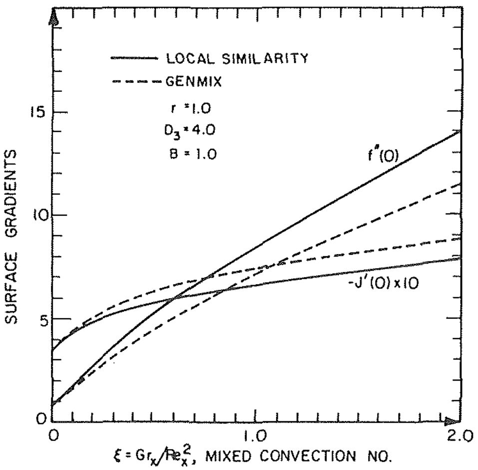

Fig. 2(*b*) Nondimensionalized surface shear stress and heat flux versus ξ for combusting mixed-mode flow mensionalized surface shear stress and heat flux as a function of ξ obtained from both local similarity and finite-difference for inert and combusting flows. The local similarity results in Fig. 2(a) coincide with [6]. The Patankar-Spalding finite-difference (GENMIX) method [10, 11] is employed for comparison. The initial profiles, stream function and boundary-layer thickness at $x = 0.01\ell$ are assumed from the Blasius solution. One hundred cross-stream grid nodes and a step size of one-twentieth of the current boundary-layer thickness are used. The deletion of derivatives with respect to ξ in equations (15 and 16a) causes ~ten and 20 percent deviation from the finite-difference results for inert and combusting cases, respectively.

For $\xi \lesssim 0.15$, the surface shear in a flame is smaller than that in an inert flow since buoyancy effects are dominated at small x by the blowing effect of pyrolysis. For $\xi > 0.15$, the wall shear with a flame is greater than the inert shear since buoyancy, which now governs the flow characteristics, is greater in the combusting case. For all ξ, the surface heat flux, proportional to $|(1 - D_3)J'(0)|$, is larger with a flame than in an inert flow.

In addition to Fig. 2, these initially unknown boundary conditions, $f''(\xi, 0)$ and $J'(\xi, 0)$, are listed to high accuracy in Table 1. The value of D_3 was chosen to permit comparison of $J'(\xi, 0)$ with the limiting forced convection case [1]. The $J'(\xi, 0)$ value for Pr = 0.72, 0.34174, is lower than the reported value for Pr = 1.0, 0.39118, due to larger thermal diffusivity. Seven significant figures are needed for $\xi > 1$ to generate accurate profiles since, in the combusting case, slight deviations from these large gradients lead to large profile errors. Due to growth of the boundary-layer thickness with ξ, the dimensional surface shear stress and heat flux decrease as $f''(\xi, 0)/\xi^{1/2}$ and $J'(0)/\xi^{1/2}$ and thus are very large near the leading edge. As ξ increases, the shear stress initially decreases as in the forced convection case. Downstream buoyancy becomes more influential, the flow accelerates and the wall shear increases. The minima in combusting and inert wall shear stresses occur at $\xi \approx 0.1$ and 0.5, respectively. Unlike the maximum velocity, the flame temperature remains constant as ξ increases. Thus the surface heat flux decreases uniformly for both inert and combusting flows. Pyrolysis absorbs the additional flux in the latter case and thus decreases similarly with ξ.

Figs. 3(a) and 3(b) show the velocity and enthalpy profiles at ξ = 0.1 and 1.0, respectively. As ξ increases, the flow accelerates due to increased buoyancy, while the chemistry-controlled flame temperature remains constant. Note that $\eta \sim x^{-1/2}$ and $\xi \sim x$ implies an ~3 fold contraction of the abscissa in Fig. 3(b) relative to Fig. 3(a). From the definition of J and the assumption that $Y_f = Y_{0x} = 0$ at the flame sheet, the flame location is given by

$$J(\xi, \eta_{f\ell}) = r/(1 + r) \tag{21}$$

The flame temperature is then from equations (8, 21)

$$h_{f\ell}(\xi, \eta_{f\ell})/h_w = (D_3 + r)/(1 + r) \tag{22}$$

As D_3 increases, both the temperature and velocity increase due to an increased heat release. As shown in Fig. 3, the mass consumption number, r, strongly effects the flame location and temperature. To qualitatively determine $y_{f\ell}(r)$, consider that the fuel and oxygen diffuse into the flame at relative rates determined by the stoichiometric ratio,

$$\dot{m}_f''/\dot{m}_{0x}'' = \nu_f M_f/\nu_{0x} M_{0x} \tag{23}$$

Assuming equal diffusivities, equation (23) becomes

$$\partial Y_f/\partial y|_{y^-{}_{f\ell}} = (\nu_f M_f/\nu_{0x} M_{0x}) \partial Y_{0x}/\partial y|_{y^+{}_{f\ell}} \tag{24}$$

Now approximate $\partial Y_f/\partial y|_{y^-{}_{f\ell}} \approx Y_{fw}/y_{f\ell}$ and $\partial Y_{0x}/\partial y|_{y^+{}_{f\ell}} \approx -Y_{0x,\infty}/(\delta - y_{f\ell})$ and solve for

$$y_{f\ell} \approx \delta/(1 + r) \tag{25}$$

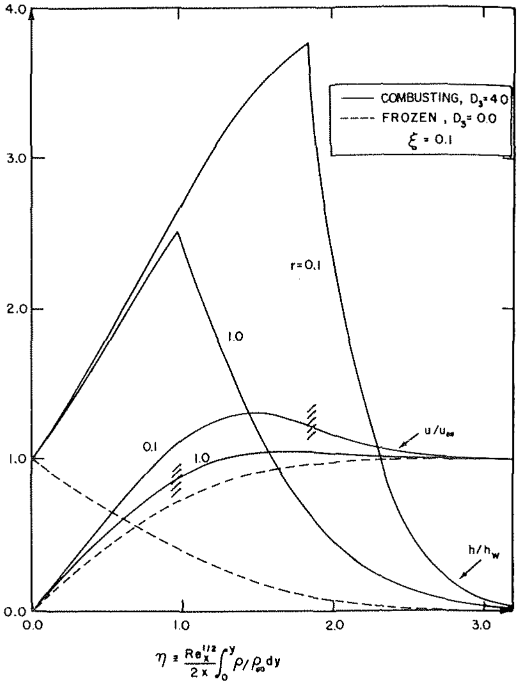

Fig. 3(a) Normalized velocity and enthalpy profiles at ξ = 0.1 parameterized in r for both inert mixed-mode flows and flames

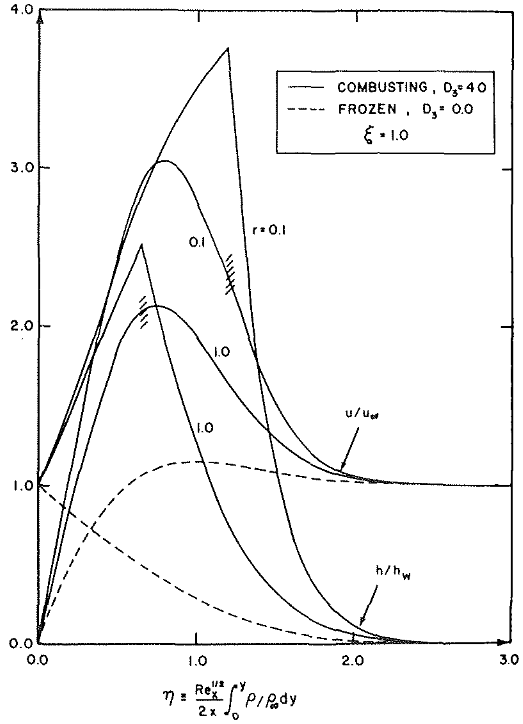

Fig. 3(b) Normalized velocity and enthalpy profiles at ξ = 1.0 parameterized in r for both inert mixed-mode flows and flames

So as r decreases, the flame location moves outward as indicated by the hatched lines in Figs. 3(a),(b). $y_{f\ell} \rightarrow \delta$ as $r \rightarrow 0$ to maintain the required oxygen flux to the flame. To qualify the influence of r on the flow field consider first the influence of r on $T_{f\ell}$ as given by equation (22). This expression can be obtained physically by equating the energy convected from both sides of the flame to the heat liberated by reaction,

$$Q_p \dot{m}_{0x}''' = (\partial h/\partial y|_{y^-{}_{f\ell}} - \partial h/\partial y|_{y^+{}_{f\ell}}) k_{f\ell}/c_{p_{f\ell}} \tag{26}$$

Approximating again $\partial h/\partial y|_{y^-{}_{f\ell}} \approx (h_{f\ell} - h_w)/y_{f\ell}$ and $\partial h/\partial y|_{y^+{}_{f\ell}} \approx h_{f\ell}/(\delta - y_{f\ell})$ and using unit Lewis number and equation (25) yields equation (22). Since $D_3 > 1$ and $r < 1$ flame temperatures increase as r decreases, as shown in Figs. 3(a),(b). For smaller r and thus larger buoyancy, the gas flows faster, inducing larger entrainment,

$$|\rho_\infty v_\infty| \approx \frac{d}{dx}\int_0^\delta \rho u dy - \dot{m}_p \tag{27}$$

Also for smaller r, the reaction zone shifts outward, tending to carry the velocity maximum outward. However, this peak-velocity shift is opposed by the increased entrainment rate, and therefore it lags the flame shift.

Not presented here for clarity of the figures are species concentration profiles. The fuel concentration distribution is almost linear inside the flame sheet. The oxygen concentration beyond the flame sheet, is also nearly linear except near the ambience where it levels off. Profiles at other values of ξ can be obtained using the listed missing initial conditions in Table 1 and integrating equations (17 and 18a).

The physical distance normal to the surface, y, is recovered by inverting the Howarth-Dorodnitzyn transformation:

$$y = \frac{2x}{\mathrm{Re}_x{}^{1/2}}\int_0^\eta (\rho_\infty/\rho)d\eta = \frac{2x}{\mathrm{Re}_x{}^{1/2}}\int_0^\eta [\phi(T_w - T_\infty)/T_\infty + 1]d\eta \tag{28}$$

For a combusting flow where large density variations occur, the usual Boussinesq assumption is invalid and the similarity displacement η is greatly compacted relative to the physical distance y. The flame stand-off distance is obtained from equation (28) as:

$$y_{f\ell} = \frac{2x}{\mathrm{Re}_x{}^{1/2}}\int_0^{\eta_{f\ell}} [\phi(T_w - T_\infty)/T_\infty + 1]d\eta \tag{29}$$

where $\eta_{f\ell}$ is given by equation (21). Fig. 4 shows $y_{f\ell}$ as a function of ξ parameterized in r. For small ξ, $y_{f\ell}$ is closely proportional to $\xi^{1/2}$ as in forced convection. As ξ increases, the integral in equation (29) decreases in contrast to a constant obtained in both pure convection limits [4]. The physical flame location, $y_{f\ell}$, which is proportional to the product of $\xi^{1/2}$ and the integral, becomes less dependent on ξ as ξ increases. It is approximately proportional to $\xi^{1/6}$ when $\xi = 2.0$ as shown by the dashed line slopes in Fig. 4.

Now consider the excess pyrolyzate generated in the mixed mode case. The local pyrolysis rate at the surface from equation (5) with $c = \frac{1}{2}$, $C = (u_\infty \nu_\infty)^{1/2}$ and the deletion of $\partial f/\partial x$, is

$$\dot{m}_p = \rho_w v_w = -\rho_\infty u_\infty \mathrm{Re}_x{}^{-1/2} f(\xi, 0)/2 \tag{30}$$

The total pyrolysis rate is obtained by integrating the local pyrolysis rate from 0 to x,

$$\dot{M}_p(x) = \int_0^x \dot{m}_p(x)dx = \frac{\rho_\infty}{2}(u_\infty \nu_\infty)^{1/2}\int_0^x [-f(\xi, 0)x^{-1/2}]dx \tag{31}$$

The excess pyrolyzate, i.e., combustible gases which are not consumed in the flames that produced them, can be obtained by evaluating the fuel flux between the fuel slab and the sheet flame as

$$\dot{M}_e(x) = \int_0^{y_{f\ell}} \rho u Y_f dy = 2\rho_\infty(u_\infty \nu_\infty x)^{1/2} Y_{fw} \times \int_0^{\eta_{f\ell}} f'\{(1 + r)J - r\}d\eta \tag{32}$$

The unburned fraction of the total pyrolyzate from 0 to ξ is then

$$\dot{M}_e(\xi)/\dot{M}_p(\xi) = \frac{2B\xi^{1/2}\int_0^{\eta_{f\ell}} f'(\xi, \eta)\{(1 + r)J(\xi, \eta) - r\}d\eta}{(B + r + 1)\int_0^\xi [-f(\xi, 0)\xi^{1/2}]d\xi} \tag{33}$$

where the transformation of x to ξ is performed at constant $\mathrm{Gr}_\ell/\mathrm{Re}_\ell{}^2$. Fig. 5 shows the excess fraction of the total pyrolyzate as a function of ξ parameterized in r. In the two previous pure convection cases [4], $\dot{M}_e(x)/\dot{M}_p(x)$ remained constant with x since the total pyrolysis rate and the streamwise fuel flux had the same x dependence. In the mixed-mode flame, this excess fraction increases as ξ increases since buoyancy effects produce larger velocities near the wall where a large amount of fuel vapor exists. Thus, as ξ increases, the fuel flux increases

Table 1 **Nondimensionalized surface shear stress and heat flux. For flames, $B = 1.03613$, $D_3 = 0.04114$, Pr = 0.72 and $f(0) = BJ'(0)/Pr$**

	Inert Pr = 0.72		r = 1.0		r = 0.1	
ξ	f"(o)	-J'(o)	f"(o)	-J'(o)	f"(o)	-J'(o)
0	1.3282300 1.32824^b	0.5912700 0.5912^a	0.6810400	0.3417400	0.6810400	0.3417400
0.1	1.8877751	0.6315331 0.6316^a	1.9317077	0.4373798	2.3053323	0.4740793
0.5	3.7001323	0.7325672	5.2863886	0.5809416	6.4983728	0.6502058
1.0	5.5673162	0.8115057 0.8116^a	8.5668836	0.6722847	10.5715533	0.7588374
1.5	7.2243569	0.8696914	11.4417937	0.7353202	14.1348623	0.8331177
2.0	8.7527834	0.9167745 0.9168^a	14.0805133	0.7847417	17.4030195	0.8911061

[a] Lloyd and Sparrow [6]
[b] Blasius

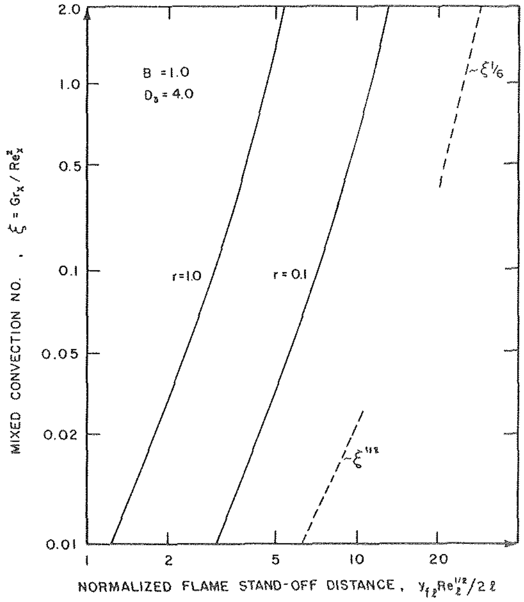

Fig. 4 Flame-sheet location along the streamwise distance parameterized in r

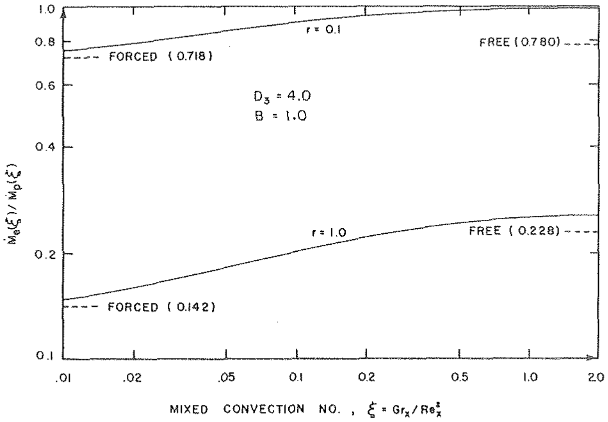

Fig. 5 Excess fraction of the total pyrolyzate versus ξ parameterized in r

faster than the total pyrolysis rate. Furthermore, since the external flow always aids the buoyancy-induced flow to transport the fuel vapor downstream, the excess fraction of the unburned fuel in the mixed-mode flame will eventually exceed that in the free convective flame.

4 Conclusions

A steady, two-dimensional, mixed-mode flame on a pyrolyzing fuel slab is analyzed. The local similarity solution lies within 20 percent of comparable finite-difference results. Five parameters, the mass transfer number B, the the mass consumption number r, the third Damköhler number D_3, the Prandtl number Pr and the mixed convection number ξ, are required to describe this laminar mixed-mode flame. In comparing combusting and inert mixed-mode flows, surface shear is smaller in the former for small ξ due to blowing and larger downstream due to increased buoyancy. The combusting case surface heat flux is always larger than its inert counterpart. In both inert and combusting flows, the wall shear stress decreases with ξ near the leading edge and then increases downstream due to buoyancy. The wall heat fluxes decrease monotonically with ξ. The velocity and enthalpy distributions in the combusting flow are largely influenced by ξ and r. As ξ increases, the flow accelerates but the flame temperature remains constant. As r decreases, the flow is heated and accelerated, the reaction zone shifts outward significantly and the velocity peak moves outward slightly. For future extensions of the present work, the numerical accuracy can be improved using the local nonsimilarity approximation. Radiation should be accounted for. Related problems of gravity unaligned with u_∞ may also be considered. Experiments are needed to compare with the current predictions.

Acknowledgments

The authors are grateful for the support from the Products Research Committee and the National Bureau of Standards Fire Research Center. The conclusions drawn herein are those of the authors and not of the Products Research Committee.

References

1 Emmons, H. W., "The Film Combustion of Liquid Fuel," *Z. Angew. Math. Mech.*, Vol. 36, 1956, pp. 60–71.

2 Kosdon, F. J., Williams, F. A., and Buman, C., "Combustion of Vertical Cellulosic Cylinders in Air," *Twelfth Symposium (Int'l) on Combustion*, pp. 253–264, The Combustion Institute, 1969.

3 Kim, J. S., deRis, J., and Krosser, F. W., "Laminar Free-Convective Burning of Fuel Surface," *Thirteenth Symposium (Int'l) on Combustion*, pp. 949–961, The Combustion Institute, 1971.

4 Pagni, P. J., and Shih, T. M., "Excess Pyrolyzate," *Sixteenth Symp. (Int'l) on Comb.*, The Combustion Institute, 1976, pp. 1329–1342.

5 Merkin, J. H., "The Effect of Buoyancy Forces on The Boundary-Layer Flow over a Semi-infinite Vertical Flat Plate in a Uniform Free Stream," *J. Fluid Mech.*, Vol. 35, 1969, pp. 439–450.

6 Lloyd, J. R., and Sparrow, E. M., "Combined Forced and Free Convection Flow on Vertical Surfaces," *Int. Journal of Heat and Mass Transfer*, Vol. 13, 1970, pp. 434–438.

7 Gryzagogridis, J., "Combined Free and Forced Convection from an Isothermal Vertical Plate," *Int. Journal of Heat and Mass Transfer*, Vol. 18, 1975, pp. 911–916.

8 Williams, F. A., *Combustion Theory*, Addison-Wesley, Reading, Mass., 1965.

9 Shih, T. M., and Pagni, P. J., "The Parametric Expansion Method for Two-Point Boundary Value Problems," in preparation.

10 Patankar, S. V., and Spalding, D. B., *Heat and Mass Transfer in Boundary Layers*, Morgan-Grampian, West Wickham, 1967.

11 Spalding, D. B., "A General Computer Program for Two-Dimensional Boundary Layer Problems," Report No. HTS/73/48, Department of Mechanical Engineering, Imperial College of Science and Technology, 1973.

12 Sparrow, E. M., Quack, H., and Boerner, C. J., "Local Nonsimilarity Boundary-Layer Solutions," *AIAA Journal*, Vol. 8, 1970, pp. 1936–1942.

13 Sparrow, E. M., and Yu, H. S., "Local Nonsimilarity Thermal Boundary-Layer Solutions," ASME JOURNAL OF HEAT TRANSFER, Vol. 93, 1971, pp. 328–334.

14 Roberts, S. M., and Shipman, J. S., *Two-point Boundary Value Problems: Shooting Methods*, American Elsevier, New York, 1972.

15 Keller, H. B., *Numerical Methods for Two-point Boundary Value Problems*, Blaisdell Co., London, 1968.

16 Rubbert, P. E., and Landahl, M. T., "Solution of Nonlinear Flow Problems through Parametric Differentiation," *Physics Fluids*, Vol. 10, 1967, pp. 831–835.

17 Na, T. Y., and Habbib, I. S., "Solution of the Natural Convection Problem by Parametric Differentiation," *Int. Journal of Heat and Mass Transfer*, Vol. 17, 1974, pp. 457–459.

APPENDIX A

Surface Fuel Mass Fraction

Species conservation written for fuel at the surface gives

$$\dot{m}_p Y_{ft} = \dot{m}_p Y_{fw} - \rho D \partial Y_f / \partial y|_w \qquad \text{(A-1)}$$

It is assumed that the Lewis No., α/D, and the Chapman const., $\rho\mu/\rho_\infty\mu_\infty$, are unity. It is also assumed that no oxygen exists inside the flame, i.e., $Y_{0x} = 0$ for $\eta \leq \eta_{f\ell}$. Therefore the fuel concentration profile can be expressed in terms of $J(\xi, \eta)$ using equations (6, 7) as

$$Y_f(\xi, \eta)/Y_{fw} = (1 + r)J(\xi, \eta) - r, \; \eta \leq \eta_{f\ell}. \qquad \text{(A-2)}$$

The surface fuel gradient is then

$$\partial Y_f/\partial y|_w = Y_{fw}(1 + r)J'(\xi, 0)\partial\eta/\partial y|_w \qquad \text{(A-3)}$$

where, from equations (3, 13)

$$\partial\eta/\partial y|_w = \rho_w \mathrm{Re}_x{}^{1/2}/(2x\rho_\infty) \qquad \text{(A-4)}$$

Substituting this $\partial Y_f/\partial y|_w$ and $\dot{m}_p$ expressed by equation (30) with the first of equations (13a) into equation (A-1) gives

$$Y_{fw} = Y_{ft}B/(B + r + 1) \qquad \text{(A-5)}$$

Solving for Y_{fw} from equations (9a and A-5) yields the surface fuel mass fraction as

$$Y_{fw} = [Y_{ft}B - Y_{0x,\infty}\nu_f M_f/\nu_{0x}M_{0x}]/(B + 1) \qquad \text{(A-6)}$$

Thus, for a given system, i.e., fuel and ambiance, Y_{fw} and, consequently, r are known a priori.

APPENDIX B

Parametric Expansion Method

The parametric expansion method is a noniterative technique [9] to solve two-point boundary value problems [14, 15] which is useful when (1) solutions are highly sensitive to the missing initial conditions and (2) wide ranges of parameters are to be examined. It improves the parametric differentiation method [16, 17] which is subject to large truncation errors due to its linear approximations. The procedure is applied below to the present combusting mixed-mode problem.

Equations (17) can be replaced by an equivalent system of five first-order equations:

$$f_1' = f_2, f_2' = f_3, f_3' = -f_1 f_3 - 8\xi\phi, f_4' = f_5, f_5' = -\mathrm{Pr}\, f_1 f_5 \qquad \text{(B-1)}$$

subject to the boundary conditions:

$$f_1(0) = \frac{B}{\mathrm{Pr}} f_5(0), f_2(0) = 0, f_2(\infty) = 2, f_4(0) = 1, f_4(\infty) = 0 \qquad \text{(B-2)}$$

The two missing initial conditions, $f_3(0)$ and $f_5(0)$, are the nondimensionalized wall shear stress and heat flux. The function f_i at an arbitrary ξ^* can be expanded about $\xi^* + \Delta\xi$:

$$f_i(\xi^* + \Delta\xi, \eta) = f_i(\xi^*, \eta) + \left.\frac{\partial f_i}{\partial \xi}\right|_{\xi^*+\Delta\xi} (\Delta\xi) - \left.\frac{\partial^2 f_i}{\partial \xi^2}\right|_{\xi^*+\Delta\xi} \frac{(\Delta\xi)^2}{2} + R_i(\xi^* + \Delta\xi, \eta) \qquad \text{(B-3)}$$

Solutions at $\xi^* + \Delta\xi$ are obtained once the first derivatives, second derivatives and the remainders are found. With the same procedure, solutions at any ξ can be obtained. For demonstration, only ξ is varied here. Differentiating equations (B-1) with respect to ξ once and then twice yields

$$g_1' = g_2, g_2' = g_3,$$

$$g_3' = -f_1 g_3 - f_3 g_1 - 8\phi - 8\xi\phi_\xi$$

$$g_4' = g_5,\ g_5' = -\Pr f_5 g_1 - \Pr f_1 g_5 \tag{B-4}$$

with the boundary conditions

$$g_1(0) = \frac{B}{\Pr} g_5(0),\ g_2(0) = g_2(\infty) = g_4(0) = g_4(\infty) = 0 \tag{B-5}$$

and

$$\begin{gathered} h_1' = h_2,\ h_2' = h_3, \\ h_3' = -f_1 h_3 - f_3 h_1 - 8\xi\phi_{\xi\xi} - 2g_1 g_3 - 16\phi_\xi, \\ h_4' = h_5,\ h_5' = -\Pr f_5 h_1 - \Pr f_1 h_5 - 2\Pr g_1 g_5 \end{gathered} \tag{B-6}$$

with the boundary conditions

$$h_1(0) = \frac{B}{\Pr} h_5(0),\ h_2(0) = h_2(\infty) = h_4(0) = h_4(\infty) = 0 \tag{B-7}$$

The missing initial conditions are defined as

$$g_3(0) = \alpha_1,\ g_5(0) = \alpha_2,\ h_3(0) = \beta_1 \quad \text{and} \quad h_5(0) = \beta_2 \tag{B-8}$$

Combining these ten functions, g_i and h_i, with thirty auxiliary functions, $g_i{}^{(k)}$ and $h_i{}^{(k)}$, (note $i = 1, 2 \ldots 5$, and $k = 1$–3) as

$$g_i = \alpha_1 g_i{}^{(1)} + \alpha_2 g_i{}^{(2)} + g_i{}^{(3)},\ h_i = \beta_1 h_i{}^{(1)} + \beta_2 h_i{}^{(2)} + h_i{}^{(3)} \tag{B-9}$$

and substituting them into equations (B-6, B-8), one obtains six sets of initial-value problems. Their initial conditions are:

$$g_1{}^{(1)}(0) = g_2{}^{(1)}(0) = g_4{}^{(1)}(0) = g_5{}^{(1)}(0) = 0,\ g_3{}^{(1)}(0) = 1, \tag{B-10}$$

$$g_1{}^{(2)}(0) = B/\Pr,\ g_2{}^{(2)}(0) = g_3{}^{(2)}(0) = g_4{}^{(2)}(0) = 0,\ g_5{}^{(2)}(0) = 1, \tag{B-11}$$

$$g_1{}^{(3)}(0) = g_2{}^{(3)}(0) = g_3{}^{(3)}(0) = g_4{}^{(3)}(0) = g_5{}^{(3)}(0) = 0, \tag{B-12}$$

$$h_1{}^{(1)}(0) = h_2{}^{(1)}(0) = h_4{}^{(1)}(0) = h_5{}^{(1)}(0) = 0,\ h_3{}^{(1)}(0) = 1, \tag{B-13}$$

$$h_1{}^{(2)}(0) = B/\Pr,\ h_2{}^{(2)}(0) = h_3{}^{(2)}(0) = h_4{}^{(2)}(0) = 0,\ h_5{}^{(2)}(0) = 1, \tag{B-14}$$

$$h_1{}^{(3)}(0) = h_2{}^{(3)}(0) = h_3{}^{(3)}(0) = h_4{}^{(3)}(0) = h_5{}^{(3)}(0) = 0 \tag{B-15}$$

All solutions at $\eta \to \infty$ can be obtained using a Runge-Kutta integration technique. From these solutions, one obtains the originally arbitrary coefficients:

$$\begin{gathered} \alpha_1 = \frac{g_2{}^{(2)}(\infty)g_4{}^{(3)}(\infty) - g_2{}^{(3)}(\infty)g_4{}^{(2)}(\infty)}{g_2{}^{(1)}(\infty)g_4{}^{(2)}(\infty) - g_2{}^{(2)}(\infty)g_4{}^{(1)}(\infty)}, \\ \alpha_2 = \frac{g_2{}^{(3)}(\infty)g_4{}^{(1)}(\infty) - g_2{}^{(1)}(\infty)g_4{}^{(3)}(\infty)}{g_2{}^{(1)}(\infty)g_4{}^{(2)}(\infty) - g_2{}^{(2)}(\infty)g_4{}^{(1)}(\infty)}, \\ \beta_1 = \frac{h_2{}^{(2)}(\infty)h_4{}^{(3)}(\infty) - h_2{}^{(3)}(\infty)h_4{}^{(2)}(\infty)}{h_2{}^{(1)}(\infty)h_4{}^{(2)}(\infty) - h_2{}^{(2)}(\infty)h_4{}^{(1)}(\infty)}, \\ \beta_2 = \frac{h_2{}^{(3)}(\infty)h_4{}^{(1)}(\infty) - h_2{}^{(1)}(\infty)h_4{}^{(3)}(\infty)}{h_2{}^{(1)}(\infty)h_4{}^{(2)}(\infty) - h_2{}^{(2)}(\infty)h_4{}^{(1)}(\infty)} \end{gathered} \tag{B-16}$$

The final form of the original missing initial conditions can be deduced from equation (B-3) as

$$f_3(0) = f_3{}^*(0) + g_3(0)[\Delta\xi] - (1 + \epsilon_3)h_3(0)[(\Delta\xi)^2/2] \tag{B-17}$$

$$f_5(0) = f_5{}^*(0) + g_5(0)[\Delta\xi] - (1 + \epsilon_5)h_5(0)[(\Delta\xi)^2/2] \tag{B-18}$$

where the remainder terms, ϵ_3 and ϵ_5 are obtained in [9] as

$$\epsilon_3 = [(\psi_{2s} - \psi_2)(\psi_{4s} - \psi_{4f3}) - (\psi_{4s} - \psi_4)(\psi_{2s} - \psi_{2f3})]/\theta(3, 5) \tag{B-19}$$

$$\epsilon_5 = [(\psi_{2s} - \psi_2)(\psi_{4s} - \psi_{4f5}) - (\psi_{4s} - \psi_4)(\psi_{2s} - \psi_{2f5})]/\theta(5, 3) \tag{B-20}$$

$$\theta(3, 5) = \psi_{4s}(\psi_{2f3} - \psi_{2f5}) - \psi_{2s}(\psi_{4f3} - \psi_{4f5}) + \psi_{4f3}\,\psi_{2f5} - \psi_{2f3}\psi_{4f5} \tag{B-21}$$

Here $\theta(5, 3)$ is obtained by interchanging 3 and 5 in $\theta(3, 5)$. ψ is the terminal-point boundary value, e.g., $\psi_2 = 2$ and $\psi_4 = 0$ in this problem. For terms ψ_{if} and ψ_{ifj}, $j = 3$ or 5, the first subscript denotes the missing initial condition, the second subscript "f" or "s" denotes first or second-order approximation, respectively, and the third subscript denotes "$f_{js}(0)/f_{jf}{}^{(0)}$" kept the same as f_{ks}". In this analysis, the parametric marching starts from simplest cases, i.e., a pure forced convection flame with $\xi = 0$ and an inert mixed-mode flow with $D_3 = 0$. The missing initial conditions thus obtained are listed in Table 1.

Shi-chune Yao[1]
R. E. Henry

Argonne National Laboratory,
Reactor Analysis and Safety Division,
Argonne, Ill.

An Investigation of the Minimum Film Boiling Temperature on Horizontal Surfaces

The frequency and magnitude of liquid-solid contacts in the film boiling of saturated ethanol and water on horizontal flat stainless steel and copper surfaces are examined with electrical conductance probes. It is observed that, at atmospheric pressure, contacts occur over a wide temperature range and are generally induced by hydrodynamic instabilities. In the ethanol system, these contacts can account for the entire heat transfer rate at the minimum film boiling temperature. The area and duration of contacts are strongly influenced by the dominant nucleation process, and thus, depend on the interface temperature and wettability of the solid. At elevated pressures, direct liquid-solid contacts in film boiling are essentially nonexistent for stainless steel and the first major contact corresponds to quenching of the surface. Under these conditions, spontaneous nucleation upon contact seems to be the controlling mechanism for the minimum film boiling temperature. The minimum point appears to be determined either by a Taylor instability vapor removal limitation or by spontaneous nucleation. The governing mechanism is the one which is stable at the lowest wall temperature.

Introduction

An understanding of liquid-solid contact behavior and the associated heat transfer mechanisms in film boiling is of importance in the interpretation of postcritical heat flux energy transfer results, in the determination of a rewet temperature for emergency core cooling systems in light water reactors, as well as in many other industrial applications where high solid temperatures are encountered.

Liquid-solid contacts, under stable film boiling conditions, were observed by Bradfield [1],[2] and it was found that the liquid subcooling and surface roughness played important roles in the occurrence of contacts. The instability induced contacts in liquid-liquid film boiling systems was also observed by Henry, et al. [2] in experiments for a lighter liquid boiling on a mercury surface. Henry, [3] postulated that such intimate contacts could produce significant thermal transients in the solid wall and that these surface transients could then lead to the progressive breakdown of the film boiling regime. Recently, Swanson, et al. [4] measured the solid surface temperature variations in film boiling and confirmed the contact hypothesis. However, through their indirect method, they were not able to arrive at a quantitative description of the contact behavior. In a recent paper by Iloeje, et al. [5], the direct contact heat transfer of drops to a wall was included in a model of dispersed flow heat transfer.

In the present experiment, the existence and importance of hydrodynamic instability induced liquid-solid contacts of saturated ethanol and water are examined by electric conductance probes. The objectives of this paper are to investigate:

a The liquid-solid contact behavior in film boiling, i.e., the area, duration, and frequency of contacts as a function of system pressure,

b The contribution of direct contact heat transfer to the overall film boiling heat transfer,

c The relationship between the minimum film boiling temperature and the system pressure.

Experimental Apparatus and Procedures

This set of experiments was conducted in a pressurized containment apparatus which is shown in Fig. 1. This test apparatus, which could operate at pressures up to 1.5 MPa, allowed visual observations of the basic film boiling behavior of water and ethanol on flat horizontal surfaces of both copper and stainless steel. Specific interest was given to boiling regimes for which large scale mechanical disturbances were always present, i.e., the liquid globules were large compared to the most dangerous wave length resulting from a Taylor instability analysis. This assured that the vapor removal was governed by such considerations, and the presence of such large disturbances increased the propensity for liquid-solid contacts and essentially precluded any metastable film boiling effects as observed in [6].

---

[1] Present address: Department of Mechanical Engineering, Carnegie-Mellon University, Pittsburgh, Pa.

[2] Numbers in brackets designate References at end of paper.

Contributed by the Heat Transfer Division for publication in the JOURNAL OF HEAT TRANSFER. Manuscript received by the Heat Transfer Division March 11, 1977.

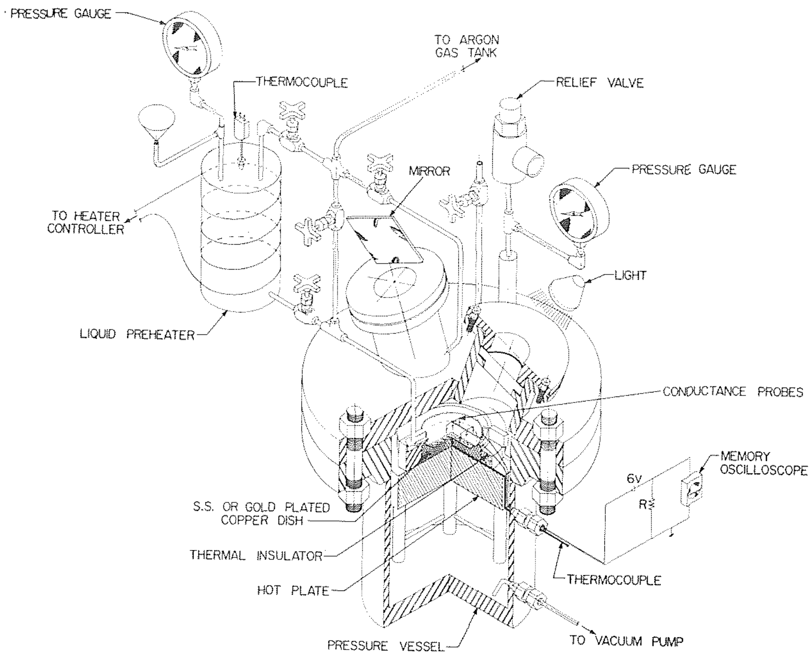

Fig. 1 Pressurized film boiling test apparatus

It has been proposed [3, 7, 8] that the thermal properties of the surface affect the minimum film boiling temperature, as the result of transient liquid-solid contact, and such dependence has been observed experimentally [9, 10]. Intimate contact between two semi-infinite slabs, with constant thermal properties, will result in the interface temperature given by [11]

$$T_i = \frac{T_s + T_\ell\sqrt{(k_\ell\rho_\ell C_\ell)/(k_s\rho_s C_s)}}{1 + \sqrt{(k_\ell\rho_\ell C_\ell)/(k_s\rho_s C_s)}} \qquad (1)$$

As shown in [12], the parabolic heat conduction equation is valid for time intervals longer than 10^{-12} seconds. Consequently, the interface temperature given by equation 1 is accurate after 10^{-12} secs and remains a valid representation until either thermal penetration of one slab occurs or vaporization is initiated at the interface. Vaporization can result from preferred sites (crevices, entrained gas bubbles, etc.) and/or spontaneously produced vapor embryos generated by density fluctuations in the liquid (spontaneous nucleation) which is highly temperature dependent [13]. However, the nucleation site density which can be produced by spontaneous nucleation is orders of magnitude larger than that characteristic of preferred sites (10^4 sites/cm^2 as reported in [14]), so that, if the necessary temperatures are established at the interface and within the thermal boundary layer to produce spontaneous nucleation, it will be the controlling phenomenon. In the time interval during which the thermal boundary layer is developed to sufficient depth to support a critical size vapor bubble [15, 16] (dia ~ 100 Å), equation 1 is an accurate representation of the contact temperature.

Since the copper and stainless steel surfaces have much larger values of thermal conductivity and density with respect to water and ethanol, the thermal transients in the metal surfaces produced by liquid-solid contacts are small, and the interface temperature is close to the measured bulk temperature. However, if significant oxidation of these surfaces occurs, the initially governing thermal physical properties at the solid interface would be those of the oxide layer. Under such conditions, the surface would experience significant thermal transients and the thermocouple within the plate, which would be insensitive to these transients, would not represent the surface temperature upon transition. In order to prevent excessive oxidation of the copper surface at the high temperatures required for the film boiling regime, the upper polished surface was plated with a 15-micron soft gold layer (99.96 percent pure). The similar thermal properties of gold and copper assure that the interface thermal behavior will not experience significant thermal transients during intimate liquid-solid contacts. In addition, experiments were conducted on both a plain stainless steel surface and a gold plated stainless steel plate. Gold plating of the steel surface was accomplished

Nomenclature

A = area
a = area ratio
C = specific heat
g = acceleration of gravity
h_{fg} = latent heat of vaporization
J = volumetric nucleation rate
k = thermal conductivity
k_1 = Boltzmann's constant
P = pressure
Q = energy transferred
q = energy transfer rate
R = electrical resistance
r = radius of a critical size cavity
T = temperature
t = time
V = battery potential
v = contact voltage
W = work required to form a nucleus $\frac{16\pi\sigma^3}{3(P_v - P_\ell)^2}$
α = thermal diffusivity
Δ = difference
λ_D = wavelength
ρ = density
σ = surface tension

Subscripts

c = contact
i = interface
ℓ = liquid
SAT = saturation
s = solid
v = vapor

by initially plating the surface with a 1 μm layer of chromium and then adding an 8 μm gold layer onto the chromium base. The comparative results enable the role of surface oxidation of the steel to be quantified. It also allows a comparison of the thermal stability of copper and stainless steel, independent of any possible differences in surface wetting characteristics (both are gold plated) which will effect spontaneous nucleation. The experiments were performed in an inert argon atmosphere and, as a final precaution, only reagent grade ethanol and triple distilled (quartz still) water were used as boiling liquids.

The plates were heated from below by a 660 W heater, and the wall temperature in each plate was measured by a grounded sheath thermocouple inserted from below to within 0.8 mm of the surface. In conducting these experiments, the dish was first heated to the desired temperature, then saturated liquid was poured onto the surface. The liquid-solid contacts during film boiling were detected by measuring the electrical conductance between the boiling liquid globule and the solid dish. Considerable care was taken in the calibration of these voltage probes in terms of the instantaneous area of contact between the boiling liquid and the solid surface, and while there is, perhaps, typically a factor of two uncertainty in the interpretation of contact area, order of magnitude behavior can be ascertained. A description of this calibration procedure is given in the Appendix. As illustrated in Fig. 1, the probes were inserted into the liquid to within 1.5 mm of the solid surface, and the voltage difference across a resistor was recorded by a memory oscilloscope. The relationship between the film boiling behavior and the voltage signals was examined by high-speed movies which simultaneously recorded the liquid behavior and the oscilloscope trace.

In the film boiling configuration, the oscillating liquid boundary and the solid wall provide a varying electrical capacitance which can confuse the interpretation of the temporal voltage signals. In order to ascertain the importance of such a varying capacitance on the voltage signals, the water electrical conductivity was varied by adding minute amounts of HNO_3 to the water. The additive will remain in the water during vaporization as opposed to being transferred to the vapor film. Consequently, no change would be expected in the voltage signals if a variable capacitance is the controlling phenomenon, but a large change would result if intimate contacts occurred. Large changes in the voltage output were indeed observed while the normalized signal shapes remained the same. Consequently, the contribution of varying capacitance was insignificant and the observed signals represent direct liquid-solid contact.

Experimental Results

Low Pressure. Intimate liquid-solid contacts in the film boiling regime, as discussed in [3], were postulated to result from the return of liquid toward the surface after the departure of a vapor bubble. As discussed above, in order to insure that such departure phenomena existed within the liquid globule, only liquid geometries with diameters greater than the fastest growing wave length [17] were considered in this experiment.

$$\lambda_D = 2\pi \left[\frac{3\sigma}{g(\rho_\ell - \rho_v)} \right]^{1/2} \tag{2}$$

For water at atmospheric pressure, the most dangerous wave length is 2.7 cm, which is in good agreement with the 3.0 cm average vapor dome spacing observed by Hosler and Westwater. [18] A similar spacing was also observed in the high speed movies of this study.

As proposed in [3], when a vapor bubble either breaks through the overlying liquid layer or detaches from the vapor film at the interface, the liquid collapses toward the solid and can produce direct liquid-solid contacts. In this investigation, the contact frequency was determined by allowing the memory oscilloscope to record all the contacts for a given interval, typically five seconds, and then divide the total by the time span. The water data demonstrated contact frequencies of 10–20 Hz for plate temperatures slightly greater than the minimum film boiling point. This is in good agreement with the bubble departure frequency observed on movies taken of these tests. However, as will be shown, these contacts were of very short duration (less than 10 m) and of little significance in the overall energy transfer. Similar measurements with ethanol show a contact frequency of 5–10 Hz, which was much less than the bubble rate for the size of the liquid mass used which was typically 6–9 cm in diameter. In contrast to the water data, the contacts in the vicinity of the minimum point demonstrate durations greater than 100 m, and these can be responsible for a significant fraction of the measured energy transfer. This is discussed in the section on energy transfer.

From the above discussion, it is not clear whether the contacts are directly induced by bubble departures, but contacts are definitely measured. In order to determine the relevance of these contacts in the film boiling regime, it is necessary to quantify their magnitude, frequency, and duration as a function of the wall, or interface, temperature. Fig. 2 shows typical contact signals, produced by ethanol in film boiling at one atmosphere on a gold plated copper surface, as a function of the interface temperature. There is a dependence of the contact behavior upon the interface temperature. As the interface temperature increases towards the homogeneous nucleation temperature of the ethanol, the magnitude and duration of the contacts are reduced to an insignificant level. At the temperature levels characteristic of nucleate, transition, and, in some cases, film boiling, the vapor formation results from preferred site nucleation (surface cavities, scratches, entrained gas bubbles, etc.), but in this elevated temperature region, nucleation can initiate within the liquid independent of these preferred sites. This spontaneous production of nucleation sites, which results from density fluctuations within the liquid, [13, 19] is strongly dependent upon temperature, and in the temperature range where such nucleation becomes significant, it is capable of producing nucleation site densities that are many orders of magnitude greater than those characteristics of preferred sites.

Spontaneous Nucleation Processes

Spontaneous nucleation can either be heterogeneous, i.e., the vapor cavities are formed by density fluctuations at the interface between the liquid and solid as a result of imperfect wetting, or homogeneous in which the nuclei are formed completely within the bulk of the liquid. The calculation of heterogeneous spontaneous nucleation rates requires a knowledge of the transient wetting behavior between the liquid and solid system on a microsecond time scale. Such experimental details are not presently available, but homogeneous nucleation rates per unit volume, which provide an upper bound on this spontaneous behavior, can be calculated by the expression

$$J = A_1(T) \exp\left(-\frac{W}{k_1 T}\right) \tag{3}$$

The pre-exponential term $A_1(T)$ contains the specific details of the molecular vaporization and condensation as summarized in [20]. Generally this term is of the order of 10^{33} when describing nucleation rates per cubic centimeter, but, as will be illustrated below, this quantity can be in error by several orders of magnitude without significantly changing the temperature at which spontaneous nucleation becomes significant. Homogeneous nucleation rates as a function of temperature are shown for ethanol and water in Tables 1 and 2, respectively, for a system pressure of 0.1 MPa. Homogeneous nucleation is of practical importance only if the temperature lies above the threshold value of approximately 195°C for ethanol and 305°C for water. However, if the temperature does lie above this value, the volumetric nucleation rate provided by density fluctuations is many orders of magnitude greater than that supplied from preferred sites. Consequently, one would then expect the energy transfer behavior to be dominated by the spontaneous nucleation behavior when the temperatures fall within this range. With such a dominant, high density nucleation mechanism, intimate liquid-solid contacts should experience an early termination as a result of the coalescence, through physical interference, of these small but numerous vapor cavities as proposed in [15]. The details of this coalescence involve nucleation site densities, thermal boundary layer development, and bubble growth characteristics, as have been quantified for liquid-liquid systems in [15]. As a result of this early termination, the liquid-solid contacts would provide an insignificant amount of energy transfer in comparison to the total energy transfer rate in film boiling at these

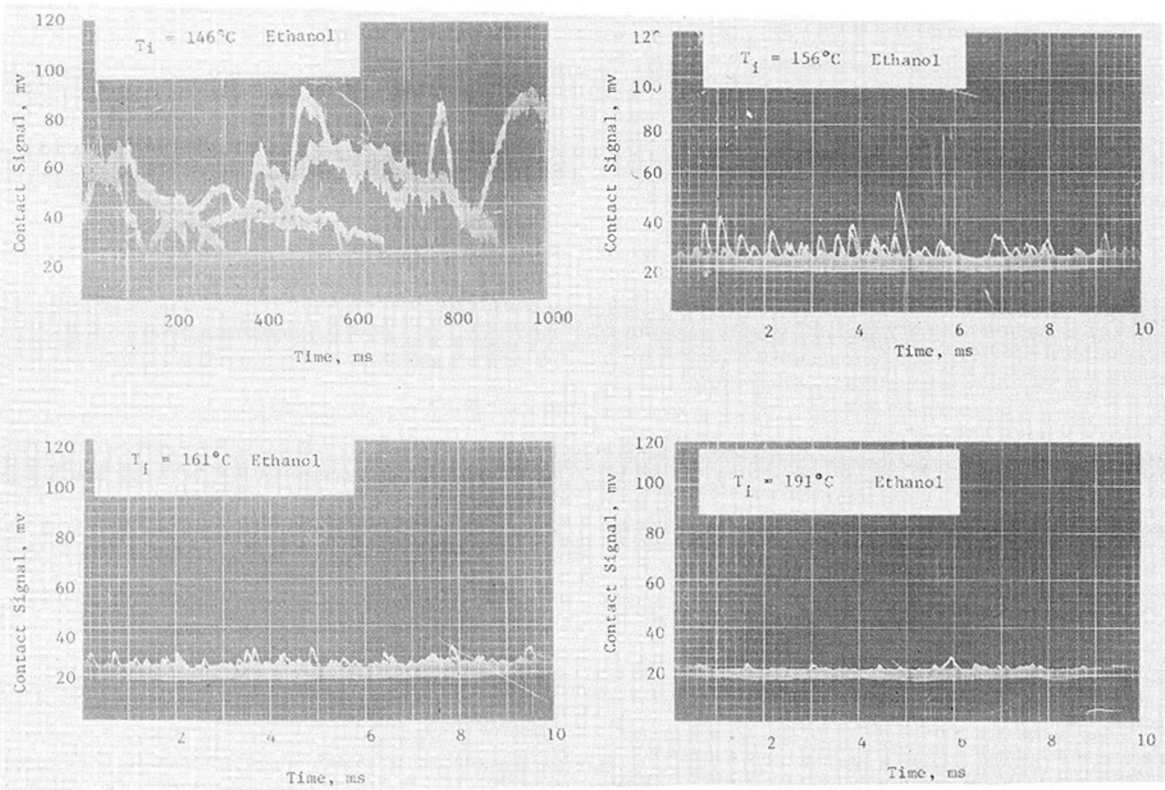

Fig. 2 Liquid-solid contacts of ethanol on a gold-plated copper surface at 0.1 MPa

Table 1 Homogeneous nucleation for ethanol

$P_\ell = 0.1$ MPa

T_ℓ °C	P_v MPa	σ N/M	r Å	J sites/cm³ s
170	1.58	0.0080	108.3	$<10^{-99}$
180	1.97	0.0067	72.0	3.3×10^{-69}
190	2.43	0.0055	47.0	3.6×10^{-2}
200	2.96	0.0043	29.8	3.0×10^{22}
210	3.58	0.0031	17.8	2.1×10^{30}

Table 2 Homogeneous nucleation for water

$P_\ell = 0.1$ MPa

T_ℓ °C	P_v MPa	σ N/M	r Å	J sites/cm³ s
290	7.44	0.0167	45.6	5.2×10^{-49}
300	8.59	0.0143	33.9	7.8×10^{-6}
310	9.87	0.0121	24.8	1.2×10^{16}
320	11.29	0.0099	17.7	1.1×10^{26}
330	12.86	0.0078	12.2	2.9×10^{30}

temperatures.

The spontaneous nucleation mechanism proposed herein is similar to the mechanism proposed by Spiegler, et al. [21] which was based upon a maximum liquid superheat as derived from a van der Waals equation of state. Such an approach gives values somewhat lower than the homogeneous nucleation limit and modifications have been proposed to account for differences with measured spontaneous nucleation temperatures. [22,23] However, this concept of a limiting liquid superheat does not describe (1) how the vapor is formed, (2) the role of surface wetting, and (3) the role of surface thermal properties. Minimum film boiling conditions have been obtained in poorly wetted systems, such as mercury on stainless steel [24] and water on surfaces coated with polyetrafluoroethylene and silicone grease, [14] with the wall temperature only slightly greater than saturation. This is due to the very low spontaneous nucleation temperature of a nonwetting system. For a completely nonwetted surface, spontaneous nucleation of the heterogeneous type is significant for any surface temperature above saturation. Consequently, while homogeneous nucleation is used for simplicity in this paper, real systems can be limited by spontaneous nucleation at considerably lower temperatures.

It is also noteworthy that the spontaneous nucleation minimum film boiling mechanism discussed herein is identical to that proposed for liquid-liquid systems. [15, 16, 25] A heated liquid surface has no interface imperfections (cracks or crevices) to act as preferred sites. Consequently, when the interface temperature upon contact is less than the value required for spontaneous nucleation sites there are no preferred sites to provide the vapor required for levitation of the liquid phase.

Elevated Pressure Results

One effective means of demonstrating the contribution of spontaneous nucleation in establishing film boiling is to measure the minimum film boiling temperatures and liquid-solid contacts at elevated pressures. Such experiments provide a very accurate measurement of the minimum point by two different techniques. In this study, the *minimum film boiling point was determined* by an increase in the rate of surface cooling as the wall temperature decreased and by visual observations as well. For the stainless steel surface, there was little uncertainty or difference in these observations.

Fig. 3 compares the minimum film boiling predictions of the Taylor instability models of Berenson [17] and Henry [3] and the limiting superheat models of Speigler [21] and Baumeister and Simon [8] with the experimental results for water on both stainless steel plates. The experimental results do not agree with each other or any of the analytical models referenced above over the entire pressure range investigated.

The stainless steel plates demonstrated a very marked transition from the film boiling regime in terms of both cooling rate and intimate liquid-solid contacts. When the surface temperature was greater than the minimum point values shown in Fig. 3, intimate contacts were essentially nonexistent similar to the ethanol data shown in Fig. 2. The first significant contact resulted in an immediate shift to tran-

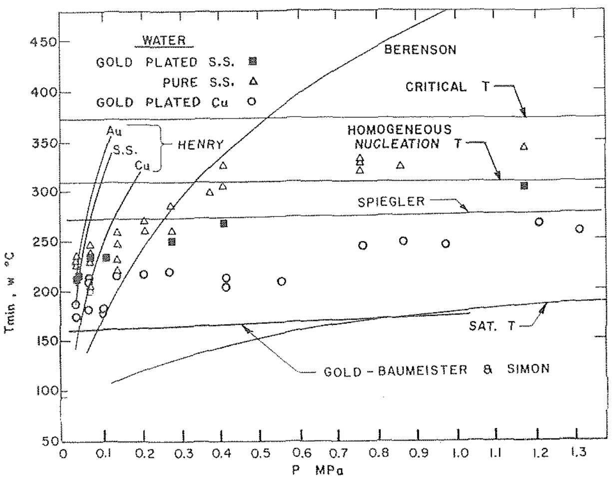

Fig. 3 Measured film boiling wall temperatures for water on various surfaces

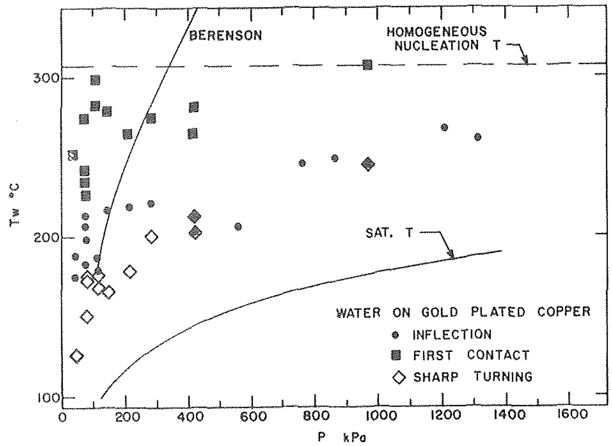

Fig. 4 Temperature for initial contact in minimum film boiling for water on a gold-plated copper surface

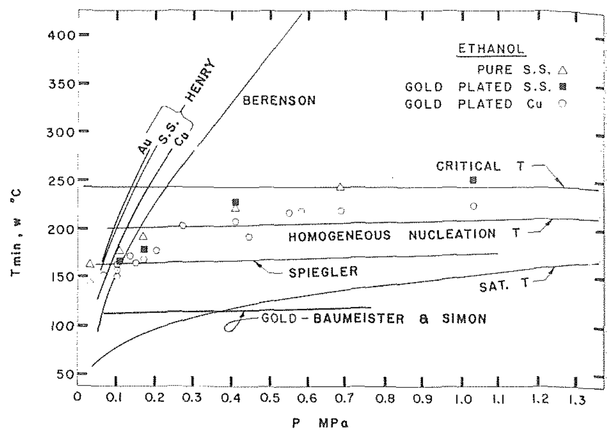

Fig. 5 Measured minimum film boiling wall temperatures for ethanol and various surfaces

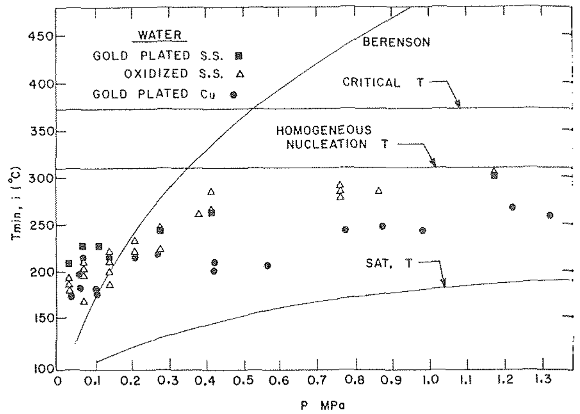

Fig. 6 Contact interface temperature at the minimum film boiling point for water

sition boiling and an increase in the contact signal to a level closely approaching complete contact. The gold plated copper surface demonstrated a significantly different behavior and, as shown in Fig. 4, considerably lower minimum film boiling temperatures. When the temperature of the copper surface was well above the homogeneous nucleation temperature, no significant contacts were observed. As illustrated in Fig. 4, when the surface temperature was in the near vicinity of this value, intimate liquid-solid contacts were observed, but the instantaneous cooling rate and visual observation both indicated that the system was in the film boiling regime, i.e., the cooling rate was decreasing as the surface cooled and the liquid mass appeared to float on the surface. At a lower temperature, the cooling rate began to increase slightly as evidenced by an inflection in the temperature versus time cooling curve. This point should closely correspond to the minimum heat flux condition, but the liquid still gave the appearance of being levitated over the surface. Finally, at the temperatures shown in Fig. 3, the cooling rate increased sharply (sharp turning of the cooling curve) and visual observation confirmed that the liquid mass was no longer levitated over the solid surface. The temperatures at which these three observations were recorded are shown in Fig. 4.

The hydrodynamic model proposed by Berenson [17] is independent of the heater surface properties and consequently there is only one prediction in Fig. 3 for all the surfaces used. Henry [3] proposed a modification to Berenson's hydrodynamic model which resulted in a correlation for the thermal stability of the wall during instantaneous contacts and microlayer evaporation. At the elevated pressures, the predictions of these hydrodynamic models are far greater than the measured values. If, as observed in this study, significant liquid-solid contacts do not occur when the wall temperature is considerably above the homogeneous nucleation limit, then the microlayer considerations of [3] would certainly not be valid. When the wall temperature decreases to the level where intimate contacts occur, such considerations are valid, but the large discrepancy between the copper-water prediction of [3] and the high pressure data indicate that the current understanding is unsatisfactory.

The foam limit model proposed by Speigler, et al. [21] is also independent of surface properties and predicts minimum film boiling temperatures that are considerably less than the measured stainless steel data and greater than that of the gold platter copper surface. This model was modified for heated surface properties by Baumeister and Simon [8], and their prediction for a gold surface is also shown in Fig. 3. This prediction is unrealistic at higher pressures since it is less than the saturation temperature.

A similar comparison of measured minimum film boiling temperatures for ethanol on various surfaces is shown in Fig. 5 along with the predictions discussed above. Again none of these analytical formulations provide reasonable predictions at elevated pressures.

For temperature ranges where spontaneous nucleation rates far exceed the preferred site density, the temperature of greatest interest in determining the propensity for film boiling is the interface temperature upon contact (equation (1)) and not the wall temperature far removed from the interface. Fig. 6 compares the experimental results from the two stainless steel dishes in terms of the interface temperature upon contact. The interface temperatures of the plain stainless steel surface are based on the properties of chromium oxide, which is the protective oxide that stainless steel forms even in the inert environment employed in this study. (Both boiling liquids contain oxygen, and the argon also contains some impurities.) For the microsecond or less time scales of interest in developing a vapor film from spontaneous nucleation, an oxide layer of 1 μm will appear to be a semi-infinite slab. For the gold plated surface, an 11 μm layer would appear to be semi-infinite in this time frame, and since the 8 μm layer approaches this thickness, the interface temperature was evaluated from the thermophysical properties of gold. The contact interface temperature provides a remarkable correlation for the two surface conditions. At elevated pressures, the interface temperatures representative of the minimum film boiling conditions closely approach the homogeneous nucleation temperature limit. At lower pressures, the interface temperatures at transition are lower than the homogeneous value but certainly in the range of measured spontaneous nucleation temperatures for water. [20]

The interface temperatures for copper is in good agreement with the stainless steel data at lower pressures, but at the elevated pressures, the copper results are consistently lower. This may indicate that the different base surfaces are limited by the same mechanism for near atmospheric pressures, but different mechanisms at elevated pressures. Future experiments and analyses will concentrate on this region.

The interface temperature representation is shown for ethanol in Fig. 7. Again very good agreement is observed between the two steel plates when the minimum film boiling point is correlated on contact interface temperature. For the stainless steel surfaces at high pressures, the first contact corresponds to transition. The gold plated copper surface did not exhibit a definite characteristic at these elevated pressures and the measured minimum film boiling temperatures are consistently less than those measured with the stainless steel surfaces. For some of the copper data shown in Fig. 7, the first contact and the onset of transition boiling occurred simultaneously, but for other tests, under similar conditions, persistent contacts began about 20–30°C above the minimum film boiling point. Consequently, while the stainless steel-ethanol system is governed by nucleation characteristics at elevated pressures, the governing mechanism for the copper surface is not as straightforward. In fact, the system appears to be very close to a boundary separating nucleation and hydrodynamic dominated behaviors. This is to be expected since the measured temperatures for stainless steel and copper are in close agreement as opposed to the elevated pressure measurements with water on the same surfaces. At the lower pressures, both the stainless steel and copper surfaces were determined by the hydrodynamic instability behavior of the ethanol as will be illustrated in the next section.

Energy Transfer Behavior

The minimum film boiling point on these horizontal solid surfaces appears to be limited by either hydrodynamic instability or spontaneous nucleation upon contact, where the controlling mechanism is the one which is stable at the lowest wall temperature. Consequently, cryogenic fluids, which typically have a comparatively small temperature difference between their normal boiling points and thermodynamic critical temperatures, are usually limited by nucleation dynamics. Conversely, the minimum film boiling of liquid metals on a horizontal solid surface is generally limited by hydrodynamic instability. However, if the liquid metal is an extremely poor wetting liquid such as mercury, spontaneous nucleation can occur at temperatures approaching local saturation, and film boiling can be governed by nucleation characteristics. If hydrodynamic instability is the controlling mechanism, sufficient and continuously available preferred nucleation sites must be present to sustain the vapor flow required to prevent the liquid from returning to the surface completely. This is the major difference between solid-liquid and liquid-liquid systems, i.e., the former has such sites with surface cracks and crevices whereas the latter does not.

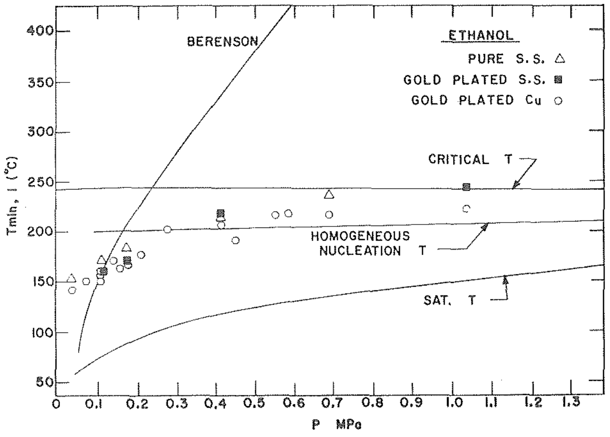

Fig. 7 Contact interface temperatures at the minimum film boiling point for ethanol

Estimates of the energy transfer to the liquid as a result of direct contacts can be made from simple conduction theory since the voltage probes provide measurements of contact area and duration. Assuming that the contact duration is sufficiently short so that both the liquid and the solid behave as semi-infinite slabs, with no nucleation within the liquid, the interface temperature upon contact is given by equation (1), and the energy transfer, which can be evaluated from the standard error function solution, is given by

$$Q_{1\ \min} = 2k_sA_c\sqrt{\frac{\Delta t}{\pi\alpha_s}}\,(T_s - T_i) \tag{4}$$

This represents the minimum energy transferred during a contact since the interface behavior is determined by conduction alone. If significant nucleation was experienced at the interface, the interfacial temperature could be considerably less than the value given by equation 1. The lower limit of the surface temperature would be the local saturation value, which would result in the maximum amount of energy transfer during a contact:

$$Q_{1\ \max} = 2k_sA_c\sqrt{\frac{\Delta t}{\pi\alpha_s}}\,(T_s - T_{\mathrm{SAT}}) \tag{5}$$

These limiting values of transient conduction heat transfer can be used to determine the importance of liquid-solid contacts in the overall energy transfer process.

The contacts were recorded on both the memory oscilloscope and FM tape. The contacts for wall temperatures in the near vicinity of, but greater than, the minimum film boiling point were evaluated for area and duration. From these measurements the energy transferred by direct contact was evaluated according to the two limiting boundary conditions discussed above. This value was divided by the time interval over which the contacts were summed (typically 10–100 s) and divided by the average area of the liquid mass to obtain an average heat flux resulting from the intimate contacts. In addition, an average heat flux to the liquid was evaluated from movies by measuring the change in projected area over a given time interval as discussed in [2].

The measured contact areas and durations are illustrated in Figs. 8 and 9 for ethanol and water, respectively. One very significant difference is immediately apparent between the two liquids. In the vicinity of the minimum film boiling point, the measured contact areas for ethanol are the same order of magnitude as the vapor dome area ($\lambda_D{}^2/2$), but for water the measured areas are an order of magnitude smaller. However, as the interface temperature approaches the homogeneous nucleation temperature, the contact areas of both liquids decrease dramatically. The contact durations for ethanol decrease by two orders of magnitude as the interface temperature approaches the homogeneous nucleation value. The water data demonstrates a significant change in the 1–10 ms contacts for temperatures approaching the homogeneous nucleation value. However, there are signals of less than a millisecond duration which are essentially independent of temperature. These may be actual contacts or they may be very local electrical discharges resulting from the high temperatures and the d-c circuitry. These are of no significance in the energy transfer, but they are included for the reader's reference.

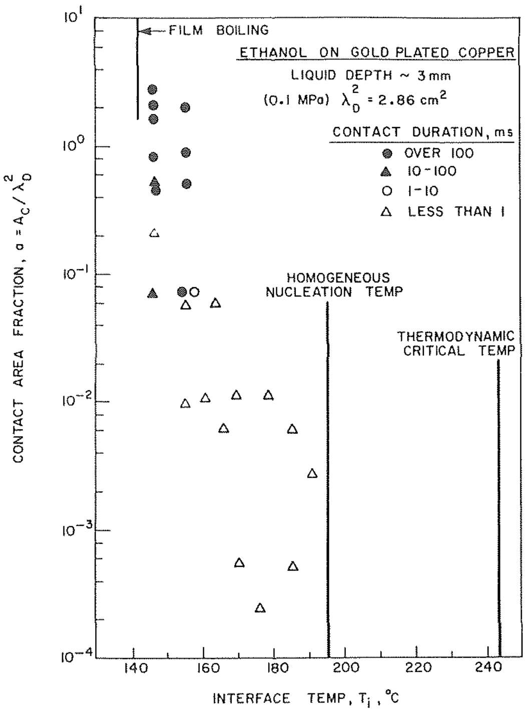

Fig. 8 **Measured contact areas as a function of interface temperature for ethanol on a gold-plated copper surface**

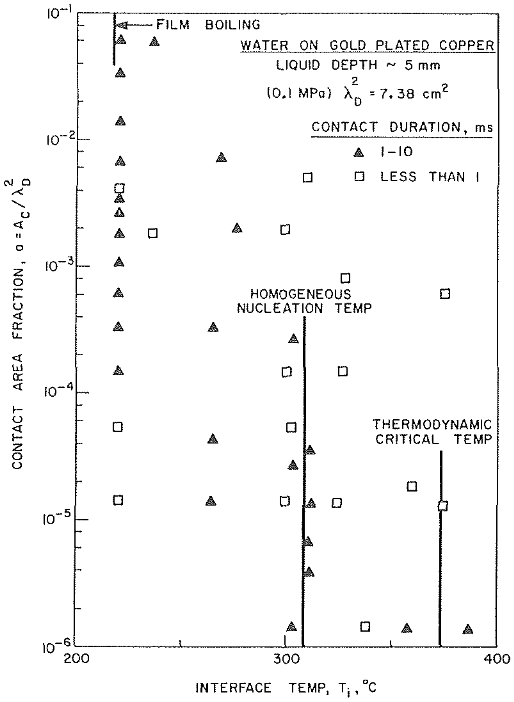

Fig. 9 **Measured contact areas as a function of interface temperature for water on a gold-plated copper surface**

The large variations shown in Figs. 8 and 9 are characteristic of the contact behavior, and do not represent experimental scatter in the true sense of the word. However, the most interesting aspect of the contact measurements is their importance in the overall energy transfer. As discussed above, the energy transfer for the interface and saturation temperature boundary conditions was summed over a given time interval and then cast in the form of an average heat flux over this interval. These calculations were made for conditions in the near vicinity of the minimum film boiling point at atmospheric pressure, and they are compared to the average heat fluxes from this and other experimental studies in Table 3. The measured minimum film boiling heat fluxes from this study are in good agreement with those measured in previous investigations [2, 18] as well as with the analytical prediction of Zuber [26] which is given by

$$\frac{q}{A} = \frac{\pi}{24} h_{fg} \rho_v \left[\frac{\sigma g (\rho_\ell - \rho_v)}{(\rho_\ell + \rho_v)} \right]^{1/4} \tag{6}$$

This comparison illustrates that the bounding calculations for the energy transferred via intimate contacts with ethanol bracket the measured minimum heat flux value, and could be the mechanism by which essentially all the energy is transferred. This is in marked contrast to the water data in which the maximum contribution is less than 20 percent of the measured heat flux. Consequently, the data indicate that the limiting mechanisms for ethanol and water at atmospheric pressure may be quite different, i.e., the ethanol appears to have a hydrodynamic limitation while the water is ostensively limited by spontaneous nucleation.

Table 3 Minimum film boiling heat fluxes

Ethanol	Water
(Experimental)	
2.0 W/cm^2—Henry, et al.	3.46 W/cm^2—Hosler and Westwater
1.7 W/cm^2—this study	3.0 W/cm^2—Henry, et al. 2.9 W/cm^2—this study
(Analytical)	
2.3 W/cm^2—Zuber	2.7 W/cm^2—Zuber
(Contact heat transfer)	
0.1 W/cm^2—interface temperature	0.02 W/cm^2—interface temperature
7.5 W/cm^2—saturation temperature	0.5 W/cm^2—saturation temperature

Conclusions

The following conclusions can be made from this study.

1 The minimum film boiling point for pool boiling on a horizontal surface can be determined either by a Taylor instability vapor removal limitation or by spontaneous nucleation upon contact. The governing mechanism is the one which is stable at the lowest wall temperature.

2 When the system is controlled by the Taylor instability, significant liquid-solid contacts are measured in the film boiling regime. For ethanol at atmospheric pressure, the transient heat conducted during these contacts can equal the total energy transferred at the minimum point. As the surface temperature is increased above the minimum point, the energy transferred by direct contact is dramatically decreased.

3 If spontaneous nucleation upon contact is the controlling mechanism, no thermally significant contacts are measured for wall temperatures above the minimum value. For systems with such a limitation, the first major contact, which occurs when the contact interface temperature drops below the level required for spontaneous nucleation, results in quenching of the surface.

Acknowledgments

The authors woul like to thank Messrs. Jeff Gabor and Bruce Hardy for their help in both the execution of the experiments and the interpretation of the data.

References

1 Bradfield, W S., "Liquid-Solid Contact in Stable Film Boiling," *I & EC Fundamentals*, Vol. 5, No. 2, May 1966, pp 200–204.

2 Henry, R. E., Quinn, D. J., and Spleha, E. A., "An Experimental Study of the Minimum Film Boiling Point for Liquid-Liquid Systems," Fifth Intl. Heat Transfer Conf., Tokyo, Japan, Sept. 3–7, 1974.

3 Henry, R. E., "A Correlation for the Minimum Film Boiling Temperature," *AIChE Sym.* Series No. 138, Vol. 70, 1974, pp 81–90.

4 Swanson, J. L., Bowman, H. F., and Smith, J. L., Jr., "Transient Surface Temperature Behavior in the Film Boiling Region," *Trans. of the CSME*, Vol. 3, 1975, pp 131–140.

5 Iloeje, O. E., Rohsenow, W. M., and Griffith, P., "Three-Step Model of

Dispersed Flow Heat Transfer (Post CHF Vertical Flow)," ASME Paper No. 75-WA/HT-1.

6 Baumeister, K. J., and Hendricks, R. C., "Metastable Leidenfrost States," NASA TN D-3226, April 1966.

7 Baumeister, K. J., Simon, F. F., and Henry, R. E., "Role of the Surface in the Measurement of the Leidenfrost Temperature," ASME Symposium, Augmentation of Convective Heat and Mass Transfer, ASME Winter Annual Meeting, New York, 1970.

8 Baumeister, K. J., and Simon, F. F., "Leidenfrost Temperature-Its Correlation for Liquid Metals, Cryogens, Hydrocarbons, and Water," ASME JOURNAL OF HEAT TRANSFER, Vol. 95, May 1973, pp 166–173.

9 Moreaux, F., Chevrier, J. C., and Beck, G., "Destabilization of Film Boiling by Means of a Thermal Resistance," *Intl. Journal of Multiphase Flow,* Vol. 2, 1975, pp 183–190.

10 Zhukov, U. M., Kazakov, G. M., Kovalev, S. A., and Kuzma-Kitcha, Yu. A., "Heat Transfer in Boiling of Liquids on Surfaces Coated With Low Thermal Conductivity Films," *Heat Transfer—Soviet Research,* Vol. 7, No. 3 May–June 1975, pp 16–26.

11 Carslaw, H., and Jaeger, J., *Conduction of Heat in Solids,* 2nd Edition, Oxford, Clarendon Press, 1959.

12 Baumeister, K. J., and Hamill, T. D., "Hyperbolic Heat-Conduction Equation-A Solution for the Semi-Infinite Body Problem," ASME JOURNAL OF HEAT TRANSFER, Vol. 91, 1969, p 543.

13 Skripov, V. P., *Metastable Liquids,* Halstead Press, Jerusalem, Israel 1974.

14 Gaertner, R. F., "Photographic Study of Nucleate Pool Boiling on a Horizontal Surface," ASME JOURNAL OF HEAT TRANSFER, Vol. 87, Feb. 1965, pp 17–29.

15 Henry, R. E., and Fauske, H. K., "Energetics of VaporExplosions," ASME Paper No. 75-HT-66.

16 Henry, R. E., and Fauske, H. K., "Nucleation Characteristics in Physical Explosions," *Proc. of the Third Specialists Meeting on Sodium/Fuel Interaction in Fast Reactors,"* PNC N251 76-12, 2, 1976, pp 595–622.

17 Berenson, P. J., "Film Boiling Heat Transfer From a Horizontal Surface," ASME JOURNAL OF HEAT TRANSFER, Vol. 83, Aug. 1961, pp 351–358.

18 Hosler, E. R., and Westwater, J. W., "Film Boiling on a Horizontal Plate," *ARS Journal,* April 1962, pp 553–558.

19 Blander, M., and Katz, J. L., "Bubble Nucleation Liquids," *AIChE Journal,* Vol. 21, Sept. 1975, pp 833–848.

20 Apfel, R. E., "Vapor Cavity Formation in Liquids," Technical Memorandum No. 62, Acoustic Research Laboratory, Harvard University, Cambridge, Ma, Feb. 1970.

21 Spiegler, P., Hopenfeld, J., Silberberg, M., Bumpus, C. F., Jr., and Norman, A., "Onset of Stable Film Boiling and the Foam Limit," Intl. Journal of Heat and Mass Transfer, Vol. *6,* 1963, pp 987–994.

22 Eberhart, J. G., "The Thermodynamic and the Kinetic Limits of Superheat of a Liquid," Paper presented at Sym. on Fund. Research in Interfacial Phen., 78th Natl. AIChE Mtg., Salt Lake City, Utah, Aug. 1974.

23 Eberhart, J., "The Thermodynamic Limit of Superheat of Sodium," *Trans. ANS,* Vol. 18, 1974, pp 202–203.

24 Lyon, R. E., Foust, A. S., and Katz, D. L., "Boiling Heat Transfer With Liquid Metals," *Chem. Eng. Prog. Sym. Series,* Vol. 51, 1955, pp 41–47.

25 Fauske, H. K., "Some Aspects of Liquid-Liquid Heat Transfer and Explosive Boiling," *Proc. Fast Reactor Safety Meeting,* Beverly Hills, Ca, CONF-740401-P2, April 1974, pp 992–1005.

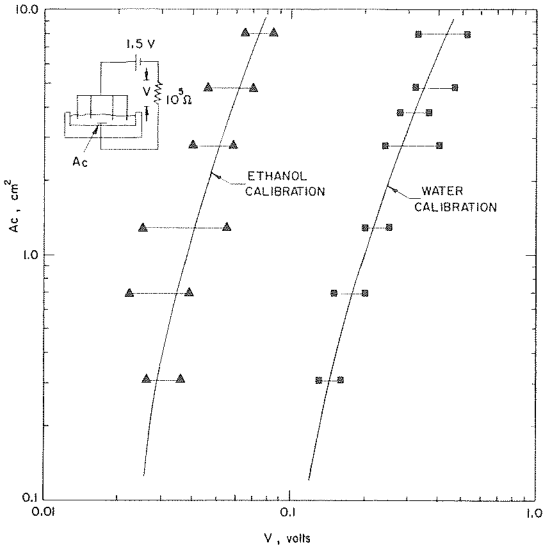

Fig. A1 Calibration of contact area and measured voltage for ethanol and water

26 Zuber, N., "On the Stability of Boiling Transfer," *Trans. ASME,* Vol. 80, April 1958, pp 711–715.

APPENDIX

Calibration of the Conductance Probes

In order to provide estimates of the contact areas, the probes were calibrated for voltage output as a function of this area. The probe tree, which was made up of six probes on each of four arms, was calibrated by measuring the voltage produced across a 100K Ω resistor by a given contact area. These areas were represented by various size copper electrodes in the base of a lucite dish which was filled with either water or ethanol, and the calibration points are shown in Fig. A.1 for both test liquids. The dependence upon angular position was investigated by rotating the lucite dish with respect to the probe tree and the error bands shown in Fig. A.1 represent these variations. Such measurements show that there can be a factor of two changes in the output voltage with the location of the contact.

The lines through the experimental data are the calibrations used to interpret the measured contacts, and thus, to provide the estimates of the energy transfer by the intimate liquid-solid contacts.

H. C. Ünal

Central Technical Institute TNO,
P.O. Box 342
Apeldoorn, The Netherlands

Determination of Void Fraction, Incipient Point of Boiling, and Initial Point of Net Vapor Generation in Sodium-Heated Helically Coiled Steam Generator Tubes

Void fraction was measured with high-speed photography in a 26.7 m and a 40.1 m long, sodium-heated helically coiled steam generator tube of 0.018 m ID. The ratio of coil diameter to tube diameter was 38.9. The operating conditions for the tests were as follows: Pressure: 4–18 MN/m^2, mass velocity: 429–1518 kg/m^{2}s, heat flux: 0.013–0.42 MW/m^2, outlet subcooling: 0.3–12.5 K, outlet steam quality: 0.000032–0.075. For vapor volumetric rate ratios greater than 0.4, the so-called distribution parameter is not affected by centrifugal forces, and is equal to 0.875. For vapor volumetric rate ratios smaller than 0.4, this parameter is affected by centrifugal forces and the aforesaid ratio. The incipient point of boiling and initial point of net vapor generation were determined with high-speed photography in the aforementioned 26.7 m long helical coil for the following range of operating conditions: Pressure: 4–18 MN/m^2, mass velocity 757–1518 kg/m^{2}s, heat flux: 0.082–0.413 MW/m^2, outlet subcooling: 4.4–12.5 K. The data were correlated by using both the average and local values of the operating conditions.

Introduction

Void fraction is of importance in determining pressure losses and instability conditions in steam generating equipment. The Incipient Point of Boiling (IPB) is the point in a boiling channel where the first bubble forms and gets detached from the heated surface. The Initial Point of Net Vapor Generation (IPNVG) is the point in a boiling channel where the activation of a significant number of nucleation centers takes place. At this point void fraction also rises suddenly. IPB and IPNVG are of importance not only for understanding boiling phenomena, but also for evaluating void fraction, instability conditions and heat transfer surfaces in steam generators.

The present paper reports the results of the experiments carried out to determine the void fraction, the IPB and the IPNVG in a sodium heated helical coil with $D_c/d = 38.9$. The experiments model the subcooled nucleate flow boiling region of a sodium heated steam generator. In the aforesaid type of boiling, the liquid bulk temperature is below the saturation temperature. A high-speed photographic technique is used to determine the void fraction, the IPB and the IPNVG.

To the knowledge of the author no literature exists on void fraction for the flow boiling of water at elevated pressures in helical coils. Data for void fraction for the adiabatic flow of gas/liquid mixtures in helical coils are given in [1–5].[1] Most of these works deal with the flow of air/water mixtures. Rippel, et al. [1] measured void fraction for the concurrent downflow of air/water, helium/water, Freon-12/water, air/2-propanal mixtures through a coil with $D_c/d = 19.9$. With the exception of high values of void fraction, the results of their air/water tests fit the correlation of Lockhart and Martinelli well [6]. This correlation is based on data obtained in horizontal tubes. Banerjee, et al. [2] also reported that the data for void fraction obtained for a wide range of fluids and coil diameters fit the aforesaid correlation well. The air/water data of Boyce, et al. [3] taken in a coil with $D_c/d = 48$ were also correlated with the aforesaid correlation. Akagawa, et al. [4] measured void fraction for the flow of air/water mixtures in two helical coils with $D_c/d = 11$ and 22.7. They correlated the data for $0.18 \leq \beta \leq 0.95$ with the equation given below

$$\beta/\alpha = 1.2 \tag{1}$$

where

Contributed by the Heat Transfer Division for publication in the JOURNAL OF HEAT TRANSFER. Manuscript received by the Heat Transfer Division August 12, 1977.

---

[1] Numbers in brackets designate References at end of paper.

$$\beta = \frac{Q_v}{Q_v + Q_L} = \frac{X}{X + (1 - X)(\rho_v/\rho_L)} \tag{2}$$

The data of the last mentioned authors do not fit the correlation of Lockhart and Martinelli well. Kasturi and Stepanek [5] obtained data for void fraction for two-phase cocurrent flows of different gas and liquid mixtures in a helical coil with $D_c/d = 53.2$, and compared the data with the correlation of Hughmark [7]. The data do not fit this correlation well.

It can be shown that the void fraction data of Rippel, et al. [1], Boyce, et al. [3], and Akagawa, et al. [4] for the flow of air/water mixtures in helical coils can be correlated within ten percent accuracy with the following equation

$$\beta/\alpha = C \tag{3}$$

where $C = 1.12$. For these data $0.18 \le \beta \le 0.99$ and $11 \le D_c/d \le 48$, and C, the so-called distribution parameter, is not affected by centrifugal forces.

It is worthwhile mentioning that for the flow of air/water mixtures in horizontal tubes the value of the distribution parameter is reported to be 1.2 [8] and 1.27 [9-10] for $0.3 \le \beta \le 0.9$. It follows from the above that for the flow of air/water mixtures the distribution parameter in horizontal tubes is greater than the distribution parameter in helical coils.

Due to the complex nature of two-phase flow in helical coils, results of the experiments given in [1-5] for the flow of gas/liquid mixtures can not be extrapolated to the flow boiling of water at elevated pressures. In the latter case, vapor velocity and radial accelerations are much lower than those in an atmospheric gas/liquid system.

A velocity field which is useful for characterizing the flow of a two-phase mixture is given in [11]

$$V_v/J = C + V_d/J \tag{4}$$

where

$$J = G(X/\rho_v + (1 - X)/\rho_L) \tag{5}$$

In order to determine the void fraction, equation (4) can be written in a different form [11]

$$\beta/\alpha = C + V_d/J \tag{6}$$

For horizontal pipes or for helical coils with small helix angle equations (4) and (6) reduce to

$$V_v/J = C = \beta/\alpha \tag{7}$$

since V_d, the drift velocity is zero or negligibly small. It follows from equation (7) that for the determination of void fraction it is sufficient to measure V_v, the weighted mean velocity of the vapor phase, since J and β in equation (7) can be predicted from the known operating conditions. In the present work, the aforesaid velocity was determined by the use of a high-speed photographic technique.

The validation of this technique for the determination of void fraction is given in [12-13] and outlined below. For vertical channels and for high pressures and mass velocities, equation (4) reduces to equation (7), since $V_d/J \ll 1$ and $C \approx 1$. In the study reported in [12], first the value of C was determined by the use of the photographic technique described in the present paper and the equation ($V_v/J = C$) for the subcooled nucleate flow boiling of water in a 10 m long vertical tube. In this study pressure varied between 4.1 and 15.9 MN/m^2 and steam quality was up to 2.9 percent. The number of data was 42. Subsequently the equation ($C = \beta/\alpha$) was compared with extensive data of various investigators taken for the saturated bulk boiling of water and for the flow of steam/water mixtures without heat addition in vertical circular tubes, annuli and rectangular channels. For these data $V_d/J \ll 1$ and the number of data was 497. The range of operating conditions and geometries for the data was: Pressure: 2-13.8 MN/m^2; mass velocity: 388-3504 kg/m^{2}s; steam quality: 0-88 percent; void fraction: 0-99 percent; heat flux: adiabatic and 0.01-2.0 MW/m^2; hydraulic diameter: 4.7-34.3 mm. The equation ($C = \beta/\alpha$) fitted the aforesaid data accurately to 12.5 percent.

To the knowledge of the author, no literature exists on data for the IPB and IPNVG in helical coils. For the subcooled nucleate flow boiling of water in vertical channels, the determination of the IPB is given in [12, 14-16] and that of the IPNVG in [17-21]. It is shown in [12, 21] that the ratio of the heat flux due to suppressed forced convection to the total heat flux (i.e. $h\Delta T_{\text{sub}}/q$) is constant at the IPB and the IPNVG for a wide range of operating conditions in vertical channels.

Experimental Apparatus and Procedure

The photographical test section was an adiabatic, square sapphire channel of 0.016 × 0.016 × 0.02 m. The wall thickness of the channel was 0.003 m. This test section was mounted at the end of a 26.7 m long test tube (i.e., 12 coils) of 0.018 m ID and of 0.026 m OD. A 0.058 m long transition piece was mounted between the photographical test section and the test tube. The cross-sectional area along the whole length of this piece was practically equal to the cross-sectional area of the test tube and of the photographical test section. This transition piece was perfectly insulated. The subcoolings used in the present study were low. It was therefore assumed that the bubbles (or plugs) did not collapse along this transition piece. This assumption was verified by measuring the bubble (or plug) diameters along the photographical test section. These diameters were approximately constant.

The test tube was manufactured from stainless steel-316 and was placed concentrically in an other helical coil of 0.049 m ID. The above described test-set-up was installed in a heat transfer loop, which is

Nomenclature

A = cross-sectional area (m^2)
B = volume of photographical test section (m^3)
C = distribution parameter
D = equivalent bubble or plug diameter (m)
D_c = mean coil diameter (m)
d = tube internal diameter (m)
e = total number of plugs and bubbles in test section
Fr = Froude number ($G^2/D_c\rho_L{}^2g$)
f = number of bubbles in a sample
G = mass velocity (kg/m^{2}s)
g = acceleration of gravity (m/s^2)
h = single-phase forced convection heat transfer coefficient (W/m^{2}K)
J = average volumetric flux density of a two-phase mixture (m/s)
K, K_1 = dimensionless constants
m = number of axial positions
Nu = Nusselt number
P = pressure (N/m^2)
Pr = Prandtl number
Q = volumetric flow rate (m^3/s)
q = heat flux (W/m^2)
Re = Reynolds number
ΔT = difference between sodium and water/steam side temperature at exit of test tube (K)
ΔT_{sub} = subcooling on water/steam side (K)
V = instantaneous bubble or plug velocity (m/s)
V_d = weighted mean drift velocity (m/s)
V_v = weighted mean velocity of vapor phase (m/s)
X = steam quality
x, y, and z = Cartesian coordinates (m)
α = void fraction, average over cross-section
β = vapor volumetric rate ratio
ρ = density (kg/m^3)

Subscripts

a = refers to average over the periphery of a helical coil
b = refers to bulk condition
I = refers to inside position in a helical coil
L = refers to liquid phase
v = refers to vapor phase

described in detail elsewhere [12, 22]. The flow in the sodium side was downwards in the annulus between the aforesaid helical coils. The flow orientation in the test tube (i.e., water/steam side) was upwards. The helix angle was 8 deg 50″.

The test tube was very heavily instrumented. It will be sufficient to mention here that values of inlet and outlet temperature, temperature at the beginning of the last coil, and pressure and mass flow at both the sodium and water/steam side were measured with precalibrated instruments, collected on an on-line data acquisition system and processed by a computer-system, Hewlett Packard-2216B. Water/steam-side temperatures were measured with inconel sheathed, chromel-alumel thermocouples of 1 mm OD and the maximum error in determining the temperature was 1.2 K. Both water/steam-side and sodium-side mass flows were measured with turbine flowmeters, which had errors less than one percent. Water/steam-side outlet pressure was measured with a dead-weight balance manometer, which had an error of 0.03 MN/m^2.

During the tests demineralized water was used with an oxygen content less than 15 ppb, with a conductivity less than 0.5 μS/cm and with a pH between 8.5 and 9.

For some void fraction experiments (i.e., $\beta > 0.12$), a 40.1 m long test tube (i.e., 18 coils) instead of the above-described test tube was used. The bore and wall thickness of the latter were equal to those of the first test tube.

The pictures of boiling were taken in two dimensions perpendicular to the direction of flow through the sapphire test section with a high-speed rotating prism camera (Hycam Model, 120 m) at a frequency of 10,000 frames per second. The schematic description of the optical system used is given in Fig. 1. This system permits following a particle on a developed film in three dimensions as illustrated in Fig. 2. A particle at the location A (x, y, z) on the $(x - y)$ plane in the sapphire channel is shown on a developed film. The three coordinates of the particle and the $(x - z)$ and $(y - z)$ planes are also indicated in the figure. The position of the sapphire channel with respect to the test tube is also shown in the figure.

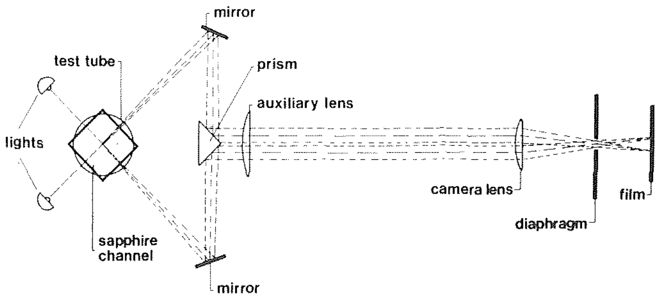

Fig. 1 Schematic description of the optical system used

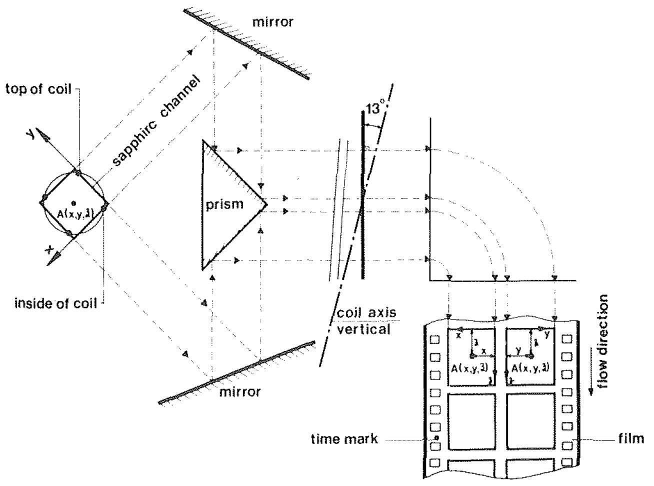

Fig. 2 System of coordinates

During the experiments, subcooling at the end of the test tube was slowly decreased, while pressure, heat flux and mass velocity were kept constant. It took half an hour to reach steady state conditions, after which photographs were taken.

Void Fraction

In total 44 runs were analyzed. In these runs bubble and plug flow regimes were observed and the range of operating conditions was: $P = 4–18$ MN/m^2; $G = 429–1518$ kg/m^2s; $q = 0.013–0.42$ MW/m^2 (average heat flux for last coil); $\Delta T_{sub} = 0.3–12.5$ K; $X = 0.000032–0.0753$; $\beta = 0.00018–0.579$; $V_v = 0.817–3.48$ m/s. After developing the films bubble (or plug) velocities and diameters were measured with a Boscar motion analyzer in order to determine V_v, the weighted mean velocity of the vapor phase.

Determination of V_v for the Plug Flow Regime. For pressures of 4 and 8.1 MN/m^2, plug flow started immediately after the initial point of net vapor generation, and one or two plugs (i.e. large bubbles) and several comparatively small bubbles in a liquid continuum were visible on the developed films, as shown schematically in Fig. 3. For almost all the test runs analyzed, the magnitude of the equivalent diameter of a plug was in the same order of magnitude as the hydraulic diameter of the sapphire channel. The first plugs appeared at the vicinity of the wall of the coil somewhere between the inside (near coil axis) and the top position. When the steam quality was increased, plugs became larger and agglomerated. A single plug was then present in the test section. For steam qualities higher than about 7 percent, wavy flow was observed and the vapor phase started to occupy the whole right-hand side of the cross section of the coil.

The velocity of every plug and bubble appearing on the film was measured at several axial positions (between 16 and 75 positions). Thus the number of velocities measured varied between 20 and 80 for each test run. The reason why the velocity of a plug or a bubble was measured at several axial positions was to determine the time-averaged value of the velocity.

Since the plugs for low values of outlet steam quality and all the bubbles were approximately elliptically shaped, the equivalent di-

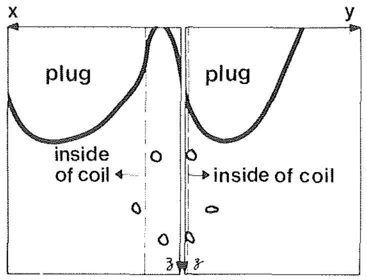

a - plug flow
($P = 8.1$ MN/m^2 ; $G = 431$ kg/m^2s ; $\Delta T_{sub} = 2$ K)

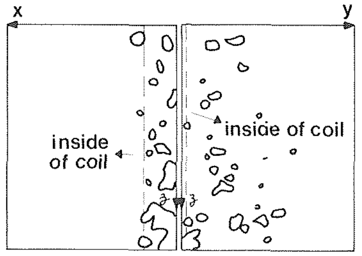

b - bubble flow
($P = 12$ MN/m^2; $G = 1495$ kg/m^2s ; $\Delta T_{sub} = 9.3$ K)

Fig. 3 Plug and bubble flow

ameter of such a plug (or a bubble) was determined by averaging the measured major and minor axes of the plug (or bubble). These axes were measured on the $(y - z)$ plane. At higher values of steam quality, plugs assumed the shape of a cylinder or a cylinder with a spherical cap. The dimensions of this type of plug were measured in the $(x - z)$ and $(y - z)$ planes, and the equivalent diameter of the plug was determined by equating the volume of the plug to that of a sphere. A cylindrical volume was approximated by the volume of a rectangular parallelepiped. No deformation in plug (or bubble) shape was observed during measurement of the velocity of a plug (or bubble).

In order to determine the weighted mean velocity of the vapor phase (or velocity of the center of gravity of the vapor phase in plug flow) the following equation was used

$$V_v \frac{\pi}{6} \rho_v \sum_{e=1}^{e} D_e{}^3 = \frac{\pi \rho_v}{6} \left(\frac{D_1{}^3}{m} \sum_{m=1}^{m} V_m + \frac{D_2{}^3}{m} \sum_{m=1}^{m} V_m + \ldots + \frac{D_e{}^3}{m} \sum_{m=1}^{m} V_m \right) \tag{8}$$

and it was possible to determine this velocity up to 72 percent void fraction. For $\beta \geq 0.12$, one large plug was present in the test section, which drastically simplifies equation (8).

Determination of V_v for the Bubble Flow Regime. For pressures of 12, 16 and 18 MN/m^2, numerous small bubbles of different sizes in a continuous liquid were visible on the developed films up to about a steam quality of one percent. This flow pattern, i.e. bubble flow, is shown schematically in Fig. 3. Bubbles were observed at the vicinity of the wall of the coil between the inside and top position. When the mass velocity was decreased from 1450 kg/m^{2}s to 760 kg/m^{2}s at 16 MN/m^2, it was clearly seen that bubbles climbed towards the top of the coil. When the steam quality was increased, bubbles began to coalesce, and wavy flow was then observed.

Since the number of bubbles was large on a film, the weighted mean velocity of the vapor phase for this flow regime was determined by a statistical method from the measured velocities of a sufficient number of bubbles taken randomly from the bubble population. For each test run, a sample of three to nine bubbles was taken from the bubble population and the velocity and diameter (or major and minor axes when they are elliptically shaped) of each bubble in the sample were measured at several axial positions (between 13 and 40 positions). Thus the number of velocities measured varied between 63 and 300 for each test run. Analyzed bubble populations were selected such that a representative bubble sample could be taken from them. For this flow regime, it was possible to determine the weighted mean velocity of the vapor phase up to 8.2 percent void fraction, and this velocity has been calculated with the formula below

$$V_v = \frac{1}{f} \sum_{f=1}^{f} \left(\frac{1}{m} \sum_{m=1}^{m} V_m \right)_f \tag{9}$$

Determination of Steam Quality. In order to determine J (see equation (5)), steam quality has to be known. During the tests heat losses were compensated by installing trace heaters in the insulation material which covered the sodium side. Steam quality was therefore calculated from the heat balance for the whole test tube by a procedure similar to that given in [12]. This was the true steam quality, i.e., the quality based on thermal nonequilibrium. The properties of sodium and water were taken from [23, 24].

The steam quality was also determined by solving the following fundamental identities, which hold for any two-phase flow

$$Q_v = V_v A_v = XGA/\rho_v \tag{10}$$

$$\alpha = A_v/(A_L + A_v) = A_v/A \tag{11}$$

as given below

$$X = \frac{\alpha \rho_v V_v}{G} \tag{12}$$

α, the void fraction in equation (12), was determined with the following equation

$$\alpha = \frac{\pi}{6} \sum_{i=1}^{e} D_i{}^3/B \tag{13}$$

The arithmetic average of the steam qualities calculated by the above-described procedures was considered for further analysis. J, calculated by the use of the aforesaid average steam quality, deviated by at most 6 percent from the J calculated by using the steam quality from the heat balance (or from equation (12)). The reason why the above-mentioned averaging procedure was used for the determination of the steam quality was that flow pattern instabilities were observed at 4 and 8.1 MN/m^2. These instabilities are discussed later. Although the determination of the steam quality may include some errors, these errors are not of much significance in predicting J, since the steam qualities were low and the pressures were high for the data presented here (see equation (5)).

Results and Discussion. The data obtained were first compared with the correlation of Lockhart and Martinelli [6]. For the experiments carried out, X_{LM}, the so-called Lockhart-Martinelli parameter, varied between 2.71 and 860. For most of the tests both water and steam were in turbulent motion. For $2.71 \leq X_{\mathrm{LM}} \leq 6.04$ the data fitted the correlation rather well. For $X_{\mathrm{LM}} > 6.04$ the agreement between the data and the correlation was far from satisfactory.

For correlation of the data, C, the distribution parameter was first determined by the use of equation (7). Next, for $0.00018 \leq \beta < 0.4$, this parameter was correlated as a function of the vapor volumetric rate ratio and the Froude number, as shown in Fig. 4. The correlation is given below

$$C = (100[40.294 - \beta^2 + 0.4\beta]^{1/2} - 633.9) \times (1 - 0.33 \exp - [10\beta + 3.5\mathrm{Fr}]) \tag{14}$$

For the data correlated, $P = 4 - 18$ MN/m^2 and $G = 754 - 1518$ kg/m^{2}s. The Froude number in equation (14) shows the ratio of centrifugal to gravity forces for the liquid phase. For $\beta < 0.4$ the centrifugal forces affect the phase distribution in the test tube and thereby the distribution parameter. For $\beta < 0.1$, the distribution parameter is found to be less than 1. It is reported in [8, 25], that for the flow of air/water mixtures and for the diabatic flow of steam/water mixtures at elevated pressures in horizontal tubes the distribution parameter is less than 1 for $\beta < 0.3$.

For $0.4 \leq \beta \leq 0.579$, the distribution parameter is not affected by centrifugal forces, and is equal to 0.875, as shown in Fig. 4. For the data considered, $P = 4.2 - 8.1$ MN/m^2 and $G = 429 - 1493$ kg/m^{2}s.

Armand and Treshchev [26] report the value of C as 0.98 and 0.95 for 4.2 and 8.1 MN/m^2 respectively for the diabatic flow of steam/water mixtures in horizontal tubes for $\beta = 0.3 - 0.9$. Analogous with the data for the flow of air/water mixtures, C, the distribution parameter for the flow of steam/water mixtures in helical coils is smaller than the distribution parameter for the flow of steam/water mixtures

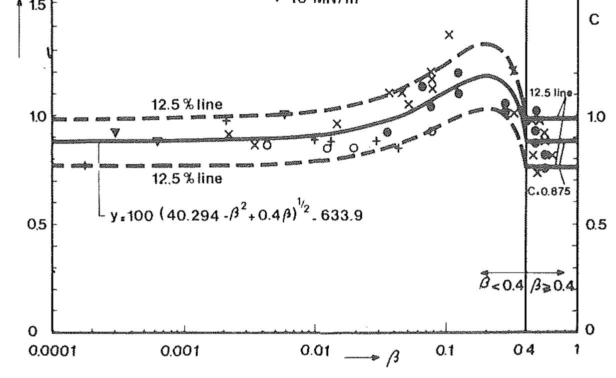

Fig. 4 Correlation of the void fraction data

in horizontal tubes for $\beta > 0.4$. It has to be indicated here, however, that the void fraction data of Armand and Treshchev were obtained by an indirect method.

IPB and IPNVG

Experimental Data. For the determination of the IPB and IPNVG, the pictures of the subcooled nucleate flow boiling were taken at constant pressure, heat flux and mass velocity, while subcooling was decreased slowly. When the first bubble was seen on a developed film, the conditions at which the film was taken were specified as those of the IPB, as given in Table 1. Per definition, void fraction increases sharply at the IPNVG. Therefore, in order to determine this point, the volume of all the bubbles on a developed film was measured and plotted versus subcooling, as shown in Fig. 5, for example for 16 MN/m^2. The best fitting curve was drawn through the experimental points. The interception of the tangent drawn to this curve with the subcooling axis gives the subcooling at the IPNVG, as illustrated in the figure. The IPNVG-data are summarized in Table 1. The heat flux at the IPB and IPNVG (i.e., at the end of the test tube) was calculated from the formula, $q_a = U\,\Delta T$. U in this formula, the overall coefficient of heat transfer, was determined for the last coil.

Correlation of Data by Using the Average Values of Operating Conditions. The data were correlated by modifying the IPB and IPNVG correlations of the author [12, 21] for vertical channels as follows

$$h_a \Delta T_{\text{sub}} \text{Pr}_b{}^{0.78}/q_a = K = \text{constant} \tag{15}$$

K, the constant in equation (15) is equal to 0.762 for the IPB and 0.434 for the IPNVG. h_a, the peripheral average heat transfer coefficient in equation (15) was evaluated by the correlation given in [27]

$$\text{Nu}_b = 0.0225\,\text{Re}_b{}^{0.8}\text{Pr}_b{}^{0.4}(1 + 3.4\,d/D_c) \tag{16}$$

This correlation fitted our heat transfer data well. The IPB and IPNVG correlations are shown in Fig. 6.

Table 1 IPB and IPNVG Data

IPB				IPNVG			
P MN/m^2	G kg/m^{2}s	ΔT_{sub} K	q_a MW/m^2	P MN/m^2	G kg/m^{2}s	ΔT_{sub} K	q_a MW/m^2
18.01	1460	12.5	0.390	18.01	1454	7.3	0.413
16.10	1458	12	0.323	16.08	1435	7.3	0.350
12.00	1471	11.8	0.263	12.00	1470	6.2	0.289
8.13	1516	11.7	0.226	8.11	1499	6.4	0.236
4.02	1518	7.3	0.148	4.03	1517	4.5	0.157
16.02	757	4.4	0.082	—	—	—	—

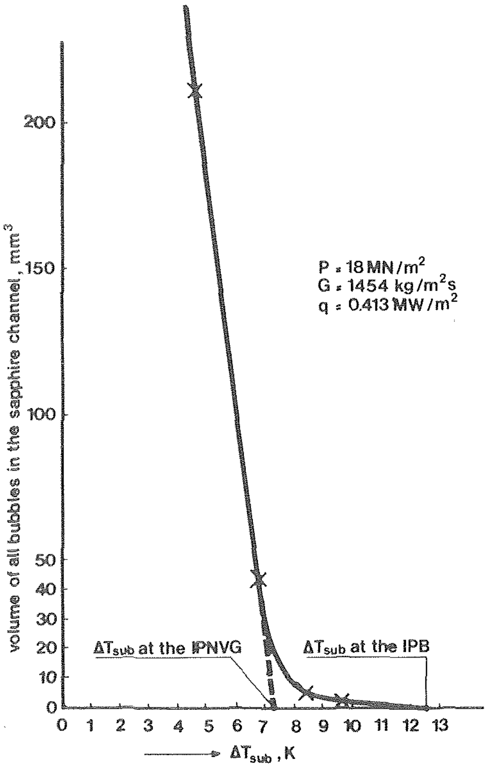

Fig. 5 Determination of the IPNVG

Correlation of Data by Using Local Values of Operating Conditions. It is shown in [12, 21] that

$$h\Delta T_{\text{sub}}/q = K_1 = \text{constant} \tag{17}$$

at the IPB and IPNVG for a wide range of operating conditions and channel geometry for the subcooled nucleate flow boiling of liquids in vertical channels. K_1, the constant in equation (17), is 0.24 for the IPNVG for velocities higher than 0.45 m/s and 0.665 for the IPB for water. Equation (17) was derived from the following heat transfer equation for subcooled nucleate flow boiling [21]

$$q = h\Delta T_{\text{sub}} + C_1 \Delta t^n \tag{18}$$

where n is a constant for a given fluid and C_1 for a given fluid, pressure and heating surface. The second term on the r.h.s. of equation (18) is the heat flux due to boiling and the first term is the heat flux due to suppressed forced convection. It follows from equations (17) and (18) that the ratio of the heat flux due to suppressed forced convection (or heat flux due to boiling) to the total heat flux is a constant at the IPB and IPNVG. This result has been verified below for the subcooled nucleate flow boiling of water in helical coils. Heat flux, heat transfer coefficient and temperature vary along the periphery of a helical coil. For an extensive range of conditions and for some of the present tests, the peripheral local values of the aforesaid quantities were also determined at 12 axial locations per coil. This was done by using the values of two temperatures measured in the wall of the test tube at known radial positions at the inside, top, outside and bottom of the test tube and by using Fourier's law of conduction and Newton's law of cooling. At the inside of the coil the wall temperature is highest, and consequently the IPB and IPNVG have to be located here. Using the local operating conditions at the aforesaid location, the IPNVG-data can be correlated as follows

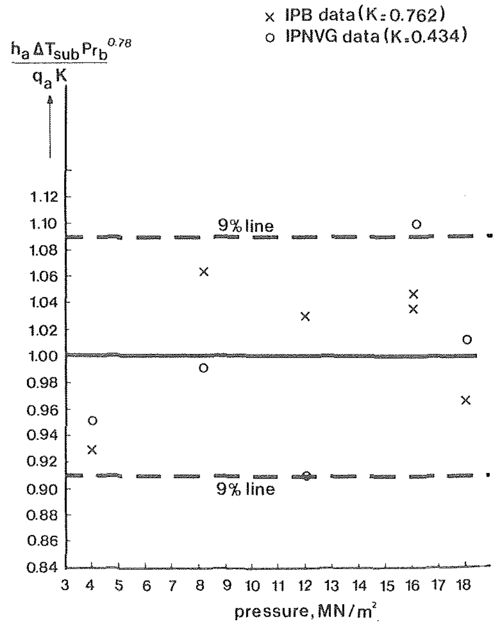

Fig. 6 Correlation of the IPB and IPNVG data by using average values of the operating conditions

$$(h/q)_I \Delta T_{\text{sub}} = 0.24 \qquad (19)$$

The data are compared with equation (19) in Fig. 7. $(h/q)_I$ in the equation was evaluated from the following correlation established by using our data and the data given in [28]

$$(h_a/q_a)/(h/q)_I = 3.12\ (d/D_c)^{0.17} \qquad (20)$$

for Re = 11800 − 439000 and $D_c/d = 17 - 104$. As stated before, equation (19) applies also to the subcooled nucleate flow boiling of water in vertical channels. From the aforementioned it is concluded that equation (18) applies to the subcooled nucleate flow boiling of water in helical coils, if local operating conditions are considered. For the IPB, K_1, the constant on the r.h.s. of equation (19), is equal to 0.445, as shown in Fig. 7.

Flow Pattern Instabilities

During the analysis of the developed films a flow pattern instability was observed. For pressures of 4 and 8.1 MN/m^2 and for low values of steam qualities, the flow regime varies from bubble flow to plug flow with a frequency of between 10 and 50 Hz. During the measurement of void fraction on a 10 m long sodium heated vertical tube of 0.008 m ID, a similar type of instability was also observed for $P = 4.3 - 14.2$ MN/m^2 and $G = 51 - 107$ kg/m^{2}s [13]. Jeglic and Yang [29] detected analogous instabilities in an electrically heated vertical tube.

In literature the cause of this type of instability is related to the variation of the pressure drop in the bubble-slug flow and in the annular flow regimes [29, 30]. Since the present test tube is very long the variation of the pressure drop in the different flow regimes can not be the cause of the instabilities observed. Moreover, no annular or wavy or stratified flow was observed during these instabilities. At present the cause of the instabilities observed is speculated to be the suppression of bubble growth. Bubbles grow at the inside wall of the test tube, depart from the heated surface, coalesce, and form a plug. Under the influence of centrifugal forces, this plug glides along the inside wall of the test tube, presses against the thin superheated liquid layer adjacent to the tube wall, and destroys this layer. This delays the growth of bubbles. For the time interval in which enough bubbles are produced to form a plug, the bubble flow regime exists in the test tube and the plug flow regime thereafter. The other type of instabilities relevant for a long steam generator tube is discussed in [22, 30–31].

Conclusions

For the flow of steam/water mixtures in helical coils and for β = 0.4–0.58, P = 4.2–8.1 MN/m^2, G = 429–1493 kg/m^{2}s and D_c/d = 38.9, the distribution parameter is not affected by centrifugal forces. It is constant and is equal to 0.875.

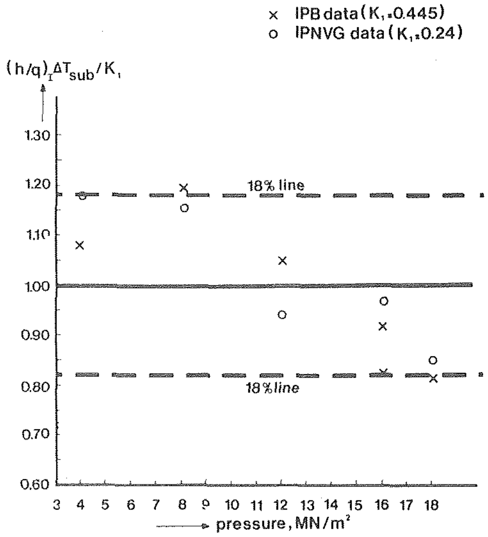

Fig. 7 Correlation of the IPB and IPNVG data by using local values of the operating conditions

For the flow of air/water mixtures in helical coils the value of the aforesaid parameter is also constant and equal to 1.1 for β = 0.18–0.99 and D_c/d = 11–48.

At elevated pressures and for $0.4 \le \beta \le 0.58$, the distribution parameter for the flow of steam/water mixtures in helical coils is smaller than the distribution parameter for the flow of steam/water mixtures in horizontal tubes. This conclusion also applies to the flow of air/water mixtures for $0.3 \le \beta \le 0.9$.

For the flow of steam/water mixtures in helical coils the distribution parameter is affected by centrifugal forces and volumetric rate ratio for β = 0.00018–0.4, P = 4–18 MN/m^2, G = 754–1518 kg/m^{2}s and D_c/d = 38.9.

At the IPB and IPNVG in helical coils, the ratio of the heat flux due to suppressed forced convection to the total heat flux (i.e., $h\ \Delta T_{\text{sub}}/q$) at the inside of the coil is constant. If the operating conditions at the inside of a helical coil are considered, the IPNVG can be predicted from the correlation given in [21], which was established for the IPNVG for vertical channels.

Acknowledgments

This study is a government sponsored work carried out by TNO. The author wishes to express his gratitude to Messrs. K. A. Warschauer, A. R. Braun, and M. L. G. van Gasselt for their encouragement during the preparation of this work. Mr. C. van Huffelen has analyzed the films.

References

1 Rippel, G. R., Eidt, C. M. Jr., and Jordan, H. B., Jr., "Two-Phase Flow in a Coiled Tube—Pressure Drop, Hold-up and Liquid Phase Axial Mixing," *Ind. Engng. Chem Process Design and Development,* Vol. 5, 1966, pp. 32–39.

2 Banerjee, S., Rhodes, E., and Scott, D. S., "Pressure Drops, Flow Patterns and Hold-up for Concurrent Gas-Liquid Flow in Helically Coiled Tubes," Paper presented at AIChE Meeting, Tampa, Florida, May, 1968.

3 Boyce, B. E., Collier, J. G., and Levy, J., "Hold-up and Pressure Drop Measurements in the Two-Phase Flow of Air-Water Mixtures in Helical Coils," *Proc. Int. Symp. on Research in Concurrent Gas-Liquid Flow,* held at the University of Waterloo, Sept. 18–19, 1968, Edited by Rhodes, E., and Scott, D. S., Plenum Press, New York, 1969, pp. 203–231.

4 Akagawa, K., Sakaguchi, T., and Ueda, M., "Study on a Gas-Liquid Two-Phase Flow in Helically Coiled Tubes," *Bulletin of the JSME,* Vol. 14, 1971, pp. 564–571.

5 Kasturi, G., and Stepanek, J. B., "Two-Phase Flow-I. Pressure Drop and Void Fraction Measurements in Cocurrent Gas-Liquid Flow in a Coil," *Chemical Engineering Science,* Vol. 27, 1972, pp. 1871–1880.

6 Lockhart, R. W., and Martinelli, R. D., "Proposed Correlation of Data for Isothermal Two-Phase, Two-Component Flow in Pipes," *Chemical Engineering Progress,* Vol. 45, 1949, pp. 39–48.

7 Hughmark, G. A., "Hold-up in Gas-Liquid Flow," *Chemical Engineering Progress,* Vol. 58, 1962, pp. 62–65.

8 Armand, A. A., "The Resistance During the Movement of a Two-Phase System in Horizontal Pipes," AERE—Report, AERE—TRANS 828, 1959

9 Neal, L. G., "*An Analysis of Slip in Gas-Liquid Flow Applicable to the* to the Bubble and Slug Flow Regimes," KR—Report, KR—62, 1963.

10 Richardson, B. L., "Some Problems in Horizontal Two-Phase Two-Component Flow," ANL—Report, ANL—5949, 1958.

11 Zuber, N., and Findlay, J. A., "Average Volumetric Concentration in Two-Phase Flow Sytems," ASME JOURNAL OF HEAT TRANSFER, Vol. 87, 1965, pp. 453–468.

12 Ünal, H. C., "Void Fraction and Incipient Point of Boiling During the Subcooled Nucleate Flow Boiling of Water," *International Journal of Heat and Mass Transfer,* Vol. 20, 1977, pp. 409–419.

13 Ünal, H. C., "Determination of the Drift Velocity and the Void Fraction for the Bubble- and Plug-Flow Regimes During the Flow Boiling of Water at Elevated Pressures," submitted for publication to *International Journal of Heat and Mass Transfer.*

14 Bergles, A. E., and Rohsenow, W. M., "The Determination of Forced Convection Surface Boiling Heat Transfer," ASME JOURNAL OF HEAT TRANSFER, Vol. 86, 1964, pp. 365–372.

15 Tarasova, N. V., and Orlov, V. M., "Heat Transfer and Hydraulic Resistance During Surface Boiling of Water in Annular Channels" in *Convective Heat Transfer in Two-Phase and One-Phase Flows,* edited by Borishanskii, V. M., and Paleev, I. I., Israel Program for Scientific Translations, Jerusalem, 1969, pp. 97–105.

16 Treshchev, G. G., "The Number of Vapor Formation Centers in Surface

Boiling" in *Convective Heat Transfer in Two-Phase and One-Phase Flows,* edited by Borishanskii, V. M., and Paleev, I. I., Israel Program for Scientific Translations, Jerusalem, 1969, pp. 135–156.

17 Bowring, R. W., "Physical Model, Based on Bubble Detachment, and Calculation of Steam Voidage in the Subcooled Region of a Heated Channel," HPR 29, Institute for Atomenergi, Halden, Norway, 1962.

18 Staub, F. W., "The Void Fraction in Subcooled Boiling—Prediction of the Initial Point of Net Vapor Generation," ASME JOURNAL OF HEAT TRANSFER, Vol. 90, 1968, pp. 151–157.

19 Levy, S., "Forced Convection Subcooled Boiling—Prediction of Vapor Volumetric Fraction," *International Journal of Heat and Mass Transfer,* Vol. 10, 1967, pp. 951–965.

20 Saha, P., and Zuber, N., "Point of Net Vapor Generation and Vapor Void Fraction in Subcooled Boiling," in *Proceedings of the Fifth International Heat Transfer Conference,* Tokyo-1974, Vol. 4, JSME-AIChE, Tokyo, 1974, pp. 175–179.

21 Ünal, H. C., "Determination of the Initial Point of Net Vapor Generation in Flow Boiling Systems," *International Journal of Heat and Mass Transfer,* Vol. 18, 1975, pp. 1095–1099.

22 Ünal, H. C., "An Investigation of the Inception Conditions of Dynamic Instabilities in Sodium Heated Steam Generator Pipes," in *Two-Phase Flows and Heat Transfer,* edited by Kakac, S., Mayinger, F., and Veziroglu, T. N., Vol. 3, Hemisphere Publishing Corporation, 1978, pp. 1425–1443.

23 Durham, M. E., "The Thermodynamic and Transport Properties of Liquid Sodium," CEGB—Report RD/B/M2479 (revised—CFR/THWP/P(72) 28 (revised), 1974.

24 The American Society of Mechnical Engineers, *"1967 ASME Steam Tables,"* ASME, New York.

25 Haywood, R. W., Knights, G. A., Middleton, G. E., and Thom, J. R. S., "Experimental Study of the Flow Conditions and Pressure Drop of Steam/Water Mixtures at High Pressures in Heated and Unheated Tubes," *Proc. Instn. Mech. Engrs.,* Vol. 175, 1961, Instn. Mech. Engrs., London, pp. 669–748.

26 Armand, A. A., and Treshchev, G. G., "Investigation of the Resistance during the Movement of Steam-Water Mixtures in a Heated Boiler Pipe at High Pressures," AERE Report, AERE Lib/Trans 816, 1959.

27 Pratt, N. H., "The Heat Transfer in a Reaction Tank Cooled by Means of a Coil," *Trans. Instn. Chem. Engrs.,* Vol. 25, 1947, pp. 163–180.

28 Seban, R. A., and McLaughlin, E. F., "Heat Transfer in Tube Coils with Laminar and Turbulent Flow," *International Journal of Heat and Mass Transfer,* Vol. 6, 1963, pp. 387–395.

29 Jeclic, F. A., and Yang, K. T., "The Incipience of Flow Oscillations in Forced—Flow Subcooled Boiling," *NASA* TM X-52081, 1965

30 Bouré, J. A., Bergles, A. E., and Tong, L. S., "Review of Two-Phase Flow Instability," *Nuclear Engineering and Design,* Vol. 25, 1973, pp. 165–192.

31 Ünal, H. C., Van Gasselt, M. L. G., and Ludwig, P. W. P. H., "Dynamic Instabilities in Tubes of a Large Capacity, Straight-Tube, Once-Through Sodium Heated Steam Generator," *International Journal of Heat and Mass Transfer,* Vol. 20, 1977, pp. 1389–1399.

R. L. Collins
Associate Professor,
Department of Mechanical Engineering,
University of Louisville, Louisville, Ky.

Choked Expansion of Subcooled Water and the I.H.E. Flow Model

The isentropic, homogeneous, equilibrium (I.H.E.) model for two-phase flows is discussed with special regard to recent experimental and theoretical information. Over the past years, the I.H.E. model has been misrepresented many times and its deficiencies have been overstated. More recent studies have indicated that the I.H.E. model may be quite valid for certain types of flows and this paper is presented to amplify these results. It is noted here that the I.H.E. model, under certain reservoir conditions, will over-predict flow rates, that an essential discontinuity of the I.H.E. sound speed may play an important role in choking, that the mass flux-pressure derivative is not continuous at the saturation line, and that the maximum error of the I.H.E. flow rate is about 60 percent at the liquid saturation line.

Introduction

Early investigations (e.g., [1], [2], [3], [4], [5])[1] of the flow of subcooled and saturated liquids through nozzles and orifices led to the conclusion that the experimental flow rates are significantly greater than those computed using the isentropic homogeneous equilibrium (I.H.E.) flow model. This result was generally attributed to the non-equilibrium effect of the super heating of the liquid to a metastable state as it passes the throat of the aperture. Further studies, such as [6] and other more recent investigations, have essentially verified the existence of metastable flows. Experimental data of these early studies appear to have been generally limited to flows from reservoirs which were saturated or only slightly subcooled liquids. The experimental data of Simoneau [7] on liquid Nitrogen, Sozzi and Sutherland [8], and Schrock, et al. [9] on water, include reservoir conditions in the highly subcooled reservoir range and provide a basis for more valid correlations with theoretical models. When these data are compared with the I.H.E. flow model, some interesting results are observed. The most important being that the I.H.E. model actually over-predicts flow rates under highly subcooled reservoir conditions. The intention here is to present additional information to reinforce recent, valid conclusions concerning the effectiveness and deficiencies of the I.H.E. flow model.

The characteristics of the choking process are fundamentally different for short, converging passages than for longer, constant area passages. It has been noted that metastable effects are stronger in low L/D apertures. Sozzi and Sutherland [8] data show metastable influence on flow lengths of less than 12 cm. Also indicated was the effect of reduced mass flux G with increased diameters, a result previously noted for saturated reservoirs by Ogasawara [10]. Moody [11] discusses the apparent existence of two choking phenomena (homogeneous and slip), dependent upon the length of a uniform pipe section attached to the aperture discharge. The emphasis of this paper will be on mass flow rate predictions of water flowing through low L/D apertures of relatively small diameter.

From observations of experimental data from highly subcooled reservoir states, it becomes apparent that choking may be controlled by the strong discontinuity of the I.H.E. acoustic speed in spite of the highly metastable character of the actual flow at the aperture exit or throat plane. In this regard, it is important to note that theoretical choking of single component I.H.E. flows from highly subcooled states do not choke at the sonic condition of $M_{CH} = 1$.

Choking of I.H.E. Flows

For short sections, where the primary cause or driving function for the change in fluid properties is reduction of area, the I.H.E. model may have some significance depending upon the capacity of the fluid to transfer heat, mass and momentum between phases. Here we consider the determination of mass flow rate for the I.H.E. model with emphasis on the expansion of subcooled water through converging channels. The theoretical basis for isentropic, homogeneous, equilibrium flow has been presented in previous papers (see especially [25]). Since most of these papers generally have been concerned with expansion from saturated liquid or two-phase reservoirs (a notable exception being [25]), a brief review is presented here for completeness. Also the occurrence of discontinuous choking is noted here.

The fluid is assumed to flow in a channel of converging cross section, accelerated by a pressure differential between reservoir and discharge.

---

[1] Numbers in brackets designate References at end of paper.

Contributed by the Heat Transfer Division for publication in the JOURNAL OF HEAT TRANSFER. Manuscript received by the Heat Transfer Division September 2, 1977.

Isentropic flow is assumed and when liquid and vapor phases are both present they are assumed to be in thermal and mechanical equilibrium. Therefore, the expansion process may be represented directly on any of the various thermodynamic property diagrams such as pressure-volume, temperature-entropy, etc. Hence, standard reference tables or equations such as those given in [12] may be used to compute required properties for various points along the expansion process. The energy equation for such a process is $h + u^2/2g_c = h_0$, and the mass flux is $G = \dot{m}/A = u/v$. Since isentropic flow is assumed, $s = s_0$ and the expansion process is completely determined by these equations for given reservoir conditions and a downstream flow property such as pressure. Assuming that the back pressure is sufficiently low, the stopping criterion will be the point at which $\overline{G}$ is a maximum. This is a point of fundamental interest here.

If $\overline{G}$ is a continuous function with continuous derivatives along the isentrope, a necessary condition that $\overline{G}$ be maximum is:

$$(d\overline{G}/d\beta)_{\overline{s}} = 0 \tag{1}$$

This condition is used extensively in the literature as a key step in determining theoretical models of choked flow (e.g., [1], [13]). It must be recalled, however, that (1) is not necessary for a maximum if $\overline{G}$ has discontinuous derivatives at some point along the isentrope since the maximum could occur there. When using the I.H.E. model, equation (1) is generally valid on the interval of the isentrope only when the reservoir is saturated liquid or a two-phase mixture. If the reservoir is subcooled, $\overline{G}$ will have discontinuous derivatives at the saturated liquid line and therefore (1) is not a necessary condition although it may still be useful in determing G_{MAX}. A brief discussion on the discontinuity of $\overline{G}$ at the saturation line is given in the appendix at the end of this paper.

The discontinuity of certain derivatives of some properties of equilibrium substances (e.g., $(\partial p/\partial v)_T$) at the saturation lines is well known. However, except for studies concerning acoustic speeds (e.g., [14], [15], [16]) in two phase media, and Perry and Bomelburg's work [17], the effect does not seem to have been sufficiently exploited in explanations of choked flow phenomena from subcooled liquid reservoirs. Keenan pointed out the possibility of this choking effect in this text [18]. Since the I.H.E. model indicates a great increase in volume when the expansion isentrope crosses the saturated liquid line, the mass flux reaches its maximum there, provided the reservoir pressure is high enough. Hence, the I.H.E. model will indicate "discontinuous choking" at the saturation line for sufficiently high reservoir pressures. As illustrated subsequently, this effect becomes most notable in experimental results at higher reservoir pressures.

The computational procedure used by this writer for calculating the I.H.E. choked flow of water from the subcooled liquid state follows. Given the reservoir conditions (β_0, θ_0) and having calculated $(\overline{s}_0, \overline{h}_0, \overline{v}_0)$ the intersection of the saturation line and the isentrope is determined by solving for θ_{SAT} from iteration of the [12] equations:

$$\beta_{\text{SAT}} = \beta(\theta_{\text{SAT}}); \quad \text{and} \quad \overline{s}(\theta_{\text{SAT}}, \beta_{\text{SAT}}) = \overline{s}_0$$

finding θ_{SAT} gives β_{SAT} and $\overline{h}_{\text{SAT}}, \overline{v}_{\text{SAT}}$ may be determined. The flow speed is determined as:

$$\overline{u}_{\text{SAT}} = [2(\overline{h}_0 - \overline{h}_{\text{SAT}})]^{1/2}$$

The homogeneous equilibrium sound speed $\overline{a}$ in the two-phase liquid-vapor region is determined from:

$$(1/\overline{a})^2 = -\{(1-x)(d\overline{v}_f/d\theta) + x(d\overline{v}_g/d\theta) - [ds_f/d\theta + x(d\overline{s}_{fg}/d\theta)]\overline{v}_{fg}/\overline{s}_{fg}\}/[\overline{v}^2(d\beta/d\theta)_{\text{SAT}}] \tag{2}$$

where the quality of $x = 0$ at the liquid saturation line. The derivatives are analytically determined from differentiation of the region 1 and region 2 property equations of [12].

The stopping criteria used is the equivalent to finding the maximum value of $\overline{G}$. The choke condition is reached whenever:

$$\overline{u} \geq \overline{a} \tag{3}$$

occurs along the isentrope as one proceeds from the reservoir state. The equality is satisfied when the expansion starts from a nearly saturated, subcooled reservoir or a saturated mixture reservoir. The inequality holds at the saturation line for sufficient expansions from the subcooled reservoir. From the subcooled reservoir the velocity increases along the isentrope but the sound speed in water is quite high, so that in the liquid portion of the expansion $u < a$ and the choke point is not reached. At the saturation line the sound speed drops drastically. For example, at 300°F the sound speed drops from over 4500 ft/s for pure liquid to about 30 ft/s on the mixture side of the saturation line at $x = 0+$. Therefore, if the reservoir enthalpy is great enough, the fluid speed at the saturation point $x = 0+$ can be considerably greater than the acoustic velocity and hence $\overline{u} > \overline{a}$ and the flow will be choked. If the reservoir is only slightly subcooled the flow velocity $\overline{u}$ will be less than $\overline{a}$ on "both sides" of the saturation line and expansion will continue on into the saturated mixture region until $\overline{u} = \overline{a}$ although $\overline{G}$ itself has a discontinuous derivative.

Fig. 1 shows four types of expansion. Type I is expansion from a saturated liquid reservoir and proceeds with continuous $d\overline{G}/d\beta$ until the maximum $\overline{G}$ is reached (or $\overline{u} = \overline{a}$) at which point the flow is choked. Type II flow begins in the subcooled region and reaches the saturation line with insufficient velocity to choke, therefore the expansion proceeds into the saturated mixture region until $\overline{u} = \overline{a}$ and the choke point is reached. Note that in this case, although the $\overline{G}$ function has discontinuous derivatives, the flow is not yet choked at the saturation line. Type III flow begins in the subcooled region and chokes at the saturation line as $\overline{u} > \overline{a}$. Type IV is similar to Type III

Nomenclature

a = acoustic or sound speed
$\overline{a}$ = reduced sound speed = $a/\sqrt{p_c v_c g_c}$
A = channel area
$\overline{A}$ = dimensionless channel area = A/A_{th}
g_c = universal inertial constant
G = mass flux = $\dot{m}/A$
$\overline{G}$ = reduced mass flux = $G\sqrt{v_c}/\sqrt{p_c g_c}$
h = enthalpy
$\overline{h}$ = reduced enthalpy = $hJ/p_c v_c$
J = energy unit conversion factor (778 ft lb/Btu, etc.)
$\dot{m}$ = mass flow rate
M_{CH} = Mach number at choke = $u/1$
P = pressure

R_0 = bubble nucleus radius
s = entropy
$\overline{s}$ = reduced entropy = $sJT_c/p_c v_c$
T = temperature
u = speed of flow
$\overline{u}$ = reduced speed of flow = $u/\sqrt{p_c v_c g_c}$
v = specific volume
$\overline{v}$ = reduced specific volume = v/v_c
x = mass fraction or quality of fluid
β = reduced pressure = p/pc
θ = reduced temperature = T/T_c

Subscripts

c = property at critical point of fluid
f = property at saturated liquid line
g = property at saturated vapor line
0 = property at reservoir
EXP = experimental data
IHE = isentropic homogeneous equilibrium value
SAT = property in saturated liquid-vapor region

Values at Critical State of H_2O

p_c = 3208.2 lb$_f$/in.^{2} = 2.17×10^7 N/m^2
T_c = 1165.14 R = 647.3 K
v_c = .05078 ft^3/lbm = 3.17×10^{-3} m^3/kg

except that choking flow cannot be reached due to the high back pressure of the nozzle.

Fig. 2 illustrates typical $\overline{G}$ function variation throughout the expansion for Types I, II, and III flows shown in Fig. 1.

Note also that at constant θ_0, as β_0 is reduced from the highly subcooled region until $M_{CH} = 1$ at the nozzle exit, the I.H.E. vapor formation plane will stand just to the downstream side of the exit plane. Further reduction of pressure (β_0) causes the vapor bubble plane to move upstream into the nozzle until the reservoir itself becomes two phase. The reservoir pressure then equals the saturation pressure ($\beta_0 = \beta_{SAT}$).

Correlation With Experimental Data

In order to properly evaluate the validity and deficiency of the I.H.E. model, it must be correlated with experimental data. Although several comparisons have been made for saturated mixture reservoir conditions, it is only in the past few years that appropriate presentations of the I.H.E. model for subcooled reservoirs have been made.

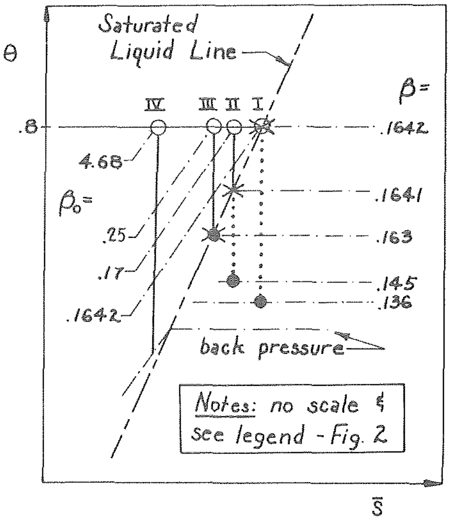

Fig. 1 Temperature-entropy diagram illustrating I.H.E. flow from four reservoir pressures at a reservoir temperature of $\theta_0 = 0.8$—not to scale

Simoneau [7] has shown I.H.E. correlation with experimental data using Nitrogen (and other cryogens) while Sozzi and Sutherland [8] have shown comparison with water at $\beta_0 = .296$ for high L/D apertures (9–140) and notes that choking flow rates are reasonably well approximated by the I.H.E. model for longer length pipes.

The experimental-theoretical comparisons of Simoneau [7] clearly indicate the existence of metastable flow conditions mixed with vapor formation in all cases. The amount of superheated liquid present and vapor present depends, to a large extent, upon the reservoir conditions. Although this data, [7], was taken using N_2, similar results using H_2O data are noted here and it is likely that these results may be considered as general for most fluids.

Subcooled reservoir data for short nozzles and orifices from several sources have been collected and compared with the I.H.E. model in this paper. Comparison is made by taking the reported reservoir pressure and temperature and inputting these values into the I.H.E. computer program. The reported mass flux is also input and the percent deviation from the computed $\overline{G}_{IHE}$ value is obtained and plotted against reservoir pressure in Figs. 3 and 4. The reservoir temperature is indicated for each data point. Also shown are approximate isotherms, faired through data, which help to indicate trends of the accuracy (or deficiency) of the I.H.E. model.

Fig. 3, which was produced mostly from data of Schrock, et al. [9], shows very definite trends in the deviation. It is clearly noted that the I.H.E. computations produce the largest error when the reservoir condition is near saturation and that the error appears to diminish considerably with increased subcooling or compression. Although the amount of data presented is less than desirable, it strongly indicates that for relatively low reservoir temperatures the I.H.E. model may over-estimate actual water flow rates, in short, converging passages. (Note: It was brought to this author's attention that the data of run number 3 of [9] was in error and that error has been corrected in the presentation of Fig. 3 data herein.)

Fig. 4 was produced from the data of Sozzi and Sutherland [8]. In order to present the data in β_0, θ_0 parameters it was necessary to compute θ_0 from the "negative quality" parameter used in [8]. This revision may have led to some error here, but the trend of the data should be reasonably accurate. Only the low L/D data presented by Sozzi is shown and it compares well with the data of [9]. The dashed isotherms of Fig. 4 are reproduced from Fig. 3.

Fig. 5 compares the I.H.E. model with the orifice data of Yarnall (see discussion in [3]). The reduced mass flux is plotted directly against reservoir pressure at constant reservoir temperature. In terms of deviation, it is observed that the trends are very much the same as

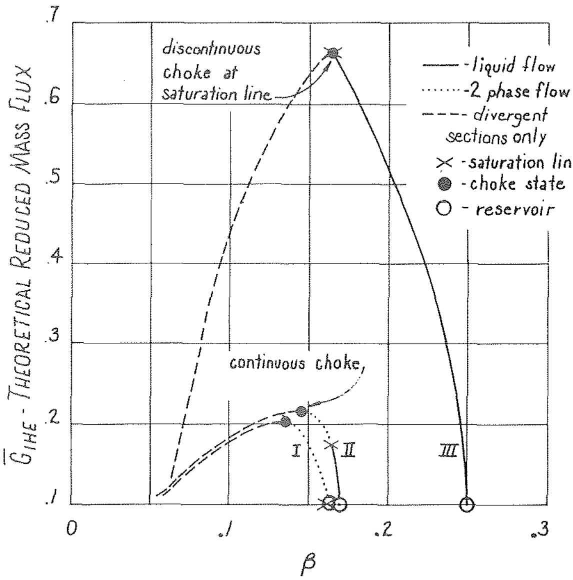

Fig. 2 Mass flux variation with pressure along an isentrope for I.H.E. expansions from three reservoir pressures at a reservoir temperature of $\theta_0 = 0.8$

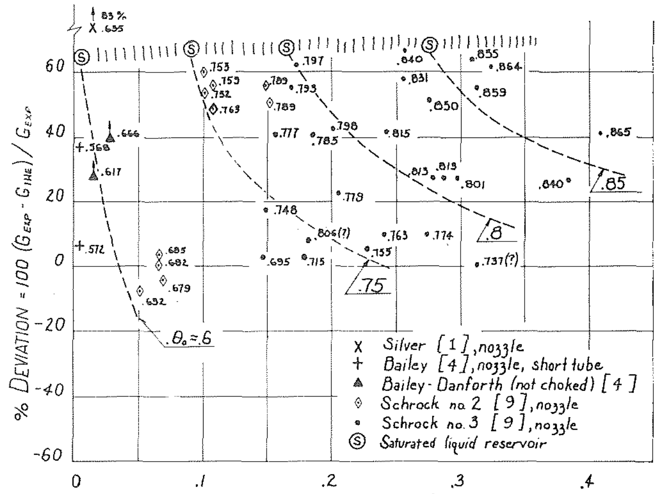

Fig. 3 I.H.E.-experimental data correlation for subcooled water reservoir. Dashed lines are estimated isotherms. Parameter indicated is reduced reservoir temperature

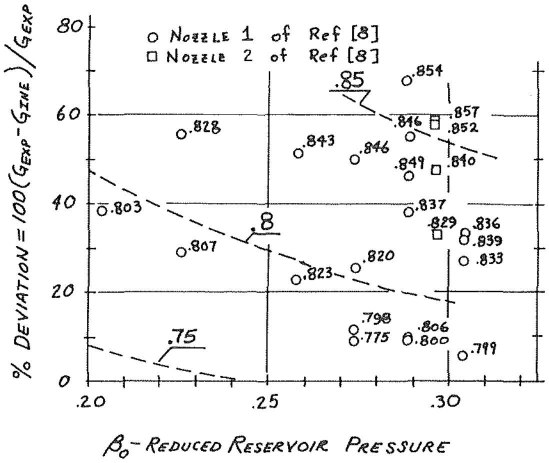

Fig. 4 I.H.E.-experimental data correlation for subcooled water reservoir. Experimental data from [8]. Dashed lines are representative isotherms from Fig. 3

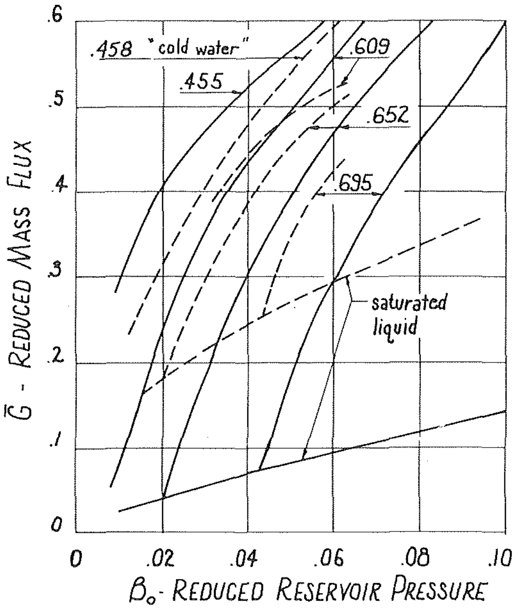

Fig. 5 I.H.E.-experimental data correlation for subcooled water reservoir. Dashed lines represent orifice data from Yarnall, [3], and solid lines are the author's I.H.E. calculations. Parameters indicated are reduced reservoir temperature

for the nozzle data of Figs. 3 and 4. The larger deviations occur for saturated reservoir conditions and smaller for highly subcooled or compressed reservoirs. The isotherm ($\theta_0 = 0.609$) indicates again the over-estimation of mass flow rate at reservoir pressures above about $\beta_0 > 0.05$.

Although flows from two-phase reservoir conditions are not the primary consideration of this paper, it is interesting to observe the I.H.E. deviation of such reservoirs as the saturation line is approached. Data typical of converging sections is given in [9] and [19]. Fig. 12 of [19] shows that percent deviation increases as the saturation line is approached through lower reservoir qualities. If the percent deviation is revised by normalizing with G_{EXP} (as done here) rather than G_{IHE} (as done in [19], then it appears that the maximum deviation approaches a value just above 60 percent as the reservoir quality x_0 approaches zero for all reservoir pressures (or temperatures).

Consideration of these results leads to the conclusion that the I.H.E. model does represent physical flows for reservoir conditions sufficiently removed from the liquid saturation line. At the saturation line the deviation from observed H_2O flows is about 60–65 percent. The significance of such observations may directly relate to the more fundamental question of the likelihood and degree of the occurrence of metastable, or superheated liquid flow.

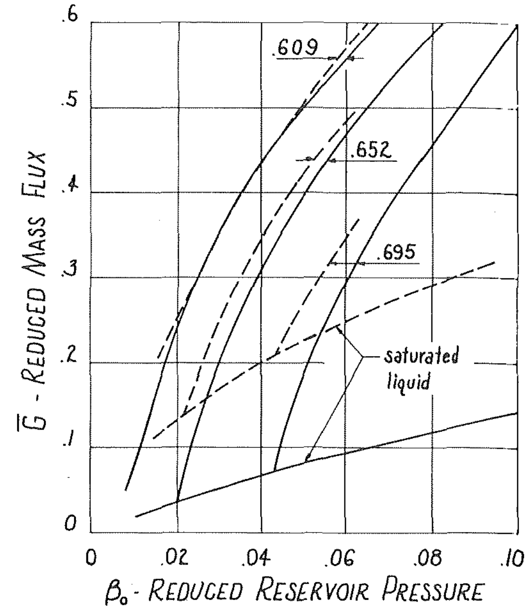

Fig. 6 Comparison of theoretical models. Dashed lines from data of Henry and Fauske [13]. Solid lines are the author's I.H.E. model. Parameters indicated are reduced reservoir temperature

Comparison With Other Models

Several mathematical models have been developed over the past years to predict flow characteristics for expansion from subcooled liquid reservoirs. Early models of Silver [1] and Bailey [4] are reasonably accurate at relatively low pressures and temperatures although somewhat cumbersome in their utility. Recent papers have described more useful and accurate models.

Henry and Fauske [13] have proposed a model which shows good correlation with experimental data. This model is quite useful as it can be used to produce flow rates and pressure distributions directly from given reservoir temperatures and pressures. Simoneau [7] suggests a necessary improvement in the model in the use of constant entropy expansion of the liquid rather than constant temperature as proposed. This model is compared to the I.H.E. result for H_2O expansions in Fig. 6. Revised theoretical data of Fig. 12 of [13], are shown to be generally superior to the I.H.E. model, especially near the saturation region when Figs. 5 and 6 are compared. The model of [13] and the I.H.E. model may also be compared in [7] and [20] for N_2 calculations.

Simoneau and Hendricks [20] have produced reduced mass flux charts from both I.H.E. computations and the improved Henry and Fauske model. Although these charts were prepared using the N_2 equation of state, they are valid for other simple molecules such as Oxygen and Methane as discussed in [26]. The mass flux of [20] is reduced as $G_r = G(v_c Z_c / g_c p_c)^{1/2}$ where: $z_c = p_c v_c / RT_c$ is the compressibility factor at the critical state. The mass flux computed in this paper is $\overline{G}_{\mathrm{IHE}}$ so that $G_r = \overline{G}_{\mathrm{IHE}} \sqrt{Z_c}$.

Fig. 7 is presented to provide a chart for the determination of H_2O (I.H.E.) mass flux as a function of reservoir pressure and temperature. The curves of Fig. 7 are primarily intended to show flow rate characteristics for subcooled reservoirs; however, results from the saturated liquid-vapor reservoir region for qualities of 10, 20 and 30 percent are also indicated.

If the curves of [20] and Fig. 7 are compared using $\sqrt{Z_c} = 0.4845$ for H_2O they show results which are essentially identical for reservoir pressures sufficiently above saturation, while some difference is found for reservoir conditions near saturation. This difference at the saturation line may be due to difference in the equations of state used in

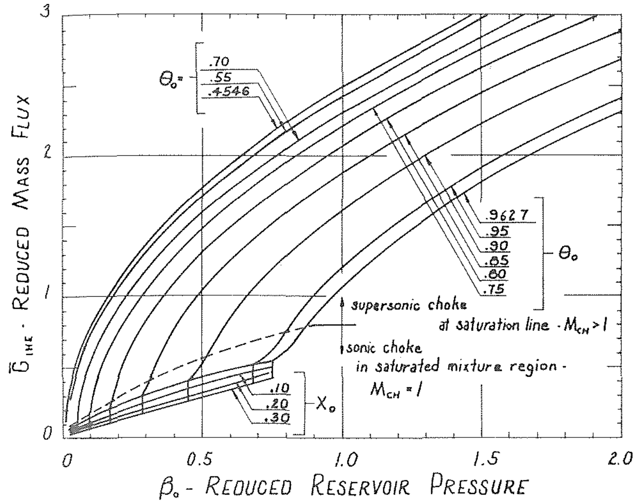

Fig. 7 Map of I.H.E. flow model for H_2O properties over extensive reservoir pressure and temperature conditions in subcooled liquid region and into two-phase reservoir region

each case (ASME, [12] versus [20]) and to the particular numerical procedures used in each case.

Concluding Remarks

Although the I.H.E. flow model is not generally reliable for use in predicting accurate choke flow rates in nozzles and orifices, the following important observations from studies of presently available experimental data can be made:

1. The I.H.E. flow model does not under-predict observed flow rates in every case but does, in fact, over-predict under certain conditions of reservoir temperature and pressure.
2. The I.H.E. model predicts choking of subcooled liquid reservoirs at the saturation line when the reservoir pressure is sufficiently above the saturation pressure at the reservoir entropy. Therefore, the condition $dG/dp = 0$ does not generally apply for the prediction of choking from subcooled reservoir states in the I.H.E. model.
3. The choking phenomena from highly subcooled states may be strongly related to the I.H.E. sound speed discontinuity at the liquid saturation line. It is therefore informative to note that the I.H.E. discontinuous choke condition produces choking Mach numbers greater than one at the downstream side of the choke plane.
4. The I.H.E. under-predicts experimental data by about 60 percent as the reservoir approaches the saturated liquid line from either the subcooled or two-phase reservoir regions.
5. The I.H.E. model has a significant role in the future development of useful flow models of the expansion of subcooled liquids in channels of varying area.

Concerning the last comment above, it is noted that flow models presented to date have some limitations. A flow model is desirable which will not only predict flow rates and choking pressures but property profiles and interface transfer effects as well. A model of such elaboration is indispensable for proper understanding of the mechanics of two-phase flows. In Giot and Fritte [22], and Smith, et al. [23], it was noted that many earlier investigators, presumably in the interest of simplicity, have not considered all available physical laws or governing equations in developing their models. Hence, they are forced to make some (arbitrary) assumptions as to certain key parameters such as velocity or slip ratio. If continuity, momentum, and energy are written for each phase, then six first order differential equations may be written. When assumptions are made on the flow, the equations may be reduced in number. Also, the reductions themselves shed considerable light on the physics of the restricted flow equations and the consequences of the assumptions.

When the I.H.E. restrictions are applied to the general two-phase system of equations, three first order differential equations arise. These equations can then be integrated along the nozzle axial coordinate and various characteristics of the flow such as heat transfer rate from liquid to interface, necessary to establish equilibrium, can be determined. Although this I.H.E. flow may not accurately represent the observed flow, it does provide a necessary basis for the study and evaluation of heat and mass transfer limits between phases and hence is very useful for developing more elaborate and accurate flow models.

The recent paper by Bouré [24] discusses this problem from a general point of view and Moody [11] derives equations for flow from consideration of the three basic laws and uses the second law of thermodynamics to establish stable slip ratio ranges by establishing the maximum slip ratio.

It is from considerations such as these which this author believes will lead to appropriate mathematical relationships for the understanding and prediction of flow rates and pressure distributions for two-phase flows.

Acknowledgments

The author wishes to thank Dr. R. W. Perry, Professor of Mechanical Engineering at the University of Louisville for his gracious aid and encouragement in these studies. The referees of this paper also provided significant contributions, especially Dr. R. J. Simoneau of NASA, Lewis Research Center.

References

1 Silver, R. S., "Temperature and Pressure Phenomena in the Flow of Saturated Liquid," *Proc. Roy. Soc., London,* Ser. A, Vol. 194, 1948, pp. 464–480.

2 Bottomley, W. T., "Flow of Boiling Water Through Orifices and Pipes," Trans. *North East Coast Institution of Engineers and Shipbuilders* (England) Vol. 53, 1936–1937, pp. 65–100.

3 Benjamin, M. W., and Miller, J. G., "The Flow of Saturated Water Through Throttling Orifices," *Trans. ASME,* Vol. 63, 1941, pp. 419–426.

4 Bailey, J. F., "Metastable Flow of Saturated Water," *Trans. ASME,* Vol. 73, Nov, 1951, pp. 1109–1116.

5 Fauske, H. K., and Min, T. C., "A Study of the Flow of Saturated Freon-11 Through Apertures and Short Tubes," Argonne National Laboratory, ANL-6667, Jan. 1963, 19 pp.

6 Lienhard, J. H., and Stephenson, J. M., "Temperature and Scale Effects Upon Cavitation and Flashing in Free and Submerged Jets," ASME *Journal of Basic Eng.,* June 1966, pp. 525–532.

7 Simoneau, R. J., "Pressure Distribution in a Converging-Diverging Nozzle During Two-Phase Choked Flow of Subcooled Nitrogen," see [21], pp. 37–45.

8 Sozzi, G. L., Sutherland, W. A., "Critical Flow of Saturated and Subcooled Water at High Pressure," General Electric Co., Report NEDO-13418, May 1975, also [21], pp. 19–25.

9 Schrock, V. E., Starkman, E. S., and Brown, R. A., "Flashing Flow of Initially Sub-Cooled Water in Convergent-Divergent Nozzles," ASME JOURNAL OF HEAT TRANSFER, Vol. 99, May 1977, pp. 263, 268.

10 Ogasawara, H., "A Theoretical Approach to Two-Phase Critical Flow," *Bull. of JSME,* Vol. 12, No. 52, 1969, pp. 847–856.

11 Moody, F. J., "Maximum Discharge Rate of Liquid-Vapor Mixtures from Vessels," see [21], pp. 27–36.

12 *1967 ASME Steam Tables* The American Society of Mechanical Engineers, Second Edition, New York, NY.

13 Henry, R. E. and Fasuke, H. K., "Two-Phase Critical Flow of One-Component Mixtures in Nozzles, Orifices, and Shot Tubes," ASME JOURNAL OF HEAT TRANSFER, May 1971, pp. 179–187.

14 Karplus, H. B., "Propagation of Pressure Waves in a Mixture of Water and Steam," Armour Research Foundation, ARF 4132-12, Jan. 1961.

15 Davies, A. L., "Speed of Sound in Mixtures of Water and Steam," *Proc. of Symp. on Two-Phase Flow Dynamics,* Sess. V, Propagation Phenomena, Eindhoven, Sept. 1967, pp. 625–638.

16 Dryndrozhik, E. I., "Critical Velocity in Two-Phase Flow," Heat Transfer—*Soviet Research,* VI, No. 4, July 1969, pp. 77–88.

17 Perry, R. W., and Bomelburg, J. H., "A One-Dimensional Computer Model for the Impingement Effects of a Small Leak in Sodium-Heated Steam Generator," LMEC Memo 70–14.

18 Keenan, J. H., *Thermodynamics,* John Wiley & Sons, Inc., New York, NY, 1941, p. 432.

19 Starkman, E. S., Schrock, V. E., Neusen, K. F., and Maneely, D. J., "Expansion of a Very Low Quality Two-Phase Fluid Through a Convergent-Divergent Nozzle," ASME *Journal of Basic Engr.,* June 1964, pp. 247–256.

20 Simoneau, R. J. and Hendricks, R. C., "Generalized Charts For Computation of Two-Phase Choked Flow of Simple Cryogenics Liquids," *Cryogenics,* Vol. 17, No. 2, Feb. 1977, pp. 73–76.

21 "Non-Equilibrium Two-Phase Flows," Collected Papers from the Winter Annual Meeting of the ASME, Houston, Texas, Dec. 1975.

22 Giot, M., and Fritte, A., "Two-Phase Two- and One-Component Critical Flows with the Variable Slip Model," *Progress in Heat and Mass Transfer,* Vol. 6, International Symposium on Two-Phase Systems, Haifa, 1971, Proc. Pub. by Pergamon Press, 1972.

23 Smith, R. V., Cousins, L. B., and Hewitt, G. F., "Critical Flow in an Annular Venturi," *Proc. of Symp. on Two-Phase Flow Dynamics,* Sess. IV, Propagation Phenomena, Eindhoven, Sept. 1967.

24 Bouré, J. A., "On a Unified Presentation of the Non-Equilibrium Two-Phase Flow Models," see [21], pp. 1–9.

25 Hendricks, R. C., Simoneau, R. J., and Ehlers, R. C., "Choked Flow of Fluid Nitrogen with Emphasis on the Thermodynamic Critical Region," *Advances in Cryogenic Engineering,* K. D. Timmerhaus, Ed., Vol. 18, pp. 150–161, Plenum Press, 1973.

26 Hendricks, R. C., Simoneau, R. J., and Barrows, R. F., "Two-Phase Choked Flow of Subcooled Oxygen and Nitrogen," NASA TN D-8169, Feb., 1976.

APPENDIX

A brief discussion on the discontinuity of $(\partial\overline{G}/\partial\beta)_s$ at the saturation line is provided in this appendix. Given that: $\overline{G} = \overline{u}/\overline{v}$ and $\overline{u} = [2(\overline{h}_0 - \overline{h})]^{1/2}$, and also noting that $(\partial\overline{h}/\partial\beta)_s = \overline{v}$, then it follows that:

$$\left(\frac{\partial\overline{G}}{\partial\beta}\right)_s = -\frac{1}{\overline{u}}\left[1 + \left(\frac{\overline{u}}{\overline{v}}\right)^2\left(\frac{\partial\overline{v}}{\partial\beta}\right)_s\right] \tag{A-1}$$

Consider the point of intersection of the expansion isentrope and the liquid saturation line. Let the liquid side of the intersection be denoted as $(-)$ and the mixture side as $(+)$. The jump J of the derivative at this point is then:

$$J = \left(\frac{\partial\overline{G}}{\partial\beta}\right)^+ - \left(\frac{\partial\overline{G}}{\partial\beta}\right)^- = -\frac{\overline{u}_{\mathrm{SAT}}}{\overline{v}_f{}^2}\left[\left(\frac{\partial\overline{v}}{\partial\beta}\right)_s^+ - \left(\frac{\partial\overline{v}}{\partial\beta}\right)_s^-\right] \tag{A-2}$$

Also the thermodynamic sound speed can be introduced as: $\overline{a}^2 = -\overline{v}^2(\partial\beta/\partial\overline{v})_s$ so that

$$\left(\frac{\partial\overline{G}}{\partial\beta}\right)_s = -\frac{1}{\overline{u}}\left[1 - \left(\frac{\overline{u}}{\overline{a}}\right)^2\right] \tag{A-3}$$

and

$$J = \overline{u}_{\mathrm{SAT}}\left[\left(\frac{1}{\overline{a}^2}\right)^+ - \left(\frac{1}{\overline{a}^2}\right)^-\right] \tag{A-4}$$

Equations of state for simple compressible substances have been developed from experimental data and tabulated (e.g., [12]). These equations have been used to determine the derivatives and equilibrium sound speeds above. Typical examples of past studies of these thermodynamic variables are found in Karplus [14] and Perry [17]. In computations used to prepare Fig. 7 of this paper, it was found that $(\overline{a})^- > (\overline{a})^+ > 0$ along the liquid saturation line, excluding the triple and critical points. Therefore, from (A-4), $J > 0$ and $(\partial\overline{G}/\partial\beta)_s$ is discontinuous along this line.

It is also evident that if $\overline{G}$ is to be a maximum at the saturation line, $(\partial\overline{G}/\partial\beta)_s$ must change sign or: $\mathrm{SIGN}(\partial\overline{G}/\partial\beta)^+ = -\,\mathrm{SIGN}(\partial\overline{G}/\partial\beta)_s^-$. Now $(\overline{a})^-$ is a large value compared to $\overline{u}_{\mathrm{SAT}}$ as long as the reservoir pressure is not too high (under 150,000 psi level for H_2O). Hence from (A-3) $(\partial\overline{G}/\partial\beta)_s^- < 0$ and the subcooled liquid does not choke. Hence for $\overline{G}_{\mathrm{MAX}}$ to occur at the saturation line it is necessary that $(\partial\overline{G}/\partial\beta)_s^+ > 0$. Using either (A-1) or (A-3) and applying these results give the necessary condition for a maximum $\overline{G}$ at the saturation line:

$$(\partial\overline{v}/\partial\beta)_s^+ < -(\overline{v}_f/\overline{u}_{\mathrm{SAT}})^2$$

or:

$$\mathrm{M_{CH}} \equiv \overline{u}_{\mathrm{SAT}}/(\overline{a})^+ > 1$$

The second condition is indicated on Fig. 7 of this paper. These computations may therefore be considered as proof of the existence of this discontinuous or supersonic choke—at least for H_2O.

G. Horvay
Professor of Civil Engineering

B. Gold
Research Associate,
Department of Mathematics

E. S. Kaczenski
Plant Engineer,
American Bosch Div. of AMBAC,
Springfield, Mass.,
formerly Graduate Student,
Dept. of Mechanical and Aerospace Engineering

University of Massachusetts,
Amherst, Mass.

Longitudinal Heat Propagation in Three-Phase Laminated Composites at High Exciting Frequencies[1]

The performance of a laminated composite depends critically on the behavior of the interfaces. This behavior cannot be explored with the usual analysis which employs a smearing out of the temperature across the widths of the laminas, but requires a rigorous solution of the problem in the vicinity of the interfaces. This task can be accomplished by augmenting the usual bilaminate arrangement of matrix M and filler F with binder layers B (of volume fractions f_M, f_F, f_B) into trilaminates MBFBMBF. . .and then considering the condition $f_B \to 0$. The unexpected result is obtained that for high exciting frequencies ω the case $f_B \to 0$ does not reduce to the case $f_B = 0$. This thrusts into the foreground two questions: (a) What are the physical implications of such an "unreasonable" result? (b) What constitutes high frequency, what constitutes low frequency? The problem posed admits a rigorous solution.

1 Introduction

In analyzing heat propagation in bilaminates in the direction x of the laminas, matrix layers of volume fraction f_M alternating with filler layers of volume fraction f_F, most of the studies in the literature use a smearing process in the transverse (our y) direction, and visualize behavior as superposition on an average temperature in each layer of a departure temperature which usually is assigned a linear variation across the layer. See, e.g., Koh [1],[2] and references cited in [1], who also surveys further approaches used in the past. Note that alternate approaches also use averages over each layer, but introduce different interaction terms to express the effect of one constituent on the other, e.g., Ben-Amoz [2] and Nayfeh [3]. It is pointed out in these studies that the statically determined equivalent diffusivity

$$\bar{\kappa}_{\text{eq}} = [f_M\bar{k}_M + f_F\bar{k}_F]/[f_M(\overline{\rho c})_M + f_F(\overline{\rho c})_F] \tag{1}$$

is applicable only at very low exciting frequencies, ω. ($\bar{k}$ = conductivity, $\overline{\rho c}$ = heat capacity; omission of bar, e.g., κ, indicates that the quantity has been *nondimensionalized with respect to length,* the physical stacking height ℓ having been assigned the dimensionless value 2π, see Fig. 1.) But little is divulged about behavior at higher frequencies, at best only recipes are provided for calculation of specific examples. Moreover, nothing is said about the very *nature of the interface of the composite.* In fact, this cannot be explored by the currently used methods of smearing in the y direction. Still, interface behavior is crucial to the performance of the composite and therefore deserves, indeed it demands, evaluation.

I In a first paper [4] by Horvay, et al., on the subject of an *MFMFM*. . .composite (for convenience of analysis it fills the half space $x \geq 0$, see Fig. 1 with $f_B = 0$) subject to a time harmonic excitation

$$T(0, y, t) = e^{-i\omega t}\chi(y) \tag{2}$$

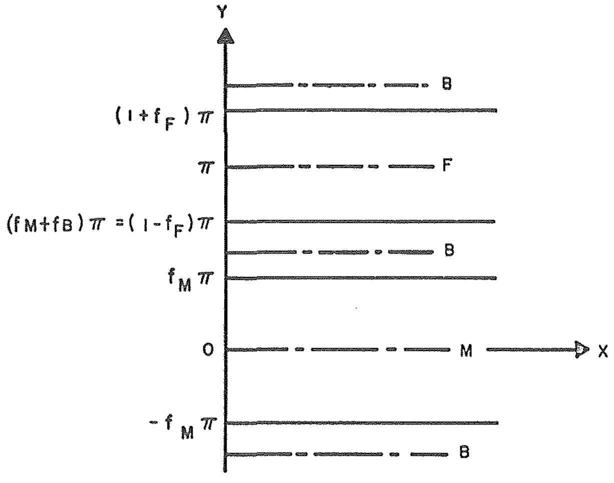

Fig. 1

---

[1] This paper is partly based on Part II of E. S. Kaczenski's thesis [8], submitted to the University of Massachusetts in partial fulfillment of the requirements for the Master of Science degree. (Part I of the thesis is condensed into [7]).

[2] Numbers in brackets designate References at end of paper.

Contributed by the Heat Transfer division and presented at the Winter Annual Meeting, Atlanta, Ga., November 27–December 2, 1977, of THE AMERICAN SOCIETY OF MECHANICAL ENGINEERS. Manuscript received by the Heat Transfer Division October, 19, 1977. Paper No. 77-WA/HT-10.

on the face $x = 0$, it was pointed out that the statically determined equivalent diffusivity (1) is valid, true to its definition, only under the condition $\omega \simeq 0$ and that at higher frequencies a dispersion relation

$$\bar{\kappa}_{\text{eq}}(\omega) = \bar{\kappa}_{\text{eq}}(0)[1 + iF(\omega)] \tag{3}$$

is appropriate. (Function F, for low frequencies, is real and linear in ω.)

II It was also shown that the problem of longitudinal heat propagation can be solved exactly so there is really no need to solve the problem approximately.

III A further result of [4] was the demonstration that the boundary distribution $\chi(y)$ may be expanded into eigenfunctions $\phi_n(y)$ of the governing equations (for the time being ignore the B equation)

$$(i + \omega^{-1}\bar{\kappa}_j\nabla^2)w_J(x, y) = 0 \qquad J = M,B,F \tag{4a}$$

$$T(x, y, t) = e^{-i\omega t}w_J(x, y) = \begin{cases} T_M \\ T_B \\ T_F \end{cases} \tag{4b}$$

$$w_{Jn} = e^{-\chi_n x} \cdot \begin{cases} \phi_{Mn}(y) \\ \phi_{Bn}(y) \\ \phi_{Fn}(y) \end{cases} \tag{4c}$$

subject to appropriate boundary conditions, using the *biorthogonal expansion formula*

$$\chi(y) = \Sigma\phi_n(y)\, \langle \chi, \Phi_n \rangle / \langle \phi_n, \Phi_n \rangle \tag{5a}$$

where

$$\Phi_n = k\phi_n \tag{5b}$$

are the "flux" eigenfunctions, and $\langle\,,\rangle$ is scalar product in the integrated sense. Conversely, if $\chi(y)$ represents boundary flux, then the expansion formula is

$$\chi(y) = \Sigma\Phi_n(y)\langle \chi, \phi_n \rangle / \langle \phi_n, \Phi_n \rangle \tag{5c}$$

IV A basic assumption must be pointed out here, used apparently by everyone in the business, but stated, insofar as the present writers were able to ascertain, only by Sun, Achenbach, and Herrmann [5]: *the periodicity* Λ *of* $\chi(y)$ *must conform to the periodicity* ℓ *of the microstructure,* i.e., $\chi(y)$ may have a period ℓ/n ($n = 1, 2, 3, \ldots$), but not a least period $\Lambda = n\ell$ ($n = 2, 3, \ldots$). This is not a severe restriction since, when ℓ is very minute (as it is in most applications), $\chi(y)$ will vary slowly over aggregates of hundreds of ℓ, and so $\chi(y)$ may be regarded as stepwise constant, where the steps are very low and are far in-between [6]. In the example of this paper we shall assume $\chi(y) =$ const. Incidentally, this is the condition used also in all papers by other authors, so they don't violate the requirement of conforming periodicity.

V The presumably simple case of equal volume fractions, $f_M = f_F = 1/2$, turns out to be, from a computational point of view, the most cumbersome of all cases [7–8], because it leads to 0/0 expressions which must be evaluated by special limiting processes.

VI The governing differential equation (4a), on taking $\omega = \infty$, reduces to $w \equiv 0$. Thus, for high frequencies the problem may not be solved by conventional perturbation methods, but requires the techniques of *singular perturbations.* This is carried out in [9]. The method has first been used for the

$$(1 + \omega^{-1}d^2/dx^2)y(x) = 0$$

equation by Carrier [10], and was further discussed by Smith [11]. Equation (4a), for $i\omega = \text{real} \rightarrow \infty$, is also treated by Eckhaus [12] (for the single phase case), but differently than it is treated here.

VII Having presented this sketch of previous work on the *MFM* . . . composite we now come to consideration of the *MBFBMB* . . . composite of Fig. 1. The binder layer has volume fraction f_B, and

$$f_M + f_B + f_F \equiv f_2 + f_F = 1 \tag{5}$$

What prompts incorporation of a binder layer? Either it is there by design, e.g., as some poorly conducting thin layer of cementing material, or by mishap, such as by segregation of impurities into the interfaces during setting or just by accumulation of tiny airpockets into the interfaces. If we want to know how a minuscule $f_B \rightarrow 0$ interface layer affects the behavior of the presumably two-phase composite we had better incorporate B with volume fraction f_B and see what happens when $f_B \rightarrow 0$. A very strange thing happens. The results do not reduce to the $f_B = 0$ case of the *MFMFM*. . .composite, at least not at high frequencies. *The* $f_B \rightarrow 0$ *case still retains dependency on the conductivity and diffusivity of the B phase, whereas in the strictly two-phase composite there is, of course, no B effect.* This is a totally unexpected result, although, in retrospect, when we recall the stress concentration factor in a plate with a hole (when the radius $r = 0$ the s.c.f. is 1, whereas for $r \rightarrow 0$ the s.c.f. > 1), it should not be surprising. For low frequencies, however, $f_B \rightarrow 0$ gives the same results as $f_B = 0$ [14]. Thus it behooves us to establish *for what* ω *we are in the low-frequency regime.* The answer is that when the magnitude of the dimensionless frequency

$$\nu \equiv (\ell/2\pi)^2[\bar{\kappa}_{\text{F}}{}^{-1} - \bar{\kappa}_{\text{M}}{}^{-1}]\omega \tag{6}$$

is $\ll 1$, we are in the low-frequency regime, and when $|\nu| \gg 1$ we are in the high-frequency regime. The value $|\nu| \sim 1$ separates the two regimes. (In the example we shall treat in Section 7, $|\nu| \sim 0.1$ will be found to be the approximate dividing point.)

VIII An important question prompted by the foregoing: given a certain two-phase composite, what frequency ω puts us on the dividing line $|\nu| = 1$? For the nickel matrix, aluminum filler, we have been using as an example in [4,6–9,13]

$$|\nu| = 1 \text{ corresponds to} \tag{7a}$$

$$\omega/2\pi = 54 \text{ megaherz when } \ell = 1\ \mu\text{m} \tag{7b}$$

i.e., for eutectoid bilaminates, as used, for instance, by turbine or compressor blade manufacturers, we shall always operate in the low-frequency regime; but

$$\omega/2\pi = 4.7 \text{ cycle per day when } \ell = 1 \text{ m} \tag{7c}$$

i.e., for geological formations of vast thicknesses, we shall frequently operate in the high-frequency regime, particularly, since the materials encountered usually have diffusivities much lower than nickel and aluminum

$$\kappa_{\text{non-metal}} \sim 10^{-3}\kappa_{\text{al}}$$

Thus cycle/year may very well be a separating frequency for some such formation.

IX A further interesting result. It is found that for $|\nu| \gtrsim 1$ the $f_B \rightarrow 0$ layer behaves as a *shock layer.* As will be shown in [14], *temperature jump* and *flux jump* occur across it.

X The practical solution of the eigenvalue equation (14), leading to complex roots $\zeta_0, \zeta_1, \zeta_2, \ldots$ (i.e., $\zeta_{M0}, \zeta_{M1}, \ldots; \zeta_{B0}, \ldots; \zeta_{F0}, \ldots$) (ranked by their moduli at very low frequencies), is of considerable interest, per se. The strange result is found that the eigenvalues ζ_0, $\zeta_3, \zeta_6, \ldots$ behave alike, and so do the $\zeta_1, \zeta_2, \zeta_4, \zeta_5, \zeta_7, \ldots$ eigenvalues. But crossings occur between members of the two families as the frequency is increased [7, 13]. For low frequencies ascending power series representation for ζ in ν may be used; for high frequencies descending power series in $\nu^{1/2}$ are appropriate. However, in order not to require the determination of too many terms in the series (the determination of five coefficients in the descending series is rather easy, but determination of three coefficients in the ascending series requires considerable effort), Padé's method [15], of representing the available terms of the power series as rational fraction of two polynomials, is used to improve the eigenvalues; and this is achieved in a spectacular manner, except for the range $0.1 \lesssim |\nu| \lesssim 10$, where Padéing is supplemented by Newton's method to achieve adequate improvement.

Outline of Paper. The governing differential equations

$$(\nabla^2 - \kappa_J{}^{-1}\partial/\partial t)T_J = 0 \qquad J = M,B,F \tag{8}$$

lead, for harmonic excitation (4b), to (4a). The temperature obeys the symmetry conditions

$$y = 0, \pi\text{: } \partial T/\partial y = 0 \tag{9a,b}$$

and the interface conditions

$$y = f_M\pi\text{: } T_M = T_B,\ k_M\partial T_M/\partial y = k_B\partial T_B/\partial y \tag{9c,d}$$

$$y = (1 - f_F)\pi\text{: } T_B = T_F,\ k_B\partial T_B/\partial y = k_F\partial T_F/\partial y \tag{9e,f}$$

in addition to the left-face condition (2), and the right-face condition:

$$\text{at } x = \infty \text{ the temperature vanishes} \tag{9g}$$

In Section 2 the eigenvalue equation (14) is established that results from substituting (4c) into (4a) and imposing (9), and the eigenmodes $\phi_{Mk}(y)$, $\phi_{Bk}(y)$, $\phi_{Fk}(y)$, (12), are also determined. Section 3 states the Fourier coefficients of $\chi(y) = 1$ in its expansion into the modes $\phi_k(y)$. Section 4 establishes the high-frequency expressions of the roots

$$\zeta_{Jk} \equiv \pi z_{Jk} \equiv \pi(x_{Jk} + iy_{Jk}) \equiv \pi(x_{Jk} - i\eta_{Jk}) \qquad J = M,B,F \tag{10}$$

of $\Delta = 0$. Section 5 lists the appropriate formulas for the two-phase composite. They cannot be obtained from the three-phase formulas by placing $f_B = 0$. In the light of the change in notation from the earlier work it was thought desirable to again list these formulas. Note that in the earlier work [3, 6–9, 13] the present symbols $f_F, f_M, \nu, \zeta, z, \phi_M, \phi_F$ were denoted by $f, 1-f, \nu/(1-f)^2, \zeta/(1-f), z/(1-f), \phi, \psi$, and that the previously used symbols $a = f/(1-f)$ and $b/a = k_F/k_M$ are now not used at all. (It would also have been desirable to redefine ν in (6) as the negative of the right hand side so as to assure that, in light of the usual situation, $\kappa_F > \kappa_M$, ν will be positive when ω is positive. However, this would have entailed an uncomfortable number of changes. Thus, it should be understood that we assign a negative value to ω in this paper in order to render ν positive.)

Section 6 derives the important result

$$\begin{aligned}(\lim f_B \to 0)[(\lim \nu \to \infty)\{\nu^{1/2}\zeta_B{}^{-1} \tan f_B\zeta_B\}] \\ = f(\kappa_M, \kappa_B, \kappa_F) \neq 0, \infty\end{aligned} \tag{11a}$$

whereas, of course,

$$(\lim \nu \to \infty)[(\lim f_B \to 0)\{\nu^{1/2}\zeta_B{}^{-1} \tan f_B\zeta_B\}] = 0 \tag{11b}$$

Because of the critical role of this factor in the eigenvalue equation (14), the results for $f_B \to 0$ do not reduce to those of $f_B = 0$ at high and moderate frequencies. The example in Section 7 shows that the singular behavior penetrates down to frequencies $\nu \sim 1$. Section 8 provides a few more comments and perspectives.

2 The Eigenvalue Equation

Substituting (4c) into (4a) leads to the differential equations[3]

$$\phi_{Jk}{}'' + (\lambda_k{}^2 + i\omega/\bar{\kappa}_J)\phi_{Jk} = 0 \qquad J = M,B,F \tag{12a}$$

where prime denotes y-differentiation. Solution of (12) subject to the conditions (9a,b) gives

$$\phi_{Mk} = A_k \cos z_{Mk}y,\ \phi_{Fk} = B_k \cos z_{Fk}(\pi - y)$$

$$\phi_{Bk} = C_k \cos z_{Bk}y + D_k \sin z_{Bk}y \tag{12b}$$

Here the eigenvalues z_{Jk} are related to the decay parameter

$$\lambda_k = \lambda_{rk} + i\lambda_{ik} \tag{13a}$$

by

$$\lambda_k{}^2 = z_{Mk}{}^2 - i\omega/\bar{\kappa}_M = z_{Fk}{}^2 - i\omega/\bar{\kappa}_F = z_{Bk}{}^2 - i\omega/\bar{\kappa}_B \tag{13b}$$

The interface conditions (9c,d,e,f) impose the requirement that the determinant of the coefficients A, B, C, D vanish. Omitting, for simpler writing, the subscript k, this leads to

$$\Delta \equiv \{k_B{}^2 \cos f_M\zeta_M \cos f_B\zeta_B \cos f_F\zeta_F\{\Delta = 0 \tag{14a}$$

Here

$$\begin{aligned}\zeta_B{}^{-1}\Delta \equiv [\zeta_B{}^2 - k_M'k_F'\zeta_M\zeta_F \tan f_M\zeta_M \tan f_F\zeta_F]\zeta_B{}^{-1} \\ \times \tan f_B\zeta_B + \Delta_2\end{aligned} \tag{14b}$$

and

$$\Delta_2 \equiv k_M'\zeta_M \tan f_M\zeta_M + k_F'\zeta_F \tan f_F\zeta_F \tag{14c}$$

It will be recalled from [4, 6–9] that $\Delta_2 = 0$ is the eigenvalue equation of the two-phase problem. We use the notation

$$k_M' = k_M/k_B,\ k_F' = k_F/k_B,\ k' = k_F/k_M \tag{15}$$

One of the coefficients A, B, C, D in (12) may be assigned arbitrarily. We select

$$C = 1 \tag{16a}$$

(In Table 2 we shall find it more advantageous to normalize to $A = 1$.) Then solution of the system gives

$$\begin{aligned}A = [\cos f_M\zeta_B + D_M \sin f_M\zeta_B]/\cos f_M\zeta_M,\ B \\ = [\cos f_2\zeta_B + D_F \sin f_2\zeta_B]/\cos f_F\zeta_F\end{aligned} \tag{16b,c}$$

In the foregoing

$$D_M = \frac{\zeta_B \tan f_M\zeta_B - k_M'\zeta_M \tan f_M\zeta_M}{\zeta_B + k_M'\zeta_M \tan f_M\zeta_M \tan f_M\zeta_B},$$

$$D_F = \frac{\zeta_B \tan f_2\zeta_B + k_F'\zeta_F \tan f_F\zeta_F}{\zeta_B - k_F'\zeta_F \tan f_2\zeta_B \tan f_F\zeta_F} \tag{16d,e}$$

are two expressions of the coefficients D, equal by virtue of (14). For detailed derivation see the Appendix of [8]. The eigenvalues are related, in the light of (13), by

$$z_F{}^2 = z_M{}^2 + i\nu, \qquad z_B{}^2 = z_M{}^2 + i\rho\nu \tag{17a,b}$$

$$\nu = (\kappa_F{}^{-1} - \kappa_M{}^{-1})\omega, \qquad \rho = (\kappa_B{}^{-1} - \kappa_M{}^{-1})/(\kappa_F{}^{-1} - \kappa_M{}^{-1}) \tag{17c,d}$$

Note that in the absence of a binder layer

$$f_B = 0, f_M = 1 - f_F \tag{18a}$$

and (14) reduces to the two region eigenvalue equation

$$\Delta_2 = 0$$

that was treated earlier, in [4, 6–9, 13].

3 Fourier Expansion

The expansion of the temperature $w(x, y)$ in terms of the eigenmodes $w_k(x, y)$ is given by

$$w(x, y) = \sum_0^\infty C_k e^{-\lambda_k x} \cdot \begin{cases}\phi_{Mk}(y), & 0 \le y \le f_M\pi \\ \phi_{Bk}(y), & f_M\pi \le y \le (1 - f_F)\pi \\ \phi_{Fk}(y), & (1 - f_F)\pi \le y \le \pi\end{cases} \tag{19a}$$

where the expansion coefficients C_k are determined from the biorthogonality formula (see [4, (20)])

$$C_k = \left[\int_0^\pi \chi(y)\Phi_k(y)dy\right] \Big/ \left[\int_0^\pi \phi_k(y)\Phi_k(y)dy\right] \tag{19b}$$

Here

---

[3] For the moment, length is dimensional. But in (14) we revert to dimensionless length.

$$\Phi_k = \begin{cases} k_M\phi_{Mk}(y), & 0 \le y \le f_M\pi \\ k_B\phi_{Bk}(y), & f_M\pi \le y \le (1-f_F)\pi \\ k_F\phi_{Fk}(y), & (1-f_F)\pi \le y \le \pi \end{cases} \tag{20}$$

are the "flux" functions. For the special excitation

$$\chi(y) = 1 \tag{21}$$

we find (omitting subscript k)

$$\begin{aligned} C = 4\{&(k_M/\zeta_M)A \sin f_M\zeta_M + (k_F/\zeta_F)B \sin f_F\zeta_F \\ &+ (k_B/\zeta_B)[\sin f_2\zeta_B - \sin \mathrm{f_M}\zeta_\mathrm{B} + D(\cos f_M\zeta_B \\ &- \cos f_2\zeta_B)]\}/\{(k_M/\zeta_M)A^2(2f_M\zeta_M + \sin 2f_M\zeta_M) \\ &+ (k_F/\zeta_F)B^2(2f_F\zeta_F + \sin 2f_F\zeta_F) + (k_B/\zeta_B)[f_B\zeta_B(1+D^2) \\ &+ (1-D^2)(\sin 2f_2\zeta_B - \sin 2f_M\zeta_B) \\ &+ 2D(\cos 2f_M\zeta_B - \cos 2f_2\zeta_B)]\} \end{aligned} \tag{22}$$

4 High-Frequency Formulas of the Roots

Reference [9] and expressions (17a, b) suggest that for $\nu \to \infty$ we should expect the roots $k = 0, 1, 2 \ldots$ to behave as

Case A: $\zeta_{Mk}{}^2 \to -i\pi^2\nu (k = 0, 3, 6, \ldots)$

Case B: $\zeta_{Fk}{}^2 \to i\pi^2\nu\ (k = 1, 2, 4, 5, 7, 8, 10, \ldots)$

Case C: $\zeta_{Mk}{}^2 \to -i\pi^2\rho\nu$

Case D: $\zeta_{Fk}{}^2 \to i\pi^2\rho\nu$ (23)

In the Appendix it is demonstrated that Cases C and D cannot exist. For Case A we write, as in Appendix B of [9],[4]

$$\begin{aligned} &\zeta_M = g_{1/2}\nu^{1/2} + g_0\nu^0 + g_{-1/2}\nu^{-1/2} + \ldots,\ \zeta_F = h_0\nu^0 + h_{-1/2}\nu^{-1/2} \\ &\quad + h_{-1}\nu^{-1} + \ldots,\ \zeta_B = j_{1/2}\nu^{1/2} + j_0\nu^0 + j_{-1/2}\nu^{-1/2} + \ldots, \\ &\qquad \tan f_F\zeta_F = e_{1/2}\nu^{1/2} + e_0\nu^0 + e_{-1/2}\nu^{-1/2} + \ldots \end{aligned} \tag{25a,b,c,d}$$

We shall adopt the notation

$$\delta = \begin{cases} -1 \\ 1 \end{cases}, \Gamma_1 = \begin{cases} i^{-1/2}/\sqrt{1-\rho} \\ i^{1/2}/\sqrt{\rho-1} \end{cases}, \Gamma_2 = \begin{cases} i^{1/2}/\sqrt{1-\rho}; & 1-\rho > 0 \\ i^{-1/2}/\sqrt{\rho-1}; & \rho - 1 > 0 \end{cases} \tag{26}$$

$$\delta = \begin{cases} -1 \\ 1 \end{cases}, \Gamma_3 = \begin{cases} i^{-1/2}/\sqrt{-\rho} \\ i^{1/2}/\sqrt{\rho} \end{cases}, \Gamma_4 = \begin{cases} i^{1/2}/\sqrt{-\rho}; & -\rho > 0 \\ i^{-1/2}/\sqrt{\rho}; & \rho > 0 \end{cases} \tag{27}$$

On substituting (25) into (14) and observing (17), the roots $k = 0$, 3, 6, ... of Case A are established in the form
$K = 0, 1, 2, \ldots$

$$\begin{aligned} h_0 &= \frac{(2K+1)\pi}{2f_F}, h_{-1/2} = -\Gamma_1\frac{(2K+1)k_F'}{2f_F{}^2}, h_{-1} \\ &= -i\frac{(2K+1)k_F'}{2f_F{}^3\pi(1-\rho)}, \\ e_{1/2} &= \Gamma_1{}^{-1}\frac{2f_F}{(2K+1)k_F'}, e_0 = \frac{2}{(2K+1)\pi}; g_{1/2} = i^{-1/2}\pi, g_0 = 0, \\ g_{-1/2} &= i^{1/2}\frac{(2K+1)^2\pi}{8f_F{}^2}, g_{-1} \\ &= -i^{1/2}\Gamma_1\frac{(2K+1)^2k_F'}{4f_F{}^3}, g_{-3/2} = i^{-1/2}\frac{(2K+1)^2}{8f_F{}^4\pi} \\ &\cdot\left[\frac{3k_F'}{1-\rho} + \frac{(2K+1)^2\pi^2}{16}\right], \mathrm{j}_{1/2} \\ &= \Gamma_2{}^{-1}, j_0 = 0, j_{-1/2} = \Gamma_2\frac{(2K+1)^2\pi}{8f_F{}^2}, \\ j_{-1} &= \delta\frac{(2K+1)^2k_F'}{4f_F{}^3(1-\rho)}, j_{-3/2} \\ &= -i\Gamma_2\frac{(2K+1)^2}{8\pi f_F{}^4(1-\rho)}\left[3k_F'^2 + \frac{(2K+1)^2\pi^2}{16}\right] \end{aligned} \tag{28}$$

Furthermore, with extremely rapid convergence (see Tables 1 and 2 of [9]),

$$\nu \gg 1: \begin{cases} \tan f_M\zeta_M \to -i \\ D, \tan f_M\zeta_B \to \mp i, \end{cases} 1 - \rho \gtrless 0 \tag{29}$$

For Case B set

$$\begin{aligned} &\zeta_F = q_{1/2}\nu^{1/2} + q_0\nu^0 + \ldots,\ \zeta_M = r_0\nu^0 + r_{-1/2}\nu^{-1/2} + \ldots, \\ &\zeta_B = p_{1/2}\nu^{1/2} + p_0\nu^0 + \ldots,\ \tan f_M\zeta_M = m_{1/2}\nu^{1/2} + m_0\nu^0 + \ldots, \end{aligned} \tag{30}$$

The roots $k = 1, 2, 4, 5, 7, \ldots$ are determined from

$K = 0, 1, 2, \ldots$

$$\begin{aligned} r_0 &= \frac{(2K+1)\pi}{2f_M}, r_{-1/2} = -\Gamma_3\frac{(2K+1)k_M'}{2f_M{}^2}, r_{-1} = i\delta\frac{(2K+1)k_M'^2}{2f_M{}^3\rho\pi}; \\ m_{1/2} &= \Gamma_3{}^{-1}\frac{2f_M}{(2K+1)k'_M}, m_0 = \frac{2}{(2K+1)\pi}; q_{1/2} \\ &= i^{1/2}\pi, q_0 = 0, q_{-1/2} = i^{-1/2}\frac{(2K+1)^2\pi}{8f_M{}^2}, \\ q_{-1} &= i^{1/2}\Gamma_4\frac{(2K+1)^2k_M'}{4f_M{}^3}, q_{-3/2} = i^{1/2}\frac{(2K+1)^2}{8\pi f_M{}^4}\left[\frac{k_M'^2}{\rho}(1+2\delta)\right. \\ &\left. + \frac{(2K+1)^2\pi^2}{16}\right]; p_{1/2} = \Gamma_4{}^{-1}\pi, p_0 = 0, p_{-1/2} \\ &= \Gamma_4\frac{(2K+1)^2\pi}{8f_M{}^2}, p_{-1} = -\delta\frac{(2K+1)k_M'}{4f_M{}^3\rho}, p_{-3/2} \\ &= i\Gamma_4\frac{(2K+1)^2}{8\pi f_M{}^4\rho}\left[k_M'^2(1+2\delta) + \frac{(2K+1)^2\pi^2}{16}\right] \end{aligned} \tag{31}$$

Furthermore

$$\nu \gg 1: \begin{cases} \tan f_F\zeta_F \to i \\ D, \tan f_2\zeta_B \to \mp i, \rho \lessgtr 0 \end{cases} \tag{32}$$

We prove (32). For $\zeta_F{}^2 \to \pi^2 i\nu$:

$$\begin{aligned} \zeta \to \pi e^{i\pi/4}\nu^{1/2}, \tan f_F\zeta_F &= \tan[\nu^{1/2}f_F\pi(1+i)/\sqrt{2}] \\ &= \frac{\tan f_F\pi\sqrt{\nu/2} + i\tanh f_F\pi\sqrt{\nu/2}}{1 - i\tan\tanh} \\ &= \frac{i}{\tanh}\,\frac{\tanh^2 - 1 + 1 - i\tan\tanh}{1 - i\tan\tanh} \\ &= \frac{i}{\tanh}\left[1 - \frac{1/\cosh^2}{1 - i\tan\tanh}\right] \to i \end{aligned} \tag{33a,b}$$

$$\zeta_B{}^2 = \zeta_F{}^2 + i\nu(\rho-1)\pi^2 \to \pi^2 i\nu\rho \tag{33c}$$

and, as above

$$\tan f_2\zeta_B \to \tan\left[\nu^{1/2}f_2\pi\begin{Bmatrix} -i(-\rho) \\ i\rho \end{Bmatrix}^{1/2}\right] \to \mp i, \rho \lessgtr 0 \tag{33d}$$

Thus, for $\rho < 0$:

$$m_{1/2} = 2i^{1/2}\sqrt{-\rho}\, f_M/(2K+1)k_M' \tag{33e}$$

The branches of the squareroot are so chosen that the phases bracket 0 as ρ is changed from negative to a positive quantity.

5 The Two Material Composite

In light of the fact that the $f_B \to 0$ case does not reduce to the $f_B = 0$ case, the formulas for $f_B = 0$ cannot be obtained by placing $f_B = 0$ into the Section 4 formulas. They must be derived directly from (25b, d, a), (30b, d, a), (10a, b), (11c). E.g., $h_{-1/2}$, g_{-1} in (28) involve the

---

[4] An intermediate step, writing (25d), as in [9, (B5)], in the form

$$\tan f_F\zeta_F = \tan[(2K+1)\pi/2 - \alpha] = \text{cotan}\,\alpha = \alpha^{-1} - \alpha/3 \ldots, \alpha \to 0 \tag{24a}$$

is also involved here. We also note (see (10)) that for $f\eta \gg 1$

$$\cos f\zeta \simeq \frac{1}{2}e^{if\zeta}, \sin f\zeta \simeq -\frac{i}{2}e^{if\zeta} \tag{24b}$$

while for $fy \gg 1$

$$\cos f\zeta \simeq \frac{1}{2}e^{-if\zeta}, \sin f\zeta \simeq \frac{i}{2}e^{-if\zeta} \tag{24c}$$

conductivity ratio $k_F' = k_F/k_B$ as well as the expression ρ, (14), involving all three diffusivities. In a strictly two material composite there cannot appear a k_B factor or a κ_B term. The appropriate two material coefficients have been listed in [3] employing the awkward former notation (see comments to (10)). We list them again in our present notation (note (14c)).

Roots $k = 0, 3, 6, \ldots; K = 0, 1, 2, \ldots$:

$$h_0 = \frac{(2K+1)\pi}{2f_F}, h_{-1/2} = -i^{-1/2}\frac{(2K+1)k'}{2f_F{}^2},$$

$$h_{-1} = -i\frac{(2K+1)k'^2}{2\pi f_F{}^3};$$

$$e_{1/2} = i^{1/2}\frac{2f_F}{(2K+1)k'}, e_0 = \frac{2}{\pi(2K+1)}; g_{1/2} = i^{-1/2}, g_0 = 0,$$

$$g_{-1/2} = i^{1/2}\frac{(2K+1)^2\pi}{8f_F{}^2}, g_{-1} = -\frac{(2K+1)^2k'}{4f_F{}^3}, g_{-3/2}$$

$$= i^{-1/2}\frac{(2K+1)^2}{8\pi f_F{}^4}\left[3k'^2 + \frac{(2K+1)^2\pi^2}{16}\right] \quad (35)$$

Furthermore (29a), i.e.,

$$\nu \gg 1: \tan f_M\zeta_M \rightarrow -i \quad (36)$$

also holds. On the other hand

Roots $k = 1, 2, 4, 5, 7, \ldots; K = 0, 1, 2, \ldots$:

$$r_0 = \frac{(2K+1)\pi}{2f_M}, r_{-1/2} = -i^{1/2}\frac{2K+1}{2f_M{}^2k'}, r_{-1} = i\frac{2K+1}{2\pi f_M{}^3k'^2},$$

$$m_{1/2} = i^{-1/2}\frac{2f_Mk'}{2K+1}, m_0 = -\frac{2}{\pi(2K+1)}; q_{1/2} = i^{1/2}\pi, q_0 = 0,$$

$$q_{-1/2} = i^{-1/2}\frac{(2K+1)^2\pi}{8f_M{}^2}, q_{-1} = -\frac{(2K+1)^2}{4f_M{}^3k'}, q_{-3/2}$$

$$= i^{1/2}\frac{(2K+1)^2}{8\pi f_M{}^4}\left[\frac{3}{k'^2} + \frac{(2K+1)^2\pi^2}{16}\right] \quad (37)$$

$$\nu \gg 1: \tan f_F\zeta_F \rightarrow i \quad (38)$$

Section 6

$$(\lim f_B \rightarrow 0)[\lim \nu \rightarrow \infty] \neq (\lim \nu \rightarrow \infty)[\lim f_B \rightarrow 0]$$

We now return to the three material composite of Section 4. The relation (11b) is obvious. On the other hand, see (26),

$k = 0, 3, 6, \ldots$:

$$\lim_{\nu\rightarrow\infty} \nu^{1/2}\zeta_B{}^{-1}\tan f_B\zeta_B = \delta i/j_{1/2} = \delta i\Gamma_2/\pi$$

$$= \frac{1}{\pi}\begin{Bmatrix}-i^{3/2}/(1-\rho)^{1/2}\\ i^{1/2}/(\rho-1)^{1/2}\end{Bmatrix} = \Gamma_1/\pi = \lim_{f_B\rightarrow 0}\lim_{\nu\rightarrow\infty} \quad (39a)$$

inasmuch as Γ_1/π is independent of f_B. Likewise,

$k = 1, 2, 4, 5, 7, \ldots$:

$$\lim_{\nu\rightarrow\infty} \nu^{1/2}\zeta_B{}^{-1}\tan f_B\zeta_B = \delta i/p_{1/2} = \Gamma_3/\pi = \lim_{f_B\rightarrow 0}\lim_{\nu\rightarrow\infty} \quad (39b)$$

7 Example. Padéing

As a representative example we return to the laminate consisting of a nickel matrix M with aluminum filler F, considered in the earlier papers, augmented by a rubber binder B. The composite is assigned the properties

$$\bar{k}_F = 174 \text{ w/mC} = 100 \text{ Btu/hr-ft-F} = 10\,\bar{k}_M = 1000\,\bar{k}_B \quad (40a)$$

$$\bar{\kappa}_F = 7.76 \times 10^{-5}\text{m}^2/\text{s} = 3.0 \text{ ft}^2/\text{h} = 10\bar{\kappa}_M = 1000\,\bar{\kappa}_B \quad (40b)$$

$$\ell = 0.076 \text{ m} = 0.08\pi \text{ ft}, \rho = -110 \quad (40c,d)$$

Five cases of volume fractions are considered ($f_B \rightarrow 0$ is denoted by $f_B = 0$, nonexistence of B by $f_B = \mathbf{0}$):

$$\begin{array}{llll}
\text{I} & f_B = 0.08 & f_M = 0.667 & f_F = 0.253 \\
\text{II} & \phantom{f_B = {}}0.01 & f_M = 0.667 & f_F = 0.323 \\
\text{III} & \phantom{f_B = {}}0.00001 & f_M = 0.667 & f_F = 0.33299 \\
\text{IV} & \phantom{f_B = {}}0 & f_M = 0.667 & f_F = 0.333 \\
\text{V} & \phantom{f_B = {}}\mathbf{0} & f_M = 0.667 & f_F = 0.333 \text{ (two-phase problem)}
\end{array} \quad (41)$$

After calculation of the j, p coefficients (28), (31), the eigenvalues were computed, carrying the expansions to the $j_{-3/2}, p_{-3/2}$ terms. These were then Padéd, as described below. Next ζ_M and ζ_F were determined from (17). Independently, these were calculated also from the g (28), q (31) coefficients for checking consistency. In the case of the two-phase composite $f_B = \mathbf{0}$ we calculated first ζ_{M0}, ζ_{F1} on the basis of g (35), q (37), and then used (17a). The Padé [2/1] eigenvalues so obtained are listed in Table 1. (In retrospect, use of the diagonal Padé [2/2] would have been preferable.) One notes that on a log-log plot, $|z_{B0}|$, $|z_{M0}|$, $|z_{B1}|$, $|z_{F1}|$ appear as straight lines, whereas $|z_{F0}|$, $|z_{M1}|$ approach their asymptotic values more slowly.

For adequate accuracy Padéing is necessary for the five-term power expansions at $\nu \lesssim 100$. Padéing the ζ_{B0} eigenvalues at $\nu = 10$ is illustrated in Table 2. At $\nu = 10$ the Padéd results were also newtonized in accordance with the recipe of [14].[5] Padéing, see [15 (1.11)], proceeds as follows. One represents

$$\zeta_B \equiv j_{1/2}\nu^{1/2} + j_0\nu^0 + j_{-1/2}\nu^{-1/2} + \ldots$$
$$\equiv \nu^{1/2}[T_0 + T_1\,\nu^{-1/2} + T_2\nu^{-1} + T_3\nu^{-3/2} + \ldots] \equiv \nu^{1/2}S \quad (42a)$$

by a rational fraction (r = row, c = column in the Table)

$$\nu^{1/2}[r/c] \equiv \nu^{1/2}N_r(\nu)/D_c(\nu) = \nu^{1/2}[N_0 + N_1\nu^{-1/2} + N_2\nu^{-1} + \ldots$$
$$+ N_r\nu^{-r/2}]/[1 + D_1\nu^{-1/2} + D_2\nu^{-1} + \ldots + D_c\nu^{-c/2}] \quad (42b)$$

then equates $[r/c]$ to the partial sums S_n of S, with $n = r + c$, clears fractions, and solves for the coefficients N and D. Baker [15, p. 77] provides a very convenient algorithm for doing this. In practice we programmed Baker's recursion formulas and solved for the highest r coefficient by evaluation at $\nu^{-1/2} = -1, 0, 1, 2$, bypassing determination of the other coefficients in $[r/c]$. We Padéd both real and imaginary parts of the roots. Table 1 shows modulus and phase of the so-determined values. Table 2 refers only to moduli. It is noted that while our five-term power series approximation [4/0] is totally misleading, the [2/1], [2/2], [1/2] Padé-adjusted values are consistent with each other and with two-phase calculation behavior.

Table 3 shows that the approach of $\nu^{1/2}\zeta_{B0}{}^{-1}\tan f_B\zeta_{B0}$ to $i^{-1/2}\pi^{-1}(1-\rho)^{-1/2}$ as ν increases sets in at already moderate frequencies $\nu \sim 1$. The case $\nu = 1$ is found to be much closer to $\nu = \infty$ than to $\nu = 0$. Note from [14] that for $\nu = 0$ the value of the expression is

$$\nu \rightarrow 0: \nu^{1/2}\zeta_{B0}{}^{-1}\tan f_B\zeta_{B0} \simeq \nu^{1/2}f_B \rightarrow 0 \quad (43)$$

8 Discussion

Some of the observations that may be drawn from the previous analysis are:

(1) The higher conductivity materials are associated with lower eigenvalues in the $k = 0$ mode.

(2) In contrast to the two-phase problem where diffusivity dependence appears only as a scale factor in the dimensionless frequency ν, in the three-phase problem the diffusivity ratios enter the calculations explicitly through appearance of ρ, (17d), in formulas (26), (27) and elsewhere. In fact, there is the tantalizing result established in Section 6, the noninterchangeability of the $\nu \rightarrow \infty$ and the $f_B \rightarrow 0$ limiting processes. This produces a persistence of the dependence of the results on ρ and on k_B/k_M, even in the limit of $f_B \rightarrow 0$, and this is the cause of the disagreement with the two-phase $f_B = \mathbf{0}$ case. The latter case is, naturally, not affected by the properties of the nonexistent phase B. The practical meaning of this observation is that *traces*

---

[5] After Padéing, the residuals $R = \Delta(\zeta_{\text{approx}})$ ranged from $R = 180.0 + 178.3i$ at $f_B = 0.08$ to $R = -609.3 - 610.5i$ at $f_B = 0.00001$. After three Newton iterations, the first became $R = 10^{-4}(-2 + 7i)$; after 12 iterations the second became $R = 10^{-4}(2 + 7i)$.

Table 1 Eigenvalues z_0 (upper table), z_1 (lower table), modulus phase (deg)

f_B	ν	10^8	10^4	10^2	10	newtonized 10
	M	10000.0000 −45.0000	99.99673 −44.9970	9.994552 −44.9669	3.156609 −44.8949	3.157653 −44.9991
.08	*B*	105356.5375 −45.0000	1053.56506 −45.0000	105.356020 −44.9997	33.316124 −44.9991	33.316223 −44.9992
	F	1.9597 .4772	1.10908 16.0663	.398451 21.6765	.226342 22.2345	.204098 22.3225
	M	10000.0000 −45.0000	99.99778 −44.9978	9.995802 −44.9741	3.157859 −44.9174	3.160132 −44.9120
.01	*B*	105356.5375 −45.0000	1053.56516 −45.0000	105.356139 −44.9998	33.316243 −44.9993	33.316458 −44.9992
	F	1.5378 .3771	.94681 14.8305	.351203 21.4571	.200061 22.1618	.183180 18.9677
	M	10000.0000 −45.0000	99.99789 −44.9978	9.995937 −44.9749	3.157995 −44.9202	3.133901 −44.3931
.00001	*B*	105356.5375 −45.0000	1053.56518 −45.0000	105.356152 −44.9998	33.316256 −44.9993	33.313948 −44.9946
	F	1.4919 .3677	.92784 14.6681	.345693 21.4261	.196998 22.1515	.525057 20.5000
	M	10000.0000 −45.0000	99.99789 −44.9979	9.995937 −44.9749	3.157995 −44.9202	3.133513 −44.3920
0	*B*	105356.5375 −45.0000	1053.56518 −45.0000	105.356162 −44.9998	33.316256 −44.9993	33.313912 −44.9946
	F	1.4919 .3693	.92782 14.6680	.345688 21.4261	.196998 22.1515	.526801 20.6698
0	*M*	10000.0000 −45.0000	99.99961 −44.9998	9.999586 −44.9976	3.161862 −44.9924	
	F	1.4043 3.3956	.33712 21.4877	.108392 22.3948	.061028 22.4676	
	M	.7492 .0436	.72595 1.7299	.564253 10.6913	.392155 16.9218	
.08 to 0	*B*	104880.8848 −45.0000	1048.8088 −45.0000	104.880331 −44.9992	33.164957 −44.9967	
	F	10000.0000 45.0000	100.00016 44.9985	10.005824 44.9152	3.175918 44.6372	
0	*M*	.7471 −.1922	.55784 −10.9737	.233837 −20.5301	.134838 −21.8537	
	F	10000.0000 45.0000	99.99942 44.9992	9.998204 44.9882	3.160292 44.9623	

Table 2 Padé Table for $|\zeta_{B0}|$ at $\nu = 10$. Upper Table $f_B = .08$, lower Table $f_B = .01$. $f_B = .08$:

$$\zeta_{B0} = 23.40434\,(1-i)\nu^{1/2} - 0.41175\,(1+i)\nu^{-1/2} - 139.07705\nu^{-1} + 17615.69752\,(1-i)\nu^{-3/2}$$

R	*C* 0	1	2	3	4
0	33.316662	33.316662	33.316611	33.745573	34.136528
1	33.316662	33.316662	31.858824	35.132820	
2	33.316714	33.316124	33.315681		
3	30.342213	33.315716			
4	280.967046				
0	33.316662	33.316662	33.316643	33.087207	33.988670
1	33.316662	33.316662	32.384711	35.170293	
2	33.316682	33.316243	33.315911		
3	31.846197	33.315930			
4	126.213275				

Table 3 $\nu^{1/2}\zeta_B{}^{-1} \tan f_B \zeta_B$

f_B	ν 10^8	10^4	10^3	10^2	10^1	10^0
.08	.021363561 −.021363561i	.021363557 −.021363577i	.021363555 −.021363625i	.021363555 −.021363777i	.021363123 −.021364101i	.021608122 −.022802018i
.01	.021363561 −.021363561i	.021363558 −.021363573i	.021363578 −.021363608i	.020976231 −.021768681i	.027394774 −.009673514i	.009984114 −.000364455i

of impurities B in the interfaces of two-phase MFMFM... composites may radically alter the anticipated behavior of the composite. Why is this so? "When the frequency goes to infinity, we can imagine the 'wavelength' of the heat disturbance going to zero. If this limit is taken first, the 'wavelength' will always be less than the thickness of the binder layer, and it is not so impossible that its presence will always be felt."[6]

An important question is whether the nonequality of (11a) and (11b) is of practical (engineering) significance. In other words, under what circumstances do we find ourselves in the high-frequency regime $|\nu| \gg 1$? This question was answered in the Introduction. Note, however, that the quantity of critical significance is the penetration distance of the temperature field from edge $x = 0$. This is, by [9, (33)] ($\kappa_F/\kappa_M \neq 1$ is assumed):

$$|\nu| \gg 1: \lambda_r^{-1} = [|\nu|/2(-1 + \kappa_F/\kappa_M)]^{-1/2} \tag{44a}$$

$$= 0.3 \text{ for } \kappa_F/\kappa_M = 10, |\nu| = 200 \tag{44b}$$

in units of $\ell/2\pi$.

Perspectives. (a) When $\kappa_F \simeq \kappa_M$, formula (6) becomes useless. Work out this case in detail.[7]

(b) Experimental evidence [16] confirms prediction in the NSF Grant Proposal GK33844 that at moderate frequencies heat propagation follows the rule

$$T(0, y, t) = \cos \omega t: T(x, y, t) = e^{-x(\omega/2\bar{\kappa}_A)^{1/2}} \cos [\omega t - x(\omega/2\bar{\kappa}_p)^{1/2}] \tag{45}$$

involving two equivalent diffusivities, $\bar{\kappa}_A$ for amplitude, $\bar{\kappa}_p$ for phase. Derive the result analytically.[7]

(c) Investigate the stress counterpart of the separation of response into low frequency and high-frequency regimes.

Acknowledgment

The exploratory paper [4], references [6–9, 13], the early version of the present paper, and the largely experimental paper [16] (plus Master's thesis [8] by E. S. Kaczenski and Ph.D. theses by A. M. Manaker and V. H. Truong) constitute the written product of NSF Grant GK33844. We are much indebted to NSF for support. We express our appreciation also to the University of Massachusetts Computing Center for use of their facilities. G. Horvay wishes to express his indebtedness also to E. L. Reiss and to J. D. Cole, who in superb Rensselaer Polytechnic Institute seminar lectures, more than a dozen years ago, awakened in him an interest in Singular Perturbations.

References

1 Weng, M. T., Koh, S. L., "A Continuum Theory of Heat Conduction in Laminates," *Proc. 2nd SMIRT Conference*, Berlin, 1973, paper L1/5.

2 Ben-Amoz, M., "On Heat Conduction in Laminated Composites," *International Journal of Engineering Science*, 1974, Vol. 12, p. 633.

3 Nayfeh, A. H., "A Continuum Mixture Theory of Heat Conduction in Laminated Composites," *Journal of Applied Mechanics*, 1975, Vol. 97, p. 399.

4 Horvay, G., Mani, R., Veluswami, M. A., and Zinsmeister, G. E. "Transient Heat Conduction in Laminated Composites," ASME JOURNAL OF HEAT TRANSFER, 1973, Vol. 95, p. 309.

5 Sun, C. T., Achenbach, J. D., Hermann, G., "Time-Harmonic waves in a stratified Medium Propagating in the Direction of the Layering," *Journal of Applied Mechanics* 1968, Vol. 90, p. 408.

6 Manaker A. M., and Horvay, G., "Thermal Response in Laminated Composites," *Zeitschrift f. Angewandte Math. u. Mech.*, 1975, Vol. 55, p. 503.

7 Kaczenski, E. S., and Horvay, G., "Thermal Response of Layered Composites," *Trans. Japan Soc. for Composite Materials* 1975, Vol. 1, p. 1.

8 Kaczenski, E. S., "Thermal Transients in Layered Composites," Master's thesis, University of Massachusetts, 1974.

9 Horvay, G., and Manaker, A. M., "Heat Flow in Laminated Composites Parallel to the Layering when the Surface Heating is of High Frequency," *Proc. 1975*, Boston AIME Conference on Composites, Vol. 2, p. 527.

10 Carrier, G. F., "Singular Perturbation Theory and Geophysics," *SIAM Review*, 1970, Vol. 12, p. 175.

11 Smith, D. R., "The Multivariate Method in Singular Perturbation Analysis," *SIAM Review*, 1975, Vol. 17, p. 221.

12 Eckhaus, W., *Matched Asymptotic Expansions and Singular Perturbations*, American Elsevier, 1973.

13 Manaker, A. M., and Horvay, G. "Frequency Response of Laminated Composites Subject to Surface Heating," *Proc. 5th International Heat Trans. Conf.*, Tokyo, 1974, paper Cu 4.2.

14 Gold, B., and Horvay, G., "Longitudinal Heat Propagation in Three-Phase Laminated Composites at Low Exciting Frequencies," in preparation

15 Baker, G. E., *Essentials of Padé Approximants*, Academic Press, 1975.

16 Truong V. H., and Zinsmeister, G. E., "Transient Heat Transfer in Laminated Composites—an Experimental Study," *International Journal of Heat and Mass Transfer*, in press.

APPENDIX

Non-existence of Cases C, D, Formulas (23)

Were we to write

$$\zeta_M = s_{1/2}\nu^{1/2} + s_0\nu^0 + \dots$$

$$\zeta_F = t_{1/2}\nu^{1/2} + t_0\nu^0 + \dots$$

$$\zeta_B = u_0\nu^0 + u_{-1/2}\nu^{-1/2} + \dots$$

in accordance with Case C

$$\zeta_M{}^2 \rightarrow -i\pi\rho\nu$$

and also

$$\tan f_B\zeta_B = \upsilon_{1/2}\nu^{1/2} + \upsilon_0\nu^0 + \upsilon_{-1/2}\nu^{-1/2} + \dots = \alpha^{-1} - \alpha/3 \dots$$

as in (25), then we would find on substituting back into the $\Delta = 0$ equation that the leading term, a $\nu^{3/2}$ power, vanishes only when $\upsilon_{1/2} = 0$. Therefore the assumption is incorrect. The Case D is handled similarly.

---

[6] For this comment we are indebted to a referee.

[7] This work is now in progress.

A. D. Kraus
Fellow ASME,
College of Engineering

A. D. Snider
College of Natural Sciences

L. F. Doty
College of Engineering

University of South Florida,
Tampa, Fla.

An Efficient Algorithm for Evaluating Arrays of Extended Surface

In the consideration of single longitudinal fins of rectangular, trapezoidal, and triangular profile and in arrays of extended surface composed of these fins, it is shown that conditions of heat flow and temperature excess at the fin or array tip induce conditions of heat flow and temperature excess at the fin or array base. In particular, there is a linear transformation between the aforementioned data at the fin tip and the fin base. The conventional fin efficiency is abandoned and single fins or arrays of extended surface are instead characterized by a single important parameter, the heat flow to temperature excess ratio, which is a function only of fin geometry and heat transfer parameters. Algorithms are provided for combining the effects of individual fins in arrays of extended surface. A modification of the procedures developed leads to an exact solution for the double stack with unequal heat distribution at opposite ends, a problem which has heretofore required iterative solution procedures.

Introduction

The heat transfer characteristics of arrays of extended surface, such as those which occur in compact heat exchangers [1],[1] are usually analyzed by a procedure expounded in [2]. Briefly, the technique is as follows:

One begins by writing the differential equations relating the heat flow and temperature excess in each fin in the array, under certain idealizing assumptions attributed to Murray [3] and Gardner [4]. Then the boundary conditions, expressing continuity at the interfaces (nodes) between adjacent fins, are listed. Finally, the operating temperatures or heat flow rates at the base surfaces are appended, and the overall system is treated as a rather complex, linear, boundary value problem.

When the individual differential equations can be integrated analytically, the problem ultimately becomes one of solving a system of linear algebraic equations; if analytic integrations are impossible, finite-difference approximations are introduced and the equations must be solved iteratively on a computer [2]. The performance of the heat exchanger is then expressed in terms of the *overall passage efficiency,* which is defined as the ratio of the actual heat dissipated or absorbed by the exchanger surfaces, to the heat that would be ideally dissipated or absorbed if all surfaces were maintained at the base temperature.

The present paper describes a new procedure which treats each fin as a lumped parameter (actually, a lumped parameter matrix) and cascades all of the fins in the array via matrix operations. This algorithm improves on the existing technique in several directions. First, the differential equations for the individual fins are uncoupled and are solved with initial-value data. This guarantees that the solutions of the equations will always be analytically well posed (in contrast to boundary value problems [5]), easily computed numerically (using Runge-Kutta methods, rather than iterative or "shooting" methods), and convenient to tabulate (because the equations are uncoupled, any solution for a given configuration is applicable to other configurations). Second, the cascading process which mathematically assembles the array characteristics from the fin characteristics is quite simple; it can easily be done on a hand calculator, and the effect of each parameter is easily isolated—an important advantage for the design engineer. Third, the heat exchanger performance is measured by the ratio of the total heat dissipated to the temperature excess (base temperature minus the coolant fluid temperature), a parameter much more closely related to design specifications than the heretofore considered overall passage efficiency. Fourth, while the analysis still evaluates heat exchangers operating under idealized conditions, some of the Murray-Gardner assumptions are relaxed.

The terminology in what follows is illustrated in Figs. 1–3. Fig. 1 depicts a fairly complex (for purposes of illustration) finned passage subjected to equal operating temperatures on right and left base surfaces. From symmetry, one can see that there is no heat flow across the imaginary surface indicated by the dashed line; hence if the heat dissipated by the "repeating section" shown in Fig. 2 can be computed, the total heat dissipated by the exchanger is obtained by simple multiplication. This feature arises often in practice but is not essential to the algorithm. It may be observed that in Fig. 2, the individual fins have been numbered and that the zero heat-flow conditions have been enforced by insulations. It illustrates that fins can have arbitrary profiles, can be connected in "series" or "parallel," and can have adiabatic conditions (zero heat flux) at the tip or along any face.

---

[1] Numbers in brackets designate References at end of paper.

Contributed by the Heat Transfer Division for publication in the JOURNAL OF HEAT TRANSFER. Manuscript received by the Heat Transfer Division May 19, 1977.

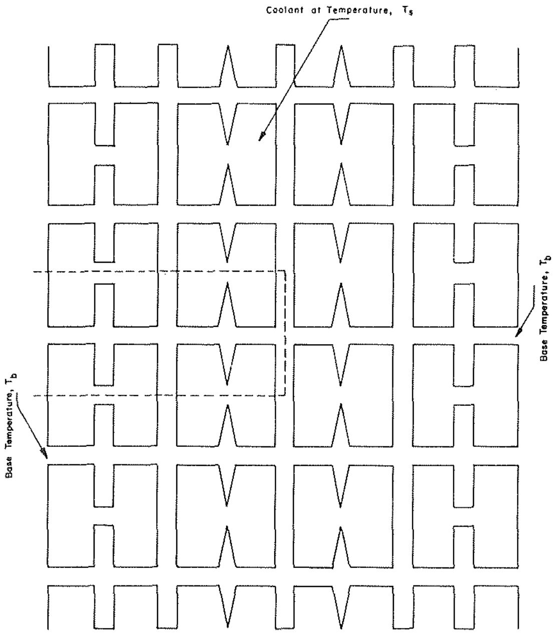

Fig. 1

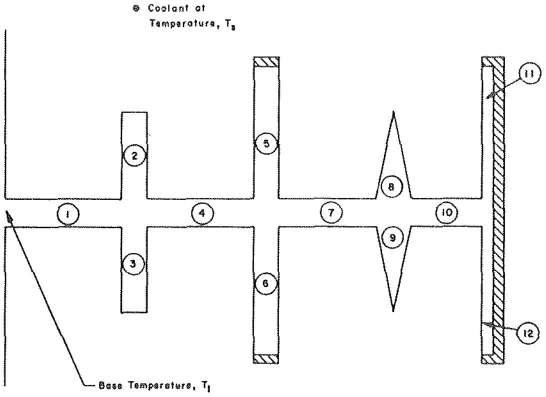

Fig. 2

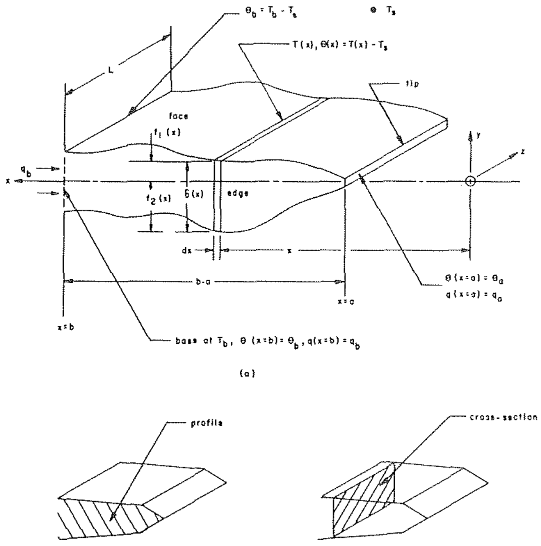

(a)

Fig. 3

Fig. 3 illustrates the terminology and defines the coordinate system which is used in this paper when discussing individual fins. It may be observed that the positive orientation of the x-coordinate is taken in a direction from fin tip to fin base and that the edges of the fin are parallel to the x, y-plane; the fin profile is characterized by two curves, $y = f_1(x)$ and $y = f_2(x)$.

Characterization of Individual Fins

In deriving the differential equation for heat flow along the fin, several of the Gardner-Murray assumptions are involved. These are as follows:

(1) There is no time dependence. Only the steady-state behavior is considered.
(2) There is no y or z-dependence (see Fig. 3). (This follows if the transverse Biot number, $h\delta/k$, is much less than unity.)
(3) The coolant temperature, T_s, is constant and uniform. This idealization assures that it is the performance of the fin itself, and not the overall cooling design, that is being evaluated.
(4) There are no heat sources within the fin itself.
(5) Heat is transferred by convection to the coolant (precluding a radiation mode).

At any point x, the heat flowing in the fin is given by the familiar equation

$$q(x) = k(x)A(x)\frac{dT(x)}{dx} \tag{1}$$

Nomenclature

A = cross-sectional area, ft^2(m^2)
a = location of tip of fin from origin of coordinate system, ft (m)
b = location of base of fin from origin of coordinate system, ft (m)
f = designates profile function, ft (m)
g = designates a bilinear function
h = heat transfer coefficient, Btu/ft^2-hr-°F (watts/m^2-°C)
I = modified Bessel Function
K = modified Bessel Function
k = thermal conductivity, Btu/ft-hr-°F (watts/m-°C)
L = fin length, ft (m)
m = fin performance factor, ft^{-1} (m^{-1})
n = fin performance factor, ft^{-1}(m^{-1})
q = heat flow, Btu/hr (watts)
S = surface area, ft^2(m^2)
T = temperature, °F(°C)
x = height coordinate, ft (m)
y = width coordinate, ft (m)
z = length coordinate, ft (m)
α = exponent dimensionless
β = exponent dimensionless
Γ = thermal transmission matrix
γ = element of thermal transmission matrix
δ = fin width, ft (m)
η = fin efficiency, dimensionless
θ = temperature excess, °F(°C)
λ = independent solution to temperature excess differential equation
μ = thermal transmission ratio, Btu/hr-°F. (watts/°C)
σ = fin height, ft (m)
ϕ = fin taper angle, deg

Subscripts

a = designates fin tip
b = designates fin base
ℓ = designates left end of configuration
r = designates right end of configuration
s = designates surroundings or coolant

where $k(x)$ is the thermal conductivity (assumed to be temperature independent) and where the customary minus sign is omitted so that a positive flow of heat is opposed to the positive sense of the x-coordinate (in this paper, all surfaces are presumed to be at a higher temperature than the surrounding coolant fluid). This requires that heat injected at the base of the fin be considered positive and that if heat is injected into the fin at the tip of the fin, the tip heat flow must be considered negative. The cross-sectional area (Fig. 3) is given by

$$A(x) = [f_1(x) - f_2(x)]L \tag{2}$$

The heat flow out of an infinitesimal surface area, $dS(x)$, is given in terms of the coefficient of heat transfer, $h(x)$, and the temperature excess, $\theta(x) = T(x) - T_s$, by

$$dq(x) = \theta(x)h(x)dS(x) \tag{3}$$

Taking into account that any of the four surface rectangles—top and bottom face and front and rear edge (Fig. 3)—bounding the element of fin at x may be considered as adiabatic, one cautiously writes (3) as

$$\begin{aligned} dq(x) = \theta(x)\{h_{\text{top}}(x)[1 + f_1'(x)^2]^{1/2} + h_{\text{bot}}(x)[1 + f_2'(x)^2]^{1/2}\}Ldx \\ + \theta(x)[h_{\text{front}}(x) + h_{\text{rear}}(x)][f_1(x) - f_2(x)]dx \end{aligned} \tag{4}$$

where any or all of the heat transfer coefficients may be zero.

Conservation of energy then yields, with $dT(x) = d\theta(x)$,

$$\begin{aligned} \frac{d}{dx}\left\{k(x)L[f_1(x) - f_2(x)]\frac{d\theta(x)}{dx}\right\} \\ - \theta(x)\{h_{\text{top}}(x)[1 + f_1'(x)^2]^{1/2} + h_{\text{bot}}(x)[1 + f_2'(x)^2]^{1/2}\}L \\ - \theta(x)[h_{\text{front}}(x) + h_{\text{rear}}(x)][f_1(x) - f_2(x)] = 0 \end{aligned} \tag{5}$$

In many cases of interest the thermal conductivity and the heat transfer coefficient are constant, and with adiabatic edges ($h_{\text{front}} = h_{\text{rear}} = 0$), (5) reduces to

$$\begin{aligned} \frac{d}{dx}\left\{[f_1(x) - f_2(x)]\frac{d\theta(x)}{dx}\right\} \\ - \left\{\frac{h_{\text{top}}}{k}[1 + f_1'(x)^2]^{1/2} + \frac{h_{\text{bot}}}{k}[1 + f_2'(x)^2]^{1/2}\right\}\theta(x) = 0 \end{aligned} \tag{6}$$

Equation (5) is a linear homogeneous second order differential equation for $\theta(x)$. It describes any fin satisfying the idealized conditions. According to the theory [5], the equation is *regular* at all points where

$$k(x)A(x) \equiv k(x)L[f_1(x) - f_2(x)] \neq 0 \tag{7}$$

and *singular* when this expression is zero. The latter situation can only arise physically when $f_1(x) = f_2(x)$, i.e., when the fin has zero thickness. This happens at the tips of certain "terminal" fins as illustrated by the triangular fins (8) and (9) in Fig. 2.

Accordingly, separate characterizations of "regular" fins, when (7) is valid, and "singular" fins, which have zero tip thickness, will now be developed.

Regular Fins

The theory [5] guarantees that (5) has two independent solutions $\lambda_1(x)$ and $\lambda_2(x)$ satisfying the initial conditions

$$\lambda_1(b) = 1; \quad \frac{d\lambda_1(b)}{dx} = 0 \tag{8}$$

and

$$\lambda_2(b) = 0 \quad \frac{d\lambda_2(b)}{dx} = \frac{1}{k(b)A(b)} \tag{9}$$

subject to certain continuity conditions that must be imposed on h and k, (indeed, if h and k happen to have discontinuities, one merely breaks the fin into shorter segments where continuous h and k prevail). The temperature excess and heat flow are then given in terms of the values at the base of the fin, θ_b and q_b, by the equations

$$\theta(x) = \theta_b\lambda_1(x) + q_b\lambda_2(x) \tag{10}$$

and

$$q(x) = k(x)A(x)[\theta_b\lambda_1'(x) + q_b\lambda_2'(x)] \tag{11}$$

Equations (10) and (11) produce a *thermal transmission matrix*, Γ, which gives tip conditions (where $x = a$) in terms of base conditions

$$\begin{bmatrix} \theta_a \\ q_a \end{bmatrix} = [\Gamma]\begin{bmatrix} \theta_b \\ q_b \end{bmatrix} = \begin{bmatrix} \gamma_{11} & \gamma_{12} \\ \gamma_{21} & \gamma_{22} \end{bmatrix}\begin{bmatrix} \theta_b \\ q_b \end{bmatrix} \tag{12}$$

where

$$\gamma_{11} = \lambda_1(a)$$

$$\gamma_{12} = \lambda_2(a)$$

$$\gamma_{21} = k(a)A(a)\lambda_1'(a)$$

$$\gamma_{22} = k(a)A(a)\lambda_2'(a)$$

The thermal transmission matrix depends only on the geometry and heat transfer properties of the fin and can easily be computed for any fin, if necessary, by Runge-Kutta integration [5]. Several examples can be extracted from the literature, with proper reinterpretation.

For the *longitudinal fin of rectangular profile*, h and k are constant, $h_{\text{top}} = h_{\text{bottom}} = h$, $h_{\text{front}} = h_{\text{rear}} = 0$, $f_1(x) = \delta/2 = -f_2(x)$, $A(x) = \delta L$, and $b - a = \sigma$. With these one obtains [2]

$$\lambda_1(x) = \cosh m(b - x) \tag{13}$$

$$\lambda_2(x) = -\frac{\sinh m(b - x)}{(2hk\delta)^{1/2}L} \tag{14}$$

where

$$m = \left(\frac{2h}{k\delta}\right)^{1/2} \tag{15}$$

hence

$$[\Gamma] = \begin{bmatrix} \cosh m\sigma & -\dfrac{\sinh m\sigma}{(2hk\delta)^{1/2}L} \\ -(2hk\delta)^{1/2}L \sinh m\sigma & \cosh m\sigma \end{bmatrix} \tag{16}$$

If one face of the longitudinal fin of rectangular profile is considered as insulated (see fins (11) and (12) in Fig. 2), $h_{\text{bot}} = 0$ and Γ becomes

$$[\Gamma] = \begin{bmatrix} \cosh m\sigma & -\dfrac{\sinh m\sigma}{(hk\sigma)^{1/2}L} \\ -(hk\delta)^{1/2}L \sinh m\sigma & \cosh m\sigma \end{bmatrix} \tag{17}$$

where in this case

$$m = \left(\frac{h}{k\delta}\right)^{1/2} \tag{18}$$

For the *longitudinal fin of trapezoidal profile* with the nomenclature of Fig. 4, one extracts from [2]

$$\lambda_1(x) = \frac{K_1(2nb^{1/2})I_0(2nx^{1/2}) + I_1(2nb^{1/2})K_0(2nx^{1/2})}{K_1(2nb^{1/2})I_0(2nb^{1/2}) + I_1(2nb^{1/2})K_0(2nb^{1/2})} \tag{19}$$

$$\lambda_2(x) = \frac{b^{1/2}}{k\delta_b Ln}\;\frac{K_0(2nb^{1/2})I_0(2nx^{1/2}) - I_0(2nb^{1/2})K_0(2nx^{1/2})}{K_1(2nb^{1/2})I_0(2nb^{1/2}) + I_1(2nb^{1/2})K_0(2nb^{1/2})} \tag{20}$$

and

$$[\Gamma] = \begin{bmatrix} \lambda_1(a) & \lambda_2(a) \\ \dfrac{ak\delta_a L}{b}\lambda_1'(a) & \dfrac{ak\delta_a L}{b}\lambda_2'(a) \end{bmatrix} \tag{21}$$

Here I and K denote modified Bessel Functions [2],

$$n = \left(\frac{h}{k \sin \phi}\right)^{1/2}$$

and

$$\lambda_1'(x) = \frac{n}{x^{1/2}} \; \frac{K_1(2nb^{1/2})I_1(2nx^{1/2}) - I_1(2nb^{1/2})K_1(2nx^{1/2})}{K_1(2nb^{1/2})I_0(2nb^{1/2}) + I_1(2nb^{1/2})K_0(2nb^{1/2})} \qquad (22)$$

$$\lambda_2'(x) = \frac{(b/x)^{1/2}}{k\delta_b L} \; \frac{K_0(2nb^{1/2})I_1(2nx^{1/2}) + I_0(2nb^{1/2})K_1(2nx^{1/2})}{K_1(2nb^{1/2})I_0(2nb^{1/2}) + I_1(2nb^{1/2})K_0(2nb^{1/2})} \qquad (23)$$

Specialists may note the deviance of this geometry from that used by Harper and Brown [6] who placed the origin at a distance $\delta_a/2$ from the fin tip.

For the *longitudinal fin of concave parabolic profile* with the nomenclature of Fig. 5, it is seen that

$$f_1(x) = \frac{\delta_b}{2}\left(\frac{x}{b}\right)^2 = -f_2(x) \qquad (24)$$

and if it is assumed that $\delta_b \ll b$ so as to neglect the $f_1'(x)$ and $f_2'(x)$ terms in (5), one finds [2]

$$\lambda_1(x) = \frac{1}{\alpha - \beta}\left[\alpha\left(\frac{x}{b}\right)^{\beta} - \beta\left(\frac{x}{b}\right)^{\alpha}\right] \qquad (25)$$

$$\lambda_2(x) = \frac{b}{k\delta_b L(\alpha - \beta)}\left[\left(\frac{x}{b}\right)^{\alpha} - \left(\frac{x}{b}\right)^{\beta}\right] \qquad (26)$$

with

$$\alpha, \beta = -\frac{1}{2} \pm \frac{1}{2}\left[1 + \frac{8h}{k\delta_b} b^2\right]^{1/2} \qquad (27)$$

Consequently

$$[\Gamma] = \begin{bmatrix} \dfrac{1}{(\alpha - \beta)}\left[\alpha\left(\dfrac{a}{b}\right)^{\beta} - \beta\left(\dfrac{a}{b}\right)^{\alpha}\right] & \dfrac{b}{k\delta_b L(\alpha - \beta)}\left[\left(\dfrac{a}{b}\right)^{\alpha} - \left(\dfrac{a}{b}\right)^{\beta}\right] \\ \dfrac{k\delta_b L\alpha\beta}{b(\alpha - \beta)}\left[\left(\dfrac{a}{b}\right)^{\beta+1} - \left(\dfrac{a}{b}\right)^{\alpha+1}\right] & \dfrac{1}{(\alpha - \beta)}\left[\alpha\left(\dfrac{a}{b}\right)^{\alpha+1} - \beta\left(\dfrac{a}{b}\right)^{\beta+1}\right] \end{bmatrix} \qquad (28)$$

Singular Fins

To see what can be expected from fins with zero tip thickness, consider the effect of letting a approach zero in the thermal transmission matrix for the concave parabolic fin, (28). One has

$$\theta_a = \frac{\theta_b}{(\alpha - \beta)}\left[\alpha\left(\frac{a}{b}\right)^{\beta} - \beta\left(\frac{a}{b}\right)^{\alpha}\right] + \frac{q_b b}{k\delta_b L(\alpha - \beta)}\left[\left(\frac{a}{b}\right)^{\alpha} - \left(\frac{a}{b}\right)^{\beta}\right] \qquad (29)$$

with $\beta < 0 < \alpha$ by (27); it is observed that θ_a will increase without bound as a approaches zero unless the terms involving a^{β} cancel each other. Hence, *the longitudinal fin of concave parabolic profile with zero tip thickness is characterized by the equation*

$$\frac{q_b}{\theta_b} = \frac{\alpha k \delta_b L}{b} \qquad (30)$$

In similar fashion, requiring θ_a to be finite as a approaches zero in (21) dictates that the *longitudinal fin of triangular profile is characterized by the equation*

$$\frac{q_b}{\theta_b} = L\left(\frac{2hk\delta_b}{\cos\phi}\right)^{1/2} \frac{I_1(2nb^{1/2})}{I_0(2nb^{1/2})} \qquad (31)$$

For both of these "singular" fins, the condition that $q_a = 0$ can be verified.

Consequently, one observes that whereas *a regular fin is characterized by a 2 × 2 thermal transmission matrix*, Γ, satisfying

$$\begin{bmatrix}\theta_a \\ q_a\end{bmatrix} = [\Gamma]\begin{bmatrix}\theta_b \\ q_b\end{bmatrix} \qquad (32)$$

a singular fin is characterized by a single *thermal transmission ratio*, μ, satisfying

$$\mu = \frac{q_b}{\theta_b} \qquad (33)$$

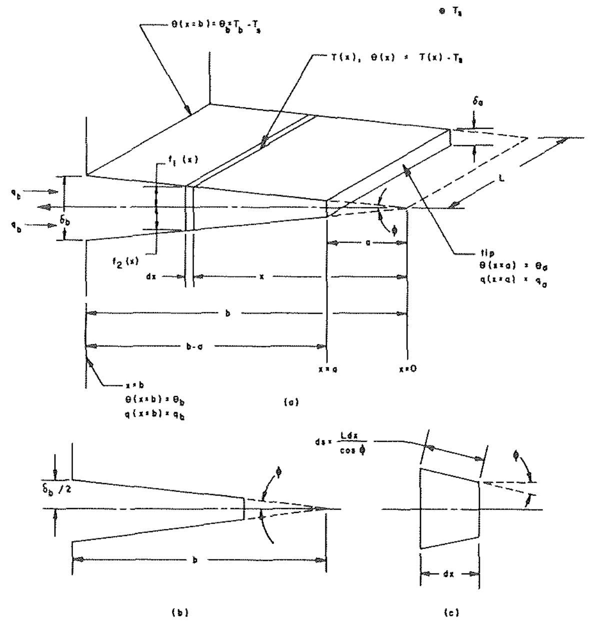

Fig. 4

Characterization of Arrays

The basic tool for analyzing an array of fins is provided by the following mathematical observation, which is easily verified: *if tip and base conditions of temperature excess and heat flow are related by a thermal transmission matrix* as in (28), *then the q:θ ratio at the tip and base are related by the bilinear transformation*

$$\frac{q_b}{\theta_b} = g\left(\frac{q_a}{\theta_a}\right) = \frac{\gamma_{21} - \gamma_{11}\left(\dfrac{q_a}{\theta_a}\right)}{-\gamma_{22} + \gamma_{12}\left(\dfrac{q_a}{\theta_a}\right)} \qquad (34)$$

with the coefficients in the transformation g drawn from the matrix

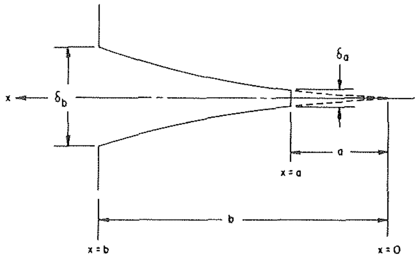

Fig. 5

Γ as displayed just below (12).

To see how this is used, consider an array like the repeating section in Fig. 2. It has the important feature that the ratio $q{:}\theta$ is immediately computable for every remote tip. Hence, because of the insulation,

$$\left.\frac{q_a}{\theta_a}\right|_5 = \left.\frac{q_a}{\theta_a}\right|_6 = \left.\frac{q_a}{\theta_a}\right|_{11} = \left.\frac{q_a}{\theta_a}\right|_{12} = 0 \tag{35}$$

The tip heat loss from fins 2 and 3, having identical tip areas, is given by

$$\left.\frac{q_a}{\theta_a}\right|_{2,3} = h(a)A(a)\Big|_{2,3} \tag{36}$$

Finally, because fins 8 and 9 have zero tip thickness,

$$\left.\frac{q_a}{\theta_a}\right|_8 = \left.\frac{q_a}{\theta_a}\right|_9 = 0 \tag{37}$$

Actually, (37) will not be used in the analysis since fins 8 and 9 are singular.

The bilinear transformations (34) are used to compute base-ratios from tip-ratios, except for the singular fins where (33) gives the ratio directly. One can successively work from the remote tips of fins 11 and 12 down to the base of fin 1, matching conditions at the nodes, to find the base heat flow to base temperature excess ratio for the entire array.

To illustrate:

(1) From (17), determine the coefficients for the bilinear transformations, $g^{(11)}$ and $g^{(12)}$, for fins 11 and 12. Then by (34) and (35)

$$\left.\frac{q_b}{\theta_b}\right|_{11} = g^{(11)}(0), \quad \left.\frac{q_b}{\theta_b}\right|_{12} = g^{(12)}(0) \tag{38}$$

(2) By continuity

$$q_{a_{10}} = q_{b_{11}} + q_{b_{12}} \tag{39}$$

and

$$\theta_{a_{10}} = \theta_{b_{11}} = \theta_{b_{12}} \tag{40}$$

Hence

$$\left.\frac{q_a}{\theta_a}\right|_{10} = \left.\frac{q_b}{\theta_b}\right|_{11} + \left.\frac{q_b}{\theta_b}\right|_{12} \tag{41}$$

(3) Read the coefficients for $g^{(10)}$ from (16) and compute

$$\left.\frac{q_b}{\theta_b}\right|_{10} = g^{(10)}\left(\left.\frac{q_a}{\theta_a}\right|_{10}\right) \tag{42}$$

by employing (34).

(4) Obtain q_b/θ_b for fins 8 and 9 from (31) and then combine as in (2)

$$\left.\frac{q_a}{\theta_a}\right|_7 = \left.\frac{q_b}{\theta_b}\right|_8 + \left.\frac{q_b}{\theta_b}\right|_9 + \left.\frac{q_b}{\theta_b}\right|_{10} \tag{43}$$

Continuing in this manner, one eventually finds $(q_b/\theta_b)_1$.

In passing, it may be observed that the effect of adhesive bonding between fins, which has been ignored in the foregoing development, can easily be incorporated by treating the adhesive layer as a short rectangular fin, with its own k and h properties.

The procedure is also applicable to configurations where the $q{:}\theta$ ratios for the tips of the most remote fins are not known a priori. Consider, for instance, the repeating section in the *unevenly loaded double stack* as shown in Fig. 6. Here two base surfaces are dissipating heat to the coolant fluid. The operating parameters are the left and right prime surface temperature excesses, θ_ℓ and θ_r, and the associated heat flows q_ℓ and q_r. If one prescribes, say, unequal temperature excesses, θ_ℓ and θ_r, then the asymmetry forbids an a priori assessment of the $q{:}\theta$ ratios at the two remote fin tips.

One could, in fact, follow the previous procedure by treating the ratio q_r/θ_r as an unknown parameter and formally carrying it through the cascade process from right to left. The result would be a bilinear relationship between the two $q{:}\theta$ ratios. However, the following matrix procedure is somewhat more illuminating. Using the transmission matrices (16) one can write, keeping in mind that a positive q indicates heat flow from right to left according to (1),

$$\begin{bmatrix}\theta_a\\ q_a\end{bmatrix}_1 = [\Gamma]_1\begin{bmatrix}\theta_\ell\\ q_\ell\end{bmatrix}; \qquad \begin{bmatrix}\theta_r\\ q_r\end{bmatrix} = [\Gamma]_4\begin{bmatrix}\theta_b\\ q_b\end{bmatrix}_4 \tag{44}$$

where opposite signs are to be expected for q_ℓ and q_r. Furthermore, it is known that

$$\theta_{a_1} = \theta_{b_2} = \theta_{b_3} = \theta_{b_4} \tag{45}$$

$$q_{b_4} = q_{a_1} - q_{b_2} - q_{b_3} \tag{46}$$

and because the tips of fins 2 and 3 are insulated

$$\left.\frac{q_b}{\theta_b}\right|_{2,3} = g^{(2,3)}(0) \tag{47}$$

A relationship that links the base condition for fin 4 to the tip condition for fin 1 can be established by a mathematical artifice:

$$\begin{bmatrix}\theta_b\\ q_b\end{bmatrix}_4 = \begin{bmatrix}\theta_a\\ q_a\end{bmatrix}_1 - \begin{bmatrix}0\\ q_b\end{bmatrix}_2 - \begin{bmatrix}0\\ q_b\end{bmatrix}_3$$
$$= \begin{bmatrix}\theta_a\\ q_a\end{bmatrix}_1 - \begin{bmatrix}0\\ g^{(2)}(0)\theta_a\end{bmatrix}_1 - \begin{bmatrix}0\\ g^{(3)}(0)\theta_a\end{bmatrix}_1$$

or

$$\begin{bmatrix}\theta_b\\ q_b\end{bmatrix}_4 = \begin{bmatrix}1 & 0\\ -g^{(2)}(0) - g^{(3)}(0) & 1\end{bmatrix}\begin{bmatrix}\theta_a\\ q_a\end{bmatrix}_1 \equiv [G]\begin{bmatrix}\theta_a\\ q_a\end{bmatrix}_1 \tag{48}$$

Hence by (44)

$$\begin{bmatrix}\theta_r\\ q_r\end{bmatrix} = [\Gamma]_4[G][\Gamma]_1\begin{bmatrix}\theta_\ell\\ q_\ell\end{bmatrix} \tag{49}$$

From (49) any two of the parameters can be related to the other two. (Keep in mind that q_r is negative.) Thus a closed form solution can be obtained, as will now be demonstrated.

Suppose the configuration shown in Fig. 6 represents a repeating section of an 11.1 plain plate fin heat exchanger [1] with splitter plates (fins 2 and 3) 0.010 in. wide. Let h = 10 Btu/ft^2-hr-°F and k = 100 Btu/ft-hr-°F and determine θ_{b1} and θ_{a4} if $|q_{b1}|$ = 10 Btu/hr and $|q_{a4}|$ = 8 Btu/hr over a 1 ft length of section (L = 1 ft).

Pertinent dimensions may be extracted from [1]. With the splitter plates 0.010 in. wide and 0.0450 in. high

$b_1 = 0.0208$ ft. $\quad \delta_1 = 5.0000 \times 10^{-4}$ ft

$b_2 = 0.0038$ ft. $\quad \delta_2 = 8.3333 \times 10^{-4}$ ft

$b_3 = 0.0038$ ft. $\quad \delta_3 = 8.3333 \times 10^{-4}$ ft

$b_4 = 0.0208$ ft. $\quad \delta_4 = 5.0000 \times 10^{-4}$ ft

Fins 2 and 3 have insulated tips because no heat can proceed across the boundaries of the repeating section. Hence from (16) and then (34) with $\gamma_{21} = -0.0751$ and $\gamma_{22} = 1.0017$,

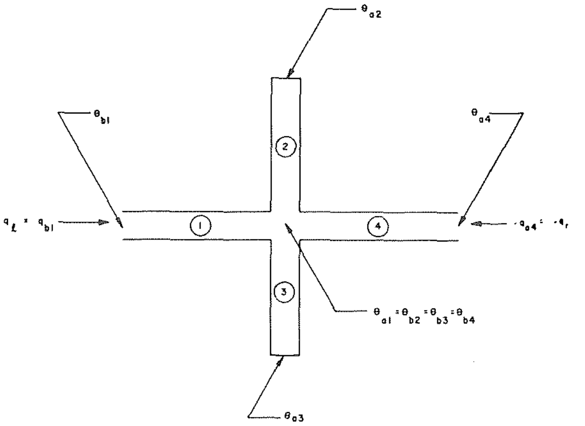

Fig. 6

$$g^{(2,3)}(0) = \frac{\gamma_{21}}{-\gamma_{22}} = \frac{-0.0751}{1.0017} = 0.0750$$

For fins 1 and 4, (16) yields

$$[\Gamma]_1 = [\Gamma]_4 = \begin{bmatrix} 1.0881 & -0.4288 \\ -0.4288 & 1.0881 \end{bmatrix}$$

Then with

$$\begin{bmatrix} 1 & 0 \\ [-g^{(2)}(0) - g^{(3)}(0)] & 1 \end{bmatrix} = \begin{bmatrix} 1 & 0 \\ -0.1500 & 1 \end{bmatrix}$$

one obtains from (49)

$$\begin{bmatrix} \theta_r \\ q_r \end{bmatrix} = \begin{bmatrix} 1.0881 & -0.4288 \\ -0.4288 & 1.0881 \end{bmatrix} \begin{bmatrix} 1 & 0 \\ -0.1500 & 1 \end{bmatrix} \begin{bmatrix} 1.0881 & -0.4288 \\ -0.4288 & 1.0881 \end{bmatrix} \begin{bmatrix} \theta_\ell \\ q_\ell \end{bmatrix}$$

or

$$\begin{bmatrix} \theta_r \\ q_r \end{bmatrix} = \begin{bmatrix} 1.4378 & -0.9608 \\ -1.1108 & 1.4378 \end{bmatrix} \begin{bmatrix} \theta_\ell \\ q_\ell \end{bmatrix}$$

This then yields, with $q_\ell = 10$ Btu/hr and $q_r = -8$ Btu/hr,

$$\theta_\ell = \frac{-8.00 - (1.4378)(10.00)}{-1.1108} = 20.15°\text{F}$$

and

$$\theta_r = 1.4378\theta_\ell - 0.9608q_\ell$$
$$= 1.4378(20.15) - 0.9608(10.00) = 19.36°\text{F}$$

Summary and Conclusions

This paper has described a new algorithm for evaluating the performance, under idealized operating conditions, of arrays of extended surface. Most individual fins are characterized by a 2 × 2 thermal transmission matrix whose entries depend only on the fin geometry and material. These matrices have been tabulated herein for the usual geometries and are easily computable by Runge-Kutta methods for exotic geometries. Fins of zero tip thickness are characterized by a thermal transmission ratio, again dependent only on geometry and material, and again tabulated herein for the usual geometries.

The heat exchange performance of an array of fins is easily computable by a straightforward process involving cascading the parameters for the individual fins. The performance is measured by the (highly practical) ratio of total heat dissipated divided by operating temperature excess.

A comparison with previous heat exchanger [1] and extended surface [2] analyses leads to the inescapable conclusion that the algorithm described herein is far simpler and more versatile than the methods heretofore used.

References

1 Kays, W. M., and London, A. L., *Compact Heat Exchangers*, 2nd Ed., McGraw-Hill Book Company, New York, 1964.

2 Kern, D. Q., and Kraus, A. D., *Extended Surface Heat Transfer*, McGraw-Hill, New York, 1972.

3 Murray, W. M., "Heat Dissipation Through an Annular Disk or Fin of Uniform Thickness," *Journal of Applied Mechanics*, J:A7B (1938).

4 Gardner, K. A., "Efficiency of Extended Surfaces," *Trans. ASME*, Vol. 67, 1945, p. 621.

5 Boyce, W. E., and DiPrima, R. C., *Elementary Differential Equations and Boundary Value Problems*, John Wiley and Sons, New York, 1965.

6 Harper, D. R., and Brown, W. B., "Mathematical Equations for Heat Conduction in the Fins of Air Cooled Engines," NACA Report 158, 1922.

T. Saitoh

Assoc. Professor,
Dept. of Mechanical Engineering II,
Tohoku University,
Sendai, Japan
Mem. JSME and Meteorol. Soc. of Japan

Numerical Method for Multi-Dimensional Freezing Problems in Arbitrary Domains

This paper presents a simple numerical method for solving two and three-dimensional freezing problems with arbitrary geometries. The change of variable method introduced by Landau for the one-dimensional problem is extended to the multi-dimensional using an independent variable which takes constant values at the boundary and the freezing front. Example calculations were performed for the Stefan type freezing problem in regular squares, triangles, and ellipses. Then some of the results were compared with the experimental ones that were obtained for the constant cooling rate.

Introduction

Heat transfer with freezing or melting is of practical importance in many instances, for example in engineering ice making, in freezing of foods, in icing of electric power plants, in aerodynamic heating of spacecraft, during the casting of metals, in many geophysical problems such as thawing of soil, in bubble growth [1][1] and collapse in boiling and cavitation, and also in the diffusion flame problem under the flame sheet model.

Mathematically, these problems belong to the so-called moving (or free) boundary problem which is characterized by the possession of moving interfaces dividing the relevant field into two regions. Such a problem becomes perfectly nonlinear because the positions of the moving interfaces are neither fixed in space nor known a priori. Due to this nonlinearity, the analytical solution can be found only in limited situations, for example in Neumann's solution for a one-dimensional problem. However, analytical solutions are important for checking approximate or numerical solutions.

To date, several analytical, approximate, and numerical methods have appeared in the literature of the two and three-dimensional freezing problem. The approximate integral method has been used by Poots [2] for the inward solidification of a uniform prism with a square cross section, subject to a constant boundary temperature. Initially, the liquid was assumed to be at the fusion temperature (i.e., two-dimensional Stefan problem).

Sikarskie and Boley [3] have found short time series solutions by using the embedding technique in which one deals mathematically with a fictitious body of known constant geometry instead of the actual one whose boundary is known. Rathjen and Jiji [4] have obtained an analytical solution of Neumann's two-dimensional problem in a corner by utilizing the Lightfoot method [5]. The solid-liquid interface was represented by the solution of a nonlinear, singular, integrodifferential equation. The Lightfoot method was also used by Budhia and Kreith [6] for melting or freezing in a wedge.

Hitherto, only a few numerical methods applicable to the arbitrary configurations have been reported.

Making use of the relaxation method, Allen and Severn [7] considered the inward solidification of a uniform prism with a square cross section when the boundary temperature is constant. Springer and Olson [8] have extended the Murray-Landis method [9] to the two-dimensional problem of axisymmetric freezing and melting of materials between two concentric cylinders of finite length. Later, Lazaridis [10] also used the Murray-Landis method to solve the multi-dimensional solidification problem in a square region.

Kroeger and Ostrach [11] devised a conformal mapping method for the steady continuous casting problem with natural convection in the liquid phase. Both solid and liquid regions were mapped into the unit circle.

Katayama and Hattori [12] have refined the conventional enthalpy method introducing Dilac's delta function and have shown that the accuracy of the solution can be considerably elevated.

More recently, Shamsunder and Sparrow [13] have presented a demonstration via enthalpy model method for general multi-dimensional cases. The solution method is equally applicable to substances that have a discrete phase change temperature and to those that do not. The other existing enthalpy method, i.e., Katayama and Hattori's, suffers from intense oscillation of the numerical solution in the case of a substance with a discrete phase change temperature.

Extensions to the two-dimensions of Haji-Sheikh and Sparrow's Monte-Carlo method [14] and a method using Biot's variational principle [15] will be forthcoming in the near future.

Among the aforementioned numerical methods, the Murray-Landis

---

[1] *Numbers in brackets designate References at end of paper.*

Contributed by the Heat Transfer Division for publication in the JOURNAL OF HEAT TRANSFER. Manuscript received by the Heat Transfer Division May 20, 1977.

type methods, for instance, those of Springer and Olson, and Lazaridis are quite complicated because special consideration is needed in the vicinity of the moving boundary in order to construct a finite difference system. Moreover, the geometry should be simple for the same reason. The enthalpy method in which latent heat is regarded as heat capacity can only be applied to problems involving a change of phase, namely those containing the latent heat term. Therefore, it is inapplicable to such problems as diffusion flames and absorption with rapid chemical reactions. The conformal mapping method developed by Kroeger and Ostrach has the capability of being applied to arbitrary configurations, but only the solution for steady problems was shown. Considerable modifications and complications may be added to extend this method to the moving boundary condition.

The present paper proposes a relatively simple numerical method for the multi-dimensional moving boundary problem by a change of the independent variable. The present scheme is an extension of Landau transformation [17] to two and three-dimensional problems.

Recently, Duda, et al. [16] have also presented an immobilization method for two-dimensional diffusive heat or mass transfer problems. The present scheme is similar to that of Duda, et al., in that the Landau transformation is extended to the multi-dimensional case; however, there is an essential difference between the two. In our method, not only the shape of the freezing front but also that of the fixed boundary can be selected arbitrarily, thereby allowing its application to more practical situations.

Sample calculations were performed for the freezing of water in regular squares, triangles, and ellipses. Further, experiments were carried out to compare these results under a constant cooling rate. The comparison revealed satisfactory agreement.

Formulation of the Problem

For the purpose of illustration, governing equations are presented for the two-dimensional freezing problem since the extension to three dimensions is accomplished in a quite similar manner. A schematic description and coordinate system for two-dimensional freezing in an arbitrary domain are shown in Fig. 1. The liquid is initially contained in a domain surrounded by a boundary represented by the function $B^+(\phi^+)$. The temperature at the boundary is given arbitrarily by the function $T_w{}^+(\phi^+, t^+)$. At the time $t^+ = t^+$, the corresponding freezing front position is assumed to be at $r^+ = F^+(\phi^+, t^+)$. The problem then is to find the freezing front $F^+(\phi^+, t^+)$ and the temperature distribution $T^+(r^+, \phi^+, t^+)$ in the solid.

For simplification, it was postulated that the temperature of the liquid is equal to the freezing temperature, and that the properties are constant.

The basic equations and the boundary conditions for this problem under the above assumptions are described below, using the cylindrical coordinate system.

$$\frac{\partial T^+}{\partial t^+} = \alpha \nabla_+{}^2 T^+ \tag{1}$$

Boundary conditions;

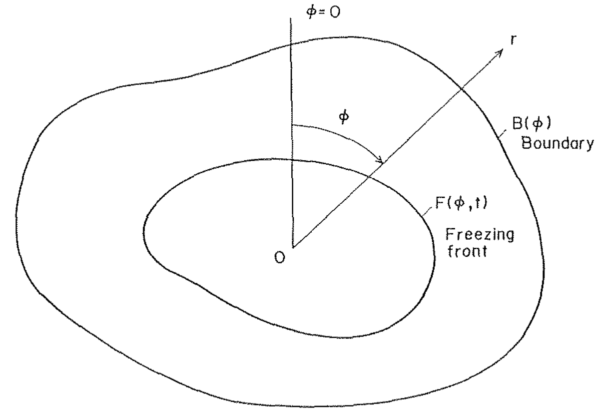

Fig. 1 Schematic description and coordinate system for two-dimensional freezing problem

$$\phi^+ = 0 \text{ and } \phi_0; \qquad \frac{\partial T^+}{\partial \phi^+} = 0 \tag{2}$$

$$\text{on } r^+ = B^+(\phi^+); \qquad T^+ = T_w{}^+(\phi^+, t^+) \tag{3}$$

$$\text{on } r^+ = F^+(\phi^+, t^+); \qquad T^+ = 0 \tag{4}$$

$$\rho L \mathbf{V}\cdot\mathbf{n} = \lambda \frac{\partial T^+}{\partial n} \tag{5}$$

$$\nabla_+{}^2 = \frac{1}{r^+}\frac{\partial}{\partial r^+}\left(r^+ \frac{\partial}{\partial r^+}\right) + \frac{1}{(r^+)^2}\frac{\partial^2}{\partial(\phi^+)^2} \tag{6}$$

The boundary condition at the free surface (5) is obtained from conservation of energy across the interface, and it is shown that this condition is represented as a heat balance equation in the radial direction, i.e.,

$$\rho L \left.\frac{\partial F^+}{\partial t^+}\right|_{r^+} = \lambda \left[1 + \left(\frac{\partial F^+}{F^+ \partial \phi^+}\right)^2\right] \frac{\partial T^+}{\partial r^+} \tag{7}$$

The above equations are nondimensionalized by the following variables.

$$r = \frac{r^+}{D}, t = \frac{\alpha t^+}{D^2}, \phi = \frac{\phi^+}{\phi_0}, T = \frac{T^+}{T_0{}^+}, F = \frac{F^+}{D}, B = \frac{B^+}{D}, T_w = \frac{T_w{}^+}{T_0{}^+} \tag{8}$$

Consequently, the governing equations are transformed into the following system.

$$\frac{\partial T}{\partial t} = \nabla^2 T \tag{9}$$

$$\phi = 0 \text{ and } 1; \qquad \frac{\partial T}{\partial \phi} = 0 \tag{10}$$

$$\text{on } r = B(\phi); \qquad T = T_w(\phi, t) \tag{11}$$

Nomenclature

α = thermal diffusivity of solid
$B(\phi)$ = boundary function
$C_1{}^+$ = cooling rate
C_p = specific heat at constant pressure
D = reference length
$F(\phi, t)$ = position of freezing front
H = side length of regular square or triangle
L = latent heat
n = normal coordinate
$\mathbf{n}$ = unit vector
r = spatial coordinate
St = Stefan number defined as St = $C_p T_0{}^+/L$
T = temperature
$T_w(\phi, t)$ = cooling surface temperature
$T_0{}^+$ = reference temperature
t = time
$\mathbf{V}$ = velocity vector
η = independent variable defined by equation (7)
λ = thermal conductivity of solid
ρ = density of solid
ϕ = angle in cylindrical coordinate
ϕ_0 = position of symmetry or insulated boundary

Subscripts

w = cooling surface
0 = reference state

Superscript

+ = dimensional quantity

$$\text{on } r = F(\phi, t); \qquad T = 0$$

$$\frac{\partial F}{\partial t} = \mathrm{St}\left[1+\left(\frac{1}{\phi_0 F}\frac{\partial F}{\partial \phi}\right)^2\right]\frac{\partial T}{\partial r} \tag{12}$$

$$\nabla^2 = \frac{1}{r}\frac{\partial}{\partial r}\left(r\frac{\partial}{\partial r}\right) + \frac{1}{r^2}\frac{\partial^2}{\partial \phi^2} \tag{13}$$

In general, besides the above equations, the Navier-Stokes and energy equations which determine the natural convection and heat transfer in the liquid region must be solved. Nevertheless, that is not within the scope of the present study.

Solution by the Boundary Fixing Method

The principal difficulties in the analysis of the multi-dimensional freezing problem derive from the fact that the position of the moving boundary is not known a priori, and that its shape is multi-dimensional. Moreover, if the boundary contour has an arbitrary shape, particular attention is likewise required for the treatment of the boundary. In consequence, the methods which are extended directly from the fixed network scheme rendered by Murray and Landis for the one-dimensional have two essential difficulties that must be resolved; one is handling of the moving boundary and the other that of the fixed boundary.

Among existing methods, only the method using the enthalpy model overcame one of the above two difficulties, i.e., the moving boundary was removed from consideration. However, the other problem remains unresolved. One of the most effective means for solving the above complexities may be adoption of the concept of *change of independent variable in two dimensions.* Duda, et al. [16] have presented the change of variable method for the two-dimensional problem. However, they focused attention only on the moving boundary and did not show a general formulation involving the handling of the fixed boundaries. Therefore, we will present another general formulation of the boundary fixing method in the following.

Specifically, the governing equations are transformed by the following variable.

$$\eta = \frac{r - F(\phi, t)}{B(\phi) - F(\phi, t)} \tag{14}$$

Making use of the above variable, the previous basic equations are changed into

$$\frac{\partial T}{\partial t} = \left[\frac{1}{(B-F)^2} + \frac{1}{R}\left(\frac{\partial \eta}{\partial \phi}\right)^2\right]\frac{\partial^2 T}{\partial \eta^2} + \left[\frac{1}{r(B-F)} - \frac{\partial \eta}{\partial t} + \frac{1}{R}\frac{\partial^2 \eta}{\partial \phi^2}\right]\frac{\partial T}{\partial \eta} + \frac{2}{R}\frac{\partial \eta}{\partial \phi}\frac{\partial^2 T}{\partial \phi \partial \eta} + \frac{1}{R}\frac{\partial^2 T}{\partial \phi^2} \tag{15}$$

$$\phi = 0 \text{ and } 1; \qquad \frac{\partial T}{\partial \phi} = 0 \tag{16}$$

$$\text{on } \eta = 0; \qquad T = 0 \tag{17}$$

$$\frac{\partial F}{\partial t} = \mathrm{St}\frac{\partial T}{\partial \eta}\frac{1}{B-F}\left[1 + \left(\frac{1}{F\phi_0}\frac{\partial F}{\partial \phi}\right)^2\right] \tag{18}$$

$$\text{on } \eta = 1; \qquad T = T_w(\phi, t) \tag{19}$$

where, $r = \eta(B - F) + F, R = (\phi_0 r)^2$.

In equation (15) the derivatives $\partial\eta/\partial t$, $\partial\eta/\partial\phi$, and $\partial^2\eta/\partial\phi^2$ are given by

$$\frac{\partial \eta}{\partial t} = -\frac{\partial F}{\partial t}\frac{1-\eta}{B-F}, \tag{20}$$

$$\frac{\partial \eta}{\partial \phi} = -\frac{1}{B-F}\left[\frac{\partial F}{\partial \phi} + \eta\left(\frac{\partial B}{\partial \phi} - \frac{\partial F}{\partial \phi}\right)\right], \tag{21}$$

$$\frac{\partial^2 \eta}{\partial \phi^2} = -\frac{1}{B-F}\left[\frac{\partial^2 F}{\partial \phi^2} + \frac{\partial \eta}{\partial \phi}\left(\frac{\partial B}{\partial \phi} - \frac{\partial F}{\partial \phi}\right) + \eta\left(\frac{\partial^2 B}{\partial \phi^2} - \frac{\partial^2 F}{\partial \phi^2}\right)\right] \tag{22}$$

In particular, at the corner portion of a regular square, the second derivative $\partial^2 B/\partial\phi^2$ in equation (22) vanishes. Therefore, the following equation is derived, by considering the heat balance in a small element shown in Fig. 2.

$$\frac{\partial T}{\partial t} = \frac{1}{r}\frac{\partial}{\partial r}\left(r\frac{\partial T}{\partial r}\right) + \frac{1}{Rd\phi}\left(\frac{\partial T}{\partial \phi}\right)_- \tag{23}$$

where $(\partial T/\partial\phi)_-$ means the value at $\phi = \pi/4 - d\phi$. Similar consideration is necessary when the boundary is not smoothly shaped.

The transformed system (15–23) constitutes an ordinary nonlinear fixed boundary heat conduction problem, except that F and the derivative of η with respect to t and ϕ are given by equations (18, 20–22). It is emphasized again that functions $B(\phi)$ and $F(\phi, t)$, representing the boundary shape and freezing front, respectively, can be chosen arbitrarily.

The present method can, of course, be applied to the usual heat conduction problem without change of phase. Extension to the three-dimensional problem is easily attained by virtue of the following variable instead of equation (7).

$$\eta = \frac{r - F(\phi, \theta, t)}{B(\phi, \theta) - F(\phi, \theta, t)} \tag{24}$$

Numerical Procedure

The numerical computation of equations (15–23) may be performed by finite differences using one of the explicit, alternating direction implicit, and unidirection implicit [18], methods. The multi-point implicit finite difference method [19] proposed by the author would be particularly efficacious for three-dimensional freezing problems from the point of view of saving computing time. Details for use of the multi-point scheme can be found in [19].

Numerical Results and Discussion

To verify the validity of the present numerical method, the numerical calculation was first performed for the cylindrical freezing problem, whose solution is well known to be expressed by the so-called quasi-steady solution [20, 21]. A typical computed result is shown in Fig. 3 in which the origin of the computation is eccentrically located at the point O, being apart from the center of the cylinder by the distance of a quarter of the diameter. The diameter is 0.08 m and the cooling rate is 1.667×10^{-3} K/s. The points marked by the circle in the figure designate the computed points, and the solid lines show the quasi-steady solution given by the next equation.

$$t = \left[\frac{2L}{C_p C_1}\{1 - R^2(1 - 2\ln R)\}\right]^{1/2} \tag{25}$$

where, C_1 denotes the cooling rate defined as

$$C_1 = -\frac{T_w(t)}{t} \tag{26}$$

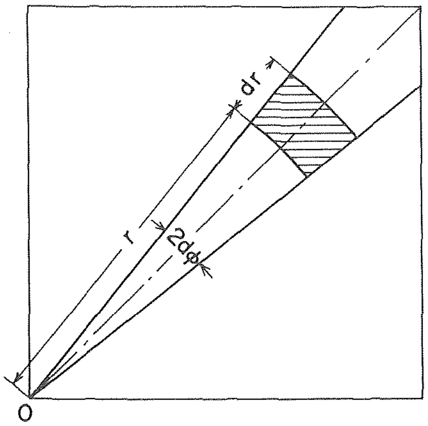

Fig. 2 Derivation of the expression for the heat conduction equation at the corner

The quasi-steady solution (25) agrees well with the exact numerical solution, with the exception of the final stage of freezing. Agreement between the numerical result using present "boundary fixing method" and the quasi-steady solution is excellent, and thus the validity of the present method is assured. The position of the boundary of the above example is represented by

$$B(\phi) = -\frac{1}{2}\cos^2\phi + \frac{1}{2}\sqrt{\cos^2\phi + 3} \tag{27}$$

The result of the numerical calculation for a regular square with side length $H = 0.079$ m is depicted in Fig. 4 when the cooling rate is $C_1{}^+ = 3.333 \times 10^{-3}$ K/s. In early time stages, the freezing contours are almost parallel to the side line of the square, showing that freezing in the normal direction has a one-dimensional aspect. The result for the constant cooling temperature is also plotted in Fig. 5, which corresponds to the two-dimensional Stefan problem. The freezing front moves according to the relation

$$F = 1 - C\sqrt{t} \tag{28}$$

in initial time stages as in the one-dimensional problem. Here, C is a constant.

Fig. 6 designates the time history curve in the perpendicular direction. The broken line shows the one-dimensional Stefan's solution, i.e., $F = 1 - 0.3536\sqrt{t}$

The comparison between the numerical result and the experiment performed by the author [20] is illustrated in Fig. 7 for a regular square with side length of 0.079 m and the cooling rate of $C_1{}^+ = 1.417 \times 10^{-3}$ K/s. The experiment was carried out by using a new technique developed for visualizing all the time histories of the freezing fronts. The freezing contours were photographed after completion of freezing. The water temperature was initially set to the freezing temperature and the cooling surface temperature was varied linearly with time.

The solid lines show the experimental result and the circle points the numerical result. In the experiment, since the cooling rate at the corner portion is slightly larger, the experimental freezing fronts are located inward of the computed points. Nevertheless, it is noted that the general agreement is fairly good. The author's experimental result has also been used by Crowley [22] to verify a numerical scheme which was based on the enthalpy method. The accordance was moderately good.

Two results for triangular geometry appear in Fig. 8 and 9 in which the cooling rates are set as $C_1{}^+ = 3.333 \times 10^{-4}$ K/s and 3.333×10^{-3}

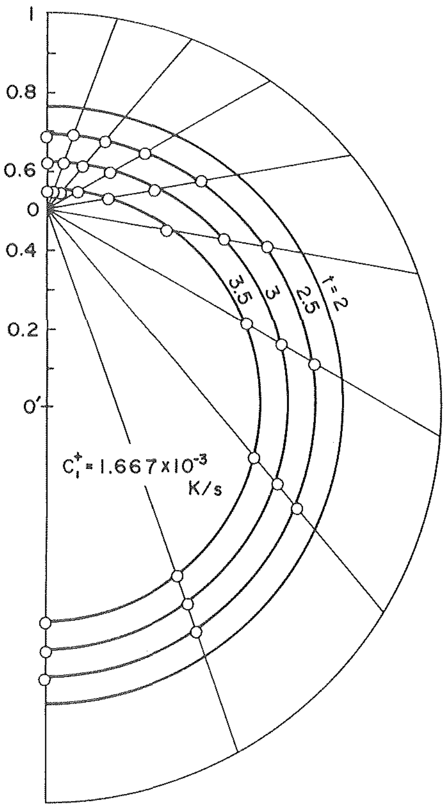

Fig. 3 Comparison of the present method with quasi-steady solution for cylindrical freezing. Diameter = 0.08 m, $C_1{}^+ = 1.667 \times 10^{-3}$ K/s

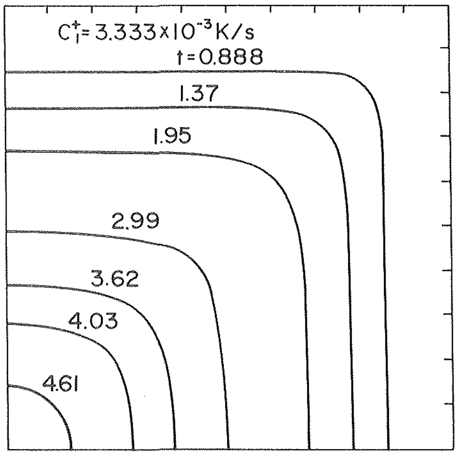

Fig. 4 Numerical result showing contours for a regular square. $H = 0.079$ m, $C_1{}^+ = 3.333 \times 10^{-3}$ K/s

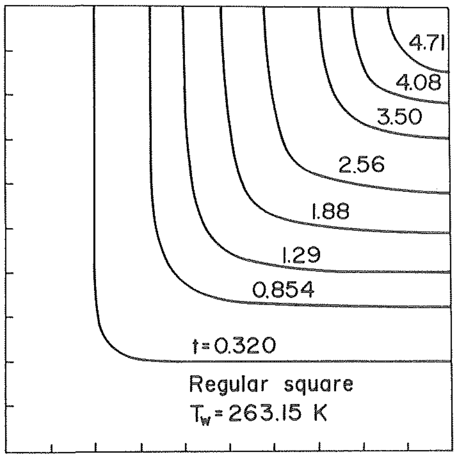

Fig. 5 Computed result for two-dimensional Stefan problem (regular square, $H = 0.079$ m)

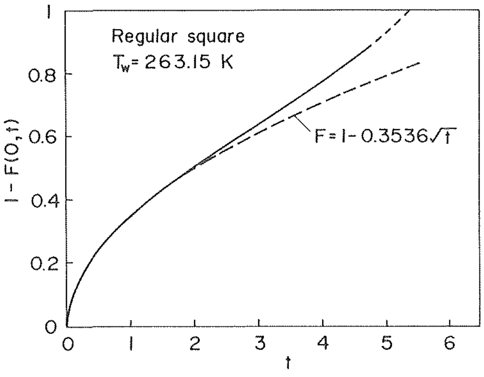

Fig. 6 Time history curve of freezing front for Stefan problem. Conditions are the same as in Fig. 5

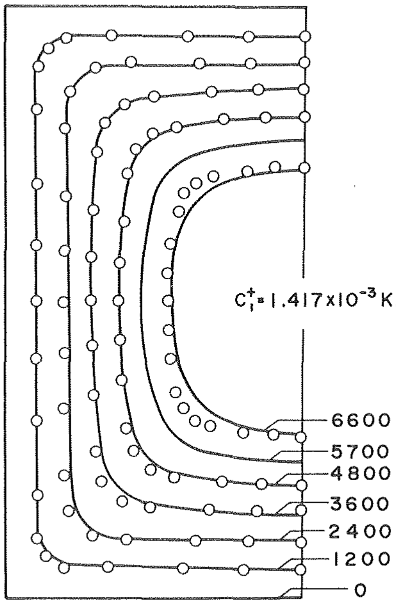

Fig. 7 Comparison between the numerical result and the experiment. Solid lines show experimental result and circles the computed points. $H = 0.079$ m, $C_1^+ = 1.417 \times 10^{-3}$ K/s

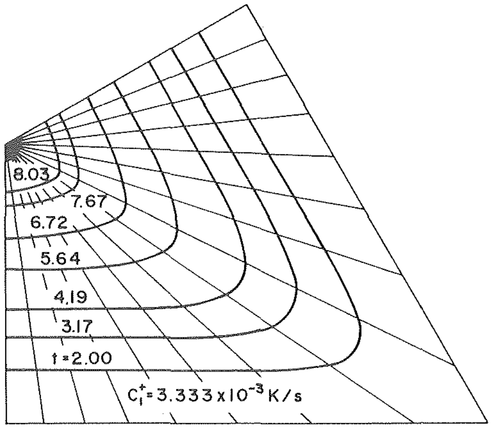

Fig. 8 Computed freezing front contours for a triangle. $H = 0.079$ m, $C_1^+ = 3.333 \times 10^{-3}$ K/s

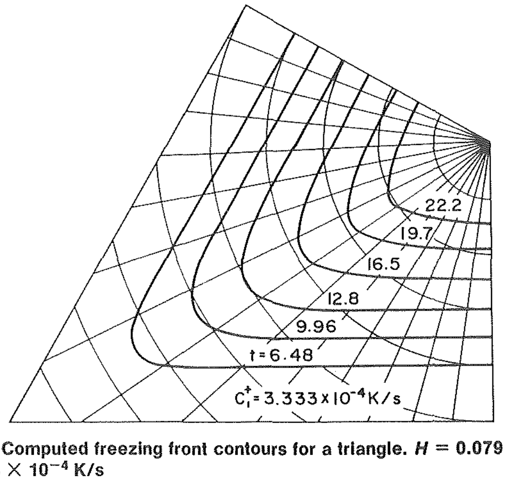

Fig. 9 Computed freezing front contours for a triangle. $H = 0.079$ m, $C_1^+ = 3.333 \times 10^{-4}$ K/s

K/s. The larger the vertical angle becomes, the faster the freezing front moves toward the origin. The boundary function $B(\phi)$ for the regular square and triangle is given by the next equation.

$$B(\phi) = 1/\cos\phi \qquad \phi < \phi_c$$

$$= 1/\cos(\phi_0 - \phi) \qquad \phi > \phi_c \tag{29}$$

Here, ϕ_c denotes half of the vertical angle, and ϕ_0 is taken to be $\pi/2$ for a regular square and $2\pi/3$ for a regular triangle.

Another result for an ellipse with a shorter diameter of 0.08 m, aspect ratio of 3/2, and a cooling rate of 3.333×10^{-3} K/s is shown in Fig. 10. The initial freezing front position F_0 can be calculated by

$$F_0(\phi, t_0) = B(\phi) - \delta\left[1 + \left(\frac{1}{B}\frac{dB}{d\phi}\right)^2\right]^{1/2} \tag{30}$$

where δ designates the initial thickness of the frozen layer. The boundary function $B(\phi)$ is expressed by the following equation.

$$B(\phi) = \{1 - 5/9 \sin^2\phi\}^{-1/2} \tag{31}$$

It is assumed that the temperature distribution within the initial frozen layer is linear. The freezing contour line remains elliptical until the last time stage. The aspect ratio at the middle time stage becomes larger since the thickness of the frozen layer in the short and long diameter directions is nearly the same.

Numerical application to other problems with different configurations is easily possible, with minor modifications.

Concluding Remarks

A numerical method for the general multi-dimensional moving boundary problem has been presented. The method utilizes the concept of change of variable and has a special feature in that it covers the arbitrary geometry of the boundary and freezing front. Further, this method has an advantage applicable to other moving boundary problems without phase change, e.g., diffusion flame, absorption with rapid chemical reactions, etc.

Sample computations were carried out for regular squares, regular triangles, and ellipses, both in cases when the cooling surface temperature varies with time and when it remains constant during freezing, namely in the case of Stefan's problem.

Extension of the numerical method is apparently feasible for resolution of three-dimensional problems and problems with more

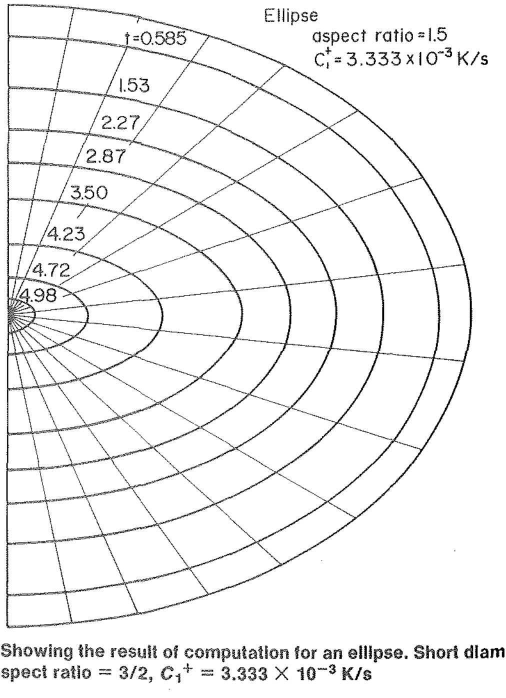

Fig. 10 Showing the result of computation for an ellipse. Short diameter = 0.08 m, aspect ratio = 3/2, $C_1^+ = 3.333 \times 10^{-3}$ K/s

complicated situations, such as the problem of natural convection flow around the freezing front. However, inquiry into these problems must be left to a later date.

Acknowledgment

The author extends his acknowledgment to the Computer Center of the Tohoku University for use of Time Sharing Systems. He is also grateful to referees who called to the author's attention the key reference [16] relating the present works.

References

1 Saitoh, T., and Shima, A., *Journal of Mechanical Engineering Science*, Vol. 19, 1977, pp. 101–108.

2 Poots, G., *International Journal of Heat and Mass Transfer*, Vol. 5, 1962, pp. 339–348.

3 Sikarskie, D. L., and Boley, B. A., *International Journal of Solids and Structure*, Vol. 1, 1965, pp. 207–234.

4 Rathjen, K. A., and Jiji, L. M., ASME JOURNAL OF HEAT TRANSFER, Vol. 93, 1971, pp. 101–109.

5 Lightfood, N. M. H., *Proceedings of London Mathematical Society*, Ser. 2, Vol. 31, 1929, pp. 97–107.

6 Budhia, H., and Kreith, F., *International Journal of Heat and Mass Transfer*, Vol. 16, 1973, pp. 195–211.

7 Allen, D. N. de G., and Severn, R. T., *Quarterly Journal of Mathematics*, Vol. 15, 1962, pp. 53–62.

8 Springer, G. S., and Olson, D. R., ASME paper No. 62-WA-246, 1962.

9 Murray, W. D., and Landis, F., ASME JOURNAL OF HEAT TRANSFER, Vol. 81, 1959, pp. 106–112.

10 Lazaridis, A., *International Journal of Heat and Mass Transfer*, Vol. 13, 1970, pp. 1459–1477.

11 Kroeger, P. G., and Ostrach, S., *International Journal of Heat and Mass Transfer*, Vol. 17, pp. 1191–1207.

12 Katayama, K., and Hattori, M., *Trans. Japan Society of Mechanical Engineers*, Vol. 40, No. 333, 1974, pp. 1404–1411.

13 Shamsunder, N., and Sparrow, E. M., ASME JOURNAL OF HEAT TRANSFER, Vol. 97, 1975, pp. 333–340.

14 Haji-Sheikh, A., and Sparrow, E. M., ASME JOURNAL OF HEAT TRANSFER, Vol. 92, 1967, pp. 121–131.

15 Agrawal, H. C., *Moving Boundary Problems in Heat Flow and Diffusion*, (J. R. Ockendon and W. R. Hodgkins eds.), Oxford Univ. Press, 1975, p. 242.

16 Duda, J. L., Michael, F. M., Notter, R. H., and Vrentas, J. S., *International Journal of Heat and Mass Transfer*, Vol. 18, 1975, pp. 901–910.

17 Landau, H. G., *Quarterly of Applied Mathematics*, Vol. 8, 1950, pp. 81–94.

18 Saitoh, T., *Applied Scientific Research*, Vol. 32, 1976, pp. 429–451.

19 Saitoh, T., *International Journal for Numerical Methods in Engineering*, Vol. 9, 1977, pp. 1439–1454.

20 Saitoh, T., *Technology Reports of Tohoku University*, Vol. 41, 1976, pp. 61–72.

21 Katto, Y., *Den-netsu-gairon*, Yokendo, 1968, p. 40.

22 Crowley, A. B., *Technical Reports of Brunel University*, TR/69, 1976, pp. 1–12.

Boris Rubinsky
Graduate Student

Avraham Shitzer
Associate Professor

Faculty of Mechanical Engineering,
Technion—Israel Institute of Technology,
Haifa, Israel

Analytic Solutions to the Heat Equation Involving a Moving Boundary with Applications to the Change of Phase Problem (the Inverse Stefan Problem)

Long time analytic solutions to the inverse Stefan problem are presented in Cartesian and spherical coordinates. This problem deals with the phase change of a substance with the boundary conditions specified at the moving boundary. The solutions, expressed in infinite series, facilitate the calculation of temperature and heat flux variations in the phase changing medium and at the interface with the heat source element. Applications of the present analysis are in aerospace engineering, e.g., controlled ablation of thermal shields; metallurgy, e.g., controlled casting; bioengineering, e.g., cryopreservation of tissues, and numerous applications in which a controlled change of phase of a substance is involved.

Introduction

Heat transfer problems dealing with phase change at constant temperature are referred to as Stefan problems, (see, e.g., [1][1]). Most of these problems are concerned with the melting or freezing of a substance with the instantaneous absorption or liberation of energy. Characteristic of these problems is the existence of an interface separating the two phases through which the latent heat is transferred. This interface is continuously changing its location with time. In the Stefan problems the boundary conditions of the problem are specified at a fixed boundary and the conditions at the moving boundary are calculated. The first to analyze this problem was Neumann in 1860 [2], but the first published results, in 1891, are due to Stefan [3]. An inverse Stefan problem, wherein the boundary conditions are specified at the moving rather than the fixed boundary, also appears in the literature [4–8]. Typically, the temporal location of the interface between the phases is given and the required temperature and heat flux variations at the fixed boundary are calculated. These solutions usually serve to provide information on the behavior of the Stefan problems, which are considered more difficult to solve.

Among the attempts in the literature to solve the Stefan problems are the works of Kolodner in 1956 [9] and Miranker in 1959 [10]. These investigators presented the problem in a Voltera type equation and thus facilitated solutions for certain problems similar to the inverse Stefan problem. Subsequent to these works several investigators have assumed specific temporal variations for the velocity of the moving boundary. These are: (a) constant velocity and (b) velocity proportional to the square root of time. Gibson in 1958 [4] obtained solutions for these conditions for the Cartesian and spherical coordinates. For the constant velocity case he employed separation of variables and obtained a confluent hypergeometric equation. For the square-root-of-time-dependent case, Gibson assumed a double layer potential temperature distribution and obtained an integral equation which was solved by the convolution method. Martynov employed a similar technique for the spherical geometry only, but represented the integrated function by a series [5]. Langford obtained solutions for the two cases through pseudosimilarity and by a series expansion [6, 7]. Langford's works were extended by Bluman, who employed the Lie theory to account for different initial conditions [8].

Inverse Stefan problems, wherein it is desirable to control the rate of freezing or melting of the moving boundary, find wide practical applications. Specific examples would be in (a) metallurgy, where the quality of a cast is determined by the rate of cooling at the solidification interface [11], (b) controlled fluidized bed baths for surface coating [12], and (c) various aspects of biological tissue destruction or preservation by alternating freezing-thawing cycles [13].

The purpose of the present study is to obtain a long time, analytic solution for the one-dimensional inverse Stefan problem subject to arbitrary conditions prescribed at the moving boundary. The solution is presented for both the Cartesian and spherical geometries and is obtained by integration and analytic iterations.

---

[1] Numbers in brackets designate References at end of paper.

Contributed by the Heat Transfer Division for publication in the JOURNAL OF HEAT TRANSFER. Manuscript received by the Heat Transfer Division November 14, 1977.

Analysis

It is assumed that the medium for which the analysis is performed is homogeneous and isotropic. Only one-dimensional problems are treated and presented separately for Cartesian and spherical coordinates.

(a) **Cartesian geometry.** The governing equation for the problem is the Fourier equation:

$$\alpha \frac{\partial^2 T}{\partial x^2} = \frac{\partial T}{\partial t}; \quad x_0 \leqslant x \leqslant \mathbf{s}(t); \quad t_0 \leqslant t \tag{1}$$

where $\mathbf{s}(t)$ is the distance of the moving boundary from the heat source element, as shown in Fig. 1.

Initial conditions are:

$$\lim_{t \to t_0} T(x, t) = T_{ph}; \quad x_0 \leqslant x \leqslant \mathbf{s}(t) \tag{2}$$

and,

$$\lim_{t \to t_0} \mathbf{s}(t) = x_0{}^+ \tag{3}$$

where T_{ph} is the phase change temperature assumed constant for the present analysis, and $\mathbf{s}(t)$ is a monotonic function of time. The analysis may be extended to include a more general initial condition by employing the well known result given by Carslaw and Jaeger [2, pp. 58–59].

The inverse Stefan problem is characterized by two boundary conditions specified at the moving front, i.e.,

$$T(\mathbf{s}(t), t) = T_{ph} \tag{4}$$

and,

$$\frac{\partial T[\mathbf{s}(t), t]}{\partial x} = F(\mathbf{s}(t), t) \tag{5}$$

where $F(\mathbf{s}(t), t)$ is an analytic function.

The domain adjoined to the one discussed is assumed to either be at the change phase temperature or to supply a known heat flux to the moving front, as is the case in fluidized bed coating problems [12].

Another useful parameter is the velocity of propagation of the moving boundary, which is given by

$$\frac{d\mathbf{s}(t)}{dt} = A(\mathbf{s}(t)) \tag{6}$$

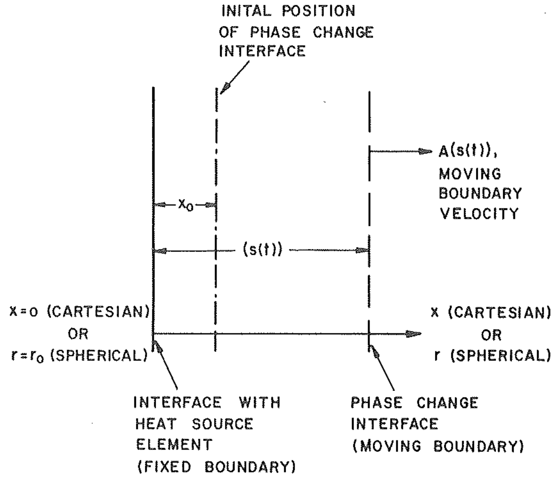

Fig. 1 Schematic drawing of model for Cartesian or spherical geometries

where $A(\mathbf{s}(t))$ is a given analytic function.

In problems which are characterized by a sharp, well-defined phase change temperature, equations (5) and (6) are related through the principle of conservation of energy applied at the moving boundary, i.e.,

$$k \frac{\partial T(\mathbf{s}(t), t)}{\partial x} - k_{ad} \frac{\partial T_{ad}(\mathbf{s}(t), t)}{\partial x} = \rho \cdot L \cdot \frac{d\mathbf{s}(t)}{dt} \tag{7}$$

where subscript *ad* denotes properties of the adjoined domain.

Now define the following nondimensional parameters,

$$u = \frac{T - T_{ph}}{T_{ex} - T_{ph}}; \quad y = \frac{x}{x_0}; \quad s = \frac{\mathbf{s}}{x_0}; \quad \tau = k \frac{(T_{ex} - T_{ph})}{\rho \cdot L \cdot x_0{}^2} \cdot t$$
$$\mathrm{Ste} = \frac{c_p(T_{ex} - T_{ph})}{L}; \quad \phi(s(\tau), \tau) = \frac{x_0 F(\mathbf{s}(t), t)}{T_{ex} - T_{ph}}; \tag{8}$$
$$\Omega(s(\tau)) = \frac{\rho L x_0 A(\mathbf{s}(t))}{k(T_{ex} - T_{ph})}$$

Introduction of these parameters into equation (1) and integration between $\xi = y$ and $\xi = s(\tau)$ yield:

Nomenclature

A = moving boundary velocity
a_n = coefficients in an infinite series, defined by equations (16–18) (Cartesian) and equations (22–24) (spherical)
c_p = specific heat in the changed phase domain
F = temperature gradient at moving boundary
k = thermal conductivity in the changed phase domain
K = proportionality constant, defined in equation (26)
L = latent heat of melting or freezing
n = summation index
r = radial coordinate
r_0 = radius of heat source element in spherical coordinates
$\mathbf{s}$ = distance from moving boundary to interface with heat source element
S = nondimensional distance of moving front, defined by equation (8)
Ste = Stefan number, defined in equation (8)
t = time
t_0 = initial time
T = temperature in the changed phase domain
x = length coordinate
x_0 = distance of phase change boundary from interface with heat source element at $t = t_0$
y = nondimensional length coordinate, defined in equation (8)
u = nondimensional temperature, defined in equation (8)
V = constant moving boundary velocity in equation (25)
α = thermal diffusivity in the changed phase domain
β = distance from moving boundary (spherical coordinates) defined by equation (21)
ζ = distance from moving boundary (Cartesian coordinates), defined by equation (15)
η = dummy variable of integration (spherical coordinates), defined by equation (21)
μ = nondimensional parameter, defined by equation (31)
ν = nondimensional parameter, defined by equation (29)
ξ = dummy variable of integration
ρ = density in the changed phase domain
τ = nondimensional time, defined in equation (8)
ϕ = nondimensional heat flux, defined in equation (8)
θ = transformation defined in equation (19)
Ω = nondimensional moving boundary velocity, defined in equation (8)

Subscripts

ad = adjoined domain
ex = external temperature
ph = phase change

$$\frac{\partial u(s(\tau),\tau)}{\partial y}-\frac{\partial u(y,\tau)}{\partial y}=\text{Ste}\cdot\int_{y}^{s(\tau)}\frac{\partial u(\xi,\tau)}{\partial\tau}\cdot d\xi \qquad (9)$$

where ξ is a dummy variable of integration. Substitution of the boundary condition (5) into (9) and a further integration between $\eta = 1$ and $\eta = y$, yield:

$$(y-1)\phi(s(\tau),\tau)-u(y,\tau)+u(1,\tau)$$

$$=\text{Ste}\int_{1}^{y}\int_{\eta}^{s(\tau)}\frac{\partial u(\xi,\tau)}{\partial\tau}\cdot d\xi\cdot d\eta \qquad (10)$$

Integration by parts operated on the double integral in equation (10) obtains:

$$u(y,\tau)=(y-1)\phi(s(\tau),\tau)+u(1,\tau)$$

$$-\text{Ste}\cdot\left\{\int_{1}^{y}\xi\cdot\frac{\partial u(\xi,\tau)}{\partial\tau}d\xi+y\int_{y}^{s(\tau)}\frac{\partial u(\xi,\tau)}{\partial\tau}d\xi\right\} \qquad (11)$$

Next, boundary condition (4) is introduced into equation (11) to yield:

$$u(1,\tau)=(1-s)\phi(s(\tau),\tau)+\text{Ste}\cdot\int_{1}^{s(\tau)}(\xi-1)\frac{\partial u(\xi,\tau)}{\partial\tau}d\xi \qquad (12)$$

Substitution of equations (6) and (12) into equation (11) and employment of Leibnitz's theorem yield the following integral equation which satisfies the boundary conditions of the problem:

$$u(y,t)=[y-s(\tau)]\phi(s(\tau),\tau)$$

$$-\Omega(s(\tau))\,\text{Ste}\cdot\frac{\partial}{\partial s}\int_{y}^{s(\tau)}(y-\xi)\cdot u(\xi,\tau)d\xi \qquad (13)$$

The Stefan number (Ste) multiplying the integral in equation (13) is smaller than unity for most practical cases. This fact implies the possibility of solving equation (13) by the method of analytic iterations wherein the first guessed solution is the long time solution to the problem. The series solution is obtained by induction following a number of iterations and is given by:

$$T(x,t)=T_{ph}+\sum_{n=0}^{\infty}a_n(\mathbf{s})\cdot\frac{\zeta^n}{n!} \qquad (14)$$

where

$$\zeta=x-\mathbf{s}(t) \qquad (15)$$

$$a_0=0 \qquad (16)$$

$$a_1=F(\mathbf{s}(t),t) \qquad (17)$$

$$a_n=\frac{A(\mathbf{s}(t))}{\alpha}\cdot\left\{\frac{da_{n-2}}{d\mathbf{s}}-a_{n-1}\right\} \qquad (18)$$

Equation (14) also satisfies the initial condition (2) of the problem.

(b) Spherical geometry. For a spherical geometry the problem can be reduced to the one presented above by the following transformation:

$$\theta=(T(x,t)-T_{ph},r \qquad (19)$$

to yield, through a similar method of solution, the following series:

$$T(r,t)=T_{ph}+\frac{1}{r}\sum_{n=0}^{\infty}a_n(\mathbf{s})\cdot\frac{\beta^n}{n!} \qquad (20)$$

where

$$\beta=r-\mathbf{s}(t) \qquad (21)$$

$$a_0=0 \qquad (22)$$

$$a_1=\mathbf{s}(t)\cdot F(\mathbf{s}(t),t) \qquad (23)$$

$$a_n=\frac{A(\mathbf{s}(t))}{\alpha}\cdot\left\{\frac{da_{n-2}}{d\mathbf{s}}-a_{n-1}\right\} \qquad (24)$$

Equations (14) and (20) are the general long time solutions to the inverse Stefan problem in Cartesian and spherical coordinates, respectively. Verification of the solutions is readily obtainable by substituting these expressions into the respective sets of equations and performing the indicated operations.

Numerical Illustrations

The freezing of a solid substance possessing properties similar to those of saturated water at atmospheric pressure, e.g., a biological tissue, is considered as an illustration of the results obtained. The element inducing freezing is assumed to be either a semi-infinite plane (Cartesian) or a sphere of radius r_0. It is further assumed that conduction is the dominant heat transfer mechanism and that the medium being frozen is homogeneous and isotropic and possesses constant thermophysical properties. Values of these and the geometrical parameters are shown in Table 1.

Two examples of the use of the results, one each for the geometries studied, are given below:

Cartesian Geometry. Both the cases of constant and square root of time dependent freezing front velocity have already been discussed in the literature for this geometry, [4–8]. These cases are two particular solutions of the present analysis and would not be repeated here. As an illustration a different case of time dependent heat flux at the moving boundary is considered along with a constant velocity of this boundary. Mathematically the problem is defined by:

$$\frac{ds}{dt}=V\quad(\text{const.}) \qquad (25)$$

$$\frac{\partial T}{\partial x}(s,t)=\frac{1}{k}\left[\rho L\frac{ds}{dt}+Kt\right] \qquad (26)$$

where K is a positive proportionality constant chosen arbitrarily in the present illustration. The physical interpretation of K is that of the rate of change of the heat flux imposed at the change of phase interface. This heat flux is supplied by the adjoined domain and the interpretation might be directly inferred from equation (7). The term Kt might, therefore, be considered as modeling the effect of some unknown temperature distribution in the adjoined domain.

When equations (25) and (26) are substituted into equation (14), with $A(s)$ replaced by V, and $F(s,t)$ replaced by the right hand side of equation (26), the solution is obtained

$$T(x,t)=T_{ph}+\frac{1}{k}(\rho L\cdot V+K\cdot t)\sum_{n=1}^{\infty}\left(-\frac{V}{\alpha}\right)^{n-1}\frac{\zeta^n}{n!}$$

$$-\frac{K}{Vk}\sum_{n=1}^{\infty}\left(-\frac{V}{\alpha}\right)^{n}\frac{n}{(n+2)!}\zeta^{n+2} \qquad (27)$$

which converges after a few manipulations to the finite expression

$$T=T_{ph}+\frac{1}{\rho cV}\{\rho LV+Kt\}[1-exp\nu]$$

$$+\frac{K}{V\cdot k}\left(\frac{\alpha}{V}\right)^2[(2-\nu)(1+exp\nu)-4] \qquad (28)$$

where

$$\nu=-\frac{V}{\alpha}\cdot\zeta \qquad (29)$$

For the case $K = 0$, equation (28) reduces to the classical solution given by Stefan [3]. This is the case of a constant heat flux at the phase-change boundary combined with a constant velocity of this front and not a unique solution to the problem of a constant velocity.

Table 1 Physical and geometrical parameters for the numerical illustrations

Thermal Diffusivity, $\alpha(\text{m}^2/s)$	Thermal Conductivity, $k(W/\text{m}^\circ\text{K})$	Density $\rho(\text{kg/m}_3)$	Phase Change Temperature, $T_{ph}(^\circ\text{C})$	Latent Heat of Freezing, $L(\text{kJ/kg})$	Radius of Spherical Element, $r_0(\text{m})$
1.5×10^{-6}	2.3	920	0	335	5×10^{-3}

Equation (28) was computed for three different values of the parameter K, namely, 0, 50 and 146 kJ/m^{2}s/s. Results for these cases are shown in Fig. 2. It is seen that the temperature distribution in the freezing medium is strongly dependent on K; low values of this parameter allow the development of moderate temperature gradients in the freezing medium. Higher values of K, however, cause sharp temperature gradients to develop. This is due to the need to extract much more energy at the freezing front caused by the rate of change of the heat flux supplied at this front. As a result, the temperature at the interface with the freezing element, i.e., $x = 0$, drops very rapidly and may reach −150° after 30 s of application only, with the frozen front located at a distance of 1.5 mm only. A hypothetical case of interest would be the assumption of negative values for K. These values may imply the removal rather than supply of heat at the moving boundary by the adjoined domain. Thus, by varying the value of K in the proper manner, control of the depth of penetration of the freezing front may be achieved. However, no actual method of employment of such a control is known to the authors and the problem remains of theoretical interest at present.

A case of particular interest is the one wherein the Stefan number approaches zero. This number, defined in equation (8), gives the ratio between the sensible and latent heat of the phase changing material. Zero value of this number would be obtained for any material for which the latent heat is much larger than the specific heat. Fig. 3 shows the temperature distribution for two cases: Ste = 0 and Ste = 0.25, both for $K = 0$. It is seen that the effect of a zero Stefan number is such that temperatures are linear and almost uniform in the solid side whereas much sharper gradients are obtained for Ste = 0.25.

Spherical Geometry. As an illustration to the results in spherical coordinates the simple case of constant heat flux along with a constant velocity of the freezing front is studied. The temperature distribution is obtained by equation (20) and is given by

$$T(r, t) = T_{ph} \frac{F(s(t), t)\alpha}{rA(s(t))} \times \left\{ g \sum_{n=1}^{\infty} \frac{\mu^n}{n!} - \frac{\alpha}{A(s(t))} \sum_{n=1}^{\infty} \frac{n}{(n+2)!} \mu^{n+2} \right\} \quad (30)$$

where

$$\mu = -\frac{A(s(t))}{\alpha} \eta \quad (31)$$

The two infinite series in equation (30) converge after a few manipulations to a finite analytic expression represented by

$$T(r, t) = T_{ph} + \frac{F(s(t), t)\alpha}{rA(s(t))} \times \left\{ g[1 - exp\mu] + \frac{\alpha}{A(s(t))} [(2 - \mu)(1 + \exp\mu) - 4] \right\} \quad (32)$$

which is similar to the expression obtained by Langford [7]. Equation (32) was computed for three constant but different velocities of the freezing front, namely, 0.01, 0.005, and 0.0025 cm/s. In all cases the radius of the spherical freezing element is the same, $r_0 = 0.5$ cm. Results shown in Fig. 4 indicate temperature distributions in the frozen region for the same locations of the freezing front. It is seen that the higher the velocity of the freezing boundary the steeper the temperature gradients in the medium. This leads, as is the case in the previous example, to lower temperatures to be required at the interface

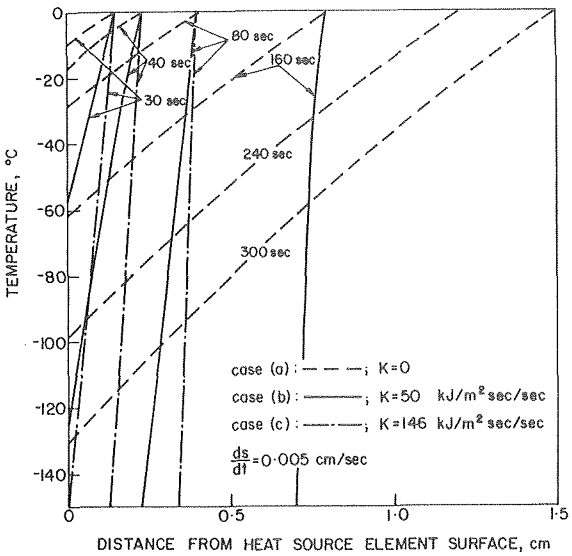

Fig. 2 Temperature distributions in a freezing medium for various heat fluxes and a constant velocity of the moving boundary. Rectangular geometry

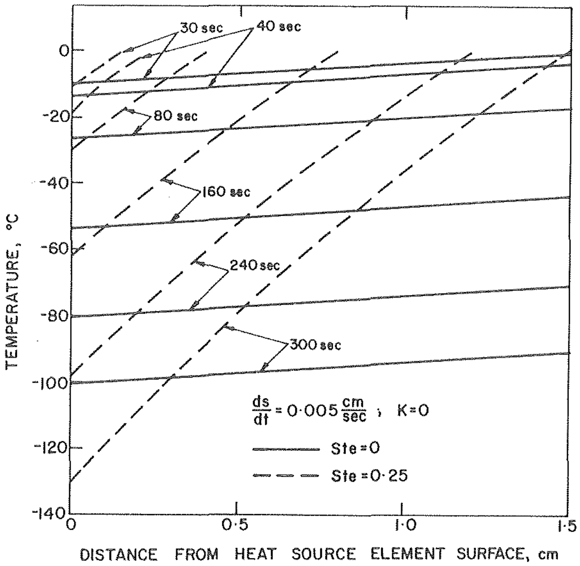

Fig. 3 Temperature distributions in a freezing medium for two values of the Stefan number. Rectangular geometry

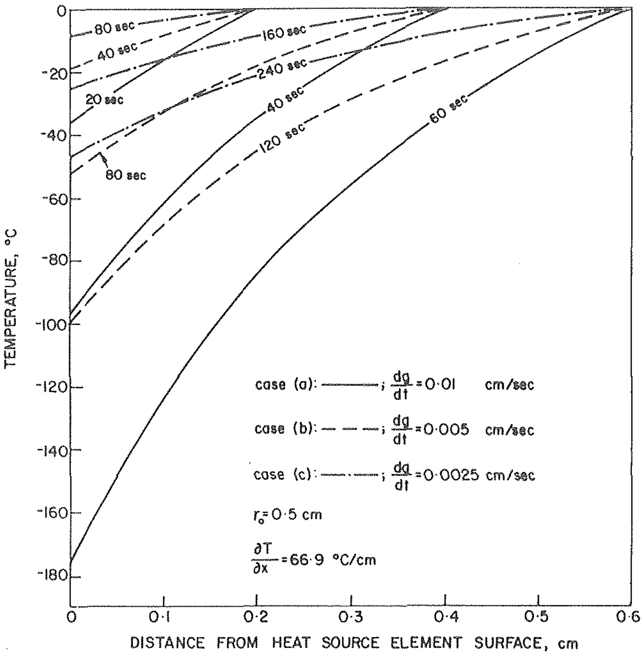

Fig. 4 Temperature distributions in a freezing medium for a constant heat flux and various velocities of the moving boundary. Spherical geometry

with the freezing element at $r = r_0$. Thus, freezing a substance to a certain depth may not be possible should the required velocity of the freezing front be too high.

The above illustrations indicate the capability of the present analysis in predicting the necessary temperature and heat flux variations that would be required at the heat source element interface. These may be calculated by specifying the required conditions at the freezing front which, in certain industrial and biomedical applications, are of utmost importance. For example, it is well known that the survival rate of preserved blood cells is dependent on the rate of temperature change when freezing them for preservation. Information on the cooling rates that will insure optimum cell survival rate can now be employed, via the analysis presented here, for better control of the freezing process. Other industrial applications to the present analysis are in ablation of flying objects thermal shields, in casting wherein nucleation is temperature dependent, and in numerous other applications involving change of phase.

References

1 Evans, G. M., Isaacson, H. E., and MacDonald, J. K. L., "Stefan-like Problems," *Quarterly of Applied Mathematics*, Vol. 8, 1950, pp. 312–319.

2 Carslaw, H. S., and Jaeger, I. C., *Conduction in Heat in Solids*, Oxford University Press, London, 1959.

3 Ibid, p. 282.

4 Gibson, R. E., "A Heat Conduction Problem Involving a Specified Moving Boundary," *Quarterly of Applied Mathematics*, Vol. 16, 1958, pp. 426–430.

5 Martynov, G. A., "Solution of the Inverse Stefan Problem in the Case of Spherical Symmetry," *Zuhurnal Tekhicheskoi Fiziki*, Vol. 2, 1960, pp. 239–241.

6 Langford, D., "Pseudo Similarity Solutions of the One-dimensional Diffusion Equation with Application to the Phase Change Problem," *Quarterly of Applied Mathematics*, Vol. 25, 1967, pp. 45–52.

7 Langford, D., "New Analytical Solutions of the One-dimensional Heat Equation for Temperature and Heat Flow Rate Both Prescribed at the Same Fixed Boundary with Applications to the Phase Change Problem," *Quarterly of Applied Mathematics*, Vol. 24, 1966, pp. 315–322.

8 Bluman, G. W., "Applications of the General Similarity Solutions of the Heat Equation to Boundary Value Problems," *Quarterly of Applied Mathematics*, Vol. 31, 1974, pp. 403–415.

9 Kolodner, I. I., "Free Body Problem for the Heat Equation with Application to Problems of Change of Phase," *Comuns. Pure and Applied Mathematics*, Vol. 9, 1956, pp. 1–31.

10 Miranker, W. L., "A Free Boundary Value Problem for the Heat Equation," *Quarterly of Applied Mathematics*, Vol. 16, 1959, pp. 121–130.

11 Peel, D. A., "Some Moving Boundary Problems in the Steel Industry," in *Moving Boundary Problems in Heat Flow and Diffusion*, Clarendon Press, Oxford, eds. J. R. Ockendon and W. R. Hodgkins, 1975.

12 Abuaf, N., and Gutfinger, C., "Heat Transfer with a Moving Boundary, Application to Fluidized Bed Coating of Thin Plates," *Int. J. Heat Mass Transfer*, Vol. 16, 1973, pp. 213–216.

13 Rubinsky, B., and Shitzer, A., "Analysis of a Stefan-like Problem in a Biological Tissue Around a Cryosurgical Probe," ASME JOURNAL OF HEAT TRANSFER, Vol. 98, 1976, pp. 514–519.

R. Farhadieh
Asso. Mem. ASME
L. Baker, Jr.
Reactor Analysis and Safety
Argonne National Laboratory,
Argonne, Ill.

Heat Transfer Phenomenology of a Hydrodynamically Unstable Melting System

An experimental study was conducted on a melting system consisting of a liquid layer overlying a solid substrate. The liquid and solid when molten were mutually miscible. To initiate melting, the liquid was heated by a heater grid suspended above the liquid-solid interface. Systems with the density of the liquid less than that of the molten solid were gravitationally stable, whereas those with the density of the liquid greater than that of the molten solid were gravitationally unstable. Total mixing of the melt layer and the liquid layer resulted in thermal mixing of the liquid. The heat transfer coefficient was found to be an increasing function of the density ratio of liquid and melted solid; this increase occurred in four stages. There was a marked enhancement of heat transfer in the system. The melting rate was also found to depend on temperature difference and conduction depth.

Introduction

The problem of melting of a horizontal layer of a solid has been extensively studied by many investigators. In the melting process, the heat transfer mode in the solid is by conduction, whereas heat transfer through the liquid phase is by either conduction or convection. The classical Stephan problem involves heat transfer by conduction through the liquid phase. An account of this problem and the analytical solution of Neumann are given by Carslaw and Jaeger [1].[1] Numerical treatment of the same problem is given by Murray and Landis [2]. A majority of solids, except for ice (Tankin and Farhadieh [3]), when melted from above, exhibit this kind of heat transfer behavior. On the other hand, when a solid is melted from below, there exists an adverse density gradient in the molten layer due to destabilizing temperature gradient. Thus the layer is thermally unstable. When a critical temperature difference is exceeded, instability sets in. That is, the buoyant forces overcome the viscous and dissipative forces, and the layer overturns; thermal convection is the heat transfer mode. The magnitude of density ratio $\Delta\rho/\rho = \alpha\Delta T$, involved in thermal convection problems, is about 10^{-4}. Tien and Yen [4], and Sparrow, Lee, and Shamsundar [5] treated this problem analytically, whereas Yen [6] and Heitz and Westwater [7] treated it experimentally. These investigators studied, respectively, the temperature distribution in the melt layer, the effect of thermal convection on the melt layer, the strength of thermal convection as the melt layer was forming, and the effect of maximum density on thermal convection.

The present study involves a melting system where the liquid phase undergoes a different kind of hydrodynamic instability. This system involves a liquid layer overlying a solid substrate. The liquid layer and the melted solid are dissimilar and hence have different thermophysical properties, but the two media, upon melting of the solid, are mutually miscible. The density of the liquid layer can be either greater or less than that of the melted solid. When the density of the liquid layer is greater than that of the melted solid, the two dissimilar liquid layers can be gravitationally unstable, even though the layers are thermally stable. When gravitationally unstable, the liquid system overturns and the two layers intermix; the resultant convective currents cause thermal mixing of the layers. We call this double mixing process "convective mixing." The process of convective mixing can affect both the flow phenomenology and the melting rate. In this study, attention is focused on the effects of variations in density on the melting rate, downward heat transfer, and flow regime. Effects of variation in initial conductive depth and temperature difference have also been investigated. It is believed that enough insight has been gained to form a basis for the analytical formulation of the problem. To the authors' knowledge, this is the first paper of the kind dealing with the effect of variation of liquid density on the mechanism of heat transfer in a melting system.

Experimental

Material selection was limited because of the experimental requirements concerning the miscibility of the melted solid and the liquid layer and the greater density of the liquid layer. Carbowax 1500 was used as the solid phase, and aqueous NaBr or KI solutions constituted the liquid layer. The initial liquid density ranged between 1068 to 1750 kg/m^3, which was obtainable by variation of the solute concentration. The thermophysical properties of both phases are given

---

[1] Numbers in brackets designate References at end of paper.

Contributed by the Heat Transfer Division for publication in the JOURNAL OF HEAT TRANSFER. Manuscript received by the Heat Transfer Division, July 20, 1977.

Table 1 Thermophysical properties of experimental materials

	Density, ρ (kg/m^3)	Melting Point, K	Thermal Conductivity, k (W/m-K)	Viscosity η (Pa·s)	Specific Heat, J/kg-K	Latent Heat λ_f (J/kg)
SOLID						
Carbowax 1500	1150 at m.p. 1095 at 323K	318	0.2508	34.5×10^{-3}	2048	1.63×10^5
SOLUTION						
NaBr	1064 1480	- -	0.540	1.0461×10^{-3} 1.8657×10^{-3}	3760 2559	- -
KI	1750	-	0.527	0.89×10^{-3}	1498	-

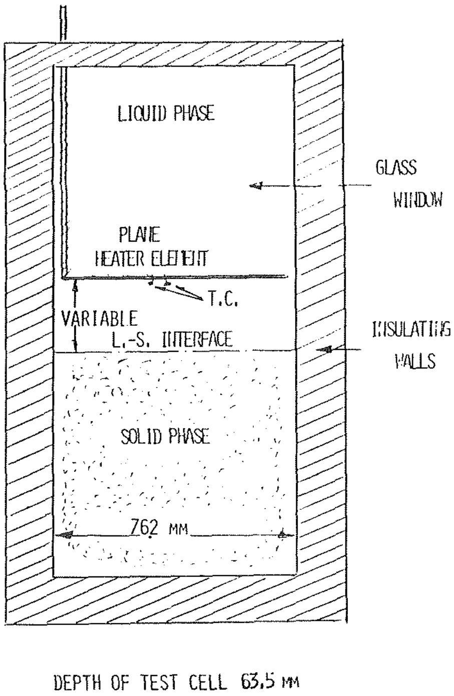

Fig. 1 Schematic drawing of the test section

in Table 1.

The one-dimensional melting experiment was conducted in an upright rectangular box (Fig. 1). The sidewalls and the bottom of the test section were insulated. Glass windows were fitted in the front and the back of the test section for the observation of interface motion and for photographic purposes. The liquid-solid interface was horizontal and had a cross section of 63.5×76 mm^2. The liquid layer, overlying the solid, was deep enough to eliminate the effect of density change which was needed to achieve steady-state conditions. The solid was deep enough to allow for steady-state measurement. A planar heater, made of Nichrome wire, was used as the heat source. The heater was suspended a fixed distance d above the liquid-solid interface. The layer temperature at the heater grid was thermostatically controlled throughout the experiment. This temperature was maintained at a value ΔT above the melting point of the solid (21K for the variable density experiments). An iron-constantain thermocouple was used to obtain the transient vertical temperature profile through the liquid phase. Temperature sensitivity of about ±0.3K was measured.

Results and Discussion

Fig. 2 is a typical sequence of photographs showing the melting of the underlying solid when the density ratio of the two media is $\rho_\ell/\rho_{sm} = \rho^* = 0.975$. The liquid layer above the heater grid is thermally unstable; heat transfer is by convection. The adverse temperature gradient resulting in thermal convection currents is about 0.67 K/mm (top of the layer is at ambient temperature). On the other hand, the liquid layer below the heater grid is stably stratified. Heat transfer through this layer is by conduction. Furthermore, the liquid layer is at all times less dense than the melted solid, and hence, the system is gravitationally stable. As can be seen after more than 11000 s (~3 hr), the 10-mm-thick melt layer has not penetrated the liquid layer. The opaqueness at the interface of the two liquids is caused by gradual diffusion of the melt into the overlying liquid.

Fig. 3 shows typical temperature profiles in the liquid phase for a system with the density ratio less than 1.093. The profiles show that the liquid layer is thermally conductive and convective mixing is not present in this case.

Fig. 4 is a typical sequence of photographs showing the advancement of the liquid-solid interface for a melting system with a density ratio $\rho^* = 1.160$. Melting had not begun at 2193 s. As before, the heat transfer in the layer above the grid is by convection. Conduction is the initial heat transfer mode in the layer beneath the heater grid. Prior to melting, narrow columns extend into the conduction layer from discreet random sites at the interface. These fingers are gravity-driven flows which appear when the dissolved interface of lighter density protrudes into the overlying heavier solution. The slight recession of the interface is caused by this gradual mass transfer process. When melting initiates at about 2200 s, the melt layer, which is lighter than the conductive layer, begins to overturn with the observation of short needle-like streamers that increase in number as melting progresses. At approximately 2800 s, large and small vortices appear at the outer edge of the streamers. These vortices can best be seen in Fig. 5, which is the enlargement of 2879 s photograph of Fig. 4. These vortices, which result in thermal mixing of the layer (convective mixing), increase in intensity as melting progresses. This type of vigorous mixing results in rapid recession of the interface, i.e., 14 mm in only 440 s.

Fig. 6 shows typical transient temperature profiles through the liquid layer for system with a density ratio $\rho^* > 1.093$. The transient

Nomenclature

A = area of the liquid-solid interface
C = constant
C_p = specific heat of solid
d = conduction depth—initial distance between heater grid and interface
d_1 = characteristic length, A/P
$\frac{dz}{dt}$ = melting rate
g = gravity
h_0 = overall heat transfer coefficient
k = thermal conductivity of melt
ℓ = characteristic length
m = constant
Nu = downward Nusselt number, $h_0\ell/k$
P = perimeter of the liquid-solid interface
Q = downward heat flux
R = Rayleigh number of layer under the grid, $g\Delta\rho\ell^3/\rho_\ell\nu\kappa$
ΔT = temperature difference between heater grid and liquid-solid interface
ΔT_s = temperature difference between melting point and initial temperature of solid
α = coefficient of volume expansion
λ_f = latent heat of solid
ρ_ℓ = liquid density
ρ_{sm} = melt density
$\rho^* = \rho_\ell/\rho_{sm}$
κ = thermal diffusivity of mixture
ν = kinematic viscosity of mixture

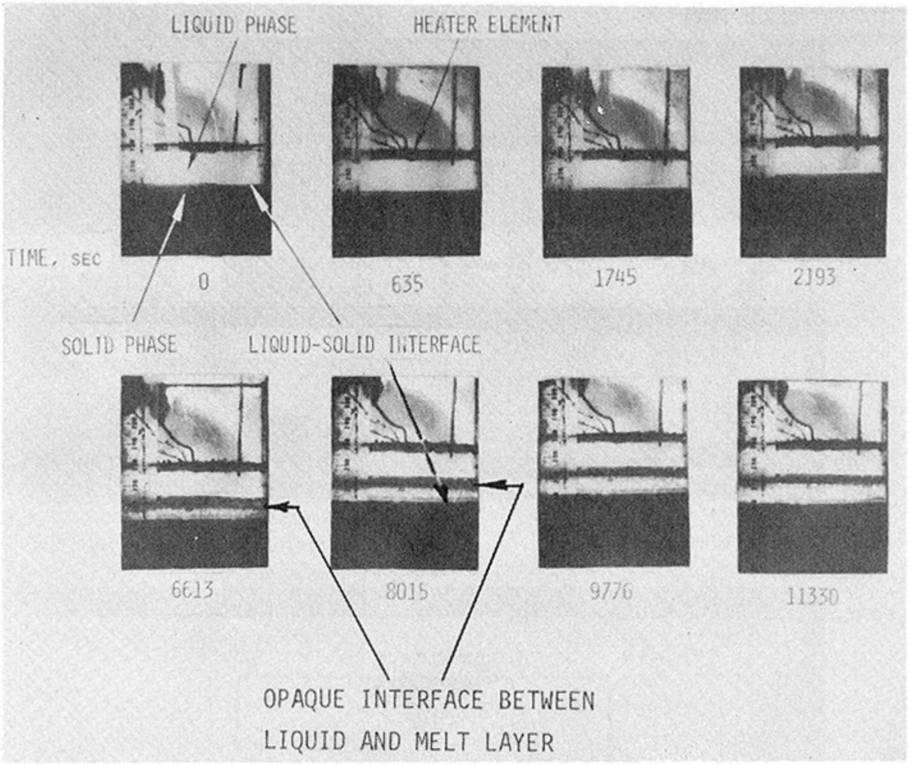

Fig. 2 Sequence of photographs showing the transient advancement of interface in a system of two miscible media; $\rho^* = 0.957$, $d = 17$ mm, and $\Delta T = 21$ K

conduction profile at 1800 s characterizes the condition when thermal mixing has not occurred even though material convection is present. The flow is characterized by needle-like streamers. The temperature profile at 2400 s is flat with a sharp gradient at the moving boundary, and this indicates that the layer is thermally mixed. This is the condition of convective mixing. The flow is characterized by the presence of vortices.

Fig. 7 shows the transient penetration distance for a melting system of two different density ratios, $\rho^* = 1.09$ and $\rho^* = 1.16$. Prior to the onset of melting, the penetration rate is controlled by gradual mass transfer and hence is small. This mass transfer is due to slight dissolution of lower density solid with the heavier liquid. After melting has initiated and the convective mixing is established, this rate increases to a much higher value. The constant slope of the curve after a penetration of about 15 mm indicates the steady-state condition of the experiment. Fig. 7 further shows that the penetration rate increases with ρ^*. Accordingly, the strength of the convective mixing process is believed to be primarily controlled by ρ^*.

The steady-state penetration rate dz/dt obtained from Fig. 7 is used to determine the overall heat transfer coefficients for the melting system. Assuming (1) the solid substrate is an insulator (heat is used entirely for melting), (2) the heat transfer is one-dimensional, and (3) steady-state conditions are maintained, the melting heat flux is given by

$$Q = \rho_{sm}(\lambda_f + C_p \Delta T_s)\frac{dz}{dt} \tag{1}$$

After convective mixing has commenced, the temperature of the fluid layer becomes uniform (flat temperature profile). The heat transfer to the liquid-solid interface can be defined as

$$Q = h_0 \Delta T \tag{2}$$

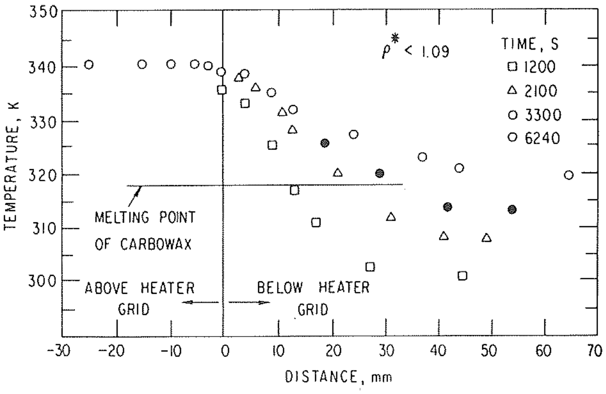

Fig. 3 Transient temperature profile in the liquid layer; $\rho^* < 1.09$

Combining the two relationships, the overall heat transfer coefficient in terms of melting rate is given by

$$h_0 = \rho_{sm}(\lambda_f + C_p \Delta T_s)\frac{dz}{dt}\bigg/\Delta T \tag{3}$$

The overall heat transfer coefficient includes the combined effects of heat and mass transfer. The former causes the melting of solid, and the latter causes the strong convective mixing which increases heat transfer. The two effects result in the rapid recession of the interface. Table 2 gives h_0 and dz/dt along with other pertinent experimental parameters.

Fig. 8 shows the steady-state h_0 versus the density ratio $\rho^* - 1$. This curve is based on experiments which involve only variations in ρ_ℓ (the liquid pool density). The strength of the convective mixing which controls the heat transfer rate to the interface depends on ρ^*, and, as a result, the overall coefficient of heat transfer increases with $\rho^* - 1$. This increase occurs in stages. Below $\rho^* = 1.09$, the layer is not thermally convecting; the flow is controlled by material convection. The

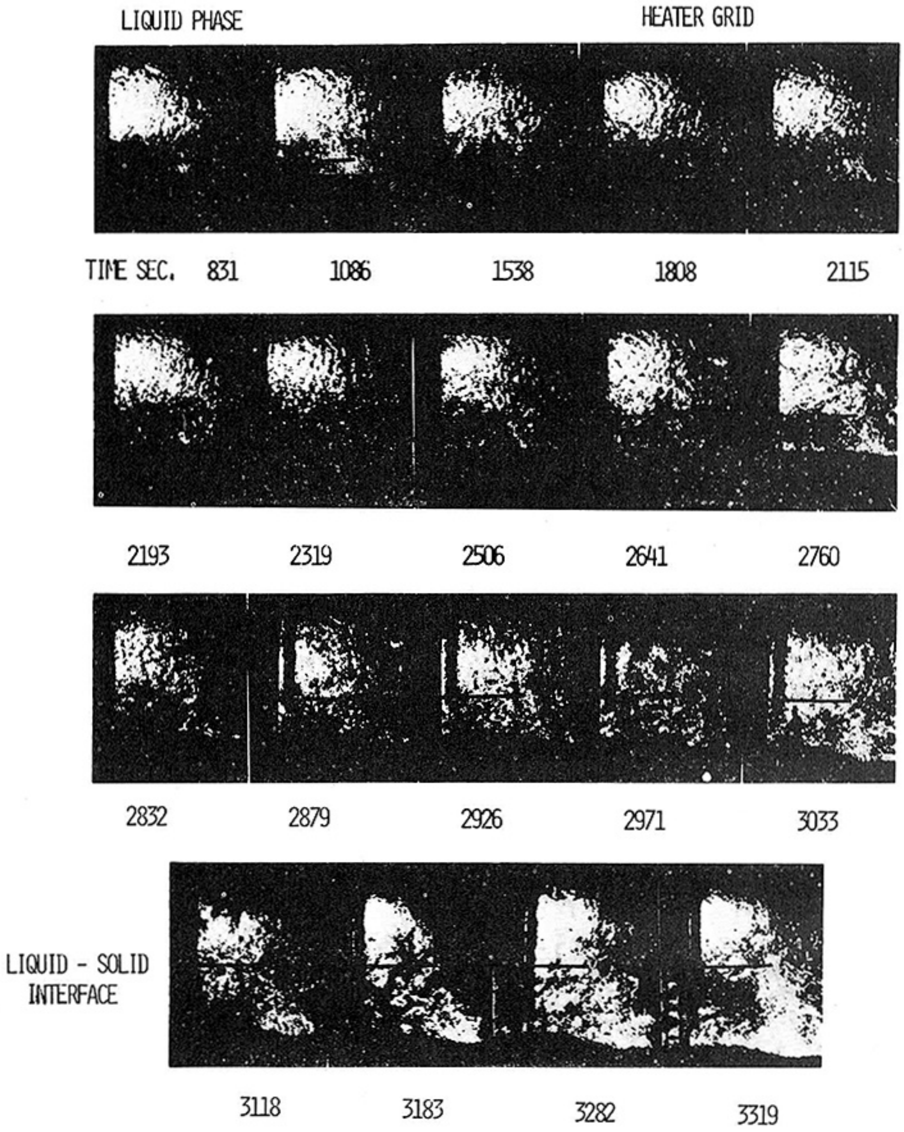

Fig. 4 **Sequence of photographs showing the transient advancement of interface in a system of two miscible media; $\rho^* = 1.16$, $d = 43$ mm, and $\Delta T = 21$ K**

flow pattern consists of needle-like streamers protruding from the conductive layer. For the density ratio ρ^* near 1.09, there exists a flow transition region where the heat transfer coefficient changes sharply. As the density ratio increases toward 1.09, the number density of the needle-like streamers increases. Small and large vortices constitute the flow pattern which occurs at the upper edge of the streamers. These vortices thermally mix the conductive layer; thus, the heat transfer mode of the layer is convection. Except for a sharp gradient at the interface, the temperature profile in the layer becomes flat. For $\rho^* < 1.09$, small and large vortices are concurrent.

Because of the observed behavior, the density regions $\rho^* < 1.09$, $\rho^* = \sim 1.09$, and $1.09 < \rho^* < 1.25$ are designated, respectively, as laminar, transition, and turbulent flow regime. In addition to these regimes, there exists an upper turbulent flow region for $\rho^* > 1.25$. Convective mixing in this region is very vigorous; only large vortices characterize the flow pattern. Needle-like streamers are confined to the vicinity of the liquid-solid interface. The melt layer is washed away by these vortices as it is formed. The slope of the heat transfer curve is the greatest in this region. This increase cannot be attributed to any change in viscosity or thermal conductivity. These quantities are essentially dependent on temperature. Density ratio is the only variable involved in the construction of Fig. 8 and, therefore, is considered to be responsible for the enhancement of heat transfer.

Fig. 9 is identical to Fig. 8 except for the transformation of the abscissa to the Rayleigh number for heat transfer and ordinate to Nusselt number. The characteristic length scale ℓ in the Rayleigh number and the Nusselt number equations is the value $d_1 \triangleq A/P$. $\Delta\rho$, the difference between the density of the liquid and the melted solid, is the only varying parameter in the Rayleigh number and equally h_0 in the Nusselt number equation. Since the Nusselt number is in reference to the heat transported to the substrate solid, it is defined as downward Nusselt number. Correlations (see [8]) for laminar natural convection ($\mathrm{Nu} = 0.54\, R^{0.25}$) and for turbulent natural convection ($\mathrm{Nu} = 0.15\, R^{1/3}$) appear in this figure. Because of the analogy between heat and mass transfer, these correlations can be applied to either heat or mass transfer problems. In the usual Bénard-Rayleigh problem involving either heat or mass transfer, the transition from laminar to turbulent convection results in a small change of slope and occurs at a Rayleigh number $\simeq 8 \times 10^6$ (see Fig. 9). Furthermore, turbulent convection continues on the same slope for Rayleigh numbers as high as 10^{10} [see [9]]. The laminar and turbulent regimes found in this study are separated by a transition region. Transition from laminar to turbulent convection occurs at a Rayleight number of about 1.5×10^6. However, the slopes of the correlations and the experimental data are

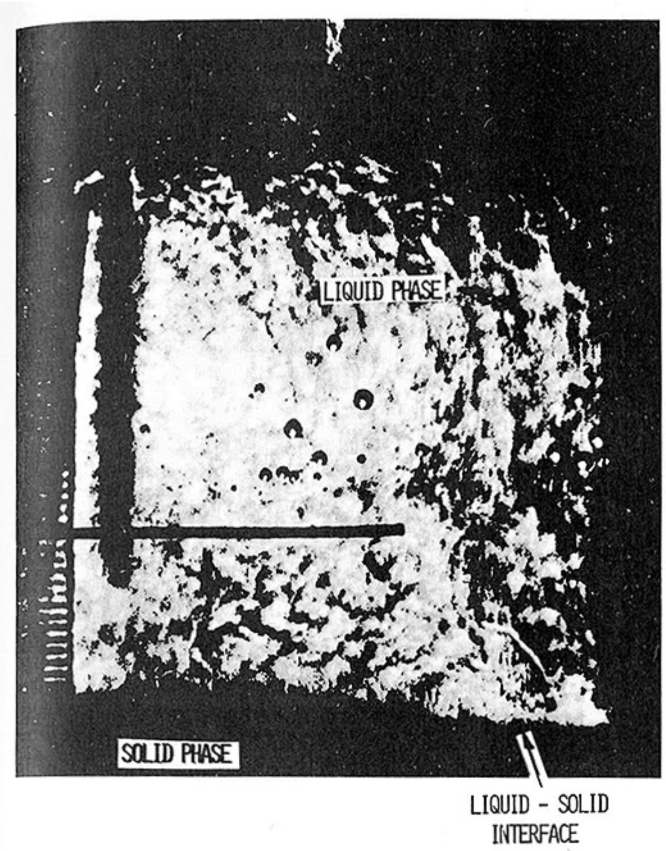

Fig. 5 Enlargement of 2879 s photograph of Fig. 4 showing large and small vortices

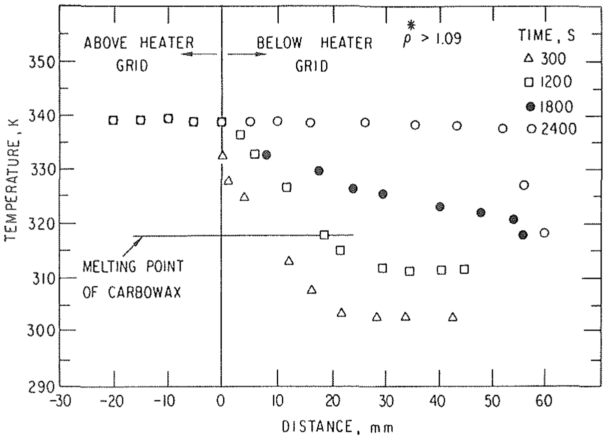

Fig. 6 Transient temperature profile in the liquid pool; $\rho^* > 1.09$

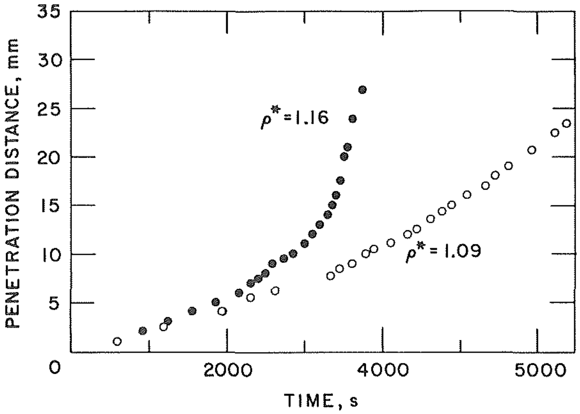

Fig. 7 Penetration depth as a function of time for two different experiments

Table 2 Tabulation of experimental parameters and results

Density ρ (kg/m^3)	Temperature differences ΔT (K)	Cond. Depth d (m)	Melting Rate dz/dt (m/s)	Heat Transfer Coefficient h_o (W/m^2 - k)
1099	21	0.017	3.080×10^{-6}	32.90
1112	21	0.017	4.400×10^{-6}	47.00
1146	21	0.017	6.994×10^{-6}	74.70
1150	21	0.017	7.294×10^{-6}	77.90
1182	21	0.017	1.760×10^{-5}	188.00
1194	21	0.017	8.239×10^{-6}	88.00
1194	21	0.017	1.133×10^{-5}	121.00
1195	21	0.017	1.114×10^{-5}	119.00
1197	21	0.017	1.591×10^{-5}	170.00
1205	21	0.017	2.397×10^{-5}	256.00
1210	21	0.017	2.415×10^{-5}	258.00
1217	21	0.017	1.451×10^{-5}	155.00
1233	21	0.017	2.481×10^{-5}	265.00
1237	21	0.017	2.677×10^{-5}	286.00
1280	21	0.017	2.696×10^{-5}	288.00
1350	21	0.017	3.080×10^{-5}	329.00
1423	21	0.017	4.204×10^{-5}	449.00
1430	21	0.017	4.597×10^{-5}	491.00
1488	21	0.017	5.149×10^{-5}	550.00
1489	21	0.017	5.496×10^{-5}	587.00
1613	21	0.017	6.404×10^{-5}	684.00
1390	21	0.044	4.600×10^{-5}	491.28
1390	21	0.034	4.100×10^{-5}	437.88
1390	21	0.025	3.750×10^{-5}	400.50
1390	21	0.017	3.500×10^{-5}	373.80
1390	21	0.008	3.300×10^{-5}	352.44
1450	16	0.040	2.650×10^{-5}	371.460
1450	21	0.040	4.900×10^{-5}	523.315
1450	24	0.040	5.950×10^{-5}	556.022
1450	29	0.040	8.150×10^{-5}	630.298
1450	37	0.040	1.050×10^{-4}	636.464

very similar. The region of strongly enhanced heat transfer is not present in the standard Bénard-Rayleigh type problem.

Penetration rate as a function of both the initial conduction depth (layer thickness under the heater grid) and the temperature difference between the heater grid and the melting point of solid are shown in Fig. 10. In the tests when conduction depth was the only variable, the initial liquid density and the temperature difference were fixed at about 1350 kg/m^3 and 21K, respectively. The conduction depth is varied by raising or lowering of the heater grid. The penetration rate was found to increase slightly with increasing depth; 83 percent increase in conduction depth increases the melting rate (or melting heat transfer) only by about 28 percent. This increase is attributed to the smaller stabilizing trmperature gradient that exists across the thick conductive layer depth d. Thus, the layer offers a lesser resistance to thermal mixing which amounts to a more vigorous convective mixing. The resultant melting heat transfer and, hence, the melting rate is increased.

When temperature difference was the only variable of the experiment, the initial conduction depth and layer density were fixed at 40 mm and 1450 ± 5 kg/m^3, respectively ($\rho^* = 1.32$). As can be seen from curve (b) of Fig. 10, the penetration rate increases with temperature difference. The increase is caused by an increase in the temperature driving force and, possibly, by a decrease in viscosity.

Conclusion

The melting system under study was found to be highly sensitive to density differences. When the density ratio $\rho^* < 1$, the system is gravitationally stable as well as thermally stable. When the density

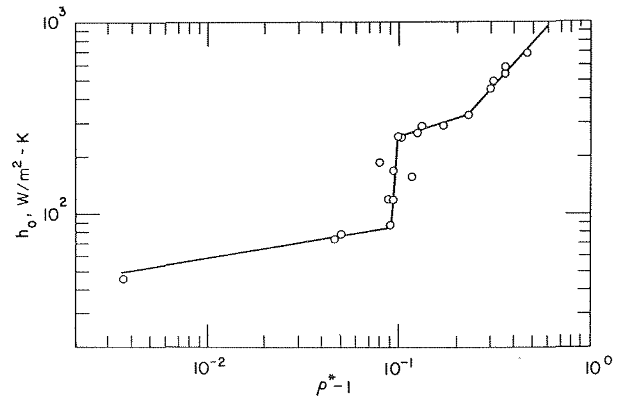

Fig. 8 Overall heat transfer coefficient as a function of density ratio — 1

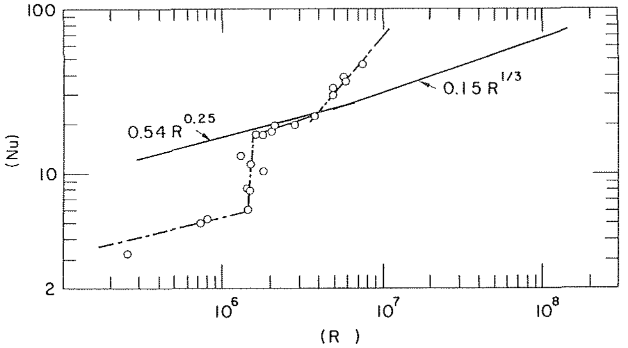

Fig. 9 Experimental Nusselt number as a function of Rayleigh number. Solid lines are correlations obtained from [8]

ratio $\rho^* > 1$, the system, although thermally stable, becomes gravitationally unstable, and convective processes are initiated. Three discreet regimes of behavior have been found for this case.

In the range of density ratios $\rho^* < 1.09$ (Rayleigh number $< 1.5 \times 10^6$), the flow regime appears to be laminar and is characterized by needle-like streamers of low density which penetrate the overlying liquid.

When the density ratio is equal to 1.09, there is a sharp transition to a turbulence region that is characterized by the presence of vortices which results in considerable increases in heat transfer and melting rate.

When the density ratio is equal to 1.25, there is a transition to a very vigorous turbulent regime characterized by an increase in vortex size and an increase in the slope of the plot of heat transfer coefficient versus density ratio minus one.

The heat transfer and melting rate were found to be weakly dependent on the initial conduction depth. However, they increased in approximately linear fashion with increasing temperature difference.

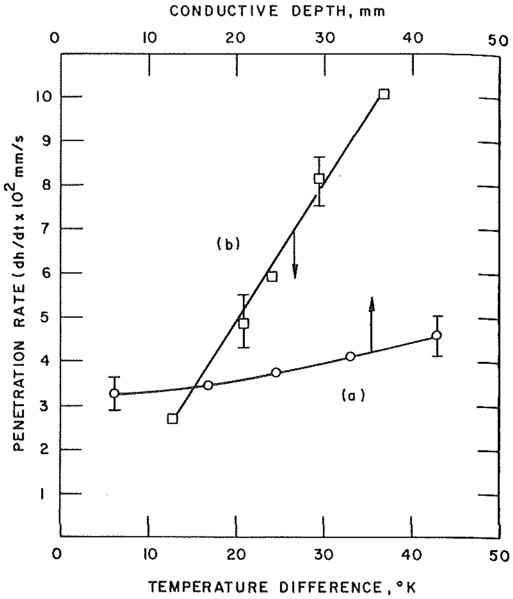

Fig. 10 Penetration rate as a function of initial temperature difference and initial conclusion depth; curve (a) ρ_ℓ = 1390 kg/m^3 and ΔT = 21°K, Curve (b) ρ_ℓ = 1450 ±5 kg/m^3

Acknowledgments

Thanks are due to Professor M. M. Chen for many hours of fruitful discussion. Also, we would like to thank Mr. J. D. Bingle for his editorial review of the paper and Mrs. E. Taylor for her expert typing of this manuscript. This work was conducted under the auspices of the U.S. Energy Research and Development Administration.

References

1 Carslaw, H. S., and Jaeger, J. C., *Conduction of Heat in Solids*, Clarendon Press, Oxford 1959.

2 Murray, W. D., and Landis, F., "Numerical and Machine Solutions of Transient Heat Conduction Problems Involving Melting or Freezing," TRANS. ASME, Vol. 81, 1959, p. 106.

3 Tankin, R. S., and Farhadieh, R., "Effect of Thermal Convection Currents on Formation of Ice," *Int. Journal of Heat Mass Transfer*, Vol. 14, 1971, p. 953.

4 Tien, C., and Yen, Y. C., "Approximate Solution of a Melting Problem with Natural Convection," *Chem. Eng. Prog. Synp. Series* 64, Vol. 62, 1960, p. 166.

5 Sparrow, E. M., Lee, L., and Shamsundar, N., "Convective Instability in a Melt Layer Heated from Below," ASME JOURNAL OF HEAT TRANSFER, Vol. 98, 1976, p. 88.

6 Yen, Y. C., "On the Effect of Density Inversion on Natural Convection in a Melted Water Layer," *Chem. Eng. Progress AIChE*, 92, Vol. 65, 1969, p. 245.

7 Heitz, W. L., and Westwake, J. W., "Critical Rayleigh Numbers for Natural Convection of Water Confined in Square Cells with L/D from 0.5 to 8," ASME JOURNAL OF HEAT TRANSFER, Vol. 93, 1971, p. 188.

8 Lloyd, J. R., and Moran, W. R., "Natural Convection Adjacent to Horizontal Surface of Various Plan Forms," ASME JOURNAL OF HEAT TRANSFER, Vol. 96, 1974, p. 443.

9 Hollands, K. G., Raithby, G. D., and Konicek, L., "Correlation Questions for Free Convection Heat Transfer in Horizontal Layers of Air and Water," *Int. Journal of Heat and Mass Transfer*, Vol. 18, 1975, p. 879.

S. I. Abdel-Khalik
T. O. Hunter[2]
Nuclear Engineering Department
and Fusion Technology Program,
University of Wisconsin
Madison, Wisc.

Assessment of Surface-Heating Problems in Laser-Fusion Reactors[1]

The surface-heating problems associated with the pulsed photon and ion irradiations of the first walls and liners of inertially-confined fusion reactor cavities are investigated. Analytical models for predicting the thermal response of these surfaces as a function of the different design and operational parameters of the system and the nature of the incident irradiations are developed. The effectiveness of residual gas as a means for protecting the wall from the ions and soft X-rays is assessed.

Introduction

Inertial confinement is one approach to the production of energy from thermonuclear fusion. Conceptual designs for commercial power reactors which utilize this mechanism are currently being developed [1].[3] Fusion is achieved by focusing high intensity laser beams of short duration onto a small deuterium-tritium pellet injected into the center of the reactor cavity. The absorption of this laser light by the pellet causes compression and heating of the fuel until ignition conditions are met. Upon ignition a microexplosion occurs in which thermonuclear energy is released. The process is repeated at a rate of 1–20 Hz with energy yields of 100–1000 MJ per pellet depending on system design. This pulsed energy is captured in the cavity walls surrounding the microexplosion and is transferred to the working fluid of a suitable power cycle.

The energy release from these microexplosions is partitioned between neutrons and other products of the fusion reaction, unburnt fuel, pellet constituents, reflected laser light, and high energy photon radiations (gamma and X-rays). The cavity walls surrounding the microexplosion will be subjected to these pulsed high-flux irradiations. Typically, the reactor cavity is a few meters in radius. At such distances, the reflected laser light and X-rays will first arrive about 10–20 ns after the burst, followed by the neutrons around 100 ns, the fast ions at approximately one μs, and finally the slower debris for as long as ten μs from thermonuclear burn.

These radiations will deposit their energy in the first wall and surrounding blanket. The high deposition rates will result in large temperature excursions at the exposed surface. If these depositions are sufficiently short in duration, thermoelastic stress waves can be generated which could induce spallation at both the exposed and rear surfaces. In addition, the combination of temperature transients and radiation damage rates can result in other effects including evaporation, sputtering, blistering, and swelling. All these effects serve to limit the lifetime of the reactor first wall. For dry-wall type cavities, the surface-heating and ablation of the first wall (or its protective liner) by the soft X-rays and charged particles emanating from the pellet and by the reflected laser light may be the limiting factors in determining the necessary cavity size to contain the microexplosion. These photons and charged particles have a relatively short range (penetration depth), and, as a result, the surface temperature of the wall may rise sharply after each pulse. The high-energy neutrons produced by the microexplosion produce an insignificant temperature rise in the first wall because of their long range. The ions arrive at the first wall much later than the photons so that the surface temperature excursion produced by the photons would be significantly reduced when the ions arrive.

Calculations of the implosion of bare D-T pellets indicate that approximately one percent of the energy yield is in the form of X-rays [1–5]. Structured pellets may produce higher X-ray fractions with softer spectra. This tends to exacerbate the surface-heating problem, since softer X-rays have a shorter range. The majority of these X-rays are produced during the thermonuclear burn which lasts about 10 ps, however, for structured pellets, the X and gamma radiation occurs over a longer time interval [1,4].

A significant portion (15–25 percent) of the energy yield from the microexplosion is released in the form of energetic charged particles. For some pellet designs, the alpha particles escaping from the pellet may carry as much as one-third of that energy; the remainder is associated with the pellet debris. The arrival times at the first wall of free-streaming charged particles and of the debris plasma depend on chamber geometry and dimensions, and on the kinetic energy and spectra of the particles. These times are also affected by the presence of a magnetic field or significant amounts of residual gas in the chamber. Knowledge of the spatial energy deposition as a function of particle energy, and the arrival time of each particle is necessary for evaluating the thermal response of the wall.

A significant fraction of the incident laser light can be reflected from the DT plasma surrounding the pellet before the critical plasma density is reached [2]. This reflection may persist for time periods of the order of 100 ps. Similar to the X-rays and charged particles, the reflected laser light will result in rapid surface heating in the first wall because of its short range.

---

[1] Work partially supported by U.S.E.R.D.A.

[2] Member Technical Staff, Sandia Laboratories, Albuquerque, N.M.

[3] Numbers in brackets designate References at end of paper.

Contributed by the Heat Transfer Division for publication in the JOURNAL OF HEAT TRANSFER. Manuscript received by the Heat Transfer Division July 25, 1977.

The purpose of this investigation is to develop general models for predicting the thermal response of laser fusion reactors first walls to the pulsed photon and ion irradiation. Upon determination of the surface temperature histories, the numerous associated effects which limit wall lifetime can be evaluated.

The response of unprotected dry walls is first investigated. A general model for evaluating the temperature response of a wall subjected to pulsed photon irradiation is developed. This model is applied to the reflected laser light and different X-ray spectra. Another model for evaluating the temperature response of a wall subjected to pulsed ion irradiations is developed. This model incorporates the slowing down properties of ions for which the range is always much less than the wall thickness.

The second part of this paper deals with the effectiveness of residual gas as a means for protecting the wall from the ions and soft X-rays. The wall thermal response to the transmitted photons is determined. A model is also developed for evaluating the wall thermal response to the pulsating heat flux radiated by the gas.

As an application to the results obtained here, the surface temperature histories are used to estimate the wall evaporation rates for typical system parameters.

Thermal Response of Unprotected Dry Walls

Response to Photon Irradiation. Reactor cavities are either spherical or cylindrical with diameters considerably larger than the first wall or liner thickness. Hence, the wall (or liner) can be represented by a slab as shown in Fig. 1(a). If the pressure inside the cavity is sufficiently low, the photons will not be attenuated and will deposit their energies directly in the liner. Under these conditions, radiative and convective heat flux at the liner's inner surface can be ignored. The outside surface can be assumed to remain at a constant temperature T_0 throughout the transient. This condition can be physically realized if the thermal time constant of the linear is considerably larger than the time between pulses. Under these conditions, the pulsating volumetric heating loads are damped, and a constant heat flux is radiated or convected from the back surface. The initial temperature distribution in the liner is assumed to be uniform and equal to T_0. This assumption should not affect the periodic steady-state solution in which we are interested.

For a pulsating flux of monoenergetic photons, the volumetric heat generation rate, g, can be represented by:

$$g(x,t) = (g_0 e^{-\mu x}) f(t) \qquad (1)$$

where g_0 is the volumetric heat generation rate at the surface, μ is the absorption coefficient, and $f(t)$ is the on/off control function shown in Fig. 1(b). The time between pulses and the pulse width are assumed to be constant and equal to ω and $\kappa\omega$, respectively. The surface heat generation rate g_0 is related to the incident flux ϕ_0, absorption coefficient μ, and photon energy ϵ_p by the relation: $g_0 = \phi_0 \mu\, \epsilon_p$. The incident flux ϕ_0 is assumed to remain constant during the "on" period so that g_0 is not a function of time. It is a straightforward matter, however, to extend the analysis to include any temporal flux variations.

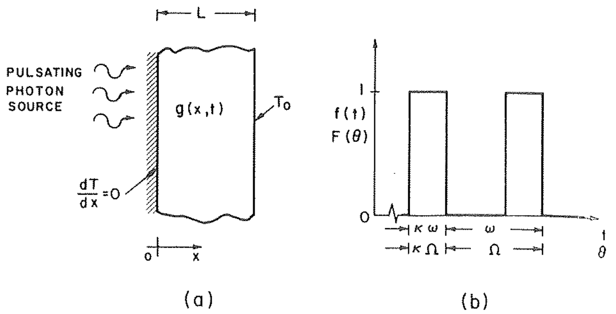

Fig. 1 Schematic representation of the liner and time dependence of the volumetric heat generation function $f(t)$

We introduce the nondimensional variables:

$$u \equiv (T - T_0)/[(g_0/\mu)\kappa\omega/\rho c L],\ \xi \equiv x/L, \text{ and } \theta \equiv \alpha t/L^2 \qquad (2)$$

In equation (2), the nondimensional temperature $u(\xi,\theta)$ is the ratio between the actual temperature rise and that obtained if the incident photons' energy were to be deposited uniformly and adiabatically. In terms of these nondimensional variables, the heat conduction equation, boundary conditions, and initial condition for the above stated problem are:

$$\frac{\partial^2 u}{\partial \xi^2} + Q(\xi)F(\theta) = \frac{\partial u}{\partial \theta} \qquad (3a)$$

$$\frac{\partial u}{\partial \xi}(0,\theta) = 0, \text{ and } u(1,\theta) = 0 \qquad (3b)$$

$$u(\xi,0) = 0 \qquad (3c)$$

The nondimensional heat generation function $Q(\xi)$ is given by: $Q(\xi) = A\, e^{-b\xi}$; $0 \leq \xi \leq 1$, where $A \equiv b/\kappa\Omega$, $b \equiv \mu L$, and $\Omega \equiv \alpha\omega/L^2$. The on/off function $F(\theta)$ is shown in Fig. 1(b).

The periodic steady-state solution, $\tilde{u}(\xi, \theta)$, for the above stated problem is given by:

$$\tilde{u}(\xi,\theta) = 2 \sum_{n=1}^{\infty} \cos\left[\left(\frac{2n-1}{2}\right)\pi\xi\right] \left\{\frac{b^2}{b^2 + \left(\frac{2n-1}{2}\pi\right)^2}\right\}$$
$$\times \left\{1 + e^{-b}\left(\frac{2n-1}{2b}\pi\right)\sin\left(\frac{2n-1}{2}\pi\right)\right\}$$

Nomenclature

A = parameter defined after equation (3)
b = nondimensional absorption coefficient
c = specific heat
C = ion slowing down parameter defined in equation 9
E = particle energy
E_1 = incident particle energy
$f(t)$, $F(\theta)$ = on/off control function in Fig. 1
g, g_0 = volumetric heat generation rates
G = Green's function
k = thermal conductivity
L = wall thickness
M = molecular weight
N = number of complete pulses prior to t
$\dot{n}$ = evaporation rate
p = vapor pressure
$\langle q \rangle$ = average heat flux
q, q_0 = surface heat flux
Q = nondimensional heat generation function
$S(E)$ = particle energy spectrum
t = time
T = temperature
T_0 = back surface temperature
u, u_a, u_b = nondimensional temperature
x = position coordinate
x_m = particle range
α = thermal diffusivity
β = nondimensional pulse width for surface heat flux model
$\delta\omega$ = time after end of previous pulse
ϵ_p = photon energy
ζ_i = parameter defined in equation (6)
θ = nondimensional time
κ = nondimensional pulse width
μ = absorption coefficient
ξ = nondimensional position coordinate
ρ = density
τ, τ^* = reference time for exponentially-decaying surface heat flux
ω = time between pulses
Ω = nondimensional time between pulses

$$\left\{\frac{\exp\left[-\left(\frac{2n-1}{2}\pi\right)^2\delta\Omega\right]}{\left(\frac{2n-1}{2}\pi\right)^2\kappa\Omega}\right\}\left\{\left[\exp\left[\left(\frac{2n-1}{2}\pi\right)^2\delta\Omega\right]-1\right]\right.$$

$$\left.+\frac{\exp\left[\left(\frac{2n-1}{2}\pi\right)^2\kappa\Omega\right]-1}{\exp\left[\left(\frac{2n-1}{2}\pi\right)^2\Omega\right]-1}\right\}\quad(0\le\delta\le\kappa)\qquad(4)$$

and

$$\bar{u}(\xi,\theta)=2\sum_{n=1}^{\infty}\cos\left[\left(\frac{2n-1}{2}\right)\pi\xi\right]\left\{\frac{b^2}{b^2+\left(\frac{2n-1}{2}\pi\right)^2}\right\}$$

$$\left\{1+e^{-b}\left(\frac{2n-1}{2b}\pi\right)\sin\left(\frac{2n-1}{2}\pi\right)\right\}\left\{\frac{\exp\left[-\left(\frac{2n-1}{2}\pi\right)^2\delta\Omega\right]}{\left(\frac{2n-1}{2}\pi\right)^2\kappa\Omega}\right\}$$

$$\times\left\{\frac{\exp\left[\left(\frac{2n-1}{2}\pi\right)^2\kappa\Omega\right]-1}{1-\exp-\left[\left(\frac{2n-1}{2}\pi\right)^2\Omega\right]}\right\}\quad(\kappa\le\delta\le1)\qquad(5)$$

In equations (4) and (5), the fraction δ is defined by: $\theta = (N + \delta)\Omega$, where N is an integer much larger than unity.

Equations (4) and (5) can be used to determine the nondimensional transient temperature distribution in the liner resulting from the pulsating exponential heat deposition given by equation (1). After a large number of pulses, the surface temperature will vary in a cyclic manner between a maximum value, $u_{\max}$, at $\delta = \kappa$ and a minimum value, $u_{\min}$, at $\delta = 1$. These temperature extremes are of particular significance when estimating the stress levels produced in the liner. These are necessary for determining whether spallation will take place.

For small values of Ω, i.e., when the time constant of the liner is considerably larger than the time between pulses, $u_{\min}$ will depend only on the nondimensional absorption coefficient b, while $u_{\max}$ will depend on both b and the nondimensional pulse width κ. Plots of $u_{\min}$ and $u_{\max}$ as functions of b and κ for $\Omega = 0.01$ are shown in Fig. 2. These results are quite general, inasmuch as they can be used for arbitrary geometry, material, absorption coefficient (i.e., photon energy), repetition rate, wall loading, and pulse width. In the following, we show how these results can be directly used to determine the surface temperature rise produced by the reflected laser light for different lasers and pellet "reflectivities." The results shown in Fig. 2 are also used, along with superposition techniques, to determine the surface temperature rise produced by the X-rays emanating from the microexplosion. A slab model is used here in order to accommodate high energy photons for which the mean free paths may be of the same order as the wall thickness.

Temperature Rise Produced by the Reflected Laser Light. For low-energy photons, the attenuation coefficient μ in the exponential heat deposition curve of equation (1) may be estimated by considering the attenuation of electromagnetic radiation in a homogeneous, isotropic, conducting medium with zero surface reflectivity. The result is $\mu = 8\pi/\lambda$ where λ is the wavelength [6]. Therefore, the results shown in Fig. 2 can be readily used to determine the surface temperature rise produced by the reflected laser light for a given system geometry and operating conditions.

A 6.5 mm thick graphite liner in a 12 m diameter cavity is considered. For a 1 MJ laser with a repetition rate of 20 s^{-1} and a pellet "reflectivity" of 15 percent, the surface temperature rise is plotted in Fig. 3 for different laser wavelength and pulse width. These results can be easily used for other conditions, since $\Delta T_{\text{surface}}$ is linearly proportional to the incident flux. It should be emphasized that the results shown in Fig. 3 do not account for any evaporation which may take place at the liner surface. Fig. 3 is quite valuable, inasmuch as it allows us to estimate the maximum tolerable pellet reflectivity corresponding to the onset of liner sublimation or spallation.

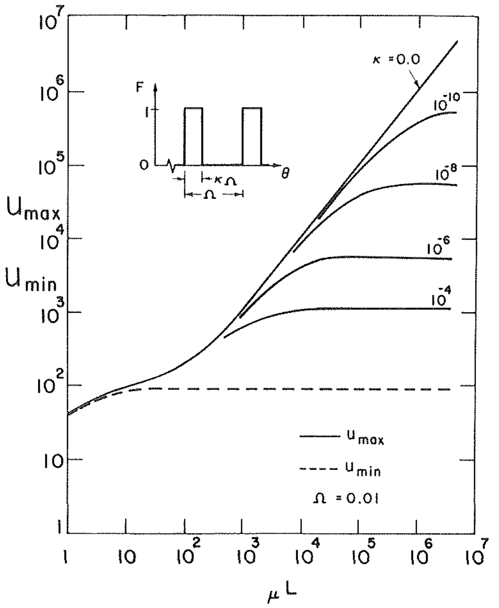

Fig. 2 Variation of the nondimensional surface temperature with pulse width and nondimensional absorption coefficient

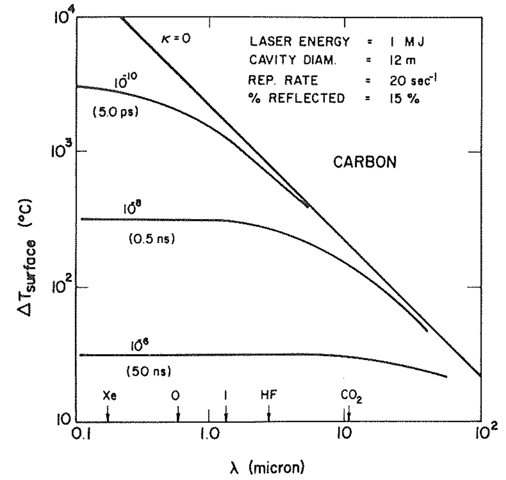

Fig. 3 Variation of the surface temperature rise produced by the reflected laser light with wavelength and pulse duration (6.5 mm thick graphite liner)

It should be emphasized that the results shown above assume a totally absorbing first wall. If the wall reflectivity is not zero, the wall will be subjected to a series of pulses with decreasing amplitudes separated by the photon transit time across the cavity. The model developed above (equations (4) and (5)) can be easily extended to solve this problem. The absorption coefficient should be modified to account for the nonzero reflectivity. The general solution is given by the sum of the contributions of the original pulses and the subsequent reflected pulses shifted in time by multiples of the photon transit time across the cavity.

Temperature Rise Produced by the X-rays. It is important to be able to determine the thermal response of the liner when subjected to a pulsating photon source with an arbitrary spectrum. This task can be readily accomplished by extending the solution for monoenergetic photons by means of superposition techniques. The X-ray spectra produced by the microexplosions are approximated by black-body radiations in the range of 0.1–2.0 keV. This range is sufficiently wide to cover pellet designs of interest.

The spectrum is divided into M bands with average photon energies $\epsilon_i, i = 1, 2, \ldots, M$. Let ζ_i be the fraction of the incident energy within band i so that:

$$\sum_{i=1}^{M} \zeta_i = 1 \tag{6}$$

The surface flux from the pulsating black-body source is given the symbol S so that the incident energy within a single pulse per unit surface area is equal to $S\kappa\omega$. We assume that the incident photons within the different bands will result in exponential heat deposition curves with absorption coefficients μ_i, $i = 1, 2, \ldots, M$, so that the corresponding net heat generation rate $g(x, t)$ can be represented by:

$$g(x, t) = f(t)S \sum_{i=1}^{M} \zeta_i \mu_i e^{-\mu_i x} \tag{7}$$

The linearity of equations (3a, b) allows the superposition of monoenergetic results so that:

$$u(\xi, \theta) = \sum_{i=1}^{M} \zeta_i u_i(\xi, \theta) \tag{8}$$

where $u_i(\xi, \theta)$ is the solution to equation (3a–c) given by equations (4) and (5) with b equal to b_i.

For graphite, the absorption coefficients are curve-fitted for five ranges of photon energies: (0.01–0.284 kev), (0.284–0.80 kev), (0.80–4.00 kev), (4.0–20.0 kev), and (20.0–100.0 kev) using relations of the form [7]:

$$(\mu/\rho)(\text{cm}^2/g) = \sum_{j=1}^{4} a_j/\epsilon_p{}^j$$

where ϵ_p is the photon energy in kev. The constants a_j, $j = 1$–4 for the five ranges of photon energies are given in [7].

A 6.5 mm thick graphite liner in a 12 m dia cavity is considered. For a pellet yield of 150 MJ, a repetition rate of 20 s^{-1}, and an X-ray fraction of 1 percent, the periodic surface temperature rise is shown in Fig. 4 for different black-body temperatures and pulse durations. Obviously, softer spectra produce higher surface temperature jumps because of their shorter range. The case $\kappa = 0$ corresponds to instantaneous deposition of the X-ray energy into the liner.

Again, it should be emphasized that the results shown in Fig. 4 do not account for any evaporation which may take place at the liner surface. However, these results should help in determining the conditions corresponding to the onset of liner sublimation or spallation.

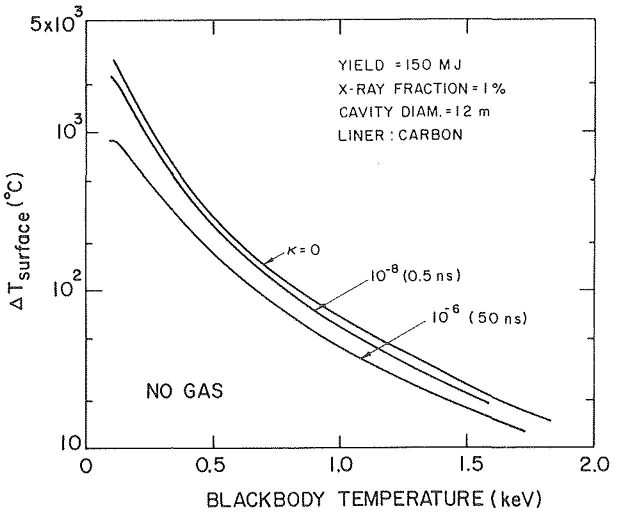

Fig. 4 Variation of the surface temperature rise produced by the X-rays with black body temperature and pulse duration (6.5 mm thick graphite liner)

Thermal Response to Pulsed Ion Sources With No Residual Gas. The thermal response of the wall (or liner) to ion pulses can be determined upon knowledge of the spatial energy deposition as a function of particle energy and arrival time of each particle. A model has been developed whereby a given spectrum of particles is initiated at the cavity center and each particle is allowed to propagate uncollided to the point of impact. The resulting particle arrival density is combined with their slowing-down characteristics to yield the spatial and temporal distribution of energy deposition. This, in turn, is used to determine the thermal response of the wall.

The particle energy loss is usually calculated as a function of its local kinetic energy. For electronic losses described by modified Lindhard (LSS) slowing down model [8], the rate of energy loss is given by

$$\frac{dE}{dx} = -C\left(\frac{E}{E_0}\right)^{1/2} \tag{9}$$

where C is a slowing down parameter determined for LSS theory. For a particle with incident energy E_1, equation (9) can be transformed from spectral to spatial dependence as:

$$\frac{dE}{dx}(x) = \frac{xC^2}{2E_0} - C\left(\frac{E_1}{E_0}\right)^{1/2} \tag{10}$$

The particle range, $x_m(E_1)$, is given by:

$$x_m(E_1) = \frac{2(E_0E_1)^{1/2}}{C} \tag{11}$$

The particles from a pulsed source will arrive at a given location with an arrival density function $f(t)$ given by:

$$\int_t f(t)dt = -\int_E S(E)dE \tag{12}$$

Here, the integral is equal to the total number of incident particles per unit surface area, and $S(E)$ is the particle energy spectrum at $x = 0$. If the kinetic energy of the particles is primarily directed along the propagation axis (i.e., small thermal component), the arrival density would be given by:

$$f(t) = 2S(E)\,E^{3/2}/B \tag{13}$$

where $B = 2.284 \times 10^{-6}RA^{1/2}$. Here, R is the distance travelled by the particles (i.e., cavity radius) in meters and A is the particle mass in amu.

The volumetric heating rate is related to the arrival density function by: $g(x, T) = f(t)dE/dx(x)$. Therefore,

$$\left.\begin{aligned} g(x, t) &= f(t)\left[\frac{A_1}{t} - A_2\,x\right]; x < \frac{2BE^{1/2}}{Ct} \\ &= 0; \qquad\qquad\qquad x > \frac{2BE_0{}^{1/2}}{Ct} \end{aligned}\right\} \tag{14}$$

where $A_1 \equiv (CB/E_0{}^{1/2})$, $A_2 \equiv C^2/2E_0$, and $(B/\sqrt{E}_{\max} < t < B/\sqrt{E}_{\min})$. Here, $E_{\min}$ and $E_{\max}$ are the limits of the spectrum.

For a semi-infinite solid with an insulated boundary at $x = 0$, and volumetric heat source $g(x, t)$, the transient temperature distribution is given by [9]:

$$T(x,t) = \int_t \int_x \frac{g(x',t')}{\rho c} G(x,t,x',t')dx'dt'$$

where G is Green's function given by:

$$G(x,t,x',t') = \frac{1}{2\sqrt{\pi\alpha(t - t')}}\{\exp[-(x - x')^2/4\alpha(t - t')] + \exp[-(x + x')^2/4\alpha(t - t')]\}$$

For the volumetric heat source given by equation (14), the above equation yields:

$$T(x, t) = \frac{1}{\rho c}\int_{t_{\min}}^{t_{\max}} f(t')\{Q_1(t',t, x)$$

$$+ Q_2(t',t,x) + Q_3(t',t,x)\}dt' \quad (15)$$

where

$$Q_1(t',t,x) = \frac{A_1}{2t'}[\operatorname{erf}(F_1) + \operatorname{erf}(F_2)],$$

$$Q_2(t',t,x) = \frac{A_2 x}{2}[\operatorname{erf}(F_2) - \operatorname{erf}(F_1) - 2\operatorname{erf}(F_0)],$$

$$Q_3(t',t,x) = A_2 \frac{\sqrt{\alpha(t-t')}}{\pi}[e^{-F^2}{}_2 + e^{-F^2}{}_1 - 2e^{-F^2}{}_0],$$

$$F_0 \equiv x/2\sqrt{\alpha(t-t')},\ F_1 = (x_m - x)/2\sqrt{2\alpha(t-t')},$$

$$F_2 = (x_m + x)/2\sqrt{2\alpha(t-t')},\ \text{and}\ x_m = 2BE_0{}^{1/2}/Ct'. \quad (16)$$

The foregoing analysis has been carried out for intermediate energy ions characteristic of pellet debris which can be described by the modified Lindhard slowing down model [8] (equation 9). For heavier ions, the inclusion of nuclear stopping will alter the deposition profiles to be more spatially uniform. Incorporation of this effect yields a result similar to equation (15). In all cases, the time integral is performed numerically, so that arbitrary spectra can be accommodated. The use of the semi-infinite solid model to predict the temperature response of the liner to ion irradiation should be quite accurate since the ions' range is extremely short compared to practical wall thicknesses. On the other hand, a slab formulation has been used for photon irradiations to accommodate high energy photons' attenuation when the mean free paths are of the same order as the wall thickness.

Results are shown for 200 kev Maxwellian spectra in a 12 m dia cavity. the thermal response of a graphite wall bombarded by helium particles is shown in Fig. 5. These results have been normalized to an ion wall loading of 1 J/cm^2 per pulse. Ion fluxes for conceptual laser fusion reactors can be much higher than 1 J/cm^2 per pulse [1]. The resulting temperatures would be too high for wall survival and protective measures must be employed. In the following, we shall investigate the effectiveness of residual gas as a means for protecting the wall from the ions and soft X-rays emanating from the microexplosion.

Effect of Residual Chamber Gas.

The gas pressure inside the reactor cavity has to be sufficiently low to allow laser propagation and focusing onto the pellet. Neon has the highest laser-induced gas breakdown threshold followed closely by helium [10]. Thus, for a given laser intensity, neon can be maintained at the highest pressure and still transmit the laser beams. For example, for 1 μm light with an on-target intensity of 10^{16} W/cm^2, the reactor activity can be filled with neon at a pressure of about 1 torr. At such pressures, the gas can significantly modify the X-ray spectra incident on the wall by absorbing the low-energy X-rays (Fig. 6). These photons would have produced high surface temperature excursions because of their short range. The wall will, therefore, be subjected to harder X-ray spectra than those produced by the microexplosion.

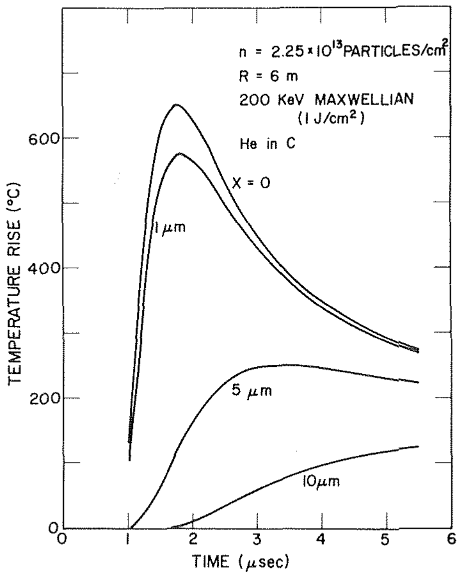

Fig. 5 Temperature response of a carbon wall bombarded by helium ions. (Ion wall loading is normalized to 1 J/cm^2 per pulse.)

Typical results showing the surface temperature rise produced by the modified X-ray spectra for different gas pressures and black body temperatures are shown in Fig. 7. These results are obtained using equation (8) after modifying the values of ζ_i to account for X-ray absorption in the gas. They pertain to a 6.5 mm thick graphite liner in a neon-filled, 12 m dia cavity with a zero pulse width. The results are plotted against the black body temperature characterizing the

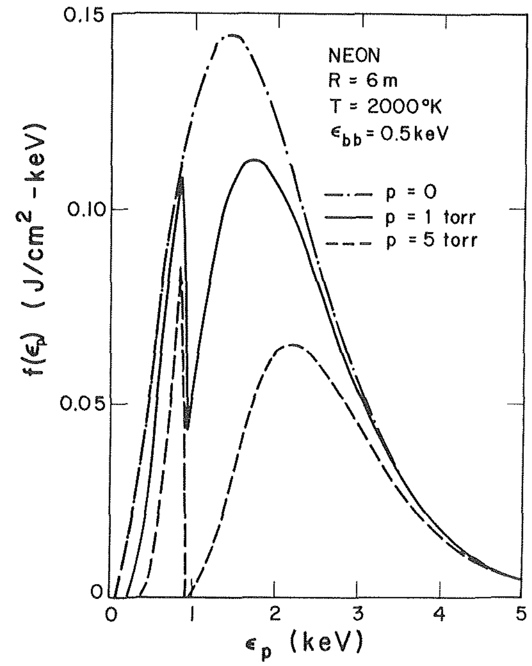

Fig. 6 Modified spectra as a function of gas pressure for a 0.5 keV black body radiation (the discontinuities result from K-edge absorption in neon)

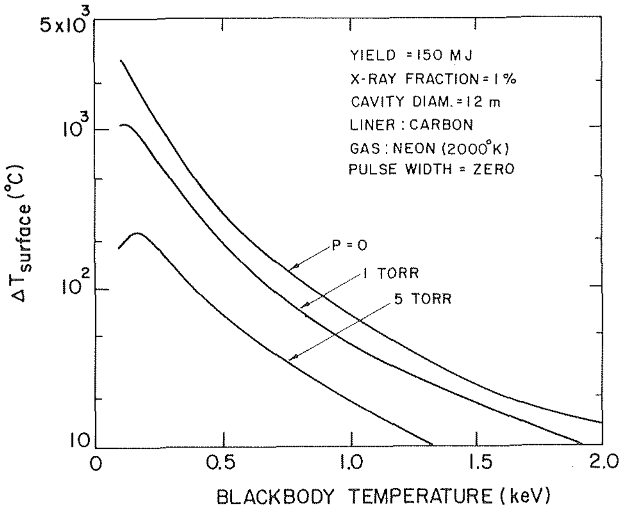

Fig. 7 Variation of the surface temperature rise produced by the modified X-ray spectra with gas pressure for a zero pulse width (6.5 mm thick graphite liner; the black body temperatures refer to the original spectrum)

original spectrum produced by the microexplosion. These results show that gas protection can be quite effective, especially if the X-rays produced by the microexplosion are soft as may be the case with structured pellets [1,4].

In addition to absorbing the soft X-rays, the gas can stop the ions produced by the microexplosion. If the wall radius exceeds the mean ion range in the gas by approximately a factor of two, all the ions' kinetic energy will be deposited in the chamber gas. The neon pressure corresponding to a mean range of six m is shown in Fig. 8 for a variety of ions. These data are based on ion range calculations using Lindhard theory in the EDEPI code [11]. These results indicate that most of the nonhydrogenic pellet constituents can be stopped in the gas at sufficiently low pressures.

The energy deposited in the gas by the X-rays and ions will be removed by radiation to the chamber walls and gas ejection through the vacuum system. (A steady stream of cold gas is allowed into the system.) Unless the energy is radiated to the wall over a sufficiently long period, excessive surface heating and ablation will result. The temporal distribution of the radiant heat flux depends on the radiation transport through the gas, as well as its ionization state. Here we consider the two limiting cases shown in Figs. 9(a) and (b). For case (a), the radiant heat flux during each pulse is assumed to remain constant and equal to q_0 over a period $\beta\omega$, where ω is the time between pulses. For case (b), the surface heat flux during each pulse is assumed to decay exponentially, so that for the $(N+1)$ pulse: $q = q_o \exp[-(t - N\omega)/\tau]$; $N\omega \le t \le (N+1)\omega$, where τ is a reference time.

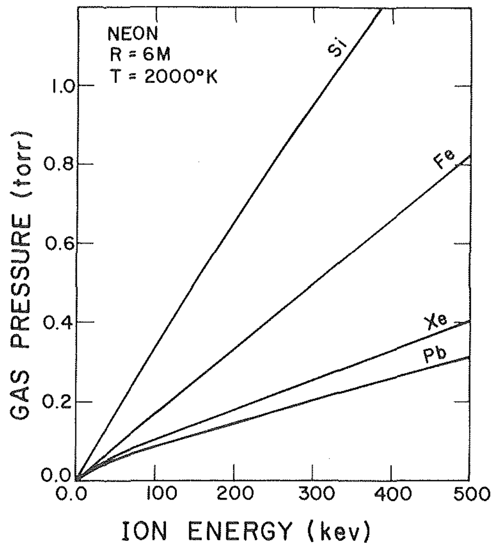

Fig. 8 **Neon pressures corresponding to a mean range of 6 m for a variety of ions**

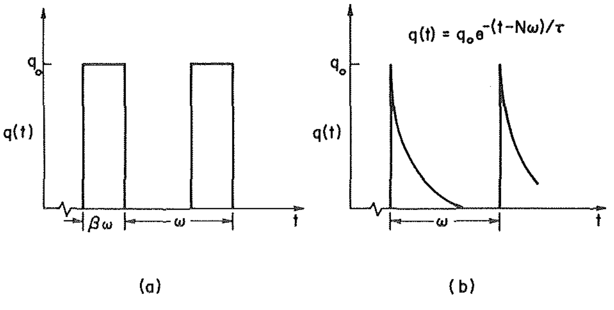

Fig. 9 **Schematic diagrams showing the two surface heat flux distributions considered in this investigation**

The thermal response of a finite slab of thickness L subjected to a sequence of these heat flux pulses can be readily obtained by either superposition or variation of parameters techniques [9]. The back surface of the slab ($x = L$) is assumed to remain at a constant temperature T_0. For case (a), the periodic steady-state solution $\tilde{u}_a(\xi, \theta)$ is given by:

$$\tilde{u}_a(\xi,\theta) = 2\sum_{m=0}^{\infty} \frac{\cos\left(\frac{2m+1}{2}\pi\xi\right)}{\left(\frac{2m+1}{2}\pi\right)^2} \left\{ \frac{\left\{\exp - \left[\left(\frac{2m+1}{2}\pi\right)^2 \delta\Omega\right]\right\}\left\{\exp\left[\left(\frac{2m+1}{2}\pi\right)^2 \beta\Omega\right] - 1\right\}}{\left\{\exp\left[\left(\frac{2m+1}{2}\pi\right)^2 \Omega\right] - 1\right\}} + \left\{1 - \exp - \left[\left(\frac{2m+1}{2}\pi\right)^2 \delta\Omega\right]\right\} \right\} \quad (0 \le \delta \le \beta) \qquad (17)$$

and,

$$\tilde{u}_a(\xi,\theta) = 2\sum_{m=0}^{\infty} \frac{\cos\left(\frac{2m+1}{2}\pi\xi\right)}{\left(\frac{2m+1}{2}\pi\right)^2} \left\{ \frac{\left\{\exp\left[\left(\frac{2m+1}{2}\pi\right)^2 \beta\Omega\right] - 1\right\}\left\{\exp\left[\left(\frac{2m+1}{2}\pi\right)^2 (1-\delta)\Omega\right]\right\}}{\left\{\exp\left[\left(\frac{2m+1}{2}\pi\right)^2 \Omega - 1\right\}} \right\} \quad (\beta \le \delta \le 1)$$

Here, the nondimensional temperature $u_a(\xi, \theta)$ is defined by: $u_a \equiv (T - T_0)/q_0L/k$. The variables ξ, θ, Ω, δ, and β have been defined before. The above analysis is valid when the pulse length, $\beta\omega$, of the surface heat flux is longer than the ions' slowing-down time in the gas.

For case (b), the periodic steady-state solution $\tilde{u}_b(\xi, \theta)$ is given by:

$$\tilde{u}_b(\xi,\theta) = 2\sum_{m=0}^{\infty} \frac{\cos\left(\frac{2m+1}{2}\pi\xi\right)}{\left[\left(\frac{2m+1}{2}\pi\right)^2 - \tau^*\right]} \left\{ \frac{\left\{\exp\left[\left(\frac{2m+1}{2}\pi\right)^2 (1-\delta)\Omega\right]\right\}\{\exp - [\Omega\tau^*] - 1\}}{\left\{\exp\left[\left(\frac{2m+1}{2}\pi\right)^2 \Omega - 1\right]\right\}} + \exp - [\delta\Omega\tau^*] \right\} \qquad (19)$$

where $\tau^* \equiv L^2/\alpha\tau$, and $u_b \equiv (T - T_0)/(q_0L/k)$.

Typical results showing the surface temperature rise in a graphite wall subjected to a train of heat flux pulses with average wall fluxes, $\langle q \rangle$, of 150 W/cm² for types (a) and (b) are shown in Figs. 10 and 11, respectively. These results do not account for any evaporation which may take place at the surface. It is obvious that the surface temperature rise, and hence the maximum surface temperature, will decrease as the pulse width is increased. For the case shown, in order to prevent excessive evaporation and spallation of the wall, the energy deposited in the gas has to be radiated over a period ≥ ~1 ms. This, in turn, can be used to determine the necessary amount of gas in the chamber to provide such a long cool-down period. An increase in the chamber gas pressure will lengthen the energy reradiation time from the gas. The

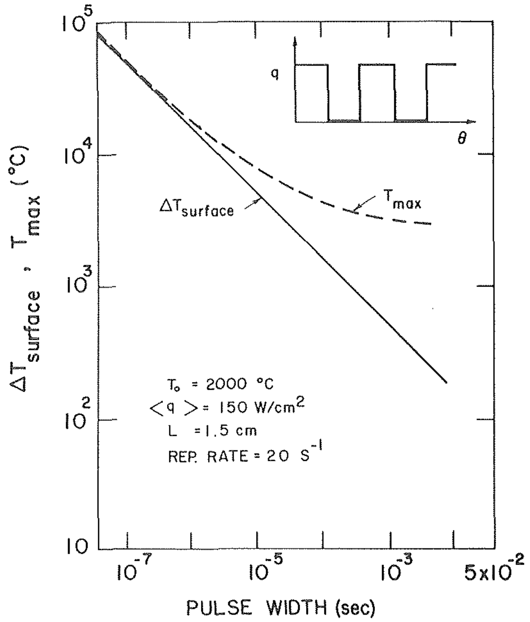

Fig. 10 Variation of temperature rise produced in a graphite wall by a train of square heat flux pulses with pulse width. (T_{max} and $\Delta T_{surface}$ are the maximum surface temperature and temperature rise respectively.)

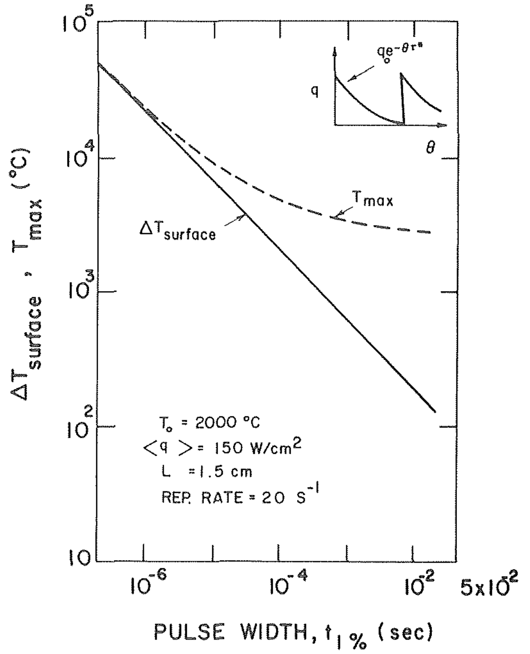

Fig. 11 Variation of temperature rise produced in a graphite wall by a train of exponentially-decaying heat flux pulses ($t_{1\ percent}$ is the time required for the surface heat flux to drop to 1 percent of its maximum value; $t_{1\ pecent} = 4.61\ \tau$)

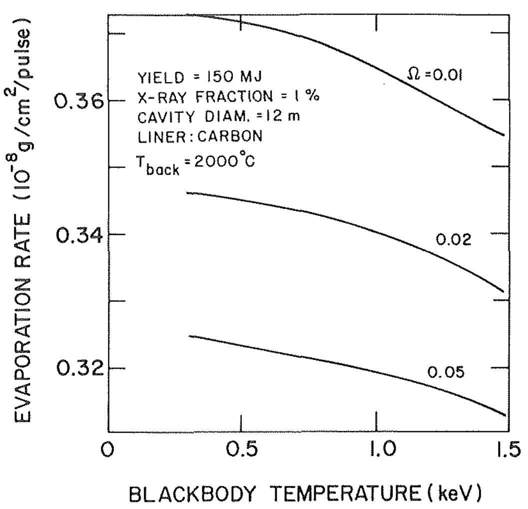

Fig. 12 Variation of amount of material evaporated during a pulse for a carbon wall with no gas protection (Ω = 0.01, 0.02, 0.05 correspond to a wall thickness of 6.5, 4.5, and 2.9 mm, respectively)

ions will be stopped in a shorter distance; however, the gas will be heated to a lower temperature since a larger number of gas atoms are present. Also, the presence of a blanket of cold gas near the wall should increase the cool-down time since the gas will not be totally transparent.

Example—Estimation of Surface Evaporation Rate. The evaporation rate from a surface at temperature T can be estimated from the equilibrium vapor pressure p of the solid material above the surface. The evaporation rate $\dot{n}(T)$ is given by [12]:

$$\dot{n}(T) = \frac{3.5 \times 10^{22}}{\sqrt{M}} \frac{p}{\sqrt{T}} \left(\frac{\text{atoms}}{\text{cm}^2\,\text{s}}\right) \tag{20}$$

where M is the molecular weight, p is in torr, and T is in K. This model is only strictly valid under equilibrium conditions. Also, for many materials, the right-hand side should be multiplied by a nonunity vaporization coefficient. However, equation (20) can be used to obtain an upper bound for the evaporation rate under the present conditions.

Vapor pressure data for several first wall materials are given in [12]. With knowledge of the surface temperature history and the corresponding vapor pressure, one can determine the evaporation rate as a function of time. These can be integrated to determine the amount of material ablated per pulse (Fig. 12). These results indicate that unless some means for wall protection is provided, excessive evaporation can take place.

Conclusions

General models for evaluating the thermal response of the first wall (or its protective liner) produced by the X-rays and charged particles emanating from the pellet and by the reflected laser light have been developed. These models are quite general inasmuch as they can be used for arbitrary geometry, wall material, spectra, repetition rate, wall loading, and pulse width. The results are presented in a parametric fashion so that the maximum tolerable limits, e.g., pellet "reflectivity", X-ray fraction, or ion wall loading, corresponding to the onset of liner spallation or sublimation can be determined.

The effect of residual chamber gas on X-ray spectra and ion-stopping has been examined. Gases such as neon at ~1 torr are observed to significantly reduce the direct X-ray heating and to stop the energetic ions. The reradiation of this energy can, however, produce large temperature excursions, unless the energy is radiated over a sufficiently long period (~1 ms).

Evaporation rates from the temperature histories of the above models indicate that materials such as carbon can suffer a significant amount of material loss unless some protection measures are provided.

Acknowledgment

This work has been supported by the Electric Power Research Institute under contract RP 237-3. Financial support for TOH has been provided by Sandia Laboratories.

References

1 Conn, R. W., et al., "SOLASE—A Laser Fusion Reactor Study," Nuclear Eng. Dept., Univ. of Wisconsin, UWFDM-220 Jan. 1978.

2 Glass, A. J., and Cummings, K. L., (eds.), "Laser Program Annual Report," Lawrence Livermore Laboratory 1975.

3 Williams, J. M., et al., "Engineering Design for Laser Controlled Thermonuclear Reactors", *Proc. 5th Symposium on Engineering Problems of Fusion Research*, Princeton, NJ 1973.

4 Frank, T. G., et al., "Heat Transfer Problems Associated with Laser Fusion," *Proc. 6th National Heat Transfer Conference*, St. Louis 1976.

5 Hovingh, J., et al., "The Preliminary Design of a Suppressed Ablation Laser-Induced Fusion Reactor," *Proc. First Topical Meeting on the Technology of Controlled Nuclear Fusion*, CONF-740402-P1, San Diego 1974.

6 Hovingh, J., "First Wall Studies of a Laser-Fusion Hybrid Reactor Design," *Proc. 2nd Topical Meeting on the Technology of Controlled Nuclear Fusion*, Richland, Washington 1976.

7 Biggs, F., and Lighthill, R., "Analytical Approximations for X-ray Cross-Sections II", SC-RR-71-0507, Sandia Laboratories (1971).

8 Lindhard, J., Scharff, M., and Schiott, H. E., *Mat. Fys. Medd. Dan. Vid. Selsk.*, Vol. 33, p. 14, 1963.

9 Carslaw H. S., and Jaeger, J. C., *Conduction of Heat in Solids*, Second Edition, Oxford University Press 1959.

10 Tomlinson, R. G., Damon, E. K., and Buscher, H. T., "The Breakdown of Noble and Atmospheric Gases by Ruby and Neodymium Laser Pulses," *Physics of Quantum Electronics*, Kelley, Lax, and Tannenwald (Eds.), p. 520, McGraw Hill, New York 1966.

11 Manning, I., and Mueller, G. P., "Depth Distribution of Energy Deposition by Ion Bombardment," *Computer Physics Communication*, Vol. 6, 1973.

12 Behrish, R., "First Wall Erosion in Fusion Reactors," *Nuclear Fusion*, Vol. 12, p. 695 1972.

J. Kern
J. W. Hemmings
Department of Chemical Engineering,
University of the Witwatersrand,
Johannesburg, South Africa

On the Analogy Between the Calorimeter Problem and Some Granulate-Fluid Exchange Processes

The solution to a generalized version of the classical calorimeter problem approximates the behavior of certain continuous exchange processes between particulate solids and a fluid. For modeling purposes, the much simpler energy-balance solution has obvious advantages, although it only holds for negligible intraparticle resistance and thus predicts too short contact times. An error diagram provides a quantitative comparison between those two results as a function of the two pertinent system parameters.

Introduction

Transient particle-fluid heat transfer, as represented by the classical calorimeter problem [1–4],[3] is a controlling mechanism in many granulate-fluid processes associated with fluidized and spouted beds [5, 6] or moving-bed regenerators. In fact, some of these processes [7, 8] can be described by exactly the same equations as the above batch problem. The neglected particle-particle interaction would lead to some inaccuracy of the results, but frequently this is more than compensated by the advantages of an analytic over a numerical solution.

For modeling purposes, one may often sacrifice some accuracy for the sake of having available a simpler result. Common simplifications, introduced in this type of analysis, are the negligibly small intraparticle or particle-fluid resistance—both these cases are well-documented in the standard literature. But the error inherent in such simplified treatments is largely unknown. From the little information available [8, 9] one cannot decide, in general, for which process conditions the simpler results will provide sufficiently accurate answers. Such information requires the comparison of these results with the solution to a generalized version of the calorimeter problem, which considers a sphere of finite thermal diffusivity in exchange with a finite extent of fluid and subject to a finite film resistance at the solid-fluid interface. The mathematical details of this solution have been discussed before [10, 11] but the result somehow seems to have escaped the traditional heat-transfer literature. This is possibly due to the fact that in these references the present problem emerges as a particular case of a mathematically more complicated problem of quite a different physical significance (see reference [11]). It may therefore be adequate to summarize the mathematical procedure before discussing the effect of the various simplifications as well as some applications.

Calorimeter Problem

In physical terms the system is represented by a spherical particle of diameter 2R and initial temperature T_0 being immersed in a finite volume of fluid of initial temperature T_{f0}. The system is perfectly insulated against the surroundings, and energy is exchanged between the two phases subject to a constant film coefficient h. The latter assumption effectively divides the fluid into a bulk part of uniform but time-dependent temperature $T_f(t)$ and a part forming a uniform boundary layer around the solid particle. It is thought that a moderately agitated solid-fluid system would follow this description reasonably well.

In mathematical terms the exchange process is given by the following equations (see nomenclature for notation):

$$\frac{\partial \theta}{\partial \tau} = \frac{1}{x^2}\frac{\partial}{\partial x}\left(x^2 \frac{\partial \theta}{\partial x}\right), \tag{1}$$

$$\theta(x, \tau = 0) = 0, \tag{2}$$

$$\left.\frac{\partial \theta}{\partial x}\right|_{x=0} = 0, \tag{3}$$

$$\left.\frac{\partial \theta}{\partial x}\right|_{x=1} = -\mathrm{Bi}(\theta_s - \theta_f), \tag{4}$$

---

[1] Present address: Balcke-Duerr AG, 4030 Ratingen, Germany.

[2] Present address: CERG-CSIR, Pretoria 0001, South Africa.

[3] Numbers in brackets designate References at end of paper.

Contributed by the Heat Transfer Division for publication in the JOURNAL OF HEAT TRANSFER. Manuscript received by the Heat Transfer Division October 3, 1977.

and

$$\frac{\partial \hat{\theta}}{\partial \tau} = -C \frac{\partial \theta_f}{\partial \tau}, \tag{5}$$

where

$$\hat{\theta}(\tau) = 3 \int_0^1 \theta x^2 dx \tag{6}$$

is the integrated average solid temperature,

$$C = \frac{m_f c_f}{mc} \text{ and } \mathrm{Bi} = \frac{hR}{k} \qquad (7), (8)$$

are the two pertinent system parameters.

From equation (5) one obtains the relationship between fluid and average solid temperature,

$$\theta_f = \frac{1 + C - \hat{\theta}}{C} \tag{9}$$

The Laplace transform of equation (1) can be solved in terms of the surface temperature, which in turn is eliminated by use of equations (4), (6), and (9). Thus, for the temperature in the Laplace domain (for details see reference [10]),

$$\bar{\theta}(x, s) = \frac{\mathrm{Bi}(1 + C)}{(3\mathrm{Bi} + Cs)\sqrt{s} \cosh\sqrt{s} + [Cs(\mathrm{Bi} - 1) - 3\mathrm{Bi}] \sinh\sqrt{s}} \times \frac{\sinh(\sqrt{s}x)}{x} \tag{10}$$

The inversion proceeds via the method of residues and involves the summation of the poles of equation (10). These poles are found from

$$\frac{\tanh \sqrt{s}}{\sqrt{s}} = \frac{3\mathrm{Bi} + Cs}{3\mathrm{Bi} - (\mathrm{Bi} - 1)Cs} \tag{11}$$

or, since for the calorimeter problem

$$s = -y^2 \leq 0,$$

from

$$\tan y = \frac{y(3\mathrm{Bi} - Cy^2)}{3\mathrm{Bi} + (\mathrm{Bi} - 1)Cy^2} \tag{12}$$

The evaluation of the residues yields for the solid temperature

$$\theta(x, \tau) = 1 - \sum_{n=1}^{\infty} \left[K_n \frac{\sin(y_n x)}{x \sin y_n} \exp(-y_n{}^2 \tau) \right] \tag{13}$$

with

$$K_n = \frac{2\mathrm{Bi}(1 + C)(Cy_n{}^2 - 3\mathrm{Bi})}{C^2 y_n{}^4 + [(\mathrm{Bi} - 1)\mathrm{Bi}C^2 - 6\mathrm{Bi}C]y_n{}^2 + 9\mathrm{Bi}^2(1 + C)}$$

and y_n being the roots of equation (12) excluding $y_0 = 0$. The somewhat anomalous character of this transcendental equation has been discussed in detail [10], but no actual values for the roots are available. Since in many situations the first three or four roots provide a sufficiently accurate answer, we present Fig. 1, which should facilitate the numerical evaluation of equation (12). The higher roots are very nearly given by

$$y_n \approx (n - 0,5)\pi \; (n > 3; C > 0,1; \mathrm{Bi} < 10) \tag{14}$$

The error is less than three percent. Further, the accuracy of a truncated-series result can be checked qualitatively from the condition

$$\sum_{n=1}^{\infty} \left[K_n \frac{\sin(y_n x)}{x \sin y_n} \right] = 1 \; (\text{at } \tau = 0) \tag{15}$$

Validity of Simplified Solutions

In the majority of heat-exchange applications, one only needs to know the average solid temperature as defined by equation (6); once this is known, the bulk fluid temperature can be evaluated from equation (9). Integration yields

$$\hat{\theta}(\tau) = 1 - \sum_{n=1}^{\infty} [L_n \exp(-y_n{}^2 \tau)] \tag{16}$$

with

$$L_n = \frac{6\mathrm{Bi}^2 C(1 + C)}{C^2 y_n{}^4 + [(\mathrm{Bi} - 1)\mathrm{Bi}C^2 - 6\mathrm{Bi}C]y_n{}^2 + 9\mathrm{Bi}^2(1 + C)} \tag{17}$$

This result will be used for comparison with the limiting solutions of negligible fluid-solid film resistance and of negligible internal solid resistance.

The "Well-Stirred" Fluid. This assumption implies that the boundary layer around the particle vanishes, leaving no thermal resistance at the fluid-particle interface. It is commonly used in calorimetric studies [1, 3], although one does not really know just how large the Biot number (h) has to be for the exchange rate to be unaffected by any other resistance. The limiting solution is known from

$$\lim_{\mathrm{Bi} \to \infty} L_n = \frac{6C(1 + C)}{9(C + 1) + Cy_n{}^2} \tag{18}$$

and is included in Fig. 2, where the effect of increasing fluid agitation is illustrated for a particular value of C. The conclusion is that, even at a value of Bi = 10, which is unusually large in practice, a significant overprediction of the exchange rate may result from the assumption of a well-stirred fluid, particularly at short times. Similar discrepancies are observed at other values of C.

The "Well-Conducting" Solid. Since for $k \to \infty$ the solid temperature is uniform over the sphere, i.e.,

$$\theta(x, \tau) \equiv \hat{\theta}(\tau) = \theta(\tau)$$

the solution is obtained from a simple energy balance:

$$3\mathrm{Bi}(\theta - \theta_f) = \frac{d\theta}{d\tau} = -C \frac{d\theta_f}{d\tau} \tag{19}$$

and hence

Nomenclature

$\mathrm{Bi} = hR/k$, Biot modulus
c = specific heat capacity
$C = m_f c_f/(mc)$ or $\dot{m}_f c_f/\dot{m}c$, capacity or capacity rate ratio
E = error relationship, equation (22)
h = heat-transfer coefficient
k = thermal conductivity
K_n, L_n = coefficients for temperature series
m = mass
$\dot{m}$ = mass flux density
r = radial coordinate
R = radius of spherical particle
s = variable in Laplace domain
t = time
T = temperature
$U = (T - T_0)/(T_{f0} - T_0)$, modified temperature, equation (25)
v = bulk velocity of solids
$x = r/R$, radial coordinate
y_n = roots of equation (12)
z = linear distance from entrance of exchanger
$\alpha = k/(\rho c)$, thermal diffusivity
$\theta = (T - T_0)/(T_\infty - T_0)$, temperature
$\hat{\theta}, \bar{\theta}$ = mean, transformed temperature
ρ = density
$\tau = t\alpha/R^2$, time

Subscripts

none = for solid where applicable
f = fluid
0 = initial
s = solid surface
∞ = at $t \to \infty$

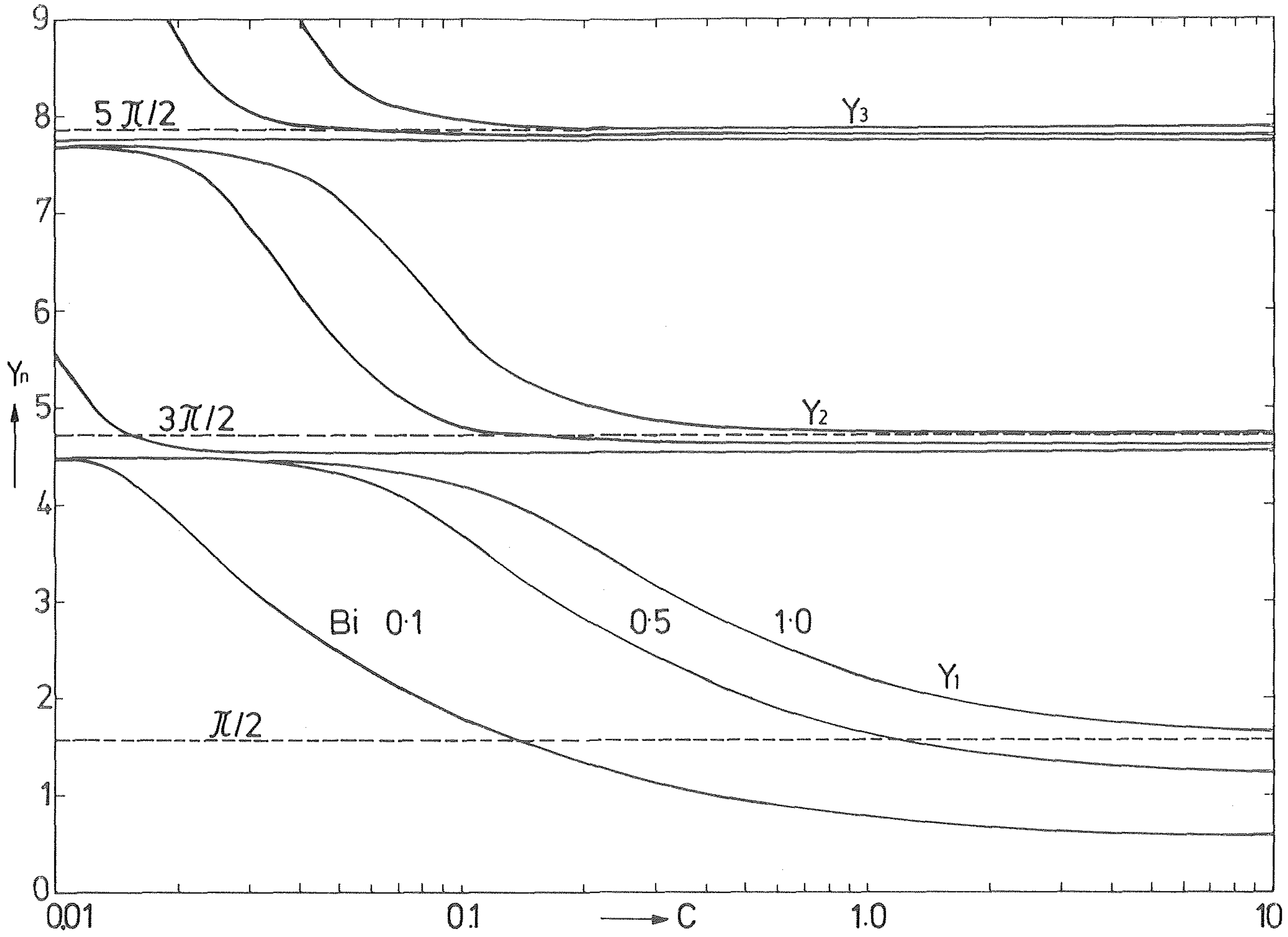

Fig. 1 The first three roots of equation (12)

$$\theta(\tau) = 1 - \exp\left(-3\mathrm{Bi}\tau \frac{1+C}{C}\right) \tag{20}$$

$$\theta_f(\tau) = 1 + \frac{1}{C}\exp\left(-3\mathrm{Bi}\tau \frac{1+C}{C}\right) \tag{21}$$

However, the use of such a simplified approach depends on how favorably equation (20) compares with the exact result, equation (16). Previous comparisons were limited to a few very special cases, such as (Bi $\leqslant$ 0.1; $C = \infty$) for which a number of textbooks quote an error of less than five percent. Other authors [8] use just three particular parameter combinations, and demonstrate that the simpler result may lead to a large over-estimation of the exchange rate. The present comparison, on the other hand, will cover the major part of paractically relevant parameter values, and will lead to a somewhat different conclusion.

A natural choice for the error inherent in the energy-balance solution is the ratio of equations (16) and (20), as expressed by

$$E(\tau) = (\theta/\hat{\theta} - 1)\ 100\ [\%] \tag{22}$$

For any given set of (Bi, C) the error reaches a maximum at some finite value of $0 < \tau < \infty$, and it is this value which has been considered in the error diagram, Fig. 3. We have plotted only three lines of constant error and assume that these characterize certain fields of application. An error of less than one percent is usually desirable for calorimetric studies, five percent for analytic and modeling work, whereas a ten percent error can often be tolerated in engineering calculations. We note further that

(i) the error is always positive because equation (20) overpredicts the rate of energy exchange,

(ii) the error decreases with decreasing fluid extent, that is, value of C, because the solid-temperature change is retarded by the fluid-temperature change, thus leaving more time for the internal temperature profile to relax and

(iii) the error in the time to reach a specified temperature is found from Fig. 3 and a first-order Taylor approximation.

In general, we conclude from the diagram that the simple result, equation (20), is a better approximation than one might have anticipated from the literature. For granulate-gas systems, in particular, where C is typically 10^{-2} to 10^{-1}, the error is seen to be surprisingly small.

Applications

So far we have been concerned with the calorimeter problem describing essentially a batchwise exchange process. The same mathematical development, together with a slightly modified physical interpretation, applies, however, to a continuous exchange process where a granular solid communicates with a fluid and both streams are flowing along the same major axis, co- or counter-currently. Such systems are quite frequent in the process industry, e.g., as a combined conveyer-heat exchanger or as a continuous energy economizer.

It is easily verified that for the analogy to hold, the following two quantities have to be redefined:

(i) contact time t is replaced by z/v, the ratio of linear distance along the flow axis and average flow velocity, thus

$$\tau = \frac{z\alpha}{vR^2}, \tag{23}$$

(ii) masses are replaced by the corresponding mass flux densities,

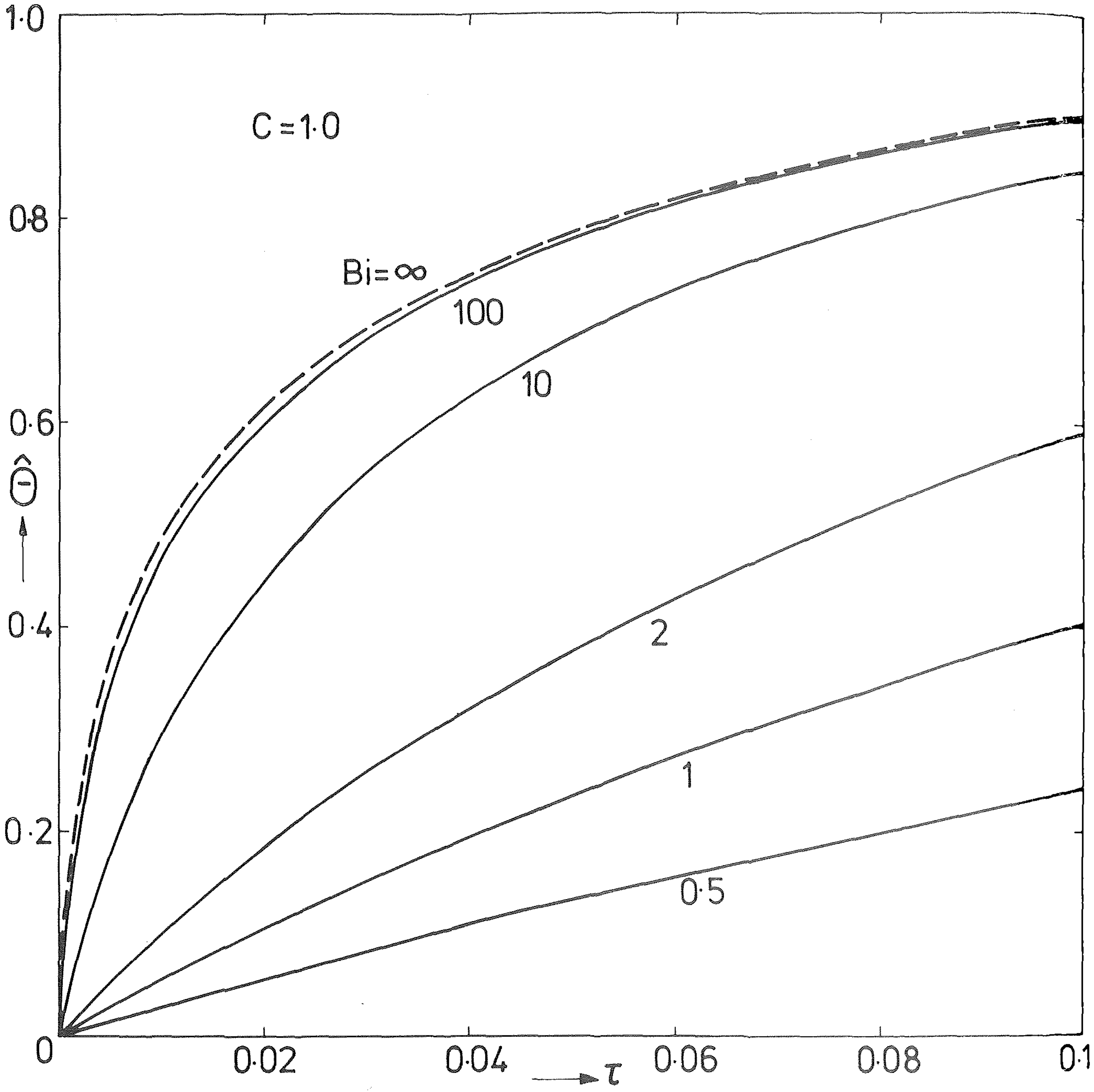

Fig. 2 Average solid temperature for fixed capacity ratio C and variable Biot number Bi. The dashed curve represents the limiting solution for negligible film resistance

so that

$$C = \frac{\dot{m}_f c_f}{\dot{m} c} \tag{24}$$

is always positive for co-current but negative for counter-current systems.

The last statement is evident from equation (5) as applied to a differential length of counter-current exchanger. Its physical and mathematical significance is, however, more readily understood when we replace the reference temperature T_∞ by T_{f0}, the fluid temperature at $z = 0$. Since a real exchanger will be of finite length (see Fig. 4), the value at $z = \infty$, T_∞, is a rather meaningless quantity in this context. With

$$U = \frac{T - T_0}{T_{f0} - T_0} = \theta \frac{C}{1 + C} \tag{25}$$

all the previous results, equations (9), (16), (20), and (21), are easily rewritten in terms of U, the new non-dimensional temperature. As is seen in Fig. 4, the co-current system ($C > 0$) leads to U and U_f gradually approaching each other, whereas the counter-current system may lead to temperature profiles which either diverge or converge in the positive z-direction. Obviously, this depends on the magnitude of C:

$0 > C > -1$, U and U_f diverge

$C < -1$, U and U_f converge

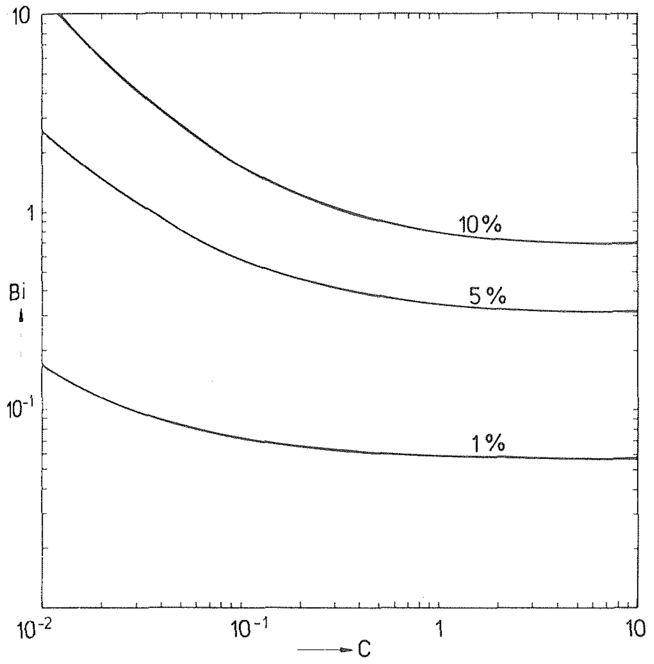

Fig. 3 Error involved in using the energy-balance solution as compared to the exact result

$$C = 1,\ U \text{ and } U_f \text{ are parallel and straight}$$

Mathematically, this is expressed in the exponentials of the results (16) and (20). For $0 > C > -1$ we find exponential growth terms indicating that U may be rising beyond all bounds. This is, however, not unreasonable, because here we are only concerned with a finite length L and not with an infinite domain. So these terms merely express the curvatures of the temperature profiles. Whereas when the energy-balance approach, which is identical to the analysis of an ordinary double-pipe heat exchanger, is unaffected by the size of C, a refinement is necessary in the case of the exact analysis. Here we have to include the possibility of positive values of s, so the step from equation (11) to (12) is no longer admissible.

Since

$$0 < \frac{\tanh \sqrt{s}}{\sqrt{s}} < 1 \text{ for } \infty > s > 0$$

one can show that the positive domain of s for which roots of equation (11) can possibly exist (but need not exist) is limited by

$$0 < s < -3\mathrm{Bi}/C \tag{26}$$

Clearly the domain only exists for $C < 0$. Thus equation (26) may have to be included in a numerical search procedure for the roots of equation (11).

Although this feature in some cases slightly complicates the calculation procedure, it does not affect the principal findings of the previous section on the batch problem. The error diagram applies to co-current and also, approximately, to counter-current systems (with C replaced by mod C) because of the physical similarities. And there are a number of other systems, not discussed here, which can be related to the calorimeter problem and, hence, analyzed on the same or a very similar basis.

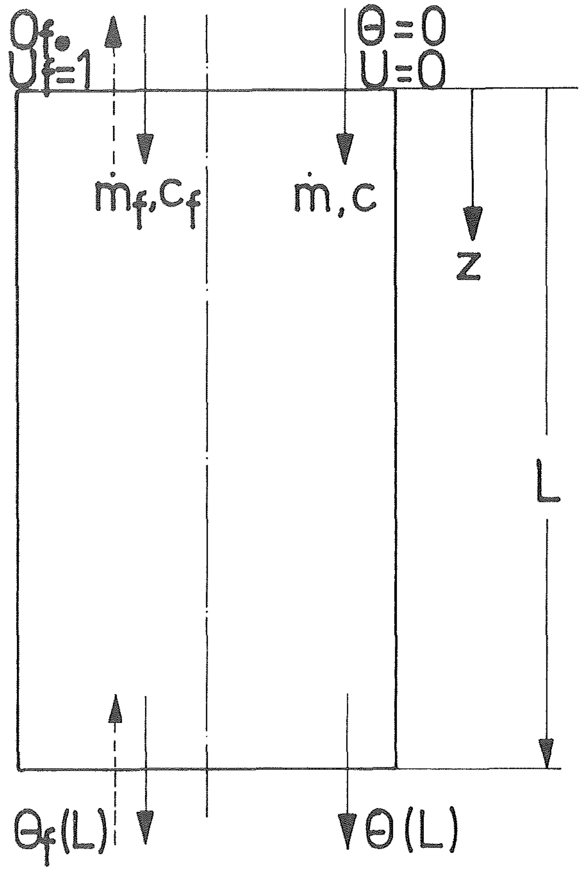

Fig. 4 Co- or counter-current granulate-fluid heat exchanger

References

1 Carslaw, H. S., and Jaeger, J. C., *Conduction of Heat in Solids*, Oxford University Press, 2nd Ed., 1959.

2 Crank, J., *The Mathematics of Diffusion*, Oxford University Press, 1956.

3 Paterson, S., The Heating or Cooling of a Solid Sphere in a Well-Stirred Fluid, *Proc. Phys. Soc.*, Vol. 59, 1947, p. 50.

4 Arpaci, V. S., *Conduction Heat Transfer*, Addison-Wesley, London, 1966.

5 Kunii, D., and Levenspiel, O., *Fluidization Engineering*, Wiley, New York, 1969.

6 Mathur, K. B., and Epstein, N., *Spouted Beds*, Academic Press, New York, 1974.

7 Kasten, P. R., and Amundsen, N. R., "Analytic Solution for Simple Systems in Moving Bed Absorbers, "*Industrial Engineering Chemistry*, Vol. 44, 1952, p. 1704.

8 Munro, W. D., and Amundsen, N. R., "Solid-Fluid Heat Exchange in Moving Beds, "*Industrial Engineering Chemistry*, Vol. 42, 1950, p. 1481.

9 Jakob, M., *Heat Transfer*, Vol. 1, Wiley, New York, 1949.

10 Edeskuty, F. J., and Amundsen, N. R., "Mathematics of Adsorption, IV," *Journal of Physical Chemistry*, Vol. 56, 1952, p. 148.

11 Amundsen, N. R., "Solid-Fluid Interactions in Fixed and Moving Beds," *Industrial Engineering Chemistry*, Vol. 48, 1956, p. 35.

Md. Alamgir
Research Assistant

J. H. Lienhard
Professor
Fellow ASME
Boiling and Phase Change Laboratory,
Mechanical Engineering Department,
University of Kentucky,
Lexington, Ky.

The Temperature Dependence of Surface Tension of Pure Fluids

The temperature dependence of the surface tension of pure liquids, in contact with their vapors, is correlated using the law of corresponding states. Molecular form is characterized by the Pitzer acentric factor. The temperature dependence reduces to a form identical to that of the van der Waals limiting liquid superheat when the Pitzer factor reaches the van der Waals value. The correlation brings together data for 91 organic and inorganic—polar and nonpolar—substances, within a constant, over the ranges of temperature for which data exist. Only water requires special modification. The accuracy of the correlation is on the order of ± one percent. This correlation will give surface tension over almost the entire range of temperature if one measured value, and the Pitzer factor, are known.

Introduction

The thermodynamic property, surface tension, σ, of saturated liquids should seemingly correlate according to the Law of Corresponding States since it is a unique function of the saturation temerature, T_s. Hence we seek a correlation of the form:

$$\sigma = \sigma_0 \text{ (molecular parameter) } f_1(T_{r_s}, \text{ molecular parameter}) \quad (1)$$

where T_{r_s} is the reduced saturation temperature, T_s/T_c; the molecular parameter could be the critical compressibility, Z_c, the Pitzer factor, ω, or the Riedel factor, and σ_0 is an as yet unformulated function of molecular structure with the dimensions of surface tension. It is customary to arrange things so σ_0 can be interpreted as $\sigma(T_s = 0 \text{ K})$.

Prior attempts to make such correlations have suggested that the corresponding states principle might be limited in bringing surface tension data together. Brock and Bird [1][1] correlated the group:

$$\sigma/p_c{}^{2/3}T_c{}^{1/3}\,k^{1/3}\,(1 - T_{r_s})^{11/9} \quad (2)$$

as a function of the Riedel factor [2] (p_c and T_c are the critical temperature and pressure). They correlated data for most fluids within an average error of three percent. However, they encountered enormous errors for light atoms and molecules, polar substances and alcohols, and carboxylic acids. They also correlated data as a function of Z_c with somewhat less success.

The work of Brock and Bird has stood up rather well. Furthermore, light has been cast on the failure of certain substances to correlate: Watkinson and Lielmezs [3], for example, have provided a quantum mechanical explanation for the departure of the light atoms and molecules. The reason is that the group $\sigma_0/p_c{}^{2/3}T_c{}^{1/3}\,k^{1/3}$deviates radically from a near near-constant value, at high values of the "de-Boer parameter."

But if the failure of Law of Corresponding States is lodged in the constant, σ_0, we can still profitably explore the possibility of generalizing the temperature dependence of σ—that is, the function, f_1, in equation (1). We must note, in that regard, that Brock and Bird do not provide evidence of having correlated data over wide ranges of temperature for specific substances. Indeed, Reid and Sherwood [4] show that Brock and Bird's correlation gives systematic changes in error of one to five percent over as small a temperature range as 15 to 40°C, in almost half the cases. Therefore, we should not be satisfied with the $(1 - T_{r_s})^{11/9}$ temperature dependence which they used, even though it has wide currency. Hakim, et al. [5] showed in 1971 that the 11/9 power should be replaced with a variable function and they discuss factors which influence the variability of σ_0, as well.

Our objective is therefore to provide a corresponding states correlation of surface tension data which accurately correlates their temperature dependence even if it involves a lead constant that defies corresponding states correlation.

Formulation

It was shown by Lienhard [6] that if one writes the Law of Corresponding States in the form

$$f(p_r, T_r, v_r, \text{ molecular parameter}) = 0 \quad (3)$$

(where v_r is the reduced specific volume), then the van der Waals equation is a member of the family of real substances. He chose Z_c as the molecular parameter, and showed that any thermodynamic property of a real substance extrapolated to the van der Waals value at the van der Waals critical compressibility, $Z_c = 3/8$.

Accordingly, we begin by asking how the surface tension for the van der Waals fluid should vary with temperature, and then translate the result to real fluids as suggested by equation (3). In doing so, we shall use the Pitzer factor, ω, as the molecular parameter. The definition of ω is:

$$\omega \equiv -[1 + \log_{10} p_{r_s}(T_{r_s} = 0.7)] \quad (4)$$

where p_{r_s} is the reduced saturation pressure.

---

[1] Numbers in brackets designate References at end of paper.

Contributed by the Heat Transfer Division for publication in the JOURNAL OF HEAT TRANSFER. Manuscript received by the Heat Transfer Division July 25, 1977.

To make use of the van der Waals surface tension, once we identify it, we must first consider a modification of equation (1). The factor $(1 - T_{r_s})^{11/9}$ is the "conventional" temperature variation of surface tension. It is known to work well for many substances; but for some, exponents other than 11/9 seem to work better. We therefore conjecture that equation (1) takes a form which isolates such an exponent:

$$\sigma(\omega, T_{r_s}) = \sigma_0 f_2(T_{r_s})^{f_3(\omega)} \tag{5}$$

where f_2 is contrived so that it approaches unity at $T_{r_s} = 0$. Thus the troublesome lead factor, σ_0, can be eliminated by logarithmic differentiation:

$$\left(\frac{\partial ln \sigma}{\partial T_{r_s}}\right)_\omega \Big/ \frac{dln f_2}{dT_{r_s}} = f_3(\omega) \tag{6}$$

if the conjecture is correct. The function $f_3(\omega)$ can thus be evaluated empirically by correlating the LHS of equation (6) against ω. We shall arrange the function $f_2(T_{r_s})$ so that $f_3(\omega_{\mathrm{vdW}} = -0.302)$[2] is unity, i.e.,

$$\frac{\sigma/\sigma_0}{(\sigma/\sigma_0)_{\mathrm{vdW}}} = f_2{}^{f_3-1} \tag{7}$$

The problem is now that of identifying the correct temperature function, f_2. The trial of several functions finally led us to the limiting liquid superheat for a van der Waals fluid. Let us next consider the implications of this.

Limiting Liquid Superheat and Surface Tension

The only information about the surface tension of a van der Waals substance was provided by van der Waals himself in 1894 [8]. Following a difficult calculation in which he considered the change of chemical potential through a surface layer he found that

$$\sigma_{\mathrm{vdW}} \sim (1 - T_{r_s})^{3/2} \tag{8}$$

near the critical point. This calculation was restudied by Fisk and Widom [9] who concluded that the exponent of 3/2 is smaller for real substances—between 1.22 and 1.33. They speculated that it might be some universal constant near 1.28 or 1.29, but they left that possibility open.

Now let us consider the limiting liquid superheat of a van der Waals substance. By this we mean the difference, ΔT_m, between the "spinodal" temperature T_m and the saturation temperature, T_s, at the same pressure, p_s. The spinodal temperature is the last temperature on a stable portion of a liquid isotherm (i.e., the point at which $(\partial p/\partial v)_T$ goes to zero.)

The calculation of $(\Delta T_{r_m})_{\mathrm{vdW}}$ must be done numerically with the help of a computer. However, near the critical point the function can be established as follows: Near the critical point the van der Waals vapor pressure curve becomes [6]

$$p_{r_s} \simeq 4T_{r_s} - 3 \tag{9}$$

but the equation for the spinodal line for a van der Waals fluid is well-known to be

$$p_{r_m} = (3v_{r_m} - 2)v_{r_m}{}^{-3} \tag{10}$$

If we write the spinodal volume as $v_{r_m} = 1 - \epsilon$, and expand the RHS noting that ϵ is small, we get, after setting p_{r_m} equal to the local saturation pressure (equation (9)),

$$\epsilon = \sqrt{4/3}(1 - T_{r_s})^{1/2} \tag{11}$$

The van der Waals equation:

$$p_{r_s} = \frac{8T_{r_m}}{3v_{r_m} - 1} - \frac{3}{v_{r_m}{}^2} \tag{12}$$

can likewise be written in terms of ϵ near the critical point. When equation (9) is substituted for p_{r_s} the result, after rearrangement, is

$$\Delta T_{r_m} = \frac{3}{2}\epsilon(1 - T_{r_s}) - \frac{3}{8}\epsilon^3 \tag{13}$$

substituting equation (11) in equation (13) yields[3]

$$\Delta T_{r_m} \rightarrow \frac{2}{\sqrt{3}}(1 - T_{r_s})^{3/2} \tag{14}$$

Thus both σ and ΔT_{r_m} depend upon T_{r_s} in the same way near the critical point.

We therefore choose f_2 proportional to $(\Delta T_{r_m})_{\mathrm{vdW}}$. The limiting value of $(\Delta T_{r_m})_{\mathrm{vdW}}$ near the critical point is given by equation (14). Since this diverges at lower values of T_{r_s}, we give the following expression which matches calculated values within 0.28 percent, down to $T_{r_s} = 0.9$.

$$(\Delta T_{r_m})_{\mathrm{vdW}} = \frac{2}{\sqrt{3}}(1 - T_{r_s})^{3/2} - 0.275(1 - T_{r_s})^{2.124};\ T_{r_s} \geq 0.9 \tag{15}$$

In [10], the following expression was fitted to the calculated values within an absolute error of 0.0016 over the whole range of T_{r_s} and with high percentage accuracy below $T_{r_s} = 0.9$:

$$(\Delta T_{r_m})_{\mathrm{vdW}} = (1 - T_{r_s}) - \frac{5}{32}(1 - T_{r_s}{}^{5.16});\ T_{r_s} \leq 0.9 \tag{16}$$

Finally, we select the constant of proportionality so f_2 will be unity at $T_{r_s} = 0$:

$$f_2 = \begin{cases} \dfrac{32}{27}(\Delta T_{r_m})_{\mathrm{vdW}}; & T_{r_s} < 0.9 \\ 1.137(\Delta T_{r_m})_{\mathrm{vdW}}; & T_{r_s} \geq 0.9 \end{cases} \tag{17}$$

---

[2] The saturated densities and the vapor pressure for a van der Waals substance were calculated in [6]. The value of −0.302 was obtained from the latter calculation.

[3] The lead constant in equation (14) was erroneously reported as $\sqrt{3}$ in [10].

Nomenclature

f_1, f_2, f_3 = specific functions defined in equations (1) and (5)
k = Boltzmann's constant
M = molecular weight
p, p_s, p_c = pressure, saturation pressure, critical pressure
T, T_s, T_c = temperature, saturation temperature, critical temperature
ΔT_m = limiting liquid superheat, $T_m - T_s$, at p_s
v = specific volume
Z_c = critical compressibility, $p_c v_c/RT_c$
ϵ = deviation of reduced critical volume from unity, $1 - v_{r_m}$
σ = surface tension between a liquid and its vapor
σ_0, σ_0' = σ evaluated at $T_s = 0$, σ_0 altered so that $f_2(T_s = 0) = 1$
ω = The Pitzer acentric factor defined by equation (4)

Subscripts

m = denoting a variable defined on the "spinodal" line, or locus of limiting liquid superheat
r = denoting a property divided by its critical value
vdW = denoting a property of a van der Waals fluid

Correlation of Data

It is first necessary to amass a large assortment of surface tension data over a wide variety of substances and a large range of reduced temperatures. Table 1 lists the 91 substances that we have considered, as well as the T_{r_s} range and the Pitzer factor for each substance. Only substances for which σ was known at at least three temperatures were considered. About two thirds of the data came from the International Critical Tables [11]. The rest came from [12], [13], [14], and [15].[4] Values of ω were largely taken from [17]. Since some of these values were obtained from the Edmister correlation (see [17]) many were cross-checked against vapor pressure data and in some cases corrected. No adjustments of negative ω's back to ω=0 were made. We have also considered water on the basis of a new IAPS release [18].

Low and Moderate T_{r_s} Correlation. Fig. 1 is a plot of the left hand side of equation (6) against ω. The derivative in the numerator was evaluated by forming local curve-fits through the σ data and differentiating these expressions. The derivative in the denominator was evaluated by differentiation of the $(\Delta T_{rm})_{vdW}$ expression in equation (16). This plot reveals an extraordinary consistency for all substances except water. However data in the range $0.9 \leqslant T_{r_s} < 1.0$ did not fall on the curve. Fig. 1 is accordingly restricted to the remaining existing data points in the range $0.37 \leqslant T_{r_s} \leqslant 0.84$. The implication is that our presumption that $f_3(\omega)$ and/or $\sigma_0(\omega)$ include no temperature dependence, is valid up to, but not at, high temperatures.

The curve is a straight line within a regression coefficient of 0.992 for $\omega \geqslant -0.002$. However it must return to a value of unity at $\omega = -0.302$ (the van der Waals limit). Fortunately, one data point for hydrogen corresponds with a large negative value of ω. It links the van der Waals limit to the straight line. We can represent this negative ω range by adding an approximate additional term and writing for

Table 1 Surface tension data used in correlation

Substance	Acentric Factor		Surface Tension, σ		σ'_0	Absolute % Error in Calculated σ/σ'_0		
	ω	Source	T_{r_s} Range of data	Source	$\frac{\text{dynes}}{\text{cm.}}$	Min.	Max.	Avg.
Organic Acids (◑)								
Acetic Acid	0.450	[15]	0.48-0.88	[10]	60.50	0.05	1.80	0.63
Propionic Acid	0.545		0.46-0.65	[10]	52.20	0.85	3.40	2.08
n-Butyric Acid	0.677		0.43-0.56	[13]	45.00	0.96	5.60	3.20
Isobutyric Acid	0.603		0.48-0.70	[10]	46.75	0.55	4.90	3.30
n-Valeric Acid	0.614		0.44-0.47	[12]	49.44	0.30	1.06	0.66
Isovaleric Acid	0.398		0.45-0.71	[10]	54.2	0.48	1.20	0.83
Alcohols (○)								
Methyl Alcohol	0.556		0.53-0.82	[10]	55.51	0.67	4.40	3.02
Ethyl Aclohol	0.635		0.55-0.82		50.36	0.01	1.10	0.58
n-Propyl Alcohol	0.600		0.50-0.69		52.55	0.02	2.40	1.60
Isopropyl Alcohol	0.773		0.55-0.70		43.2	0.06	0.57	0.30
n-Butyl Alcohol	0.596		0.48-0.72		51.03	0.01	0.23	0.09
Isobutyl Alcohol	0.604		0.53-0.74		49.44	0.29	1.52	0.77
Sec. Butyl Alcohol	0.579		0.52-0.66		50.2	0.29	0.31	0.30
Tert. Butyl Alcohol	0.619		0.58-0.70		46.31	1.72	2.30	1.91
n-Amyl Alcohol	0.513		0.50-0.52	[12]	54.50	0.01	0.05	0.03
Tert. Amyl Alcohol	0.496		0.52-0.56		52.79	0.08	0.10	0.06
n-Octyl Alcohol	0.452		0.43-0.46		51.77	0.10	0.43	0.29
Allyl Alcohol	0.568		0.51-0.68	[10]	57.28	0.00	2.91	1.50
Ethers (⦶)								
Diethyl Ether	0.192	[12]*	0.62-0.99		71.00	0.78	4.30	2.20
Ethyl Phenyl Ether	0.445	[15]	0.45-0.58		65.0	0.70	1.99	1.40
Ethyl Propyl Ether	0.306	[15]	0.54-0.59		59.7	0.06	0.07	0.07
Methyl Ethyl Ether	0.230	[12]*	0.64-0.73	[12]	70.56	0.14	1.50	1.02
Methylal	0.290	[15]	0.59-0.62	[12]	68.60	0.21	0.22	0.22
Esters (△)								
Methyl Formate (T_{r_s} < 0.85)	0.272	[15]	0.58-0.80	[10]	84.10	0.84	1.21	0.96
(T_{r_s} > 0.85)**	0.272		0.86-0.992		73.50	2.51	3.32	2.96
Ethyl Acetate	0.365		0.58-0.81		64.9	0.99	3.01	1.50
n-Propyl Acetate	0.395		0.49-0.74		59.4	0.29	2.52	1.45
Methyl n-Butyrate	0.380		0.51-0.73		61.4	1.60	3.76	2.48
Methyl Isobutyrate	0.370		0.52-0.79		60.3	0.36	2.24	1.32
Methyl Propionate	0.363		0.53-0.76		66.0	0.10	0.93	0.42
Ethyl n-Pelargonate	0.601		0.42-0.45	[12]	49.2	0.02	0.76	0.44
Ethyl n-Caprylate	0.537		0.43-0.46		53.2	0.32	1.24	0.72
Ethyl n-Butyrate	0.455		0.51-.054		55.9	0.96	0.98	0.97
Ethyl Propionate	0.396		0.52-0.56		60.7	0.23	0.25	0.24
Ketones (□)								
Acetone	0.318	[15]	0.53-0.70	[10]	70.4	0.07	0.92	0.51
Diethyl Ketone	0.365		0.48-0.58		61.5	0.00	0.10	0.06
Methyl Ethyl Ketone	0.337		0.51-0.65		66.7	0.25	0.87	0.57
Methyl n-Propyl Ketone	0.349		0.52-0.58		67.7	0.92	0.97	0.95
Halides (⊖)								
Chlorobenzene	0.255		0.44-0.95		79.70	0.92	3.30	1.46
Carbon Tetrachloride	0.202		0.50-0.94		78.72	0.18	3.03	2.22
(T_{r_s} > 0.85)**	0.202		0.94-0.98		65.00	0.02	0.62	0.32
Chloroform	0.214		0.52-0.66		81.20	0.14	0.93	0.56
Methyl Chloride	0.158		0.65-0.71		89.1	0.19	1.22	0.83
Ethyl Bromide	0.310		0.56-0.63		73.3	0.21	0.47	0.32
Iodobenzene	0.255		0.40-0.47		82.3	0.10	0.27	0.20
Hydrogen Bromide	0.083		0.50-0.57	[13]	91.0	2.63	4.31	3.37
Hydrogen Chloride	0.133		0.50-0.60	[13]	80.2	0.02	2.88	2.24
Bromobenzene	0.255		0.43-0.46	[12]	80.2	0.16	2.61	2.12
Allyl Chloride	0.161		0.56-0.59	[12]	77.2	0.00	0.31	0.19
Nitrogen Compounds (◓)								
Piperidine	0.248		0.46-0.68	[10]	77.4	0.71	2.30	1.45
Ethyl Amine	0.303		0.63-0.68	[12]	74.2	0.15	1.58	1.07
n-Propyl Amine	0.306		0.57-0.64	[10]	70.1	0.10	1.63	0.81
Hydrogen Cyanide	0.399		0.62-0.66		59.4	0.08	0.17	0.11
Acetonitrile	0.319		0.51-0.67		78.1	0.08	0.68	0.51
Propionitrile	0.328		0.50-0.65		68.2	0.72	2.39	1.41
Sulfur Compounds (▲)								
Carbon disulfide	0.123		0.49-0.61		99.5	0.27	2.10	0.82
Diethyl Sulfide	0.303		0.50-0.66		53.1	0.93	5.35	3.71
Dimethyl Sulfide	0.199		0.56-0.66		85.1	0.27	1.47	0.99
Methyl Mercaptan	0.177		0.43-0.55		68.0	0.31	1.57	1.01
Ethyl Mercaptan	0.173		0.54-0.59		78.3	0.07	0.19	0.12
Hydrogen Sulfide	0.100		0.50-0.57	[13]	98.0	0.27	1.22	0.81
Paraffins (⊕)								
n-Hexane	0.290		0.56-0.62	[11]	56.1	0.00	0.05	0.03
n-Heptane	0.352		0.52-0.60		53.0	0.17	0.93	0.62
n-Octane	0.408		0.49-0.57		50.9	0.97	1.76	1.40
n-Nonane	0.441		0.49-0.53		49.9	0.06	0.87	0.55
n-Decane	0.586		0.47-0.51		45.5	0.22	1.11	0.79
n-Pentadecane	0.650		0.41-0.51		44.3	1.79	3.02	2.49
n-Hexadecane	0.704	[15]	0.40-0.44	[11]	43.8	0.09	1.42	1.06
n-Nonadecane	*0.772*		*0.38-0.42*		*42.9*	*0.21*	*1.01*	*0.88*
n-Eicosane	0.710		0.37-0.41		44.3	0.07	1.62	1.08
Cyclohexane	0.186		0.52-0.55	[12]	72.8	0.18	0.38	0.30
Cyclopentane	0.193		0.56-0.60	[12]	72.5	1.22	1.66	1.36
Methyl Cyclohexane	0.244		0.51-0.55	[11]	63.1	0.02	0.14	0.07
Olefins (◐)								
Acetylene	0.186		0.63-0.69	[14]	70.0	0.30	3.03	2.09
Cyclopentene	0.207		0.55-0.60	[12]	72.4	0.30	3.10	2.12
Aldehyde (■)								
Acetaldehyde	0.314		0.59-0.70	[10]	75.3	0.28	1.22	1.14
Aromatics (◒)								
Benzene (T_{r_s} < 0.85)	0.215		0.48-0.85	[10]	81.8	0.02	4.76	1.36
(T_{r_s} > 0.85)**	0.215		0.85-0.994		71.5	0.00	3.43	1.65
Toluene	0.279		0.47-0.68		69.7	0.40	5.61	1.74
Ethyl Benzene	0.322		0.44-0.66		65.7	0.31	2.19	0.79
Mesitylene	0.417		0.46-0.50	[11]	60.0	0.00	0.84	0.51
m-Xylene	0.330		0.44-0.66	[10]	66.1	0.56	1.41	0.99
p-Xylene	0.303		0.44-0.66	[10]	66.0	0.36	2.06	0.87
Oxides (◆)								
Carbon dioxide**	0.263	[12]*	0.89-0.997		66.5	0.00	6.40	2.62
Nitrous Oxide**	0.160	[15]	0.91-0.97		62.0	0.01	6.80	3.08
Ethylene Oxide	0.157		0.46-0.63	[14]	94.5	1.53	3.36	2.52
Water	0.348		0.42-0.99	[16]	--	--	--	--
Elements (▼)								
Hydrogen	-0.215	*	0.44-0.62	[14]	8.09	0.01	6.86	4.01
Oxygen	-0.04	[15]	0.46-0.59		50.00	0.04	2.98	2.03
Argon	-0.002		0.57-0.60		49.90	0.73	0.77	0.75
Neon	0.		0.54-0.64		20.8	0.81	2.56	1.52
Nitrogen	0.04		0.56-0.72		40.0	1.52	4.60	2.94
Chlorine	0.074		0.66-0.73	[10]	109.0	0.01	2.75	2.09
Bromine	0.132		0.47-0.56	[10]	116.0	0.02	0.86	0.45

* *Calculated from experimental vapor pressure data or Antoine equation.*

** Use of high temperature correlation, equation (24) recommended.

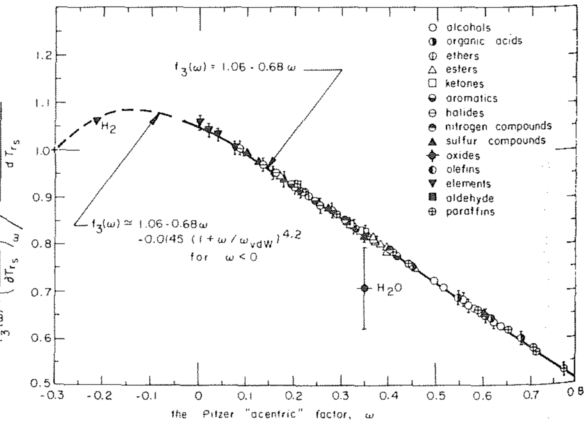

Fig. 1 Correlation of the exponent $f_3(\omega)$ from experimental data

---

[4] We subsequently found Jasper's [16] important listing of surface tension data. Careful checking revealed that use of his data would not require revision of our correlation curves.

$f_3(\omega)$:

$$f_3(\omega)\begin{cases}\simeq 1.06 - 0.68\,\omega & \omega \geqslant 0\\ = 1.06 - 0.68\,\omega - 0.0145(1 + \omega/\omega_{\text{vdW}})^{4.2}, & \omega < 0\end{cases} \quad (18)$$

in the range $0.37 \leqslant T_{r_s} \leqslant 0.84$.

To show how well experimental surface tension data follow the temperature dependence proposed in equation (17), we have plotted $(\sigma_{\text{expt'l.}}/\sigma_0')^{1/f_3}$ against T_{r_s} in Fig. 2 where, for a particular liquid,

$$\sigma_0' \equiv \sigma_0\left(\frac{32}{27}\right)^{f_3} = \left[\frac{\sigma_{\text{expt'l.}}}{(\Delta T_{r_m})_{\text{vdW}}{}^{f_3}}\right] \quad (19)$$

The RHS is averaged over the temperature range of the data. Fig. 2 also includes the plot of $(\Delta T_{r_m})_{\text{vdW}}$ from equations (15) and (16). The average deviation of all data but water from the correlation is 1.37 percent on this curve and the rms deviation is 1.4 percent. The accuracy of σ/σ_0 is still better for most liquids as can be seen in Table 1. However, *all* other substances which have previously caused difficulty in corresponding states correlations are well-behaved.

An Approximate Correlation for σ_0'. The lead constants, $\sigma_0'(\omega)$, are correlated against ω in Fig. 3. (The numerical values $\sigma_0'(\omega)$, are given for each substance in Table 1.) The data all come together nicely, with the exception of the light elements. Watkinson and Lielmezs have shown that those data cannot correlate, so that is to be expected. The remaining data (including polar substances and carboxylic acids) are represented by:

$$\sigma_0'(\omega) = 42\omega^{-0.37}{}_{\omega > 0.05,\ 0.37 \leqslant T_{r_s} \leqslant 0.84} \quad (20)$$

with an average error of 7.8 percent and an rms error of 5.7 percent. It should be pointed out that since σ_0' is dimensional, the ordinate of Fig. 3 should be divided by a reference value—probably the van der Waals, or $\omega = -0.302$, value. Since this reference cannot be specified precisely it is omitted, but with no loss of generality. As a matter of interest, the dimensionless correlation $\sigma_0/p_c{}^{2/3}T_c{}^{1/3}k^{1/3} = f(\omega)$ was also attempted and found to be completely unsuccessful in a correlating σ_0.

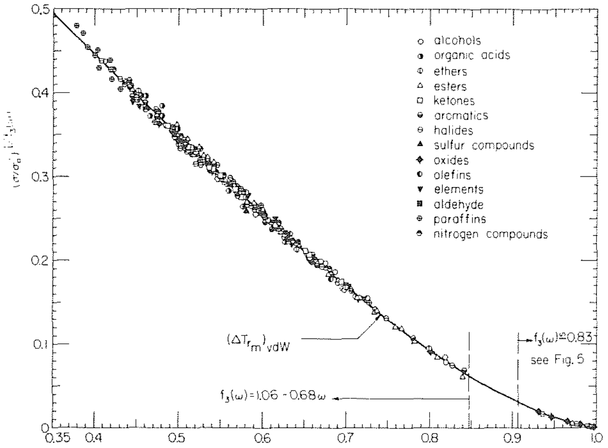

Fig. 2 Temperature dependence function for surface tension: low and moderate temperatures

A final correlation can be written as the product of the very accurate $(f_2)^{f_3}$ term and the less accurate σ_0' term.

$$\sigma = 42\omega^{-0.37}\left[(1 - T_{r_s}) - \frac{5}{32}(1 - T_{r_s}{}^{5.16})\right]^{1.06 - 0.68\omega} \quad (21)$$

which is valid for $0.37 \leqslant T_{r_s} \leqslant 0.84$ and $\omega > 0.05$.

It should be emphasized that if a single piece of surface tension data exists, it can be used in place of equation (20) to evaluate σ_0' for that fluid. Then it will be possible to predict $\sigma(T_s)$ for that fluid with great accuracy.

Water. It turns out that water can be correlated to a form consistent with the present correlation if we acknowledge temperature dependence in σ_0'. Thus equation (21) will describe water within 0.32 percent in the low temperature range $0.422 \leqslant T_{r_s} \leqslant 0.84$ if we replace $42\omega^{-0.37}$ with $110.1\,(1 + 0.939\,T_{r_s})$. Under such a change, f_3 becomes 0.8234 which lies on the correlation line in Fig. 1. The result:

$$\sigma = 110.1\,(1 + 0.939\,T_{r_s})(\Delta T_{r_m})_{\text{vdW}}{}^{0.8234} \quad (22)$$

retains much of the logic of the present work and is almost as accurate as the IAPS curve fit:

$$\sigma = 235.8\,(1 - T_{r_s})^{1.256}[1 - 0.625\,(1 - T_{r_s})] \quad (23)$$

which represents the data within 0.5 percent in this range.

High temperature correlation. There is a gap in available data between 0.84 and about 0.9 in our curves since the extant data (other than water) did not allow us to form the derivative $(\partial \ln\sigma/\partial T_{r_s})\omega$ in that range. We must therefore pass to the range $T_{r_s} > 0.9$ which exhibits substantially different behavior.

Fig. 4 shows $f_3(\omega)$ as obtained from data near the critical point—generally from the range of $0.93 \lesssim T_{r_s} < 1.0$. Only five fluids provided data over a very narrow range of ω. Other surface tension data were available but there were either too few points to form a derivative at high temperature or else the experimental error was too large. Ethanol and methanol data fell on the dashed trend line shown in the figure, near $\omega \simeq 0.6$, but experimental errors for these substances were greater than the reported values of σ at high T_{r_s}.

Since there are insufficient data to form an accurate functional relation for $f_3(\omega)$ at high temperatures we must be content to observe that this function is far weaker than it was at low temperature. Indeed, in the relatively narrow ω range of available data

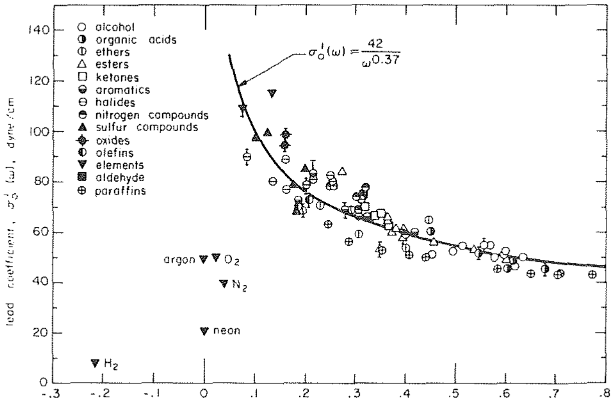

Fig. 3 Correlation of surface tension lead coefficients

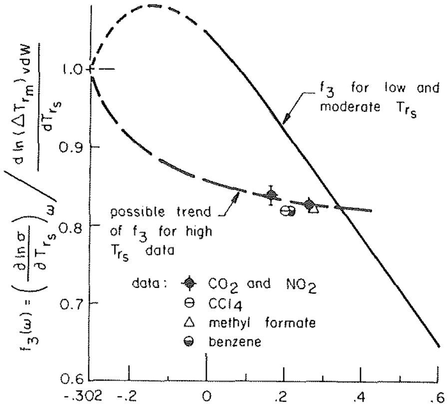

Fig. 4 Evaluation of $f_3(\omega)$ for very high T_{r_s}

$$(f_3)_{\text{high temp.}} = 0.83 \pm 0.012, \quad 0.16 \leqslant \omega \leqslant 0.272 \tag{24}$$

With this we can form the appropriate high temperature surface tension equation

$$\frac{\sigma}{\sigma_0'} = \left[\frac{2}{\sqrt{3}}(1 - T_{r_s})^{3/2} - 0.275\,(1 - T_{r_s})^{2.124}\right]^{0.83} \tag{25}$$

Fig. 5 shows the comparison of this expression with data. For a particular liquid the high temperature σ_0' has been evaluted as in equation (19), using equation (15) for $(\Delta T_{r_m})_{vdW}$. Equation (25) describes the data within an average error of 2.1 percent and an rms error of 1.2 percent. (The data upon which the comparison is based are generally subject to larger experimental errors than these.) Values of the lead constant, σ_0' are shown in the inset. They averaged about 66 dynes/cm and seem to show some upward trend with increasing ω. But these data are too meager to permit the formulation of a correlating equation.

Discussion

The preceding correlations raise a number of questions which merit consideration:

How Good is the 11/9 Power-law? Fig. 6 shows $\sigma(T_{r_s})/\sigma_0$ as calculated using equations (5), (17) and (18) for several values of ω. The 11/9 power law is included for comparison. It is clear that the latter is a rough, but not unreasonable, approximation for ω up to 0.2 or 0.3. Beyond that it is seriously in error. At high temperatures, equation (25) describes only a single temperature dependence since f_3 is so weakly dependent on ω. In the limit, as $T_{r_s} \to 1$, equation (24) reduces to a 1.245 power law which is valid near $\omega = 0.2$. This line meshes rather well with either $[1.137(\Delta T_{r_m})_{vdW}]^{f_3}$ for $\omega = 0.2$, or the 11/9 (or 1.222) power-law.

What About Fisk and Widom's 1.28 or 1.29 High-Temperature Power-Law Conjecture? It is not impossible that $f_3(\omega)$ settles on a constant value for all ω's greater than zero. Our limited data suggest a constant value of 0.83 which leads to a power law of 1.245. Certainly a universal value would be no higher than this. For water ($\omega = 0.348$) the power law appears to be 1.20 or even less. A great deal of hard-to-measure high-temperature data are needed to answer this question.

Is there a Physical Principle Which says that σ is Proportional to ΔT_{r_m} for Real Substances? The present formulation does not give a direct basis for inferring the ΔT_{r_m} values of a real substance once its surface tension is known. Nevertheless a direct proportionality appears to exist between these variables for a van der Waals fluid.

Reliable measurements of ΔT_{r_m} (or, at least, of temperature differences very close to ΔT_{r_m}) over a range of temperature exist only for two fluids. These are Pavlov and Skripov's [19] data for benzene and n-hexane. The data for each substance are multiplied by an appropriate constant and plotted along with the surface tension data for that substance in Fig. 7. The ΔT_{r_m} and σ data for benzene overlap and match perfectly. The n-hexane data only overlap at one point, but their slopes match perfectly. On the basis of the best available information, we cannot claim such a proportionality for water.

Conclusions

1 The functional dependence of surface tension on ω and temperature has has been given by:

$$\sigma(T_{r_s}, \omega) = \sigma_0'(\omega)[(\Delta T_{r_m})_{vdW}]^{f_3(\omega)}$$

for all substances but water and for $T_{r_s} \leqslant 0.84$ or greater.

2 The preceding expression gives a very accurate representation of the temperature dependence of σ. With $f_3 = 1.06 - 0.68\omega$, it predicts

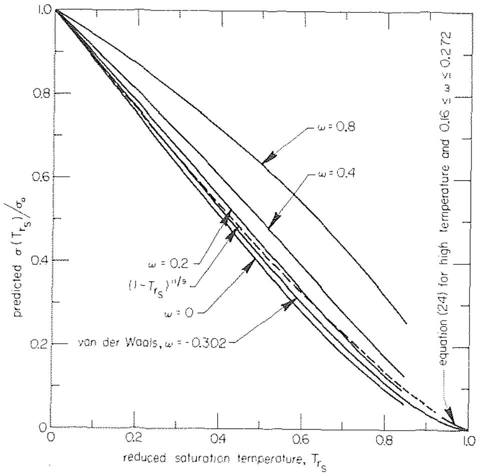

Fig. 6 The physical variation of surface tension with temperature for various kinds of substances

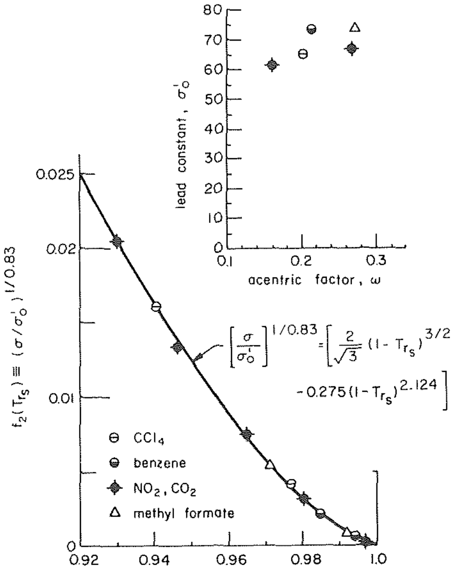

Fig. 5 The temperature dependence function, and lead constant, for surface tension at high temperature

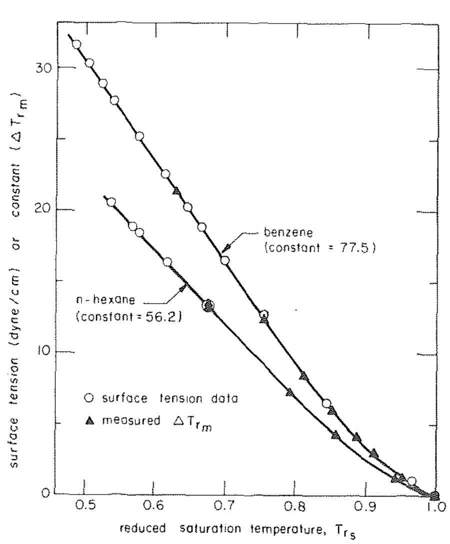

Fig. 7 An experimental comparison of the temperature dependence of ΔT_{r_m} with that of σ

σ/σ_0' within an rms error of about 1 percent. An additional term is needed in f_3 if $\omega < 0$.

3 The lead constant, σ_0', can be obtained from a measurement of surface tension at a single temperature (or from Table 1). If no data exist, it can be estimated with the help of equation (20) for $\omega > 0.05$. This estimate is subject to an rms error of 5.7 percent, but it includes all substances except water.

4 Substances for which $\omega < 0.05$ obey the present correlation of temperature dependence, but the lead constants are not given by equation (20).

5 Limited surface tension data at high temperatures (in the small range of ω around 0.2) have a temperature dependence of the form of equation (25) with an rms error of 1.2 percent.

Acknowledgment

The present work was done under the support of the Electric Power Research Institute, Research Project 687-1 with B. Sehgal as Project Manager. We are especially grateful to Dr. M. Trela, Professor J. Straley, and A. Karimi for their counsel in the work.

References

1 Brock, J. R., and Bird, R. B., "Surface Tension and the Principle of Corresponding States," *AIChE Journal*, Vol. 1, 1955, p. 174.

2 Riedel, L., "Eine Neue Universelle Dampfdruckformel," *Chemie-Ing-Techn.*, Vol. 26, 1954, p. 83.

3 Watkinson, A. P., and Lielmezs, J., "Corresponding-States Principle and Surface Tension," *J. Chem. Phys.*, Vol. 47, 1967, p. 1158.

4 Reid, R. C., and Sherwood, T. K., *The Properties of Gases and Liquids*, McGraw-Hill, New York, Second ed., 1966, Table 8-4.

5 Hakim, D. I., Steinberg, D., Stiel, L. I., "Generalized Relationship for the Surface Tension of Polar Fluids," *Ind. Engr. Chem. Fundam.*, Vol. 10, No. 1, 1971, pp. 174–75.

6 Lienhard, J. H., "Relation between van der Waals' Fluid and Real Substances," *Iranian Journal of Sci. and Tech.*, Vol. 5, 1976, p. 111.

7 See, e.g., Reid, R. C., and Sherwood, T. K. op. cit., Section 8.3.

8 Van der Waals, J. D., "Thermodynamische Theorie der Kapillarität unter Voraussetzung stetiger Dichteänderung," *Zeit. Phys. Chemie.*, Vol. 13, 1894, p. 657.

9 Fisk, S., and Widom, B., "Structure and Free Energy of the Interface between Fluid Phases in Equilibrium near the Critical Point," *Jour. Chem. Phys.*, Vol. 50, No. 8, 1969, p. 3219.

10 Lienhard, J. H., "Correlation for the Limiting Liquid Superheat," *Chem. Engr. Sci.*, Vol. 31, 1976, p. 847.

11 *International Critical Tables*, Vol. IV, McGraw-Hill, New York, First ed., 1928.

12 Dreisbach, R. R., *Physical Properties of Chemical Compounds*, American Chemical Society, 1959, Nos. 15, 22 and 29.

13 Timmermans, J., *Physico-chemical Constants of Pure Compounds*, Elsevier Publishing Co., Amsterdam, 1950.

14 Landölt-Bornstein, *Physikalisch-chemische Tabellen*, Springer, Berlin, Fifth ed., 1923.

15 *Lange's Handbook of Chemistry*, McGraw-Hill, New York, 1973.

16 Jasper, J. J., "The Surface Tension of Pure Liquid Compounds," *Journal of Physical and Chemical Reference Data*, Vol. 1, No. 4, 1972, pp. 841–1010.

17 Reid, R. C., and Sherwood, T. K., op. cit., Section 2–7 and App. A.

18 "Release of Surface Tension of Water Substance," The Int. Assn. for the Properties of Steam, Dec., 1976, available from the Executive Secretary IAPS, Office of Std. Ref. Data, Nat'l. Bur. of Stds.

19 Skripov, V. P., and Pavlov, P. A., "Explosive Boiling of Liquids and Fluctuation Nucleus Formation," *Teplofizika Vysokih Temp.*, Vol. 8, No. 4, 1970.

20 Pavlov, P. A., and Skripov, V. P., "Kinetics of Spontaneous Nucleation in Strongly Heated Liquids," *Teplofizika Vysokih Temp.*, Vol. 8, No. 3, 1970, pp. 579–585.

R. E. Taylor

Properties Research Laboratory,
School of Mechanical Engineering,
Purdue University,
West Lafayette, Ind.

Thermal Properties of Tungsten SRM'S 730 and 799

Samples of sintered and arc-cast tungsten are available from NBS as thermal conductivity (SRM 730) and electrical resistivity (SRM 799) standards for the temperature range from 4 to 3000K. NBS recommended values for these properties above room temperature are based on results of various researchers during a previous international program which included arc-cast and sintered tungsten. The sintered tungsten used in this program was found to be unsuited for use as a standard material due to inhomogeneity and high temperature instability. The present paper gives results at high temperatures for thermal conductivity, electrical resistivity, specific heat, thermal diffusivity and Wiedemann-Franz-Lorenz ratio for a sample of the NBS sintered tungsten using the Properties Research Laboratory's multiproperty apparatus. These results are compared to values recommended by the Thermophysical Properties Research Center, NBS, and an international program.

Introduction

Samples of both sintered and arc-cast tungsten are available from the National Bureau of Standards Office of Standard Reference Materials as SRM 730 and SRM 799. These materials have been certified for a thermal conductivity (SRM 730) and electrical resistivity (SRM 799) reference material from 4 to 3000K even though their properties were not directly measured above 300K [1].[1] These high temperature certifications are based mainly on a report [2] of the AGARD[2] task group which investigated the transport properties of a number of materials including arc-cast tungsten. The present SRM certification of the thermal conductivity of sintered tungsten closely follows the AGARD results for arc-cast tungsten.

The NBS sintered-tungsten is 99.98 percent pure with 10 to 100 ppm Si and Mo present along with trace amounts (<10 ppm) of Ca, Fe, Cr, Cu and Mg. The density is 19.23 ± 0.05 g/cm^3. The material is useful up to 2800 K if annealed up to 2300 K for one hour.

The present work has the objective of comparing the thermal conductivity results on sintered tungsten with the previous results on arc-cast tungsten to verify the SRM certification. The certified values are believed accurate within five percent from 300 to 2000K and within eight percent above 2000K [1]. Further, since PRL possesses a unique capability to measure extremely accurately a number of properties at high temperature on the same sample, specific heat values were also measured on this material. The specific heat values are useful in clarifying the ambiguity in calculated thermal conductivity values from previous thermal diffusivity-specific heat determinations noted during the AGARD program [3].

Apparatus

The PRL multi-property apparatus was developed in the late 1960s and early 1970s. The apparatus has been continuously upgraded since then—primarily in the software used in conjunction with the mini-computer-based digital data aquisition system which controls parts of the experiments, collects all the data, and computes and outputs results. The apparatus is described in publications [4,5]. The sample is suspended between one fixed and one movable electrode and heated by direct passage of electrical current through it. Through measurement of brightness temperature, voltage drop and current, the electrical resistivity and total hemispherical emittance as a function of brightness temperature are determined. The electrical resistivity is also measured as a function of true temperature by measuring the sample when an auxiliary furnace surrounds it. Thus, total hemispherical emittance and normal spectral emittance can be calculated as a function of temperature. Temperature profiles are determined on the sample when the electrodes are moved closer together, effectively shortening the sample. These data, combined with the electrical resistivity and hemispherical emittance are used to compute thermal conductivity using SPLINE [6] procedures. All measured quantities (voltage, current, length, temperature, mass and time) are directly traceable to NBS or equivalent standards.

Procedures

Electrical Resistivity. Two voltage probes are spot welded about one cm apart in the central portion of the sample. The voltage probe separation distance "L" is determined electrically from the ratio of the voltage drop between the probes and the voltage drop between two accurately spaced knife blades placed on the same region. This can be done conveniently in a thermostated water bath holder and the electrical resistivity measured from room temperature to about 80°C at the same time.

To determine the electrical resistivity at moderate temperature (20–800°C), a modified Kohlrausch setup was used with thermocouples for both voltage probes and temperature measurements. For higher temperature measurements the sample minus the thermo-

---

[1] Numbers in brackets designate References at end of paper.

[2] Advisory Group for Aerospace Research and Development.

Contributed by the Heat Transfer Division for publication in the JOURNAL OF HEAT TRANSFER. Manuscript received by the Heat Transfer Division July 25, 1977.

couples is inserted within a tantalum tube heater and its surrounding heat shields. Slots are provided in the heater and heat shields so that an optical pyrometer can view the sample and a portion of the interior furnace surface. The sample is connected to one fixed and one movable electrode and the heater is connected to separate electrodes. The brightness temperature of the sample and interior heater surface are made to nearly coincide by separately adjusting the current to each. When the sample disappears, a near black body condition is achieved, and the temperature, voltage drop, and current are measured with the sample current flowing in both directions.

Thermal Conductivity. Temperature profiles are measured on the sample after the electrodes are moved closer together, effectively making a short sample. These data are adjusted automatically to the values which would be obtained if the average current were flowing during each measurement. These data along with the appropriate geometrical constants (length and diameter), current, and coefficients for fits of resistivity and total hemispherical emittance as a function of temperature are used to calculate thermal conductivity as a function of temperature. First the temperature versus position data are fitted by SPLINE fits to yield the calculated temperature data. Then the derivatives of calculated temperature data are used as input to the SPLINE program to determine second derivatives of temperature versus position. With these data an array such as shown in Table 1 is set up. The column marked "ρ" is the resistivity, the column marked E_H is the total hemispherical emittance, and the column marked "F" is the fourth term minus the third term in the equation:

$$\lambda\, d^2T/dx^2 + (d\lambda/dT)\,(dT/dx)^2 + I^2\rho/A^2 - PE_H\sigma\,(T^4 - T_0{}^4)/A - \mu I(dT/dx)/A = 0.$$

In this equation λ is the thermal conductivity, I is the current, ρ is the electrical resistivity, A is the cross-sectional area, P is the circumference, σ is the Stefan-Boltzmann constant, T_0 is the ambient temperature, and μ is the Thomson coefficient. The values for $\lambda, d\lambda/dT$ and μ are found in the following fashion:

Assume: $\lambda = \lambda_0 + \lambda_1 T$

then $d\lambda/dT = \lambda_1$

and

$$\lambda(d^2T/dz^2) + d\lambda/dT(dT/dz)^2 + \mu(I/A)(dT/dz) = F \text{ becomes}$$
$$\lambda_0(d^2T/dz^2) + \lambda_1(T(d^2T/dz^2) + (d\lambda/dT)^2) + \mu(I/A)(dT/dz) = F.$$

The array of Table 1 is then solved for the best values (in the least squares sense) of λ_0, λ_1 and μ. This procedure yields the values of λ versus T given at the bottom of Table 1. The value of I was 160.63 amps and A was 0.08006 cm^2 for this experiment.

Table 1 Array for calculating thermal conductivity (data of run TU 4)

POSITION (cm)	TEMPERATURE (K)	dT/dx (K·cm^{-1})	d^{2}T/dx^2 (K·cm^{-2})	ρ (μΩ·cm)	E_H	F (w·cm^{-3})
0.000	1475.15	206.43	-88.025	40.2597	0.1933	-97.143
0.100	1495.36	197.81	-85.504	40.9255	0.1957	-95.354
0.200	1514.72	189.40	-83.090	41.5649	0.1979	-93.419
0.300	1533.25	181.20	-80.782	42.1786	0.2000	-91.357
0.400	1550.97	173.21	-78.582	42.7669	0.2021	-89.185
0.600	1584.06	157.85	-74.503	43.8695	0.2060	-84.582
0.800	1614.16	143.32	-70.852	44.8768	0.2095	-79.743
1.000	1641.44	129.58	-67.629	45.7932	0.2127	-74.789
1.400	1688.03	103.73	-62.099	47.3663	0.2181	-64.995
1.800	1724.70	79.95	-55.696	48.6114	0.2224	-56.023
2.200	1752.37	59.02	-48.053	49.5551	0.2264	-48.463
2.800	1779.98	34.28	-36.732	50.5002	0.2289	-40.210
3.200	1790.84	20.12	-33.401	50.8729	0.2301	-36.761
3.800	1796.80	- 0.16	-34.814	51.0776	0.2308	-34.818
4.400	1790.38	- 21.53	-37.122	50.8571	0.2301	-36.908
4.800	1778.76	- 36.71	-37.978	50.4582	0.2287	-40.591
5.200	1760.94	- 52.47	-40.309	49.8480	0.2266	-45.980
5.400	1749.64	- 60.57	-42.785	49.4618	0.2253	-49.241
5.600	1736.68	- 69.24	-46.136	49.0194	0.2238	-52.836
5.800	1721.88	- 78.92	-50.360	48.5154	0.2221	-56.754
6.000	1705.04	- 89.60	-55.459	47.9432	0.2201	-60.976
6.200	1685.97	-101.29	-60.507	47.2966	0.2179	-65.465
6.400	1664.46	-113.92	-64.581	46.5693	0.2154	-70.116
6.600	1640.37	-127.07	-67.681	45.7573	0.2125	-74.994
6.800	1613.60	-140.68	-69.806	44.8582	0.2094	-79.838
7.000	1584.07	-154.74	-70.957	43.8699	0.2060	-84.580
7.200	1551.68	-169.26	-71.134	42.7906	0.2022	-89.094

Temperature (K)	λ(watts m^{-1} k^{-1})
1500	109.6
1550	108.7
1600	107.8
1650	107.0
1700	106.1
1750	105.2

Specific Heat. The specific heat (C_p) measurements are made by subjecting the sample to a small step-function change in power after the sample has attained a stable condition. Voltage and current measurements are made as a function of time. The governing equation is:

$$C_p = [(E \cdot I)_t - (E \cdot I)_{eq}]/m\ (dT/dt)$$

where m is the mass and the subscripts "eq" and "t" refer to equilibrium and transition conditions, respectively. The current may be increased, in which case $(E \cdot I)_t$ is greater than $(E \cdot I)_{eq}$ and dT/dt is positive (heating curve) or the current may be decreased in which case $(E \cdot I)_t$ is less than $(E \cdot I)_{eq}$ and dT/dt is negative (cooling curve). In practice both heating and cooling data were taken over the same temperature interval. Several hundred data points were taken over a short interval (usually about six seconds). The temperature was determined from the resistivity and dT/dt was determined by fitting temperature-time data to curves and differentiating and by determining $dT/d\rho$ and $d\rho/dT$ at each point and multiplying these terms together. The results for a typical run are given in Table 2.

Results

Electrical Resistivity. The electrical resistivity results, uncorrected for expansion, are plotted in Fig. 1. These values can be approximated within a standard deviation of 0.21 microhm cm by the equation

$$\rho(\mu\Omega\text{cm}) = -2.7626 + 0.2511377 \times 10^{-1}T + 0.2440221 \times 10^{-5}T^2 - 0.7974080 \times 10^{-10}T^3 \qquad 1150 < T < 2650$$

over the range 1150 to 2650 K. In the range from 300 to 800 K, the resistivity can be approximated within a standard deviation of 0.021 microhm cm by the equation

$$\rho(\mu\Omega\text{cm}) = -0.223865 + 0.1537791 \times 10^{-1}T + 0.1400266 \times 10^{-4}T^2 - 0.43543094 \times 10^{-8}T^3 \qquad 300 < T < 800$$

The electrical resistivity values given for SRM 799 [1] with an uncertainty of ±2 percent [1], also uncorrected for expansion, are within 1 percent of the present results.

Thermal Conductivity. The thermal conductivity results are plotted in Fig. 2. These values are smoothed to give the best representation of the thermal conductivity values and the smoothed results are also plotted in Fig. 2. The smoothed results lie above both the SRM certification [1] and TPRC recommended [7] curves below 2400 K and between these two curves above this temperature. However, the present curve is well within the combined uncertainties of the present curve and either recommended curve over the entire temperature range. The smoothed values were corrected for thermal expansion (which in the present case was a $(1 + \Delta L/L_0)^{-3}$ correction factor [8]) and the corrected results are included in Fig. 2. The corrected curve can be represented by the equation

$$\lambda(W \cdot M^{-1}K^{-1} = 148.60 - 0.40332 \times 10^{-1}T + 0.11161 \times 10^{-4}T^2 - 0.14644 \times 10^{-8}T^3 \pm 0.08 \qquad 1200 < T < 3000$$

The corrected results are between the NBS and TPRC [8] recommended values (both of which are uncorrected for expansion) between 1200 and 2400 K, but decrease below the TPRC curve at 2400 and is

Table 2 Specific heat results for run TUCOOL

E (volts)	I (amps)	Time (sec)	RHO (μΩcm)	TEMP (K)	dT/dt (K/sec)	$E \cdot I_{eq}$ (W)	$C_p^{\ 1}$ (W sec $gm^{-1}K^{-1}$)	$C_p^{\ 2}$ (W sec $gm^{-1}K^{-1}$)
0.1689	118.66	0.00	59.78	2093.5	-62.22	52.21	0.1782	0.1780
0.1671	118.64	0.296	59.17	2075.7	-58.66	50.06	0.1775	0.1774
0.1655	118.64	0.592	58.59	2058.8	-55.40	48.09	0.1768	0.1767
0.1640	118.64	0.887	58.05	2042.8	-52.41	46.27	0.1761	0.1761
0.1625	118.63	1.184	57.53	2027.8	-49.65	44.61	0.1755	0.1756
0.1611	118.63	1.479	57.05	2013.5	-47.08	43.07	0.1751	0.1751
0.1598	118.63	1.775	56.58	1999.9	-44.69	41.64	0.1747	0.1747
0.1586	118.63	2.071	56.15	1987.0	-42.47	40.33	0.1743	0.1743
0.1574	118.63	2.367	55.73	1974.7	-40.40	39.10	0.1740	0.1740
0.1563	118.63	2.663	55.34	1963.1	-38.48	37.96	0.1737	0.1737
0.1552	118.63	2.959	54.96	1951.9	-36.69	36.90	0.1733	0.1733
0.1542	118.63	3.255	54.61	1941.3	-35.03	35.90	0.1730	0.1730
0.1533	118.63	3.550	54.26	1931.2	-33.48	34.97	0.1726	0.1726
0.1523	118.63	3.846	53.94	1921.5	-32.03	34.09	0.1722	0.1722
0.1515	118.62	4.142	53.63	1912.2	-30.27	33.27	0.1718	0.1718
0.1506	118.62	4.348	53.33	1903.4	-29.33	32.50	0.1716	0.1716

Diameter = 0.1253 cm
Density = 19.285 gm cm^{-3}
Length = 1.89404 cm

$C_p^{\ 1}$ calculated with dT/dt = (dT/dρ)(dρ/dt)

$C_p^{\ 2}$ calculated with dT/dt determined directly

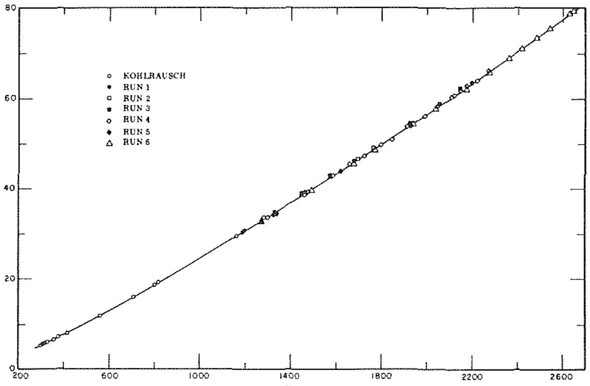

Fig. 1 Electrical resistivity of tungsten

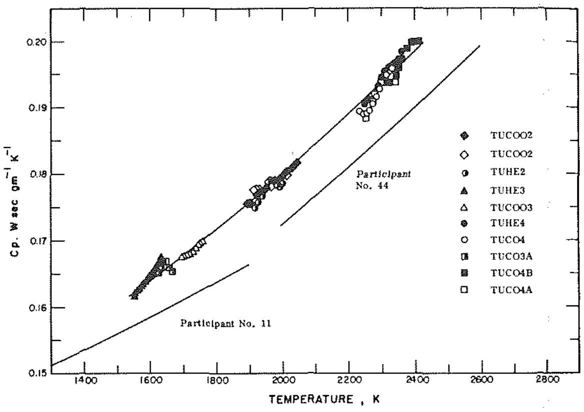

Fig. 3 Specific heat

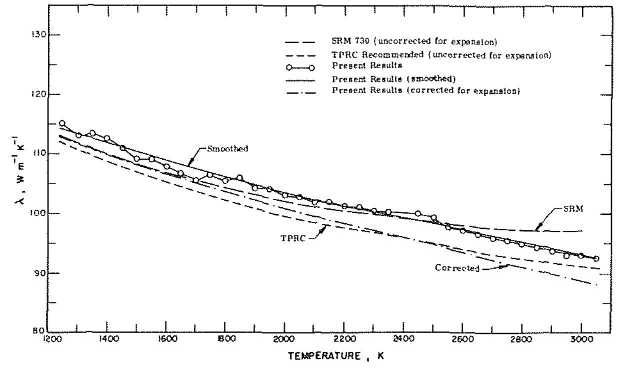

Fig. 2 Thermal conductivity

three percent below the TPRC curve and nine percent below the NBS curve at 3000 K.

Specific Heat. The specific heat results are plotted in Fig. 3. Ten heating or cooling runs were made. Runs designated "HE" are heating runs, and runs designated "CO" are cooling runs. Heating and cooling rates at the same temperature were usually about a factor of two different, but the results were in excellent agreement (Fig. 3). Smoothed values for the specific heat can be represented by the equation

$$C_p = 0.0956 + 0.621586 \times 10^{-4}T - 0.197747 \times 10^{-7}T^2 + 0.42197 \times 10^{-11}T^3$$

within a maximum deviation of 0.1 percent and a standard deviation of 0.00006. Specific heat values calculated from the equation are provided in Table 3. The results are compared to those obtained by AGARD participants [2] on sintered tungsten in Fig. 3. The present results are in good agreement with participant no. 44.

Discussion

Three properties of the SRM tungsten were measured; ρ, λ, and C_p. The major errors associated with the resistivity measurements are the temperature measurement and the diameter measurement. The inaccuracy with the temperature measurement is ±5° at 1200 K increasing to ±13° at 2600 K or 0.5 percent. The diameter measurement is accurate to one part in 1250 but enters as a square term leading to a 0.16 percent uncertainty. All other errors are much smaller than these two so the maximum inaccuracy is ±0.7 percent.

The inaccuracies of the thermal conductivity measurements have been discussed in detail in a critical evaluation [9]. From this evaluation, updated to account for recent imporvements in the software, it is concluded that the smoothed values are accurate within ±2 percent from 1250 to 3050 K.

The accuracy of the specific heat values is controlled by the accuracy of the derivative dT/dt. Consequently this quantity is determined by two different methods and the results (Table 2) are generally

Table 3 Properties of sintered tungsten corrected for thermal expansion

Temp. K	$\rho \times 10^{-8}$ (Ωm)	λ (W m^{-1} K^{-1})	$C_p \times 10^{-3}$ (W·sec·m^{-1} K^{-1})	L x 10^8 (WΩK^{-2})	$\alpha \times 10^4$ (m^{2}sec^{-1})
1300	34.002	111.8		2.925	
1350	35.577	110.9		2.921	
1400	37.164	110.0		2.919	
1450	38.762	109.1		2.917	
1500	40.372	108.2		2.913	
1550	41.993	107.4	0.1602	2.911	0.3544
1600	43.626	106.6	0.1618	2.906	0.3484
1650	45.257	105.9	0.1633	2.904	0.3429
1700	46.925	105.0	0.1649	2.898	0.3374
1750	48.591	104.3	0.1665	2.895	0.3320
1800	50.269	103.6	0.1681	2.893	0.3270
1850	51.958	102.9	0.1697	2.890	0.3221
1900	53.659	102.1	0.1713	2.884	0.3169
1950	55.370	101.5	0.1730	2.881	0.3120
2000	57.093	100.9	0.1746	2.880	0.3077
2050	58.827	100.2	0.1763	2.875	0.3029
2100	60.572	99.5	0.1781	2.871	0.2981
2150	62.329	98.9	0.1798	2.868	0.2939
2200	64.096	98.3	0.1816	2.864	0.2893
2250	65.875	97.7	0.1835	2.860	0.2848
2300	67.665	97.1	0.1853	2.857	0.2807
2350	69.466	96.4	0.1873	2.850	0.2760
2400	71.279	95.8	0.1893	2.846	0.2717
2450	73.103	95.3		2.842	
2500	74.937	94.7		2.838	
2550	76.784	94.1		2.833	
2600	78.641	93.5		2.828	

in very good agreement (0.2 percent). The overall accuracy of the smoothed data should be within 1.5 percent.

The values of ρ, λ, and C_p corrected for expansion at even temperature intervals are given in Table 3. These values are used to generate two additional properties "L" (Wiedemann-Franz-Lorenz ratio) and "α" (thermal diffusivity). These values are included in Table 3. The classical value of L for good metals is $2.44 \times 10^{-8} V^2 K^{-2}$, so the value for tungsten is about 20 percent above the classical value. An increase in the value of L above the classical value is often attributed to phonon conduction. However, in the present case, the increased value is probably due to an additional electronic contribution since the temperature dependency of L above 1300 K is very small and a significant phonon conduction would lead to an appreciable decrease in the value of L.

Calculated values of the thermal diffusivity decrease from 0.354 $\times 10^{-4} m^2 s^{-1}$ at 1550 K to 0.272 $\times 10^{-4} m^2 s^{-1}$ at 2400 K. This follows the results of one of the AGARD participants who measured thermal diffusivity, but is contrary to the general trend which had a much smaller temperature dependency than the present results (Fig. 4).

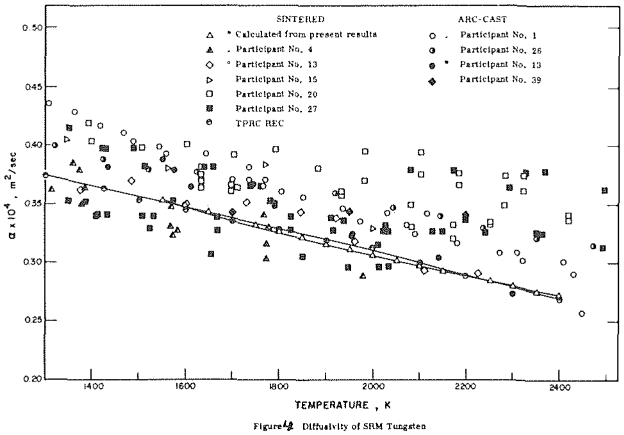

Fig. 4 Diffusivity of SRM tungsten

References

1 Hust, J. G., and Giarratano, P. J., "Standard Reference Materials: Thermal Conductivity and Electrical Resistivity Standard Reference Materials: Tungsten SRM'S 730 and 799, from 4 to 3000K," NBS Publication 260-52, September 1975.

2 Fitzer, E., "Thermophysical Properties of Solid Materials, Project Section II, Cooperative Measurements on Heat Transport Phenomena of Solid Materials at High Temperatures," AGARD-R-606, March, 1973, Available from NTIS.

3 Minges, M., "Evaluation of Selected Refractories as High Temperature Thermophysical Property Calibration Materials," AFML-TR-74-96, August, 1975.

4 Powell, R. W., and Taylor, R. E., "Multi-Property Apparatus and Procedures for High Temperature Determinations," *Revue Internationale Hautes Temperatures et des Refractaires,* Vol. 7, 1970, pp. 298–304.

5 Taylor, R. E., Davis, F. E., and Powell, R. W., "Direct Heating Methods for Measuring Thermal Conductivity of Solids at High Temperatures," *High Temperature-High Pressures,* Vol. 1, 1970, pp. 663–673.

6 Rice, J. R., Pyrodynamics, Vol. 6, pp. 231–256, 1968.

7 Ho, C. Y., Powell, R. W., and Liley, P. E., "Thermal Conductivity of the Elements," *J. Phys. Chem. Ref. Data,* Vol. 1, Ser. 2, 1972, pp. 279–421.

8 Taylor, R. E., "On Correcting Thermophysical Property Data for Thermal Expansion Effects," *Proceedings of the 15th International Thermal Conductivity Conference* IFI/Plenum, New York (in preparation).

9 Taylor, R. E., and Hartge, L. C., Jr., "Evaluation of Direct Heating Methods for Measuring Thermal Conductivity of Solids at High Temperatures," *High Temperatures-High Pressures,* Vol. 2, 1970, pp. 641–650.

R. G. Bennett
Graduate Student.

M. W. Golay
Associate Professor.
Mem. ASME

Dept. of Nuclear Engineering, Massachusetts
Institute of Technology, Cambridge, Mass.

Interferometric Investigation of Turbulently Fluctuating Temperature in an LMFBR Outlet Plenum Geometry

A novel optical technique is developed for the measurement of turbulently fluctuating temperature is a transparent fluid flow. The turbulent sodium mixing in the ANL $^1/_{15}$-scale FFTF outlet plenum is investigated with a scale-model outlet mixing plenum, using flows of air. The electrical analogue and the power spectral density of the fluctuating temperature are observed experimentally at seven stations in the flow.

Introduction

The conservative design of nuclear reactor structural components, guarding against thermal transients in the upper mixing plenum of liquid-metal-cooled fast-breeder reactors (LMFBRs), requires a predictive knowledge of the turbulent sodium mixing. Specifically, the eddy diffusivity of heat, ϵ_{Hij}:

$$\epsilon_{Hij}(\underset{\sim}{x}) \equiv \frac{\langle T(\underset{\sim}{x}, t) v_i(\underset{\sim}{x}, t)\rangle}{\langle \partial T(\underset{\sim}{x}, t)/\partial x_j \rangle} \tag{1}$$

describes the turbulent mixing that lessens thermal shock on the structural components. The eddy diffusivity of heat is often expediently defined in terms of conveniently known quantities [1][1] that fall short of describing the mixing accurately. Calculation of the eddy diffusivity of heat from equation (1) demands the mapping of the turbulently fluctuating temperature and velocity for any particular flow geometry.

This paper approaches the LMFBR turbulent sodium mixing problem with a transparent fluid scale model, measuring the fluctuating temperature by a novel optical method. The fluctuating velocity is not measured in this paper, but could be found with standard Laser-Doppler anemometry techniques. This combination of optical systems could achieve the extremely fast time response needed to follow faithfully the turbulent fluctuations, while not intruding into the flow and disturbing its structure.

The recently developed [2, 3] optical system for temperature measurements uses a Mach-Zehnder interferometer [4] of extremely short field (about 0.5 mm) in real time. Due to the short field and other considerations, the instrument defines a temperature sensitive volume of 1 mm^3. The detector system produces a nearly linear electrical analog of the fluctuating temperature over most of the 67°C (120°F) range of the instrument. The frequency response range is greater than 10 kHz for the inexpensive photodetector used in this work. The average temperature is not currently available from this optical technique, but could be incorporated into the analog temperature signal by simply biasing the analog with an appropriate dc voltage. The average temperature is measured mechanically at a symmetrical, but remote, station in the flow.

The experiments reported seek to establish the capabilities of the temperature measurement technique and to visualize the transport and mixing of heat in a $^1/_{15}$-scale Fast Flux Test Facility (FFTF) outlet plenum model. The experimental results are not meant to be conclusive with regard to LMFBRs; rather, the results will be used to validate a computer code for plenum flows that is currently under development for LMFBR analysis.

The characterization of the turbulent temperature proceeds with photographic studies of the electrical temperature analogue; Fourier analysis of the analogue yields data regarding the power spectral density of the fluctuating temperature.

Optical Technique

The optical technique developed in this work requires that the flowing fluid be transparent. A flow of water is unsuitable in this application due to the large variation of the index of refraction of water with temperature, which would require that the thickness of the test cell be less than 100 μm. A flow of air is much more suitable; the exact thickness that is required is developed later in this section. Also, the Prandtl number for air is about $^1/_{10}$ that of water at room temperature,

---

[1] Numbers in brackets designate References at end of paper.

Contributed by the Heat Transfer Division for presentation at the Winter Annual Meeting, New York, N. Y., December 5, 1976 of THE AMERICAN SOCIETY OF MECHANICAL ENGINEERS. Manuscript received at ASME Headquarters August 18, 1976. Paper No. 76-WA/HT-82.

which makes air closer to, though admittedly very far from, liquid sodium as a heat-transfer medium.

The index of refraction of air varies, most importantly, with its temperature and pressure. The variation is quite small, being about 1×10^{-6} per °C with temperature [5], and about 3×10^{-7} per millibar with pressure.[2] In this paper, the Mach-Zehnder interferometer is used as a differential refractometer [6] in which an extremely sensitive measurement is made of the *difference* of the index of refraction between a test fluid and a standard fluid. The design of the experiments imposes the responsibility for insuring that the temperature fluctuations always induce a much larger effect than the pressure fluctuations.

The Mach-Zehnder interferometer is shown schematically in Fig. 1. The incident monochromatic light ray divides in amplitude in the first beamsplitter; the rays reflect in their own mirrors, and recombine at the second beamsplitter. If the rays encounter different conditions in the two cells through which they pass, their phases will generally differ, and they will interfere when recombined. All of the mirrors and beamsplitters are mutually parallel, and the two arms are of equal *geometrical* length. The *optical* path lengths experienced by the rays are governed by the refractive indices of the media through which the respective rays pass, as either $\int_{OA'B} n(s)ds$ or $\int_{OAB} n(s)ds$. With ideal optical components, total destructive interference of the two rays occurs when the condition [7]

$$\oint_{OABA'O} n(s)ds = \pm m \frac{\lambda_0}{2} \qquad (2)$$

is satisfied, where odd integer values of m are the "order of interference." The transmitted intensity generally obeys the relation:

$$I = I_0 \cos^2 \left[\frac{\pi}{\lambda_0} \oint n(s)ds \right] \qquad (3)$$

The argument of equation three must be kept within a range of $\pi/2$ as the idex of refraction in the test cell fluctuates, so that the analogue output intensity will correspond to a single value of the temperature. Further, the analogue intensity is linear only in a broad range about the half-maximum of equation (3). To illustrate these points the interferometer characteristic (equation (3)) is sketched on the right-hand side of Fig. 2. From these considerations, the maximum temperature range of the instrument should be specified to be somewhat larger than the expected range of the temperature fluctuations, so that the analogue fluctuations will be linear; the maximum permissible thickness of the test cell is then governed by this maximum temperature range through equation (2). For this work, the temperature fluctuations ranged through approximately 45 Centigrade degrees, and the maximum range of the instrument is 67°C above the ambient air temperature. The inside thickness of the test cell is 0.64 cm (0.025 in.), which corresponds to the first minimum condition ($m = 1$) of equation (2) for a uniform temperature distribution over the thickness of the test cell.

Schlieren effects, which can cause a misalignment of the interferometer in several ways, have been considered, and they have been found to produce less than 1 percent error in the temperature analogue.

The analogue output intensity of the interferometer is detected by a simple battery-powered photoconductive diode circuit. The characteristic curve of the photodiode is included on the left-hand side of Fig. 2. In Fig. 2, a uniform test cell temperature of 33°C above ambient corresponds to a detector voltage of about 8 V. The nonideal fringe contrast is entirely suppressed with the oscilloscope preamplifier so that the display of the electrical analogue is always a full-scale waveform of $\cos^2[(\pi/\lambda_0) \oint n(s)ds]$. In the work being reported, the electrical analogue is displayed on a storage oscilloscope and recorded via still photography. Additionally, the power spectral density of the analog is measured electronically, and recorded similarly with still photography.

Experiments

The Argonne National Lab (ANL) $^1\!/_{15}$-scale FFTF liquid sodium *test loop is the standard geometry for the flow experiments.* A cross section of the cylindrical ANL test loop is represented by the thin (0.63-cm inside gap width) test assembly of Fig. 3. The positioning of the optical components about the test cell is shown in Fig. 4.

The average recirculating flow pattern in the test cell must be re-

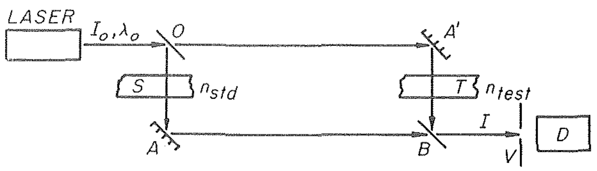

Fig. 1. Mach-Zehnder interferometer applied to temperature measurements. A, A'—mirrors; O, B—beamsplitters; D—photodiode detector system; V—variable aperture; S—standard cell with index of refraction n_{std}; T—test cell with index of refraction n_{test}. The initial laser intensity I_0 is reduced to intensity I by the interferometer.

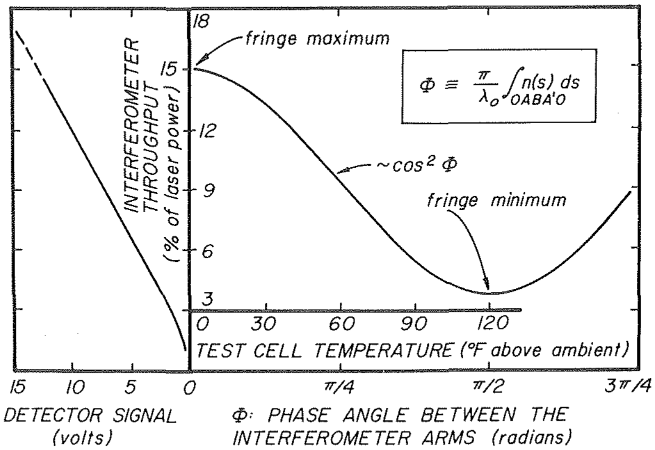

Fig. 2. Visualization of parameters for interferometric temperature measurements. The interferometer characteristic curve on the right and the photodetector characteristic curve on the left share the interferometer throughput as a common axis.

---

[2] This is the value of the derivative of the Biot and Arago formula (5) with respect to pressure at STP.

Nomenclature

I = intensity of the light transmitted by the interferometer, mW/cm^2

I_0 = the maximum interferometer throughput, expressed as an intensity, mW/cm^2

m = the order of interference, an odd integer

$n(s)$ = index of refraction at the path length, s

n_{std} = index of refraction of the ambient air

n_{test} = index of refraction in the test cell

t = time, s

$T(\underline{x}, t)$ = fluctuating temperature at point $\underline{x}$, °C

$v_i(\underline{x}, t)$ = fluctuating velocity in the x_i direction at point $\underline{x}$, cm/s

$\epsilon_{Hij}(\underline{x})$ = eddy diffusivity of heat, a second rank tensor, cm^2/s

λ_0 = wavelength of the laser beam, 6328×10^{-8} cm

$\langle \ldots \rangle$ denotes averaged over time

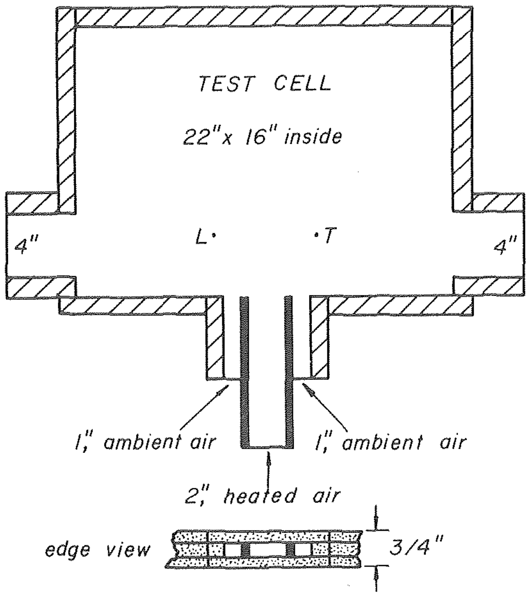

Fig. 3. Test cell dimensions. The test cell is constructed entirely of 0.64-cm (0.25-in.) laminated plexiglass. *L*—typical laser measurement station; *T*—typical thermocouple measurement station.

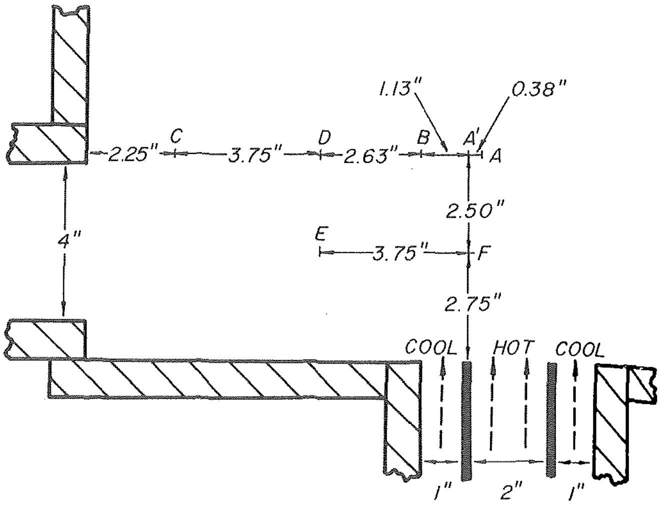

Fig. 5. View of the seven interferometric temperature measurement stations in the test cell of Fig. 3. The average temperatures at the stations during rated flow conditions are listed in Table 1.

Table 1 Average temperatures during steady flow heating

Re = 9300
Ambient inlet at 65°F
Heated inlet at 155°F

Station	Average Temperature °F	°C
A	117	47
A'	109	43
B	79	26
C	76	25
D	65	18
E	65	18
F	104	40

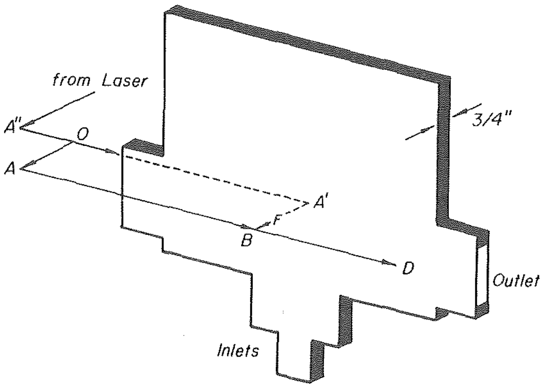

Fig. 4. View of the optical components (from Fig. 1) and the test cell (from Fig. 3). All of the optics are outside of the test cell, and the temperature is being measured at station F (see Fig. 5). A" is a mirror. The inlets and outlets are connected to large hoses for the experiments.

stricted to two dimensions in order to facilitate the temperature measurements. The test assembly is slightly larger than the ANL model in order to permit large Reynolds numbers, while decreasing the large flow rates. Even so, an entrance velocity of air of 119 m/s (390 ft/s) is needed to match the ANL inlet Reynolds numbers. The Reynolds numbers of the air flows investigated are about ten times smaller than those of the ANL model.

The experiments investigate the steady mixing of hot and cold coflowing inlet streams. The central 5-cm (2-in.) inlet admits hot air at about 56°C (100°F) above ambient. The two adjacent 2.5-cm (1-in.) inlets admit ambient air. The difference in the average temperatures of the inlet flows is referred to as the *inlet temperature upset*. The entire flow is maintained by ¼-hp blower, with about half of the flow being heated before entering the central inlet. Heated inlet Reynolds numbers of 10,000 and 20,000 are investigated. The inlet air velocities are matched with the flow heater turned off. When the central flow of air is heated, its velocity increased along with its specific volume, and shearing of the hot and cold inlet flows takes place. The effect of this flow slip on the average recirculating flow properties is not known accurately.

Due to the heating of the test cell walls, an unknown phase angle is opened between the arms of the interferometer. The rate of variation of the index of refraction of plexiglass with temperature is several orders of magnitude larger than that for air. This slow (but large) variation completely masks a measurement of the average temperature in the flow. Additionally, free convection of the air outside of the test cell introduces another slowly fluctuating phase angle, but this is greatly suppressed by wrapping the entire interferometer in thick fiberglass insulation, especially near the warm test cell. The turbulence of the flow within the cell produces a smaller but much faster variation in the analogue output intensity. This work seeks to examine only this rapidly fluctuating analogue and rejects the time-average of the analogue as spurious information since it includes the wall heating and uses a separate measurement of the average temperature to replace the mean. The symmetry of the test cell is exploited by placing a thin thermocouple in the flow at a station that is symmetric with respect to the laser station (see Fig. 3). A fine chromel-alumel thermocouple protrudes into the middle of the test cell through a 1.6-mm ($^1/_{16}$-in.) dia hole in the front face of the cell. The thermocouple wires are 28-gauge, or 0.40 mm (0.0156 in.) in diameter.

Experimental Results

Temperature Analogue Traces. Several illustrative traces of the temperature analogue are presented here. Fig. 5 presents a closeup view of the lower left-hand portion of the test cell shown in Fig. 3, and it serves as a key to the seven laser measurement stations of the study. Table 1 includes the representative average temperatures at the seven stations under typical running conditions.

A typical noise trace (taken at station F) is presented in Fig. 6. The noise is independent of the particular station, and it shows a moderate frequency (several hundred Hz) ripple due to the motor-induced acoustical vibrations of the optical components of the interferometer. The noise generally represents a ±3°C (5°F) error in the temperature signal. An equally strong source of low-frequency noise in the data is due to the shaking of the building. However, due to the very short (10 ms) duration of the data trace, the shaking of the building (of the order of 10 Hz) cannot be seen. These errors in the temperature analogue are certainly not fundamental, and can be reduced with more careful isolation of the interferometer. Note carefully that the ordinates of the temperature traces are nonlinear—they are obtained from an inversion of equation (3), and they are very nearly linear in the *central* 33°C range.

The two most vigorously fluctuating traces observed at Re = 10,000 are presented in Figs. 7 and 8. The data of Fig. 7 are taken at station F, which is closest to the confluence of a hot and a cold inlet stream. The 40°C average temperature at station F (see Table 1) is very close to the mean temperature of the two streams, and the trace exhibits a very strong 300 Hz character. The trace is very suggestive of the initially uniform breakup of a shearing flow. A power spectral density trace of this signal is presented in the next section. The data of Fig. 8 are taken from station B, which is further along in the flow. The data trace has a much more random character and is representative of the traces obtained at stations A and A′, which differ only slightly from this data trace. The data trace taken at station C (not presented here) exhibits much less mixing. Note that station C is much farther along on the average streamlines of the recirculating flow of Fig. 3. The traces from stations D and E (also not presented here) show no measurable fluctuations above background noise. This is in agreement with the average temperatures for stations D and E quoted in Table 1, which hover near the ambient inlet temperature during the experiments.

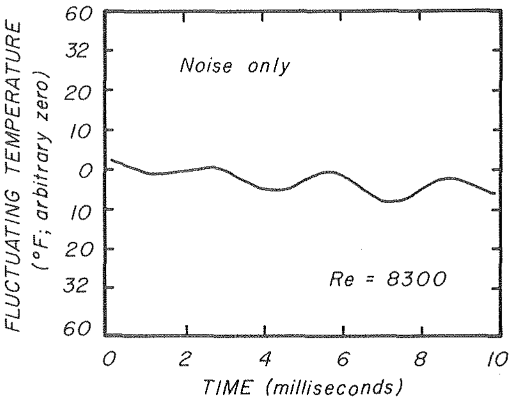

Fig. 6. Noise in the temperature analogue; Re = 8300, and all of the inlets are at ambient temperature. The nonlinear ordinate is discussed in the text.

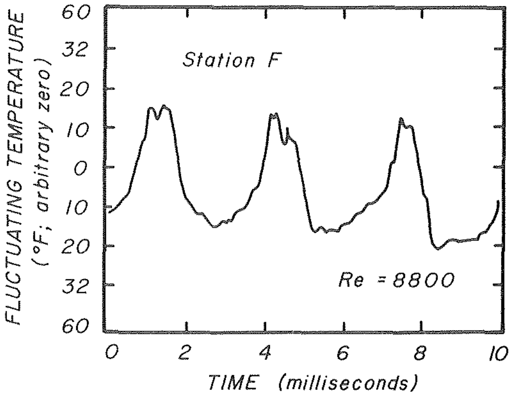

Fig. 7. Temperature trace at station F (see Fig. 5); Re = 8800, and the heated inlet is at 47°C (85°F) above ambient. The nonlinear ordinate is discussed in the text.

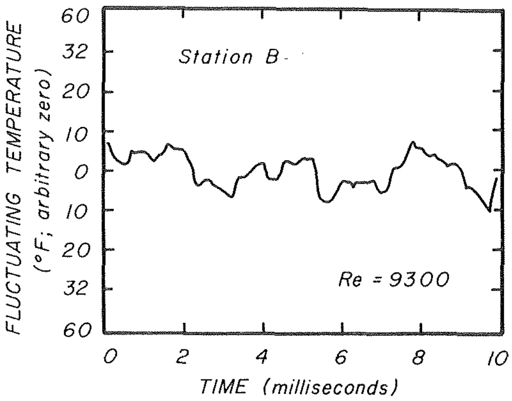

Fig. 8. Temperature trace at station B (see Fig. 5); Re = 9300, and the heated inlet is at 47°C (85°F) above ambient. The nonlinear ordinate is discussed in the text.

Power Spectral Densities. Several traces of the power spectral densities are also presented. Separate power spectral density (PSD) measurements are made of the temperature analogue and of the background noise trace at each station. The background root-mean-square fluctuation at each frequency value is subtracted from the root-mean-square fluctuation data curve of the temperature analogue in order to correct for the noise signal. The resultant PSD curves are normalized to unit area. Some error is introduced during the normalization because the *full* range of the PSD data is not determined experimentally. The composite error in the PSD curves is about 30 percent. Generally, the PSD technique suffers from short sampling times, but the qualitative behavior shown by the results is clear.

The PSD curves for stations F and B are presented in Figs. 9 and 10, respectively. The spectral bandwidths of all of the various components in the temperature analogue are shown in Fig. 11. It is found that the Fourier analysis is especially noise-free above several hundred Hertz. The PSD data curve at station F (Fig. 9) exhibits a strong 300 Hz component and a harmonic of substantially less magnitude. A significant PSD signal persists well into the kHz range, even at this relatively low Reynolds number of 8800. The PSD data curve at station B (Fig. 10) shows the reduced intensity of the 300 Hz component and the decay of the higher frequencies as the flow progresses. Note that both of the PSD curves do not resolve the low-frequency behavior of the analogue signal due to the high noise level, while the high-frequency behavior is very well represented; this is quite contrary to the usual fast-response temperature measurement results [8, 9].

Inlet Temperature Upset. Several PSD data curves at various inlet temperature upsets are shown in Fig. 12. The data of all of these curves are taken at station A′. The inlet temperature upset is found to have no measurable effect on the spectral distribution of the PSD, at least for stations similar to A′. That is, the turbulent mixing in these experiments is not measurably enhanced with the additional buoyant forces. Note that the higher Reynolds number (Re = 19,000) in this experiment causes the PSD to extend to considerably higher frequencies than the Re = 8800 results of Fig. 9.

The information foregone by normalizing the PSD curves to unit area[3] has been regained in a different experiment. The spectrum analyzer is stopped at 1500 Hz, and is used to measure the value of the Fourier component at 1500 for different values of the inlet temperature upset. This frequency is chosen because the measurement technique is most sensitive at this value, i.e., the highest signal-to-noise ratio is obtained here. The output data fluctuations are smoothed for several seconds in an integrating circuit, and the resulting data are plotted as a function of the applied temperature upset in Fig. 13. Two separate regressions are quoted in Fig. 13. They indicate that the rms fluctuation (at 1500 Hz) increases very nearly lin-

---

[3] The PSD curves have unit area by convention.

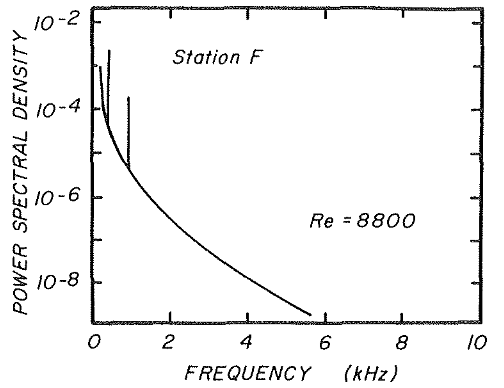

Fig. 9. Power spectral density curve at station F (see Fig. 5); Re = 8800 and the heated inlet is at 49°C (88°F) above ambient.

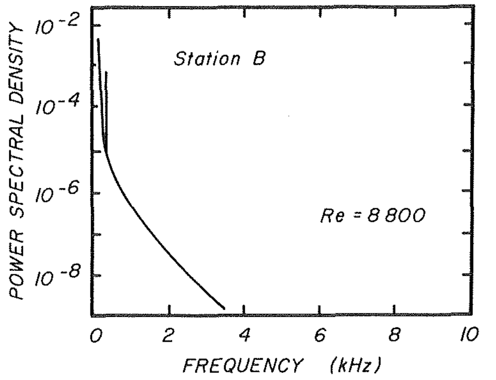

Fig. 10. Power spectral density curve at station B (see Fig. 5); Re = 8800, and the heated inlet is at 44°C (80°F) above ambient.

early with the temperature upset. Note that the inlet temperature upset may affect the average flow pattern in the test cell.

Conclusions

The following conclusions have been derived in this work.

1 The temperature measurement method presented in this paper is an effective, and potentially a very accurate, way to implement an unintrusive turbulent temperature measurement.

2 The accuracy of the temperature analogue, in its linear region, is about ±3°C (5°F), with most of the noise originating from building vibrations and room noise affecting the interferometer. The accuracy may be improved in a straightforward manner, by seeking a quieter room and by upgrading the quality of the optical bench. A special geometry for the incorporation of feedback to stabilize the system and to refine the temperature analogue has been considered [10].

3 The frequency response of the temperature analogue is limited only by the choice of the photodetector. For the inexpensive detector in this work, the frequency response range is greater than 10 kHz.

4 The fluctuating temperature has a strong position dependence in the test cell. A large 300 Hz component in the power spectral density is generated in the inlet shearing layer, and it decays as the flow progresses along the average streamlines. This component is probably stimulated by a forced vibration of the inlet air columns; this is suggested by considering the typical velocity and lengthscales at the inlets.

5 The results demonstrate that the temperature upset in the test cell does not drive any measurable instabilities in the flow with buoyant forces. In effect, the temperature serves only to "color" the turbulent mixing that is driven almost solely by the shearing of the inlet flows.

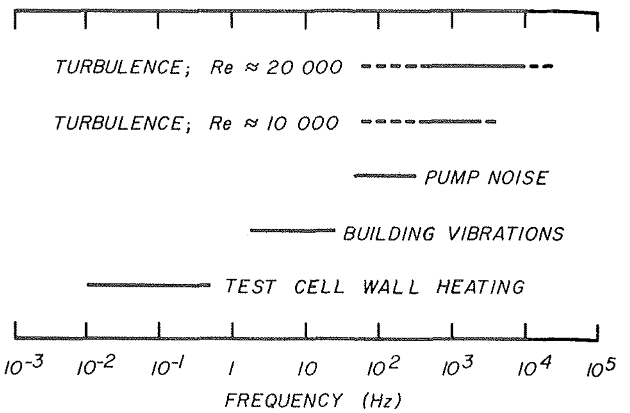

Fig. 11. Frequency bandwidths of the component signals in the temperature analogue. The three lower bands are all sources of noise in the analogue. The solid portions of the two upper bands show the frequencies observed in the turbulent mixing experiments.

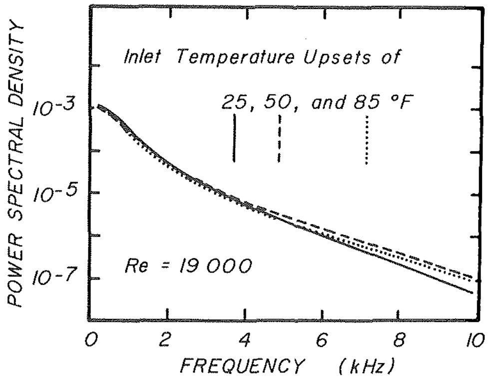

Fig. 12. Power spectral density curves at various inlet temperature upsets. The curves were found at station A′.

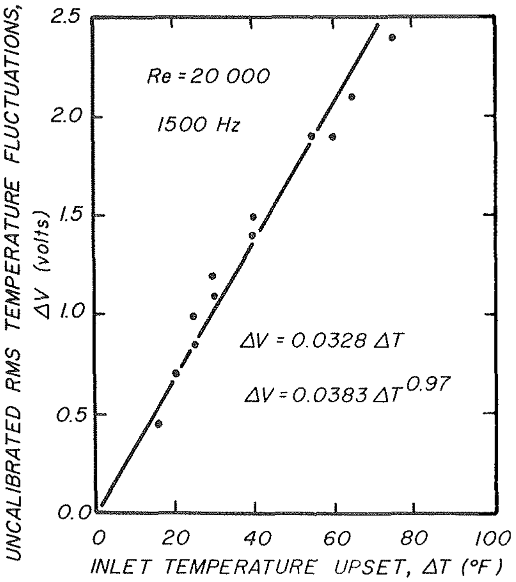

Fig. 13. Variation of the rms fluctuation (measured as ΔV) in the temperature signal at 1500 Hz versus the applied inlet temperature upset. The data are modeled by the two different regressions in the figure. The solid curve is the linear regression.

Acknowledgment

This research was conducted as part of the "Coolant Mixing in LMFBR Rod Bundles Project," contract AT(11-1)-224 sponsored by the U.S. Energy Research and Development Administration.

References

1 Johannsen, K., "Heat Transfer Analysis of Reactor Fuel Rod Bundles," Notes E.1–4, MIT Course 22.313, Spring, 1975.

2 Bennett, R. G., and Golay, M.W., "Development of an Optical Method for Measurement of Temperature Fluctuations in Turbulent Flows," *Transactions of the American Nuclear Society,* Vol. 22, Nov. 1975, p. 581.

3 Miller, A., Hussmann, E. K., and McLaughlin, W. L., "Interferometer for Measuring Fast Changes of Refractive Index and Temperature in Transparent Liquids," *Review of the Scientific Instruments,* Vol. 46, No. 12, Dec. 1975, pp. 1635–1638.

4 Born, M., and Wolf, E., *Principles of Optics,* 5th ed., Pergamon Press, New York, 1975, pp. 213–315.

5 Forsythe, W. E., *Smithsonian Physical Tables,* 9th ed., Smithsonian Institute, Washington, D.C., 1956, Tables 553 and 554.

6 Fishter, G. E., "Refractometry," *Applied Optics and Optical Engineering,* Vol. 4, Kingslake, R., ed., Academic Press, New York, 1967, p. 375.

7 Cook, A. H., *The Interference of Electromagnetic Waves,* Clarendon Press, Oxford, 1971, p. 78.

8 LaRue, J. C., Deaton, T., and Gibson, C. H., "Measurement of High-Frequency Turbulent Temperature," *Review of the Scientific Instruments,* Vol. 46, No. 6, June 1975, pp. 757–764.

9 Hughes, G., "Detection of Rapid Electrical Conductivity Fluctuations in High Temperature Liquid Metals," *Journal of Physics E: Scientific Instruments,* Vol. 5, April 1972, pp. 349–353.

10 Bennett, R. G., and Golay, M. W., "Interferometric Investigation of Turbulently Fluctuating Temperature in an LMFBR Outlet Plenum Geometry," MIT Report C00-2245-29TR, May 1976.

M. Hishida
Professor

Y. Nagano
Lecturer

Nagoya Institute of Technology,
Showa-ku, Nagoya, Japan

Simultaneous Measurements of Velocity and Temperature in Nonisothermal Flows

A two-wire probe technique has been developed for the simultaneous and continuous measurements of instantaneous velocity and temperature in nonisothermal flows. The equations of the thermal equilibrium of two adjacent fine wires, one hot and one only a little above the fluid temperature, are solved by employing analog technique, wherein not only the difference of the heat transfer coefficients between two wires but also their variations with both the velocity and temperature are taken into consideration. The measuring system proposed in this study is founded on fairly strict principles of analysis and, hence, provides automatic compensation even for very large amplitude velocity and temperature fluctuations over a frequency range of d-c to six kHz.

Introduction

Simultaneous velocity and temperature measurements are essential in the experimental studies of heat transfer and combustion. In nonisothermal flows, an effect of varying temperature on a hot-wire anemometer output is comparable to that of varying velocity, so it is impossible to distinguish a single hot-wire anemometer output into its velocity and temperature components without additional information. Theoretically, these two kinds of components can be separated by using two fine wire probes operated in different modes. Analog circuits of the two probes can be designed so that simultaneous temperature and corrected velocity signals are made available. The relevant techniques hitherto reported [1-3][1], however, are still not satisfactory, because they involve a number of assumptions and abbreviations based on the underlying analytic principles concerned, which result in a lack of an automatic compensation system for the large velocity and temperature fluctuations and an excessive calibration procedure for the time constant setting.

The technique described here has been developed to permit the aforementioned problems to be solved. First, an analysis is given of the thermal behaviors of hot and cold fine wires, together with the underlying principle of compensation. Secondly, the complete compensation circuit and the setting procedure of circuit parameters are described. Finally, some results are given of measurements of the velocity and temperature in a nonisothermal flow of air.

Governing Equations

With the assumption of the uniform radial temperature distribution within a fine wire, the thermal equilibrium of the wire in a fluid of temperature t gives the following equation:

$$\pi r_0^2 c_w \gamma_w d\theta/d\tau + 2\pi r_0 h(\theta - t) - ji^2 R = 0 \tag{1}$$

where R denotes the electric resistance of the wire per unit length.

The temperature dependence of the wire resistance may be expressed as follows:

$$R = R_0\{1 + \beta(\theta - \theta_0)\} \tag{2}$$

With equation (2), rewriting equation (1) in terms of wire resistances gives:

$$\frac{r_0 c_w \gamma_w}{2h}\frac{dR}{d\tau} + \left(1 - \frac{ji^2\beta R_0}{2\pi r_0 h}\right) R = R_a \tag{3}$$

in which R_a denotes the wire resistance corresponding to an ambient fluid temperature t, i.e.,

$$R_a = R_0\{1 + \beta(t - \theta_0)\} \tag{4}$$

Heat Transfer from Fine Wires

The empirical relation evolved by Collis and Williams [4] is considered to express well the heat transfer rate from a fine wire to flow. However, for the sake of simplicity and convenience in the electronics, we use in this study the Kramers relation [5] describing a Nusselt number dependence on the square root of the Reynolds number, so that:

$$\mathrm{Nu}_f = 0.42\,\mathrm{Pr}_f^{0.2} + 0.57\,\mathrm{Pr}_f^{0.33}\,\mathrm{Re}_f^{0.5} \tag{5}$$

in which the fluid properties are to be evaluated at the film temperature $t_f = (\theta + t)/2$. When a wire of 5 μm dia is used in an air flow, equation (5) gives satisfactory results in the range of fluid velocity 3 m/s $< u <$ 30 m/s. If the fluid velocities are out of this range, it is recommended that we first process and arrange the data according

---

[1] Numbers in brackets designate References at end of paper.

Contributed by the Heat Transfer Division for publication in the JOURNAL OF HEAT TRANSFER. Manuscript received by the Heat Transfer Division November 15, 1977.

to the Kramers relation (5) and then correct the final results as required.

Heat transfer coefficient h derived from equation (5) becomes:

$$h = A + B\sqrt{u} \tag{6}$$

with

$$A = 0.42\,\mathrm{Pr}_f^{0.2}\lambda_f/2r_0$$
$$B = \frac{0.57\,\mathrm{Pr}_f^{0.33}\lambda_f}{(2r_0\nu_f)^{0.5}} = \frac{0.57(c_f\gamma_f\lambda_f)^{0.5}}{(2r_0)^{0.5}\mathrm{Pr}_f^{0.17}}$$

in which c, γ, and λ are the specific heat, the specific weight, and the thermal conductivity of fluid, respectively. For many gases, A is well approximated by the linear function of temperature t_f, while the variations of B with temperature are negligible (the converse being true for water). Hence we shall consider B to be constant and write A as follows:

$$A = A_0 + a(t_f - \theta_0) \tag{7}$$

For air and $\theta_0 = 0°\mathrm{C}$, $2r_0 = 5\,\mu\mathrm{m}$, for example, we obtain:

$$A = 1.63 \times 10^3 + 4.98\,t_f\ \mathrm{kcal/m^2}h°\mathrm{C}$$
$$B = 1.29 \times 10^3\ \mathrm{kcal/m^2}h°\mathrm{C}\sqrt{\mathrm{m/s}}$$

Basic Equations for Measurement with Two Fine Wires

In nonisothermal flows, the continuous signals of the velocity and temperature are not readily obtainable by a single hot-wire output. The simultaneous use of two wires operating in different modes, however, provides two simultaneous equations to solve for the velocity and temperature. While the combination of two wires yields various modes of operation, we shall confine ourselves to the simplest, i.e., one wire is operated as a constant temperature hot wire providing a signal with information on both the velocity and temperature, whereas the other is a cold wire operated with so low a current as to have a negligible current heating. We assume further both hot and cold wires consist of the same material with the same diameters, but resistances R_0 at a reference temperature θ_0 may differ from each other.

Considering that a hot wire keeps a resistance constant and a cold wire has a negligible current heating, the following equations for hot and cold wires are obtained from equation (3):

$$R_1 - R_{a1} - \frac{ji_1^2\beta R_{01}}{2\pi r_0 h_1}R_1 = 0 \tag{8}$$

$$\frac{r_0 c_w \gamma_w}{2h_2}\frac{dR_2}{d\tau} + R_2 - R_{a2} = 0 \tag{9}$$

where subscripts 1 and 2 refer to the hot and cold wires, respectively.

For the hot wire, multiplying equation (8) by constant current i_2, we get:

$$\frac{j\beta R_{01}i_2}{2\pi r_0 R_1 h_1}(i_1R_1)^2 = i_2R_1 - i_2R_{a1}$$

Writing

$$\epsilon = R_{a1}/R_{a2} = R_{01}/R_{02},\quad V_1 = i_1R_1,$$
$$V_2 = i_2R_2,\quad V_{a2} = i_2R_{a2},\quad V_{21} = i_2R_1$$

and substituting these into the above equation, we get:

$$2K_1h_1 = V_1^2/(V_{21} - \epsilon V_{a2}) \tag{10}$$

where K_1 is a constant given by:

$$K_1 = (\pi r_0/j\beta)(R_1/R_{01})/i_2 \tag{11}$$

In equation (10), V_1 refers to an output voltage of the hot wire and V_{a2} corresponds to a signal linearly related to fluid temperature, while ϵ and V_{21} are constants for given types of wires and for the pertinent operating conditions.

For the cold wire, upon multiplying equation (9) by constant i_2, we obtain the following relation:

$$V_{a2} = \frac{r_0 c_w \gamma_w}{2h_2}\frac{dV_2}{d\tau} + V_2 \tag{12}$$

in which V_2 refers to an output voltage of the cold wire. The quantities h_1 and V_{a2}, which are related respectively to the fluid velocity (as described in more detail in the next section) and to the fluid temperature, are obtainable by solving equations (10) and (12), provided that the relation between h_1 and h_2 is given.

In general, the difference in heat transfer coefficients between the hot and cold wires cannot be neglected because the relevant film temperatures differ considerably from each other. The heat transfer coefficients h_1 and h_2 are given by equations (6) and (7):

$$h_1 = A_0 + a(t_{f1} - \theta_0) + B\sqrt{u} \tag{13(a)}$$

$$h_2 = A_0 + a(t_{f2} - \theta_0) + B\sqrt{u}$$
$$\simeq A_0 + a(t - \theta_0) + B\sqrt{u} \tag{13(b)}$$

where

$$t_{f1} = (\theta_1 + t)/2 \text{ and } t_{f2} = (\theta_2 + t)/2$$

The approximation in equation (13(b)) is valid, provided $(\theta_2 - t)/2 \ll (t - \theta_0)$, which is generally true, since the difference between wire temperature θ_2 and fluid temperature t is very slight. From equations (13(a)) and (13(b)) we obtain the following relation between h_1 and h_2:

Nomenclature

A = defined by equation (6)
A_0 = constant, equation (7)
a = constant, equation (7)
B = defined by equation (6)
c = specific heat
E_0 = constant (voltage), equation (20)
E_1 = voltage = $2K_1h_1$
h = heat transfer coefficient
h_0 = heat transfer coefficient at temperature t_0, equation (22)
i = current
j = conversion constant
K_1 = constant, equation (11)
K_2 = constant, equation (18(a))
K_3 = constant, equation (18(b))
M = time constant of wire, equation (18(c))
Nu = Nusselt number = $2r_0h/\lambda$
Pr = Prandtl number
R = resistance of wire
R_0 = resistance of wire at reference temperature θ_0
R_a = resistance of wire at temperature t
Re = Reynolds number = $2r_0u/\nu$
r_0 = wire radius
t = instantaneous local temperature of fluid
t_f = film temperature = $(\theta + t)/2$
u = instantaneous total velocity of fluid
V = voltage = iR
V_a = voltage = iR_a
V_{21} = constant (voltage) = i_2R_1
β = temperature coefficient of resistivity defined at θ_0
γ = specific weight
ϵ = resistance ratio = R_{01}/R_{02}
θ = wire temperature
θ_0 = reference temperature
λ = thermal conductivity
ν = kinematic viscosity
τ = time

Subscripts

1 = hot wire
2 = cold wire
f = value evaluated at film temperature t_f
w = property of wire
Properties without subscript denote those of fluid.

$$h_2 = h_1 - \frac{a(\theta_1 - t)}{2} = h_1 - \frac{a}{2\beta i_2 R_{01}}(V_{21} - \epsilon V_{a2}) \tag{14}$$

With equation (10), this again gives:

$$h_2 = \frac{1}{2K_1}\frac{V_1^2}{V_{21} - \epsilon V_{a2}} - \frac{a}{2\beta i_2 R_{01}}(V_{21} - \epsilon V_{a2}) \tag{15}$$

Substituting equation (15) into equation (12), and putting

$$E_1 = V_1^2/(V_{21} - \epsilon V_{a2}) \tag{16}$$

for the cold wire, we finally obtain:

$$V_{a2} = \frac{K_2}{E_1 - K_3 a(V_{21} - \epsilon V_{a2})}\frac{dV_2}{d\tau} + V_2 \tag{17}$$

$$= M dV_2/d\tau + V_2 \tag{17(a)}$$

where

$$K_2 = r_0 c_w \gamma_w K_1 = \frac{\pi r_0^2 c_w \gamma_w}{j\beta}\frac{R_1}{R_{01}}\frac{1}{i_2} \tag{18(a)}$$

$$K_3 = \frac{K_1}{\beta i_2 R_{01}} = \frac{\pi r_0}{j\beta^2}\frac{R_1}{R_{01}^2}\frac{1}{i_2^2} \tag{18(b)}$$

$$M = \frac{K_2}{E_1 - K_3 a(V_{21} - \epsilon V_{a2})} = \frac{r_0 c_w \gamma_w}{2}\frac{1}{h_2} \tag{18(c)}$$

M denotes the time constant of the cold wire, and is a function of both the fluid velocity and temperature. By solving equations (10) and (17), with measured values V_1 and V_2, we obtain h_1 and V_{a2} by the analog technique described later.

Equation for Measurement of Velocity

With equation (13(a)), the fluid velocity u is directly obtainable from the measured heat transfer coefficient h_1. Although it is mainly the effect of $\sqrt{u}$ that determines the heat-transfer coefficient, the effect of the fluid temperature changes, as seen from equation (13(a)), cannot be neglected. Therefore the additional correction is necessary for the measurement of velocity in flows with temperature fluctuations.

The film temperature is expressed as a function of V_{a2} by using equations (2) and (4) as follows:

$$\begin{aligned} t_{f1} - \theta_0 &= (\theta_1 - \theta_0) - (\theta_1 - t)/2 \\ &= (R_1 - R_{01})/\beta R_{01} - (R_1 - R_{a1})/2\beta R_{01} \\ &= (R_1 - R_{01})/\beta R_{01} - (V_{21} - \epsilon V_{a2})/2\beta i_2 R_{01} \end{aligned}$$

Substituting the above equation into equation (13(a)) and using equations (10), (16) and (18(b)), the following equation for the fluid velocity u is obtained:

$$2K_1 B\sqrt{u} = E_1 - E_0 + K_3 a(V_{21} - \epsilon V_{a2}) \tag{19}$$

where E_0 is a constant expressed as:

$$E_0 = 2K_1\left(A_0 + \frac{a}{\beta}\frac{R_1 - R_{01}}{R_{01}}\right) \tag{20}$$

Solutions by Analog Technique

When signals V_1 and V_2 from the hot and cold wires, respectively, are available, we can obtain h_1 and V_{a2} from equations (10) and (17) so that u also may be derived from equation (19). These simultaneous equations can be solved by employing a suitable analog technique, as shown schematically in Fig. 1. The analog technique provides not only outputs proportional to flow and temperature, but frequency compensation as well. The output E_u and V_{a2} proportional to the velocity and temperature of fluid, respectively, are on the right side of the block diagram of compensation. Heat transfer coefficient h_1 is also obtainable, if necessary, from an intermediate signal E_1.

The evaluation of constants K_2 and K_3 given by equations (18(a)) and (18(b)) involves some difficulties, and hence, for practical applications, the following procedure is to be recommended. First, setting all compensation circuits under the normal operating conditions, we place both the hot and cold wires in a flow of a constant velocity and room temperature t_a. Secondly, we feed a certain additional current into the cold wire so that the wire temperature rises to θ_i. Sudden removal of the added current from this state works as the step-response test of the cold wire as illustrated in Fig. 2. The corresponding situation may be the step change of the fluid temperature from t_i to t_a, as shown by A in the figure, in which $t_i \simeq \theta_i$ may hold. An uncompensated signal V_2, corresponding to a cold-wire temperature θ_2, usually deviates from the true input curve. By employing a compensation based on equation (17(a)), the signal V_2 is, however, to be restored to the precise signal V_{a2}, which shows the step change given by A in the figure. Inaccurate settings for K_2 and K_3 result in either under or overcompensation, illustrated by B or C in the figure, respectively. Consequently, the proper settings for K_2 and K_3 to accord with equations (18(a)) and (18(b)) are achieved by adjusting these constants until the compensated output V_{a2} indicates the correct stepwise change, as shown by A in Fig. 2. In practice it will be more appropriate to adjust K_2 first in a flow at room temperature and then K_3 at a high temperature.

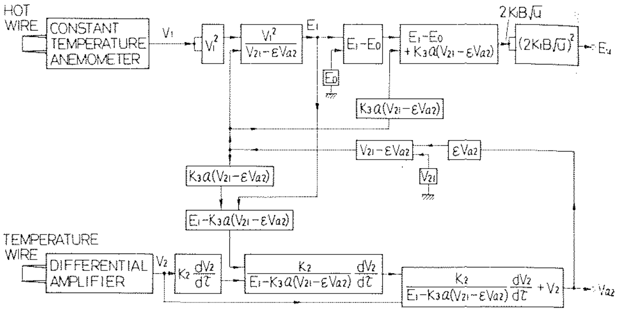

Fig. 1 Block diagram of compensation

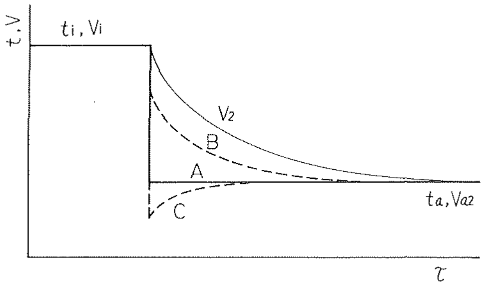

Fig. 2 Setting for time constant of cold wire

Although the constant E_0 in equation (19) can be calculated from equation (20), its practical evaluation is performed as follows. Set the wires in a static fluid $u = 0$, then from equation (19) the intermediate signal E_1 is given by a linear function of the output V_{a2} as:

$$E_1 = E_0 - K_3 a(V_{21} - \epsilon V_{a2})$$

Hence, the estimation of E_0 and $K_3 a$ in the compensation circuit can be made from the measured relation between E_1 and $(V_{21} - \epsilon V_{a2})$ at various fluid temperatures.

Possible Shortcuts for Moderate Temperature Fluctuations

The time constant M in equation (17(a)) is given by equation (18(c)) as a function of the fluid velocity and temperature. Except for very large temperature fluctuations, we can approximate equation (18(c)) as:

$$M \simeq \frac{r_0 c_w \gamma_w}{2}\frac{h_{01}}{h_{02}}\frac{1}{h_1} \tag{21}$$

where h_{01} and h_{02} are the heat transfer coefficients of the hot and cold wires, respectively, at a given fluid temperature t_0 and are expressed as follows:

$$h_{01} = A_0 + a(t_0/2 + \theta_1/2 - \theta_0) + B\sqrt{u} \qquad (22(a))$$

$$h_{02} = A_0 + a(t_0 - \theta_0) + B\sqrt{u} \qquad (22(b))$$

Now since, from equation (18(*c*)), the true time constant M_{tr} is written as:

$$M_{tr} = r_0 c_w \gamma_w / 2h_2$$

we obtain:

$$\frac{M}{M_{tr}} = \frac{h_{01}}{h_{02}}\frac{h_2}{h_1}$$

Equations (13) and (22) combine into the following:

$$h_1 = h_{01} + a(t - t_0)/2, \quad h_2 = h_{02} + a(t - t_0)$$

Substitution in the above equation then yields:

$$\frac{M}{M_{tr}} = \frac{1 + a(t - t_0)/h_{02}}{1 + a(t - t_0)/2h_{01}}$$

or

$$\frac{M - M_{tr}}{M_{tr}} = \frac{a(t - t_0)(1/h_{02} - 1/2h_{01})}{1 + a(t - t_0)/2h_{01}}$$

Since from equation (6), $a(t - t_0)/2h_{01} = (h_1 - h_{01})/h_{01} \leq 0.046$ holds for $2r_0 \geq 5\ \mu\text{m}$, $u \geq 5$ m/s and $t - t_0 \leq 100°\text{C}$, we may put $a(t - t_0)/2h_{01} \ll 1$ and approximate the above equation as follows:

$$\frac{M - M_{tr}}{M_{tr}} \simeq a(t - t_0)\left(\frac{1}{h_{02}} - \frac{1}{2h_{01}}\right) \qquad (23)$$

Equation (23) gives the resulting error due to the approximation to the time constant with equation (21). When $2r_0 = 5\ \mu m$ and $u = 5$ m/s, the absolute error in M remains less than 5.8 percent even though $t - t_0 = 100°\text{C}$. The ratio h_{01}/h_{02} decreases by only 4.0 percent even though the fluid velocity increases from 5 to 30 m/s. Accordingly, h_{01}/h_{02} in equation (21) is considered to be a constant independent of velocity. With equation (10), we can write:

$$M = \frac{h_{01}}{h_{02}}\frac{K_2}{V_1{}^2/(V_{21} - \epsilon V_{a2})} = \frac{h_{01}}{h_{02}}\frac{K_2}{E_1}$$

Thus we obtain the approximation for V_{a2} as:

$$V_{a2} = \frac{h_{01}}{h_{02}}\frac{K_2}{E_1}\frac{dV_2}{d\tau} + V_2 \qquad (24)$$

in which $K_2 h_{01}/h_{02}$ is a constant.

The block diagram of the complete system in this case becomes simpler, as illustrated in Fig. 3. The proper setting for the time constant of the cold wire is accomplished by the adjustment of $(h_{01}/h_{02})K_2$ in equation (24) at room temperature in the way previously described. This need be done only once for a given type of wire.

Instrument for Measurements of Velocity and Temperature in Heated Air Flows

A practical instrument for measurements in nonisothermal air flows is described here, together with some remarks about the application and possible significance of the results. A two-wire probe consisting of 5 μm dia tungsten wires with copper plated ends was used as shown in Fig. 4. The downstream wire was the 1 mm long hot wire and the upstream one the 2 mm long cold wire separated by 0.7 mm to avoid any mutual interference.

Fig. 5 shows the result of probe orientation tests to identify the region of negligible wake interference. The two wires are parallel and are held normal to an air flow. Such a probe configuration is highly effective in the study of turbulent shear flow. The fluid velocity u measured by the downstream hot wire starts to deviate significantly from the true fluid velocity u_∞ when the distance x separating the two wires becomes less than 150 wire diameters. This critical distance is practically unaffected by the Reynolds number $\text{Re} = u_\infty d/\nu$. In exceptionally low velocity situations, a slight phase shift is introduced between the signals of hot and cold wires by the physical distance separating the two wires. This corresponds, for instance, to a delay of the order of 0.7×10^{-3} s in the case of $u_\infty = 1$ m/s and $x = 0.7$ mm. When the precision control of the phase shift is required in such an exceptional case, a delay line should be inserted in the circuit before compensation is performed.

A compensation circuit was built up on the basis of the block diagram for moderate temperature fluctuations given in Fig. 3. In Fig. 6, the schematic of the complete compensating circuit is presented in detail. An anemometer unit on the market was used for constant temperature operation. The current supplied to the cold wire was 1 m*A*. The wire-temperature rise caused by current heating was measured and proved to remain less than 0.1°C provided $i_2 \leq 1$ m*A*. The output of the cold wire was amplified by the differential amplifier made of Fairchild μA 725C instrumentation operational amplifier at a gain of 1000. The differential amplifier gave a flat frequency response up to 40 kHz, which was quite adequate, and 108 dB common mode rejection ratio for a signal with a frequency of 60 Hz. The total

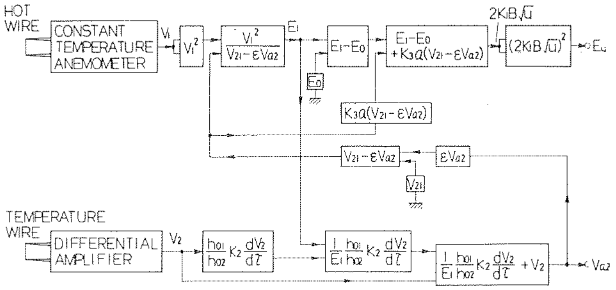

Fig. 3 Block diagram of compensation for moderate temperature fluctuation

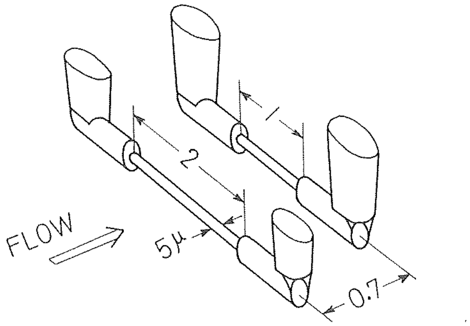

Fig. 4 Probe configuration (all dimensions in millimeters)

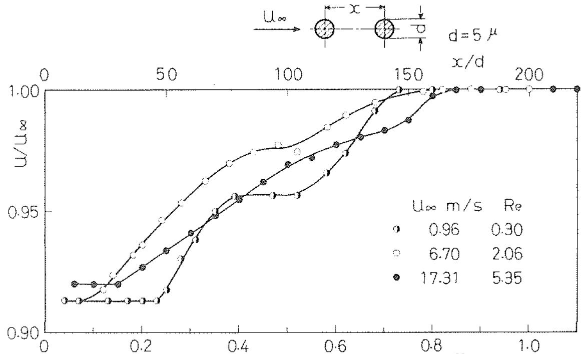

Fig. 5 Effect of upstream wire on output of downstream one

noise voltage referred to input was 1.2 μV (r.m.s) for a bandwidth of 10 kHz, which resulted in the corresponding error in temperature of 0.05°C at the most. The multiplier and divider were made from NEC μPC 132D wideband four quadrant multipliers, the operational errors of which were less than 0.8 percent.

The proper setting for the time constant of the cold wire could be accomplished, as described previously, by applying the on-off added currents to the wire and adjusting the feedback resistance (potentiometer) until the output V_{a2} indicated the correct step response. Fig. 7 shows typical traces illustrating the step response of the cold wire obtained by the compensation setting. It was our experience that the readjustment for the compensation was not needed with the changes of the fluid temperature from 20 to 100°C and of the velocity from 5 to 25 m/s.

The frequency response of the compensating circuit is shown in Fig. 8. The gain of the velocity measuring circuit is presented with the ratio of the output E_u to the input V_1. The frequency response of the complete temperature measuring circuit is shown by a solid curve derived from the combination of the measured frequency response of the electronic circuit (V_{a2} versus V_2) and the calculated frequency response of the uncompensated cold wire shown by a dot-dash line. The gain thus corresponds to the ratio of the output V_{a2} to the signal of virtual voltage fluctuation proportional to the fluid temperature fluctuation. In Fig. 8, the d-c gains of both the velocity and temperature measuring circuits are fixed so as to indicate 0 dB. With a view towards preventing the undesired contribution of noise with frequencies higher than the range of interest, the differentiating action in the temperature measuring circuit was restricted up to a frequency of 6 kHz, which is more than adequate for most turbulence research [6, 7]. The phase shift contributed by the compensators is seen to be quite acceptable over the frequency range of interest [8, 9]. In general, the overall response of the compensating circuit is limited only by the electronic properties of the devices used.

The calibration curves between the linearizer output E_u and the velocity measured by Pitot tube at various temperatures are presented in Fig. 9. The figure clearly shows that the velocity calibration curves of the uncompensated hot-wire anemometer output, which indeed vary widely with temperature, can be reduced to a single one, regardless of temperature changes, when the temperature compensations are performed with this proposed circuit.

To verify the effectiveness of the compensation for fluctuations, sample oscillograph records (Fig. 10) of velocity and temperature fluctuations were measured with this instrument in a heated pipe flow.

Another set of reference flow fluctuation data in fully developed pipe flow is shown in Fig. 11, in which the distributions of intensities of velocity and temperature fluctuations normalized by the friction velocity u_* and the friction temperature t_* are presented as a function of dimensionless distance from wall y/r_p (r_p being pipe radius). The data of Bremhorst, et al. [7] are those obtained by the conventional constant-current method introduced first by Corrsin [10]. Such conventional measurements of turbulent intensities, however, are bound to be erroneous due to nonlinearity of the hot-wire response and additional assumptions needed to find the sensitivities to fluctuations [11, 12]. As seen from Fig. 11, the effect of heat input on the

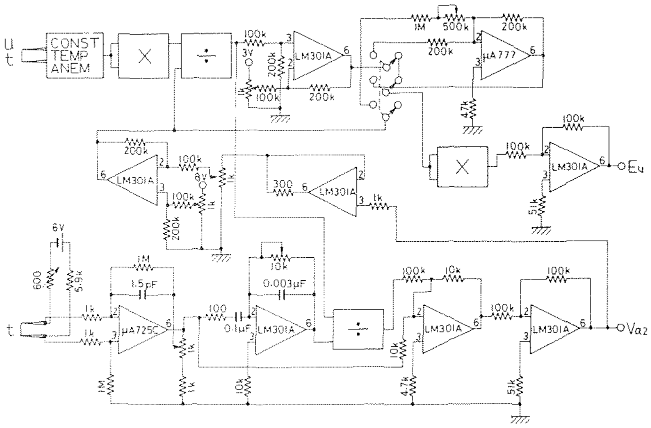

Fig. 6 Compensating circuit

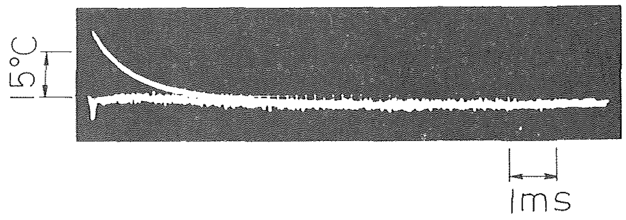

Fig. 7 Step response of cold wire

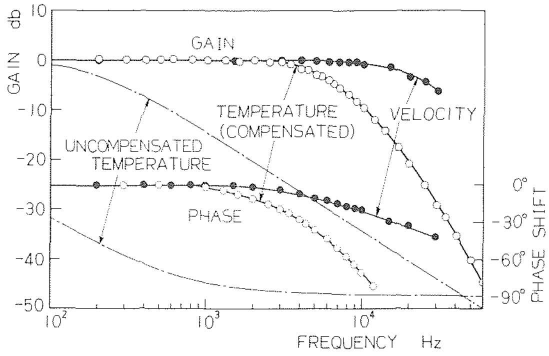

Fig. 8 Frequency response of compensating circuit

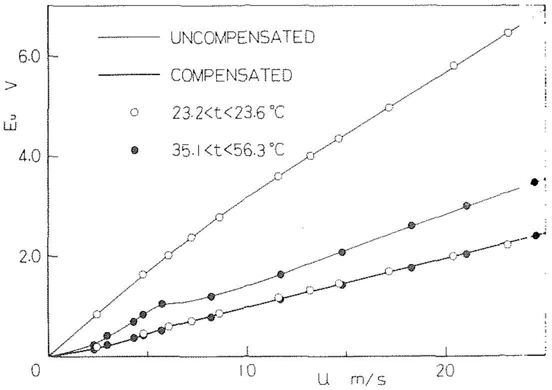

Fig. 9 Results of compensation

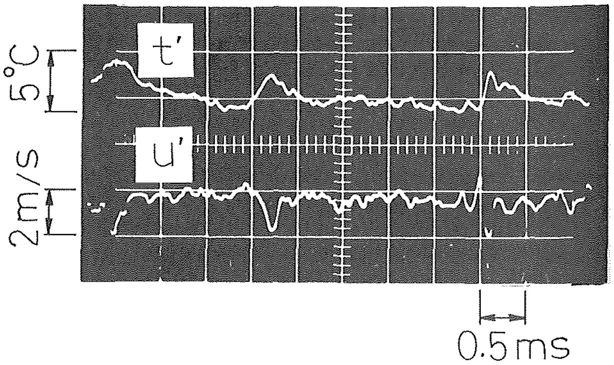

Fig. 10 Velocity and temperature fluctuations in a heated pipe flow

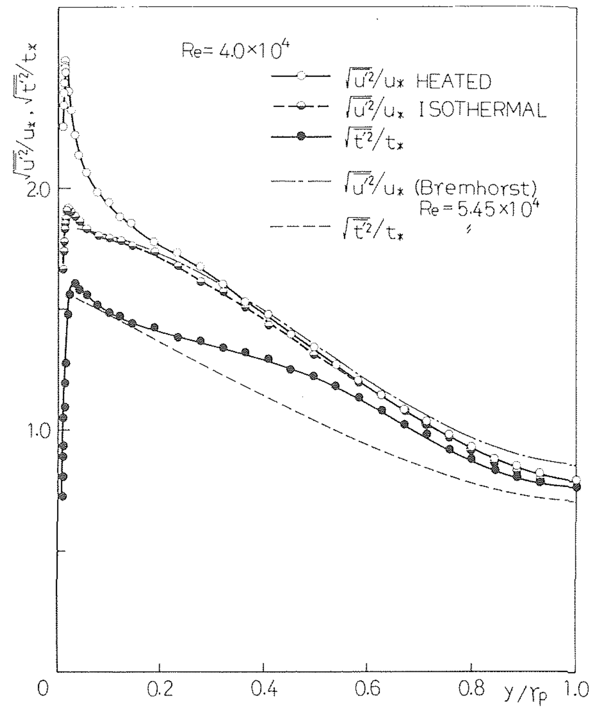

Fig. 11 Intensities of velocity and temperature fluctuations in fully developed pipe flow

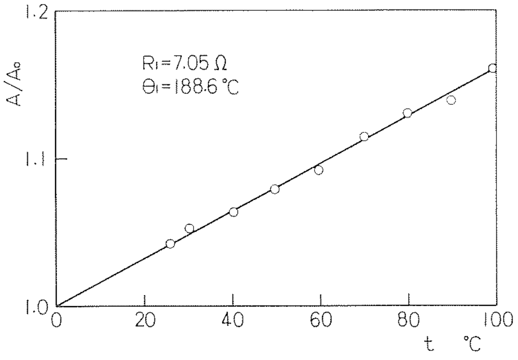

Fig. 12 Variation of *A* with fluid temperature

$\sqrt{\overline{U'^2}}/U_*$ distribution is chiefly produced in the wall region, and in the core region there is no longer a definite effect of added heat. Details of fine structures of turbulent velocity and temperature fields in fully developed pipe flow, and extensive turbulence studies on the thermal entrance region of a pipe, will be given in other reports [13, 14].

The relation between A in equation (6) and film temperature t_f is obtained through the evaluation of h_1 from the intermediate signal E_1 measured in still air at various temperatures, since from equation (6), $h = A$ for $u = 0$. Fig. 12 shows the experimental result of the relation between A and fluid temperature t, in which A_0 denotes the value of A at 0°C. The assumed linear relation (7) between A and t_f has been proven acceptable for air in the temperature range of 20 to 100°C.

Conclusions

The results of this investigation pertaining to simultaneous measurements of velocity and temperature can be summarized in the following conclusions:

1 Considering the difference of the heat transfer coefficients between hot and cold wires, the analysis has been presented in as strict a form as possible.

2 For simplicity of presentation, the analysis involves the use of Kramers heat transfer equation, which has proved to be an expression acceptable enough to warrant its use in practice.

3 Separate and simultaneous signals of the velocity and temperature are obtained by employing analog technique in which the time constant of the cold wire is automatically evaluated from the signal directly proportional to the heat transfer coefficient of the hot wire.

4 Compensation for the effects of fluid temperature on the heat transfer coefficient has been accomplished through compensating circuits.

5 Possible shortcuts for moderate temperature fluctuations are described.

6 A measuring system has been built by using a two-wire probe consisting of 5 μm dia tungsten wires. The unit has been tested in a controlled environment, and the corresponding results have proven very satisfactory for the measurements of velocity and temperature fluctuations in ordinary turbulent fluids.

References

1 Hoshino, T., and Sawada, T., "Development of a Method for Measuring Rapidly Varying Gas Temperatures and Velocities," *Transactions of the Japan Society of Mechanical Engineers,* Vol. 38, No. 305, Jan. 1972, pp. 139–147, in Japanese.

2 Chevray, R., and Tutu, N. K., "Simultaneous Measurements of Temperature and Velocity in Heated Flows," *The Review of Scientific Instruments,* Vol. 43, No. 10, Oct. 1972, pp. 1417–1421.

3 Pessoni, D. H., and Chao, B. T., "A Simple Technique for Turbulence Measurements in Nonisothermal Air Flows," *Proceedings of the 5th International Heat Transfer Conference,* Vol. 5, 1974, pp. 278–282.

4 Collis, D. C., and Williams, M. J., "Two-Dimensional Convection from Heated Wires at Low Reynolds Numbers," *Journal of Fluid Mechanics,* Vol. 6, 1959, pp. 357–384.

5 Kramers, H., "Heat Transfer from Spheres to Flowing Media," *Physica,* Vol. 12, 1946, pp. 61–120.

6 Miller, J. A., "A Simple Linearized Hot-Wire Anemometer," *ASME Journal of Fluids Engineering,* Vol. 98, 1976, pp. 749–752.

7 Bremhorst, K., and Bullock, K. J., "Spectral Measurements of Temperature and Longitudinal Velocity Fluctuations in Fully Developed Pipe Flow," *International Journal of Heat and Mass Transfer,* Vol. 13, 1970, pp. 1313–1329.

8 Kovásznay, L. S. G., "Development of Turbulence-Measuring Equipment," NACA Report 1209, 1954.

9 Nieuwvelt, C., Bessem, J. M., and Trines, G. R. M., "A Rapid Thermometer for Measurement in Turbulent Flow," *International Journal of Heat and Mass Transfer,* Vol. 19, 1976, pp. 975–980.

10 Corrsin, S., "Extended Applications of the Hot-Wire Anemometer," NACA TN No. 1864, 1949.

11 Chevray, R., and Tutu, L. K., "On Velocity Measurements in Non-Isothermal Turbulent Flows," *Proceedings of Symposium on Turbulence in Liquids,* 1972, pp. 19–25.

12 Hinze, J. O., Turbulence, Second Ed., McGraw-Hill, 1975, pp. 135–138.

13 Hishida, M., and Nagano, Y., "Structure of Turbulent Velocity and Temperature Fluctuations in Fully Developed Pipe Flow," submitted to ASME JOURNAL OF HEAT TRANSFER, 1978.

14 Hishida, M., and Nagano, Y., "Structure of Turbulent Temperature and Velocity Fluctuations in the Thermal Entrance Region of a Pipe," *Proceedings of Sixth International Heat Transfer Conference* (in Canada), 1978, (in press).

J. P. Chiou

Professor of Mechanical Engineering,
University of Detroit,
Detroit, Michigan
Mem. ASME

The Effect of Longitudinal Heat Conduction on Crossflow Heat Exchanger

A numerical method to determine the effectiveness of the crossflow heat exchanger, accounting for the effect of the two-dimensional longitudinal heat conduction through the exchanger wall structure in the directions of fluid flows, is presented. The exchanger effectiveness and its deterioration due to the conduction effect have been calculated for various design and operating conditions of the exchanger. The results indicate that the thermal performance deterioration of the exchanger may become significant for some typical applications.

Introduction

Longitudinal heat conduction through the heat exchanger wall structure in the directions of fluid flows has the effect of decreasing the exchanger performance. Investigations of this effect have been done for storage type periodic-flow heat exchangers [1–5],[1] and for the direct transfer type counterflow heat exchangers [6–8]. Reporting on the investigation of this effect for the direct transfer type crossflow heat exchanger is very limited [9].

This paper presents the results of the study of the thermal performance deterioration in the direct transfer type single pass crossflow heat exchanger. The deterioration is the result of the two-dimensional longitudinal heat conductions through the exchanger wall in the directions of the two fluid flows. Heat transfer rate equations for the two fluids and the heat exchanger wall are first formulated. By using a successive substitution technique, these three equations are reduced to a single equation with the wall temperature alone as the unknown variable. The two-dimensional temperature distribution of the exchanger wall is then determined. Next, the temperature distributions of both fluids in the heat exchanger are calculated. Finally the exchanger heat transfer effectiveness and its deterioration due to this longitudinal heat conduction effect are determined for various design and operating conditions.

Analysis

Many types of heat transfer matrices are used in direct transfer type heat exchangers. The heat transfer matrices generally can be classified into plate-fin surfaces and tubular surfaces. When the two-dimensional longitudinal heat conduction through the exchanger wall is taken into consideration, the thermal performance deterioration is more significant for the plate-fin heat exchanger than for the tubular heat exchanger. Thus, in this investigation, a plate-fin heat exchanger is considered. The subject heat exchanger may be visualized as a wall separating the two fluid streams flowing at right angles and with plate-fins on both sides as shown in Fig. 1. In most heat exchangers,

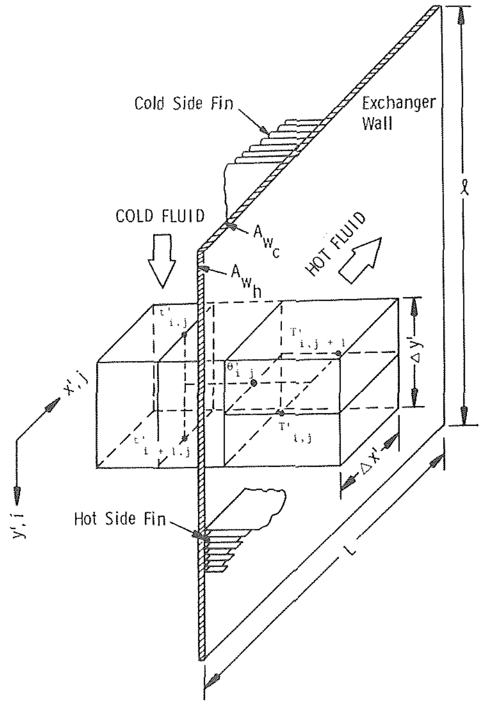

Fig. 1 Single pass crossflow heat exchanger

---

[1] Numbers in brackets designate References at end of paper.

Contributed by the Heat Transfer Division for publication in the JOURNAL OF HEAT TRANSFER. Manuscript received by the Heat Transfer Division October 29, 1976.

the thickness of the exchanger wall is small compared with its other two dimensions, so the thermal resistance through the exchanger wall in the direction normal to the fluid flows is small enough to be neglected. The fin thickness, especially in the plate-fin heat exchanger, is much thinner than the exchanger wall; it is also small compared with the fin height and fin width. Therefore, the temperature gradient across the fin thickness may be neglected. For the same reason, the heat transfer rate across the fin in the direction of the fluid flow (on the same side of the fin concerned) is also very low and can be neglected, especially when the off-set or interrupted-fin is used. In other words, one-dimensional heat transfer fin concept is assumed in this investigation. Other assumptions of this analysis are:

1 Steady state condition.

2 Both fluids considered are nonliquid metal type. Their temperatures remain constant and uniform over their respective inlet sections. Their mass velocities are also constant with respect to time.

3 Both fluids pass in crossflow pattern on both sides of the exchanger wall. Each stream is assumed to have been broken up into a large number of separate flow tubes for passage through the exchanger with no cross or transverse mixing [2]. Change of flow distribution inside the exchanger is neglected.

4 Thermal-physical properties of both fluids and the exchanger wall and fin are independent with respect to the temperatures.

5 The convection heat transfer coefficient between either fluid and its respective heat transfer surface is constant throughout the exchanger.

6 The heat transfer surface configurations and the heat transfer areas on both sides per unit base area are constant and uniform throughout the exchanger.

7 No heat generates within the exchanger. No phase change occurs in the fluid streams flowing through the exchanger. Heat transfer between the exchanger and the surrounding is negligible.

Based on these assumptions, the governing differential equations of the heat transfer activities of the subject system are formulated as shown below:

Heat transfer between the hot fluid and the exchanger wall:

$$-\frac{C_h}{\ell}\frac{\partial T'}{\partial x'} = (\eta h a')_h(T' - \theta') \qquad (1)$$

Heat transfer between the exchanger wall and the cold fluid:

$$\frac{C_c}{L}\frac{\partial t'}{\partial y'} = (\eta h a')_c(\theta' - t') \qquad (2)$$

Two-dimensional longitudinal heat conduction in the wall:

$$\frac{(kA_w)_h}{\ell}\frac{\partial^2\theta'}{\partial x'^2} + \frac{(kA_w)_c}{L}\frac{\partial^2\theta'}{\partial y'^2} - \frac{C_h}{\ell}\frac{\partial T'}{\partial x'} - \frac{C_c}{L}\frac{\partial t'}{\partial y'} = 0 \qquad (3)$$

The boundary conditions are:

$$T'(0, y') = T'_{in}; \qquad t'(x', 0) = t'_{in}$$
$$\frac{\partial\theta'(0, y')}{\partial x'} = \frac{\partial\theta'(L, y')}{\partial x'} = 0; \qquad \frac{\partial\theta'(x', 0)}{\partial y'} = \frac{\partial\theta'(x', \ell)}{\partial y'} = 0 \qquad (4)$$

Let:

$$\lambda_h = \frac{1}{L}\,[(kA_w)/C]_h; \qquad \lambda_c = \frac{1}{\ell}\,[(kA_w)/C]_c \qquad (5)$$

then equations (1)–(3) can be expressed as:

$$\frac{\partial T}{\partial x} + \mathrm{NTU}_h(T - \theta) = 0 \qquad (6)$$

Nomenclature

a' = heat transfer area per unit base area, dimensionless

a = total heat transfer area ($= a'\ell L$), ft^2

A = a dimensionless parameter defined by equations (17), and (18)–(20)

A_w = total solid area available for longitudinal heat conduction, ft^2

B and B' = dimensionless parameters defined by equation (10)

c_p = specific heat of fluid at constant pressure, Btu/Lbm. F

$C = Mc_p$ = fluid heat capacity rate, Btu/hr F

D = a dimensionless parameter defined by equation (10)

E, E' and F = dimensionless parameters defined by equation (15)

G and H = dimensionless parameters defined by equation (17)

h = convection heat transfer coefficient, Btu/hr sq ft F

I = subscript of the one-dimensional variable θ^* as defined in equation (21)

i and j = subscripts of the two-dimensional variable θ. i specified i-th row and j specifies j-th column

k = thermal conductivity of exchanger wall, Btu/hr ft F

L, ℓ = the length of the exchanger in the x' or y' directions respectively. ft

m = number of subdivisions in y' direction.

M = mass flow rate, Lbm./hr.

n = number of subdivisions in x' direction.

NTU$_h$ = number of transfer units on the hot side = $(\eta ha)_h/C_h$, dimensionless

NTU$_c$ = number of transfer of units on the cold side = $(\eta ha)_c/C_c$, dimensionless

NTU = number of transfer units of the heat exchanger = $\dfrac{1}{C_{\min}\left[\left(\dfrac{1}{\eta ha}\right)_h + \left(\dfrac{1}{\eta ha}\right)_c\right]}$, dimensionless

P_1, P_2, P_3, P_4 and R = dimensionless parameters defined in equation (17)

r = an integer

$S = (\eta ha)_h/(\eta ha)_c$, dimensionless

$T = (T' - t'_{in})/(T'_{in} - t'_{in})$; $t = (t' - t'_{in})/(T'_{in} - t'_{in})$, dimensionless

T', t' = fluid temperature on hot or cold side, F

$V = C_c/C_h$, dimensionless

W = a dimensionless parameter as defined in equation (17)

$x = x'/L$, dimensionless coordinate in x'-direction

x' = coordinate in x'-direction (direction of hot fluid flow), ft

$\Delta x = x/n$, the length of the subdivision in x'-direction

$y = y'/\ell$, dimensionless coordinate in y'-direction

y' = coordinate in y'-direction (direction of cold fluid flow), ft

$\Delta y = y/m$, the length of the subdivision in y'-direction

Z = a dimensionless parameter as defined in equation (17)

ϵ = exchange heat transfer effectiveness $= \dfrac{C_h(T'_{in} - T'_{exit})}{C_{\min}(T'_{in} - t'_{in})} = \dfrac{C_c(t'_{exit} - t'_{in})}{C_{\min}(T'_{in} - t'_{in})}$, dimensionless

$\Delta\epsilon$ = deterioration of exchanger effectiveness due to longitudinal conduction effect, dimensionless

λ = longitudinal heat conduction parameter as defined in equation (5), dimensionless

η = overall surface efficiency, dimensionless

θ = double subscripts dimensionless temperature of exchanger wall = $(\theta' - t'_{in})/(T'_{in} - t'_{in})$

θ' = exchanger wall temperature, F

θ^* = single subscript dimensionless temperature of exchanger wall

τ = conduction effect factor as defined by equation (23)

Subscripts

c = cold side or in the direction of cold fluid flow

exit = exit

h = hot side or in the direction of hot fluid flow

in = inlet

max = maximum magnitude

min = minimum magnitude

$$\frac{\partial t}{\partial y} + \mathrm{NTU_c}(t - \theta) = 0 \tag{7}$$

$$\lambda_\mathrm{h} \frac{\partial^2 \theta}{\partial x^2} + \lambda_\mathrm{c} V \frac{\partial^2 \theta}{\partial y^2} - \frac{\partial T}{\partial x} - V \frac{\partial t}{\partial y} = 0 \tag{8}$$

The boundary conditions are:

$$\begin{aligned} &T(0, y) = 1.0; && t(x, 0) = 0.0 \\ &\frac{\partial \theta(0, y)}{\partial x} = \frac{\partial \theta(1, y)}{\partial x} = 0; && \frac{\partial \theta(x, 0)}{\partial y} = \frac{\partial \theta(x, 1)}{\partial y} = 0 \end{aligned} \tag{9}$$

Subdivide the $x' - y'$ plane of the exchanger into $m \times n$ small subdivisions as shown in Fig. 2. The finite-difference representations of the governing differential equations are obtained as shown below:

Center Region Subdivisions. Let:

$$B' = \mathrm{NTU_h} \Delta x; \quad B = (1 - \tfrac{1}{2}B')/B'; \quad D = (1 + \tfrac{1}{2}B')/B' \tag{10}$$

equation (6) can be expressed as,

$$\theta_{i,j} + BT_{i,j} - DT_{i,j+1} = 0 \tag{11}$$

By means of successive substitution, the hot fluid temperature T, at any position (i, j), can be related to the wall temperature of all the upstream subdivisions in the same flow channel i, and the inlet temperature of the hot fluid, $T_{i,1}$ which is given. Thus,

$$\begin{aligned} T_{i,j} = \frac{1}{D} \Bigg[&\theta_{i,j-1} + \left(\frac{B}{D}\right) \theta_{i,j-2} + \left(\frac{B}{D}\right)^2 \theta_{i,j-3} + \left(\frac{B}{D}\right)^3 \theta_{i,j-4} + \ldots \\ &+ \left(\frac{B}{D}\right)^r \theta_{i,j-r-1} + \ldots + \left(\frac{B}{D}\right)^{j-2} \theta_{i,1} \Bigg] + \left(\frac{B}{D}\right)^{j-1} T_{i,1} \end{aligned} \tag{12}$$

Similarly, equation (7) can be expressed as,

$$\theta_{i,j} + Et_{i,j} - Ft_{i+1,j} = 0 \tag{13}$$

then,

$$\begin{aligned} t_{i,j} = \frac{1}{F} \Bigg[&\theta_{i-1,j} + \left(\frac{E}{F}\right) \theta_{i-2,j} + \left(\frac{E}{F}\right)^2 \theta_{i-3,j} + \left(\frac{E}{F}\right)^3 \theta_{i-4,j} + \ldots \\ &+ \left(\frac{E}{F}\right)^r \theta_{i-r-1,j} + \ldots + \left(\frac{E}{F}\right)^{i-2} \theta_{1,j} \Bigg] + \left(\frac{E}{F}\right)^{i-1} t_{1,j} \end{aligned} \tag{14}$$

Here,

$$E' = \mathrm{NTU_c} \Delta y; \quad E = (1 - \tfrac{1}{2}E')/E'; \quad F = (1 + \tfrac{1}{2}E')/E' \tag{15}$$

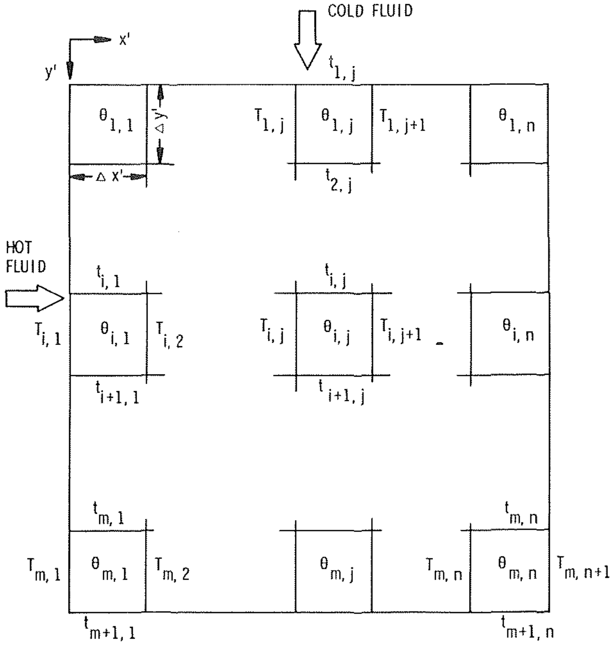

Fig. 2 Subdivision of crossflow heat exchanger

Equation (14) indicates that the cold fluid temperature t, at any position (i, j), can be related to the wall temperature of all the upstream subdivisions in the same flow channel j; and the inlet temperature of the cold fluid, $t_{1,j}$, which is also known.

By means of the same successive substitution technique, equation (8) can be written as,

$$\begin{aligned} &G\theta_{i,j+1} + H\theta_{i+1,j} + W\theta_{i,j} + P_1\theta_{i,j-1} + P_2\theta_{i-1,j} \\ &\quad + P_3 \left[\theta_{i,j-2} + \left(\frac{B}{D}\right) \theta_{i,j-3} + \left(\frac{B}{D}\right)^2 \theta_{i,j-4} + \ldots + \left(\frac{B}{D}\right)^{j-3} \theta_{i,1} \right] \\ &\quad + P_4 \left[\theta_{i-2,j} + \left(\frac{E}{F}\right) \theta_{i-3,j} + \left(\frac{E}{F}\right)^2 \theta_{i-4,j} + \ldots + \left(\frac{E}{F}\right)^{i-3} \theta_{1,j} \right] \\ &\qquad = -R \left(1 + \frac{B}{D}\right) \left(\frac{B}{D}\right)^{j-1} T_{i,1} - Z \left(1 + \frac{E}{F}\right) \left(\frac{E}{F}\right)^{i-1} t_{1,j} \end{aligned} \tag{16}$$

Here:

$$A = -\frac{2\lambda_\mathrm{h}}{(\Delta x)^2} - \frac{2\lambda_\mathrm{c} V}{(\Delta y)^2} - \mathrm{NTU_h} - V \cdot \mathrm{NTU_c}$$

$$G = \lambda_\mathrm{h}/(\Delta x)^2; H = \lambda_\mathrm{c} V/(\Delta y)^2; R = \tfrac{1}{2}\mathrm{NTU_h}; Z = \tfrac{1}{2}V \cdot \mathrm{NTU_c}$$

$$W = A + \frac{R}{D} + \frac{Z}{F}; P_1 = G + \frac{R}{D}\left(1 + \frac{B}{D}\right); P_2 = H + \frac{Z}{F}\left(1 + \frac{E}{F}\right)$$

$$P_3 = \frac{R}{D}\left(1 + \frac{B}{D}\right)\left(\frac{B}{D}\right); P_4 = \frac{Z}{F}\left(1 + \frac{E}{F}\right)\left(\frac{E}{F}\right) \tag{17}$$

Equation (16) is used to determine the wall temperature, $\theta_{i,j}$, in the center region of the system. This equation is also used to determine the wall temperature of all the boundary region subdivisions with certain restrictions and limitations as discussed in the next section.

Boundary Region Subdivisions. Following the same analysis as the Center Region equations (6), (7) and (8) can be written into similar finite-difference forms for the boundary region subdivisions. Therefore, all the finite difference equations developed for the center region subdivisions can be used for all the boundary region subdivisions with the following restrictions:

a Only those terms of $T_{i,j}$ are retained if $1 \le i \le m$ and $1 \le j \le n + 1$.

b Only those terms of $t_{i,j}$ are retained if $1 \le i \le m + 1$ and $1 \le j \le n$.

c Only those terms of $\theta_{i,j}$ are retained if $1 \le i \le m$ and $1 \le j \le n$.

d The parameter, A, for various boundary region subdivisions are:

For the four corner subdivisions,

$$A = -\frac{\lambda_\mathrm{h}}{(\Delta x)^2} - \frac{\lambda_\mathrm{c} V}{(\Delta y)^2} - \mathrm{NTU_h} - V \cdot \mathrm{NTU_c} \tag{18}$$

For the top and bottom center subdivisions,

$$A = -\frac{2\lambda_\mathrm{h}}{(\Delta x)^2} - \frac{\lambda_\mathrm{c} V}{(\Delta y)^2} - \mathrm{NTU_h} - V \cdot \mathrm{NTU_c} \tag{19}$$

For the left and right center subdivisions,

$$A = -\frac{\lambda_\mathrm{h}}{(\Delta x)^2} - \frac{2\lambda_\mathrm{c} V}{(\Delta y)^2} - \mathrm{NTU_h} - V \cdot \mathrm{NTU_c} \tag{20}$$

Equation (16) must be formulated for every subdivision of the system. There are $m \times n$ equations to form a set of simultaneous equations. The unknown variables of equation (16) are the wall temperatures of the related subdivisions. These related subdivisions are:

a the subdivision concerned,

b the immediate downstream subdivision of both fluids (up to the last row or/and last column subdivisions),

c all subdivisions in the upstream directions of both fluids (up to the first row or/and first column subdivisions).

Solving θ alone by equation (16) is much simpler than solving θ, T

and t simultaneously. The advantage of using the successive substitution technique to obtain equation (16) is therefore obvious.

Numerical Solutions

In equation (16), the wall temperature, $\theta(i, j)$, is expressed in a two-dimensional array. Because the wall temperatures of all the related subdivisions are present, identification of each element and its coefficient in the matrix is complicated. In order to simplify this problem, the two-dimensionsl array $\theta(i, j)$ is transformed into one-dimensional array $\theta^*(\mathrm{I})$, here

$$\mathrm{I} = (i-1)n + j \tag{21}$$

The general arrangement of the one-dimensional array, θ^*, is shown in Fig. 3. After this transformation, equation (16) can be written as

$$\begin{aligned} &G\theta^*{}_{\mathrm{I}+1} + H\theta^*{}_{\mathrm{I}+n} + W\theta^*{}_{\mathrm{I}} + P_1\theta^*{}_{\mathrm{I}-1} + P_2\theta^*{}_{\mathrm{I}-n} \\ &+ P_3\left[\theta^*{}_{\mathrm{I}-2} + \left(\frac{B}{D}\right)\theta^*{}_{\mathrm{I}-3} + \left(\frac{B}{D}\right)^2\theta^*{}_{\mathrm{I}-4} + \ldots + \left(\frac{B}{D}\right)^{j-3}\theta^*{}_{\mathrm{I}-j+1}\right] \\ &+ P_4\left[\theta^*{}_{\mathrm{I}-2n} + \left(\frac{E}{F}\right)\theta^*{}_{\mathrm{I}-3n} + \left(\frac{E}{F}\right)\theta^*{}_{\mathrm{I}-4n} + \ldots + \left(\frac{E}{F}\right)^{i-3}\theta^*{}_{j}\right] \\ &= -R\left(1+\frac{B}{D}\right)\left(\frac{B}{D}\right)^{j-1} T_{i,1} - Z\left(1+\frac{E}{F}\right)\left(\frac{E}{F}\right)^{i-1} t_{1,j} \end{aligned} \tag{22}$$

The node I and its related nodes in equation (22) are also shown in Fig. 3. There are $m \times n$ equations of the type of equation (22) in the system. After θ^* are determined, $\theta_{i,j}$, the temperature distributions of the two fluid streams and their average values can then be calculated.

The Conduction Effect Factor, τ, is introduced to illustrate the influence of the two-dimensional longitudinal heat conduction on the deterioration of exchanger performance.

$$\tau = \frac{\Delta\epsilon}{\epsilon} = \frac{\epsilon_{\text{no conduction}} - \epsilon_{\text{with conduction}}}{\epsilon_{\text{no conduction}}} \tag{23}$$

The conduction effect factor directly shows the degree of deterioration of the exchanger heat transfer effectiveness due to the longitudinal heat conduction. The larger this factor is, the greater is the deterioration of the exchanger effectiveness.

The $\mathrm{NTU_h}$ and $\mathrm{NTU_c}$ used in the various equations developed before are determined from V, S and NTU as shown below.

For the case when C_h is $C_{\min}$,

$$\mathrm{NTU_h} = \mathrm{NTU}\,(1+S);\ \mathrm{NTU_c} = \mathrm{NTU}\left(1+\frac{1}{S}\right)\Big/ V \tag{24}$$

For the case when C_c is $C_{\min}$,

$$\mathrm{NTU_h} = \mathrm{NTU}\cdot V(1+S);\ \mathrm{NTU_c} = \mathrm{NTU}\left(1+\frac{1}{S}\right) \tag{25}$$

Results

The accuracy of the solution obtained by finite-difference mathematics depends on the number of the subdivisions used. Use of a greater number of subdivisions not only can produce results of higher accuracy but can also enhance the convergence. Practically, the number of subdivisions used is determined by a compromise between the accuracy desired and the time required on the computer. It was found that when a 10 × 10 matrix was used, the results were accurate to the third digit for most cases, as compared with the near-exact solution [2, 10]. This accuracy is believed to be sufficient for most engineering applications. Thus, a 10 × 10 matrix arrangement was used throughout this investigation.

In this study, the ranges of the design and operating parameters of the exchanger under consideration are:

$C_\mathrm{c}/C_\mathrm{h}$ = 0.1 to 10.0

$\lambda_\mathrm{c}/\lambda_\mathrm{h}$ = 0.5, 1.0, and 2.0

λ_h = 0.00, 0.04, 0.06, 0.08, 0.10, 0.20, and 0.40

$(\eta ha)_\mathrm{h}/(\eta ha)_\mathrm{c}$ = 0.5, 1.0, and 2.0

NTU = 1.0, 2.0, 4.0, 6.0, 8.0, and 10.0 to 100.0 at an interval of 10.0

The parameters covered are in the range of general interest. The methods developed, however, are not limited to within these ranges and also can be applied to treat various other heat exchanger problems as well [11, 12]. Useful data of τ for various exchanger design and operating conditions are presented in [9].

Fig. 4 shows the exit temperature distribution of both fluids with

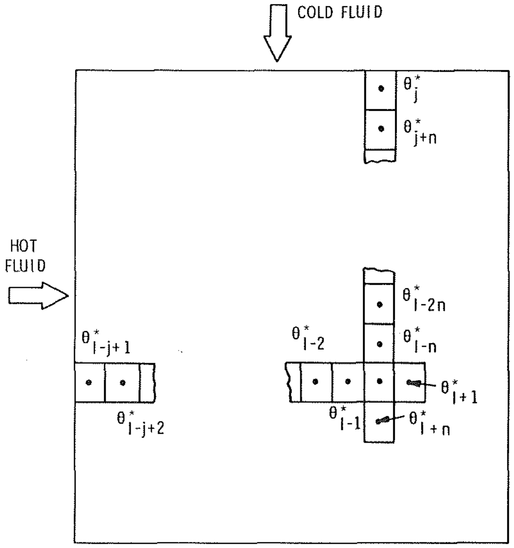

Note: $\theta^*(\mathrm{I}) = \theta\,(i, j)$
$\mathrm{I} = (i-1)n+j$

Fig. 3 Related nodes in equation (22)

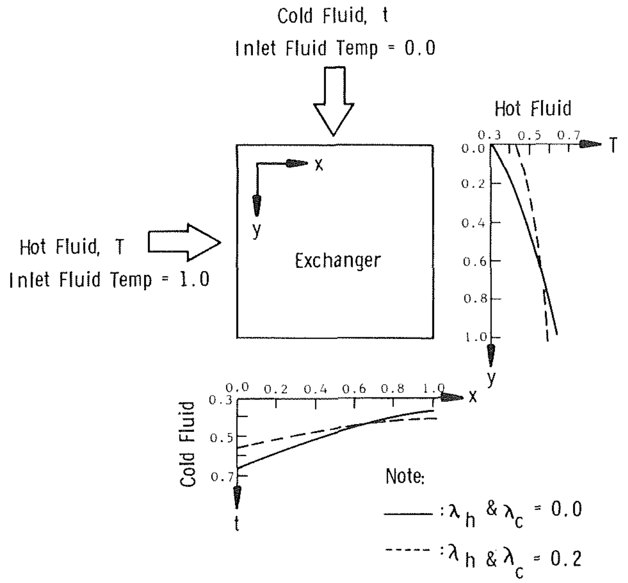

CONDITIONS: $C_c/C_h = 1.0$
$(\eta ha)_h/(\eta ha)_c = 1.0$
NTU = 1.0

Fig. 4 Fluid temperature distributions at exits of exchanger

λ_h (and λ_c) = 0.0 and 0.2 respectively. In this figure, exchanger NTU, C_c/C_h and $(\eta ha)_h/(\eta ha)_c$ are all equal to unity. When λ_h (and λ_c) = 0.2, the exit temperature of the hot fluid is warmer and that of the cold fluid is colder in most regions than those of the respective fluids when λ_h (and λ_c) = 0.0. This results in lower thermal performance of the exchanger when the longitudinal heat conduction in the wall cannot be neglected.

For the case of $C_c/C_h = 1.0$, the conduction effect factor increases as the exchanger NTU increases as shown in Figs. 5 and 6. For the cases of $C_c/C_h = 0.5$ and 2.0, the conduction effect factor generally increases with NTU until NTU reaches approximately 10, then it decreases with the increase of NTU as shown in Figs. 5 and 7. These results are due to the exchanger unbalanced flow stream capacity rates which suppress the longitudinal conduction effect, and are similar to those observed by other investigators [1, 2, 7].

Relations between $(\eta ha)_h/(\eta ha)_c$ and τ used C_c/C_h and λ_c/λ_h as parameters are presented in Fig. 8.

For all other parameters held constant, the conduction effect factor, τ, is maximum when $C_c/C_h = 1.0$ as shown in Fig. 9. In other words, the deterioration of the exchanger effectiveness is the greatest when the flow stream capacity rates on both sides are equal. This result is similar to those of previous reports [1, 2, 7].

From the results presented in this paper, it is noted that the thermal

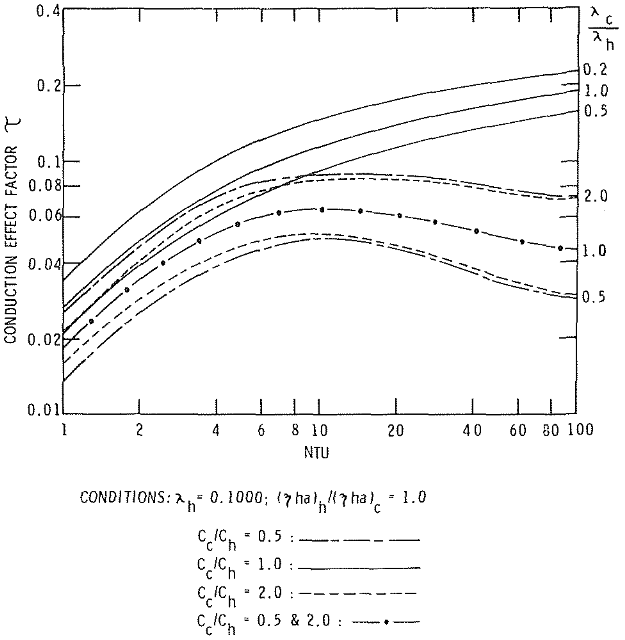

Fig. 5 **Relations between conduction effect factor τ and other parameters**

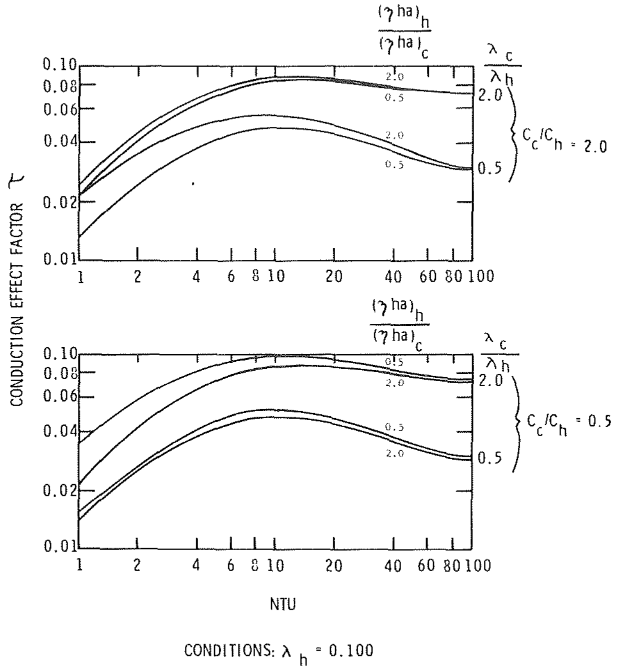

Fig. 7 **Relations between conduction effect factor τ and other parameters**

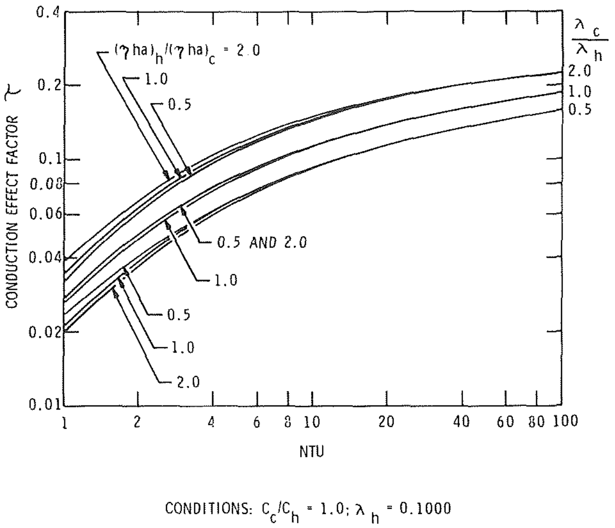

Fig. 6 **Relations between conduction effect factor τ and other parameters**

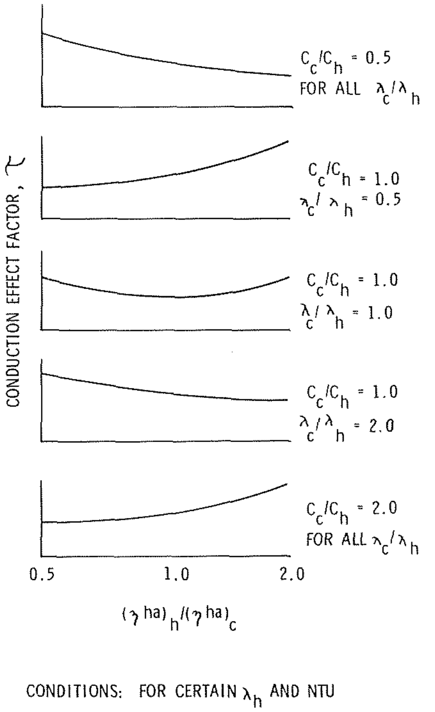

Fig. 8 **Relations between conduction effect factor τ and other parameters**

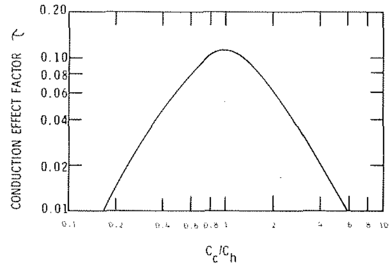

CONDITIONS: NTU = 10.0; λ_h = 0.100; λ_c/λ_h = 1.000; $(\eta ha)_h/(\eta ha)_c$ = 1.000

Fig. 9 Relations between conduction effect factor τ and other parameters

performance deterioration of crossflow heat exchanger due to longitudinal conduction through the wall structure is not always negligible, especially when the capacity rate ratio of both fluids is equal to 1.0, and when the longitudinal conduction parameter is large.

References

1 Bahnke, G. D., and Howard, C. P., "The Effect of Longitudinal Heat Conduction on Periodic-Flow Heat Exchanger Performance," ASME *Journal of Engineering for Power*, Vol. 86, 1964, pp. 105–120.

2 Kays, W., and London, A. L., *Compact Heat Exchangers*, 2nd ed., McGraw-Hill, New York, 1964.

3 Lamberton, T. J., "Performance Factors of a Periodic-Flow Heat Exchanger," TRANS. ASME, April 1958, pp. 586–592.

4 Schultz, B. H., "Regenerators with Longitudinal Heat Conduction," IME-ASME General Discussion on Heat Transfer, London, England, 1951, pp. 440–443.

5 Theoclitus, G., and Eckrich, T. L., "Parallel Flow Through the Rotary Heat Exchanger," Proceedings of Third International Heat Transfer Conference, 1966, Vol. I, pp. 130–138.

6 Hahnemann, H. W., "Approximate Calculation of Thermal Ratios in Heat Exchangers Including Heat Conduction in Direction of Flow," National Gas Turbine Establishment Memorandum, No. M36, 1948.

7 Kroeger, P. G., "Performance Deterioration in High Effectiveness Heat Exchanger Due to Axial Heat Conduction Effects," 1966 Cryogenic Engineering Conference, Boulder, Colo.

8 Landau, H. G., and Hlinka, J. W., "Steady State Temperature Distribution in a Counterflow Heat Exchanger Including Longitudinal conduction in the Wall," ASME paper, No. 60-WA-236, 1960.

9 Chiou, J. P., "Thermal Performance Deterioration in Crossflow Heat Exchanger due to Longitudinal Heat Conduction in the Wall," ASME 76-WA/HT-8, paper presented at ASME Winter Annual Meeting, Dec. 5, 1976, New York, N.Y.

10 Mason, J. L., "Heat Transfer in Crossflow," Proceedings of Applied Mechanics Second U.S. National Congress, 1954, pp. 801–803.

11 Chiou, J. P., "The Effect of Nonuniform Fluid Flow Distribution on the Thermal Performance of Crossflow Heat Exchanger," ASME 77-WA/HT-3, paper presented at 1977 Winter Annual Meeting of American Society of Mechanical Engineers, Atlanta, Ga., Nov. 1977.

12 Chiou, J. P., "Thermal Performance Deterioration in Crossflow Heat Exchanger due to Flow Nonuniformity on Both Hot and Cold Sides," To be presented at Sixth International Heat Transfer Conference, Toronto, Canada, Aug. 1978 (also to appear in the Conference Proceedings).

B. R. Hollworth
Assistant Professor,
Mechanical and Industrial Engineering Department,
Clarkson College of Technology,
Potsdam, N. Y.
Mem. ASME

R. D. Berry
Utilities Development Engineer,
Kodak,
Kodak Park,
Rochester, N. Y.
Assoc. Mem. ASME

Heat Transfer From Arrays of Impinging Jets with Large Jet-to-Jet Spacing

Local and average convective heat transfer coefficients were measured for arrays of widely spaced impinging air jets and correlated in terms of system geometry, air flow, and fluid properties. The configurations were square arrays of circular turbulent jets (spaced from 10–25 diameters apart) incident upon a flat isothermal target surface. Independent parameters were varied over ranges generally corresponding to gas turbine cooling applications. Local heat transfer coefficients were influenced by interference from neighboring jets only when the target plate and the jet orifice plate were less than five jet diameters apart. Average heat transfer coefficients were nearly equal for all the arrays tested as long as the coolant flow per unit area of target surface was held constant. In fact, there was a tendency for the more widely spaced configurations to produce slightly higher average heat transfer under such conditions.

Introduction

Impinging fluid jets are widely used for heating and cooling solid surfaces. Applications include the processing of glass and some metals, the drying of paper stock, and the cooling of electronic components. Impinging jets provide an especially attractive means of cooling critical gas turbine parts; they produce very high convective heat transfer rates with minimal expenditures of cooling air.

A single jet directed at a target surface tends to produce very localized cooling; hence, most practical impingement systems consist of an array of many cooling jets laid out in a regular pattern (often a square matrix) to produce more uniform heat transfer. Several investigators have measured average and local convective heat transfer coefficients for such multi-jet systems; these include Friedman and Mueller [1],[1] Gardon and Cobonpue [2], Huang [3], Daane and Han [4], Kercher and Tabakoff [5], and Chance [6]. They determined, in their investigations, how heat transfer coefficients varied with coolant flow rate, fluid properties, and system geometry.

In certain gas turbine applications, the coolant flow (per unit area of cooled surface) and the available pressure drop are set, within narrow limits, by the overall design of the engine. Corresponding situations may exist for the other applications cited above. In these cases where the flow is relatively low and the pressure drop is high, the designer is forced to use an array of cooling jets spaced far (15 or more diameters) apart to provide the desired metering—though this may or may not be the optimum array with regard to magnitude and uniformity of heat transfer. Though there is presently an extensive body of heat transfer data for impinging jet systems, the information for arrays having holes more than 10–12 diameters apart is scant.

The purpose of this study, then, was to measure both average and local convective heat transfer coefficients for arrays of turbulent air jets with jet-to-jet spacing varying from 10–25 diameters. Often, knowledge of only the space-averaged heat transfer coefficient is adequate for design calculations. However, the heat transfer distribution for widely spaced jets tends to be quite nonuniform, with isolated cool spots beneath individual jets. Such a situation has the potential for producing severe thermal stresses or distortions in the target surface. The local heat transfer measurements may be used in conjunction with heat transfer and stress analysis computer routines to establish the level of thermal stresses and strains.

The data obtained were correlated in terms of relevant independent parameters involving flow rate, fluid properties, and system geometry. These parameters were varied over ranges generally appropriate to gas turbine cooling, though this information is certainly of use to designers in those other areas where impinging jets find use. Table 1 summarizes the ranges of variation of the test variables involved. The jets were formed by 4×4 square arrays of circular orifices on a flat surface oriented parallel to the target plate as shown in Fig. 1, and spent air was exhausted along all four edges of the enclosure. The orifices themselves were square-edged with length/diameter = 1.0, which is typical of the sort used in practical applications. The working fluid was air near S.T.P.

---

[1] Numbers in brackets designate References at end of paper.

Contributed by the Gas Turbine Division for presentation at the Gas Turbine Conference, London, England, April 9–13, 1978, of THE AMERICAN SOCIETY OF MECHANICAL ENGINEERS. Manuscript received at ASME Headquarters December 22, 1977. Paper No. 78-GT-117.

Table 1 Ranges of test variables

Nominal jet diameter	d	2.5, 5.0 mm[2]
Jet spacing/jet diameter	X/d	10, 15, 20, 25
Plate spacing/jet diameter	Z/d	1, 2.5, 5, 10, X/d
Jet Reynolds number	Re	3000–35,000
Jet exit Mach number	*	0.06–0.40
Jet exit velocity	V	20–130 m/s

[2] Nominal diameters were 2.5 and 5.0 mm. Actual diameters were 2.54 and 5.08 mm.

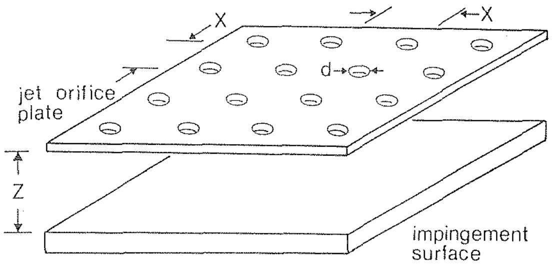

Fig. 1 Impingement system, with nomenclature

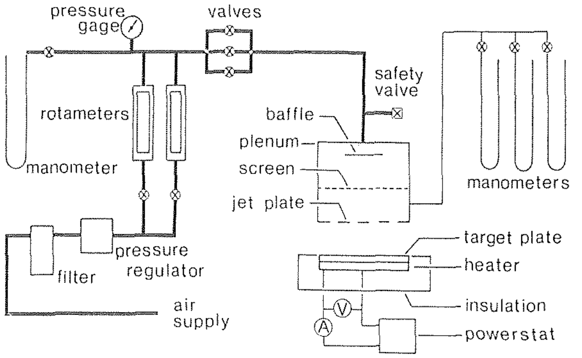

Fig. 2 The test rig

Experimental Apparatus and Procedures

The test system is shown in Fig. 2. Impingement air is supplied by a compressor, and dried and filtered upstream of the heat transfer rig. The flow to the jet array is regulated with manually-operated valves and measured with a bank of precision (±1 percent) rotameters. The constant supply pressure provided by the regulator and the constant jet discharge pressure (i.e., ambient pressure) insure that the flow rate does not vary during a test. Cooling air enters the jet plenum at room temperature; and a baffle and screen in the plenum insure that the air is evenly distributed among the several jet orifices. Total pressure and temperature are measured in the plenum. Interchangeable orifice plates are used to provide the eight impingement geometries (two values of d and four values of X/d) indicated in Table 1. The spacing, Z, between the orifice plate and the target plate is set and maintained using wooden spacers machined to the appropriate lengths. The spacers are small wooden dowels located at the four corners of the plates. They are set as far as possible from the jet array to minimize their effect on the crossflow between the plates. Wood has a fairly low thermal conductivity, tending therefore to minimize the fin effect (i.e., the conduction of heat away from the target plate along the dowels).

Air jets issuing from the orifice plate impinge upon a flat isothermal surface consisting of a 6 mm thick copper target plate heated by resistance heater pads glued to its back face. In fact there is one such plate (square, with dimensions 4X × 4X) for each of the eight arrays tested. Electric power is supplied to the heaters with a powerstat, and the heat input is determined by measuring current (I) and voltage (E) in the heater circuit. Each plate is insulated with 6 cm of balsa wood to reduce heat leak from its edges and back to the surroundings.

Each target plate is instrumented with five 30 gas iron-constantan thermocouples to measure surface temperature. They are installed in holes drilled in from the back surface to within 1.0 mm of the impingement side. The TC's (thermocouples) are forced into the (tight) holes and held in place by peening the metal to clamp the leads where they enter the plate. The holes are drilled inclined at 45 deg to the plate to keep a greater length of the leads in thermal contact with the plate, thereby reducing conduction error. Leads are routed out to the edge of the plate along slots milled into the back face of the plate, and finally through tight holes drilled through the balsa insulation. Measuring junctions are located at sites near the four jet orifices at the center of the array. For an x-y co-ordinate system with axes parallel to the edges of the target plate and origin at its center, the locations are

$$\text{TC1 } x = 0 \text{ and } y = 0$$

$$\text{TC2 } x = X/2 \text{ and } y = 0$$

$$\text{TC3 } x = 0 \text{ and } y = X/4$$

$$\text{TC4 } x = X/2 \text{ and } y = X/2$$

$$\text{TC5 } x = X/4 \text{ and } y = X/4$$

One copper plate (the one with $X/d = 25$ and $d = 5.0$ mm) is instrumented with 12 thermocouples—the five listed above plus seven at sites near the edges of the plate. During the entire test program this plate, presumably a "worst case," remained acceptably isothermal. The maximum and minimum readings never differed by more than 7°C; the difference was usually less than 4°C.

In addition, one target plate is instrumented with a microfoil heat

Nomenclature

A = area of target plate, m^2
d = nominal diameter of jet orifices, mm
E = voltage supplied to target plate heater, volts
$\bar{h}$ = average impingement heat transfer coefficient, W/m$^2\cdot$°C
h = local impingement heat transfer coefficient, W/m$^2\cdot$°C
I = current supplied to target plate heater, amps
k = thermal conductivity of test fluid, W/m – °C
$\overline{\text{Nu}}$ = average Nusselt number, $\bar{h}d/k$
Nu = local Nusselt number, hd/k
Pr = Prandtl number
q = heat flux, W/m^2
q_r = radiant heat flux, W/m^2
Re = jet Reynolds number, $\rho Vd/\mu$
r = radial distance from jet stagnation point, mm
T_a = fluid temperature used in defining $\bar{h}$ and h, °C
T_0 = jet plenum temperature, °C
T_∞ = ambient (room) temperature, °C
T_s = target surface temperature, °C
T_r = jet centerline recovery temperature, °C
V = jet discharge velocity, m/s
X = center-to-center spacing of jet orifices, mm
Z = normal distance between orifice plate and target plate, mm
μ = test fluid dynamic viscosity, Pa·s
ρ = test fluid density, kg/m^3

flux sensor (having a sensing area of 0.7 mm × 1.0 mm) located at the center of its impingement surface. This plate was traversed beneath jet arrays to determine local heat fluxes and local heat transfer coefficients. The heat flux sensor (a commercial unit available from RdF Corporation of Hudson, N.H.) consists of two thermopiles affixed to opposite faces of a 0.025 mm thick Kapton thermal barrier, with this assembly sandwiched between two more Kapton sheets of the same thickness. The thermopiles are wired so that their emf's "buck" one another and the net emf produced is proportional to the heat flux, q, through the barrier. The manufacturer furnishes a calibration with each unit.

Space-average heat transfer coefficients were computed using

$$\bar{h} = \frac{EI}{A(T_s - T_a)} - \Delta\bar{h} \tag{1}$$

where A is the target surface area (16 X^2), and T_s is the target surface temperature obtained by taking the arithmetic mean of the readings from the five thermocouples imbedded in the heated plate. The term $\Delta\bar{h}$ accounts for heat lost by radiation, and by conduction through the insulation. Its value was determined by performing a calibration with the cooling jets inoperative, and correcting for free convection using the appropriate correlation from Kreith [7]. In this fashion, it was determined that $\Delta\bar{h}$ = 4.0 W/m^2 – °C.

During these tests, air arrived at the test rig at room temperature. Because the jet velocity was always low (≤130 m/s) it was presumed that it would be justified to use T_0 (the total temperature of the air measured in the plenum) as the effective air temperature in equation (1). As testing proceeded, it was observed that there was radiation heat transfer between the heated target plate and the orifice plate which warmed the air in the plenum; the condition was, of course, most pronounced when running arrays with large X/d at low flows. In fact, over the whole program, T_0 averaged 4–5°C above room temperature. Because this difference was significant compared to the overall ΔT (($T_s - T_0$) ≅ 65°C was used) measurements of the recovery or adiabatic wall temperature were made, and these values were used for T_a in equation (1). These measurements were made with a thermocouple buried in a cylindrical aluminum slug (length = 5 mm, dia = 6 mm) which was imbedded in a large flat balsa wood block flush with the surface. The block was traversed beneath the jet array to determine the spatial variation of recovery temperatures on the target surface.

Local heat transfer coefficients were calculated from local heat fluxes measured with the heat flux sensor using

$$h = \frac{q - q_r}{T_s - T_a} \tag{2}$$

where q_r is the radiant heat flux from the sensor surface. The radiation correction was calculated using an emissivity value for the Kapton sensor which was provided by the manufacturer. The surface temperature (T_s) was measured using one TC in the thermopile nearest the air-side surface of the sensor, and a small correction was made for the temperature drop across the intervening layer of Kapton. Again, the recovery temperature was used as the effective air temperature (T_a) in equation (2). There is a tendency for there to be a local cold spot at the sensor site. To discourage this tendency and keep a fairly isothermal target surface, a roughly circular region (dia ≅ 300 mm) around the sensor was masked with a sheet of Kapton having the same thermal impedance as the sensor itself.

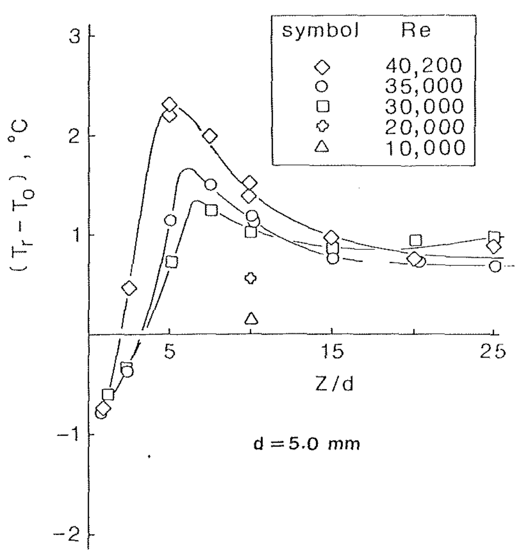

Fig. 3 Stagnation point recovery temperatures

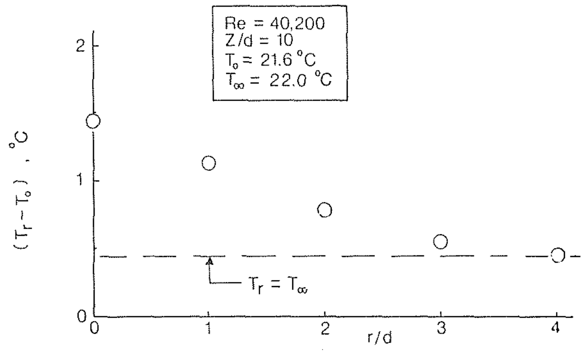

Fig. 4 Radial variation of recovery temperature

Results and Discussion

Recovery Temperatures. Recovery temperatures were measured, using the methods previously described, while V and Z/d were varied over the same ranges which would be used when measuring heat transfer coefficients. Fig. 3 shows the recovery temperature (T_r) at the jet stagnation point. Measurements were made on a 5.0 mm jet, and the highest Re shown (40,200) corresponds to a jet exit velocity of 130 m/s. For Z/d < 2 or 3, the recovery temperature is somewhat lower than the jet plenum temperature (T_0). For 3 ≤ Z/d ≤ 15, the recovery temperature exceeds the plenum temperature. The jets expand to a temperature below ambient, and are subsequently heated by mixing with warmer ambient air so that, upon impingement, they have a total temperature (and recovery temperature) which exceeds the plenum temperature. This behavior was noted also by Gardon [2] and Sparrow, et al. [8]. For large Z/d, the recovery temperature is equal to ambient temperature (T_∞). During these tests, ambient temperature was approximately 1.0°C higher than the plenum temperature, hence ($T_r - T_0$) approaches 1.0°C for large Z/d. Fig. 4 shows the radial variation of the recovery temperature measured for Z/d = 10 and V = 130 m/s, which is the highest jet velocity for which heat transfer data was taken.

It was decided that the most suitable air temperature to use in correlating heat transfer data would be the area-averaged recovery temperature, and that this temperature could be adequately approximated (see Fig. 4) by

$$T_a = \frac{1}{2}(T_r + T_\infty) \tag{3}$$

The centerline recovery temperature (T_r) was calculated in the following way. For small Z/d (<5), it was assumed that T_r was not influenced by T_∞ as mixing had not penetrated to the jet axis (see Abramovitch [9]); values of T_r were taken directly from Fig. 3. For Z/d > 15, it was assumed (see Fig. 3) that $T_r = T_\infty$. Finally, for 5 < Z/d < 15, T_r was obtained from a linear interpretation (based on the value of Z/d) between the value of T_r at Z/d = 5 (from Fig. 3) and the value of T_r at Z/d = 15 (i.e., $T_r = T_\infty$). This method of determining T_r eliminates the need to measure the recovery temperature each time a heat transfer measurement is made. In fact, equation (3) gives a value of T_a that never differs from the arithmetic mean of T_0 and T_∞ by more than 1°C.

Average Heat Transfer Coefficients. Average heat transfer coefficients were found to correlate well using a relation of the form

$$\overline{\mathrm{Nu}} = \frac{\overline{h}d}{k} = \mathrm{Re}^m \mathrm{Pr}^n f(X/d, Z/d) \qquad (4)$$

where all fluid properties (μ, k, etc.) were evaluated at a "film" temperature halfway between T_0 and T_s. The Prandtl number (Pr) was constant at 0.72 for this study and the traditional assumption $n = 1/3$ was used. Fig. 5 shows average heat transfer coefficients obtained in this study for the smallest jet-to-jet spacing ($X/d = 10$), compared to measurements made by other investigators. Results compare favorably, though some basic differences in the test configurations preclude better agreement. Gardon and Cobonpue (Curve II) used jets produced by arrays of long nozzles instead of by perforated plates. Kercher and Tabakoff, Chance, and Daane and Han (Curves I, III, and IV respectively) reported data for systems in which spent air was constrained to exhaust at one end of a rectangular enclosure. In both instances, the crossflow pattern (hence the heat transfer rates) must be expected to differ somewhat from those obtained here.

Figs. 6 and 7 show average heat transfer for the rest of the arrays tested, X/d = 15, 20, and 25. It was noted that there was no hole-size effect: at the same Re, Z/d, and X/d, jets formed by 2.5 and 5.0 mm dia. orifices yielded virtually the same $\overline{\mathrm{Nu}}$. Fig. 6 shows this for arrays with $X/d = 20$; it was true for arrays with X/d = 10, 15, and 25 as well. It was noted, also, that there was no effect due to varying ΔT ($\Delta T = T_s - T_0$). Several tests were run using $\Delta T = 32$°C, and the resulting values of $\overline{\mathrm{Nu}}$ were virtually identical to those measured using $\Delta T = 65$°C. The slopes, m, of the $\overline{\mathrm{Nu}}$ versus Re curves (Figs. 5, 6, and 7) vary between 0.74 and 0.86, depending upon both X/d and Z/d. The most apparent trend was that m decreased with increasing Z/d, as these figures clearly indicate. The method of least squares was used to determine that the value which best fit all data was $m = 0.80$. Despite the variation of m discussed above, the data correlated well (see Fig. 8) with

$$\frac{\overline{\mathrm{Nu}}}{\mathrm{Re}^{0.80}\mathrm{Pr}^{0.33}} = f\left(\frac{X}{d}, \frac{Z}{d}\right) \qquad (5)$$

The geometry function, f, is portrayed graphically, as no simple algabraeic representation was found. The data of [2, 4, 5, 6] may in general be reduced to the form of equation (5). Daane and Han used exactly the same form with $m = 0.78$. Chance and Kercher and Tabakoff used virtually the same form, but both found that m increases with X/d for $X/d < 12$. At $X/d = 10$, they obtained $m = 0.84$ and $m = 0.94$ (respectively) for turbulent Reynolds numbers. The correlations of Kercher and Tabakoff and Chance contains also a "crossflow degradation" factor ϕ_2; for large X/d and relatively few rows of jets the crossflow effect on average heat transfer is small and $\phi_2 \cong 1.0$.

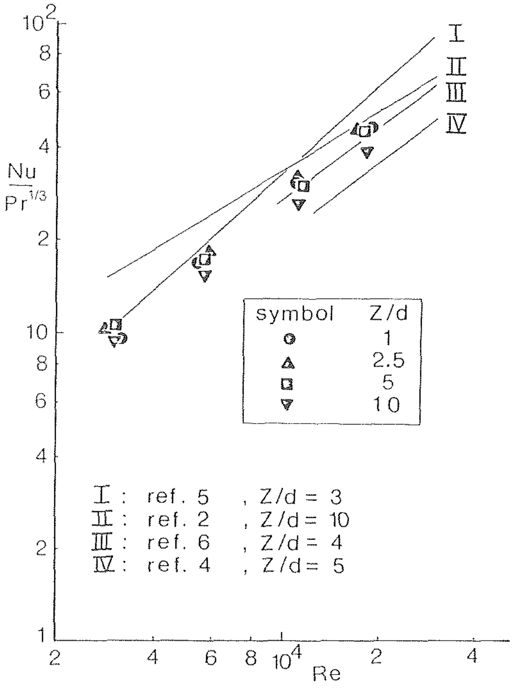

Fig. 5 Average heat transfer coefficients for X/d = 10, d = 2.5 mm

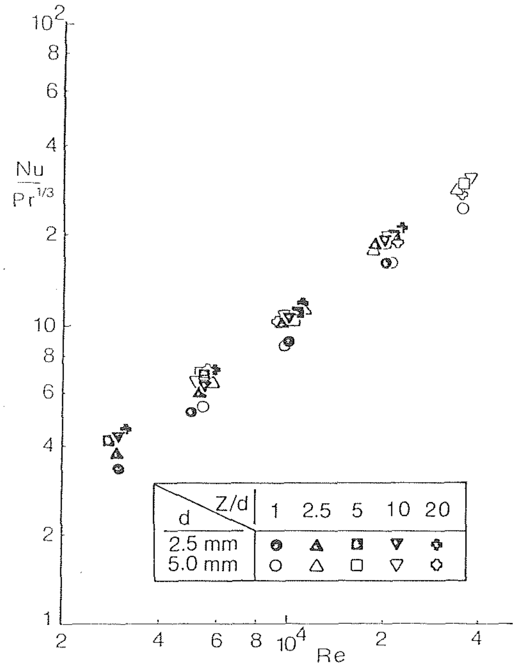

Fig. 6 Average heat transfer coefficients for X/d = 20, d = 2.5 and 5.0 mm

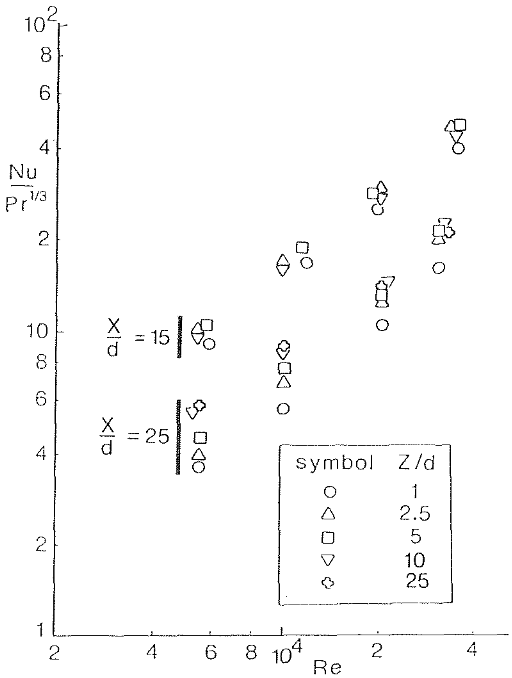

Fig. 7 Average heat transfer coefficients for X/d = 15 and 25, d = 5.0 mm

Gardon and Cobonpue correlated their data using Nusselt and Reynolds numbers in which X is the significant length, and the Reynolds number contained the fictitious "arrival" velocity of the jet. However, their correlation can be recast in the form of equation (5) with $m = 0.625$.

From inspection of the same figure, several useful observations may be made. For all arrays tested, the average heat transfer coefficient was sensitive to Z for $Z/d \leq 5$. The "tightest" array ($X/d = 10$) exhibited a marked decay in $\overline{\text{Nu}}$ as Z/d was increased past 5; the same tendency (though less pronounced) was exhibited by the array with $X/d = 15$. However, for the most widely-spaced arrays ($X/d = 20, 25$), $\overline{\text{Nu}}$ is virtually independent of Z for $5 \leq Z/d \leq X/d$. For the designer whose requirements demand an array with $X/d > 15$, the implication is apparent. If space limitations permit, use $Z \geq 5d$ for maximum heat transfer; as long as $Z < X$, the actual value of Z selected has no significant effect on $\overline{\text{Nu}}$.

It has been generally accepted that the "best" impingement systems have $X/d \leq 10$. It may be true that such geometries produce high average heat transfer, but the total required coolant flow is also high. This is an important consideration in gas turbine applications, where a penalty (in terms of overall power plant efficiency) is exacted for air diverted for cooling purposes. Accordingly, arrays having differing X/d should be rated by comparing their respective heat transfer rates at the same coolant flow per unit area of cooled target surface. Fig. 9 shows $\overline{\text{Nu}}$ plotted against the parameter Re*, for the several values of X/d considered here. This parameter is a Reynolds number based upon the flow rate per unit area, G, of target surface, and is defined as

$$\text{Re}^* = \frac{4}{\pi}\frac{Gd}{\mu} = \text{Re}(d/X)^2 \qquad (6)$$

Fig. 9 was constructed for $Z/d = 5$, which is nearly optimum orifice plate-to-target plate spacing for all arrays. At constant Re* (i.e., at constant G) average heat transfer increases steadily as X/d increases; and the array with $X/d = 25$ yields $\overline{\text{Nu}}$ about 20 percent higher than that produced by the array with $X/d = 10$.

Local Heat Transfer Coefficients. Measurements were made, also, of local convective heat transfer coefficients beneath individual jets in the arrays. These measurements were made with and without the remaining jets operational, to determine the extent to which local heat transfer coefficients were influenced by crossflow from neighboring jets. All such data were taken at the following conditions:

$$\text{Re} = 20{,}000$$

$$d = 5.0 \text{ mm}$$

$$X/d = 10, 15$$

$$Z/d = 1, 5, 10, 15$$

Figs. 10 and 11 show typical radial variations of local heat transfer coefficients for $X/d = 10$. The solid lines represent the author's measurements of local heat transfer coefficients with all jets plugged except the one for which measurements were being made. For $Z/d = 1$ (Fig. 10) secondary heat transfer peaks occur near $r/d = 1$–2; these same peaks were observed by Gardon and Cobonpue [2] and later attributed by Gardon and Akfirat [10] to variations in jet turbulence. There is apparently some degree of jet interaction. For $1 \leq r/d \leq 2$, local Nu values are increased due to the influence of nearby jets. At larger r/d, Nu values differ, depending upon which radius one selects to make the measurements; this must be attributed also to jet interaction. For $Z/d = 10$ (Fig. 11) the jet within an array yields virtually the same heat transfer profile as a single jet operating at the same conditions. Measurements at $Z/d = 5$ (not shown) also show no appreciable distortion of the profile. The same measurements were repeated for $X/d = 15$. For $Z/d = 1$, the same behavior was observed (though less pronounced) as for $X/d = 10$. For $Z/d = 5, 10, 15$ the profiles were essentially unaffected by jet interaction.

It must be pointed out that while the heat transfer profiles in Figs. 10 and 11 are generally typical for such impingement systems, the profiles must, in fact, change shape continuously throughout the

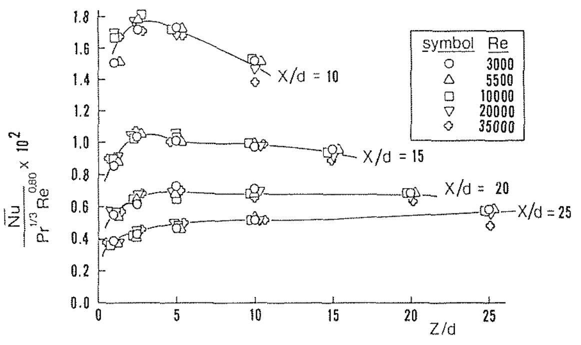

Fig. 8 Effect of Z/d on average heat transfer coefficients

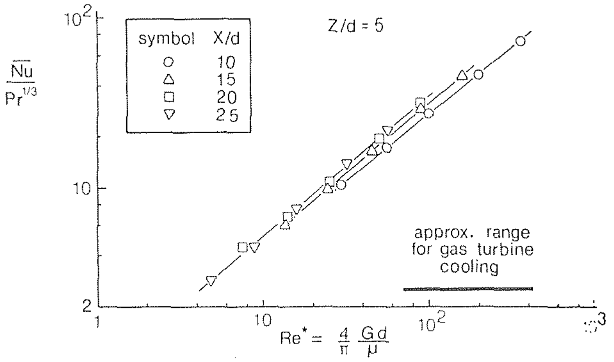

Fig. 9 Average heat transfer coefficients versus flow rate per unit area of target surface

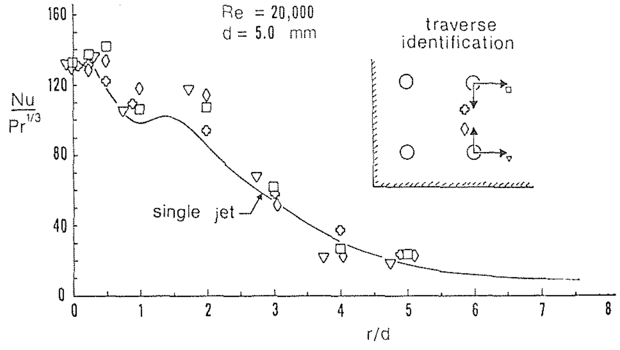

Fig. 10 Local heat transfer coefficients for $X/d = 10$, $Z/d = 1$

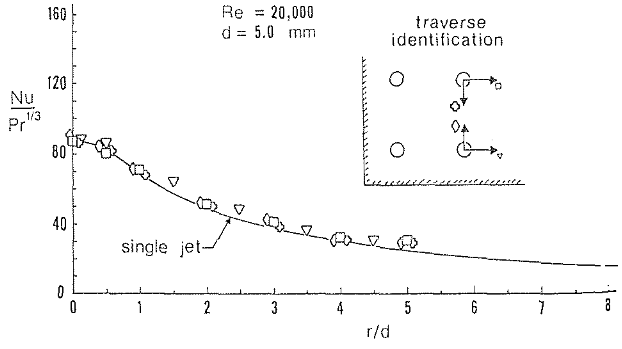

Fig. 11 Local heat transfer coefficients for $X/d = 10$, $Z/d = 10$

impingement region. This occurs for two reasons:

1 Crossflow is cumulative. For a square region $L \times L$ in the center of the array, the coolant mass flow is proportional to L^2 while the exit area for the same flow in proportional to L. Jets farther from the center of the array find themselves, therefore, in a stronger wind and one must expect a correspondingly larger distortion of the local h-distribution. Because this study concerned itself with widely spaced jets, this crossflow effect is less pronounced than it would be for more closely-packed arrays.

2 There is an edge effect. The flow field near the periphery of the array is affected by the absence of additional jets farther out. The measurements reported here were all made on 4×4 jet arrays. Hence there is some small measure of "edge effect" undoubtedly reflected in all the local h's measured.

All local heat transfer measurements were made at Re = 20,000 for this study. The author cautions that these heat transfer profiles cannot be applied to jets operating at significantly different Re. For a single impinging jet, $h \sim \mathrm{Re}^{0.5}$ near the stagnation point of the jet (where the boundary layer is laminar), while $h \sim \mathrm{Re}^{0.8}$ at large r/d (where the boundary layer is turbulent). Therefore h-profiles for low Re are relatively more peaked near $r/d = 0$ than are those for large Re. The data reported in a recent paper by Martin [11] clearly show this behavior.

Conclusions

The heat transfer data obtained from this experimental investigation should provide the practicing engineer with sufficient information to design impingement cooling configurations consisting of square arrays of axisymmetric turbulent jets, spaced from 10–25 diameters apart. Significant conclusions resulting from this study are the following:

1 Local h's beneath individual jets in such an array are affected by interference from neighboring jets only for small Z/d. For $Z/d \geq 5$, each jet produces virtually the same h-profile as would be produced by a single isolated impinging jet.

2 For large X/d ($X/d = 20, 25$) average h's are nearly independent of Z (and are maximum) for $5d \leq Z \leq X$. Moreover, local h-profiles are flatter (see Figs. 10 and 11) for large Z—thereby reducing temperature gradients in the target surface. For such arrays, then, it is best to use $Z \to X$ if space permits.

3 At constant coolant flow per unit area of target surface, average h's increase with X/d for $10 \leq X/d \leq 25$. One does not, therefore, pay a penalty in terms of total heat transfer if obliged to use a widely-spaced array. It remains true, however, that such arrays still produce more nonuniform cooling than more tightly packed jet arrays.

Acknowledgments

The authors wish to thank the National Science Foundation, who sponsored this study through an NSF Initiation Grant.

References

1 Friedman, S. J., and Mueller, A. C., "Heat Transfer to Flat Surfaces," *Proceedings, General Discussion on Heat Transfer,* the Institute of Mechanical Engineers, London, England, 1951, pp. 138–142.

2 Gardon, R., and Cobonpue, J., "Heat Transfer Between a Flat Plate and Jets of Air Impinging on It," International Developments in Heat Transfer, *Proceedings of 2nd International Heat Transfer Conference,* ASME, New York, N.Y., 1962, pp. 454–460.

3 Huang, G. C., "Investigations of Heat Transfer Coefficients for Air Flow Through Round Jets Impinging Normal to a Heat Transfer Surface," ASME *Journal of Heat Transfer,* Vol. 85, 1963, pp. 237–243.

4 Daane, R. A., and Han, S. T., "An Analysis of Air Impingement Drying," *Tappi,* Vol. 44, 1961, pp. 73–80.

5 Kercher, D. M., and Tabakoff, W., "Heat Transfer by a Square Array of Round Air Jets Impinging Perpendicular to a Flat Surface Including the Effect of Spent Air," ASME JOURNAL OF ENGINEERING FOR POWER, Vol. 92, No. 1, Jan. 1970, pp. 73–82.

6 Chance, J. L., "Experimental Investigation of Air Impingement Heat Transfer Under an Array of Round Jets," *Tappi,* Vol. 57, No. 6, 1974, pp. 108–112.

7 Kreith, F., *Principles of Heat Transfer,* 3rd ed., Intext, New York and London, 1973, pp. 383–413.

8 Sparrow, E. M., Goldstein, R. J., and Rouf, M. A., "Effect of Nozzle-Surface Separation Distance on Impingement Heat Transfer for a Jet in a Crossflow," ASME *Journal of Heat Transfer,* Vol. 97, 1975, pp. 528–533.

9 Abramovitch, G. N., *The Theory of Turbulent Jets,* Trans. by Scripta Technica, M.I.T. Press, Cambridge, Mass., 1963, pp. 89–102.

10 Gardon, R., and Akfirat, J. C., "The Role of Turbulence in Determining the Heat Transfer Characteristics of Impinging Jets," *International Journal of Heat and Mass Transfer,* Vol. 8, 1965, pp. 1261–1272.

11 Martin, H., "Heat and Mass Transfer Between Impinging Gas Jets and Solid Surfaces," *Advances in Heat Transfer,* Vol. 13, 1977, pp. 1–60.

J. L. S. Chen
Associate Professor,
Department of Mechanical Engineering,
University of Pittsburgh,
Pittsburgh, Pa.
Mem. ASME.

T. N. Smith
McDonnell Douglas Corp.,
St. Louis, Mo.

Forced Convection Heat Transfer from Nonisothermal Thin Needles

The steady laminar forced convection heat transfer from nonisothermal thin needles in nonuniform incompressible flows is investigated analytically. Similarity temperature fields and heat transfer characteristics for needles with power-law thermal variations in (1) wall temperature, and (2) surface heat flux, are obtained. The influence of needle size and Prandtl number on the thermal behavior of the flow is examined for a uniform as well as an accelerating flow.

Introduction

An important aspect of experimental studies of flow and heat transfer characteristics is the measurements of velocity and temperature profiles of the flow field. The probe of the measuring devices, such as a hot wire anemometer or shielded thermocouple, is often a very thin wire or "needle." The detailed analysis of the flow over such slender needle-shaped bodies, therefore, is of considerable practical interest. The axisymmetric boundary layer flow past a thin paraboloid of revolution has been investigated by Mark [1],[1] Lee [2], and Miller [3]. These problems are closely related to the flow problem on a long thin cylinder considered by Glauert and Lighthill [4]. Free-convention heat transfer from vertical thin needles has been examined by many investigators in recent years [5–9]. Since Cebeci, et al. [10] extended Mark's [1] analysis to forced-convection heat transfer, considerable efforts have been very usefully devoted to forced convection [11, 12] as well as combined forced and free convection [13, 14] from thin needles. However, these investigations have been concerned only with uniform surface temperature or uniform surface heat flux.

This analysis is primarily intended to cover the problem of forced heat transfer from nonisothermal thin needles. Similarity solutions are presented for the steady, incompressible forced heat transfer from needles having arbitrary power-law variations in (1) wall temperature, and (2) wall heat flux. To the authors' knowledge, solutions for nonisothermal needles have not been reported previously in the literature. Results for temperature fields and heat transfer characteristics with negligible viscous dissipation are obtained. It is also shown that the existence of similarity solutions depends upon pressure variations along the needle when viscous dissipation is considered.

Analysis

Consider a steady, incompressible, laminar boundary-layer axisymmetric flow past a thin needle. The needle is considered thin when its thickness does not exceed that of the boundary layer over it. Under this assumption, the effect of transverse curvature is of importance, but the pressure variation along the surface due to the presence of the needle can be neglected [2, 12]. Clearly, the solution so obtained is not applicable in the region near the front stagnation of the needle. To study a more general flow with axial pressure gradient, however, we impose a variable mainstream velocity of the form $U(x) = u_1 x^m$. When $m = 0$, it reduces to the cases of uniform flow reported in [1–4, 12]. The mainstream fluid is maintained at a uniform temperature T_∞. Assuming constant fluid properties, the governing boundary layer equations of continuity, momentum, and energy use, respectively,

$$\frac{\partial(ru)}{\partial x} + \frac{\partial(rv)}{\partial r} = 0 \tag{1}$$

$$u\frac{\partial u}{\partial x} + v\frac{\partial u}{\partial r} = U\frac{dU}{dx} + \frac{\nu}{r}\frac{\partial}{\partial r}\left(r\frac{\partial u}{\partial r}\right) \tag{2}$$

$$u\frac{\partial T}{\partial x} + v\frac{\partial T}{\partial r} = \frac{\alpha}{r}\frac{\partial}{\partial r}\left(r\frac{\partial T}{\partial r}\right) + \frac{\nu}{c_p}\left(\frac{\partial u}{\partial r}\right)^2 \tag{3}$$

As a preliminary part of the investigation, we retain the viscous dissipation term in (3) and find whether there is a similarity solution of (1) to (3) with appropriate boundary conditions.

Introducing the axisymmetric stream function Ψ, we define the similarity variable z:

$$\Psi = \nu x f(z) \tag{4}$$

$$z = u_1 r^2 x^{m-1}/\nu \tag{5}$$

The surfaces of constant $z = a$ correspond to the surfaces of revolution and refer to the walls of the needles. For example, at $z = a$, surfaces are paraboloids of revolution when $m = 0$, cylinders when $m = 1$, and cones when $m = -1$.

Continuity equation, (1), is identically satisfied when the velcocity components are expressed as

$$u = 2U(x)f'(z),\ v = -\frac{\nu f}{r} - \frac{(m-1)\nu z f'}{r} \tag{6}$$

where the primes denote differentiations with respect to z. Substituting (5) and (6) into (2) gives

$$8zf''' + 4(2+f)f'' - 4m(f')^2 + m = 0 \tag{7}$$

---

[1] Numbers in brackets designate References at end of paper.

Contributed by the Heat Transfer Division for publication in the JOURNAL OF HEAT TRANSFER. Manuscript received by the Heat Transfer Division July 12, 1977.

The boundary conditions for f can be obtained as

$$f(a) = f'(a) = 0; f'(\infty) = 1/2 \tag{8}$$

It is noted that by setting $m = 0$ in (7), the flow problem reduces to that considered by Lee [2] and Narian and Uberoi [12]; and $m = 0.5$ to that reported in [14] when the forced-convection dominated flow is considered therein. The skin friction coefficient can be readily determined to have

$$C_f = \frac{\nu \left(\frac{\partial u}{\partial r}\right)_w}{\frac{1}{2} U^2} = 8a^{1/2}\mathrm{Re}^{-1/2} f''(a) \tag{9}$$

We next seek to transform the energy equation, (3), for needles with nonisothermal surfaces.

Variable Surface Temperature Needles. By using (5) and (6) in (3) with the definition of dimensionless temperature

$$\theta(z) = \frac{T - T_\infty}{T_w - T_\infty} \tag{10}$$

it can be shown that (3) reduces to an ordinary differential equation in z only if

$$T_w = T_\infty + T_1 x^n \tag{11}$$

and

$$n = 2m \tag{12}$$

The resulting dimensionless energy equation becomes then

$$2z\theta'' + 2\theta' + \mathrm{Pr}(f\theta' - nf'\theta) + 8\mathrm{EPr}z(f'')^2 = 0 \tag{13}$$

and the boundary conditions

$$\theta(a) = 1; \theta(\infty) = 0 \tag{14}$$

Thus, similarity solutions are possible for only a restricted power-law surface temperature, as dictated by (11) and (12), whenever the effects of viscous dissipation must be considered. Fortunately, in a great majority of practical applications in low speed flows such effects are negligible. In this case the restriction (12) is no longer necessary, and the value of n is independent of m, i.e., the wall temperature given by (11) is independent of the imposed axial pressure variations. Accordingly, (13) reduces to

$$2z\theta'' + 2\theta' + \mathrm{Pr}(f\theta' - nf'\theta) = 0 \tag{15}$$

where n is an arbitrary constant.

The local Nusselt number is

$$\mathrm{Nu} = \frac{-x \left(\frac{\partial T}{\partial r}\right)_w}{T_w - T_\infty} = -2a^{1/2}\mathrm{Re}^{1/2}\theta'(a) \tag{16}$$

and in terms of the Stanton number, (16) becomes

$$\mathrm{StRe}^{1/2} = -2a^{1/2}\mathrm{Pr}^{-1}\theta'(a) \tag{17}$$

Variable Surface Heat Flux Needles. In this case, we define a dimensionless temperature as

$$\theta(z) = \frac{T - T_\infty}{\frac{q_w}{k}\left(\frac{\nu x}{4aU}\right)^{1/2}} \tag{18}$$

and (3) transforms to

$$2z\theta'' + 2\theta' + \mathrm{Pr}f\theta' - \mathrm{Pr}\left(S + \frac{1-m}{2}\right) f'\theta + 16\mathrm{E}_1\mathrm{Pr}z(f'')^2 = 0 \tag{19}$$

under the restrictions of

$$q_w = q_1 x^S \tag{20}$$

and

$$S = \frac{1}{2}(5m - 1) \tag{21}$$

If the viscous dissipation is important, then a similarity temperature field exists only if there is a power-law variation in surface heat flux given by (20). It also depends on the needle shape and the axial variation of mainstream velocity through (21). Similar to the preceding case, however, if the viscous dissipation is negligible, the restriction (21) can be disregarded. It follows that similarity solutions are possible for an arbitrary power-law variation in surface heat flux, and (19) is simplified, neglecting viscous dissipation, to

$$2z\theta'' + 2\theta' + \mathrm{Pr}f\theta' - \mathrm{Pr}\left(S + \frac{1-m}{2}\right) f'\theta = 0 \tag{22}$$

with the boundary conditions

$$\theta'(a) = -1; \theta(\infty) = 0 \tag{23}$$

where S and m are independent constants. It is noted that when $S = 0$ and $m = 3/5$, the problem is reduced to that treated by Narain and Uberoi [14] for a uniform heat flux needle when the heat transfer mode is dominated by forced convection.

Using (18) in the definition of local Nusselt number yields

$$\mathrm{Nu} = \frac{xq_w}{k(T_w - T_\infty)} = 2a^{1/2}\mathrm{Re}^{1/2}\theta^{-1}(a) \tag{24}$$

Nomenclature

a = needle size
b = 1-maPr/4, parameter in F
$C = b + n$, parameter in F
C_f = skin-friction coefficient
c_p = fluid specific heat
E = Eckert number, $u_1{}^2/c_pT_1$
E_1 = Eckert number, $u_1{}^2k(au_1/\nu)^{1/2}/c_pq_1$
F = solution of Kummer's equation, defined by (29)
f = dimensionless stream function
k = fluid thermal conductivity
M = Kummer's function
m = axial potential flow index
n = surface temperature distribution index
Nu = Nusselt number defined by (15) or (24)
Pr = Prandtl number, ν/α
q = heat flux
q_1 = constant in (20)
r = radial coordinate
Re = Reynolds number, Ux/ν
S = surface heat flux distribution index
St = Stanton number, Nu/RePr
T = temperature
T_1 = constant in (10)
u = axial velocity
U = mainstream flow velocity
u_1 = constant
v = radial velocity
x = axial coordinate measured from needle leading edge
y = Prz/4
z = similarity variable defined by (5)
α = fluid thermal diffusivity
Γ = gamma function
θ = dimensionless temperature defined by (9) or (18)
ν = kinematic viscosity
Ψ = axisymmetric stream function

Subscripts

w = needle surface condition
∞ = mainstream condition
Also, ′ denotes differentiation with respect to z or y, whichever is appropriate.

or in terms of the Stanton number

$$\mathrm{St}\mathrm{Re}^{1/2} = 2a^{1/2}\mathrm{Pr}^{-1}\theta^{-1}(a) \qquad (25)$$

Results and Discussion

Local velocity profiles and skin friction coefficients for needles with variable mainstream velocity can be obtained by integrating (7) with the boundary conditions (8). Numerical results for a uniform flow ($m = 0$) and an accelerated flow ($m = 0.5$) are given in Table 1 for the needle sizes $a = 0.1, 0.01$, and 0.001. Mark [1], and Narain and Uberoi [12] reported skin friction coefficients along with values of $f''(a)$ for the case of $m = 0$. In this case we find that our results for $f''(a)$ agree with theirs to four decimal places, although the results of skin friction coefficients for $a = 0.1$ and 0.001 given in [12] are believed to be slightly in error. The dimensionless axial velocity profiles for various needle sizes are displayed in Fig. 1 for $m = 0$ and 0.5. As expected, the velocity boundary layers are thinner for accelerated flows at a given needle size and thicker for larger needles placed in a given potential stream.

The velocity profiles are applicable to the heat transfer problems of thin needles having either variable surface temperature or variable surface heat flux. Results for these two cases with negligible viscous dissipation are presented as follows.

Variable Surface Temperature Needles. In this case, (7) with (8) and (15) with (14) are numerically integrated using "shooting" methods until mainstream conditions are satisfied. The dimensionless fluid temperature distributions for $a = 0.1$ with isothermal ($n = 0$) and linear ($n = 1$) wall temperatures are graphically displayed in Figs. 2(a) and 2(b), respectively, for $m = 0$ and 0.5.

Table 2 lists the wall values with heat transfer results. There appear to be no solutions available in the literature except for isothermal needles in a uniform stream [12] and in an accelerated flow with $m = 0.5$ [14]. For these cases the results agree with our data.

The effect of Pr is clearly seen. At a given needle size and a surface temperature distribution, the smaller the Pr, the thicker the thermal boundary layer, as is expected. When $\mathrm{Pr} = 0.02$ for a prescribed wall temperature variation, the influence of m on the dimensionless temperature distributions and heat transfer processes from the needle is quite small. This behavior is analogous to the cases of forced-convection heat transfer from two-dimensional wedges in Newtonian flow [15, 16] and in power-law non-Newtonian flow [17] when Pr is small. A physical explanation given by Chen and Chao [15] is that, under this circumstance, the velocity boundary layer thickness is only a small fraction of that of the thermal boundary layer. It is interesting to note that the influence of m is indeed small as revealed by the following analysis of the limiting case of $\mathrm{Pr} \to 0$.

In this case, the velocity boundary layer might be neglected entirely,

Table 1 Local Skin-friction coefficient over thin needles for $m = 0$ and 0.5

	$f''(a)$		$C_f\mathrm{Re}^{0.5}$	
a	$m = 0$	$m = 0.5$	$m = 0$	$m = 0.5$
0.1	1.28881	1.72178	3.26045	4.35579
0.01	8.49244	10.35056	6.79395	8.28045
0.001	62.16372	71.66594	15.72632	18.13021

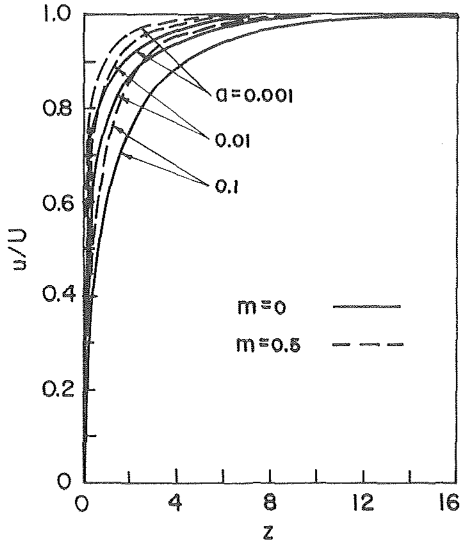

Fig. 1 Axial velocity distribution

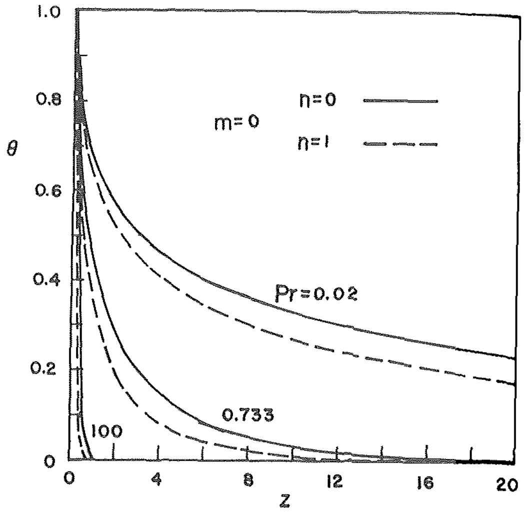

Fig. 2(a) Temperature fields for a uniform flow ($m = 0$) past a needle ($a = 0.1$) with variable wall temperature

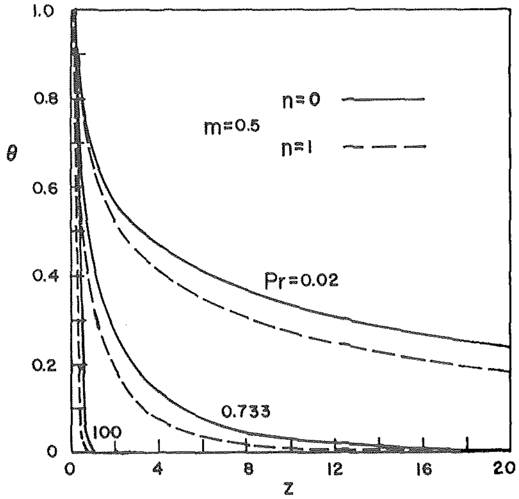

Fig. 2(b) Temperature fields for an accelerating flow ($m = 0.5$) past a needle with variable wall temperature

Table 2 Values of $\mathrm{StRe}^{0.5}$ and $\theta'(a)$ for $a = 0.1$. Values in parentheses are of $\theta'(a)$.

	$m = 0$		$m = 0.5$	
Pr	$n = 0$	$n = 1$	$n = 0$	$n = 1$
0.02	46.145 (−1.459)	51.275 (−1.621)	46.295 (−1.464)	51.639 (−1.633)
0.733	2.100 (−2.434)	2.519 (−2.920)	2.161 (−2.505)	2.611 (−3.026)
100.0	0.045 (−7.046)	0.058 (−9.100)	0.048 (−7.555)	0.062 (−9.808)

and the velocity components can be approximated by

$$u \simeq U(x) = u_1 x^m, \; v \simeq \frac{1}{2} m v r^{-1}(a - z) \tag{26}$$

The energy equation (15) with (14) has the simplified form

$$y\theta'' + \left(1 - \frac{\Pr}{4} ma + y\right)\theta' - n\theta = 0 \quad \text{for } \Pr \to 0 \tag{27}$$

with

$$\theta\left(\frac{\Pr}{4} a\right) = 1; \theta(\infty) = 0$$

where $y = \Pr z/4$. It can be readily demonstrated that the solution of (27) is

$$\theta = \frac{F(C, b, \Pr z/4)}{F(C, b, \Pr a/4)} \exp\left[\Pr(a - z)/4\right], \text{ for } \Pr \to 0 \tag{28}$$

where F is related to the Kummer's functions $M(C, b, y)$ by [18] the expression

$$F(C, b, y) = \frac{\pi}{\sin \pi b}\left[\frac{M(C, b, y)}{\Gamma(1 + C - b)\Gamma(b)} - y^{1-b}\frac{M(1 + C - b, 2 - b, y)}{\Gamma(C)\Gamma(2 - b)}\right] \tag{29}$$

in which $b = 1 - \Pr ma/4$, $C = b + n$. The local dimensionless temperature gradient corresponding to (28) is

$$\theta'(a) = -\frac{\Pr}{4}\frac{F(C, b + 1, \Pr a/4)}{F(C, b, \Pr a/4)}, \text{ for } \Pr \to 0 \tag{30}$$

Equations (27) to (30) suggest that, for sufficiently small needle size and Pr, the effect of m is quite insignificant. In the limit as $\Pr \to 0$, b approaches unity, and the dimensionless temperature distribution is independent of m. The influence of flow acceleration, however, increases with progressively increasing Pr. For large Pr, the thermal boundary layer is confined within the velocity boundary layer, and the presence of the latter can no longer be ignored. Data for the accelerated flow $m = 0.5$ deviate significantly from that for the uniform flow $m = 0$ for $\Pr = 100$ at a given surface temperature distribution $n = 0$ or 1. The relatively higher convective transport is clearly due to a greater flow acceleration. As expected on the other hand, imposing a linear axial surface temperature variation ($n = 1$) upon a needle in lieu of an isothermal distribution ($n = 0$) results in a higher heat transfer rate.

The effect of needle size on the dimensionless temperature distribution for $n = 1$ is illustrated in Figs. 3(a) and 3(b) for $\Pr = 0.733$ and 100, respectively. Local heat transfer data corresponding to Fig. 3 are given in Table 3.

The results show that the thermal boundary layer increases with increasing needle size, as it does in the case of isothermal needles in uniform flows reported in [10, 12]. This means that the effect of needle transverse curvature is of importance and a more slender needle facilitates heat transfer. The dependence of heat transfer on m is again such that accelerating flow promotes heat convection in relatively large Pr fluids.

Variable Surface Heat Flux Needles. Neglecting viscous dissipation, (22) and (23) are numerically integrated by the same method as in the preceding treatment of needles with variable surface temperatures. Figs. 4(a) and 4(b) show the dimensionless temperature distributions for two flows $m = 0$ and 0.5 past a needle of size $a = 0.1$. Results of wall temperature and wall heat transfer corresponding to Fig. 4 are given in Table 4.

Unlike the preceding case of variable surface temperature, the data in Table 4 appear to lack uniformity. For $\Pr = 0.02$, the wall value increases with m at a given value of S. For the remaining two Pr's, it decreases. This behavior is similar to that of heat transfer from wedges having a uniform wall heat flux [15]. At present, a satisfactory physical explanation is lacking.

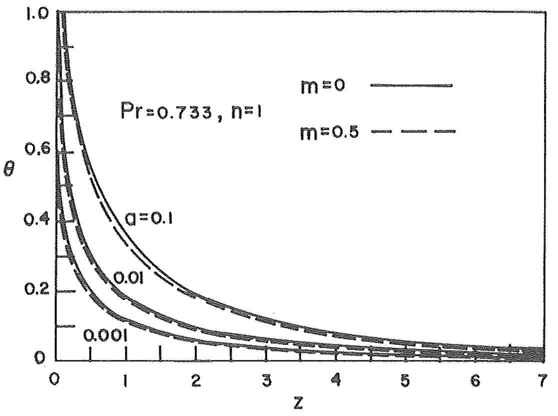

Fig. 3(a) Effect of needle size on temperature fields for $n = 1.0$ and $\Pr = 0.733$

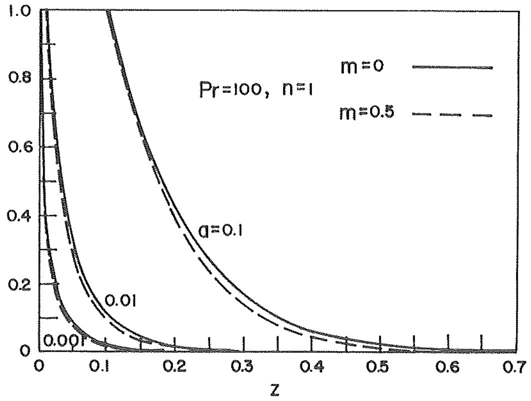

Fig. 3(b) Effect of needle size on temperature fields for $n = 1.0$ and $\Pr = 100$

Table 3 Effect of needle size on $\mathrm{StRe}^{0.5}$ for $n = 1$

	$m = 0$		$m = 0.5$	
a	Pr = 0.733	Pr = 100	Pr = 0.733	Pr = 100
0.1	2.519	0.058	2.611	0.062
0.01	5.103	0.092	5.203	0.096
0.001	11.574	0.172	11.706	0.176

Due to the definition of θ given by (18) and the wall flux condition of (23), all curves in Fig. 4 have identical slopes at $z = a$. The thermal boundary layer follows the usual expectation that it is thinner for larger Pr fluids. The wall temperature decreases with increasing Pr for given m and n.

In departure from the case of variable surface temperature needles, the effect of m is more discernible for $\Pr = 0.02$. We have also examined the solution for vanishingly small Pr when variable wall flux is imposed. Using the velocity profile given by (26) in (22) yields

$$y\theta'' + \left(1 - \frac{\Pr}{4} ma + y\right)\theta' - \left(S + \frac{1 - m}{2}\right)\theta = 0 \quad \text{for } \Pr \to 0 \tag{31}$$

with

$$\theta'\left(\frac{\Pr}{4} a\right) = -1, \theta(\infty) = 0$$

where, again, $y = \Pr z/4$. It is readily shown that the solution of (31) is

$$\theta = 4\Pr^{-1}\frac{F(d, b, \Pr z/4)}{F(d, b + 1, \Pr a/4)} \exp\left[\Pr(a - z)/4\right], \quad \text{for } \Pr \to 0 \tag{32}$$

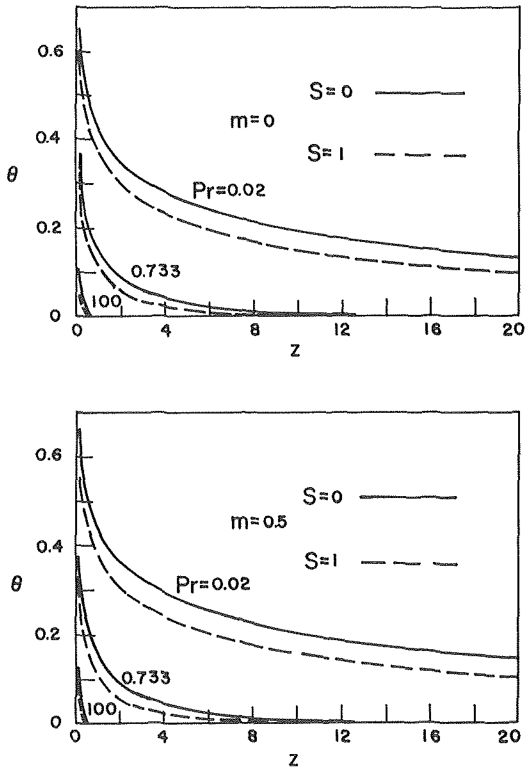

Fig. 4 Temperature fields for $a = 0.1$ with variable wall heat flux (a) for $m = 0$, (b) for $m = 0.5$

Table 4 Values of $StRe^{0.5}$ and $\theta(a)$ for $a = 0.1$. Values in parentheses are of $\theta(a)$

	$m = 0$		$m = 0.5$	
Pr	$S = 0$	$S = 1$	$S = 0$	$S = 1$
0.02	48.985	53.190	47.859	52.681
	(0.646)	(0.595)	(0.661)	(0.600)
0.733	2.345	2.658	2.304	2.690
	(0.377)	(0.325).	(0.375)	(0.321)
100.0	0.052	0.062	0.052	0.064
	(0.122)	(0.102)	(0.121)	(0.099)

where $d = b + S + (1 - m)/2$.

It is then seen from (31) that, as Pr → 0, the dimensionless temperature depends upon m as well as S—unlike the previous case described by (27) which does not involve m for vanishingly small Pr fluids.

Finally, we note that the results of (28) and (32) for the limiting case Pr → 0 should be used with caution due to the assumption of absent velocity boundary layers. For Pr = 0.02 and $a = 0.1$, for example, the results for the wall temperature gradient given by (30) and the wall temperature by (32) are about 14 to 23 percent too high as compared to numerical data for various values of m, n, and S considered herein. As has been demonstrated by Chen [16], the potential flow theory does not suffice to yield sufficiently accurate results for practical applications where the fluids have small but *finite* Pr.

References

1 Mark, R. M., "Laminar Boundary Layer on Slender Bodies of Revolution in Axial Flow," Rept. 21, Guggenheim Aeronautical Laboratory, Calif. Inst. of Technology, July 1954.

2 Lee, L. L., "Boundary Layer Over a Thin Needle," *Physics of Fluids*, Vol. 10, No. 4, 1967, pp. 820–822.

3 Miller, D. R., "The Boundary Layer on a Paraboloid of Revolution," *Proceedings of the Cambridge Philosophical Society*, Vol. 65, 1969, pp. 285–299.

4 Glauert, M. B., and Lighthill, M. J., "The Axisymmetric Boundary Layer on a Long Thin Cylinder," *Proceedings of the Royal Society*, Series A, No. 230, 1955, pp. 188–203.

5 Cebeci, T., and Na, T. Y., "Laminar Free-Convection Heat Transfer from a Needle," *Physics of Fluids*, Vol. 12, No. 2, Feb., 1969, pp. 463–465.

6 Govindarajula, T., "Comments on 'Laminar Free-Convection from a Needle," *Physics of Fluids*, Vol. 15, No. 1, Jan., 1972, pp. 211–212.

7 Van Dyke, M., "Free Convection from a Vertical Needle," *Problems of Hydrodynamics and Continum Mechanics*, Ed. I. E. Block, 1970, pp. 748–761.

8 Narain, J. P., and Uberoi, M. S., "Laminar Free Convection from Thin Vertical Needles," *Physics of Fluids*, Vol. 15, No. 5, May, 1972, pp. 928–929.

9 Raithby, G. D., and Hollands, K. G. T., "Free Convection Heat Transfer from Vertical Needles," ASME JOURNAL OF HEAT TRANSFER, Vol. 98, 1976, pp. 522–523.

10 Cebeci, T., Na, T. Y., and Mosinskis, G., "Laminar Boundary Layers on Slender Paraboloids," *Journal of AIAA*, Vol. 7, 1969, pp. 1372–1374.

11 Tam, K. K., "On the Asymptotic Solution of Viscous Incompressible Flow Past a Heated Paraboloid of Revolution," *SIAM Journal of Appl. Math.*, Vol. 20, No. 4, 1971, pp. 714–721.

12 Narain, J. P. and Uberoi, M. S., "Forced Heat Transfer over Thin Needles," ASME JOURNAL OF HEAT TRANSFER, Vol. 94, 1972, pp. 240–242.

13 Narain, J. P., and Uberoi, M. S., "Combined Forced and Free-Convection Heat Transfer from Thin Needles in a Uniform Stream," *Physics of Fluids*, Vol. 15, No. 11, Nov., 1972, pp. 1879–1882.

14 Narian, J. P., and Uberoi, M. S., "Combined Forced and Free-Convection over Thin Needles," *Int. Journal of Heat and Mass Transfer*, Vol. 16, No. 8, Aug., 1973, pp. 1505–1511.

15 Chen, J. L. S., and Chao, B. T., "Thermal Response Behavior of Laminar Boundary Layers in Wedge Flow," *Int. Journal of Heat and Mass Transfer*, Vol. 13, 1970, pp. 1101–1114.

16 Chen, J. L. S., "Laminar Forced-Convection at Small Prandtl Numbers," *Acta Mechanica*, Vol. 17, 1973, pp. 315–322.

17 Chen, J. L. S. and Radulovic, P. T., "Heat Transfer in Non-Newtonian Flow Past a Wedge with Non-Isothermal Surfaces," ASME JOURNAL OF HEAT TRANSFER, Vol. 95, 1973, pp. 498–504.

18 Abramowitz, M., and Stegun, I. A., eds., *Handbook of Math. Functions*. Dover Publications, Inc., N. Y., 1965, pp. 504–509.

R. L. Mussulman

Assistant Professor,
Department of Mechanical Engineering,
Montana State University,
Bozeman, Mont.

Effect of an Elevated Pipeline on Moss Covered Ground Temperature

Elevated pipelines in cold regions will lose heat to the environment and raise the ground temperature below the pipe. The maximum temperature in the ground is the (steady) solution of Laplace's equation with boundary condtions appropriate for summer months which are complicated by the insulating effects of mossy vegetation that grows in cold regions. A linear decomposition of the problem was accomplished to permit isolation of the thermal effects for the pipeline. That is, increases in ground and vegetation temperature due to the presence of the pipeline were obtained so that the environmental impact of a pipeline can be assessed.

Introduction

An elevated pipeline in a cold climate will lose heat to the environment and increase ground temperature below the pipe. Brown [1][1] has described the types of measurements (core drilling, etc.) that are routinely made as part of site investigations for construction projects in permafrost regions. Ground thermal conductivity, ground temperature profiles, vegetation characteristics, and depth of the so-called "active layer" which thaws each summer are quantities essential to assessment of the thermal impact of a proposed pipeline. Gilpin and Wong [2] have developed analytical models to predict annual ground temperature variations that occur in permafrost regions in the absence of man-made structures. The results of this work permit rapid calculation of ground temperature increases that would be caused by an elevated pipeline. The temperature increases from this work can be combined with known temperatures in the absence of the pipeline to determine the possible increase of the "active layer" thickness that would be caused by the pipeline as well as the ground surface and vegetation temperatures. This information can be used by engineers concerned with foundation design and also by those charged with predicting the environmental impact of the pipeline.

Analysis and Formulation

The geometry of the problem investigated is shown in Fig. 1. Insulating effects of mossy vegetation which covers the ground in cold tundra regions must be accounted for in a realistic analysis. Gilpin [3] has shown that the insulating effects of moss are minimized when the moss is moist throughout. That case is appropriate for this study since it will result in a maximum ground temperature increase. Gilpin's measurements indicate that a moist moss layer can be modeled by a simple conductor with all convective and radiative heat transport taking place only at the moss surface. Brazel and Outcalt [4] have shown that latent heat transfer from moist moss can be accurately modeled using saturation pressures based on temperatures of the moss surface and ambient air.

The maximum temperature increase that could occur is the steady temperature profile increase for boundary conditions appropriate to summer conditions. The year-round warming from the pipeline will cause the ground temperature increase due to the pipeline to penetrate deeper in successive years. The maximum temperature increase will thereby be more closely approached year by year. The impact of two unusually warm years in succession could then be a surprise to engineers operating a pipeline that encountered no foundation problems in previous years.

The steady value of ground temperature satisfies Laplace's equa-

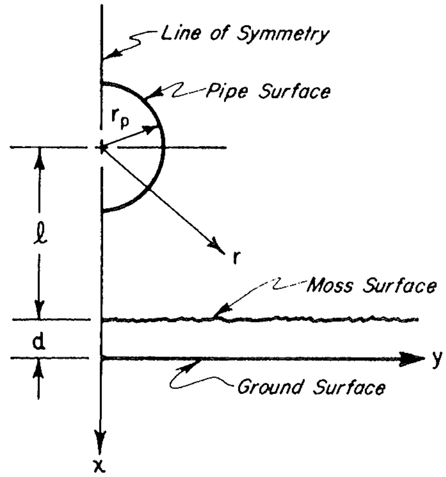

Fig. 1 Geometry

---

[1] Numbers in brackets designate References at end of paper.

Contributed by the Heat Transfer Division for publication in the JOURNAL OF HEAT TRANSFER. Manuscript received by the Heat Transfer Division August 1, 1977.

tion:

$$T_{xx}(x, y) + T_{yy}(x, y) = 0, x > 0 \qquad (1)$$

The solution of equation (1) is very difficult to obtain in the present case because of insulating effects of the moss and the complicated nature of the boundary condition on the moss surface. The moss surface boundary condition is illustrated schematically in Fig. 2. As indicated in the figure, net heat flux to the moss surface is

$$R_s + R_L{}^{\downarrow} - R_L{}^{\uparrow}(y) - S(y) - L(y) + R_p(y) = Q(y) \qquad (2)$$

The term $R_p(y)$ is long wavelength radiative heat flux absorbed through the moss surface due to the presence of the pipeline. The other terms are defined in the nomenclature.

In principle, one must also solve Laplace's equation for the temperature distribution in the moss layer. In practice, however, a simple one-dimensional model for the heat transfer through the moss layer may be applied. Such a model is appropriate whenever the moss thermal conductivity is small compared to ground thermal conductivity. To see that this is true, consider the moss-ground interface. Heat flux across that interfacial surface must be continuous:

$$k_m \left(\frac{\partial T_m}{\partial x}\right)_{x=0} = k \left(\frac{\partial T}{\partial x}\right)_{x=0} \qquad (3)$$

Also, continuity of temperature across the surface requires that

$$\left(\frac{\partial T_m}{\partial y}\right)_{x=0} = \left(\frac{\partial T}{\partial y}\right)_{x=0} \qquad (4)$$

Dividing equation (4) by equation (3) leads to

$$\tan \Theta_m = \frac{k_m}{k} \tan \Theta \qquad (5)$$

where Θ is the angle the ground temperature gradient makes with a direction normal to the interface surface, and Θ_m is the angle the moss temperature gradient makes with the normal. A small conductivity ratio in equation (5) will cause Θ_m to be small even if Θ is not particularly small. So it is assumed in this work that $\Theta_m = 0$, which is a mathematical statement that heat transfer through the moss layer is one-dimensional. Conservation of energy for the moss layer then gives

$$Q(y) = \frac{k_m}{d}\,[T_s(y) - T(0, y)] = -kT_x(0, y) \qquad (6)$$

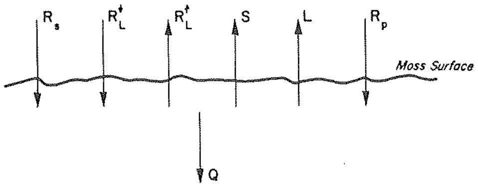

Fig. 2 Moss surface heat flux balance

In order to evaluate effects of the pipeline on ground and moss temperatures, one must compare those temperatures with temperatures that would occur in the absence of the pipeline. In the absence of the pipeline, equations (1), (2) and (6) would be replaced by

$$T_0''(x) = 0, x > 0 \qquad (7)$$

$$R_s + R_L{}^{\downarrow} - R_{L0}{}^{\uparrow} - S_0 - L_0 = Q_0, \text{ and} \qquad (8)$$

$$Q_0 = \frac{k_m}{d}\,[T_{s0} - T_0(0)] = kT_0'(0) \qquad (9)$$

Subtraction of equations (7), (8) and (9) from equations (1), (2) and (6) yields

$$t_{xx}(x, y) + t_{yy}(x, y) = 0, x > 0 \qquad (10)$$

$$-[R_L{}^{\uparrow}(y) - R_{L0}{}^{\uparrow}] - [S(y) - S_0] - [L(y) - L_0] + R_p(y) = q(y) \qquad (11)$$

and

$$q(y) = \frac{k_m}{d}\,[t_s(y) - t(0, y)] = -kt_x(0, y) \qquad (12)$$

where the lower case quantities,

$$t(x, y) = T(x, y) - T_0(x),$$

$$t_s(y) = T_s(y) - T_{s0}, \text{ and}$$

$$q(y) = Q(y) - Q_0$$

represent effects of the pipeline on the upper case quantities. For example, the first of these quantities is the ground temperature increase that occurs as a result of the presence of the pipeline.

Terms in equation (11) must be expressed as functions of the moss

Nomenclature

A = function defined by equation (33)
B = function defined by equation (35)
c = specific heat of air
d = moss layer thickness
D = thermal diffusivity between moss surface and air
h = total effective film coefficient (equation 21)
H = latent heat for water evaporation or condensation
k = ground thermal conductivity
k_e = effective ground thermal conductivity (equation 25)
k_m = moist moss thermal conductivity
ℓ = elevation of pipe centerline above moss surface
L = latent heat flux from moss surface
P = atmospheric pressure
P_a = saturation pressure at atmospheric temperature
P_s = saturation pressure at moss surface temperature
Q = heat flux through moss layer
q = heat flux increase through moss layer caused by pipeline
Q_p = radiative flux due to presence of pipeline (equations (18, 19))
r = distance from pipe centerline
r_p = pipe outer surface radius
$R_L{}^{\downarrow}$ = long wavelength radiation absorbed through moss surface
$R_L{}^{\uparrow}$ = long wavelength radiation emitted by moss surface
R_p = pipe radiative heat flux absorbed through moss surface (equation (18))
R_s = short wavelength radiation absorbed through moss surface
S = sensible convective heat flux from moss surface
T = absolute ground temperature
t = ground temperature increase caused by pipeline
T_m = absolute moss temperature
T_p = absolute pipe surface temperature
T_s = absolute moss surface temperature
t_s = moss surface temperature increase caused by pipeline
U = wind speed
x = distance below ground surface
y = horizontal distance from pipe centerline
β = Biot number (equation (30))
β_m = Biot number for moss layer (equation (23))
ϵ = long wavelength moss surface emissivity
ϵ_p = long wavelength pipe surface emissivity
ρ = mass density of air
σ = Stefan-Boltzmann constant (5.67×10^{-8} W/m^{2}K^4)
ϕ = quantity defined by equation (26)

Subscripts

0 = property value in the absence of pipeline
x = differentiation with respect to x
y = differentiation with respect to y

surface temperature increase to make the appropriate solution of equation (10) possible. The first terms are long wavelength radiative fluxes emitted by the moss surface and are expressed in terms of moss surface emissivity, ϵ, as

$$R_L{}^{\uparrow}(y) - R_{L0}{}^{\uparrow} = \epsilon\sigma[T_s{}^4(y) - T_{s0}{}^4] \tag{13}$$

The bracketed quantity in equation (13) can be linearized with respect to moss temperatures as

$$T_s{}^4(y) - T_{s0}{}^4 \simeq 4T_{s0}{}^3[T_s(y) - T_{s0}] = 4T_{s0}{}^3 t_s(y) \tag{14}$$

This linearization is accurate whenever the temperature difference, $t_s(y)$, is small compared to the absolute temperature, T_{s0}, and is called the small temperature difference approximation.

The next two terms are sensible convective heat fluxes from the moss surface to the atmosphere. These terms are expressed [3] as

$$\begin{aligned} S(y) - S_0 &= \rho c D[T_s(y) - T_a] - \rho c D(T_{s0} - T_a) \\ &= \rho c D t_s(y) \end{aligned} \tag{15}$$

where D is the diffusivity between the moss surface and air.

The next two terms are latent energy fluxes between the moss surface and air. These terms account for moisture evaporation, and are expressed [4] as

$$\begin{aligned} L(y) - L_0 &= 0.622\rho HD \frac{[P_s(y) - P_a] - [P_{s0} - P_a]}{P} \\ &= 0.622\rho HD[P_s(y) - P_{s0}]/P \end{aligned} \tag{16}$$

Saturation pressure is a function of temperature, so that the saturation pressure difference can be approximated from a truncated Taylor's series as

$$\begin{aligned} P_s(y) - P_{s0} &= P_{s0} + \left(\frac{dP_s}{dT_s}\right)_{T_{s0}} [T_s(y) - T_{s0}] \ldots - P_{s0} \\ &\simeq \left(\frac{dP_s}{dT_s}\right)_{T_{s0}} t_s(y) \end{aligned} \tag{17}$$

This expression could also be called a small temperature difference approximation. The approximation is not particularly accurate for large moss surface temperature increases. For example, Keenan and Keyes [5] give

$$\frac{dP_s}{dT} = 0.001084 \text{ Atm/°C at } 15°\text{C},$$

while the correct value that should replace this derivative in equation (17) for a 5°C temperature increase would be

$$\frac{P_s(20°\text{C}) - P_s(15°\text{C})}{5c} = 0.001248 \text{ Atm/°C},$$

so that the value recommended in equation (17) is 13 percent low. Errors caused by this approximation will be discussed in more detail later.

Finally, the last term is radiative heating of the moss surface that occurs due to the presence of the pipeline. The y-dependence of this function is easily derived if radiative flux due to the pipe is diffuse. Diffuse radiation will decrease by a factor inversely proportional to the distance from the pipe centerline. Finding the x-component of that flux, evaluating at the moss surface level, and multiplying by moss absorptivity (assumed here to equal long wavelength emissivity ϵ) gives

$$R_p(y) = \frac{\epsilon r_p Q_p}{r}\frac{\ell}{r} = \frac{\epsilon r_p \ell Q_p}{\ell^2 + y^2} \tag{18}$$

where Q_p is the diffuse radiative flux due to the presence of the pipeline evaluated at the pipe surface.

The pipe contributes to Q_p by three mechanisms. The first is emission by the pipe surface, $\epsilon_p\sigma T_p{}^4$. The other two mechanisms are diffuse reflection of radiant energy incident on the pipe and shadowing of radiation by the physical presence of the pipe. In order to estimate the contributions of these mechanisms, one can imagine that the ground surface and atmosphere form an isothermal surface enclosing the pipe. The temperature of the isothermal surface can be approximated for computational purposes as T_{s0}. Then,

$$Q_p = \epsilon_p\sigma(T_p{}^4 - T_{s0}{}^4) \tag{19}$$

This approximation introduces some error since neither the ground surface nor the atmospheric air will be at exactly the temperature T_{s0}. The relative error is small, however, because we are dealing here with small differences in *absolute* temperature. In order for the atmosphere to form an enclosure, it must be opaque to long wavelength radiation. This also is not strictly true, but the atmosphere is over 90 percent opaque to long wavelength radiation [6, 7].

The effects of shadowing and reflection of short wavelength solar radiation by the pipe are ignored in this analysis. Ignoring shadowing of solar radiation which occurs throughout the day during summer months in permafrost regions (with the shadow in constant motion) causes this analysis to be slightly conservative. That is, the results of this study slightly overestimate ground temperature increase. More accurate estimates of Q_p require extensive data from the proposed pipeline site. It is important that equation (16) is thermodynamically consistent in that the pipe can only heat the moss surface if the pipe is at a higher temperature than the surface.

Combining the equations (13) through (17) with equation (11) yields

$$q(y) = -ht_s(y) + R_p(y) \tag{20}$$

where the total effective film coefficient is

$$h = h_c + h_\ell + h_r \tag{21}$$

with

$$h_c = \rho c D,\ h_\ell = 0.622\frac{\rho HD}{P}\left(\frac{dP_s}{dT_{s0}}\right)_{T_{s0}},$$

and $h_r = 4\epsilon\sigma T_{s0}{}^3$ being the convective, latent and radiative film coefficients, respectively. Since h_ℓ constitutes only a fraction of the total quantity h, errors in equation (17) are reduced in final results employing h.

Solution of the Equations

Equation (2) and the first of the two equations (12) can be combined to eliminate the moss heat flux increase, $q(y)$. The resulting equation may then be solved for moss surface temperature increase as

$$t_s(y) = \left[t(0, y) + \frac{d}{k_m}R_p(y)\right] \Big/ (1 + \beta_m), \tag{22}$$

where

$$\beta_m = hd/k_m \tag{23}$$

is a Biot number based on moss properties. Equation (22) may then be combined with the last of the equations (12) to yield

$$t_x(0, y) - \frac{h}{k_e}t(0, y) = -R_p(y)/k_e, \tag{24}$$

where

$$k_e = k(1 + \beta_m) \tag{25}$$

is a modified ground conductivity accounting for effects of the mossy insulation on the boundary condition. Equation (24) is the boundary condition for equation (10). The solution to those equations is facilitated by the substitution

$$\phi(x, y) = t_x(x, y) - \frac{h}{k_e}t(x, y). \tag{26}$$

Then equations (10) and (24) are transformed to

$$\phi_{xx}(x, y) + \phi_{yy}(x, y) = 0, \tag{27}$$

$$\phi(0, y) = -R_p(y)/k_e. \tag{28}$$

The solution to equations (27) and (28) is readily available [8] as

$$\phi(x, y) = -\frac{x}{\pi k_e} \int_{-\infty}^{\infty} \frac{R_p(z)dz}{x^2 + (y - z)^2} \tag{29}$$

With $\phi(x, y)$ now taken as known, equation (26) is regarded as a first order differential equation for temperature increase. The solution to that equation which satisfies the boundary condition,

$$\lim_{x \to \infty} t(x, y) = 0$$

is

$$t(x, y) = -e^{\beta x/\ell} \int_{x}^{\infty} \bar{e}^{\beta w/\ell} \phi(w, y)dw \tag{30}$$

where

$$\beta = h\ell/k_e$$

is another Biot number.

Substitution of equation (18) into equation (29) and nondimensionalization of the integration variable yields

$$\phi(x, y) = -\frac{\epsilon r_p Q_p x}{\pi k_e \ell^2} A(x/\ell, y/\ell) \tag{31}$$

where

$$A(\xi, \eta) = \int_{-\infty}^{\infty} \frac{d\zeta}{(1 + \zeta^2)[\xi^2 + (\zeta - \eta)^2]}. \tag{32}$$

This integral was evaluated by means of complex contour integration [9] as

$$A(\xi, \eta) = \pi \frac{(1 + \xi)(\eta^2 + \xi^2 - 2\xi + 1)}{\xi[(\eta^2 + \xi^2 - 1)^2 + 4\eta^2]} \tag{33}$$

Substitution of equations (31) and (33) into equation (30) gives the temperature increase as

$$t(x, y) = \frac{\epsilon r_p Q_p}{k_e} e^{\beta x/\ell} \int_{x/\ell}^{\infty} \bar{e}^{\beta \xi} B(\xi, y/\ell)d\xi \tag{34}$$

where

$$B(\xi, \eta) = (1 + \xi) \frac{(\eta^2 + \xi^2 - 2\xi + 1)}{(\eta^2 + \xi^2 - 1)^2 + 4\eta^2} \tag{35}$$

Along the line of symmetry ($y = 0$), the integral in equation (34) is easily performed because of the simple form of the function B there:

$$B(\xi, 0) = \frac{1}{1 + \xi} \tag{36}$$

So along the line of symmetry, temperature increase is

$$t(x, 0) = \frac{\epsilon r_p Q_p}{k_e} e^{\beta(1+x/\ell)} E_1[\beta(1 + x/\ell)], \tag{37}$$

where E_1 is the first exponential integral and is a tabulated function [10]. The maximum ground temperature increase is

$$t(0, 0) = \frac{\epsilon r_p Q_p}{k_e} e^{\beta} E_1(\beta). \tag{38}$$

Equations (22) and (38) may now be combined to give the moss surface temperature increase:

$$t_s(0) = t(0, 0) \left(1 + \frac{\beta_m}{\beta e^{\beta} E(\beta)}\right) \Big/ (1 + \beta) \tag{39}$$

Equations (37), (38) and (39) give the desired environmental temperature increase caused by the pipeline. Errors in results from equations (38) and (39) due to small temperature difference approximations can easily be corrected by successive substitution.

Results and Discussion

Equations (38) and (39) can be used not only as tools to estimate evironmental temperature increases, but also as design tools to control those increases. For example, if the anticipated ground temperature increase is too high, it can be reduced by changing various design parameters. In order to evaluate the effects of those parameters, the following numerical example was evaluated:

T_{s0} = 285 K (53°F)
T_p = 310 K (98°F)
ϵ = 0.98, ϵ_p = 0.80
k = 2.22 W/mK (ice)
k_m = 0.15 W/mK (from Gilpin [1])
d = 0.15m, ℓ = 1.00m, r_p = 0.50m
U = 0.50m/s (wind velocity = 1.12 mph)

Sellers [6] suggests that for flat open country, thermal diffusivity between the moss surface and air can be expressed as the linear function

$$D = f + gU \tag{40}$$

where f = 0.003m/s and g = 0.002. Temperature increases for the above numerical example were

$$t(0, 0) = 1.5 \text{ K, and } t_s(0) = 3.4 \text{ K.}$$

Effects from variations in the above tabulated quantities were studied separately by maintaining all quantities constant, except for the quantity being considered.

Fig. 3 shows the insulating effect of the mossy ground cover. An increase in the moss thickness is seen to decrease ground surface temperature but to have little effect on the moss surface temperature.

Fig. 4 shows the effect of pipe elevation on environmental tem-

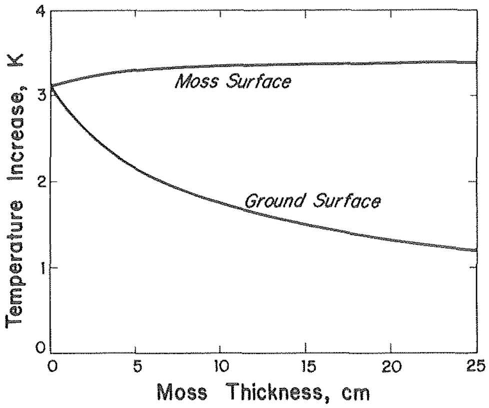

Fig. 3 Effect of moss thickness on moss surface and ground surface temperature increases

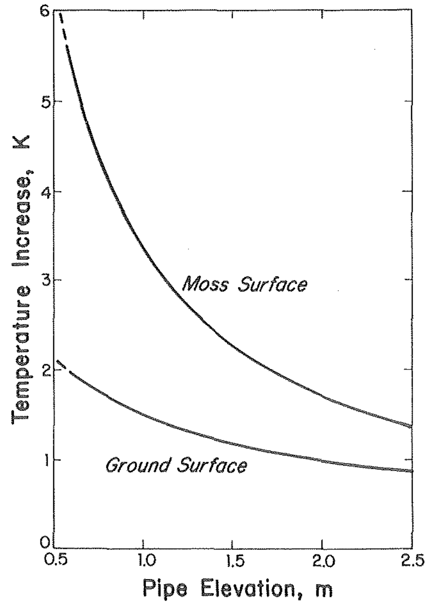

Fig. 4 Effect of pipe elevation on moss surface and ground surface temperature increases

peratures. Raising the pipe reduces the temperature increases caused by the pipeline. Because of the insulating property of the moss cover, this tactic affects moss surface temperature strongly, but has little effect on the ground temperature.

Fig. 5 shows the effect of the pipe surface temperature on environmental temperatures. The curves are fourth order in pipe surface temperature, but they appear to be nearly linear because of the relatively small absolute temperature differences involved. Pipe surface temperature is controlled by pipe insulation.

Other effects were also studied. For example, higher wind velocities reduce the environmental temperature increases. Short time period fluctuations in wind speed would have negligible effect on ground surface temperature, since the diffusion time for temperature change penetration through the moss is quite large. A smaller value for either ground conductivity or pipe emissivity would reduce environmental temperature increases.

The results of this work permit estimation of environmental increases that would occur as a result of a proposed elevated and heated pipeline in a tundra region. Application of the results requires adequate data for the proposed sited. Minimal data required includes peak temperatures at the site in the absence of the pipeline, moss thickness, and ground and moss thermal conductivities. Gilpin [3] has shown that the effective thermal resistance of the moss layer increases significantly if even a thin surface layer dries out. It would be somewhat risky, however, to design a pipeline based on the assumption that such a dry layer is going to exist during every summer of the pipeline service life.

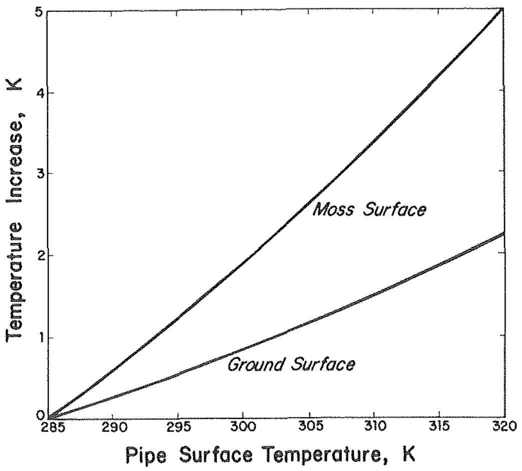

Fig. 5 Effect of pipe surface temperature on moss surface and ground surface temperature increases

References

1 Brown, R. J. E., *Permafrost in Canada*, University of Toronto Press, Toronto, Canada, 1970.

2 Gilpin, R. R., and Wong, B. K., "Heat Valve Effect in the Ground Thermal Regime," ASME JOURNAL OF HEAT TRANSFER, Nov. 1976, p. 537.

3 Gilpin, R. R., "The Ground Temperature Boundary Condition Provided by a Moss Covered Surface," ASME Paper No. 76-WA/HT-61, New York, 1976.

4 Brazel, A. J., and Outcalt, S. I., "The Observation and Simulation of Diurnal Evaporation Contrasts in an Alaskan Alpine Pass," *Journal of Applied Meteorology*, Vol. 12, 1973, pp. 1134–1143.

5 Keenan, J. H., and Keys, F. G. *Thermodynamic Properties of Steam*, John Wiley and Sons, New York, 1936.

6 Sellers, W. D., *Physical Climatology*, U. of Chicago Press, Chicago Press, Chicago, 1969.

7 Matvev, L. T., *Fundamentals of General Meteorology—Physics of the Atmosphere*, (Translated from Russian) U. S. Dept. of Commerce Clearinghouse for Federal Scientific and Technical Information, Springfield, VA.

8 Carslaw, H. S., and Jaeger, J. C., *Conduction of Heat in Solids*, 2nd ed., Oxford Press, London, 1959, p. 166.

9 Wylie, C. R., *Advanced Engineering Mathematics*, 4th Ed., McGraw-Hill, New York, 1975.

10 Abramowitz, M., and Stegun, I. A., *Handbook of Mathematical Functions*, National Bureau of Standards, 1964.

ERRATUM

Erratum: S. V. Patankar, S. Ramadhyani, and E. M. Sparrow, "Effect of Circumferentially Nonuniform Heating on Laminar Combined Convection in a Horizontal Tube," published in the February, 1978 issue of the JOURNAL OF HEAT TRANSFER, pp. 63–70. The quantity $(2/\pi)Gr^+$, which appears either on the abscissa or as a parameter in Figs. 1 through 8 of the paper, should be replaced by $(4/\pi)Gr^+$. A similar replacement should be made throughout the discussion of results, wherever reference is made to the figures. These corrections are needed to rectify a misinterpretation of the computer print-outs that was made when the graphs were plotted.

With the renaming of the abscissa of Figs. 1 and 2 as $(4/\pi)Gr^+$, it is also necessary to shift the short-dash curves, which represent the results of reference [5], to the right. The shift is accomplished by multiplying the abscissa coordinate of each point of the respective curve by two. Inasmuch as the shift is slight, the characteristics discussed in the paper remain unchanged.

journal of heat transfer

technical notes

This section contains shorter technical papers. These shorter papers will be subjected to the same review process as that for full papers.

Melting and Natural Convection Due to a Vertical Embedded Heater

J. W. Ramsey[1] and E. M. Sparrow[1]

Introduction

In this paper, experiments are described which provide definitive information about the heat transfer processes which occur when a solid is melted by a vertical cylindrical heat source embedded within the solid. The analytical approach to solid/liquid phase change problems that has been standard in the heat transfer literature is based on conduction as the sole transport mechanism, as witnessed by numerous literature surveys [1–5].[2] On the other hand, it can be reasoned that the temperature differences which necessarily exist in the melt region will result in buoyancy forces which, in turn, will generate natural convection motions. The importance of natural convection in the melting of a solid by an embedded heater was not experimentally confirmed in the heat transfer literature until the very recent past. Those experiments [6, 7] demonstrated the dominance of natural convection for the case where the heat source was a horizontal cylinder.

The present study was undertaken to investigate the role of natural convection in a melting configuration in which the direction of the buoyancy force, relative to the heating surface, differs from that of [6] and [7]. Consideration is given here to melting caused by a vertical heating cylinder embedded in a solid whose temperature is at the fusion point. During each data run, the heat input from the cylinder to the melting phase-change medium was maintained constant, and the response of the cylinder surface temperature as a function of time was recorded. The time varying shape of the melt region was determined by running a sequence of experiments, each of which was terminated at a successively longer time. Upon termination of the run, the melted material was removed, and the remaining solid was sectioned and photographed.

The experiments were performed with naphthalene as the phase change medium (fusion temperature $\cong 80°C$). Two power densities were employed, with the resulting Rayleigh number (based on the cylinder diameter) being in the range of $6–7 \times 10^6$.

Both the surface temperature histories and the melt region shapes offer clear testimony affirming the importance of natural convection.

During the Journal review process, a prior paper [8], published in the aerospace literature, was called to the authors' attention. That paper deals with a melting situation which has some similarities to that described here. The relationship between the experiments of [8] and the present work will be discussed later, after the results have been presented.

Experimental Apparatus and Procedure

For the melting experiments, the phase-change medium was contained in an open-topped, cylindrical stainless steel vessel, 12 cm in diameter and 18 cm high ($4\frac{3}{4} \times 7$ in.). The heating cylinder was positioned along the vertical centerline of the vessel, with its lower end about 2.5 cm (1 in.) above the bottom of the vessel and its upper end flush with the surface of the phase change medium in its unmelted state. The containment vessel was situated in a thermostatically controlled circulating bath whose temperature was maintained well within one degree of the fusion temperature of the naphthalene medium. A shroud was placed just above the top of the vessel to preclude contact between the room air and the naphthalene.

The cylindrical heater consisted of a smooth-walled stainless steel sheath encasing a closely spaced helical electrical heating element. d-c current was supplied to the heater via leads which extended from its upper end. The cylinder was 1.27 cm ($\frac{1}{2}$ in.) in diameter and 14.6 cm ($5\frac{3}{4}$ in.) long. It was suspended in the naphthalene with the aid of a specially designed insulating fixture made of a phenolic laminate. Three 30-gage chromel-alumel thermocouples were spot welded to the surface of the heater at approximately equal intervals along its height. The thermocouple wires extending from the respective junctions were run axially along the surface of the heater and secured by fine wire ties.

Each data run required a number of preparatory steps. First, a suitable quantity of naphthalene was placed in the test vessel and liquified, whereupon the vertical heating element was fixed in place. The freezing of the naphthalene was painstakingly performed to avoid potential cavities and depressions associated with the contraction that accompanies solidification. The actual freezing was accomplished with the vessel mounted on a high-frequency, low amplitude vibrator. Not only did the vibrator effectively avoid internal contraction cavities, but it also eliminated the small air bubbles which initially existed in the molten material. Additional molten naphthalene was added to the test vessel at the end of the freezing process to attain a final solid configuration in which the top surface was flat and flush with the top of the heater.

Once freezing was accomplished, the test vessel was returned to the constant temperature bath and allowed to equilibrate until the entire mass of naphthalene attained a temperature that was within 1°C (or better) of the fusion temperature. The data run was initiated by energizing the heater to a preselected power level and maintaining it constant thereafter. Power levels of 24.5 and 49 W were employed. At each power level, three data runs were made with respective durations of $\frac{1}{2}$, 2, and 4 hrs at the lower power and $\frac{1}{4}$, 1, and 2 hrs at the higher. Surface temperature data were collected throughout the run.

---

[1] Department of Mechanical Engineering, University of Minnesota, Minneapolis, Minn.

[2] Numbers in bracket designate References at end of technical note.

Contributed by the Heat Transfer Divison for publication in the JOURNAL OF HEAT TRANSFER. Manuscript received by the Heat Transfer Division March 3, 1978.

At the end of the data run, the power input was terminated, and the test vessel was immediately removed from the constant temperature bath and the melted naphthalene poured off. Subsequently, the unmelted naphthalene was taken out of the vessel and cut along a vertical plane that had contained the axis of the heater. In order to obtain a clear photographic record of the shape of the melt region, the melt cavity in one of the halves of the sectioned material was filled with a dark sand. In addition, prior to photographing the section, a thin white-painted rectangular slab whose length and width correspond respectively to the length and diameter of the heater was positioned at the location of the heater.

The fusion temperature of the naphthalene was determined to be 80.0°C from auxiliary experiments in which temperature versus time cooling curves were measured.

Results and Discussion

The progress of the melting at a succession of times is displayed photographically in Figs. 1 and 2, respectively, for surface heat fluxes of 0.42 and 0.84 W/cm^2. The successive photographs in Fig. 1 correspond to run times of $\frac{1}{2}$, 2, and 4 hrs, while those of Fig. 2 correspond to $\frac{1}{4}$, 1, and 2 hr runs. In each photograph, the heater is represented by the white vertical rectangle, and the white cup-shaped region is the unmelted solid. The initial volume of the solid naphthalene is outlined by the outer perimeter of the remaining solid and by the white dotted lines. The slight irregularities of the liquid-solid interfaces in evidence in the figures are due primarily to unavoidable chipping that occurred at the melt cavity surface during the cutting operation.

It is evident from the figures that there is substantially more melting adjacent to the upper part of the heater than adjacent to the lower part, and this behavior is accentuated as time progresses. These melt layer shapes are in sharp contrast with the vertical annuli that would be predicted by an analysis based on pure conduction. Clearly, conduction is not the transport mechanism that is responsible for the melting patterns displayed in Figs. 1 and 2.

Rather, the experimentally determined melt shapes are consistent with the presence of a recirculating natural convection flow. As the buoyancy-induced flow moves upward along the heated cylinder, the fluid temperature increases. Therefore, the maximum fluid temperature occurs at the top of the heater and, as a result, the highest rates of melting also occur in that region. The recirculating flow passes downward along the solid-liquid interface and is progressively cooled, thereby weakening its melting capabilities.

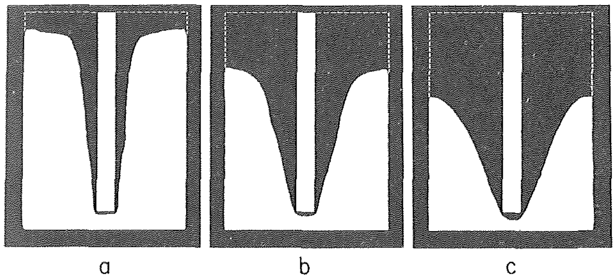

Fig. 1. Progress of melting at a succession of times for surface heat flux = 0.42 W/cm^2. Duration of melting period: (a) $\frac{1}{2}$ hr, (b) 2 hrs, (c) 4 hrs

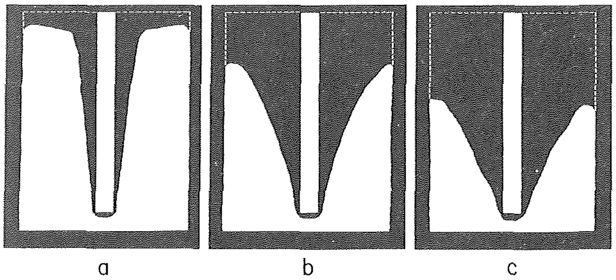

Fig. 2 Progress of melting at a succession of times for surface heat flux = 0.84 W/cm^2. Duration of melting period: (a) $\frac{1}{4}$ hr, (b) 1 hr, (c) 2 hrs

The melting patterns of Fig. 2 correspond to twice the heat flux and half the run times of Fig. 1. Although there are some differences in detail, the corresponding melt shapes for the two cases are quite similar. This outcome is not unexpected in view of the fact that the Rayleigh numbers for the two cases are nearly equal, 6.5×10^6 and 7.0×10^6, respectively. These Rayleigh number values are based on the heater diameter, on the difference between the heater and interface temperatures, and on fluid properties evaluated at the film temperature.

The finding that the highest rates of melting occurred near the top of the heater are consistent with the experimental results of [6, 7] for melting adjacent to a horizontal embedded cylinder. There it was found that melting primarily occurred above the cylinder, with very little melting below.

Representative time histories of the heater surface temperature are presented in Fig. 3. The ordinate variable is the difference between the surface temperature (measured at the mid-height position) and the fusion temperature. The plotted data correspond to the data runs which culminated in the melt shapes pictured in Fig. 1, (b) and (c).

Inspection of Fig. 3 reveals a pattern whereby the temperature difference rises rapidly from an initially small value and attains a maximum, whereafter it decreases and ultimately takes on a steady value. Since the heat flux is independent of time, the reciprocal of the temperature difference is proportional to the heat transfer coefficient. Thus, it is seen that the heat transfer coefficient is very large at small values of time but decreases rapidly and then reaches a minimum, after which it increases to a steady-state value. In contrast, a pure conduction model would predict a monotonic decrease in the heat transfer coefficient for all times, starting with high initial values. Thus, it would appear that conduction only plays an important role at early times, but that natural convection is dominant thereafter. This finding is in accord with the results of [6, 7] for melting due to an embedded horizontal heat source.

The attainment of steady-state heat transfer coefficients is worthy of note, especially since the position of the solid-liquid interface continues to change as time proceeds. This suggests that the thermal resistance of the transfer processes that occur adjacent to the heater surface is substantially greater than the thermal resistance at the interface. This may, in part, be due to the significantly greater transfer area at the interface compared with that of the heater.

The melt layer shapes and the temperature histories both demonstrate the dominant role played by natural convection for melting due to a vertical embedded heater. These findings reinforce those of [6, 7] for the case of a horizontal embedded heater.

The experiments of [8] and those reported here appear to have some similarities. However, the highly abbreviated description of the apparatus and test procedure presented in [8] makes it difficult to fully understand the nature of the experiment performed there. In general,

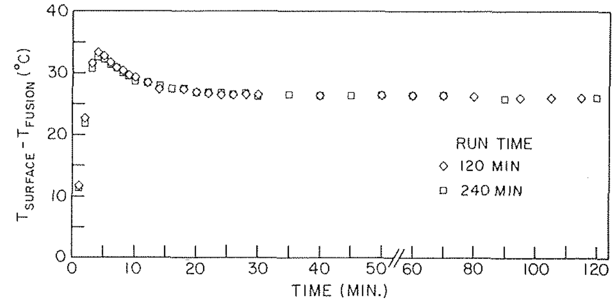

Fig. 3 Representative time histories of the heater surface temperature

the apparatus consisted of a relatively short (length/diameter <4) vertically oriented cylindrical heater situated in an annular volume of paraffin. The entire outer surface of the paraffin was surrounded by an insulated plexiglass enclosure. Thus, unlike the present test set-up, where the top of the phase change medium was unconstrained, that of [8] was constrained by a rigid boundary. The paraffin was initially solid and underwent melting when energy was supplied by the heater. Temperatures at various positions within the paraffin were recorded during the melting process and are reported.

Unlike the present investigation, direct visual determinations of the melt region shape were not made in [8], nor were results obtained relevant to the heat transfer coefficient. From the temperature distributions measured in the paraffin, it was inferred that the melting rate increases with increasing height, which is consistent with the findings presented in Figs. 1 and 2.

References

1 Muehlbauer, J. C., and Sunderland, J. E., "Heat Conduction with Freezing or Melting," *Applied Mechanics Reviews*, Vol. 18, 1965, pp. 951–959.

2 Boley, B. A., "The Analysis of Problems of Heat Conduction and Melting, in High Temperature Structures and Materials," *Proceedings 3rd Symposium on Naval Structural Mechanics*, edited by A. M. Freudenthal, B. A. Boley, and H. Liebowitz, Pergamon, New York, 1963, pp. 260–315.

3 Rubinstein, L. I., "The Stefan Problem," *American Mathematical Society Translations*, Providence, Rhode Island, Vol. 27, 1971.

4 Bankoff, S. G., "Heat Conduction or Diffusion with Change of Phase," in *Advances in Chemical Engineering*, edited by T. B. Drew, Vol. 5, 1964, pp. 75–150.

5 Shamsundar, N., and Sparrow, E. M., "Analysis of Multidimensional Conduction Phase Change Via the Enthalpy Model," ASME JOURNAL OF HEAT TRANSFER, Vol. 97, 1975, pp. 333–340.

6 White, R. D., Bathelt, A. G., Leidenfrost, W., and Viskanta, R., "Study of Heat Transfer and Melting Front from a Cylinder Imbedded in a Phase Change Material," ASME Paper 77-HT-42, National Heat Transfer Conference, Salt Lake City, Utah, August, 1977.

7 Sparrow, E. M., Schmidt, R. R., and Ramsey, J. W., "Experiments on the Role of Natural Convection in the Melting of Solids," ASME JOURNAL OF HEAT TRANSFER, Vol. 100, 1978, pp. 11–16.

8 Bain, R. L., Stermole, F. J., and Golden, J. O., "Liquefaction Dynamics of n-Octadecane in Cylindrical Coordinates," *Journal of Spacecraft and Rockets*, Vol. 11, 1974, pp. 335–339.

Acknowledgment

This research was performed under the auspices of ERDA grant E(11-1)-2595. The involvement of David C. Dunnigan and Roger R. Schmidt in various aspects of the experimental work is gratefully acknowledged.

A Note on the General Formulation of Phase Change Problem as Heat Conduction Problem with a Moving Heat Source

M. Necati Özişik[1]

The liberation (or absorption) of heat during solidification (or melting) can be treated as a moving surface heat source (or sink) located at the solid-liquid interface for pure substances having a discrete melting point temperature. Then the phase change problem can be replaced by an equivalent heat conduction problem with a moving surface heat source for a region with stationary boundaries. This approach, originally proposed by Lightfoot [1][2] and discussed in [2] for the solution of one-dimensional transient phase change problems, was used by several investigators [3–7] under different names such as the *moving heat source method*, the *integral equation method* and the *Green's function method*. In these investigations a heuristic argument is used to derive the appropriate moving heat source term for each particular case studied, or lengthy analysis is presented [7] just to obtain a solution in terms of Green's function. However, if, once and for all, the moving boundary problem is recast explicitly in the form of a general three-dimensional standard heat conduction problem with a moving surface heat source, its solution can immediately be written in terms of Green's function using the standard solutions in the literature [8]. Then, there would be no need to derive for each specific case the appropriate heat source term or the solution in terms of Green's function. The problems of existence, uniqueness, and stability of the solution of multifront Stefan problem have been discussed in [9], and an infinite medium Green's function is used to transform the solution of a two-dimensional phase change problem into a nonlinear integral equation for the location of phase front; but the results are not in a form from which an appropriate moving surface heat source term can be obtained. Therefore, the purpose of this note is to recast a general moving boundary problem explictly as a three-dimensional time dependent heat conduction problem with a moving surface heat source, show the equivalence of the two problems, and discuss how the standard solutions can be utilized to transform the resulting heat conduction problem into an integral equation for the location of the solid-liquid interface.

We consider a three-dimensional solidification problem for a substance which has a discrete melting point temperature; that is, the liquid and solid phases are separated by a sharp interface at the melting phase temperature. We assume the density to be the same for both phases so that the convective velocity resulting from the volumetric effects are neglected; also the thermal diffusivities for the solid and liquid phases are taken to be equal. The differential equations of heat conduction for the solid and liquid phases are given respectively as

$$\nabla^2\theta_s(\mathbf{r},t)=\frac{1}{\alpha}\frac{\partial\theta_s(\mathbf{r},t)}{\partial t}\quad\text{in region } R_s,\ t>0 \tag{1a}$$

$$\nabla^2\theta_\ell(\mathbf{r},t)=\frac{1}{\alpha}\frac{\partial\theta_\ell(\mathbf{r},t)}{\partial t}\quad\text{in region } R_\ell,\ t>0 \tag{1b}$$

where t is the time, α is the thermal diffusivity, and the dimensionless temperature θ_s for the solid and θ_ℓ for the liquid phase are defined as

$$\theta_s(\mathbf{r},t)=\frac{T_s(\mathbf{r},t)-T_m}{\Delta T},\quad \theta_\ell(\mathbf{r},t)=\frac{k_\ell}{k_s}\frac{T_\ell(\mathbf{r},t)-T_m}{\Delta T}$$

Here T_m is the melting point temperature, ΔT is a reference temperature difference, and k_ℓ and k_s are the thermal conductivities for the liquid and solid phases, respectively.

Let the location of the solid-liquid interface be defined by the equation $F(\mathbf{r}, t) = 0$. The boundary conditions at the interface are given as

$$\theta_s(\mathbf{r},t)=\theta_\ell(\mathbf{r},t)=0\quad\text{on } F(\mathbf{r},t)=0,\ t>0 \tag{2a}$$

$$\frac{\partial\theta_s}{\partial n}-\frac{\partial\theta_\ell}{\partial n}=\frac{\rho L}{k_s\Delta T}V_n(t)\quad\text{on } F(\mathbf{r},t)=0,\ t>0 \tag{2b}$$

Here ρ is the density, L is the latent heat per unit mass, $V_n(t)$ is the normal velocity of the solid-liquid interface in the direction of a unit normal vector $\hat{\mathbf{n}}$ at any point p at the interface and pointing into the liquid phase, and $\partial/\partial n$ is the derivative along the unit normal vector $\hat{\mathbf{n}}$. Finally, we assume that:

$$\left[\begin{array}{c}\text{Appropriate boundary conditions are specified}\\ \text{on the outer boundaries of the regions } R_s\\ \text{and } R_\ell \text{ for } t>0\text{; and the initial conditions}\\ \text{are given.}\end{array}\right] \tag{3}$$

---

[1] Department of Mechanical and Aerospace Engineering, North Carolina State University, Raleigh N. C.

[2] Numbers in brackets designate References at end of technical note.

Contributed by the Heat Transfer Division for publication in the JOURNAL OF HEAT TRANSFER. Manuscript received by the Heat Transfer Division October 21, 1977.

the apparatus consisted of a relatively short (length/diameter <4) vertically oriented cylindrical heater situated in an annular volume of paraffin. The entire outer surface of the paraffin was surrounded by an insulated plexiglass enclosure. Thus, unlike the present test set-up, where the top of the phase change medium was unconstrained, that of [8] was constrained by a rigid boundary. The paraffin was initially solid and underwent melting when energy was supplied by the heater. Temperatures at various positions within the paraffin were recorded during the melting process and are reported.

Unlike the present investigation, direct visual determinations of the melt region shape were not made in [8], nor were results obtained relevant to the heat transfer coefficient. From the temperature distributions measured in the paraffin, it was inferred that the melting rate increases with increasing height, which is consistent with the findings presented in Figs. 1 and 2.

References

1 Muehlbauer, J. C., and Sunderland, J. E., "Heat Conduction with Freezing or Melting," *Applied Mechanics Reviews*, Vol. 18, 1965, pp. 951–959.

2 Boley, B. A., "The Analysis of Problems of Heat Conduction and Melting, in High Temperature Structures and Materials," *Proceedings 3rd Symposium on Naval Structural Mechanics*, edited by A. M. Freudenthal, B. A. Boley, and H. Liebowitz, Pergamon, New York, 1963, pp. 260–315.

3 Rubinstein, L. I., "The Stefan Problem," *American Mathematical Society Translations*, Providence, Rhode Island, Vol. 27, 1971.

4 Bankoff, S. G., "Heat Conduction or Diffusion with Change of Phase," in *Advances in Chemical Engineering*, edited by T. B. Drew, Vol. 5, 1964, pp. 75–150.

5 Shamsundar, N., and Sparrow, E. M., "Analysis of Multidimensional Conduction Phase Change Via the Enthalpy Model," ASME JOURNAL OF HEAT TRANSFER, Vol. 97, 1975, pp. 333–340.

6 White, R. D., Bathelt, A. G., Leidenfrost, W., and Viskanta, R., "Study of Heat Transfer and Melting Front from a Cylinder Imbedded in a Phase Change Material," ASME Paper 77-HT-42, National Heat Transfer Conference, Salt Lake City, Utah, August, 1977.

7 Sparrow, E. M., Schmidt, R. R., and Ramsey, J. W., "Experiments on the Role of Natural Convection in the Melting of Solids," ASME JOURNAL OF HEAT TRANSFER, Vol. 100, 1978, pp. 11–16.

8 Bain, R. L., Stermole, F. J., and Golden, J. O., "Liquefaction Dynamics of n-Octadecane in Cylindrical Coordinates," *Journal of Spacecraft and Rockets*, Vol. 11, 1974, pp. 335–339.

Acknowledgment

This research was performed under the auspices of ERDA grant E(11-1)-2595. The involvement of David C. Dunnigan and Roger R. Schmidt in various aspects of the experimental work is gratefully acknowledged.

A Note on the General Formulation of Phase Change Problem as Heat Conduction Problem with a Moving Heat Source

M. Necati Özişik[1]

The liberation (or absorption) of heat during solidification (or melting) can be treated as a moving surface heat source (or sink) located at the solid-liquid interface for pure substances having a discrete melting point temperature. Then the phase change problem can be replaced by an equivalent heat conduction problem with a moving surface heat source for a region with stationary boundaries. This approach, originally proposed by Lightfoot [1][2] and discussed in [2] for the solution of one-dimensional transient phase change problems, was used by several investigators [3–7] under different names such as the *moving heat source method*, the *integral equation method* and the *Green's function method.* In these investigations a heuristic argument is used to derive the appropriate moving heat source term for each particular case studied, or lengthy analysis is presented [7] just to obtain a solution in terms of Green's function. However, if, once and for all, the moving boundary problem is recast explicitly in the form of a general three-dimensional standard heat conduction problem with a moving surface heat source, its solution can immediately be written in terms of Green's function using the standard solutions in the literature [8]. Then, there would be no need to derive for each specific case the appropriate heat source term or the solution in terms of Green's function. The problems of existence, uniqueness, and stability of the solution of multifront Stefan problem have been discussed in [9], and an infinite medium Green's function is used to transform the solution of a two-dimensional phase change problem into a nonlinear integral equation for the location of phase front; but the results are not in a form from which an appropriate moving surface heat source term can be obtained. Therefore, the purpose of this note is to recast a general moving boundary problem explictly as a three-dimensional time dependent heat conduction problem with a moving surface heat source, show the equivalence of the two problems, and discuss how the standard solutions can be utilized to transform the resulting heat conduction problem into an integral equation for the location of the solid-liquid interface.

We consider a three-dimensional solidification problem for a substance which has a discrete melting point temperature; that is, the liquid and solid phases are separated by a sharp interface at the melting phase temperature. We assume the density to be the same for both phases so that the convective velocity resulting from the volumetric effects are neglected; also the thermal diffusivities for the solid and liquid phases are taken to be equal. The differential equations of heat conduction for the solid and liquid phases are given respectively as

$$\nabla^2\theta_s(\mathbf{r},t)=\frac{1}{\alpha}\frac{\partial\theta_s(\mathbf{r},t)}{\partial t}\quad \text{in region } R_s,\ t>0 \tag{1a}$$

$$\nabla^2\theta_\ell(\mathbf{r},t)=\frac{1}{\alpha}\frac{\partial\theta_\ell(\mathbf{r},t)}{\partial t}\quad \text{in region } R_\ell,\ t>0 \tag{1b}$$

where t is the time, α is the thermal diffusivity, and the dimensionless temperature θ_s for the solid and θ_ℓ for the liquid phase are defined as

$$\theta_s(\mathbf{r},t)=\frac{T_s(\mathbf{r},t)-T_m}{\Delta T},\qquad \theta_\ell(\mathbf{r},t)=\frac{k_\ell}{k_s}\frac{T_\ell(\mathbf{r},t)-T_m}{\Delta T}$$

Here T_m is the melting point temperature, ΔT is a reference temperature difference, and k_ℓ and k_s are the thermal conductivities for the liquid and solid phases, respectively.

Let the location of the solid-liquid interface be defined by the equation $F(\mathbf{r},t)=0$. The boundary conditions at the interface are given as

$$\theta_s(\mathbf{r},t)=\theta_\ell(\mathbf{r},t)=0\quad \text{on } F(\mathbf{r},t)=0,\ t>0 \tag{2a}$$

$$\frac{\partial\theta_s}{\partial n}-\frac{\partial\theta_\ell}{\partial n}=\frac{\rho L}{k_s\Delta T}V_n(t)\quad \text{on } F(\mathbf{r},t)=0,\ t>0 \tag{2b}$$

Here ρ is the density, L is the latent heat per unit mass, $V_n(t)$ is the normal velocity of the solid-liquid interface in the direction of a unit normal vector $\hat{\mathbf{n}}$ at any point p at the interface and pointing into the liquid phase, and $\partial/\partial n$ is the derivative along the unit normal vector $\hat{\mathbf{n}}$. Finally, we assume that:

$$\left[\begin{array}{c}\text{Appropriate boundary conditions are specified}\\ \text{on the outer boundaries of the regions } R_s\\ \text{and } R_\ell \text{ for } t>0\text{; and the initial conditions}\\ \text{are given.}\end{array}\right] \tag{3}$$

---

[1] Department of Mechanical and Aerospace Engineering, North Carolina State University, Raleigh N. C.

[2] Numbers in brackets designate References at end of technical note.

Contributed by the Heat Transfer Division for publication in the JOURNAL OF HEAT TRANSFER. Manuscript received by the Heat Transfer Division October 21, 1977.

Equations (1), (2), and (3) describe the complete mathematical formulation of the solidification problem considered here in which the solid-liquid interface moves in the direction of $\hat{\mathbf{n}}$.

We now consider the following time dependent heat conduction problem with a moving heat source, for the region $(R_s + R_\ell)$:

$$\nabla^2\theta(\mathbf{r},t)+\frac{1}{k_s}g(\mathbf{r},t)=\frac{1}{\alpha}\frac{\partial\theta(\mathbf{r},t)}{\partial t} \quad \text{in } (R_s+R_\ell),\ t>0 \tag{4a}$$

$$\text{where } g(\mathbf{r},t)\equiv\frac{\rho L}{\Delta T}V_n(t)\delta(n-n_0) \tag{4b}$$

Here, $\delta(n - n_0)$ is the Dirac delta function with n denoting the distance measured along the normal vector $\hat{\mathbf{n}}$ at a point P on the interface $F(\mathbf{r}, t) = 0$ and n_0 the location of the point P. Thus, $g(\mathbf{r}, t)$ represents a moving surface heat source at the solid-liquid interface.

We now impose the requirement that the temperature $\theta(\mathbf{r}, t)$ should be zero over the surface $F(\mathbf{r}, t) = 0$, which is the location of the solid-liquid interface; thus we have

$$\theta(\mathbf{r},t)=0 \quad \begin{pmatrix}\text{on the surface } F(\mathbf{r},t)=0,\text{ within}\\ \text{the region } R_s+R_\ell,\text{ for } t>0\end{pmatrix} \tag{5}$$

We now have to show that the solution of the heat conduction problem defined by equations (4) and (5) subject to the boundary and inital conditions (3) is equivalent to the solution of the above phase change problem.

The heat conduction equation (4) reduces to equation (1a) in the region R_s and to equation (1b) in the region R_ℓ because of the delta function type heat source. The requirement given by equation (5) is equivalent to the interface boundary condition (2a) of the phase change problem. Finally, we need to prove that equation (4a) satisifies the jump boundary condition (2b) of the phase change problem. This can readily be verified by integrating equation (4a) over a small volume element across the interface, changing the volume integral to the surface intergral, and then letting the thickness ϵ of this volume element become zero, so that the volume element in the limit as $\epsilon \to 0$ coincides with the interface $F(\mathbf{r}, t) = 0$. The procedure is straightforward. Thus the two problems are identical.

The moving surface heat source term $g(\mathbf{r}, t)$ specified in the form given by equation (4b) is not convenient for numerical or analytical computations. Depending on the coordinate system used and the functional form of $F(\mathbf{r}, t) = 0$, it can be expressed in alternative forms. To illustrate this matter we now consider a three-dimensional problem in the rectangular coordinate system and assume that the equation for the interface is given in the form

$$F(\mathbf{r},t)=z-S(x,y,t)=0 \tag{6}$$

The distance n measured along $\hat{\mathbf{n}}$ is related to the distance along the z axis by the relation

$$n=\frac{z}{\hat{\mathbf{n}}\cdot\hat{\mathbf{k}}} \tag{7}$$

where $\hat{\mathbf{k}}$ is the unit direction vector along the z-axis. Then

$$\delta(n-n_0)=\frac{1}{\hat{\mathbf{n}}\cdot\hat{\mathbf{k}}}\delta(z-z_0) \tag{8}$$

Here, z_0 is the z coordinate of the point n_0 on the surface $F(\mathbf{r}, t) = 0$. We also have the relations

$$\hat{\mathbf{n}}\cdot\hat{\mathbf{k}}=-\frac{\partial F/\partial z}{|\nabla F|} \tag{9a}$$

$$V_n(t)=\frac{\partial F/\partial t}{|\nabla F|} \tag{9b}$$

Introducing equations (8) and (9) into (4b) we find

$$g(\mathbf{r},t)=-\frac{\rho L}{\Delta T}\frac{\partial F/\partial t}{\partial F/\partial z}\delta(z-z_0) \tag{10}$$

In view of the relation (6), this expression is written as

$$g(x,y,z,t)=\frac{\rho L}{\Delta T}\frac{\partial S(x,y,t)}{\partial t}\delta(z-z_0) \tag{11}$$

For the two and one-dimensional problems, equation (11) yields the heat source terms used in [4] and [1], respectively.

The advantage of the formulation of phase change problem as a heat induction equation (4a) is that its solution for $\theta(\mathbf{r}, t)$ is immediately written in terms of Green's function using the standard solutions [8, chapter 5]. When the condition (5) is imposed on this solution, an integral equation is obtained for the location of the solid-liquid interface.

Acknowledgment.

This work was supported in part by the National Science Foundation through Grant ENG 77-12949.

References

1 Lightfoot, N. M. H., "The Solidification of Molten Steel," *Proc. London Math. Soc.*, Vol. 31, 1929, pp. 97–119.

2 Carslaw, H. S., and Jaeger, J. C., *Conduction of Heat in Solids*, 2nd ed. Oxford at the Clarendon Press, London, 1959.

3 Chuang, Y. K., and Szekely, J., "The Use of Green's Functions for Solving Melting or Freezing Problems," *Int. Journal of Heat and Mass Transfer*, Vol. 14, 1971, pp. 1285–1295.

4 Rathjen, K. A., and Jiji, L. M., "Heat Conduction with Melting or Freezing in a Corner," ASME JOURNAL OF HEAT TRANSFER, Vol. 93, 1971, pp. 101–109.

5 Chuang, Y. K., and Szekely, J., "The Use of Green's Functions for Solving Melting or Solidification Problems in Cylindrical Coordinate System," *Int. Journal of Heat and Mass Transfer*, Vol. 15, 1972, pp. 1171–1175.

6 Budhia, H., and Kreith, F., "Heat Transfer with Melting or Freezing in a Wedge," *Int. Journal of Heat and Mass Transfer*, Vol. 16, 1973, pp. 195–211.

7 Chuang, Y., "On the Integral Technique for Spherical Growth Problems," *Int. Journal of Heat and Mass Transfer*, Vol. 17, 1974, pp. 945–953.

8 M. N. Özisik, *Boundary Value Problems of Heat Conduction*, International Textbook Co., Scranton, Pa, 1968.

9 Budak B. M., and Moskal, M. Z., "Classical Solution of the Multidimensional Multifront Stefan Problem, Soviet Mathematics," *Dokl. Akad. Nauk SSSR*, Vol. 10, No. 5, 1969, pp. 1043–1046.

Thermocline Degradation in a Packed Bed Thermal Storage Tank[1]

S. B. Margolis[2]

Nomenclature

c_f, c_s = fluid, solid heat capacities (constants)
h' = volumetric heat transfer coefficient
L = tank length
λ_f, λ_s = effective fluid, solid thermal conductivities (constants)
y_n = roots of transcendental equation
T_f, T_s = fluid, solid temperatures (functions of x, t)
$T_{f,0}$, $T_{s,0}$ = initial conditions on T_f, T_s
T_A = ambient outside temperature
T_0 = reference temperature
$(\Delta T)_0$ = characteristic temperature difference
t = time variable
U_f = fluid velocity in bed
x = space variable

---

[1] This work was supported by the United States Department of Energy. Contract Number AT-(29-1)-789.

[2] Applied Mathematics Division 8322, Sandia Laboratories, Livermore, Calif.

Contributed by the Heat Transfer Division for publication in the JOURNAL OF HEAT TRANSFER. Manuscript received by the Heat Transfer Division September 2, 1977.

Equations (1), (2), and (3) describe the complete mathematical formulation of the solidification problem considered here in which the solid-liquid interface moves in the direction of $\hat{\mathbf{n}}$.

We now consider the following time dependent heat conduction problem with a moving heat source, for the region $(R_s + R_\ell)$:

$$\nabla^2\theta(\mathbf{r}, t) + \frac{1}{k_s} g(\mathbf{r}, t) = \frac{1}{\alpha}\frac{\partial\theta(\mathbf{r}, t)}{\partial t} \quad \text{in } (R_s + R_\ell),\ t > 0 \tag{4a}$$

$$\text{where } g(\mathbf{r}, t) \equiv \frac{\rho L}{\Delta T} V_n(t)\delta(n - n_0) \tag{4b}$$

Here, $\delta(n - n_0)$ is the Dirac delta function with n denoting the distance measured along the normal vector $\hat{\mathbf{n}}$ at a point P on the interface $F(\mathbf{r}, t) = 0$ and n_0 the location of the point P. Thus, $g(\mathbf{r}, t)$ represents a moving surface heat source at the solid-liquid interface.

We now impose the requirement that the temperature $\theta(\mathbf{r}, t)$ should be zero over the surface $F(\mathbf{r}, t) = 0$, which is the location of the solid-liquid interface; thus we have

$$\theta(\mathbf{r}, t) = 0 \quad \begin{pmatrix} \text{on the surface } F(\mathbf{r}, t) = 0, \text{ within} \\ \text{the region } R_s + R_\ell, \text{ for } t > 0 \end{pmatrix} \tag{5}$$

We now have to show that the solution of the heat conduction problem defined by equations (4) and (5) subject to the boundary and inital conditions (3) is equivalent to the solution of the above phase change problem.

The heat conduction equation (4) reduces to equation (1a) in the region R_s and to equation (1b) in the region R_ℓ because of the delta function type heat source. The requirement given by equation (5) is equivalent to the interface boundary condition (2a) of the phase change problem. Finally, we need to prove that equation (4a) satisifies the jump boundary condition (2b) of the phase change problem. This can readily be verified by integrating equation (4a) over a small volume element across the interface, changing the volume integral to the surface intergral, and then letting the thickness ϵ of this volume element become zero, so that the volume element in the limit as $\epsilon \rightarrow 0$ coincides with the interface $F(\mathbf{r}, t) = 0$. The procedure is straightforward. Thus the two problems are identical.

The moving surface heat source term $g(\mathbf{r}, t)$ specified in the form given by equation (4b) is not convenient for numerical or analytical computations. Depending on the coordinate system used and the functional form of $F(\mathbf{r}, t) = 0$, it can be expressed in alternative forms. To illustrate this matter we now consider a three-dimensional problem in the rectangular coordinate system and assume that the equation for the interface is given in the form

$$F(\mathbf{r}, t) = z - S(x, y, t) = 0 \tag{6}$$

The distance n measured along $\hat{\mathbf{n}}$ is related to the distance along the z axis by the relation

$$n = \frac{z}{\hat{\mathbf{n}} \cdot \hat{\mathbf{k}}} \tag{7}$$

where $\hat{\mathbf{k}}$ is the unit direction vector along the z-axis. Then

$$\delta(n - n_0) = \frac{1}{\hat{\mathbf{n}} \cdot \hat{\mathbf{k}}} \delta(z - z_0) \tag{8}$$

Here, z_0 is the z coordinate of the point n_0 on the surface $F(\mathbf{r}, t) = 0$. We also have the relations

$$\hat{\mathbf{n}} \cdot \hat{\mathbf{k}} = -\frac{\partial F/\partial z}{|\nabla F|} \tag{9a}$$

$$V_n(t) = \frac{\partial F/\partial t}{|\nabla F|} \tag{9b}$$

Introducing equations (8) and (9) into (4b) we find

$$g(\mathbf{r}, t) = -\frac{\rho L}{\Delta T}\frac{\partial F/\partial t}{\partial F/\partial z}\delta(z - z_0) \tag{10}$$

In view of the relation (6), this expression is written as

$$g(x, y, z, t) = \frac{\rho L}{\Delta T}\frac{\partial S(x, y, t)}{\partial t}\delta(z - z_0) \tag{11}$$

For the two and one-dimensional problems, equation (11) yields the heat source terms used in [4] and [1], respectively.

The advantage of the formulation of phase change problem as a heat induction equation (4a) is that its solution for $\theta(\mathbf{r}, t)$ is immediately written in terms of Green's function using the standard solutions [8, chapter 5]. When the condition (5) is imposed on this solution, an integral equation is obtained for the location of the solid-liquid interface.

Acknowledgment.

This work was supported in part by the National Science Foundation through Grant ENG 77-12949.

References

1 Lightfoot, N. M. H., "The Solidification of Molten Steel," *Proc. London Math. Soc.*, Vol. 31, 1929, pp. 97–119.
2 Carslaw, H. S., and Jaeger, J. C., *Conduction of Heat in Solids*, 2nd ed. Oxford at the Clarendon Press, London, 1959.
3 Chuang, Y. K., and Szekely, J., "The Use of Green's Functions for Solving Melting or Freezing Problems," *Int. Journal of Heat and Mass Transfer*, Vol. 14, 1971, pp. 1285–1295.
4 Rathjen, K. A., and Jiji, L. M., "Heat Conduction with Melting or Freezing in a Corner," ASME JOURNAL OF HEAT TRANSFER, Vol. 93, 1971, pp. 101–109.
5 Chuang, Y. K., and Szekely, J., "The Use of Green's Functions for Solving Melting or Solidification Problems in Cylindrical Coordinate System," *Int. Journal of Heat and Mass Transfer*, Vol. 15, 1972, pp. 1171–1175.
6 Budhia, H., and Kreith, F., "Heat Transfer with Melting or Freezing in a Wedge," *Int. Journal of Heat and Mass Transfer*, Vol. 16, 1973, pp. 195–211.
7 Chuang, Y., "On the Integral Technique for Spherical Growth Problems," *Int. Journal of Heat and Mass Transfer*, Vol. 17, 1974, pp. 945–953.
8 M. N. Özisik, *Boundary Value Problems of Heat Conduction*, International Textbook Co., Scranton, Pa, 1968.
9 Budak B. M., and Moskal, M. Z., "Classical Solution of the Multidimensional Multifront Stefan Problem, Soviet Mathematics," *Dokl. Akad. Nauk SSSR*, Vol. 10, No. 5, 1969, pp. 1043–1046.

Thermocline Degradation in a Packed Bed Thermal Storage Tank[1]

S. B. Margolis[2]

Nomenclature

c_f, c_s = fluid, solid heat capacities (constants)
h' = volumetric heat transfer coefficient
L = tank length
λ_f, λ_s = effective fluid, solid thermal conductivities (constants)
y_n = roots of transcendental equation
T_f, T_s = fluid, solid temperatures (functions of x, t)
$T_{f,0}$, $T_{s,0}$ = initial conditions on T_f, T_s
T_A = ambient outside temperature
T_0 = reference temperature
$(\Delta T)_0$ = characteristic temperature difference
t = time variable
U_f = fluid velocity in bed
x = space variable

---

[1] This work was supported by the United States Department of Energy. Contract Number AT-(29-1)-789.

[2] Applied Mathematics Division 8322, Sandia Laboratories, Livermore, Calif.

Contributed by the Heat Transfer Division for publication in the JOURNAL OF HEAT TRANSFER. Manuscript received by the Heat Transfer Division September 2, 1977.

β = void fraction of bed
ϵ = dimensionless heat transfer coefficient
ρ_f, ρ_s = fluid, solid densities (constants)

1 Introduction

The problem of thermocline degradation in a packed bed thermal storage tank arises in the analysis of a central solar receiver facility. By passing hot fluid, heated by the sun in the receiver portion of the system, through a cold bed (charging), heat energy is transferred from the fluid to the solid portions of the tank. This stored heat energy may then be reclaimed by the reverse process at a later time by passing cold fluid through the hot bed (discharging). Both processes usually result in a moving narrow region, called a thermocline, in which the temperature gradients of the fluid and solid are relatively large and monotonic. For the general case of a partially charged bed, maintaining a sharp thermocline between the hot and cold regions of the bed for reasonably long holding times is essential in order to keep the hot end of the tank at or near its original charged temperature. Accordingly, this paper presents a time-dependent mathematical analysis of the fluid and solid temperature profiles of the bed during holding periods when no new fluid enters the tank.

The general case of fluid flowing through a packed bed consisting of crushed material (Fig. 1) was first treated mathematically by Schumann [1].[3] In that paper, the assumptions of constant fluid and material properties, zero thermal conductivity in the flow direction, and infinite thermal conductivity in the direction normal to the flow, permitted a closed form solution of the one-dimensional semi-infinite problem. Other papers have since extended these results to allow for heat generation due to chemical reactions (cf. Hung and Nevins [2]). Although the diffusion terms are usually small compared to those describing the heat transfer between fluid and solid when the inlet fluid velocity is nonzero, the neglect of these terms does not permit the modelling of the thermocline degradation when the fluid is at rest. Hence, the present contribution deals with the special case where the inlet fluid velocity is zero, but incorporates the additional effects of thermal conduction and finite tank length.

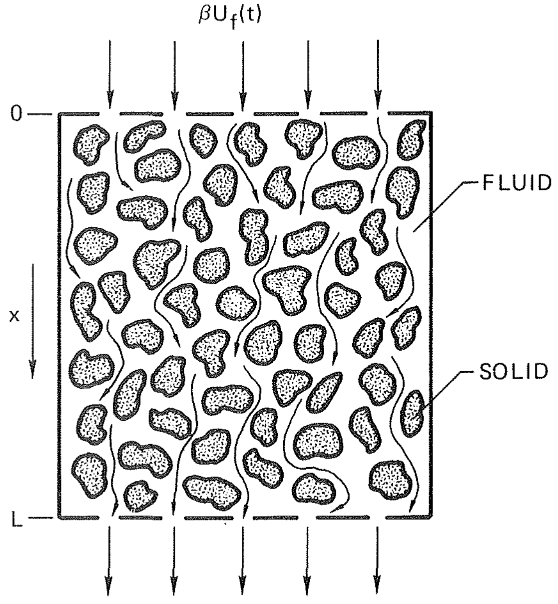

Fig. 1 Sketch of fluid flow through a packed bed

2 Governing Equations

Assuming the fluid to be incompressible and the problem to be globally one-dimensional, the problem reduces to the solution of the energy equations for the fluid and solid portions of the bed. Assuming constant thermal properties, these are

$$\frac{\partial T_f}{\partial t} + U_f(t)\frac{\partial T_f}{\partial x} = \frac{h'}{\beta \rho_f c_f}(T_s - T_f) + \frac{\lambda_f}{\rho_f c_f}\frac{\partial^2 T_f}{\partial x^2} \qquad (1a)$$

$$\frac{\partial T_s}{\partial t} = \frac{h'}{(1-\beta)\rho_s c_s}(T_f - T_s) + \frac{\lambda_s}{\rho_s c_s}\frac{\partial^2 T_s}{\partial x^2} \qquad (1b)$$

The semi-empirical terms containing h' account for the heat transfer between fluid and solid in the direction(s) perpendicular to the flow, whereas the terms containing λ_f, λ_s (which denote *effective* thermal conductivities) account for the diffusion of heat in the direction parallel to the flow. In deriving these equations, it has been assumed that the solid particles in the bed are sufficiently small relative to the dimensions of the tank so that a continuum formulation is possible. This justifies the use of the one-dimensional Fourier law of heat conduction, provided that the thermal conductivities of the fluid and solid are replaced by their "effective" values to take into account the more intricate paths followed by the heat transport process.

The above equations, without the diffusion terms, constitute Schumann's original model. Setting $U_f = 0$, they govern the behavior of the fluid and solid temperature profiles, subject to appropriate initial and boundary conditions, when no new fluid is allowed to enter the tank. Of course, the one-dimensional formulation does not permit one to impose a nontrivial boundary condition, such as a heat flux, on the tank side walls, but practical applications indicate that such possible heat losses are small compared to end losses when the horizontal tank dimension(s) are at least comparable to the vertical length of the tank. This (experimental) result (cf. [3]) is due both to the presence of piping which allows for the passage of fluid into and out of the bed during charging or discharging cycles and to the contact of the bottom of the tank with a foundation (especially the latter).

Introducing the nondimensional quantities

$$x^* = \frac{x}{L}; \quad t^* = \frac{t\lambda_s}{\rho_s c_s L^2}; \quad T^* = \frac{T - T_0}{(\Delta T)_0} \qquad (2a,b,c)$$

where $\rho_s c_s L^2/\lambda_s$ is a diffusive time scale based on the thermal diffusivity $\lambda_s/\rho_s c_s$ of the solid, the governing equations become

$$\frac{\partial T_f^*}{\partial t^*} = h_f(T_s^* - T_f^*) + \alpha\frac{\partial^2 T_f^*}{\partial x^{*2}} \qquad (3a)$$

$$\frac{\partial T_s^*}{\partial t^*} = h_s(T_f^* - T_s^*) + \frac{\partial^2 T_s^*}{\partial x^{*2}} \qquad (3b)$$

where the pure numbers h_f, h_s, α are

$$h_f \equiv \frac{h' L^2 \rho_s c_s}{\beta \lambda_s \rho_f c_f}; \quad h_s \equiv \frac{h' L^2}{(1-\beta)\lambda_s}; \quad \alpha \equiv \frac{\lambda_f \rho_s c_s}{\lambda_s \rho_f c_f} \qquad (4a,b,c)$$

It should be pointed out that correlated values for h' are not readily available for cases where $U_f \to 0$. The volumetric heat transfer terms in equations (1) should thus be interpreted as first, semi-empirical approximations to the actual mechanism of heat transfer between the fluid and solid portions of the bed.

3 Analysis

The solution to the coupled system (3) for arbitrary boundary conditions may be obtained by introducing the Laplace transforms

$$\bar{T}_{f,s}(x^*; p) = \int_0^\infty \exp(-pt^*) T_{f,s}^*(x^*, t^*) dt^* \qquad (5)$$

where the subscript f, s indicates that the definition holds for both the fluid and solid variables. Defining

$$\bar{R}_{f,s} = \frac{d\bar{T}_{f,s}}{dx^*} \qquad (6)$$

one obtains the ordinary system

---

[3] Numbers in brackets designate References at end of technical note.

$$\frac{d}{dx^*}\begin{bmatrix}\tilde{T}_f\\ \tilde{T}_s\\ \tilde{R}_f\\ \tilde{R}_s\end{bmatrix}=\begin{bmatrix}0 & 0 & 1 & 0\\ 0 & 0 & 0 & 1\\ \frac{1}{\alpha}(h_f+p) & -\frac{1}{\alpha}h_f & 0 & 0\\ -h_s & h_s+p & 0 & 0\end{bmatrix}\begin{bmatrix}\tilde{T}_f\\ \tilde{T}_s\\ \tilde{R}_f\\ \tilde{R}_s\end{bmatrix}+\begin{bmatrix}0\\ 0\\ -\frac{1}{\alpha}T^*_{f,0}(x^*)\\ -T^*_{s,0}(x^*)\end{bmatrix} \qquad (7)$$

where $T^*_{f,0}$, $T^*_{s,0}$ are the initial profiles at $t^* = 0$. The formal solution of equation (7) is

$$\begin{bmatrix}\tilde{T}_f\\ \tilde{T}_s\\ \tilde{R}_f\\ \tilde{R}_s\end{bmatrix}=\exp(\mathbf{A}x^*)\int^{x^*}\exp(-\mathbf{A}\bar{x})\begin{bmatrix}0\\ 0\\ -\frac{1}{\alpha}T^*_{f,0}(\bar{x})\\ -T^*_{s,0}(\bar{x})\end{bmatrix}d\bar{x}+\exp(\mathbf{A}x^*)\begin{bmatrix}c_1(p)\\ c_2(p)\\ c_3(p)\\ c_4(p)\end{bmatrix} \qquad (8)$$

where $\mathbf{A}$ is the matrix in (7) and c_1, c_2, c_3, c_4 are p-dependent constants of integration which are in principle determined by the boundary conditions in the transformed space. Owing to the simple structure of $\mathbf{A}$ the matrices $\exp(\pm\mathbf{A}x^*)$, and hence the solution (8), are tractable (cf. [4]) and the physical solution is then given by the inversion formula

$$T^*_{f,s}(x^*, t^*) = \frac{1}{2\pi i}\int_{c-i\infty}^{c+i\infty}\exp(pt^*)\tilde{T}_{f,s}(x^*; p)dp \qquad (9)$$

where c is chosen so that the path of integration in the complex p-plane lies to the right of all singularities of the integrand.

For solar energy applications, one has that $h_f, h_s \gg 1$ and thus only minute temperature differences are maintained between the fluid and solid portions of the bed. Hence, diffusion takes place in both materials at essentially the same rate, and it is therefore reasonable to drop the volumetric heat transfer terms in the governing equations and to replace the separate diffusivities with a single mean diffusivity for the bed as a whole. That is, $T^*_f \approx T^*_s \equiv T^*$ (as shown in [4], this is rigorously true independent of h_f, h_s when $\alpha = 1$ and T^*_f, T^*_s satisfy the same initial and boundary conditions). The result therefore is simply the classical heat conduction equation for the mean bed temperature $T^*(x^*, t^*)$. In the context of the above analysis, one may set $h_f = h_s \approx 0$, $\alpha = 1$ to obtain

$$\begin{bmatrix}\tilde{T}\\ \tilde{R}\end{bmatrix}=\exp(\mathbf{A}_c x^*)\int^{x^*}\exp(-\mathbf{A}_c\bar{x})\begin{bmatrix}0\\ -T^*_0(\bar{x})\end{bmatrix}d\bar{x}+\exp(\mathbf{A}_c x^*)\begin{bmatrix}c_1(p)\\ c_3(p)\end{bmatrix} \qquad (10)$$

where $\exp(\pm\mathbf{A}_c x^*)$ is the compressed matrix

$$\exp(\pm\mathbf{A}_c x^*)=\begin{bmatrix}\cosh\Lambda x^* & \pm\frac{1}{\Lambda}\sinh\Lambda x^*\\ \pm\Lambda\sinh\Lambda x^* & \cosh\Lambda x^*\end{bmatrix} \qquad (11)$$

with $\Lambda \equiv p^{1/2}$.

4 Results

To illustrate the analysis and to indicate the dominating effects of imperfect insulation on the degradation of the initial temperature profiles, consider the case of a tank which is perfectly insulated at the top but allowed to lose heat out the bottom surface according to Newton's law of cooling. For the single-phase approximation, the boundary conditions are thus

$$\frac{\partial T^*}{\partial x^*} = 0 \text{ at } x^* = 0; \quad \frac{\partial T^*}{\partial x^*} = -\epsilon(T^* - T^*_A) \text{ at } x^* = 1 \qquad (12a,b)$$

where $\epsilon \geqq 0$ is the dimensionless heat transfer coefficient and T^*_A is the ambient temperature of the medium outside the tank (in dimensional units, the heat transfer coefficient is $\epsilon\lambda/L$). The thermocline-like initial profile is taken to be

$$T^*_0(x^*) = A(x^*)^2 + B(x^*)^3 \qquad (13)$$

where

$$A = \frac{27}{4}\left(\frac{2+\epsilon}{3+\epsilon}\right)^2; \quad B = -\frac{27}{4}\left(\frac{2+\epsilon}{3+\epsilon}\right)^3 \qquad (14a,b)$$

This profile, which is shown in Fig. 2(a) for several choices of ϵ, is zero at $x^* = 0$, has a maximum of unity at $x^* = -2A/3B = 2(3+\epsilon)/3(2+\epsilon)$, and is consistent with the boundary conditions at $x^* = 0$ and 1.

The resulting solution for $\epsilon > 0$ according to the analysis of Section 3 (cf. [4]) is

$$T^*(x^*, t^*; \epsilon > 0) = T^*_A + \sum_{n=0}^{\infty}\frac{2}{y_n^4} \times \frac{-\gamma_1 y_n^2 + \gamma_2 + \gamma_3\cos y_n + \gamma_4 y_n^{-1}\sin y_n}{\cos y_n + (1+\epsilon)y_n^{-1}\sin y_n} \times \cos(y_n x^*)\exp(-y_n^2 t^*) \qquad (15)$$

where the y_n's are the positive roots of $\epsilon/y = \tan y$ and are obtained numerically using a Newton-Raphson technique. (The integrand in (9) has a nonsimple pole at the origin and simple poles at $p = -y_n^2$, $n = 0, 1, \ldots$, where $y_n \approx n\pi$ for $n \gg 1$.) Here,

$$\gamma_1 = \epsilon T^*_A - A(2+\epsilon) - B(3+\epsilon) \qquad (16a)$$

$$\gamma_2 = -2\epsilon A - 6B(1+\epsilon); \quad \gamma_3 = 6B; \quad \gamma_4 = 6\epsilon B \qquad (16b, c, d)$$

For $\epsilon = 0$ (perfectly insulated tank) one obtains

$$T^*(x^*, t^*; \epsilon = 0) = \frac{1}{2} - \sum_{n=1}^{\infty}\frac{48}{(2n-1)^4\pi^4}\cos[(2n-1)\pi x^*]\exp[-(2n-1)^2\pi^2 t^*] \qquad (17)$$

Note that

$$\lim_{t^*\to\infty} T^* = \begin{cases}1/2, & \epsilon = 0\\ T^*_A, & \epsilon > 0\end{cases} \qquad (18)$$

Fig. 2(b) and (c) show the time evolution of the profiles according

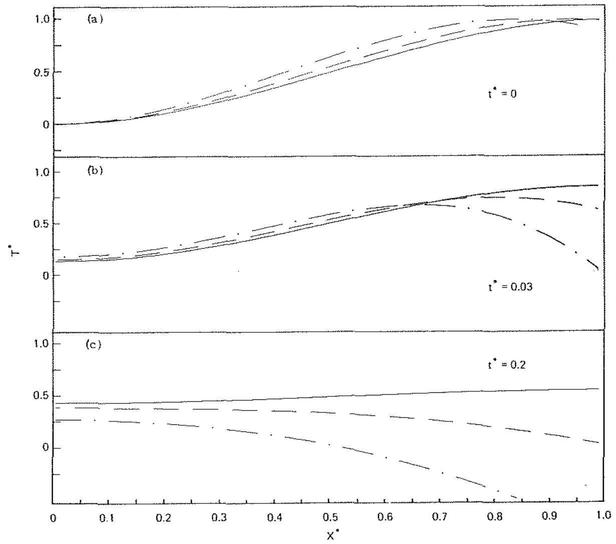

Fig. 2(a–c) **Time evolution of temperature profile for the imperfectly insulated tank of Section 4. ————, $\epsilon = 0$; — — —, $\epsilon = 0.5$; — · — · —, $\epsilon = 2.0$**

to the solutions given above. The dimensionless ambient temperature $T_A^* \equiv (T_A - T_0)(\Delta T)_0$ was taken to be -2, which corresponds to a typical case in which T_A is room temperature, the minimum initial bed temperature $T_0 = T_A + 194$ K, and the difference between the maximum and minimum initial bed temperatures is $(\Delta T)_0 = 97$ K. For a tank length L of 6.1 m and a typical mean bed conductivity λ of 1.7 W/m − K, even the largest value of ϵ used in the figures apparently represents a relatively low value for the dimensionless heat transfer coefficient at the surface of the tank in contact with a foundation (cf. [3]). A comparison of the time evolution of the temperature profile for the $\epsilon = 0$ case with those for $\epsilon > 0$ clearly illustrates how heat losses due to imperfect insulation dominate over internal thermal conduction effects alone in causing the degradation of the temperature profile. (The initial heat content of the bed is an increasing function of ϵ for $0 \leqq \epsilon < 6$ so that the enhanced degradation for $\epsilon > 0$ is not attributable to lower initial heat content.) For a typical mean bed thermal diffusivity of 5×10^{-7} m^2/s, the profiles of Fig. 2(b) show the profiles after approximately 90 hours.

References

1 Schumann, T. E. W., "Heat Transfer—A Liquid Flowing Through a Porous Prism," *J. Franklin Institute*, Vol. 208, 1929, p. 405.

2 Hung, F. T. and Nevins, R. G., "Unsteady-State Heat Transfer With a Flowing Fluid Through Porous Solids," *ASME*-65-HT-10, 1965.

3 "Central Receiver Solar Thermal Power System, Vol. 5: Thermal Storage Subsystem," McDonnell Douglas Report MDC G6776, 1977.

4 Margolis, S. B., "Thermocline Degradation in a Packed Bed Thermal Storage Tank," Sandia Laboratories Report SAND77-8032, 1977.

Radial Heat Transfer and Critical Biot Number With Radiation, Uniform Surface Heat Generation, and Curvature Effects in Convection

T. H. Kuehn[1]

Nomenclature

b = constant, $(X - X_\infty)/(T - T_\infty)$
$B = (\partial r/\partial T)/(\partial c/\partial T)$, $B = 0$ when $R = 0$
Bi_{cr} = critical Biot number, Nu/K
c = external convective heat flux
c_p = external fluid constant pressure specific heat
C = constant
D_i = outside diameter of inner cylinder
D = outside diameter of solid surrounding the inner cylinder
F = shape factor for radiation
g = gravitational acceleration
G = ratio of heat flux from surface heat generation to heat flux from convection, s/c
h = mean external convective heat transfer coefficient
$h = C(T - T_\infty)^n D^{-m}$
h_{pc} = enthalpy of sublimation for phase change substance
H = height of vertical cylinder
k_s = thermal conductivity of solid
k_f = thermal conductivity of external fluid
K = ratio of solid to external fluid thermal conductivity, k_s/k_f
Le = Lewis number, Pr/Sc
m = exponent of D in the expression for variable external convective heat transfer coefficient
n = exponent of $(T - T_\infty)$ in the expression for variable external convective heat transfer coefficient
Nu = external Nusselt number, hD/k_f
Pr = external fluid Prandtl number
r = radiative heat flux
R = ratio of radiative heat flux to convective heat flux, r/c
Ra = Rayleigh number, $g\beta D^3 (T - T_\infty)/\nu\alpha$
s = heat flux due to surface heat generation
Sc = external fluid Schmidt number
T_i = temperature of inner cylinder
T = temperature of solid external surface
T_∞ = temperature of surroundings
X = mole fraction of phase change substance at solid-fluid interface
X_∞ = mole fraction of phase change substance in surroundings
α = external fluid thermal diffusivity
β = external fluid thermal coefficient of volumetric expansion
ϵ = hemispherical emissivity of solid
ν = external fluid kinematic viscosity
σ = Stefan-Boltzmann constant

Introduction

Radial heat transfer by combined conduction and convection including the concept of a critical radius has been discussed for many years in standard heat transfer texts [1, 2].[2] In these references, the external convective heat transfer coefficient is assumed to be constant. Sparrow [3] incorporated the effect of a variable convective coefficient dependent on both cylinder radius and temperature. Simmons [4] gave a relation for the critical radius using an exact expression for radiation. The variable convection coefficients were determined from laminar boundary layer theory. The purpose of this note is to add the effect of uniform surface heat generation due to a phase change at the external convective boundary. More accurate expressions for natural convection heat transfer coefficients are given. These are valid at small Rayleigh numbers where curvature effects make boundary layer solutions inaccurate. The resulting critical radius equation is cast into dimensionless form in terms of a critical Biot number. An application is the solidification of a vapor from a gas-vapor mixture including frosting of refrigeration tubes.

Analysis

The rate of steady heat conduction per unit length through a cylindrical annulus with convection, radiation, and uniform surface heat generation on the external surface can be expressed as

$$\frac{2\pi k_s(T_i - T)}{\ln D/D_i} = \pi Dh(T - T_\infty) + \pi D\epsilon F\sigma(T^4 - T_\infty{}^4) + \frac{\pi Dh(X - X_\infty)h_{pc}}{\mathrm{Le}c_p} \qquad (1)$$

The inner and outer boundaries of the annulus are each assumed to be at a uniform temperature. The Lewis analogy is used to relate the mass transfer of the phase change material to the convective heat transfer. For many gases and vapors Pr ≈ Sc so that Le ≈ 1. The concentration difference can be written in terms of the temperature difference, $(X - X_\infty) = b(T - T_\infty)$, when the phase change substance is saturated at the solid surface and in the surrounding fluid. This is a good approximation for enclosed spaces and small temperature differences. Bottemanne [5] found that natural convection heat and mass transfer coefficients are virtually independent providing the body forces are aligned, Pr ≈ Sc, and the rate of mass transfer is small.

Considering the temperature difference $(T_i - T_\infty)$ to be constant, the critical radius equation describing the conditions of maximum heat transfer can be written in dimensionless form. This becomes an expression for the critical Biot number which is more general than the relations for the dimensional critical radius used in the past.

---

[1] Department of Mechanical Engineering, Iowa State University, Ames, Iowa.

Contributed by the Heat Transfer Division for publication in the JOURNAL OF HEAT TRANSFER. Manuscript received by the Heat Transfer Division December 5, 1977.

[2] Numbers in brackets designate References at end of technical note.

to the solutions given above. The dimensionless ambient temperature $T_A^* \equiv (T_A - T_0)(\Delta T)_0$ was taken to be −2, which corresponds to a typical case in which T_A is room temperature, the minimum initial bed temperature $T_0 = T_A + 194$ K, and the difference between the maximum and minimum initial bed temperatures is $(\Delta T)_0 = 97$ K. For a tank length L of 6.1 m and a typical mean bed conductivity λ of 1.7 W/m − K, even the largest value of ϵ used in the figures apparently represents a relatively low value for the dimensionless heat transfer coefficient at the surface of the tank in contact with a foundation (cf. [3]). A comparison of the time evolution of the temperature profile for the $\epsilon = 0$ case with those for $\epsilon > 0$ clearly illustrates how heat losses due to imperfect insulation dominate over internal thermal conduction effects alone in causing the degradation of the temperature profile. (The initial heat content of the bed is an increasing function of ϵ for $0 \leqq \epsilon < 6$ so that the enhanced degradation for $\epsilon > 0$ is not attributable to lower initial heat content.) For a typical mean bed thermal diffusivity of 5×10^{-7} m²/s, the profiles of Fig. 2(b) show the profiles after approximately 90 hours.

References

1 Schumann, T. E. W., "Heat Transfer—A Liquid Flowing Through a Porous Prism," *J. Franklin Institute*, Vol. 208, 1929, p. 405.

2 Hung, F. T. and Nevins, R. G., "Unsteady-State Heat Transfer With a Flowing Fluid Through Porous Solids," *ASME*-65-HT-10, 1965.

3 "Central Receiver Solar Thermal Power System, Vol. 5: Thermal Storage Subsystem," McDonnell Douglas Report MDC G6776, 1977.

4 Margolis, S. B., "Thermocline Degradation in a Packed Bed Thermal Storage Tank," Sandia Laboratories Report SAND77-8032, 1977.

Radial Heat Transfer and Critical Biot Number With Radiation, Uniform Surface Heat Generation, and Curvature Effects in Convection

T. H. Kuehn[1]

Nomenclature

b = constant, $(X - X_\infty)/(T - T_\infty)$

$B = (\partial r/\partial T)/(\partial c/\partial T)$, $B = 0$ when $R = 0$

Bi_{cr} = critical Biot number, Nu/K

c = external convective heat flux

c_p = external fluid constant pressure specific heat

C = constant

D_i = outside diameter of inner cylinder

D = outside diameter of solid surrounding the inner cylinder

F = shape factor for radiation

g = gravitational acceleration

G = ratio of heat flux from surface heat generation to heat flux from convection, s/c

h = mean external convective heat transfer coefficient

$h = C(T - T_\infty)^n D^{-m}$

h_{pc} = enthalpy of sublimation for phase change substance

H = height of vertical cylinder

k_s = thermal conductivity of solid

k_f = thermal conductivity of external fluid

K = ratio of solid to external fluid thermal conductivity, k_s/k_f

Le = Lewis number, Pr/Sc

m = exponent of D in the expression for variable external convective heat transfer coefficient

n = exponent of $(T - T_\infty)$ in the expression for variable external convective heat transfer coefficient

Nu = external Nusselt number, hD/k_f

Pr = external fluid Prandtl number

r = radiative heat flux

R = ratio of radiative heat flux to convective heat flux, r/c

Ra = Rayleigh number, $g\beta D^3 (T - T_\infty)/\nu\alpha$

s = heat flux due to surface heat generation

Sc = external fluid Schmidt number

T_i = temperature of inner cylinder

T = temperature of solid external surface

T_∞ = temperature of surroundings

X = mole fraction of phase change substance at solid-fluid interface

X_∞ = mole fraction of phase change substance in surroundings

α = external fluid thermal diffusivity

β = external fluid thermal coefficient of volumetric expansion

ϵ = hemispherical emissivity of solid

ν = external fluid kinematic viscosity

σ = Stefan-Boltzmann constant

Introduction

Radial heat transfer by combined conduction and convection including the concept of a critical radius has been discussed for many years in standard heat transfer texts [1, 2].[2] In these references, the external convective heat transfer coefficient is assumed to be constant. Sparrow [3] incorporated the effect of a variable convective coefficient dependent on both cylinder radius and temperature. Simmons [4] gave a relation for the critical radius using an exact expression for radiation. The variable convection coefficients were determined from laminar boundary layer theory. The purpose of this note is to add the effect of uniform surface heat generation due to a phase change at the external convective boundary. More accurate expressions for natural convection heat transfer coefficients are given. These are valid at small Rayleigh numbers where curvature effects make boundary layer solutions inaccurate. The resulting critical radius equation is cast into dimensionless form in terms of a critical Biot number. An application is the solidification of a vapor from a gas-vapor mixture including frosting of refrigeration tubes.

Analysis

The rate of steady heat conduction per unit length through a cylindrical annulus with convection, radiation, and uniform surface heat generation on the external surface can be expressed as

$$\frac{2\pi k_s(T_i - T)}{\ln D/D_i} = \pi D h(T - T_\infty) + \pi D \epsilon F \sigma (T^4 - T_\infty{}^4) + \frac{\pi D h (X - X_\infty) h_{pc}}{\mathrm{Le} c_p} \qquad (1)$$

The inner and outer boundaries of the annulus are each assumed to be at a uniform temperature. The Lewis analogy is used to relate the mass transfer of the phase change material to the convective heat transfer. For many gases and vapors Pr ≈ Sc so that Le ≈ 1. The concentration difference can be written in terms of the temperature difference, $(X - X_\infty) = b(T - T_\infty)$, when the phase change substance is saturated at the solid surface and in the surrounding fluid. This is a good approximation for enclosed spaces and small temperature differences. Bottemanne [5] found that natural convection heat and mass transfer coefficients are virtually independent providing the body forces are aligned, Pr ≈ Sc, and the rate of mass transfer is small.

Considering the temperature difference $(T_i - T_\infty)$ to be constant, the critical radius equation describing the conditions of maximum heat transfer can be written in dimensionless form. This becomes an expression for the critical Biot number which is more general than the relations for the dimensional critical radius used in the past.

---

[1] Department of Mechanical Engineering, Iowa State University, Ames, Iowa.

Contributed by the Heat Transfer Division for publication in the JOURNAL OF HEAT TRANSFER. Manuscript received by the Heat Transfer Division December 5, 1977.

[2] Numbers in brackets designate References at end of technical note.

$$\mathrm{Bi}_{cr} = \frac{2[(1-m)(1+G)+R]}{[(1+n)(1+G)+B][1+G+R]} \qquad (2)$$

This becomes equivalent to equation (7) of [4] when $G = 0$. When both radiation and surface heat generation are zero this reduces to

$$\mathrm{Bi}_{cr} = \frac{2(1-m)}{1+n} \qquad (3)$$

which can be easily obtained from the relation for the critical radius given in [3].

The values for m and n in natural convection ($m = 1 - 3n$) depend on the Rayleigh number, Prandtl number and in some cases dimensionless geometry terms. The variation of n with Rayleigh number and Prandtl number for natural convection about a horizontal cylinder is shown in Fig. 1(a). The curves were obtained from the following correlation given in [6]:

$$\mathrm{Nu} = \frac{2}{\ln\left[1 + \dfrac{2}{\left\{\left(0.518\,\mathrm{Ra}^{1/4}\left[1+\left(\dfrac{0.559}{\mathrm{Pr}}\right)^{3/5}\right]^{-5/12}\right)^{15} + (0.1\,\mathrm{Ra}^{1/3})^{15}\right\}^{1/15}}\right]} \qquad (4)$$

This correlation gives accurate heat transfer coefficients at low Rayleigh numbers where curvature effects make boundary layer solutions invalid. The value of n for laminar boundary layer flow, $n = 1/4$, is asymptotically approached when the Prandtl number is large and the Rayleigh number increases to 10^7. Curvature effects force n to be lower than this until the transition to turbulence. At larger Rayleigh numbers n becomes $1/3$ indicating turbulent flow.

The variation of n with Rayleigh number and D/H at Pr = 0.7 for natural convection from the sides of a vertical cylinder is shown in Fig. 1(b). This is obtained from the following equation which approaches the flat plate correlation as $D/H \to \infty$ (7):

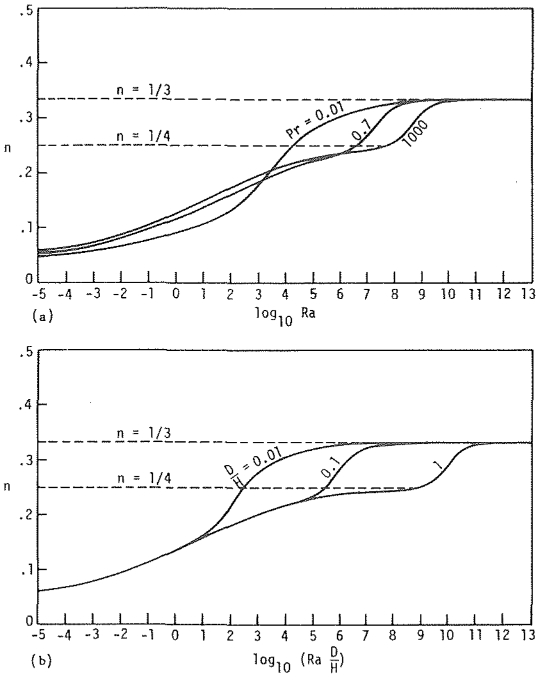

Fig. 1 Variation of n for natural convection from a) horizontal cylinder, b) vertical cylinder

$$\mathrm{Nu} = \frac{2}{\ln\left[1 + \dfrac{2}{\left\{\left(0.67\left(\mathrm{Ra}\dfrac{D}{H}\right)^{1/4}\left[1+\left(\dfrac{0.559}{\mathrm{Pr}}\right)^{3/5}\right]^{-5/12}\right)^{15} + 0.1(\mathrm{Ra}^{1/3})^{15}\right\}^{1/15}}\right]} \qquad (5)$$

The value for laminar boundary layer flow, $n = 1/4$, is merely a limit for laminar flow before the transition to turbulence.

Variation of the critical Biot number with Rayleigh number, R, B, and G at Pr = 0.7 is shown in Fig. 2 for natural convection about a horizontal cylinder. The critical Biot number varies the most with Rayleigh number when convection dominates as the external heat transfer mechanism. Increased radiation or surface heat generation decreases the variation since the total heat transfer depends less on the variable convective coefficient.

Application

An example of the discussion above is heat transfer to a horizontal refrigeration tube under frosting conditions. Data used in the computations are listed in Table 1. Heat transfer results are shown in Fig. 3 using various methods of determining the critical conditions. The addition of radiation, curvature effects in the convective coefficient and surface heat generation all increase the maximum heat transfer and decrease the critical radius. This example shows that frost buildup can increase the heat transfer to a refrigeration tube until critical conditions are reached.

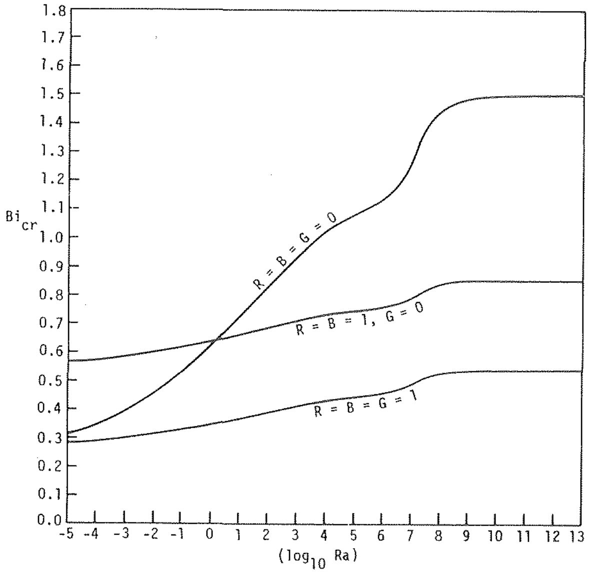

Fig. 2 Variation of Bi_{cr} for natural convection from a horizontal cylinder at Pr = 0.7 under various external heat transfer conditions

Table 1 Values used to calculate heat transfer to a horizontal tube during frost buildup.

$D_i = 0.635$ cm (0.25 in.)

$T_i = -10$ °C

$T_\infty = -5$ °C

$\epsilon_{\mathrm{frost}} = 0.95$

$K = 5.0$

$F = 1.0$

$b = 0.000282\ {}^\circ\mathrm{C}^{-1}$

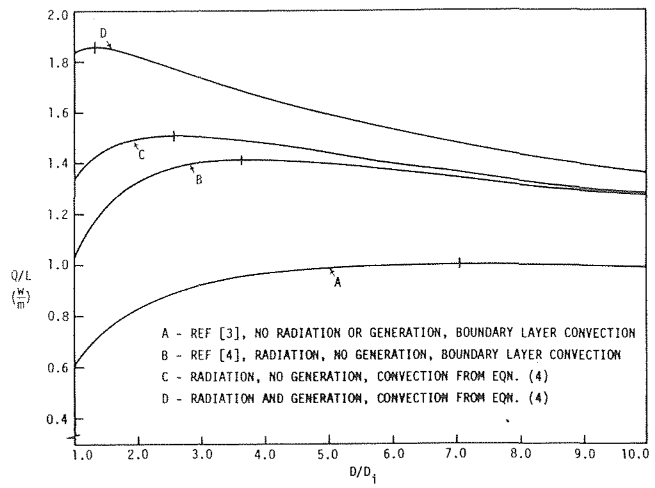

Fig. 3. Heat transfer to a horizontal tube during frost buildup; comparison of various methods of obtaining critical conditions

References

1 McAdams, W. H., *Heat Transmission,* Third ed., McGraw-Hill, New York, 1954, p. 415.

2 Kreith, F., *Principles of Heat Transfer,* Third ed., Intext Educational, New York, 1973, pp. 44–46.

3 Sparrow, E. M., "Re-examination and Correction of the Critical Radius for Radial Heat Conduction," *AIChE J.,* Vol. 16, 1970, p. 149.

4 Simmons, L. D., "Critical Thickness of Insulation Accounding for Variable Convection Coefficient and Radiation Loss," ASME, JOURNAL OF HEAT TRANSFER, Vol. 98, 1976, pp. 150–152.

5 Bottemanne, F. A., "Experimental Results of Pure and Simultaneous Heat and Mass Transfer by Free Convection About a Vertical Cylinder for Pr = 0.71 and Sc = 0.63," *Appl. Sci. Res.,* Vol. 25, 1972, pp. 372–382.

6 Kuehn, T. H. and Goldstein, R. J., "Correlating Equations for Natural Convection Heat Transfer Between Horizontal Circular Cylinders," *Intl J. of Heat and Mass Transfer,* Vol. 19, 1976, pp. 1127–1134.

7 Kuehn, T. H., "Natural Convection Heat Transfer from a Horizontal Circular Cylinder to a Surrounding Cylindrical Enclosure," Ph.D. Thesis, University of Minnesota, 1976, pp. 243–247.

Contributed by the Heat Transfer Division for publication in the JOURNAL OF HEAT TRANSFER. Manuscript received by the Heat Transfer Division May 5, 1977.

Thermal Instability of a Volumetrically-Heated Pool With Phase Change and a Free Upper Surface[1]

L. S. Yao[2] and I. Catton[3]

Nomenclature

a = wave number, Fig. 3
g = gravitational acceleration
ℓ = depth of the liquid layers, Fig. 1
q_0 = internal heat source, Fig. 1
Ra = Rayleigh number, $\beta g q_0 \ell^5/\nu\alpha^2$
T_h = upper free surface temperature
T_m = phase-change temperature
α = thermal diffusivity
β = thermal expansion coefficient
ϵ = Stefen number
θ_h = stabilizing boundary temperature $(T_h - T_m)\alpha/q_0\ell^2$
ν = kinematic viscosity
ζ = dimensionless depth of the liquid layer with internal heat sources, Fig. 1

Introduction

Much attention, both experimental and theoretical, has been given to thermal convection in fluids between horizontal surfaces, resulting from volumetric heating. This problem represents one of the fundamental phenomena in reactor accidents. Several recent reports [1–3][4] have been published on the prediction of heat fluxes from a fluid layer, which contains internal heat sources.

After the onset of a hypothetical core disrupture accident (HCDA) in a nuclear reactor, the molten fuel will form a pool. The fission products trapped in the molten pool will continuously release heat. The temperature distribution within the molten pool and the thermal loads on the surrounding structures will be changed by thermal convection, caused by the internal heat generation. These effects are completely different from those resulting from heat conduction alone, and must be known for the prediction of the development of the molten fuel pool and for its interaction with the surrounding structures.

Under some circumstances, the accident will not be contained in the core area of the nuclear reactor; therefore, post-accident heat removal (PAHR) devices are required to isolate the hot, radioactive materials from contaminating the environment. The prediction of thermal loads is needed for the design of these PAHR devices. Furthermore, this information is important in the planning of underground storage for the radioactive wastes, because the surrounding structure might collapse during a postulated accident. The effects of phase change on the thermal instability in the molten pool are also important in the understanding of the development of an accident.

Most of the early works were restricted to a fluid layer with fixed thickness. Recently, Sparrow, et al. [4] studied convective instability in a melt layer heated from below. Later, Seki, et al. [5] extended the solution for a horizontal melted water layer with a free upper surface. The onset of thermal instability with a downward phase change which is caused by a uniformly distributed internal heat sources was studied by Yao, et al. [6]. They assumed that a thin crust was formed on top of the molten fuel; therefore, the no-slip boundary condition applied to the top of the pool. Their results show that the critical Rayleigh number decreases with increasing speed of the advancing phase-change front; and that it greatly depends on the distribution of the internal heat sources. Since the accidents are most likely to be confined in a closed system, and the temperatures of the surrounding environments are also high, a thin crust may not exist on top of the molten pool, and its temperature could be much higher than the melting temperature of the fuels.

The physical system considered (Fig. 1) is a layer of hot fluid, containing heat sources, on top of a solid bed. The solid bed is constructed of the same material as the molten fluid, but is without heat generation. Furthermore, we assume that the thickness of the fluid layer is much smaller than the horizontal dimensions of the cavity. The side-wall effects can then be neglected in the study of thermal instability in the central region of the pool, and the pool can be assumed to be of infinite horizontal extent. The temperature of the solid bed is held at its melting point. It starts to melt as soon as it contacts with the hot fluid, then, a second fluid layer forms between the top hot fluid layer and the solid bed. Before the Rayleigh number grows beyond its critical value, there is no convective motion in either of the two fluid layers. Since the mass diffusion of the fission products is small, it is reasonable to assume that the middle layer does not contain any heat sources. As more solid becomes melted, the thickness of the

---

[1] This work was supported, in part, by the U.S. Nuclear Regulatory Commission.

[2] The Rand Corporation, Santa Monica, Calif.

[3] University of California, Los Angeles, Calif.

Contributed by the Heat Transfer Division for publication in the JOURNAL OF HEAT TRANSFER. Manuscript received by the Heat Transfer Division March 3, 1978.

[4] Numbers in brackets designate References at end of Technical Note.

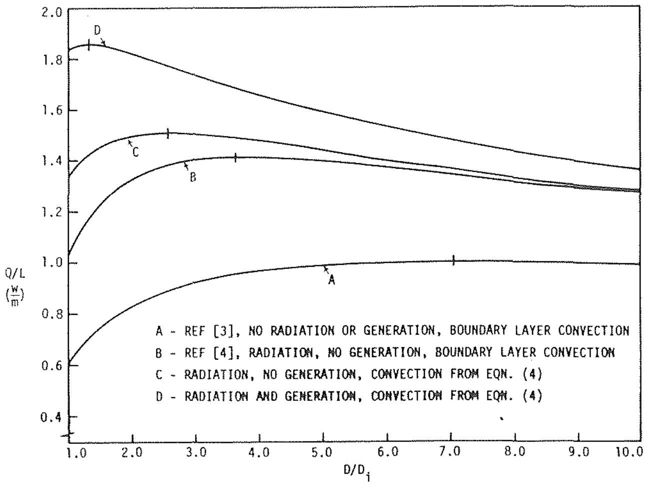

Fig. 3. Heat transfer to a horizontal tube during frost buildup; comparison of various methods of obtaining critical conditions

References

1 McAdams, W. H., *Heat Transmission,* Third ed., McGraw-Hill, New York, 1954, p. 415.

2 Kreith, F., *Principles of Heat Transfer,* Third ed., Intext Educational, New York, 1973, pp. 44–46.

3 Sparrow, E. M., "Re-examination and Correction of the Critical Radius for Radial Heat Conduction," *AIChE J.,* Vol. 16, 1970, p. 149.

4 Simmons, L. D., "Critical Thickness of Insulation Accounding for Variable Convection Coefficient and Radiation Loss," ASME, JOURNAL OF HEAT TRANSFER, Vol. 98, 1976, pp. 150–152.

5 Bottemanne, F. A., "Experimental Results of Pure and Simultaneous Heat and Mass Transfer by Free Convection About a Vertical Cylinder for Pr = 0.71 and Sc = 0.63," *Appl. Sci. Res.,* Vol. 25, 1972, pp. 372–382.

6 Kuehn, T. H. and Goldstein, R. J., "Correlating Equations for Natural Convection Heat Transfer Between Horizontal Circular Cylinders," *Intl J. of Heat and Mass Transfer,* Vol. 19, 1976, pp. 1127–1134.

7 Kuehn, T. H., "Natural Convection Heat Transfer from a Horizontal Circular Cylinder to a Surrounding Cylindrical Enclosure," Ph.D. Thesis, University of Minnesota, 1976, pp. 243–247.

Contributed by the Heat Transfer Division for publication in the JOURNAL OF HEAT TRANSFER. Manuscript received by the Heat Transfer Division May 5, 1977.

Thermal Instability of a Volumetrically-Heated Pool With Phase Change and a Free Upper Surface[1]

L. S. Yao[2] and I. Catton[3]

Nomenclature

a = wave number, Fig. 3
g = gravitational acceleration
ℓ = depth of the liquid layers, Fig. 1
q_0 = internal heat source, Fig. 1
Ra = Rayleigh number, $\beta g q_0 \ell^5/\nu\alpha^2$
T_h = upper free surface temperature
T_m = phase-change temperature
α = thermal diffusivity
β = thermal expansion coefficient
ϵ = Stefen number
θ_h = stabilizing boundary temperature $(T_h - T_m)\alpha/q_0\ell^2$
ν = kinematic viscosity
ζ = dimensionless depth of the liquid layer with internal heat sources, Fig. 1

Introduction

Much attention, both experimental and theoretical, has been given to thermal convection in fluids between horizontal surfaces, resulting from volumetric heating. This problem represents one of the fundamental phenomena in reactor accidents. Several recent reports [1–3][4] have been published on the prediction of heat fluxes from a fluid layer, which contains internal heat sources.

After the onset of a hypothetical core disrupture accident (HCDA) in a nuclear reactor, the molten fuel will form a pool. The fission products trapped in the molten pool will continuously release heat. The temperature distribution within the molten pool and the thermal loads on the surrounding structures will be changed by thermal convection, caused by the internal heat generation. These effects are completely different from those resulting from heat conduction alone, and must be known for the prediction of the development of the molten fuel pool and for its interaction with the surrounding structures.

Under some circumstances, the accident will not be contained in the core area of the nuclear reactor; therefore, post-accident heat removal (PAHR) devices are required to isolate the hot, radioactive materials from contaminating the environment. The prediction of thermal loads is needed for the design of these PAHR devices. Furthermore, this information is important in the planning of underground storage for the radioactive wastes, because the surrounding structure might collapse during a postulated accident. The effects of phase change on the thermal instability in the molten pool are also important in the understanding of the development of an accident.

Most of the early works were restricted to a fluid layer with fixed thickness. Recently, Sparrow, et al. [4] studied convective instability in a melt layer heated from below. Later, Seki, et al. [5] extended the solution for a horizontal melted water layer with a free upper surface. The onset of thermal instability with a downward phase change which is caused by a uniformly distributed internal heat sources was studied by Yao, et al. [6]. They assumed that a thin crust was formed on top of the molten fuel; therefore, the no-slip boundary condition applied to the top of the pool. Their results show that the critical Rayleigh number decreases with increasing speed of the advancing phase-change front; and that it greatly depends on the distribution of the internal heat sources. Since the accidents are most likely to be confined in a closed system, and the temperatures of the surrounding environments are also high, a thin crust may not exist on top of the molten pool, and its temperature could be much higher than the melting temperature of the fuels.

The physical system considered (Fig. 1) is a layer of hot fluid, containing heat sources, on top of a solid bed. The solid bed is constructed of the same material as the molten fluid, but is without heat generation. Furthermore, we assume that the thickness of the fluid layer is much smaller than the horizontal dimensions of the cavity. The side-wall effects can then be neglected in the study of thermal instability in the central region of the pool, and the pool can be assumed to be of infinite horizontal extent. The temperature of the solid bed is held at its melting point. It starts to melt as soon as it contacts with the hot fluid, then, a second fluid layer forms between the top hot fluid layer and the solid bed. Before the Rayleigh number grows beyond its critical value, there is no convective motion in either of the two fluid layers. Since the mass diffusion of the fission products is small, it is reasonable to assume that the middle layer does not contain any heat sources. As more solid becomes melted, the thickness of the

---

[1] This work was supported, in part, by the U.S. Nuclear Regulatory Commission.

[2] The Rand Corporation, Santa Monica, Calif.

[3] University of California, Los Angeles, Calif.

Contributed by the Heat Transfer Division for publication in the JOURNAL OF HEAT TRANSFER. Manuscript received by the Heat Transfer Division March 3, 1978.

[4] Numbers in brackets designate References at end of Technical Note.

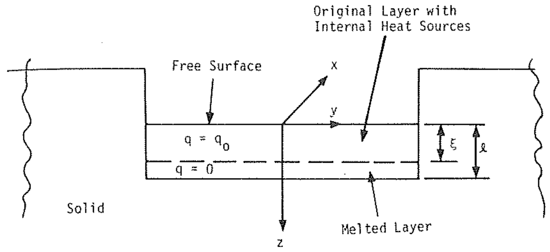

Fig. 1 Physical coordinates

middle layer grows, and so does the total depth of the fluid layers. The restraint on the fluid motion is gradually decreased and thermal convection occurs when the Rayleigh number reaches its critical value.

This note reports the effect of the downward phase change on the thermal instability, possible convection patterns, and temperature redistribution of an internally-heated pool with a stabilizing temperature gradient and a free top surface.

The mathematical formulation and the method of solution are similar to those in [6]. One more parameter in this study is θ_h which is the dimensionless temperature of the upper free surface. The mathematical detail is not repeated here, but can be found in [7].

Onset of Thermal Instability

The critical Rayleigh numbers and wave numbers are plotted in Figs. 2 and 3 for $\epsilon = 0$. They increase with decreasing ζ, because the unstable temperature region in the top layer shrinks as ζ decreases (see equation (4c)). However, it has been shown [6] that the originally quiescent layers will become unstable when ζ is reduced by increasing the total depth of the fluid layers. When the Stefen number increases, i.e., the rate of melting increases, the fluid particles have more freedom to move. Consequently, the critical Rayleigh number and the critical wave number decrease. The decreasing amounts are too small to be shown in the scale of Figs. 2 and 3. This agrees with the results given by Sparrow, Lee, and Shamsunder [4] for a melted layer heated from below. The temperature difference, θ_h, has a strong stabilizing effect on the fluid layers. The fluid layers become unconditionally stable when $\theta_h \geq 0$. The higher the value of θ_h, the larger the critical Rayleigh number decreases with increasing Stefen number. For $\zeta = 1$, the critical Rayleigh number is independent of the Stefen number, and its value equals the critical Rayleigh number of an internally heated pool without phase change at the boundary [1, 2].

Convection Pattern

The pattern of the thermal convection is shown in Fig. 4. For $\zeta = 0.1$ ($\theta_h = \epsilon = 0$), there are five cells. The cell amplitudes vary as a function of z and have a maximum near $z = 0$. The number of cells decreases when ζ increases, and the location of the maximum amplitude moves into the top layer. For $\zeta \geq 0.6$, there is only one cell. The number of cells increases when the stabilizing boundary temperature, θ_h, rises (Fig. 4). It can be concluded that there are several cells for the more stable layers, and only a single cell for the less stable ones. A comparison of the convection patterns of the free top surface with the one of the rigid top surface [6] indicates that the free top surface imposes less restraint on the fluid motion; therefore it has a lower critical Rayleigh number and a smaller number of convective cells. The boundary of the convection cell is not at the same location as the interface of the two liquid layers. This indicates that the melted layer will be carried upward and be mixed with the top layer. The internal heat sources, originally distributed in the top layer, will be redistributed and will invalidate the assumption that they stay in the top layer. Since the critical Rayleigh number decreases with increasing ζ, the redistribution of the internal heat sources enhances the convective motion after the fluid layers become supercritical, and increases the thermal load on the solid layer underneath the molten pool. It is different from an internally heated pool without phase change on the bottom [1–3], where the downward heat flux is reduced

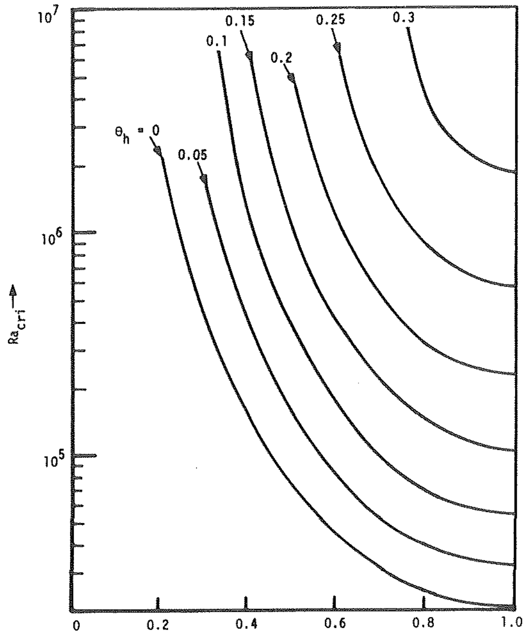

Fig. 2 Critical Rayleigh number for $\epsilon = 0$

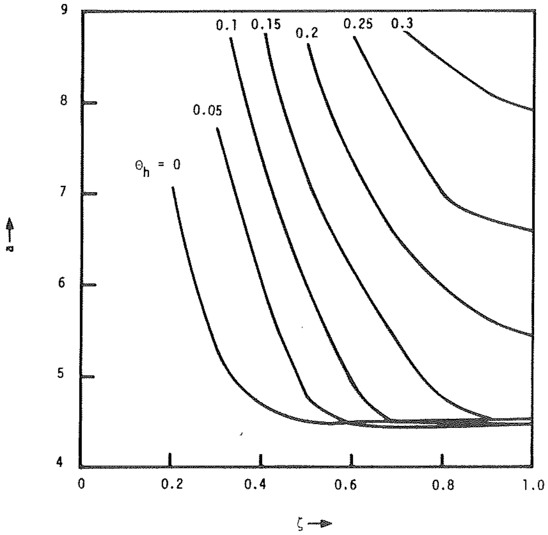

Fig. 3 Critical wave number for $\epsilon = 0$

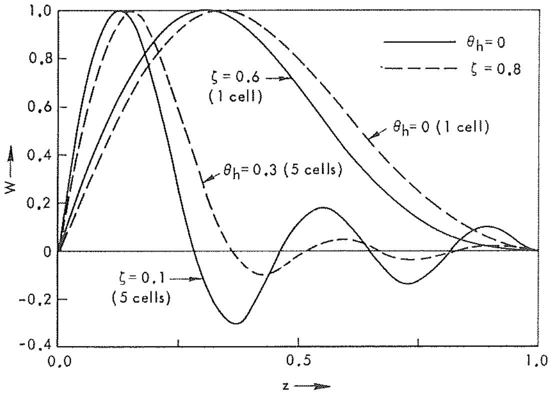

Fig. 4 Convective cells

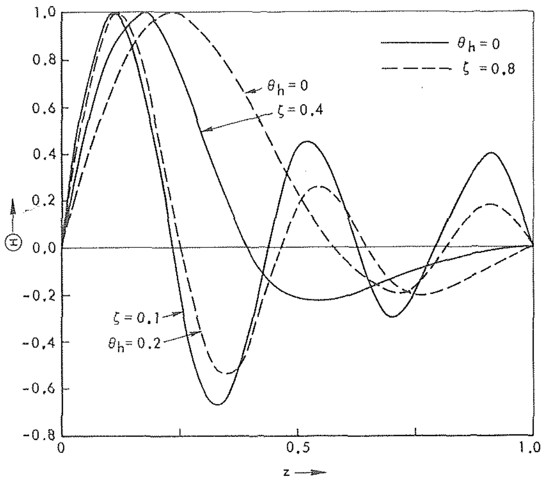

Fig. 5 Perturbation of temperature

by the thermal convection. The redistribution of internal heat sources, caused by mass convection, has to be coupled with the thermal convection, in order to predict the temperature distribution inside the molten pool and the heat fluxes out of the molten pool.

The temperature fluctuation, due to the convective motion, is shown in Fig. 5. The pattern of the temperature disturbance is similar to that of fluid velocity. However, the boundary of the temperature cells does not coincide with the boundary of the fluid convection cells, because the fluid is conducting and viscous.

Summary and Conclusions

The effect of phase change on the thermal instability of an internally heated layer with a free upper surface has been determined. It was found that the temperature boundary condition, θ_h, and the molten layer thickness, ζ, had a stabilizing effect on the fluid layers, whereas the melting rate, ϵ, and the increase of ℓ by melting, had a destabilizing effect. These competing factors may lead to an unstable layer. The redistribution of the internal heat source after the onset of the thermal instability will enhance the thermal convection and increase the heat transfer to the liquid-solid interface. It is estimated that the thermal load on the solid bed by heat conduction through a quiescent melted layer will be too low for PAHR. On the other hand, the top layer is cooled by mixing with the melted layer. This may prevent the top layer from boiling up during HCDA. The heat fluxes out of the molten layer can only be evaluated by coupling the thermal and mass convection.

References

1 Catton, Ivan, and Suo-Anttila, A. J., "Heat Transfer from a Volumetrically Heated Horizontal Fluid Layer," *Proc. 5th International Heat Transfer Conference*, Tokyo, Japan, Sept. 1974.

2 Suo-Anttila, A. J., and Catton, Ivan, "The Effect of a Stabilizing Temperature Gradient on Heat Transfer from a Molten Fuel Layer with Volumetric Heating," *ASME*. JOURNAL OF HEAT TRANSFER, Vol. 97, No. 4, 1975, pp. 544–548.

3 Kulacki, F. A., and Goldstein, R. J., "Thermal Convection in a Horizontal Fluid Layer with Uniform Volumetric Energy Sources," *J. Fluid Mech*, Vol. 55, 1972, pp. 271–287.

4 Sparrow, E. M., Lee, L., and Shamsundar, N., "Convective Instability in a Melted Layer Heated From Below," *ASME* JOURNAL OF HEAT TRANSFER, Vol. 98, No. 1, 1976, pp. 88–94.

5 Seki, N., Fukusako, S., and Sugawara, M., "A Criterion of Onset of Free Convection in a Horizontal Melted Water Layer with Free Surface," *ASME* JOURNAL OF HEAT TRANSFER, Vol. 99, No. 1, 1977, pp. 92–98.

6 Yao, L. S., Catton, Ivan, and Suo-Anttila, A. J., "The Effect of Phase Change on the Thermal Instability of a Volumetrically Heated Layer," presented at 17th National Heat Transfer Conference, Salt Lake City, Utah, Aug. 1977.

7 Yao, L. S., and Catton, Ivan, "Thermal Instability of a Volumetrically-Heated Pool with Phase Change and a Free Upper Surface," Rand Report No. P-6069, 1978.

Heat Transfer by Natural Convection Between a Vertical Surface and a Stably Stratified Fluid

G. D. Raithby,[1] and K. G. T. Hollands[1]

Chen and Eichhorn [1][2] recently reported measurements of the heat transfer by natural convection from a vertical isothermal surface to thermally-stratified water. They also reported an analysis, based on the local nonsimilarity method (e.g., [2]), which predicted the heat transfer for both water and air. Excellent agreement between predictions and the water measurements was found.

The first purpose of this note is to apply the approximate method of Raithby, Hollands and Unny [3] (a generalization of the method reported in [4], [5], etc.) to this problem and to compare these predictions with the results obtained by Chen and Eichhorn.

The approximate method of [3, 4, 5] has now been applied to many problems in natural convection. Based on this experience, the authors have gained some appreciation of both the strengths and limitations of the method. The second purpose of this paper is to assist potential users by describing these limitations. A comparison of the predictions of the approximate method with the family of similarity solutions reported by Yang, et al. [6] is used for demonstration.

Approximate Solution for Chen-Eichhorn Problem

Fig. 1 describes the geometry and boundary conditions for this problem. The notation of Chen and Eichhorn is used in this section wherever possible, mostly without redefinition. The stratification of

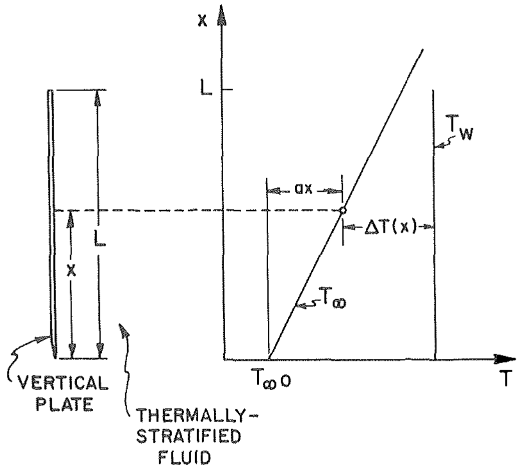

Fig. 1 Geometry and boundary conditions for heat transfer to a thermally stratified fluid

---

[1] Thermal Engineering Group, Mechanical Engineering Department, University of Waterloo, Waterloo, Ontario, Canada. Associate Members, ASME.

[2] Numbers in brackets designate References at end of Technical Note.

Contributed by the Heat Transfer Division for publication in the JOURNAL OF HEAT TRANSFER. Manuscript received March 21, 1978.

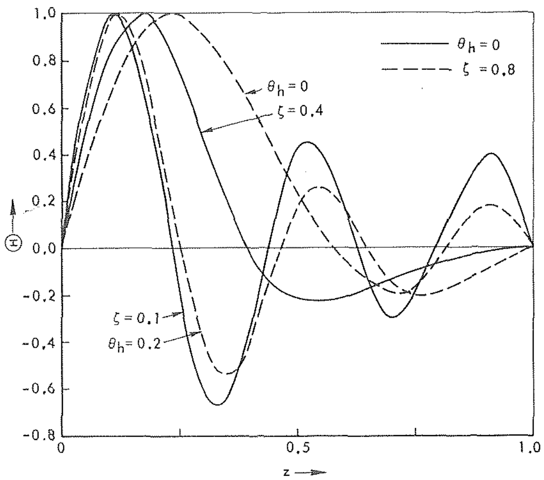

Fig. 5 Perturbation of temperature

by the thermal convection. The redistribution of internal heat sources, caused by mass convection, has to be coupled with the thermal convection, in order to predict the temperature distribution inside the molten pool and the heat fluxes out of the molten pool.

The temperature fluctuation, due to the convective motion, is shown in Fig. 5. The pattern of the temperature disturbance is similar to that of fluid velocity. However, the boundary of the temperature cells does not coincide with the boundary of the fluid convection cells, because the fluid is conducting and viscous.

Summary and Conclusions

The effect of phase change on the thermal instability of an internally heated layer with a free upper surface has been determined. It was found that the temperature boundary condition, θ_h, and the molten layer thickness, ζ, had a stabilizing effect on the fluid layers, whereas the melting rate, ϵ, and the increase of ℓ by melting, had a destabilizing effect. These competing factors may lead to an unstable layer. The redistribution of the internal heat source after the onset of the thermal instability will enhance the thermal convection and increase the heat transfer to the liquid-solid interface. It is estimated that the thermal load on the solid bed by heat conduction through a quiescent melted layer will be too low for PAHR. On the other hand, the top layer is cooled by mixing with the melted layer. This may prevent the top layer from boiling up during HCDA. The heat fluxes out of the molten layer can only be evaluated by coupling the thermal and mass convection.

References

1 Catton, Ivan, and Suo-Anttila, A. J., "Heat Transfer from a Volumetrically Heated Horizontal Fluid Layer," *Proc. 5th International Heat Transfer Conference*, Tokyo, Japan, Sept. 1974.

2 Suo-Anttila, A. J., and Catton, Ivan, "The Effect of a Stabilizing Temperature Gradient on Heat Transfer from a Molten Fuel Layer with Volumetric Heating," *ASME*. JOURNAL OF HEAT TRANSFER, Vol. 97, No. 4, 1975, pp. 544–548.

3 Kulacki, F. A., and Goldstein, R. J., "Thermal Convection in a Horizontal Fluid Layer with Uniform Volumetric Energy Sources," *J. Fluid Mech*, Vol. 55, 1972, pp. 271–287.

4 Sparrow, E. M., Lee, L., and Shamsundar, N., "Convective Instability in a Melted Layer Heated From Below," *ASME* JOURNAL OF HEAT TRANSFER, Vol. 98, No. 1, 1976, pp. 88–94.

5 Seki, N., Fukusako, S., and Sugawara, M., "A Criterion of Onset of Free Convection in a Horizontal Melted Water Layer with Free Surface," *ASME* JOURNAL OF HEAT TRANSFER, Vol. 99, No. 1, 1977, pp. 92–98.

6 Yao, L. S., Catton, Ivan, and Suo-Anttila, A. J., "The Effect of Phase Change on the Thermal Instability of a Volumetrically Heated Layer," presented at 17th National Heat Transfer Conference, Salt Lake City, Utah, Aug. 1977.

7 Yao, L. S., and Catton, Ivan, "Thermal Instability of a Volumetrically-Heated Pool with Phase Change and a Free Upper Surface," Rand Report No. P-6069, 1978.

Heat Transfer by Natural Convection Between a Vertical Surface and a Stably Stratified Fluid

G. D. Raithby,[1] and K. G. T. Hollands[1]

Chen and Eichhorn [1][2] recently reported measurements of the heat transfer by natural convection from a vertical isothermal surface to thermally-stratified water. They also reported an analysis, based on the local nonsimilarity method (e.g., [2]), which predicted the heat transfer for both water and air. Excellent agreement between predictions and the water measurements was found.

The first purpose of this note is to apply the approximate method of Raithby, Hollands and Unny [3] (a generalization of the method reported in [4], [5], etc.) to this problem and to compare these predictions with the results obtained by Chen and Eichhorn.

The approximate method of [3, 4, 5] has now been applied to many problems in natural convection. Based on this experience, the authors have gained some appreciation of both the strengths and limitations of the method. The second purpose of this paper is to assist potential users by describing these limitations. A comparison of the predictions of the approximate method with the family of similarity solutions reported by Yang, et al. [6] is used for demonstration.

Approximate Solution for Chen-Eichhorn Problem

Fig. 1 describes the geometry and boundary conditions for this problem. The notation of Chen and Eichhorn is used in this section wherever possible, mostly without redefinition. The stratification of

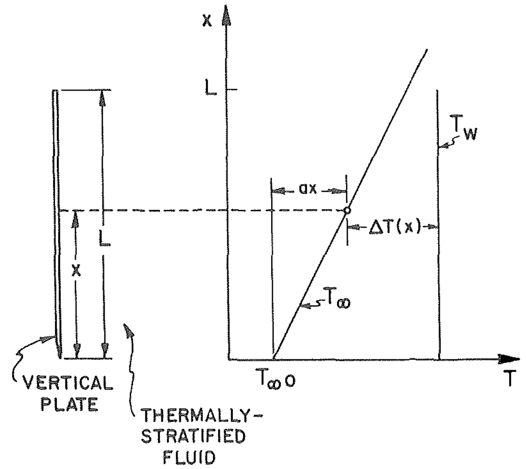

Fig. 1 Geometry and boundary conditions for heat transfer to a thermally stratified fluid

---

[1] Thermal Engineering Group, Mechanical Engineering Department, University of Waterloo, Waterloo, Ontario, Canada. Associate Members, ASME.

[2] Numbers in brackets designate References at end of Technical Note.

Contributed by the Heat Transfer Division for publication in the JOURNAL OF HEAT TRANSFER. Manuscript received March 21, 1978.

Table 1 Values of $F(b, S)$, defined by equation (7)

$b \rightarrow$	1/6	1/2	2/3	2/3	1.0	4/3	5/3	2.0	3.0	4.0
$n \rightarrow$	1.25	1.75	2.0	2.125	2.5	3.0	3.5	4.0	5.5	7.0
Pr $\rightarrow$	$\rightarrow \infty$		≈ 10		≈ 5		≈ 0.7			
$S \downarrow$										
0.0	1.000	1.000	1.000	1.000	1.000	1.000	1.000	1.000	1.000	1.000
0.25	0.980	0.988	0.992	0.994	1.000	1.008	1.015	1.023	1.045	1.067
0.50	0.965	0.979	0.986	0.990	1.000	1.013	1.027	1.040	1.077	1.112
0.75	0.954	0.973	0.982	0.987	1.000	1.018	1.035	1.051	1.098	1.140
1.00	0.946	0.968	0.979	0.984	1.000	1.020	1.040	1.059	1.111	1.158
1.25	0.940	0.965	0.977	0.983	1.000	1.022	1.044	1.064	1.119	1.168
1.50	0.936	0.963	0.975	0.982	1.000	1.023	1.046	1.067	1.124	1.173
1.75	0.934	0.961	0.974	0.981	1.000	1.024	1.047	1.068	1.126	1.176
2.00	0.933	0.961	0.974	0.981	1.000	1.024	1.047	1.069	1.127	1.178

the ambient fluid is defined in terms of the parameter $S = La/\Delta T_m$, where $a = dT_\infty/dx$ and ΔT_m is the mean temperature difference between the plate and the fluid. For $S < 2$, the heat transfer flows *from* the plate at all locations. For $S > 2$, the fluid temperature drops below the wall temperature somewhere between the mid-height and top of the plate, causing heat to flow *to* the plate over part of its area. The analyses in the following two sections address these problems separately.

Approximate Analysis for $S \leq 2$. For the special case of a flat plate, the approximate solution [3] for the local heat transfer from a surface of arbitrary temperature distribution, T_w, to a fluid of arbitrary T_∞ becomes

$$q = C_\ell k \left[\frac{g\beta}{\nu\alpha}\right]^{1/4} (T_w - T_\infty)^{5/3} G^{1/4} \Big/ \left[\int_0^x (T_w - T_\infty)^{5/3} G\, dx\right]^{1/4} \tag{1}$$

where

$$G = \exp\left[\int_0^x \frac{4(n+1)}{3(T_w - T_\infty)} \frac{dT_\infty}{dx} dx\right] \tag{2}$$

$$C_\ell = 0.50/[1 + (0.49/\mathrm{Pr})^{9/16}]^{4/9} \tag{3}$$

where x is positive in the flow direction. For $T_\infty > T_w$, $(T_w - T_\infty)$ is replaced by $(T_\infty - T_w)$ and the intergrand in (2) changes sign. Note that T_h and $\overline{T}$ in [3] are rewritten here as T_w and T_∞ respectively. The "constants" C_ℓ and n are parameters which depend on the profile distributions of velocity and temperature which, in the approximate-method approach, are taken to be functions of Prandtl number only. The selection and universality of C_ℓ have been discussed previously [5]. Of the problems previously studied, only in [3] was G not unity (i.e., $dT_\infty/dx \neq 0$). In that paper, very crude estimates of n were found to be sufficient since the heat transfer was virtually independent of the value of n chosen. The present predictions require better estimates of n. The values tabulated in equation (4) have been obtained by utilizing the results of similarity solutions of Yang, et al. [6]; the procedure is described in the second section of this paper.

$$\begin{array}{lll} \mathrm{Pr} \rightarrow \infty & n \approx 1.25 & b \approx 1/6 \\ \mathrm{Pr} = 10 & n \approx 2.0 & b \approx 2/3 \\ \mathrm{Pr} = 0.72 & n \approx 3.5 & b \approx 5/3 \end{array} \tag{4}$$

For uniform T_w and the linear distribution of T_∞ (shown in Fig. 1), the local heat flux q is readily obtained from equations (1) and (2). Integrating this local flux over the surface to obtain the total flux, and converting this to a mean Nusselt number, yields

$$\overline{\mathrm{Nu}} = (4C_\ell/3)\mathrm{Ra}^{1/4}\,[(S+2)/2]^{1/2}\,F(b, S) \tag{5}$$

where

$$b = 2(n-1)/3 \tag{6}$$

$$F(b, S) = \left(\frac{S+2}{2}\right)^{3/2} \frac{\frac{3}{4}}{(2bS)^{3/4}} \left[\frac{\Gamma\left(\frac{1}{b}\right)\Gamma\left(\frac{3}{4}\right)}{\Gamma\left(\frac{1}{b}+\frac{3}{4}\right)} - \int_0^{[(2-S/2+S)]^{2b}} \frac{dt}{t^{1-1/b}(1-t)^{1/4}}\right] \tag{7}$$

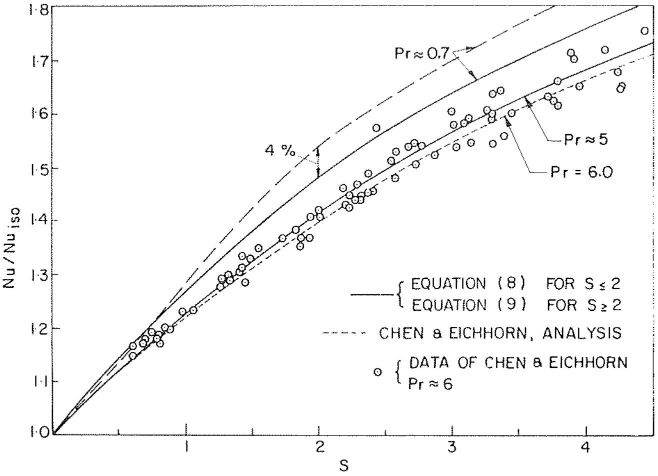

Fig. 2 A comparison of present predictions with analysis and measurements of Chen and Eichhorn

Here, Ra is based on the plate length and the mean temperature difference, ΔT_m. The gamma functions (Γ) are readily available [7] but the second integral, an incomplete beta function, has not to the authors' knowledge been tabulated for the 1/4-power on $(1 - t)$. A numerical integration yielded the values of $F(b, S)$ in Table 1. For $b = 1$ (or $n = 2$, or, by interpolation between the values in equation (4), $\mathrm{Pr} \approx 5$), the integration is straightforward, yielding $F(1, S) = 1.0$. It can be seen from the table that F does not depart greatly from unity for other values of b in the range of interest.

The value of $\overline{\mathrm{Nu}}_{iso}$, the average Nusselt number for heat transfer between T_w and an isothermal medium with the same ΔT_m is $\overline{\mathrm{Nu}}_{iso} = (4C_\ell/3)\mathrm{Ra}^{1/4}$ (equation (1) with T_w and T_∞ constant). Therefore, for $S \leq 2$,

$$\overline{\mathrm{Nu}}/\overline{\mathrm{Nu}}_{iso} = [(S+2)/2]^{1/2}\,F(b, S) \tag{8a}$$

$$= [(S+2)/2]^{1/2} \qquad (\text{for } b = 1, \mathrm{Pr} \approx 5) \tag{8b}$$

Good agreement between equation (8b) and both the data of Chen and Eichhorn for water ($\mathrm{Pr} \approx 6$) and their analysis ($\mathrm{Pr} = 6.0$) is demonstrated in Fig. 2.

Approximate Analysis for $S \geq 2$. For $S \geq 2$, ΔT is zero at $L' = L(2 + S)/2S$. Following the procedure of Chen and Eichhorn, the above analysis is applied for $0 \leq x \leq L'$ to determine the heat transfer *from* the plate to the surrounding fluid. Similarly, the same analysis is applied to $L' \leq x \leq L$ to find the heat transfer *to* the upper part of the surface from the fluid. Summing these, converting the result to a Nusselt number, and taking the ratio of this to $\overline{\mathrm{Nu}}_{iso}$, one obtains

$$\overline{\mathrm{Nu}}/\overline{\mathrm{Nu}}_{iso} = 2^{1/4} S^{1/4} \cdot F(b, 2) \tag{9a}$$

$$= 2^{1/4} S^{1/4} \qquad (\text{for } b = 1, \Pr \approx 5) \tag{9b}$$

Equation (9b) for $\Pr \approx 5$ agrees in form with the equation obtained by Chen and Eichhorn for $\Pr = 6.0$. The coefficient, $2^{1/4}$, is 1.2 percent larger than their value of 1.179. Both equations are plotted along with their data in Fig. 2.

Also shown in the figure is a comparison of the predictions of Chen and Eichhorn for $\Pr = 0.7$ with equation (8a) for $S \leq 2$ and (9a) for $S \geq 2$ using a value of $b = 5/3$ ($\Pr \approx 0.72$ from equation (4)). The functions $F(b, S)$ are taken from Table 1. The trends of the approximate analysis are correct, and there is also reasonable quantitative agreement for the value of b used.

The method of calculating the heat transfer from separate analyses for $x \leq L'$ and $x \geq L'$ may be open to question because of inertial effects, as pointed out by Chen and Eichhorn. However, it is consistent with the framework of the present analysis since it was assumed in the derivation of equation (1) that the heat transfer is controlled mainly by the "inner region" in the boundary layer where inertial effects were neglected.

Discussion of Approximate Method

T_w, T_∞ Uniform. The application of the approximate method to problems in this class has been discussed in [4] and [8]. Compared to more exact solutions of the "thin-layer" equations (expressed in terms of local Cartesian coordinates [5]), the local Nusselt numbers usually agree to within about 1 percent for $\Pr > 1$, while differences of up to about 5 percent have been found on the rear portions of blunt bodies. The average Nusselt numbers are in better agreement. Larger differences are expected for $\Pr \ll 1$. Accounting for turbulent heat transfer and curvature effects is generally much more important than these differences.

Uniform Heat Flux, Uniform T_∞. For these thermal boundary conditions, the approximate method predicts average heat transfer rates which are low by about 5 percent for plates and circular cylinders for $\Pr \gtrsim 0.7$ when compared to more precise solutions of the thin-layer equations. Experience to date suggests that the approximate method may be accurate to a few percent for a wide range of geometries for this boundary condition if C_ℓ is replaced by $1.05\, C_\ell$. Again, turbulent heat transfer and curvature effects will often be more important than these differences.

Variable T_∞ and T_w. For a vertical plate with the following distributions of wall and fluid temperature

$$T_w - T_r \propto (M + 1)x^N; \quad T_\infty - T_r \propto Mx^N$$

where T_r is a reference temperature and M and N are constants, equations (1) and (2) give the following local Nusselt number

$$\mathrm{Nu}_x/\mathrm{Ra}_x{}^{1/4} = C_\ell[1 + 5N/3 + 4(n + 1)MN/3]^{1/4} \tag{10}$$

where Ra_x is the Rayleigh number based on distance from the leading edge and on the local temperature difference. Yang, et al. [6] obtained similarity solutions to this problem, while Sparrow and Gregg [9] earlier examined the special case, $M = 0$. These predictions of $\mathrm{Nu}_x/\mathrm{Ra}_x{}^{1/4}$ are plotted together with equation (10) in Fig. 3 for the stable stratification case ($MN \geq 0$). The values of n used in this comparison (equation (4)) were obtained by forcing equation (10) to agree with the similarity results for $M = -1.0$ (uniform wall temperature) on the average for values of N in the range $0 \leq N \leq 1.0$.

It is seen from the figure that for uniform T_w ($M = -1.0$) a single value of n is totally adequate for all $T_\infty - T_r \propto -x^N$ for $\Pr = 10$, but small errors occur for $\Pr = 0.72$. The results in the previous section verify that these same values of n are adequate also for the Chen-Eichhorn problem. Previous experience suggests that the same values of n should be adequate also for other geometries with the same thermal boundary conditions.

For $M \neq -1.0$, the errors in the approximate method increase to a maximum as $M \to 0$ (uniform T_∞, $T_w - T_r \propto x^N$). For $N = 1.0$, the figure shows discrepancies of 14 percent while errors of 20 percent were found earlier for $N = 3.0$ [4]. The inaccuracy of the approximate method under these conditions has already been discussed in [4], and amounts to a failure of the parameter C_ℓ to be universally dependent on Pr alone.

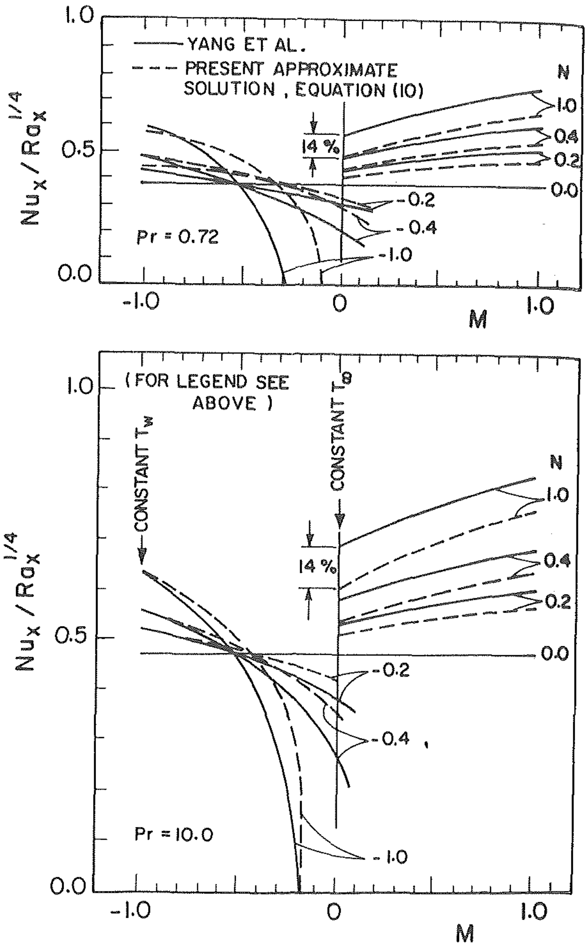

Fig. 3 A comparison of the predictions of the approximate method for power law variations in wall and fluid temperatures with the similarity solution of Yang, et al.

Again, the practical importance of curvature and turbulent heat transfer should be kept clearly in mind, even for the flat plate geometry.

Acknowledgments

Dr. I. McGee of the Applied Mathematics Department of the University of Waterloo carried out the integration to the form appearing in equation (7). We are grateful to Dr. Chen and Dr. Eichhorn for the use of their data and for helpful discussions, and to Dr. Yang for providing their predictions. This work was supported by operating grants from the National Research Council of Canada.

References

1 Chen, C. C., Eichhorn, R., "Natural Convection from a Vertical Surface to a Thermally Stratified Fluid," ASME JOURNAL OF HEAT TRANSFER, Vol. 98, 1976, pp. 446–451.

2 Sparrow, E. M., Yu, H. S., "Local Non-Similarity Thermal Boundary-Layer Solutions," ASME JOURNAL OF HEAT TRANSFER, Vol. 93, 1971, pp. 328–334.

3 Raithby, G. D., Hollands, K. G. T., Unny, T. E., "Analysis of Heat Transfer by Natural Convection Across Vertical Fluid Layers," ASME JOURNAL OF HEAT TRANSFER, Vol. 99, 1977, pp. 287–293.

4 Raithby, G. D., Hollands, K. G. T., "A General Method of Obtaining Approximate Solutions to Laminar and Turbulent Free Convection Problems," *Advances in Heat Transfer*, Academic Press, Vol. 11, 1975.

5 Raithby, G. D., Hollands, K. G. T., "Laminar and Turbulent Free Convection from Elliptic Cylinders, with a Vertical Plate and Horizontal Cylinder

as Special Cases," ASME JOURNAL OF HEAT TRANSFER, Vol. 98, 1976, pp. 72–80.

6 Yang, Y. T., Novotny, J. L., Cheng, Y. S., "Laminar Free Convection from a Nonisothermal Plate Immersed in a Temperature Stratified Medium," *International Journal of Heat and Mass Transfer,* Vol. 15, 1972, pp. 1097–1109.

7 Selby, S., Editor, *Handbook of Tables for Mathematics,* CRC Press Inc., Cleveland, Ohio.

8 Raithby, G. D., Hollands, K. G. T., "Analysis of Heat Transfer by Natural Convection (or Film Condensation) for Three-Dimensional Flows," to be presented at 6th International Heat Transfer Conference, Toronto, Canada, 1978.

9 Sparrow, E. M., Gregg, J. L., "Similar Solutions for Free Convection from a Nonisothermal Vertical Plate," *TRANS. ASME,* Vol. 79, 1957, pp. 379–386.

Effect of Flow Direction on Calibration of Hot-Film Anemometers at Low Velocities

H. Shaukatullah[1] and B. Gebhart[2]

Nomenclature

d = diameter of sensor
E = anemometer output voltage
E_0 = anemometer output voltage at zero velocity
Gr = Grashof number = $g\,\beta(T_s - T_\infty)d^3/\nu^2$
g = gravitational acceleration
Re = Reynolds number = Ud/ν
T_s = sensor temperature
T_∞ = ambient temperature
U = velocity of flow
β = coefficient of thermal expansion of water
ν = kinematic viscosity of water

Introduction

It has been found that when a hot-wire/film anemometer is calibrated at low velocities with flow in the horizontal direction, the heat transfer from the probe may be less than when the imposed velocity is zero. This peculiar effect of flow direction on calibration of anemometer probes seems to have been first observed by Ower and Johansen in 1931 and later confirmed by Cooper and Linton [1].[3] Subsequent investigators [2–11] also found this effect on heat transfer from cylinders and anemometer probes when the imposed flow was at angles of 90 deg or more, where the angle of flow is measured from vertical and is zero when the flow is vertically up. Davis [12], however, calibrated a hot-wire probe in air at flow inclinations of 0 deg, 90 deg, and 180 deg, and found no difference between these calibrations.

The effect of inclination between 0 and 90 deg on calibration has not been investigated. Calibration results are presented here for imposed flow angles of 0 deg, 15 deg, 30 deg, 45 deg, 60 deg, 75 deg and 90 deg.

Apparatus

A constant temperature anemometer (Disa type 55D01) with a quartz coated cylindrical hot-film probe (Disa type 55F20) was used. The sensor has approximately 2 μm thick coating of quartz [13]. The diameter and active length of the sensor, measured with a travelling microscope, were 0.0711 and 1.13 mm, respectively. A sketch of the probe is shown in Fig. 1. The probe was calibrated, with the sensor horizontal, in water at a temperature of 19.5°C. The probe temperature was 46.9°C and corresponded to a resistance ratio of about 1.1. Details of calibration apparatus and procedure are given in [14] and [15]. Essentially, the probe was moved in a water tank at a constant velocity. The bridge output voltage corresponding to the velocity was measured, and velocity was determined by measuring the time for the probe to travel a known distance.

Calibration Results

The calibration curves for flow at 0 deg and 90 deg are shown in Fig. 2. Results are presented in terms of $[(E/E_0)^2 - 1]$, versus the imposed velocity U. Here E_0 is the anemometer output voltage at zero velocity, and E is the output voltage at velocity U. For vertically upward flow, 0 deg, the curve is a single valued function of U and increases monotonically. However, at 90 deg a minimum occurs at a nonzero value of U. Between 0 and 0.22 cm/s two values of U result in the same output voltage, and there would be an ambiguity in converting bridge output voltage to velocity. The two calibration curves eventually merge at about 1.6 cm/s.

The curves for all seven angles are shown on an enlarged scale in Fig. 3. There is no appreciable difference between the calibration points for the angles of 0 deg, 15 deg and 30 deg. Also the results at 75 deg and 90 deg have the same form; i.e., each curve goes through a minimum before again reaching the no-flow values.

Thus, at low velocities, the present study shows that a large error arises if the actual direction of flow is not accounted for. Consider, as a specific measurement, $[(E/E_0)^2 - 1]$ equal to 0.05 in Fig. 3. The calibration curve for flow at 0 deg gives a velocity of 0.15 cm/s, whereas that for flow at 90 deg gives 0.32 cm/s, an uncertainty of a factor of about 2. This uncertainty decreases with increasing velocity, and in the present study becomes negligible at 1.6 cm/s. In addition, for imposed flow near horizontal, the results show that it is not possible to determine velocities from measured output below a certain level even if the direction of flow is known. This limit for the present case

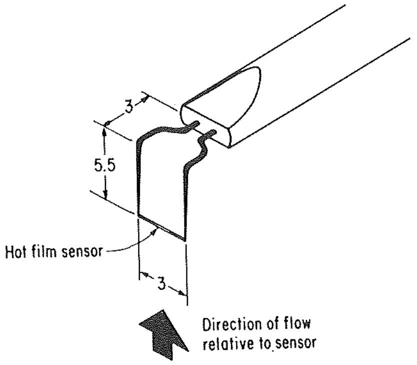

Fig. 1 Schematic of Disa 55F20 hot-film probe. All dimensions are in millimeters

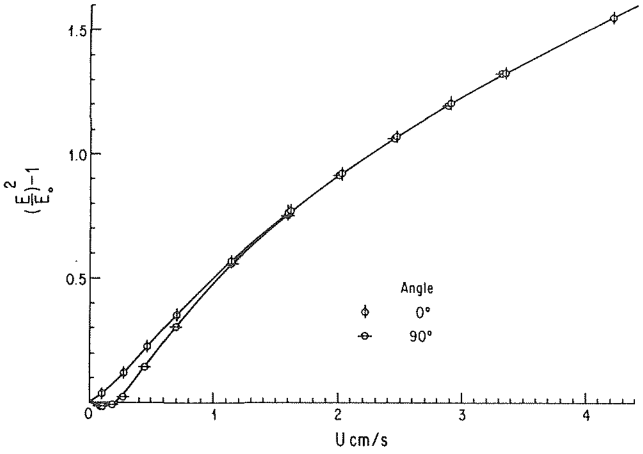

Fig. 2 Calibration curves for hot-film probe. Operating resistance 5.63 ohm, water temperature 19.5°C. $E_0 = 6.506 \pm 0.004$ volts

---

[1] Visiting Assistant Professor, Mechanical Engineering Department, State University of N. Y. at Buffalo, Amherst, N. Y.

[2] Professor and Chairman, Mechanical Engineering Department, State University of N. Y. at Buffalo, Amherst, N. Y.

[3] Numbers in brackets designate References at end of technical note.

Contributed by the Heat Transfer Division for publication in the JOURNAL OF HEAT TRANSFER. Manuscript received by the Heat Transfer Division November 22, 1977.

as Special Cases," ASME JOURNAL OF HEAT TRANSFER, Vol. 98, 1976, pp. 72–80.

6 Yang, Y. T., Novotny, J. L., Cheng, Y. S., "Laminar Free Convection from a Nonisothermal Plate Immersed in a Temperature Stratified Medium," *International Journal of Heat and Mass Transfer,* Vol. 15, 1972, pp. 1097–1109.

7 Selby, S., Editor, *Handbook of Tables for Mathematics,* CRC Press Inc., Cleveland, Ohio.

8 Raithby, G. D., Hollands, K. G. T., "Analysis of Heat Transfer by Natural Convection (or Film Condensation) for Three-Dimensional Flows," to be presented at 6th International Heat Transfer Conference, Toronto, Canada, 1978.

9 Sparrow, E. M., Gregg, J. L., "Similar Solutions for Free Convection from a Nonisothermal Vertical Plate," *TRANS. ASME,* Vol. 79, 1957, pp. 379–386.

Effect of Flow Direction on Calibration of Hot-Film Anemometers at Low Velocities

H. Shaukatullah[1] **and B. Gebhart**[2]

Nomenclature

d = diameter of sensor
E = anemometer output voltage
E_0 = anemometer output voltage at zero velocity
Gr = Grashof number = $g\,\beta(T_s - T_\infty)d^3/\nu^2$
g = gravitational acceleration
Re = Reynolds number = Ud/ν
T_s = sensor temperature
T_∞ = ambient temperature
U = velocity of flow
β = coefficient of thermal expansion of water
ν = kinematic viscosity of water

Introduction

It has been found that when a hot-wire/film anemometer is calibrated at low velocities with flow in the horizontal direction, the heat transfer from the probe may be less than when the imposed velocity is zero. This peculiar effect of flow direction on calibration of anemometer probes seems to have been first observed by Ower and Johansen in 1931 and later confirmed by Cooper and Linton [1].[3] Subsequent investigators [2–11] also found this effect on heat transfer from cylinders and anemometer probes when the imposed flow was at angles of 90 deg or more, where the angle of flow is measured from vertical and is zero when the flow is vertically up. Davis [12], however, calibrated a hot-wire probe in air at flow inclinations of 0 deg, 90 deg, and 180 deg, and found no difference between these calibrations.

The effect of inclination between 0 and 90 deg on calibration has not been investigated. Calibration results are presented here for imposed flow angles of 0 deg, 15 deg, 30 deg, 45 deg, 60 deg, 75 deg and 90 deg.

Apparatus

A constant temperature anemometer (Disa type 55D01) with a quartz coated cylindrical hot-film probe (Disa type 55F20) was used. The sensor has approximately 2 μm thick coating of quartz [13]. The diameter and active length of the sensor, measured with a travelling microscope, were 0.0711 and 1.13 mm, respectively. A sketch of the probe is shown in Fig. 1. The probe was calibrated, with the sensor horizontal, in water at a temperature of 19.5°C. The probe temperature was 46.9°C and corresponded to a resistance ratio of about 1.1. Details of calibration apparatus and procedure are given in [14] and [15]. Essentially, the probe was moved in a water tank at a constant velocity. The bridge output voltage corresponding to the velocity was measured, and velocity was determined by measuring the time for the probe to travel a known distance.

Calibration Results

The calibration curves for flow at 0 deg and 90 deg are shown in Fig. 2. Results are presented in terms of $[(E/E_0)^2 - 1]$, versus the imposed velocity U. Here E_0 is the anemometer output voltage at zero velocity, and E is the output voltage at velocity U. For vertically upward flow, 0 deg, the curve is a single valued function of U and increases monotonically. However, at 90 deg a minimum occurs at a nonzero value of U. Between 0 and 0.22 cm/s two values of U result in the same output voltage, and there would be an ambiguity in converting bridge output voltage to velocity. The two calibration curves eventually merge at about 1.6 cm/s.

The curves for all seven angles are shown on an enlarged scale in Fig. 3. There is no appreciable difference between the calibration points for the angles of 0 deg, 15 deg and 30 deg. Also the results at 75 deg and 90 deg have the same form; i.e., each curve goes through a minimum before again reaching the no-flow values.

Thus, at low velocities, the present study shows that a large error arises if the actual direction of flow is not accounted for. Consider, as a specific measurement, $[(E/E_0)^2 - 1]$ equal to 0.05 in Fig. 3. The calibration curve for flow at 0 deg gives a velocity of 0.15 cm/s, whereas that for flow at 90 deg gives 0.32 cm/s, an uncertainty of a factor of about 2. This uncertainty decreases with increasing velocity, and in the present study becomes negligible at 1.6 cm/s. In addition, for imposed flow near horizontal, the results show that it is not possible to determine velocities from measured output below a certain level even if the direction of flow is known. This limit for the present case

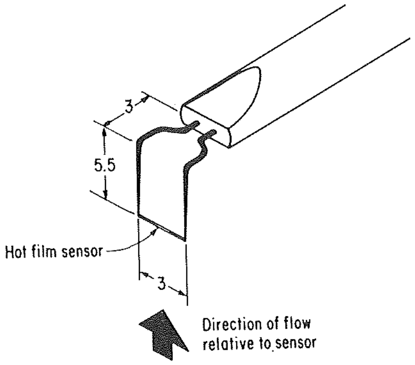

Fig. 1 Schematic of Disa 55F20 hot-film probe. All dimensions are in millimeters

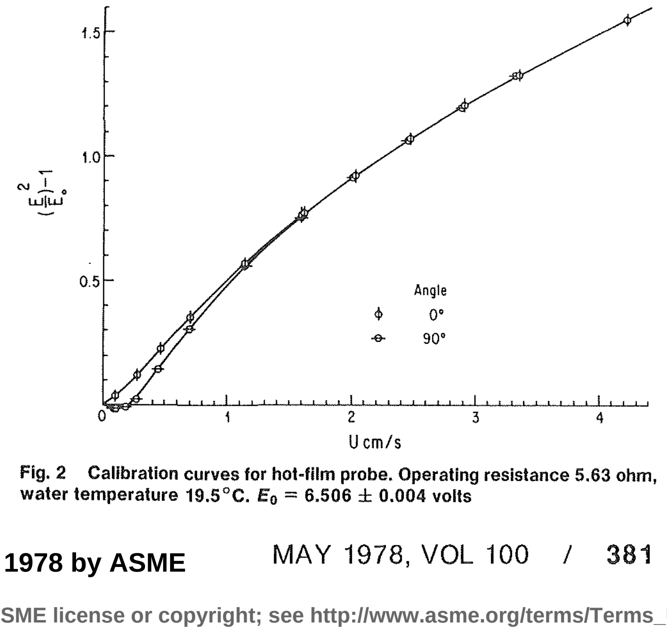

Fig. 2 Calibration curves for hot-film probe. Operating resistance 5.63 ohm, water temperature 19.5°C. E_0 = 6.506 ± 0.004 volts

---

[1] Visiting Assistant Professor, Mechanical Engineering Department, State University of N. Y. at Buffalo, Amherst, N. Y.

[2] Professor and Chairman, Mechanical Engineering Department, State University of N. Y. at Buffalo, Amherst, N. Y.

[3] Numbers in brackets designate References at end of technical note.

Contributed by the Heat Transfer Division for publication in the JOURNAL OF HEAT TRANSFER. Manuscript received by the Heat Transfer Division November 22, 1977.

is 0.22 cm/s for flow at 90 deg and 0.17 cm/s at 75 deg.

The conditions under which an imposed velocity may cause the output of the anemometer to again become equal to the output at zero velocity are of particular importance. Collis and Williams [5] showed that, for flow at 90 deg, such limiting conditions are correlated by $Re = C\ Gr^{1/3}$, where the value of C is taken as 1 and the Reynolds and Grashof numbers are evaluated at ambient conditions. This relation is shown in Fig. 4, along with data of Collis and Williams, a point from the present study, a point from Fand and Keswani [10] and a point from Coulbert [3]. For the data point from this study the properties are evaluated at ambient temperature of 19.5°C. The total body of data, which spans almost thirteen decades of Grashof number and six decades of Reynolds number, agrees reasonably well with the correlation. It is not possible to infer additional comparison points from yet other material in the literature, since complete information is not provided to calculate the pertinent nondimensional numbers.

Conclusions

A hot-film probe was calibrated at a resistance ratio of 1.1 in water, at seven imposed flow angles from vertically up to horizontal. It was found that there was no appreciable difference between calibrations at flow angles between 0 deg (vertically up) and 30 deg. For angles greater than 30 deg the effect was appreciable, and for flows in the neighborhood of horizontal there was a lower limit of velocity below which the output from a single sensor did not unambiguously determine velocity, even if the direction was otherwise known.

Acknowledgments

We would like to acknowledge the help of Mrs. B. Boskat in the preparation of the manuscript. Financial support was provided under NSF grants GK-18529, ENG-75 05466 and ENG-75 22623.

References

1 Ower, E., and Pankhurst, R. C., *The Measurements of Air Flow,* 4th Edition, Pergamon Press, Oxford, 1966, pp. 314–317.

2 Hukill, W. V., "Characteristics of Thermocouple Anemometers," Temperature—Its Measurement and Control in Science and Industry, Reinhold Publishing Corp., New York, 1941, pp. 666–672.

3 Coulbert, C. D., "Mach-Zehnder Interferometer Applications," *Mechanical Engineering,* Vol. 74, No. 12, 1952, pp. 1005–1010.

4 Hromas, L. A., and Kentzer, C. P., "Calibration of a Hot Wire Anemometer for Low Velocities in Steady Flow with Temperature Gradients," *Proc. of the IV Midwestern Conference on Fluid Mechanics,* Purdue University, Lafayette, Indiana, 1955, pp. 23–44.

5 Collis, D. C., and Williams, M. J., "Two-dimensional Convection from Heated Wires at Low Reynolds Number," *Journal of Fluid Mechanics,* Vol. 6, Part 3, 1959, pp. 357–384.

6 Sharma, G. K., and Sukhatme, S. P., "Combined Free and Forced Convection Heat Transfer from a Heated Tube to a Transverse Air Stream," ASME JOURNAL OF HEAT TRANSFER, Vol. 91, No. 3, 1969, pp. 457–459.

7 Oosthuizen, P. H. and Madan, S., "The Effect of Flow Direction on Combined Convective Heat Transfer from Cylinders to Air," ASME JOURNAL OF HEAT TRANSFER, Vol. 93, No. 2, 1971, pp. 240–242.

8 Hatton, A. P., James, D. D., and Swire, H. W., "Combined Forced and Natural Convection with Low-Speed Air Flow over Horizontal Cylinders," *Journal of Fluid Mech.,* Vol. 42, Part 1, 1970, pp. 17–31.

9 Warpinski, N. R., Nagib, H. M. and Lavan, Z., "Experimental Investigation of Recirculating Cells in Laminar Coaxial Jets," AIAA Journal, Vol. 10, No. 9, 1972, pp. 1204–1210.

10 Fand, R. M., and Keswani, K. K., "Combined Natural and Forced Convection Heat Transfer from Horizontal Cylinders to Water," *Int. Journal of Heat and Mass Transfer,* Vol. 18, No. 6, 1973, pp. 1175–1191.

11 Anonymous, "Measurements in Low Velocities with Hot-Wire Anemometers," Technical Bulletin TB14, Thermo-Systems Inc., St. Paul, Minnesota, 1973.

12 Davis, M. R. "Heat Transfer from Hot Wire and Film Anemometer Probe," Heat and Mass Transfer in Boundary Layers, Afgan, N., Zaric, Z., and Anastasijevic, P., eds., Vol. II, Pergamon Press, Oxford, 1972, pp. 577–583.

13 Anonymous, "Newcomers to the Disa Standard Probe Line," *Disa Information* No. 11, 1971, pp. 46–47.

14 Shaukatullah, H., "An Experimental Investigation of Natural Convection Boundary Layers over a Uniform Flux inclined Surface," Ph.D. Thesis, Cornell University, Ithaca, New York 1977.

15 Shaukatullah, H., and Gebhart, B., "Hot Film Anemometer Calibration and Use in Fluids at Varying Background Temperature," *Letters in Heat and Mass Transfer,* Vol. 4, No. 5, 1977, pp. 309–317.

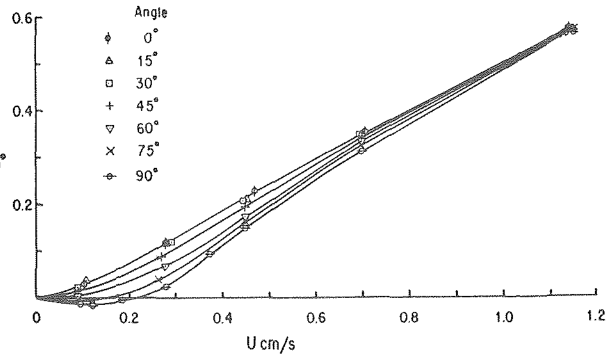

Fig. 3 Calibration curves for hot-film probe. Conditions same as in Fig. 1

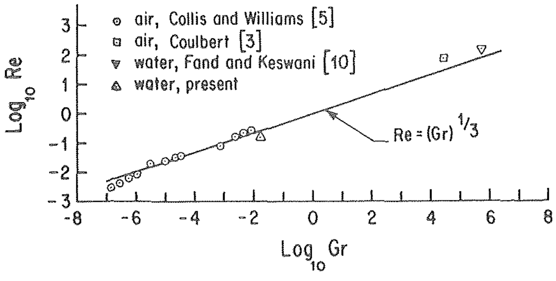

Fig. 4 Limiting values of Reynolds number below which the calibration is ambiguous for flow at 90 deg. All properties evaluated at ambient temperature

---

Measurements of Transition Boiling Data for Water Under Forced Convective Conditions

S. C. Cheng,[1] W. W. L. Ng,[1] K. T. Heng,[1] and D. C. Groeneveld[2]

Introduction

Accurate analysis of the thermal behavior of a hot surface during rewetting (e.g. a nuclear fuel bundle during emergency core cooling) requires a reliable transition boiling correlation. However, due to the scarcity of relevant data, existing transition boiling correlations have a very limited range of applicability and must be suspected because of their unreliable data base.

In this investigation, forced convective transition boiling data were obtained both during steady state and transient conditions. The test section used was designed to have a high thermal capacity; this extended the transition boiling time during transient tests, thus permitting frequent and accurate determination of transition boiling temperatures and heat flux values. The measuring technique used

---

[1] Department of Mechanical Engineering, University of Ottawa, Ottawa, Canada.

[2] Atomic Energy of Canada Ltd., Chalk River, Ontario, Canada.

Contributed by the Heat Transfer Division for publication in the JOURNAL OF HEAT TRANSFER. Manuscript received by the Heat Transfer Division October 7, 1977.

is 0.22 cm/s for flow at 90 deg and 0.17 cm/s at 75 deg.

The conditions under which an imposed velocity may cause the output of the anemometer to again become equal to the output at zero velocity are of particular importance. Collis and Williams [5] showed that, for flow at 90 deg, such limiting conditions are correlated by Re $= C\ \mathrm{Gr}^{1/3}$, where the value of C is taken as 1 and the Reynolds and Grashof numbers are evaluated at ambient conditions. This relation is shown in Fig. 4, along with data of Collis and Williams, a point from the present study, a point from Fand and Keswani [10] and a point from Coulbert [3]. For the data point from this study the properties are evaluated at ambient temperature of 19.5°C. The total body of data, which spans almost thirteen decades of Grashof number and six decades of Reynolds number, agrees reasonably well with the correlation. It is not possible to infer additional comparison points from yet other material in the literature, since complete information is not provided to calculate the pertinent nondimensional numbers.

Conclusions

A hot-film probe was calibrated at a resistance ratio of 1.1 in water, at seven imposed flow angles from vertically up to horizontal. It was found that there was no appreciable difference between calibrations at flow angles between 0 deg (vertically up) and 30 deg. For angles greater than 30 deg the effect was appreciable, and for flows in the neighborhood of horizontal there was a lower limit of velocity below which the output from a single sensor did not unambiguously determine velocity, even if the direction was otherwise known.

Acknowledgments

We would like to acknowledge the help of Mrs. B. Boskat in the preparation of the manuscript. Financial support was provided under NSF grants GK-18529, ENG-75 05466 and ENG-75 22623.

References

1 Ower, E., and Pankhurst, R. C., *The Measurements of Air Flow,* 4th Edition, Pergamon Press, Oxford, 1966, pp. 314–317.

2 Hukill, W. V., "Characteristics of Thermocouple Anemometers," Temperature—Its Measurement and Control in Science and Industry, Reinhold Publishing Corp., New York, 1941, pp. 666–672.

3 Coulbert, C. D., "Mach-Zehnder Interferometer Applications," *Mechanical Engineering,* Vol. 74, No. 12, 1952, pp. 1005–1010.

4 Hromas, L. A., and Kentzer, C. P., "Calibration of a Hot Wire Anemometer for Low Velocities in Steady Flow with Temperature Gradients," *Proc. of the IV Midwestern Conference on Fluid Mechanics,* Purdue University, Lafayette, Indiana, 1955, pp. 23–44.

5 Collis, D. C., and Williams, M. J., "Two-dimensional Convection from Heated Wires at Low Reynolds Number," *Journal of Fluid Mechanics,* Vol. 6, Part 3, 1959, pp. 357–384.

6 Sharma, G. K., and Sukhatme, S. P., "Combined Free and Forced Convection Heat Transfer from a Heated Tube to a Transverse Air Stream," ASME JOURNAL OF HEAT TRANSFER, Vol. 91, No. 3, 1969, pp. 457–459.

7 Oosthuizen, P. H. and Madan, S., "The Effect of Flow Direction on Combined Convective Heat Transfer from Cylinders to Air," ASME JOURNAL OF HEAT TRANSFER, Vol. 93, No. 2, 1971, pp. 240–242.

8 Hatton, A. P., James, D. D., and Swire, H. W., "Combined Forced and Natural Convection with Low-Speed Air Flow over Horizontal Cylinders," *Journal of Fluid Mech.,* Vol. 42, Part 1, 1970, pp. 17–31.

9 Warpinski, N. R., Nagib, H. M. and Lavan, Z., "Experimental Investigation of Recirculating Cells in Laminar Coaxial Jets," AIAA Journal, Vol. 10, No. 9, 1972, pp. 1204–1210.

10 Fand, R. M., and Keswani, K. K., "Combined Natural and Forced Convection Heat Transfer from Horizontal Cylinders to Water," *Int. Journal of Heat and Mass Transfer,* Vol. 18, No. 6, 1973, pp. 1175–1191.

11 Anonymous, "Measurements in Low Velocities with Hot-Wire Anemometers," Technical Bulletin TB14, Thermo-Systems Inc., St. Paul, Minnesota, 1973.

12 Davis, M. R. "Heat Transfer from Hot Wire and Film Anemometer Probe," Heat and Mass Transfer in Boundary Layers, Afgan, N., Zaric, Z., and Anastasijevic, P., eds., Vol. II, Pergamon Press, Oxford, 1972, pp. 577–583.

13 Anonymous, "Newcomers to the Disa Standard Probe Line," *Disa Information* No. 11, 1971, pp. 46–47.

14 Shaukatullah, H., "An Experimental Investigation of Natural Convection Boundary Layers over a Uniform Flux inclined Surface," Ph.D. Thesis, Cornell University, Ithaca, New York 1977.

15 Shaukatullah, H., and Gebhart, B., "Hot Film Anemometer Calibration and Use in Fluids at Varying Background Temperature," *Letters in Heat and Mass Transfer,* Vol. 4, No. 5, 1977, pp. 309–317.

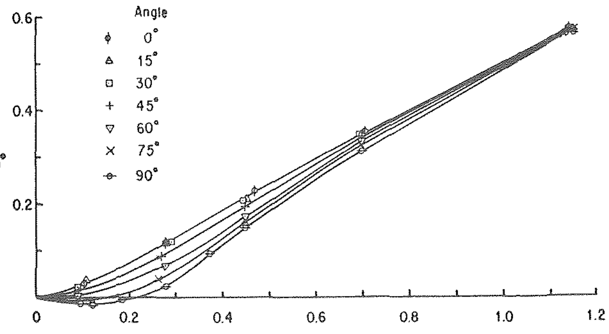

Fig. 3 Calibration curves for hot-film probe. Conditions same as in Fig. 1

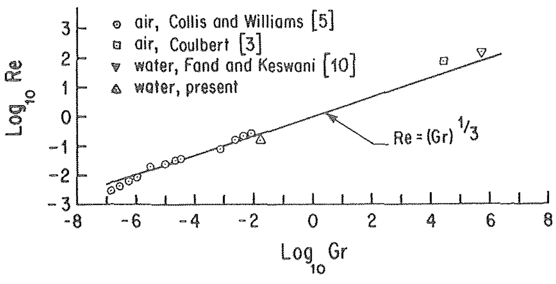

Fig. 4 Limiting values of Reynolds number below which the calibration is ambiguous for flow at 90 deg. All properties evaluated at ambient temperature

---

Measurements of Transition Boiling Data for Water Under Forced Convective Conditions

S. C. Cheng,[1] W. W. L. Ng,[1] K. T. Heng,[1] and D. C. Groeneveld[2]

Introduction

Accurate analysis of the thermal behavior of a hot surface during rewetting (e.g. a nuclear fuel bundle during emergency core cooling) requires a reliable transition boiling correlation. However, due to the scarcity of relevant data, existing transition boiling correlations have a very limited range of applicability and must be suspected because of their unreliable data base.

In this investigation, forced convective transition boiling data were obtained both during steady state and transient conditions. The test section used was designed to have a high thermal capacity; this extended the transition boiling time during transient tests, thus permitting frequent and accurate determination of transition boiling temperatures and heat flux values. The measuring technique used

---

[1] Department of Mechanical Engineering, University of Ottawa, Ottawa, Canada.

[2] Atomic Energy of Canada Ltd., Chalk River, Ontario, Canada.

Contributed by the Heat Transfer Division for publication in the JOURNAL OF HEAT TRANSFER. Manuscript received by the Heat Transfer Division October 7, 1977.

in this investigation permits the construction of complete boiling curves under forced convective conditions over a wide range of mass flows and subcoolings.

Experimental Apparatus

Distilled water was heated to the required inlet temperature in a hot water tank and subsequently circulated through a pump and a flow meter to the test section. Provisions for bypassing the pump and the test section were incorporated to stabilize the flow. Thermocouples were installed to measure temperatures of the flow at the inlet and exit of the test section.

The test section shown in Fig. 1, consists of a 5.72 cm long copper cylinder with a 9.53 cm outside diameter and a 1.27 cm diameter central flow channel. The location of the seven test section thermocouples and the twelve cartridge heaters (250 W each) is also shown in Fig. 1. Thermocouples A3, B3 and C3 were used for data thermocouples. The test section heat loss was minimized by using an asbestos gasket at the inlet and outlet of the test section and by lagging the test section with a 5 cm thick ceramic fiber insulation. A temperature controller was used to control the test section temperature during the steady-state operation. Further details of the experimental apparatus and procedures may be found in [1, 2].[3]

Experimental Results

From typical temperature-time traces based on the three data thermocouples for a mass flux of 136 kg/m^{2}s, a subcooling of 13.9°C and atmospheric pressure, it appears that axial conduction is insignificant. Boiling curves based on these thermocouple traces were constructed using the technique developed in [3, 4] and are presented in Fig. 2. Basically, the technique allows one to calculate heat flux from the test section to the fluid between time t to $t + \Delta t$ by computing the change in stored heat in the test section, minus heat losses through outside wall during the time interval Δt. In the data reduction it was assumed that the heater presence did not affect the temperature transients. This is justified since (a) the volumetric heat capacity (ρc_p) of the heaters is similar to that of copper, (b) the heaters only occupy 10 percent of the test section volume and (c) the heaters are distributed evenly around the periphery of the test section and do not introduce a nonuniform circumferential temperature distribution at the inside heated surface. During the steady-state runs, the heat flux to the fluid was obtained directly from the power input to the heaters after correction for heat losses. Fig. 3 illustrates the effect of inlet

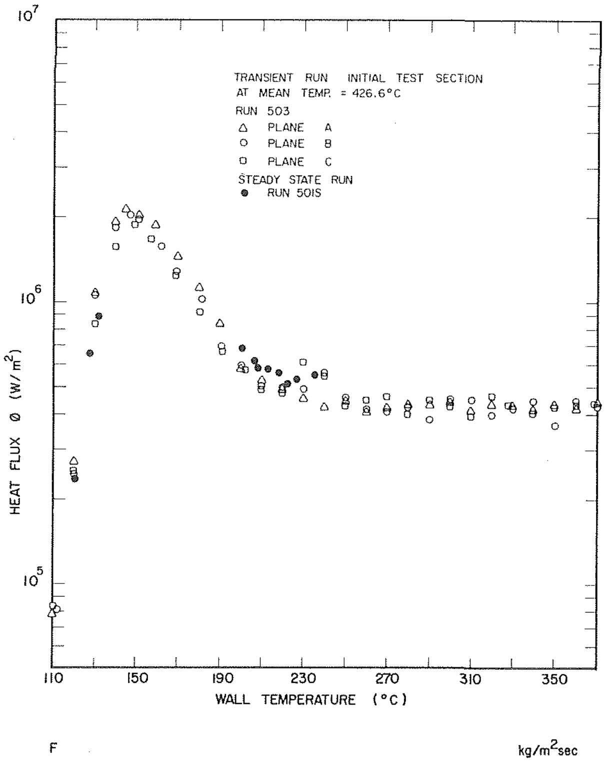

Fig. 2 Boiling curves of distilled water for G = 136 kg/m^{2}s and ΔT_{sub} = 13.9°C

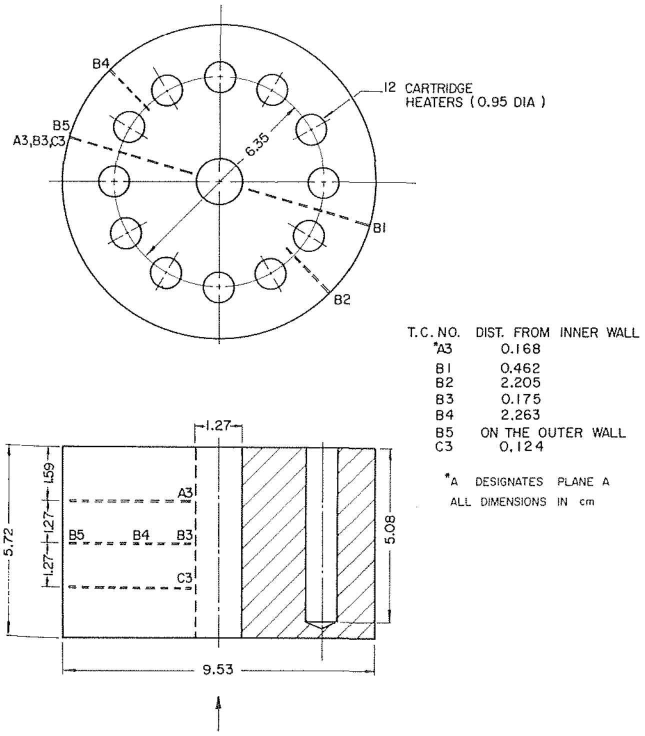

Fig. 1 Test section

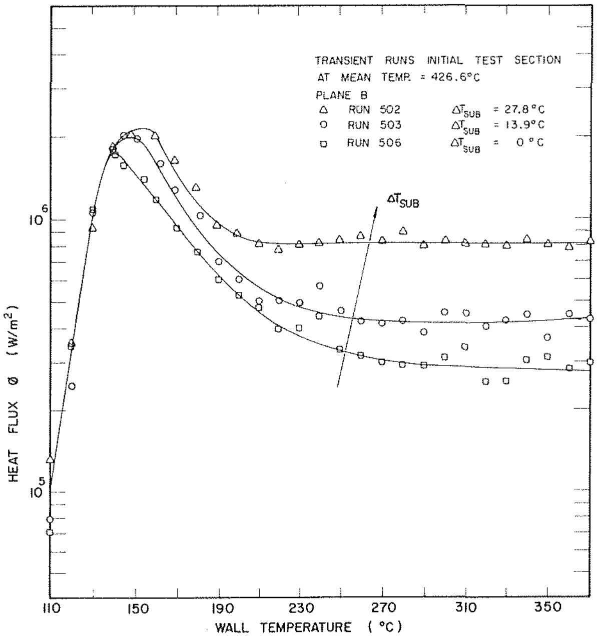

Fig. 3 Effect of subcooling on boiling curves of distilled water for G = 136 kg/m^{2}s

---

[3] Numbers in brackets designate References at end of technical note.

subcooling on the boiling curves for a mass flux of 136 kg/m^{2}s, while the effect of mass flux for a subcooling of 0°C is shown in Fig. 4.

Discussion

Newbold's [5] and Fung's [6] experimental data suggest that the film boiling portion of the boiling curve is almost independent of wall superheat. Figs. 2–4 show that our experimental results display a similar trend. Some fluctuation in surface temperature and heat flux was observed at lower subcooling runs, e.g., Run 506 in Fig. 3. This is thought to be due to the presence of slug flow. A subsequent study by Ragheb [7] using a transparent section near the test section showed that slug formation occurred during transition boiling. The associated variation in the heat transfer coefficient could have resulted in the observed fluctuation in surface temperature.

During some of the runs, steady-state data were obtained in addition to the transient results. Fig. 2 shows that the difference between the steady-state and transient results is negligible. This was expected as the high thermal capacity of test section slowed down the quenching process to make the system act in a pseudo-steady-state manner.

Fig. 5 presents an example of our data and Fung's transition boiling results obtained in a similar test section. It was found that, for the mass flux range and subcooling range studied, Berenson's type transition boiling correlation [8] having the form

$$\frac{\phi}{\mathrm{CHF}} = \left(\frac{\Delta T_{\mathrm{sat}}}{T_{\mathrm{CHF}} - T_{\mathrm{sat}}}\right)^{-1.25}$$

agreed with our data. Other correlations, such as Hsu's transition and film boiling correlation [9] and Ellion's transition boiling correlation [10] are also shown for comparison. Both Hsu's and Ellion's correlations only predict a general trend of the boiling curve and do not show an effect of subcooling.

Conclusions

1 The boiling curves obtained via both transient and steady-state methods, in general, are in good agreement. Transition boiling heat flux increases with increasing subcooling and mass flux within the range of the flow parameters investigated (mass flux range 68–203 kg/m^{2}s and subcooling range 0–28°C). Present transition boiling correlations do not display such an effect and should, therefore, be suspected.

2 The experimental data show no effect of subcooling and mass flux on the nucleate boiling curves (Figs. 2–4). This is in agreement with the data and correlations of Thom [11] and Jens and Lottes [12].

3 Caution should be exercised when extrapolating the boiling curves to heated surfaces other than copper. The high thermal diffusivity of copper may affect the shape of the boiling curve in the transition and nucleate boiling regimes. A further study on the effect of heated surface properties is in progress.

Acknowledgments

The authors wish to express their gratitude to the U.S. Nuclear Regulatory Commission for providing the financial support for this project.

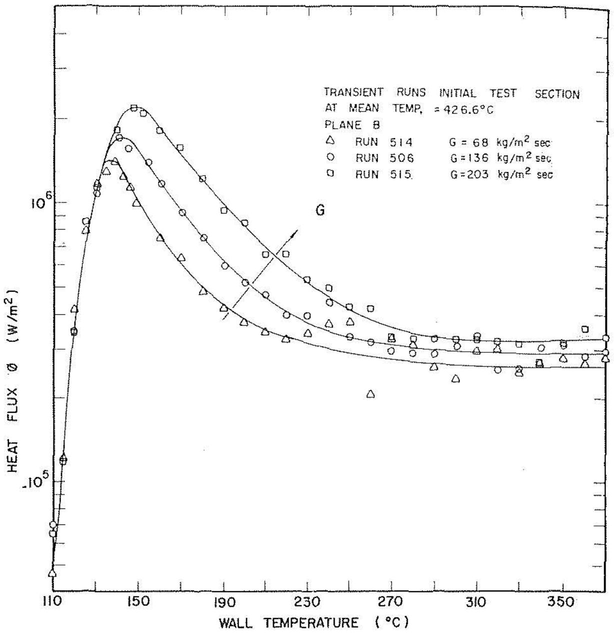

F DISTILLED

Fig. 4 Effect of mass flux on boiling curves of distilled water for $\Delta T_{\mathrm{sub}} =$ 0°C

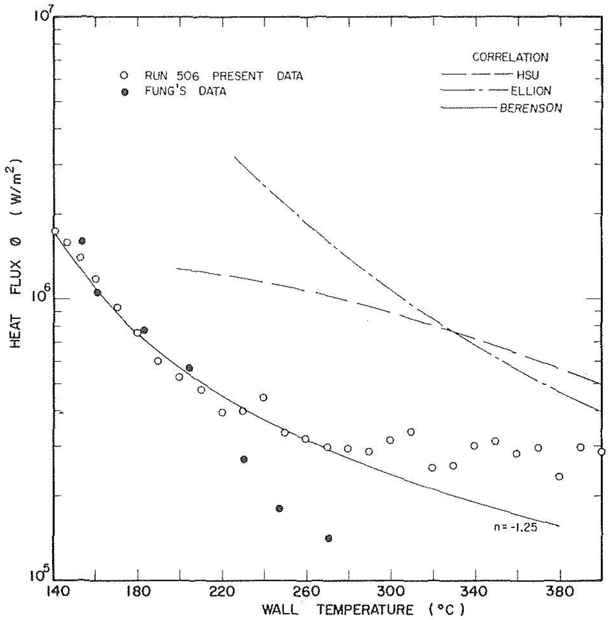

Fig. 5 Comparison of data in the transition and film boiling regimes for $G =$ 136 kg/m^{2}s and $\Delta T_{\mathrm{sub}} = 0$°C

References

1 Cheng, S. C., and Ng, W., "Transition Boiling Heat Transfer in Forced Vertical Flow Via a High Thermal Capacity Heating Process," *Letters in Heat and Mass Transfer Journal,* Vol. 3, 1976 pp. 333–342.

2 Cheng, S. C., Ng, W. W. L., Heng, K. T., and Ragheb, H., "Transition Boiling Heat Transfer in Forced Vertical Flow," Final Report, for the period June 1976–June 1977, Argonne Contract No. 31-109-38-3564, June 1977.

3 Cheng, S. C., and Heng, K. T., "A Technique to Construct a Boiling Curve from Quenching Data," *Letters in Heat and Mass Transfer Journal,* Vol. 3, 1976, pp. 413–420.

4 Cheng, S. C., Heng, K. T., and Ng, W., "A Technique to Construct a Boiling Curve from Quenching Data Considering Heat Loss," *Int. Journal of Multiphase Flow,* Vol. 3, 1977, pp. 495–499.

5 Newbold, F. J., Ralph, J. C., and Ward, J. A., "Post-Dryout Heat Transfer Under Low Flow and Low Quality Conditions," AERE-R8390, 1976.

6 Fung, K. K., "Forced Convective Transition Boiling," M.A.Sc. Thesis, Dept. of Mechanical Engineering, University of Toronto, 1976.

7 Ragheb, H., "Development of Probe to Detect Phase Change at a Heated Surface," M.A.Sc. Thesis, Dept. of Mechanical Engineering, University of Ottawa, December 1977.

8 Berenson, P. J., "Transition Boiling Heat Transfer from a Horizontal Surface," MIT Technical Report No. 17, 1960.

9 Hsu, Y. Y., "Tentative Correlation of Reflood Heat Transfer," presented at the Third Water Reactor Safety Information Meeting, Germantown, Maryland, 1975.

10 Ellion, M. E., "A Study of the Mechanism of Boiling Heat Transfer," California Inst. of Technology Report, JPL-MEMO-20-88, 1954.

11 Thom, J. R. S., Walker, W. M., Fallon, T. A., and Reising, G. F. S., "Boiling in Subcooled Water During Flow up Heated Tubes or Annuli," Paper 6 presented at the Symposium on Boiling Heat Transfer in Steam Generating Units and Heat Exchangers, Manchester, September, 1965.

12 Jens, W. H., and Lottes, P. A., "Analysis of Heat Transfer Burnout, Pressure Drop and Density Data for High Pressure Water," ANL-4627, May 1951.